

# PERPENDICULAR BLADE VORTEX INTERACTION AND ITS IMPLICATIONS FOR HELICOPTER NOISE PREDICTION

Final technical report to NASA Langley on  
research performed under grant NAG-1-1119  
"Wave-Number Frequency Spectra in a Trailing Vortex for BWI Noise Prediction"  
for the period ending 15th August 1993

William J. Devenport\*, Stewart A. L. Glegg\*\*,  
(Principal Investigators)  
Kenneth S. Wittmer\* and Michael C. Rife\*  
(Graduate Assistants)

August 1993

GRANT  
IN-71-CR  
179672  
p. 367

(NASA-CR-193623) PERPENDICULAR  
BLADE VORTEX INTERACTION AND ITS  
IMPLICATIONS FOR HELICOPTER NOISE  
PREDICTION: WAVE-NUMBER FREQUENCY  
SPECTRA IN A TRAILING VORTEX FOR  
BWI NOISE PREDICTION Final  
Technical Report, period ending 15  
Aug. 1993 (Virginia Polytechnic  
Inst. and State Univ.) 367 p

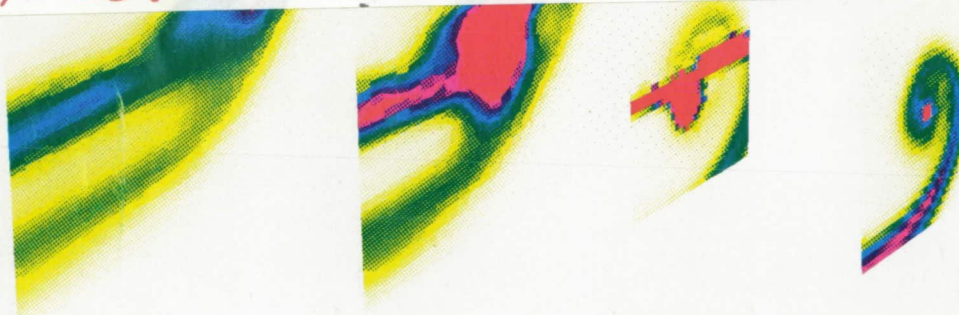
N94-10752

Unclas

G3/71 0179672

456383

~~456383~~



\*A.O.E. Department,  
Virginia Tech,  
215 Randolph Hall,  
Blacksburg VA 24061

\*\*Ocean Engineering Department,  
Florida Atlantic University,  
NW 28th St.,  
Boca Raton FL 33431

## ABSTRACT

~~ORIGINAL CONTAINS~~  
~~CLASSIFIED INFORMATION~~

Perpendicular blade vortex interactions are a common occurrence in helicopter rotor flows. Under certain conditions they produce a substantial proportion of the acoustic noise. However, the mechanism of noise generation is not well understood. Specifically, turbulence associated with the trailing vortices shed from the blade tips appears insufficient to account for the noise generated. In this report we examine the hypothesis that the first perpendicular interaction experienced by a trailing vortex alters its turbulence structure in such a way as to increase the acoustic noise generated by subsequent interactions. To investigate this hypothesis a two-part investigation has been carried out.

In the first part, experiments were performed to examine the behavior of a streamwise vortex as it passed over and downstream of a spanwise blade in incompressible flow. Blade vortex separations between  $\pm 1/8$  chord were studied for at a chord Reynolds number of 200,000. Three-component velocity and turbulence measurements were made in the flow from 4 chordlengths upstream to 15 chordlengths downstream of the blade using miniature 4-sensor hot-wire probes. These measurements show that the interaction of the vortex with the blade and its wake causes the vortex core to lose circulation and diffuse much more rapidly than it otherwise would. Core radius increases and peak tangential velocity decreases with distance downstream of the blade. True turbulence levels within the core are much larger downstream than upstream of the blade. The net result is a much larger and more intense region of turbulent flow than that presented by the original vortex and thus, by implication, a greater potential for generating acoustic noise.

In the second part, the turbulence measurements described above were used to derive the necessary inputs to a BWI noise prediction scheme. This resulted in significantly improved agreement between measurements and calculations of the BWI noise spectrum especially for the spectral peak at low frequencies, which previously was poorly predicted.



## ACKNOWLEDGEMENTS

The authors would like to thank NASA Langley, in particular Tom Brooks and Mike Marcolini, for their support under grant NAG-1-1119. The assistance of Mark Engel, Chris Schively and Lee Fugelstad in taking many of the measurements presented here is also gratefully acknowledged.

## **PART I - EXPERIMENTS**

## CONTENTS

1. INTRODUCTION	1-1
2. APPARATUS AND INSTRUMENTATION	2-1
2.1 Wind Tunnel	2-1
2.2 Wing models	2-1
2.3 Hot-wire anemometry	2-2
2.4 Helium Bubble Flow Visualizations	2-6
3. RESULTS AND DISCUSSION	3-1
3.1 Coordinate System, Flow Conditions and Table of Measurements	3-1
3.2 Summary of relevant flow-visualization results	3-2
3.3 The approach vortex	3-3
3.4 Flow over the blade	3-7
3.5 Flow downstream of the blade as a function of $\Delta$ .	3-13
<u>3.5.1 Velocity grids</u>	3-13
<u>3.5.2 Velocity profiles</u>	3-16
<u>3.5.3 Velocity autospectra</u>	3-19
3.6 Flow downstream of the blade as a function of $x$ .	3-20
<u>3.6.1 Velocity grids</u>	3-21
<u>3.6.2 Velocity profiles</u>	3-22
<u>3.6.3 Velocity autospectra</u>	3-24
4. CONCLUSIONS	4-1
5. REFERENCES	5-1
APPENDIX . BETZ'S THEORY APPLIED TO AN ARBITRARY LIFT DISTRIBUTION	A-1

## 1. INTRODUCTION

When a helicopter blade passes through or near the tip vortex shed by a previous blade, noise is generated. When the vortex is approximately parallel to the blade (figure 1.1a), noise is generated as a consequence of the unsteady lift produced by the blade as it passes through the steady swirling flow of the vortex. When the vortex is more or less perpendicular (figure 1.1b), the noise is generated by the blade passing through turbulence associated with the vortex (Brooks et al. (1987), Glegg (1989)). Most research in rotor aerodynamics and acoustics has focussed on parallel interactions. Perpendicular interactions (also known as Blade Wake Interactions or BWIs) have received relatively little attention, despite the fact that they are the most important contributor to helicopter noise during level flight and mild climb conditions (Brooks and Martin (1987)).

One of the difficulties of BWI noise prediction is that it requires knowledge of the turbulence structure and spectrum of the vortex as it passes the blade (Glegg (1989)). Devenport et al. (1992) attempted to provide this knowledge by studying the turbulence structure of trailing vortices in isolation. The assumption here was that the impact of the blade would not significantly alter the turbulence structure from the point of view of noise prediction. However, upon incorporating their results into the BWI noise prediction method of Glegg (1989) they found the turbulence structure of the isolated vortex to be insufficient to account for all the BWI noise generation. There are two possible explanations for this result; either changes in the flow structure during the interaction strongly effect the noise produced or the vortex structure is significantly altered by its encounter with the blade, changing the nature of all subsequent interactions. In either case a study of the details of the interaction and the flow it produces is required.

With the exception of the present investigation there has been surprisingly little research into the fluid mechanics of BWI. What has been done has concentrated primarily on the aerodynamic characteristics of the blade rather than on the vortex itself.



Perpendicular blade vortex interactions at transonic speeds have been studied by Kalkhoran et al. (1992) and Phillippe and Armand (1978). Kalkhoran et al. examined the influence of a trailing vortex on a rectangular NACA 0012 section blade at zero angle of attack for Mach numbers between 0.7 and 0.8 (figure 1.2). They took total pressure surveys of the vortex at the leading and trailing edge of the blade as well as pressure measurements on the blade surface under the vortex for blade-vortex separations  $\Delta$  of 0.3, 0.2 and 0.1 chordlengths (figure 1.1b). They found the vortex to significantly affect the pressure distribution on the blade especially upstream of its maximum thickness. The magnitude of this disturbance increased with reduction in  $\Delta$ . Their total pressure measurements show unsteadiness in the approaching vortex and some gross mean-flow features of the interaction, such as the relative location of the vortex and blade and vortex-generator wakes. In particular they observe a spanwise drift of the vortex as it passes over the blade under the influence of its image in the blade surface. Phillippe and Armand (1978) studied the influence of a trailing vortex on the integrated lift and drag characteristics of also used a rectangular NACA 0012 blade for  $M=0.6$  (configuration shown in figure 1.3). They varied both the blade angle of attack and vortex strength while apparently holding the nominal blade-vortex separation constant. They found the vortex reduced the blade lift coefficient by a fairly constant amount over the angle of attack range of the blade (figure 1.4a) as though a negative camber had been added to the blade. They also found the blade drag coefficient to be increased by as much as 40% in the presence of the vortex (figure 1.4b).

Incompressible perpendicular blade vortex interactions have been studied by Seath and Wilson (1986), Müller (1990) and Ham (1975). Seath and Wilson used a rectangular NACA 64A015 blade (figure 1.5) at zero angle of attack for a chord Reynolds number of 417,000. They considered a range of trailing vortex strengths  $\Gamma_0$  and of blade vortex separations  $\Delta$ . Like Kalkhoran et al. they observed significant changes in the pressure distribution on the blade in the vicinity of the vortex and the spanwise drift of the vortex over the blade surface. The spanwise drift reached a maximum for  $\Delta \approx 7\%$  chord and increased with vortex strength. They also present a flow visualizations performed on the blade surface which show three-dimensional separation and reattachment lines induced by the nearby vortex. Muller (1990) used laser Doppler

anemometry to examine the mean flow structure immediately downstream of a blade-vortex interaction for a chord Reynolds number of 100,000. He used a blade with a varying twist angle to simulate the lift distribution on a helicopter rotor (figure 1.6). He considered only one vortex strength, blade angle of attack and blade vortex separation, for which the vortex passed close to the pressure side of the blade near its tip. His mean velocity vectors downstream of blade show the trailing vortex and blade tip vortex. He postulates, based on his measurements and theoretical considerations, that the disturbance of the vortex to the blade lift distribution causes the local shedding of a 'mid-span' vortex from the blade with a strength of one quarter to one third of that of the blade tip vortex. Ham (1975) measured blade surface pressure distributions in the configuration shown in figure 1.7. He considered a range of vortex strengths and blade pitch and yaw angles. Rather than fixing the blade vortex separation distance he oscillated the vortex generator to move the vortex periodically across the blade leading edge. Ham concluded that the disturbance to the blade pressure distribution cannot exceed a certain peak value, beyond which the flow under the vortex stalls. He argues that this peak value is dependent on the two thirds power of the vortex circulation but is largely independent of blade pitch or yaw angle.

Overall very little is known about the influence of a perpendicular blade on a trailing vortex. The work described above includes only a few mean flow measurements and flow visualizations. Nothing is known about the turbulence structure or the development of the flow for any significant distance downstream of the blade. There is therefore little to base predictions of BWI noise upon.

The aim of the present investigation is remedy this situation. Specifically, to document the details of perpendicular blade vortex interactions and the flows they produce over a range of conditions and then incorporate that information into a theoretical BWI noise prediction method. The experimental investigation was performed at Virginia Tech in two parts;

- (i) helium-bubble flow visualizations to examine the nature of the interactions and the gross features of the resulting flows, and

- (ii) detailed three-component hot-wire velocity and turbulence measurements.

The theoretical work was performed at Florida Atlantic University.

## Perpendicular BVI Part I

This report describes the results of the velocity and turbulence measurements and of the theoretical investigation. Flow visualizations results, already presented by Rife et al. (1993), are only summarized here.

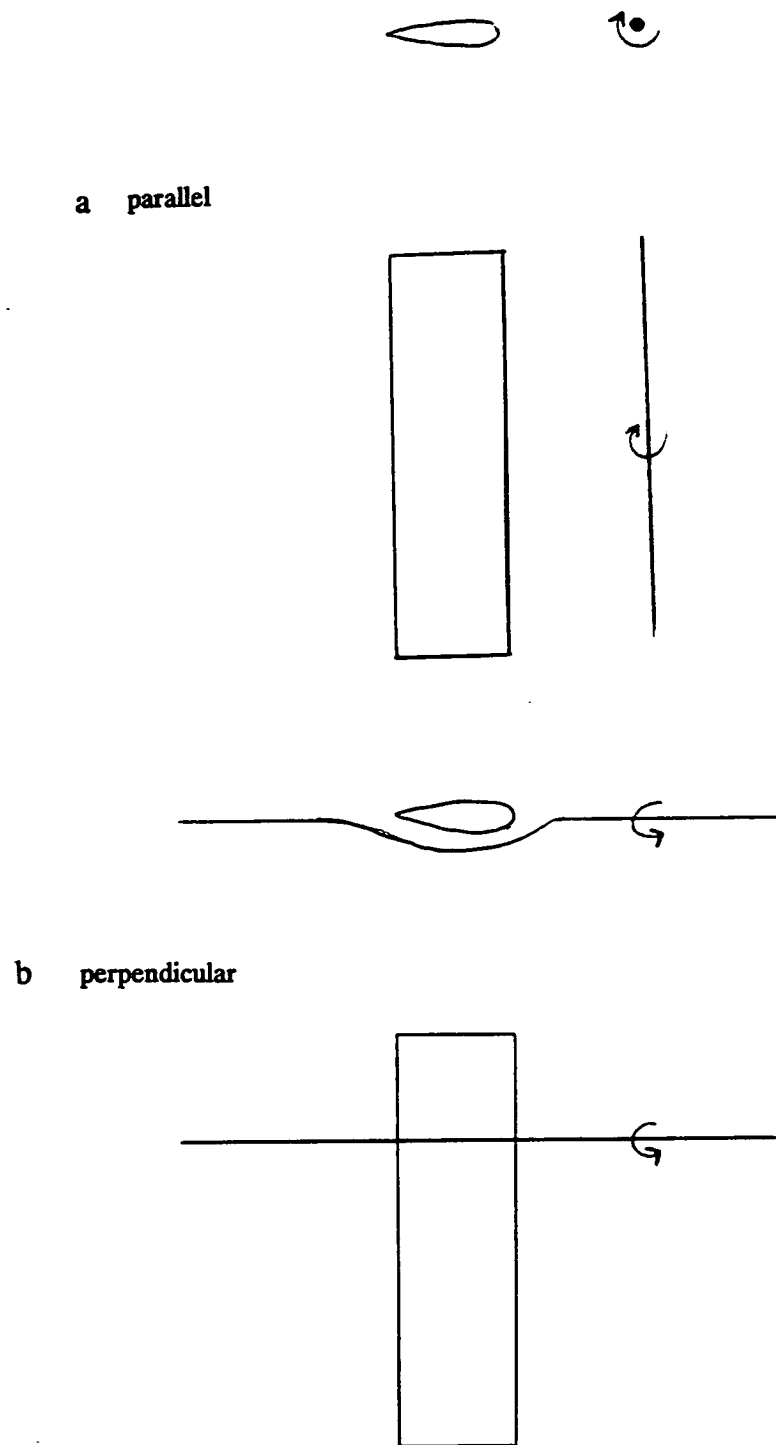


Figure 1.1 Two types of blade vortex interactions.



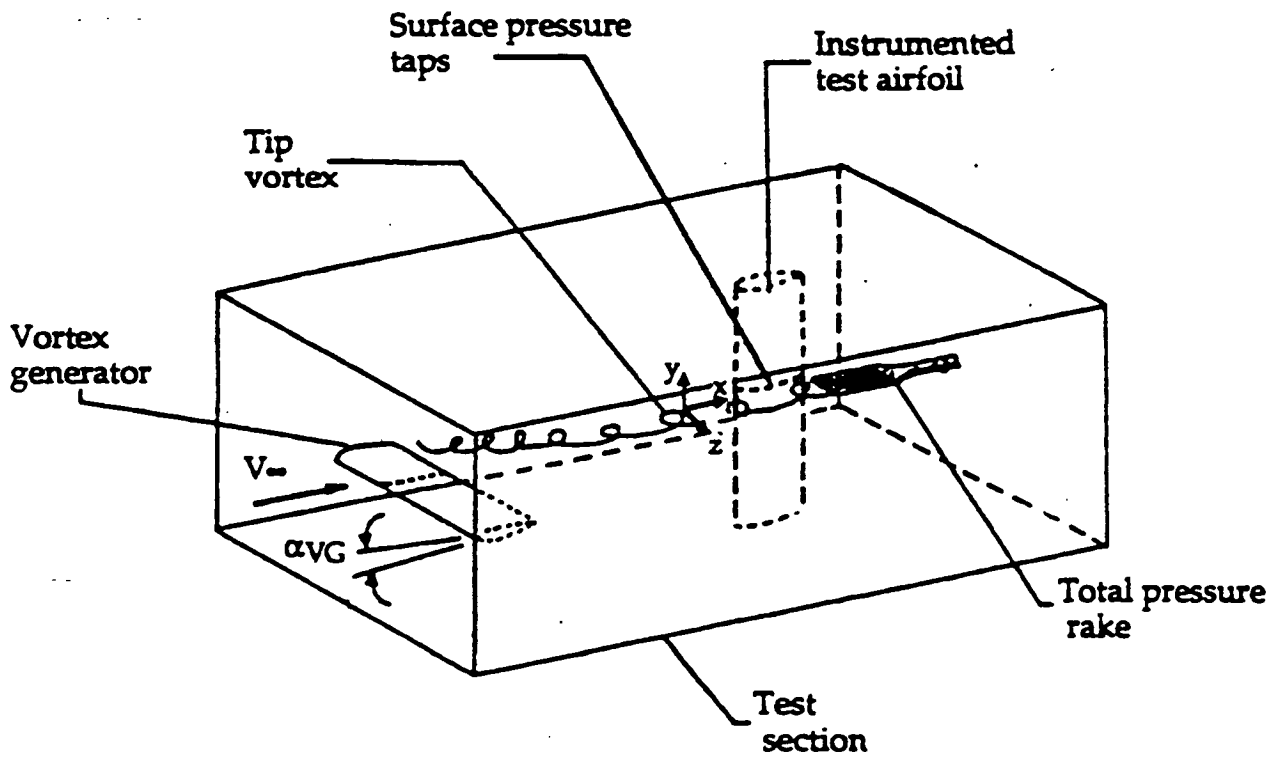


Figure 1.2 Configuration studied by Kalkhoran et al. (1992).  
Figure from Kalkhoran et al. (1992).

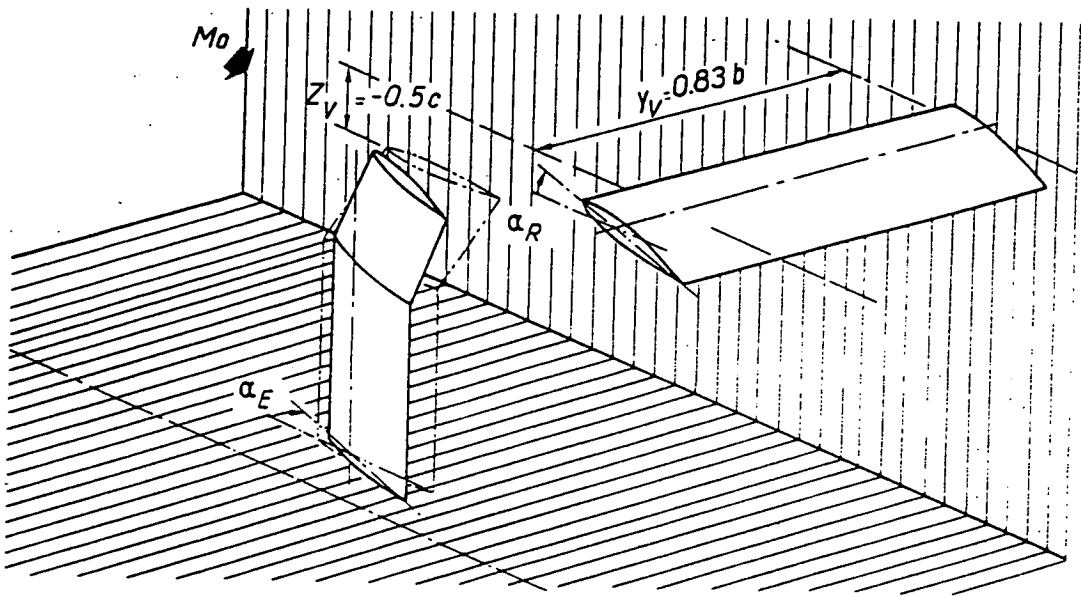


Figure 1.3 Configuration studied by Phillipe and Armand (1978).  
Figure from Phillipe and Armand (1978).

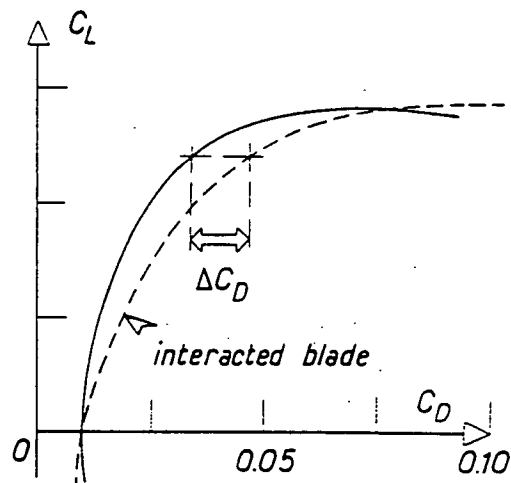
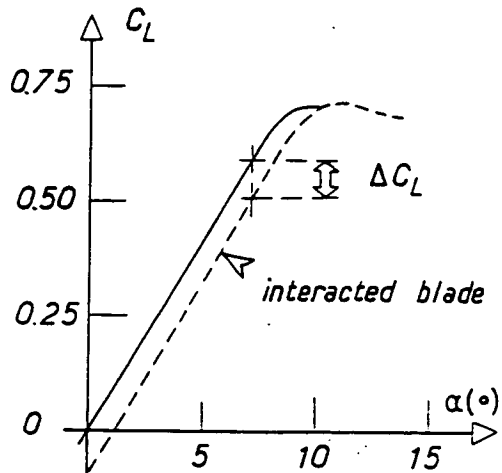


Figure 1.4 Effects of perpendicular blade vortex interaction on blade characteristics. (a) lift coefficient. (b) Drag coefficient.

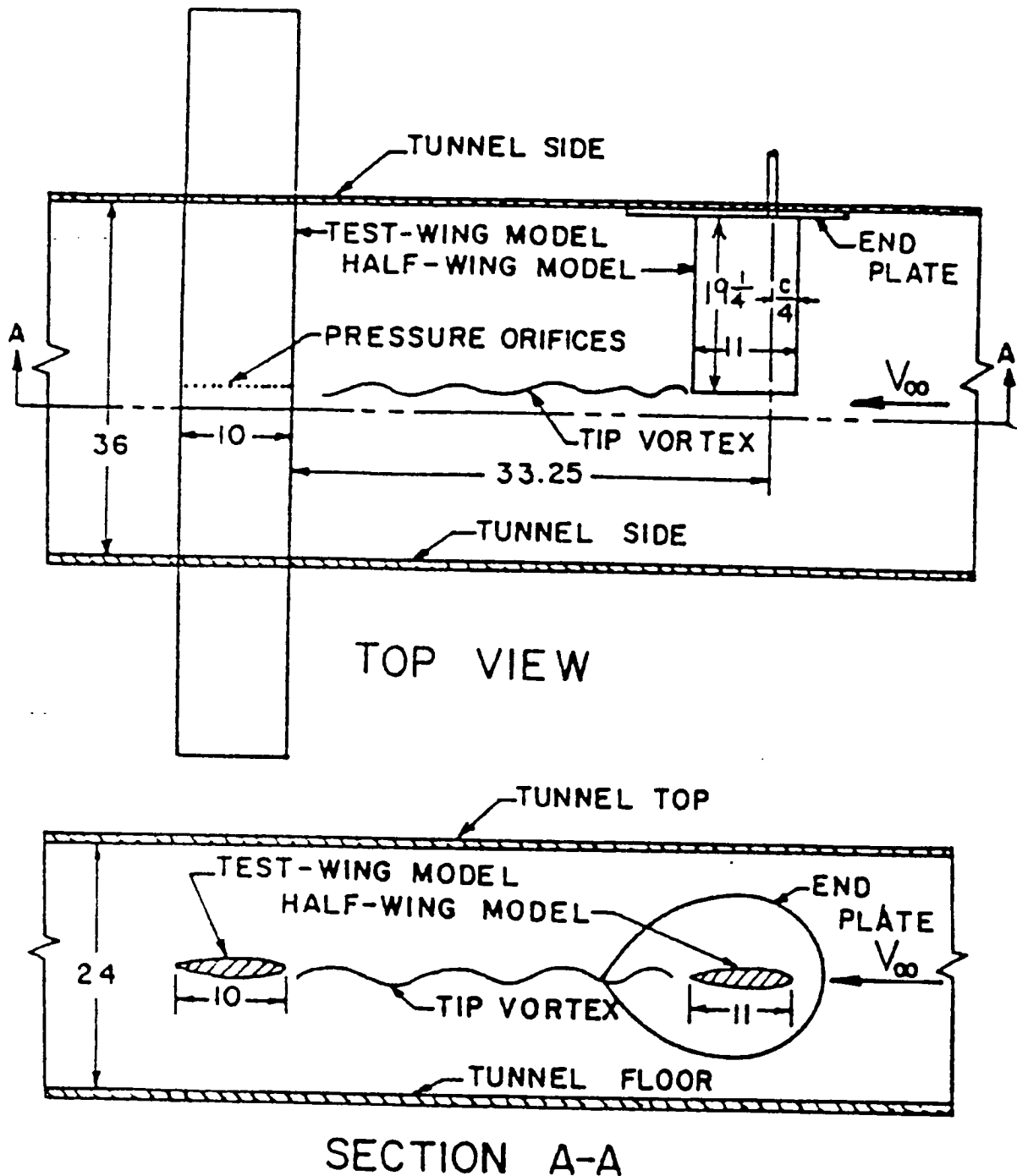


Figure 1.5 Configuration studied by Seath and Wilson (1986).  
Figure from Seath and Wilson (1986).



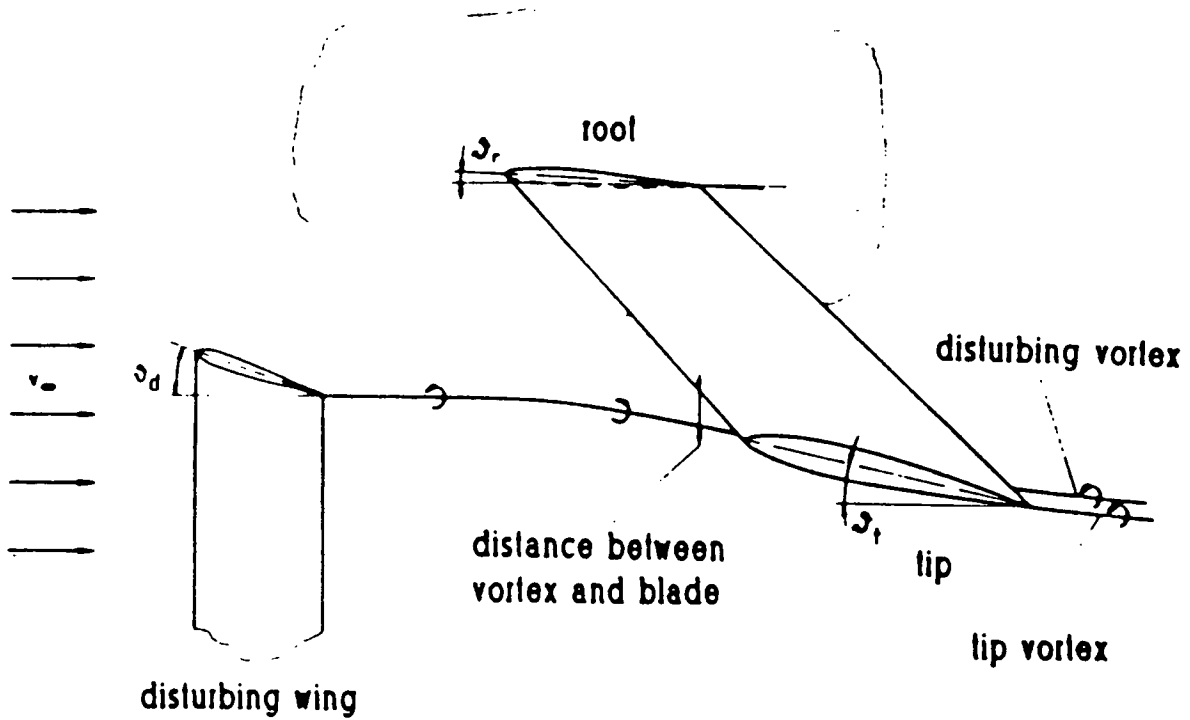


Figure 1.6 Configuration studied by Muller (1990).  
Figure from Muller (1990).

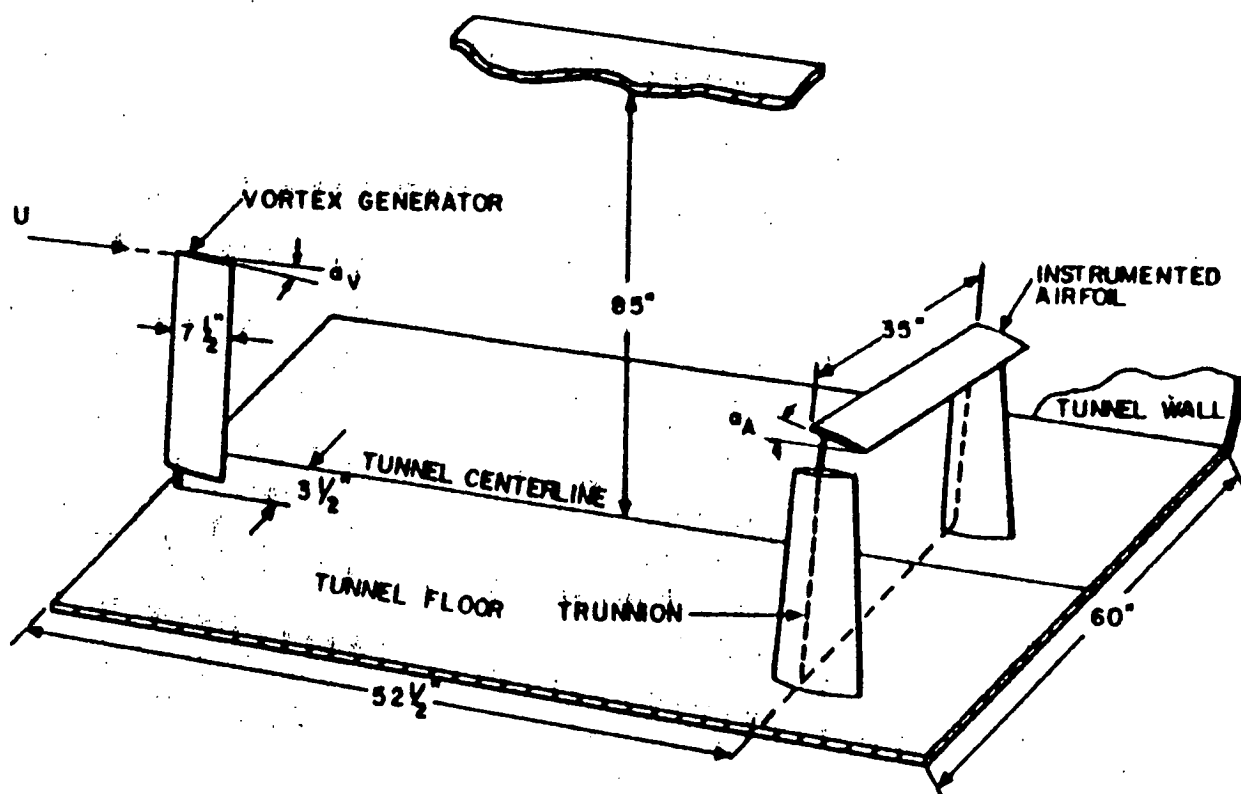


Figure 1.7 Configuration studied by Ham (1975).  
Figure from Ham (1975).

## 2. APPARATUS AND INSTRUMENTATION

Much of the apparatus and instrumentation has already been described in detail by Devenport et al. (1993). Only brief descriptions of these items are therefore included here.

### 2.1 Wind Tunnel

Experiments were performed in the Virginia Tech Stability Wind Tunnel (figure 2.1). It is a closed-circuit tunnel powered by a 600 horsepower axial fan. The test section is square with a cross section of 1.83m X 1.83m and a length of 7.33m. Flow in the empty test section is closely uniform with a turbulence intensity of less than 0.05% (Choi and Simpson (1987)). For speeds between 6 and 30 m/s there is a slight favorable pressure gradient along the test section  $\partial C_p / \partial x = -0.003/m$  as a consequence of the growth of the side-wall boundary layers (Reynolds (1979)). This acceleration causes some convergence of the streamlines. Choi and Simpson (1987) showed the convergence, illustrated in figure 2.2, to be centered roughly in the middle of the test section at speeds of 15 and 37.5 m/s. Flow angles produced by the convergence are small near the middle of the test section but increase to about  $2^\circ$  near the walls.

During operation of the wind tunnel the free stream dynamic pressure and flow temperature are monitored continuously. The former is measured using a pitot-static probe located at the upstream end of the test section connected to a Barocell electronic manometer. The latter is sensed using an Omega thermocouple located within the test section boundary layer, there being no significant temperature gradient across the boundary layer.

### 2.2 Wing models

Mason and Marchman's (1972) wing model was used along with a copy produced on a numerically controlled milling machine. Both models have a rectangular planform, NACA 0012 airfoil section and a blunt wing tip. The chord and span are .20 m and 1.22m respectively.

Mason and Marchman's wing is made from solid brass while the copy is made from solid aluminum. Surfaces of both wings are accurate to within  $\pm 0.25\text{mm}$ .

The aluminum model was used as the vortex generator. It was mounted vertically as a half wing at the center of the upper wall of the test section entrance (figure 2.3). Its root was held cantilever fashion in a turntable and cable assembly (figure 2.4), this allowing the wing to be rotated to angle of attack about its quarter chord location. In this arrangement 0.88m of this wing protruded into the test section flow. The brass model, used as the interaction blade, was mounted in a similar manner 14 chord lengths downstream (figure 2.3), its effective span being 1.0m. Here the mount consisted primarily of two large aluminum beams resting on the tunnel superstructure (figure 2.5). These allowed the angle of attack and lateral position to be independently adjusted.

The wing models were initially placed at zero angle of attack, with an accuracy of  $\pm 0.2^\circ$  by using a removable wing tip holding 48 static pressure ports. The tip was first placed on the rear wing and used to position it at zero angle of attack by equalizing the static pressures on both sides. The forward wing was then put in place and zeroed in a similar manner.

To eliminate possible unsteadiness and non-uniformity that might result from natural transition, the boundary layers on the wings were tripped. Glass beads with a diameter of 0.5mm were glued to the wings in a random pattern in a strip extending between 20% and 40% chord locations. Average density was 200 beads/cm<sup>2</sup>. The resulting turbulent boundary layers were documented for a range of angles of attack by Devenport et al. (1992).

### 2.3 Hot-wire anemometry

An Auspex Corporation four-sensor hot-wire probe, type AVOP-4-100, was used to make three-component velocity measurements. The probe, shown in figure 2.6, consists of two orthogonal X-wire arrays with each wire inclined at a nominal  $45^\circ$  angle to the probe axis. Eight prongs, 75 $\mu\text{m}$  in diameter at their tips, position the wires some 40mm upstream of the main part of the probe. Each wire is 0.8mm long and 5 $\mu\text{m}$  in diameter. The total measurement volume is roughly 1.1mm<sup>3</sup>.

## Perpendicular BVI Part I

The probe was operated using four Dantec 56C17 bridges and four 56C01 constant temperature anemometer units mounted in a Dantec 56B12 main frame. The output voltages from the anemometer bridges were recorded by the IBM AT compatible computer using an Analogic 12 bit HSDAS-12 A/D converter having an input voltage range of 0-5 volts and 12 bit resolution. The HSDAS-12 can sample up to four of its sixteen channels simultaneously at a maximum rate of 100 kHz per channel. In addition to those channels used for hot wire signals, two other channels of HSDAS-12 were used to measure flow temperature and free-stream pitot-static pressure. Raw hot wire signals were linearized and processed in the computer using an 18-8 laboratories PL1250 array processor. Optical disc cartridges were used to store the raw and processed data.

A nominal overheat of 1.7 was used. The wires were calibrated frequently by placing the probe in the free stream and comparing the wire output voltages ( $E$ ) with cooling velocities ( $U_{eff}$ ) determined from the velocity sensed by the pitot-static probe located at the test-section entrance and the wire angles. The absolute wire angles were determined in advance by pitching and yawing the probe in the uniform potential core of a jet. The absolute flow direction at the calibration location was determined in advance using a 7-hole yaw probe. King's law

$$E^2 = A + BU_{eff}^n \quad (1)$$

was used. The exponent  $n$  was taken as 0.45 the constants  $A$  and  $B$  were determined via linear regression from 10 to 20 calibration points. Root mean square errors between the points and the King's-law fit were typically less than 0.5% in velocity. Flow temperature in the stability wind tunnel was found to drift by typically 1 to 2°C per hour. Hot wire signals were corrected for temperature changes using the method of Bearman (1970). The anemometer bridges were balanced to give a frequency response of better than 20kHz.

A probe holder, shown in figure 2.7 was used to attach the to the wind-tunnel traverse gear. The holder was designed to position the measurement point of the probes 0.84m upstream of the leading edge of the traverse. It consisted of a 23.6mm diameter steel tube aligned with the free stream and two 6.2mm diameter rods normal to it. The purpose of the rods was to offset the

axis of the probe from that of the tube by 114mm. Thus the tube did not have to be placed in or near the vortex core for measurements to be made there. For all measurements the axis of the probe and tube were held parallel to the test section axis and thus free-stream flow direction. The probe was not pitched or yawed to face the local mean flow direction since, as demonstrated by Mason and Marchman (1972), this can seriously disrupt a trailing vortex flow.

To turn the four effective velocities obtained simultaneously from the hot-wire probe into velocity components the following analysis was used. Consider the velocity components and wire angles defined in figure 2.6. Following Jorgensen (1971) we would expect the effective velocities to be related to the velocity components through the relations,

$$\begin{aligned} U_{eff1}^2 &= (U\sin\theta_1 + V\cos\theta_1)^2 + k_1^2(U\cos\theta_1 - V\sin\theta_1)^2 + h_1 W^2 \\ U_{eff2}^2 &= (U\sin\theta_2 + W\cos\theta_2)^2 + k_2^2(U\cos\theta_2 - W\sin\theta_2)^2 + h_2 V^2 \\ U_{eff3}^2 &= (U\sin\theta_3 - V\cos\theta_3)^2 + k_3^2(U\cos\theta_3 + V\sin\theta_3)^2 + h_3 W^2 \\ U_{eff4}^2 &= (U\sin\theta_4 - W\cos\theta_4)^2 + k_4^2(U\cos\theta_4 + W\sin\theta_4)^2 + h_4 V^2 \end{aligned} \quad (2)$$

where  $k$  and  $h$  refer to the axial and pitch sensitivity of each wire. Splitting velocity components into mean and fluctuating parts, taking the square root and ignoring second order terms leads to the expressions

$$\begin{aligned}
 U_{eff1} &= \sqrt{A_1}U + \frac{D}{\sqrt{A_1}}V \\
 U_{eff2} &= \sqrt{A_2}U + \frac{D}{\sqrt{A_2}}W \\
 U_{eff3} &= \sqrt{A_3}U + \frac{D}{\sqrt{A_3}}V \\
 U_{eff4} &= \sqrt{A_4}U + \frac{D}{\sqrt{A_4}}W
 \end{aligned} \tag{3}$$

where

$$\begin{aligned}
 A_1 &= \sin^2\theta_1 + k_1^2 \cos^2\theta_1 & D_1 &= \frac{1}{2}\sin 2\theta_1(1 - k_1^2) \\
 A_2 &= \sin^2\theta_2 + k_2^2 \cos^2\theta_2 & D_2 &= \frac{1}{2}\sin 2\theta_2(1 - k_2^2) \\
 A_3 &= \sin^2\theta_3 + k_3^2 \cos^2\theta_3 & D_3 &= -\frac{1}{2}\sin 2\theta_3(1 - k_3^2) \\
 A_4 &= \sin^2\theta_4 + k_4^2 \cos^2\theta_4 & D_4 &= -\frac{1}{2}\sin 2\theta_4(1 - k_4^2)
 \end{aligned} \tag{4}$$

rearranging equations 3 gives, finally,

$$\begin{aligned}
 V &= \frac{A_1\sqrt{A_3}U_{eff3} - A_3\sqrt{A_1}U_{eff1}}{A_1D_3 - A_3D_1} \\
 W &= \frac{A_2\sqrt{A_4}U_{eff4} - A_4\sqrt{A_2}U_{eff2}}{A_2D_4 - A_4D_2} \\
 U &= \frac{U_{eff1}}{\sqrt{A_1}} - \frac{D_1}{A_1}V \\
 U &= \frac{U_{eff2}}{\sqrt{A_2}} - \frac{D_2}{A_2}W
 \end{aligned} \tag{5}$$

The above analysis treats the probe as two orthogonal X-wire arrays and thus gives two estimates of  $U$ . As discussed by Devenport et al (1992) measurements of axial velocity  $U$  with X-wire arrays can be contaminated by streamwise vorticity because of the finite size of the probe. However, the two X-wire arrays of the present probe are influenced by streamwise vorticity to in an and opposite fashion. Averaging the two estimates of  $U$  therefore tends to eliminate this contamination, i.e.  $U$  is calculated as

$$U = \frac{1}{2} \left( \frac{U_{eff1}}{\sqrt{A_1}} - \frac{D_1}{A_1}V + \frac{U_{eff2}}{\sqrt{A_2}} - \frac{D_2}{A_2}W \right) \tag{6}$$

the above equations were used to determine the instantaneous velocity components from the instantaneous effective velocities. Averaging was then used to determine mean velocities and Reynolds stresses, fast Fourier transforms were employed to compute velocity spectra.

## 2.4 Helium Bubble Flow Visualizations



## Perpendicular BVI Part I

The helium bubble flow visualization system used by Rife et al. (1993) was used in setting up the blade position, see section 3.1. For a full description of this system see Rife et al.

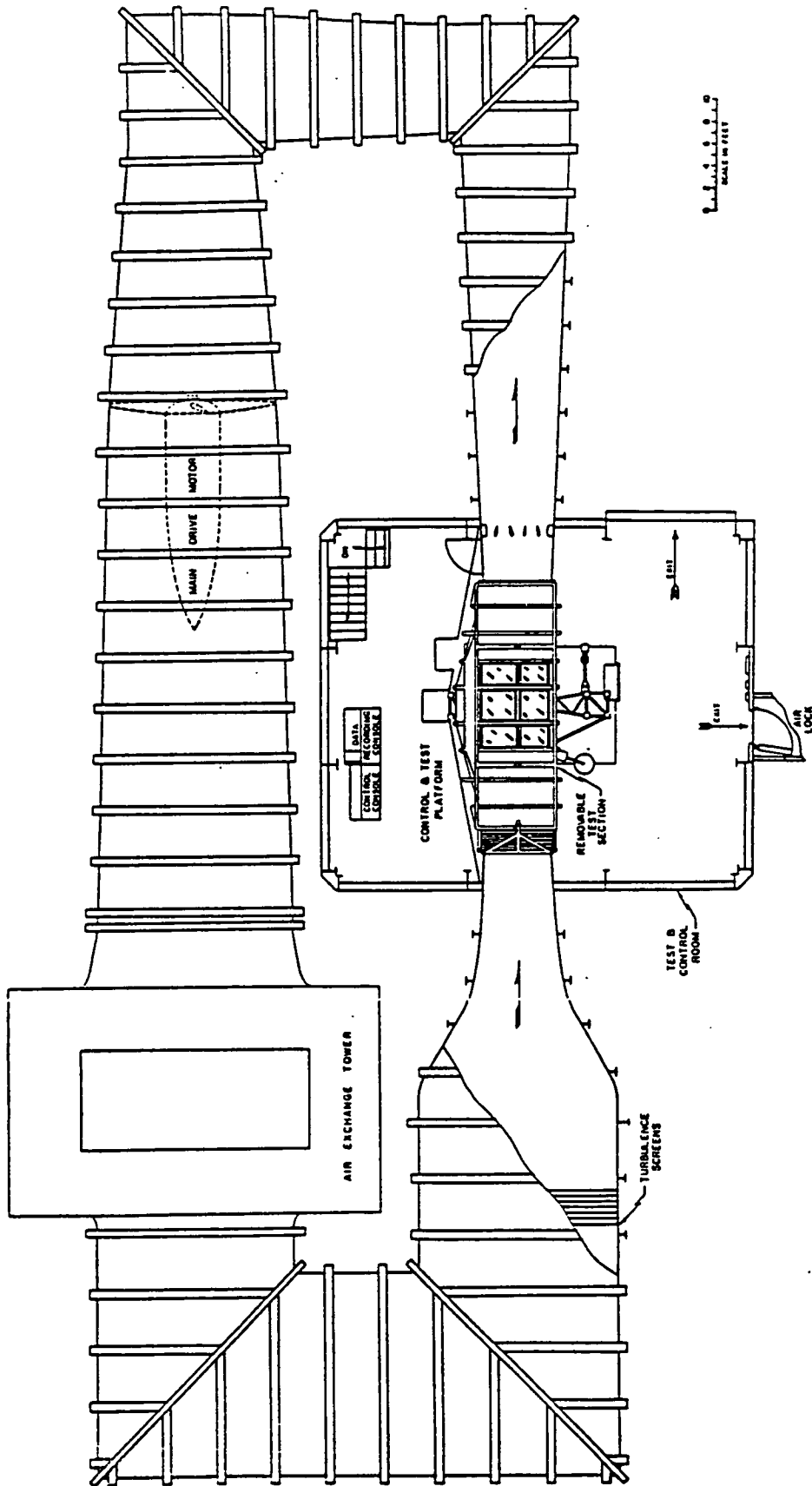
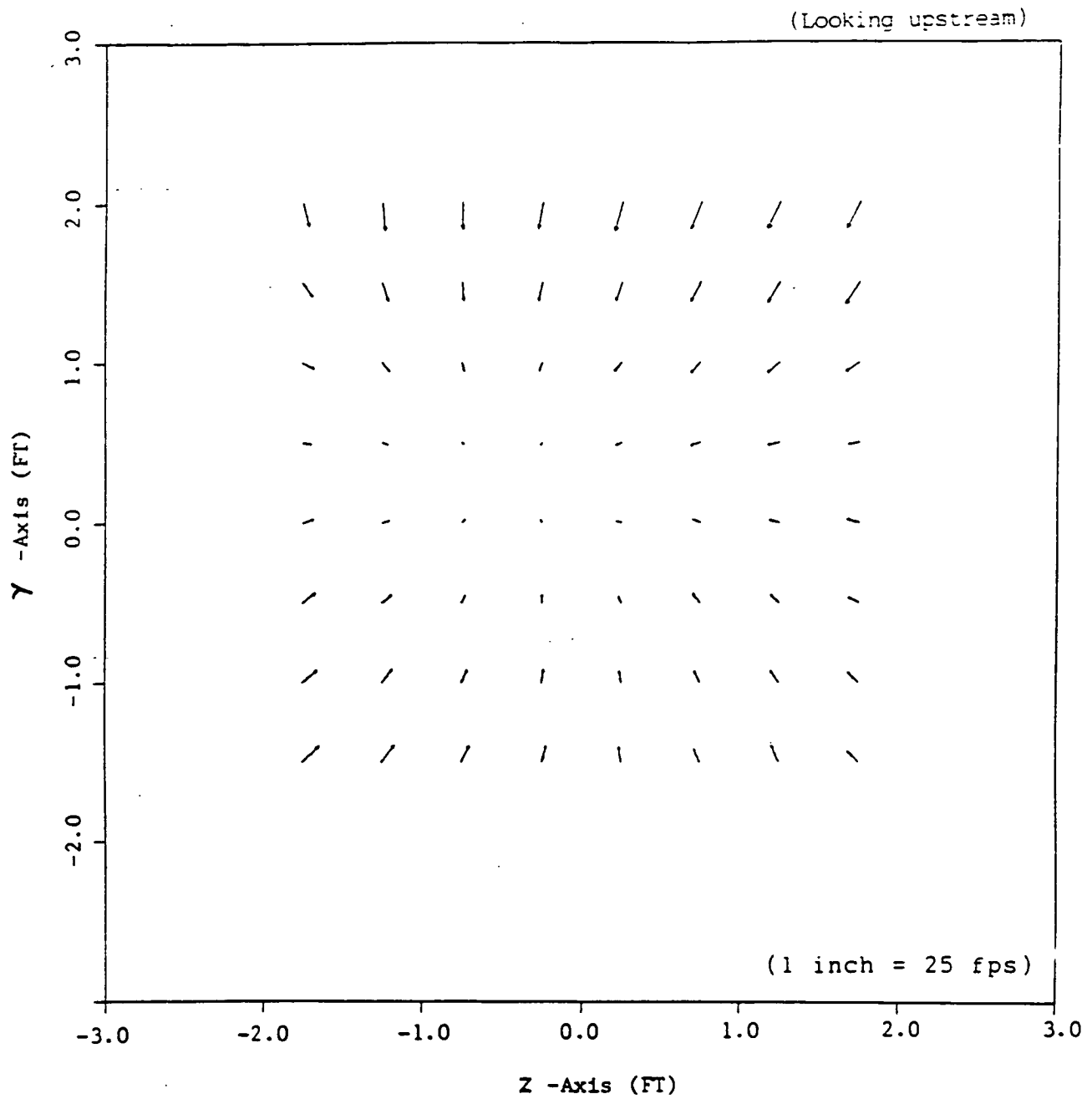


Figure 2.1 Schematic of the Virginia Tech Stability Wind Tunnel.



**Figure 2.2** Convergence of flow through the empty test section and 37.5m/s (125fps).  
From Choi and Simpson (1987).

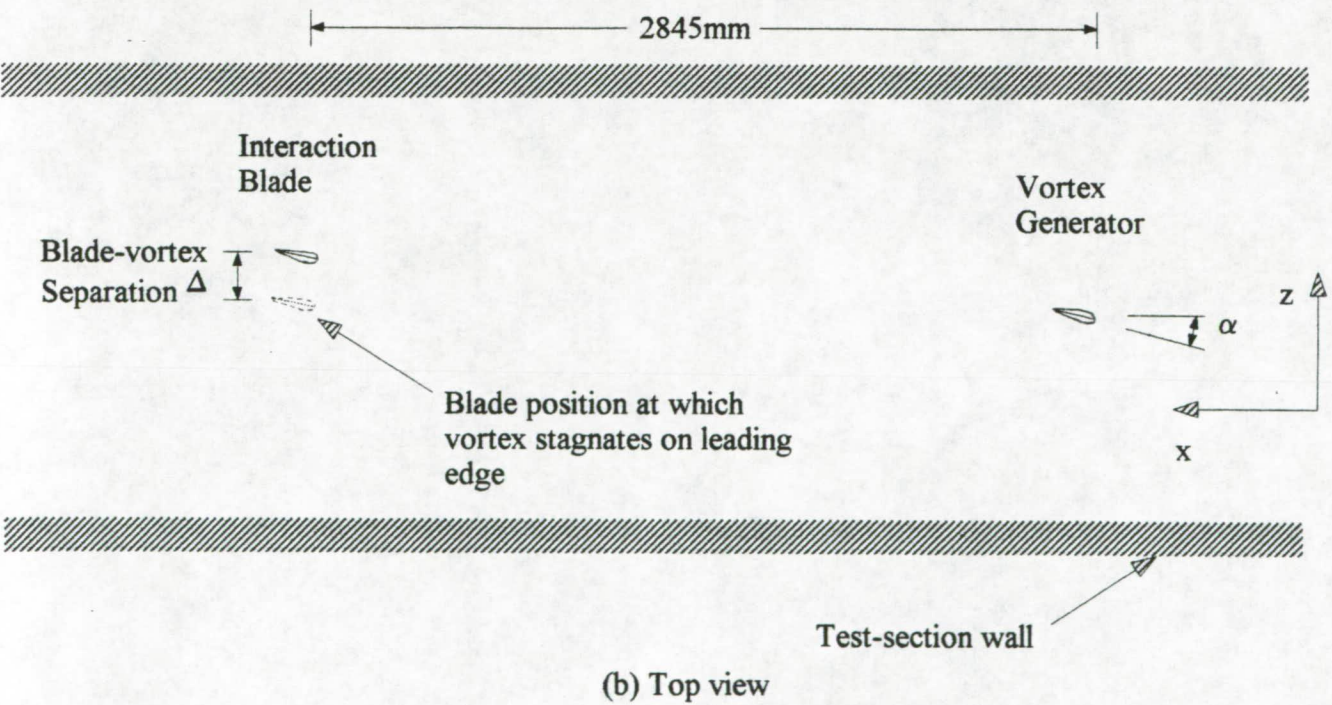
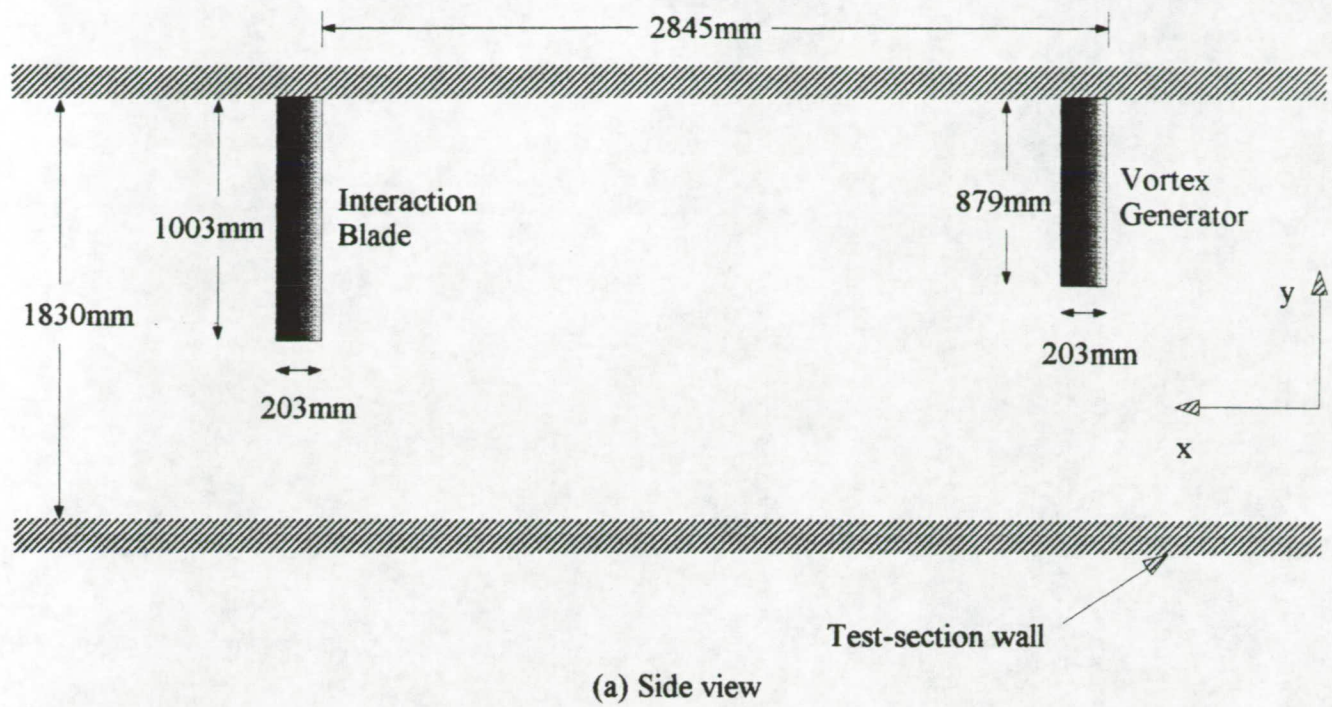


Figure 2.3 Orthogonal views of the test section showing the vortex generator, interaction blade and coordinate system.

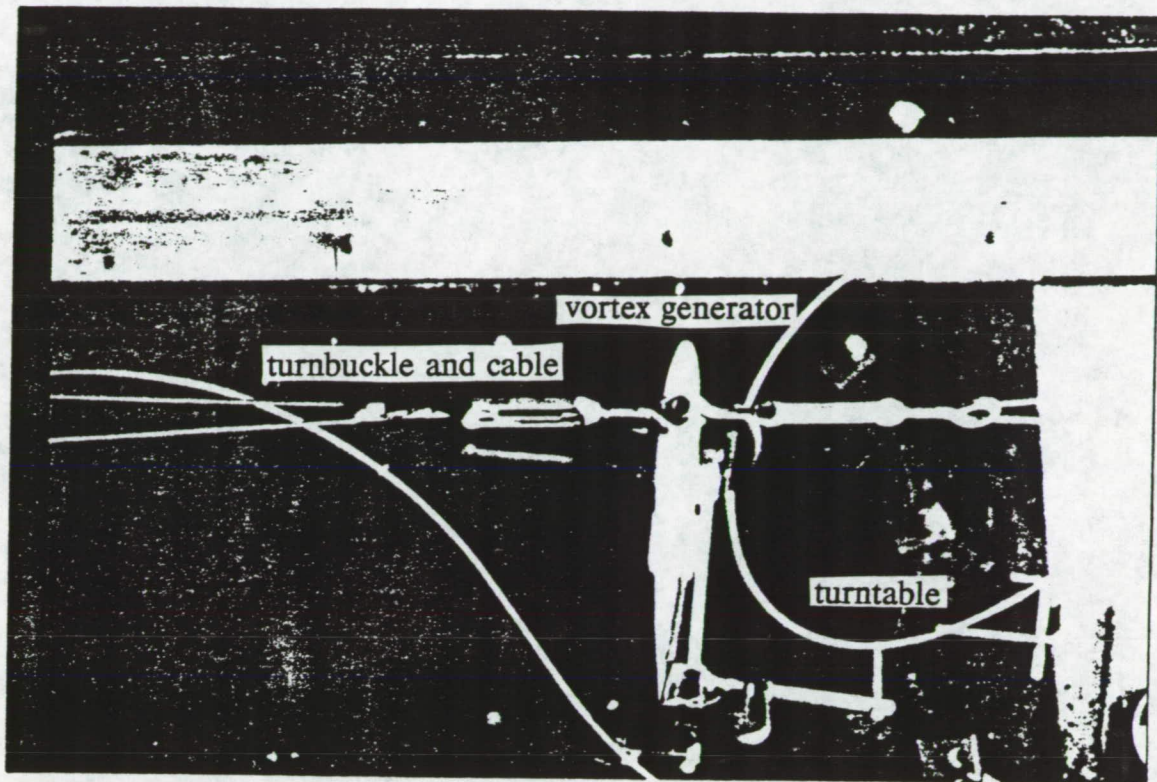


Figure 2.4 Top view of vortex-generator mount.

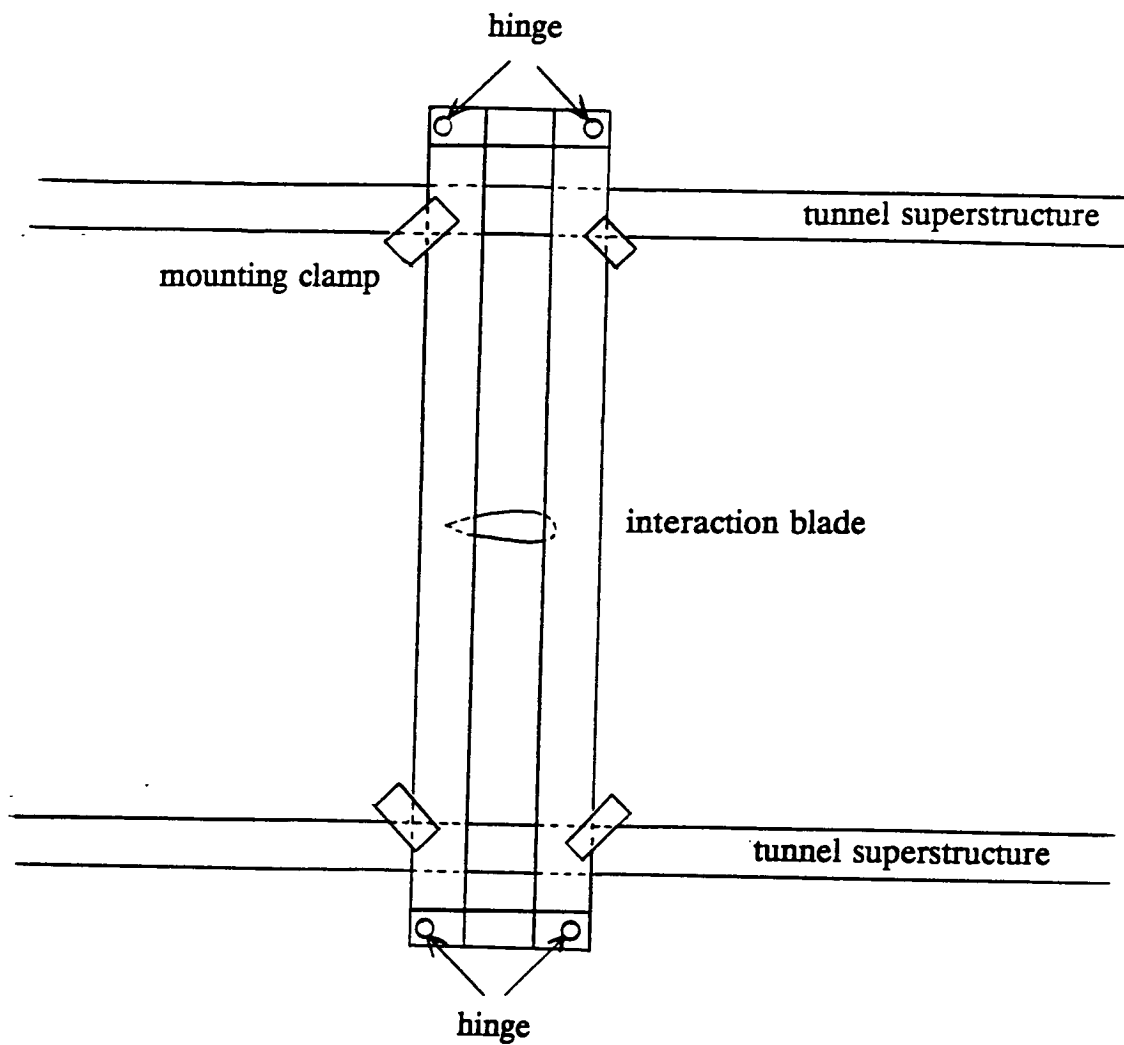
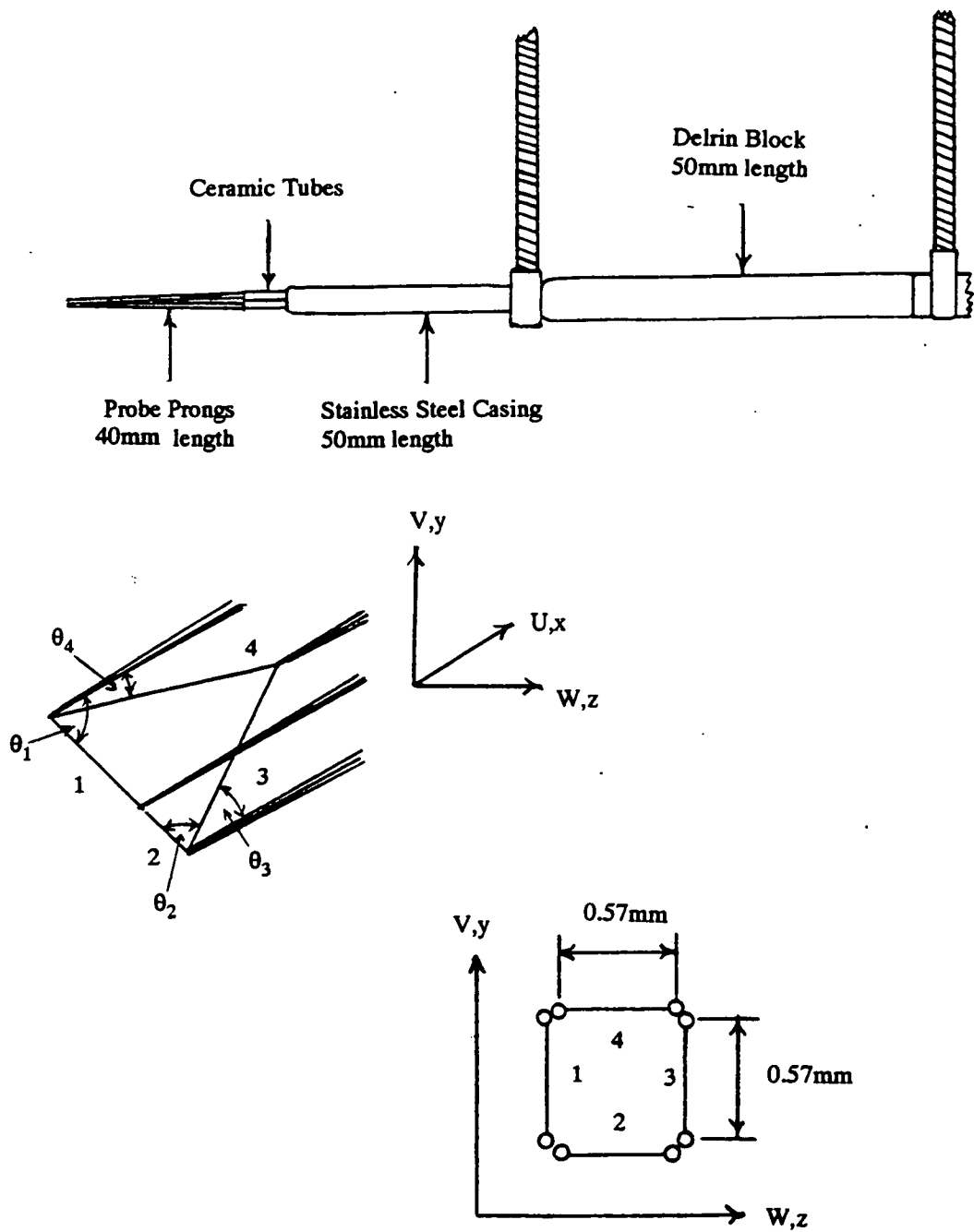
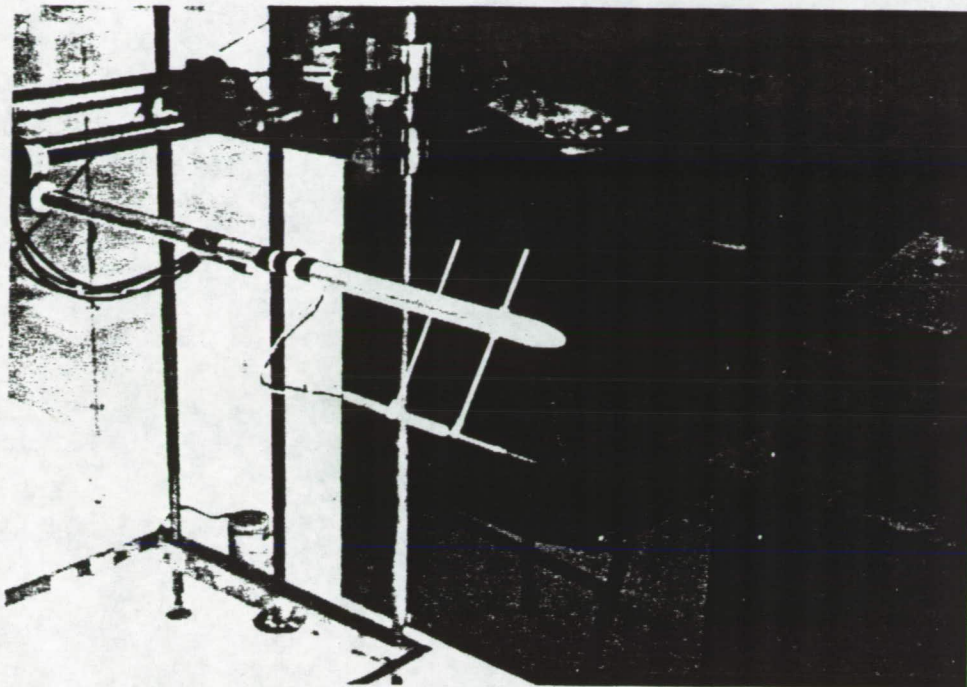


Figure 2.5 Schematic of interaction blade mount.

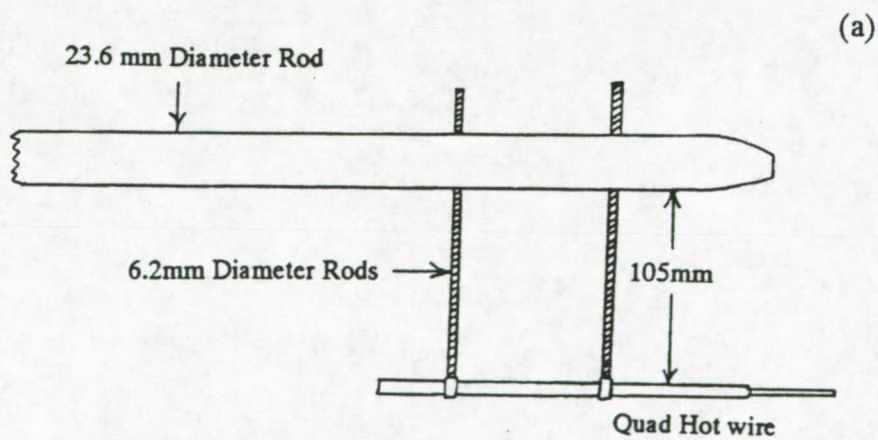




**Figure 2.6** Schematic of quad hot-wire probe showing dimensions, wire configuration and velocity components used in analysis.



(b)



(a)

Figure 2.7 (a) Diagram of the probe holder. (b) View of the probe holder and quad-hot wire attached to the wind-tunnel traverse gear.



### 3. RESULTS AND DISCUSSION

#### 3.1 Coordinate System, Flow Conditions and Table of Measurements

The wind-tunnel fixed coordinate system shown in figure 2.3 will be used in presenting results. The direction of the free stream flow is along the X axis, Y is parallel to the wing spans and, Z is opposite to the direction of lift. The origin of the coordinate system is the leading edge of the tip of the vortex-generator. In this system the leading edge of the blade is at  $X/c = 14$  and its tip is at  $Y/c = -0.613$ , where  $c$  is the chord length. Mean velocity components  $U$ ,  $V$ ,  $W$  and fluctuating components  $u'$ ,  $v'$  and  $w'$  are defined in the X, Y and Z directions respectively.

All velocity measurements were performed at a Reynolds number based on chord  $c$  ( $Re_c = U_{ref}c/\nu$ ) of 260,000, corresponding to a free-stream velocity  $U_{ref}$  of 20 m/s. The free stream velocity  $U_{ref}$  was monitored using a pitot static tube placed at  $(3.9c, 2.8c, 3.0c)$ . Both blade and vortex generator were fixed at 5 degrees angle of attack, measured according to the right-hand rule for the negative Y axis. The vortex was therefore rotating according to the right hand rule in the positive X direction. Measurements were made for several lateral ( $z$ ) positions of the blade measured in terms of the blade-vortex separation distance  $\Delta$ , defined in figure 2.3<sup>1</sup>. Zero  $\Delta$  corresponds to the blade position where the streamline marking the vortex center stagnates upon the blade leading edge. This blade position was determined at the start of the hot wire measurements by using helium-filled soap bubbles to visualize the vortex core.  $\Delta$  is negative when the vortex passes to the pressure side of the blade and positive when it passes to the suction side.

Table 3.1 lists all the conditions and locations at which velocity measurements were made. Measurements were made upstream of the blade location, at  $X/c=10$  (for which the blade was actually removed), and downstream of the blade at  $X/c=30$  (15c downstream of the blade trailing edge) for  $\Delta/c = -0.125, -0.0625, 0, 0.0625$  and  $0.125$ . For the closest pressure-side passage,  $\Delta/c$

---

<sup>1</sup>Note that Rife et al. (1993) used  $z_s$  to denote blade-vortex separation.  $\Delta = -z_s$ .

= -0.0625, measurements were also performed at  $X/c=15.33$  (0.33c downstream of the blade trailing edge) and  $X/c=22.6$  (7.6c from the blade trailing edge). For the closest suction side passage additional measurements were made only at  $X/c=22.6$ . At most locations and conditions grids of mean velocity and turbulence stress measurements were made to reveal the overall flow structure, detailed profiles were measured through the core center(s) and velocity spectra were measured at representative locations. Note that in presenting many of these data we shall use for convenience the coordinates  $y$  and  $z$ , identical to  $Y$  and  $Z$ , except measured relative to the center of the largest measurement grid at each streamwise location. In the text below positions will be referred to in coordinate pairs, for example,  $(1,2)_R$  will refer to a  $(y,z)$  position and  $(1,2)_A$  a  $(Y,Z)$  position. Uncertainty estimates for velocity measurements are listed in table 3.2.

### 3.2 Summary of relevant flow-visualization results

Rife et al. (1993) performed helium bubble visualizations to reveal the gross features of the blade vortex interaction. Visualizations were performed for a number of vortex generator/blade angle of attack combinations and a range of blade-vortex separations  $\Delta$ .

For the conditions of interest here (i.e. vortex generator and blade at  $5^\circ$  angle of attack) a range of phenomena were observed depending on  $\Delta$ . For  $\Delta$  greater than a few percent chord (figures 3.1 to 3.4) the vortex was deflected as it passed the blade under the influence of the local streamline curvature and its image in the blade. During a pressure side passage (figures 3.1 and 3.2) the image deflected the vortex inboard as it passed the blade. The reverse occurred for suction-side passage (figures 3.3 and 3.4). Initially the interaction appeared to have no influence on the core. Downstream, of the blade however, the vortex core began to diffuse and grow, presumably as a consequence of its interaction with the blade wake. The core also interacted with the blade tip vortex, the two rotating slowly about each other with distance downstream. The magnitude of these effects increased with reduction in  $\Delta$ . For  $\Delta$  near zero the form of the interaction changed. With both vortex generator and blade at  $5^\circ$  angle of attack (figure 3.5) the vortex appeared to split into two filaments at the leading edge of the blade, one passing on the pressure and one passing on the suction side.

Table 3.3 and figures 3.6 and 3.7 present quantitative data taken from the flow visualizations and relevant to the present velocity measurements. Figure 3.6 presents measurements of the spanwise drift of the vortex over the blade as a function of  $\Delta$ . Figure 3.7 gives estimates of the divergence angle of the bubble stream marking the core downstream of the blade. These data are also listed in table 3.3 along with estimates of the maximum amplitude of any vortex wandering motions observed in the flow visualizations. Wandering is often a serious problem when tip vortices are generated in wind tunnel test sections. As discussed by Devenport et al. (1992) wandering motions in the present flows are small (a few percent chord), when compared to those present in other studies. However, they should be taken into account when interpreting velocity measurements made in and very close to the vortex core. Note that the estimates in table 3.3 are very definitely upper limits on wandering motions. Velocity measurements presented below suggest that in many cases the actual amplitude of wandering was considerably smaller than these values.

### 3.3 The approach vortex

The overall structure of the approach vortex is shown in figures 3.8 to 3.12 in terms of mean cross flow velocity vectors and contours of axial mean velocity  $U/U_{ref}$ , mean vorticity  $\omega_x c/U_{ref}$ , normal stress  $\overline{u^2}/U_{ref}^2$ , and turbulence kinetic energy  $k/U_{ref}^2$ . Here  $\omega_x = \frac{\partial W}{\partial y} - \frac{\partial V}{\partial z}$ , determined by linear central difference, and  $k = \frac{1}{2}(\overline{u^2} + \overline{v^2} + \overline{w^2})$ . Results are presented on two scales reflecting the coarse and fine measurement grids. The vectors, figure 3.8a and b, show the strong rotational flow associated with the vortex, the vortex center appearing at  $(0,0)_R$ . Its absolute location  $(0.18, -0.058)_A$  is somewhat inboard of the generator tip, as one would expect (see table 3.4).

The structure of this rotating flow, most clearly shown in figures 3.9-3.12, consists of a central core of high axial vorticity (figure 3.10), where there is a significant axial velocity deficit (figure 3.9) and turbulence levels appear high (figure 3.11 and 3.12). Spectra to be presented

below show the high turbulence levels within the core to be a consequence of core wandering motions rather than true turbulence. Surrounding the core there is no substantial region of axisymmetric turbulent flow. Instead the wake of the vortex generating wing wake is wound in a loose spiral. This wake contains the un-rolled-up portion of the vortex sheet shed by the generator and thus has a significant streamwise vorticity (figure 3.10). This, and the curvature and straining of the wake in the rotational velocity field of the vortex, have a significant influence on its turbulence structure.

Far from the core the turbulence structure of the wake is presumably much like that of a two-dimensional wake (see for example Wygnanski et al. (1986)). Approaching the core peak turbulence levels first rise as the wake begins to curve (figures 3.11 and 3.12) reaching a maximum of  $\overline{u^2}/U_{ref}^2 \approx 0.00035$  and  $k/U_{ref}^2 \approx 0.0005$  near  $(0.2, 0.4)_R$ . They then fall by more than a factor of two as the wake wraps  $180^\circ$  around the core to a minimum near  $z/c = -0.15$ . It is unclear whether the fall continues from this point on or not because of the possible influence of wandering on turbulence levels closer to the core.

A plausible explanation of the decrease in wake turbulence levels is that the vorticity, rotational rate of strain and axial vorticity inhibit the formation of large scale coherent structures in the wake. There is no equivalent explanation of the initial increase in turbulence levels. This phenomenon has been seen before by Zsoldos and Devenport (1992) who found increases of up to 50% in peak turbulence levels in the spiral wakes of a pair of interacting trailing vortices. One possibility is that this effect has nothing directly to do with the influence of the vortex but is a consequence of initial non-uniformity in the wake produced by the three-dimensionality of flow over the generating wing. Alternatively it may be that the lengthening of the wake as it is wound into a spiral initially causes some stretching and intensification of its spanwise turbulence structures.

Mean-velocity and normal turbulence stress profiles along the line  $y=0$  are presented in figures 3.13 and 3.14. Near the vortex center (figure 3.14) the mean  $V$  profile shows a core radius of  $3.8\%c$  and peak tangential velocity of  $27\% U_{ref}$ , implying a core circulation of  $27\%\Gamma_0$ ,  $\Gamma_0$  being the root circulation of the wing calculated using lifting line theory. The axial velocity

profile shows a deficit of 15%  $U_{ref}$  at the core center - presumably a consequence of the drag of the generating wing and the gradual decay of the vortex (see Batchelor (1964), Moore and Saffman (1973)). The normal stresses, especially  $\overline{v'^2}$  and  $\overline{w'^2}$ , reach fairly substantial maxima in the core of about  $0.006 U_{ref}^2$ . Spectra presented below show these maxima to be primarily a consequence of the wandering motions, even though the implied magnitude of these motions is small. Core motions of an r.m.s. amplitude of only  $0.005c$  (7% core diameter) would be sufficient to produce these entire stresses given the steep tangential velocity gradient in the core. In reality the motions were probably smaller than this since some of these stresses would have been produced by true turbulence.

Looking at these profiles on a larger scale in figure 3.13 we see the regions where they cut the spiral wake. The wake produces shallow dips and inflections in the  $U$  and  $V$  profiles respectively (at  $z/c = -0.2$  and  $0.35$ ) and local maxima in the turbulence stresses. Overall the wake structure seen in these profiles appears much like that observed and discussed by Devenport et al. (1992).

Figure 3.15 and 3.16 compare mean tangential ( $V$ ) velocity and circulation profiles deduced from the above measurements with predictions from Betz's theory. Measured circulations were calculated by assuming axisymmetry, i.e. as  $2\pi rV$ . Betz's theory, described by Donaldson and Bilanin (1975) and others, relates the spanwise distribution of circulation on a wing to the radial distribution of circulation and tangential velocity in the tip vortex it sheds. It was applied using the equations derived in appendix 1 and a lifting line theory calculation of the vortex-generator circulation distribution. Wall interference effects were ignored in this calculation since they should have been negligible. Betz's theory assumes potential flow and thus cannot account for the presence of the core. It also assumes axisymmetry and so does not model the spiral wake of the vortex. Given these limitations it does a remarkably good job of predicting the tangential velocity profile all the way in to the edge of the core (figure 3.15). The agreement is not as good in the circulation profile (figure 3.16) primarily because of the large deviations in measured circulation around  $z/c = 0.35$  and  $-0.2$  produced where the spiral wake cuts the profile. The

non-axisymmetry of the real flow may also explain why the measured circulation profile falls some 4 to 10% below Betz's at large radius.

Velocity autospectra were measured at a number of locations along the center of the spiral wake and on a radial profile into the core, see figure 3.17(a). The spectra, normalized as

$$\frac{G_{uu}}{U_{ref}^3 c}, \frac{G_{vv}}{U_{ref}^3 c}, \frac{G_{ww}}{U_{ref}^3 c} \quad \text{vs.} \quad \frac{fc}{U_{ref}}$$

where  $G$  is the power spectral density per Hertz and  $f$  is frequency in Hertz, are plotted in figure 3.17b through g. Furthest from the core, at point A the spectra look qualitatively like those of a two-dimensional turbulent wake (see Wygnanski et al. (1986), Antonia and Britz (1989)). The  $U$  spectrum (figure 3.17b), fairly constant at low frequencies, begins to roll off near  $fc/U_{ref} = 2$ . The roll off shows a clear inertial subrange ( $-5/3$  slope) between  $fc/U_{ref} = 2$  and 20 and the beginnings of a dissipation range ( $-7$  slope) thereafter. The  $V$  and  $W$  spectra (figures 3.17d and f) are similar except that they show a peak near  $fc/U_{ref} = 3.4$ . This peak, strongest in  $W$ , presumably marks the typical passage frequency of large scale structures in the wake. Assuming Taylor's hypothesis gives these structures a characteristic length scale of  $c/3.4$ , almost exactly the width of the wake at this location.

Moving inward along the wake towards  $y/c = -.02$ ,  $z/c = -.13$   $U$  spectral levels at low frequencies,  $fc/U_{ref} < 10$ , fall monotonically (figure 3.17b). This tends to confirm our hypothesis that the additional strain rates, curvature and embedded vorticity experienced by the wake nearer the core center inhibit the formation of larger scale structures. At frequencies above  $fc/U_{ref} = 10$  spectral levels remain almost unaltered, however. This is a little surprising and difficult to explain, especially when one recalls that those parts of the wake near  $y/c = -.02$ ,  $z/c = -.13$  and near  $y/c = 0.41$  and  $z/c = 0.40$  have developed under quite different conditions. Intuitively one would expect the suppression of low-frequency motions to produce a drop in the amplitude of high-frequency motions through the energy cascade. Obviously, this does not happen. Similar effects are seen in the  $V$  and  $W$  autospectra (figures 3.17d and f). Here the loss of low-frequency energy is closely associated with the flattening and eventual disappearance of the peak at  $fc/U_{ref}$

= 3.4. The development of this peak is obscured to a certain extent by the rotation of the wake with respect to our rectangular coordinate system, which has a tendency to shift the peak from the W to the V component over this range of positions.

Fairly dramatic changes are seen in those spectra measured in the final tail of the wake and in the core region. At low frequencies  $fc/U_{ref} < 10$  spectral levels increase, especially in the V and W components, because of the coherent wandering of the core (figure 3.17e and g). Because these motions are small the velocity spectrum they produce at different locations has more or less the same shape. At higher frequencies, spectral levels fall by as much as an order of magnitude. Within the core there is little sign of an inertial subrange in any of the components but a dissipation range is clearly visible extending to relatively low frequencies. The implication is that any turbulence inside the core is of low effective Reynolds number.

A striking feature seen in those spectra measured in or near the core center is a fairly sharp spike at a frequency of about  $fc/U_{ref} = 5$ . In U this spike is strongest at  $z/c = .02$ . In V it is clearest at the core center and edge;  $z/c = 0.0$  and  $0.04$ . In W the peak at  $fc/U_{ref} = 5$  only appears at the core center (point P) - at the core edge (point N) a spike is seen but at approximately double the frequency. After having considered many possibilities we are still mystified as to the fluid mechanics producing these features, though we suspect that they are generated by some kind of core wave. The frequency doubling in the W component would seem to rule out any type of probe or sensor vibration as the source.

### 3.4 Flow over the blade

The leading edge of the blade was positioned 4 chordlengths downstream of the above measurement location. The flow visualizations of figures 3.1 to 3.4 show the vortex center passing the blade leading edge  $85\%c^2$  from the tip ( $Y/c = 0.21$ ), this distance varying by no more than  $\pm 3\%c$  with  $\Delta$ . We therefore conclude there was an inboard movement of the vortex of about  $10\%c$  between  $X/c = 10$  and this location.

---

<sup>2</sup>This distance was mis-stated by Rife et al. (1993) at  $92\%c$ .

Figures 3.18 and 3.19 show the probable structure of the flow over the blade and immediately downstream as a function of  $\Delta$ . With the vortex passing to the pressure side of the blade ( $\Delta < 0$  figure 3.18) it drifts inboard under the action of its image in the blade surface. The rotational flow of the vortex has a strong influence on the local angle of attack of the blade  $\alpha$ . Outboard of the vortex center  $\alpha$  is increased, inboard it is decreased. Judging from the tangential velocity profile at  $X/c=10$  (figures 3.13a and 3.14a) the effect could be as much as  $15^\circ$  close to the vortex core, and about  $2^\circ$  at the blade tip. Bearing in mind the geometric angle of attack of the blade of  $5^\circ$ ,  $\alpha$  could be large enough outboard of the vortex center to cause local stall or at least a substantial thickening of the suction side boundary layer. The changes in  $\alpha$  with spanwise distance  $Y$  along the blade should cause the shedding of streamwise vorticity from the blade trailing edge. Outside the immediate vicinity of the core  $\partial\alpha/\partial Y$  is positive and thus positive vorticity is shed. Only close to the core is negative vorticity shed. Downstream of the blade trailing edge we would expect the vortex to interact with this shed vortex sheet and the blade tip vortex. The flow visualizations showed the vortices to rotate about each other as a consequence of their mutual induction. The influence of the vortex on the blade boundary layer is not limited to angle of attack effects. Between its center and the pressure side of the blade the vortex induces a spanwise flow that runs counter to the natural outwash on the blade. The negative streamwise vorticity produced by the friction between this flow and the blade surface is the same as that inferred from changes in the local angle of attack. Inboard of its center the vortex is tending to lift this spanwise flow away from the blade surface. This would be likely to produce some thickening of the pressure-side boundary layer here.

With the vortex passing the suction side of the blade (figure 3.19) its effects on the local angle of attack and thus the shed vorticity distribution are qualitatively the same as those described above. Other aspects of the flow structure, however, are not the same. First, the vortex drifts outboard under the action of its image. Second, the spanwise flow that it generates is found primarily on the suction side of the blade and is outward towards the tip (though this is still in opposition to the natural inwash that would otherwise be found here.) Third, and perhaps most significant, the vortex is rotating so as to lift the flow outboard of its center away from the



suction side surface of the blade. In contrast to the pressure side case, the outward flow generated by the vortex and the variations it produces in local angle of attack therefore act together here to thicken the boundary layer and promote separation.

With the vortex stagnating on the blade leading edge it would still have the same effects on local angle of attack and shed vorticity described above. Its other effects on the boundary layer structure are hard to predict without detailed knowledge of the fate of the vortex core. Assuming the flow visualizations are accurate in this respect and the vortex core splits in two, one would expect the flow structure to be a combination of that drawn in figures 3.18 and 3.19.

No measurements were made over the blade surface to confirm the above discussion. However, measurements were made just (0.33c) downstream of the trailing edge with the vortex passing the pressure side of the blade. The blade-vortex separation for this case was  $\Delta/c = -0.0625$ . Measurements made in grids at this station are presented as vectors and contours in figures 3.20 to 3.27. In addition to those properties plotted for the approach vortex contours of turbulence shear stresses  $\tau_a/U_{ref}^2$  and  $\tau_c/U_{ref}^2$  and of turbulence kinetic energy production  $Pc/U_{ref}^3$  are presented<sup>3</sup>.  $\tau_a$  represents the magnitude of the shear stresses associated with the axial velocity component  $\sqrt{u'v'^2 + u'w'^2}$ , this quantity being invariant under rotation about the X axis.  $\tau_c$  represents the cross flow shear stress  $\overline{v'w'}$  rotated such that  $v'$  lies in the local mean cross-flow direction and  $w'$  normal to it.  $P$  is turbulence kinetic energy production neglecting streamwise derivatives,

$$P = -\overline{v'^2} \frac{\partial V}{\partial y} - \overline{w'^2} \frac{\partial W}{\partial z} - \overline{u'v'} \frac{\partial U}{\partial y} - \overline{u'w'} \frac{\partial U}{\partial z} - \overline{v'w'} \left( \frac{\partial W}{\partial y} + \frac{\partial V}{\partial z} \right) \quad (8)$$

Note that all quantities except  $P$  are plotted on two scales corresponding to the coarse and fine grid measurements. The coarse grid spacing was too large for accurate estimates of  $P$ .

---

<sup>3</sup> Note that, due to a computer programming error, shear stress measurements were not recorded for the inflow plane.

The contours of turbulence quantities and streamwise vorticity (figures 3.22 to 3.27) show the blade to have cut the spiral wake of the vortex generator in two, the core lying just to the pressure side of the blade wake. Due to the influence of its image in the blade surface the core has indeed drifted inboard. The mean velocity vectors (figure 3.20a and b) show the core to be centered at  $(0.02, 0.04)_R$   $(0.33, 0.02)_A$ , 94%*c* inboard of the blade tip. This indicates a total spanwise (*Y*) drift over the blade of 9%*c* inboard, in approximate agreement with the flow visualizations, see table 3.3.

The flow structure in this plane may be split into three fairly distinct regions; the spiral wake, the blade wake and the vortex core. Qualitatively the spiral wake appears little different than at  $X/c=10$ , except for having been cut in two. Turbulence kinetic energy and axial normal stress levels still fall with distance along the spiral towards the core (figures 3.24a and 3.23a). Axial and cross-flow turbulence shear stress magnitudes (figures 3.25a and 3.26a) also drop. Overall turbulence levels in the spiral are lower than at  $X/c=10$ , but this is probably due to the natural decay of the turbulence rather than any effect of the blade.

By contrast, flow properties in the blade wake reveal much about the flow over the blade surface and the influence of the vortex upon it. The blade wake is, not surprisingly, a region of intense turbulent activity where  $k$ ,  $\overline{u'^2}$ , axial shear stress magnitude  $\tau_a$  and turbulence production  $P$  reach relatively large values (3.23, 3.24, 3.25 and 3.27). It is also a region of substantial cross-flow shear stress  $\tau_c$  (figure 3.26) presumably associated with a significant amount of streamwise vorticity embedded within it (figure 3.22a) and of significant axial velocity deficit (figure 3.21). As might be expected from our arguments above, the properties of the wake appear quite different inboard and outboard of the vortex core. Most obvious is the fact that the wake is thicker and more turbulent outboard of the vortex center than inboard. This thickening is presumably due to the predicted effects of the vortex on the local angle of attack. Lifting of fluid away from the blade surface by the rotational motion of the vortex may also increase the wake thickness inboard of the vortex center, but this effect is clearly smaller here. Both inboard and outboard of the core the positive streamwise vorticity shed from the blade is visible in its wake (figure 3.22a). This vorticity is associated with significant negative cross-flow shear stress (figure

3.26a). Interestingly there is also a thin region of positive cross-flow stress on the suction side of the outboard part of the wake (figure 3.26a,  $z/c=-0.12$   $y/c<0$ ). We speculate that this may be due to early separation of the boundary layer from the blade surface under the influence of the vortex. The negative vorticity shed in the vicinity of the core is also visible, near  $(0.1,0)_R$  in figure 3.22. This negative region appears to form part of a tongue of relatively turbulent fluid that extends around the periphery of the core from the wake on its inboard side (figures 3.23, 3.24, 3.25, 3.26). The implication is that this fluid is in the process of being ingested into the core.

Turbulence levels in the core center appear somewhat lower than at its edge, presumably because of the stabilizing effects of rotation. Production here is also strongly negative, there being a strong positive region between the core and blade wake at  $(0.02,-0.02)_R$ , figure 3.27. Note that a portion of this production could be due to coherent motions of the core rather than true turbulent motions.

A Z-wise profile of mean velocity and Reynolds stress components measured through the vortex core blade wake and vortex core at  $y/c=0$  is plotted in figures 3.28 and 3.29. The U-profile (figure 3.28a and 3.29a) shows the axial velocity deficit in the core which occupies the region between  $z/c=-.01$  and  $.12$ . At most locations within this region the deficit is larger than in the approach vortex (figure 3.14a). The maximum, of about 19%  $U_{ref}$  occurs off center, near  $z/c=-.025$ . This same profile also shows a substantial dip, near  $z/c=-.045$  associated with the blade wake and lesser minima centered at  $z/c=0.5$  and  $-0.25$  associated with the vortex generator wake. Corresponding maxima are visible in the turbulence stress profiles.

The tangential velocity profile, visible in the V component shows a peak tangential velocity  $v_{\theta 1}$  of  $0.19U_{ref}$  (compared with  $0.27 U_{ref}$  upstream) and a core radius  $r_1$  of  $3.1\%c$  (compared to  $3.8\%c$  upstream). The apparent decrease in core radius may be due to the core having become non-circular as a result of interaction with its image. Trailing vortex pairs do tend to develop elliptical cores, see Zsoldos and Dévenport (1992) and references therein. The implied core circulation  $2\pi r_1 v_{\theta 1}$  is only 16% of the root circulation of the vortex generator  $\Gamma_o$ , compared to  $27\%\Gamma_o$  upstream. This low value implies that some of the negative vorticity produced on the blade surface and shed into its wake has become ingested into the core, even at this early stage.

Many previous authors have observed the loss of core circulation that results from vortex/boundary layer interaction, see for example Shabaka et al. (1985).

Figures 3.28b and 3.29b show the region of elevated turbulence stresses around the core to be significantly broader than at  $X/c=10$ . However, peak  $W$  and  $V$  normal stresses ( $.0047U_{ref}^2$  and  $.003U_{ref}^2$  respectively) are lower. In making this comparison it should be remembered that almost all the normal stress in the core at  $X/c=10$  was attributed to coherent vortex wandering motions, based on autospectra and the fact that the variations in normal stresses here are similar to those of the mean velocity gradient. This may not be the case here where the normal stresses reach broad maxima and are approximately constant in the core region, despite the fact that the mean-velocity gradients vary substantially. Furthermore  $\overline{u^2}/U_{ref}^2$  reaches approximately the same maximum value as  $\overline{v^2}/U_{ref}^2$  and  $\overline{w^2}/U_{ref}^2$  although the crossflow gradients of  $V$  and  $W$  are much larger than those of  $U$ .

$U$ ,  $V$  and  $W$  autospectra measured at representative locations over the cross section are presented in figure 3.30. Figure 3.30a shows the locations. Figures 3.30b, d and f show those spectra measured furthest from the vortex core. These fall into two groups depending on whether they were measured in the vortex generator or blade wakes. Spectra from the generator wake (points A,B,D,E,F, and G) are very similar to those measured in this wake at  $X/c=10$ . Their shape is the same and they show the same fall in low-frequency spectral levels as the core is approached. The only difference is that these spectra are shifted to slightly lower frequency and energy as a consequence of the growth and decay of the wake between these two locations. The peak in the  $V$  and  $W$  spectra attributed to the typical passage frequency of large scale structures is centered at  $fc/U_{ref}=2.7$  compared to  $fc/U_{ref}=3.4$  at  $X/c=10$ .

The two spectra from the blade wake (points C and H) are of much higher characteristic frequency and energy because of the much shorter distance over which this wake has grown. This distance,  $0.33c$ , is probably not sufficient for the transition from boundary layer to wake to have been completed which may explain why these spectra have a more rounded appearance than those of the generator wake. Both  $W$  autospectra show peaks that can be attributed to large-scale

structures. Outboard of the vortex core, at point C, the peak lies at a frequency  $fc/U_{ref}=5$ . Inboard, at point H, it occurs at  $fc/U_{ref}=6.7$ . This difference is consistent with the wake being thicker on the outboard side due to the effects of the vortex on the local angle of attack. Assuming Taylor's hypothesis is valid these frequencies imply length scales of  $0.1c$  and  $0.15c$  respectively. The ratio of these is close to the ratio of blade wake thicknesses at these two locations, as judged from the turbulence kinetic energy contours.

Figures 3.c, e and g show those spectra measured in the vicinity of the vortex core. Points I through L appear to be associated with the inner part of the vortex generator wake. The peak in the V and W spectra shows a slight shift to higher frequencies as the core is approached and a peak appears in the U spectrum. Similar effects were observed in the vicinity of the core at  $X/c=10$ . The spectra at points M and N have the more rounded appearance of the blade wake spectrum (see especially  $G_{vv}$ , figure 3.30e). These points presumably lie in the ring of blade wake fluid apparently entrained by the core that was observed in the contour plots of turbulence stresses. The only point lying within the core is point O. At  $(0, 0.02c)$  it is  $2.8\%c$  from the core center, the core radius being  $3.3\%c$ . Unlike the spectra measured inside the core upstream of the blade this spectrum has a clear  $-5/3$  region in all components. Also, spectral levels at high frequencies are either of similar to or greater than those measured outside the core. The implication here is that the blade vortex interaction substantially alters the turbulence structure of the core, increasing true turbulence levels and the effective turbulence Reynolds number. At low frequencies spectral levels are at least slightly lower than those at corresponding locations in the approach vortex, suggesting some reduction in the amplitude of wandering motions.

### 3.5 Flow downstream of the blade as a function of $\Delta$ .

In this section we present and discuss the measurements made at  $X/c=30$  for  $\Delta/c = -0.125, -0.0625, 0, 0.0625$  and  $0.125$ . These measurements reveal not only the structure of the primary vortex following its interaction with the blade but also that of the tip vortex shed by the blade.

#### 3.5.1 Velocity grids

Figures 3.31 to 3.38 show cross sections through each of these flows in terms of velocity vectors and contours<sup>4</sup>. These figures show both the primary vortex and the blade tip vortex. The mean velocity vectors (figures 3.31) show the sum of these two secondary flow velocity fields, and are thus not useful for distinguishing the vortices. However, the contours of streamwise vorticity (figure 3.33) clearly show the locations of the primary and blade tip vortex cores. In all these figures the blade tip vortex core is located towards the top left hand corner and the primary vortex core towards the center. The relative and absolute locations of the core centers are listed in table 3.4 and plotted in figure 3.39. This figure shows the movement of the vortices as  $\Delta$  was varied by moving the blade. In the absence of any interaction the blade tip vortex would move exactly with  $\Delta$  and the primary vortex would remain fixed. Instead the blade tip vortex core moves considerably less than the blade, by  $0.1c$  for a change in  $\Delta$  of  $0.25c$ . Presumably this is because of the rotation of the blade tip and primary vortices about each other. Rotation apparently plays a large part in determining the location of the primary vortex as well. For  $\Delta < 0$  (pressure side passage) the core ends up at a substantially lower  $Y$  than if  $\Delta \geq 0$ . This is exactly the opposite of the situation at the blade trailing edge, as seen in the flow visualizations and illustrated in figures 3.18 and 3.19. Here the position of the primary vortex core is determined by its drift across the blade under the action of its image. The drift is inboard ( $+Y$ ) for  $\Delta < 0$  and outboard ( $-Y$ ) for  $\Delta > 0$ .

The vorticity contours also give some idea of the degree of organization in the primary vortex core. Following the impingement of the vortex on the blade leading edge ( $\Delta/c=0$ , figure 3.33c) the vorticity in its core is relatively weak and is spread out over a non-circular region aligned approximately with the blade wake. With the vortex passing just to the pressure side of the blade ( $\Delta/c=-0.0625$ , figure 3.33b) it is only slightly more organized, the peak vorticity at its center being about 50% greater than for  $\Delta/c=0$ . A more substantial change is seen between  $\Delta/c=-0.0625$  and  $-0.125$  (figure 3.33a) where the vorticity of the core is much more intense and

---

<sup>4</sup>Contours of turbulence kinetic energy production are only plotted for  $\Delta/c=-0.0625$  since in all other cases the grid resolution was too coarse for the appropriate derivatives to be estimated accurately.

axisymmetric. With the vortex passing to the suction side of the blade (figures 3.33d and e) a similar but more rapid change is seen. The core appears as organized and intense for  $\Delta/c=0.0625$  (figure 3.33d) as with the vortex passing twice the distance from the pressure side of the blade. In none of these cases is the region of negative vorticity produced by the blade-vortex interaction visible, suggesting that it is quickly cancelled by positive vorticity in the core. (Note that some small regions of negative vorticity are seen adjacent to the blade vortex core in some of the figures, but these appear to be a consequence of the limited grid resolution.)

The contours of  $\overline{u'^2}$  and  $k$  (figures 3.34 and 3.35) show a similar effect in the turbulence distributions. For  $\Delta/c=0$  turbulence levels are elevated over a large non-circular region in the vicinity of the primary vortex core. With increase or decrease in  $\Delta$  the region shrinks but turbulence levels at the core center rise, presumably as a consequence of the steeper mean-velocity gradients in the more organized core coupled with coherent wandering motions. The flow structure around the core is in all cases quite different then for the approach vortex. Gone is the loose spiral of the vortex generator wake and, if anything, the core appears well imbedded in the blade wake. The two wakes may be most easily distinguished inboard of the core. For all values of  $\Delta$  the vortex generator wake appears below the blade wake, though the distance between the two shrinks with increase in  $\Delta$ . For  $\Delta/c \geq 0$  they are close enough to overlap.

Outboard of the primary vortex core a highly curved section of blade wake connects it to the blade tip vortex. Qualitatively the turbulence structure of this section of wake and the blade tip-vortex core is similar to that seen in the spiral wake and core of the approach vortex. Turbulence kinetic energy and axial normal stress levels fall with distance along the wake towards the core presumably because of the suppression of large scale turbulent structures by the greater curvature and straining of the mean-velocity field. In the vicinity of the core they then increase as a consequence of coherent wandering motions. Quantitatively, however, turbulence levels in this part of the flow are a strong function of  $\Delta$ , increasing monotonically with this variable. Consider, for example,  $\overline{u'^2}$  levels in the most elevated (i.e. most negative  $z$ ) section of

the blade wake. For  $\Delta/c=-0.125$  (figure 3.34a)  $\overline{u'^2}$  reaches a peak value of about  $1 \times 10^{-4}$  here. For  $\Delta/c=0.125$  (figure 3.34e) the peak value is about 3.5 times greater. Effects of similar magnitude are visible along this entire section of wake and in the blade tip vortex core. The only satisfactory explanation of this effect appears to be in the influence of the primary vortex on the blade boundary layer. As discussed above, with the vortex on the pressure side of the blade (negative  $\Delta$ ) local angles of attack outboard of its core are increased and therefore so is the thickness and intensity of the blade wake. As  $\Delta$  is increased to zero the magnitude of this effect should increase producing the more turbulent section of blade wake seen here. For positive  $\Delta$  (vortex passing to the suction side of the blade) the lifting of fluid away from the blade surface by the vortex acts in concert with the increase in angle of attack to further thickening and intensifying the blade wake.

The contours of axial and cross-flow shear stress are more difficult to interpret (figures 3.36 and 3.37) since in most cases the grid resolution is really not sufficient to reveal the detailed spatial variations of these quantities. At most one can infer that  $\tau_a$  and  $\tau_c$  reach large magnitudes in the vicinity of the vortex cores. For the most part  $\tau_c$  is negative but some intense positive regions are visible near the vortex cores, especially for  $\Delta>0$ . One exception to this limitation is the case  $\Delta/c=-0.0625$  for which a fine grid of measurements were made in the vicinity of the primary vortex core (figures 3.36b(ii), 3.37b(ii) and 3.38). Here we see the core to be bordered above and below by strip shaped regions of high shear stress and turbulence kinetic energy production aligned approximately with the blade wake. This may be an effect of the primary vortex stretching the blade wake as it rolls it in. Stretching would tend to intensify any spanwise structure remaining in the wake and turbulence levels associated with it.

### 3.5.2 Velocity profiles

Z-wise profiles of mean velocities and Reynolds stresses measured through the primary vortex core for  $\Delta/c=-0.125$ ,  $-0.0625$ ,  $0.0625$  and  $0.125$  are shown in figures 3.40 and 3.41. The arrows in these figures mark the core center locations. Detailed views of the core regions are shown in figures 3.42 and 3.43.



The axial velocity deficit in the primary vortex core is clearly visible in these figures. Its dependence on  $\Delta$  is illustrated in figure 3.44. Between  $\Delta/c = -0.125$  and  $-0.0625$  the deficit at the core center falls from  $10.2\%U_{ref}$  to  $6.3\%$  but the size of the region affected by the deficit grows. The reverse occurs for  $\Delta/c > 0$ , the peak deficit rising from  $7.2\%U_{ref}$  at  $\Delta/c = 0.0625$  to  $13.8\%U_{ref}$  at  $\Delta/c = 0.125$ . These observations are consistent with a lower blade-vortex separation resulting in a more diffuse and less organized core. Note that the peak axial velocity deficit for the approach vortex was  $15\%U_{ref}$ .

Far less clear in these plots is the tangential velocity profile of the primary vortex. The V component profile, where it should be visible, also contains substantial contributions from the velocity field of the blade tip vortex. Assuming this superposition to be linear the influence of the blade tip vortex may be subtracted out. All that is required is an independent estimate of its velocity field. We used Betz's theory to provide this estimate, applying it to the theoretical circulation distribution on the blade. Out of necessity the influence of the primary vortex upon the blade circulation distribution was ignored. The estimated velocity field, centered at the measured location of the blade tip vortex, was then subtracted out of the V profile. Figures 3.45 and 3.46 show the results of the subtraction in terms of measured tangential velocity profiles and circulation profiles estimated from them assuming axisymmetry. All profiles are compared with the measurements and Betz's theory estimates for the approach vortex.

These figures show the peak tangential velocity of the primary vortex to be substantially lower and the core radius to be greater at  $X/c = 30$  than upstream of the blade. Peak tangential velocity  $v_{\theta 1}/U_{ref}$ , core radius  $r_1/c$  and core circulation  $\Gamma_1/\Gamma_0$  are plotted as functions of  $\Delta/c$  in figure 3.47 and listed in table 3.5. Consistent with our observations above  $v_{\theta 1}$  falls and  $r_1$  increases as the blade vortex separation falls. The magnitude of these changes is larger for pressure side passage. Despite the substantial changes in  $v_{\theta 1}$  and  $r_1$  the core circulation remains surprisingly constant at  $15\text{--}17\%\Gamma_0$  between  $\Delta/c = -0.125$  and  $0.0625$ , rising to  $23\%\Gamma_0$  at  $\Delta/c = 0.125$ . These compare with  $27\%\Gamma_0$  for the approach vortex. It may be that there is a substantial range of blade vortex separations over which the amount of negative vorticity shed by the blade and ingested into the core is roughly constant.

The agreement between these profiles and the prediction from Betz's theory is, on the whole, very poor even at large radius. At first we were concerned that this poor agreement was due to inaccuracies in the procedure used to subtract the influence of the blade tip vortex. To test this hypothesis we varied the root circulation used in calculating the blade tip vortex and repeated the subtraction process. As can be seen from a comparison of figures 3.46 and 3.48 this had little effect. The poor agreement with Betz's theory has two explanations. Firstly, it is quite possible that the interaction with the blade causes a change in the overall circulation distribution of the vortex - lines of vorticity associated with the trailing vortex could join to some of those associated with the bound vortex on the blade (the loss of core circulation is direct evidence of this). Secondly, even with the velocity field of the blade tip vortex subtracted, flow downstream of the blade is unlikely to have been very axisymmetric and thus cannot really be compared with Betz's results. This second suggestion appears to be supported by the measured circulation profiles of figure 3.46. These profiles, calculated assuming axisymmetry, show erratic and unlikely variations in the total vortex circulation, from  $35\%\Gamma_0$  at  $\Delta/c=-0.125$  to  $70\%\Gamma_0$  at  $\Delta/c=0.125$ .

Figures 3.41 and 3.43 show the turbulence stress distributions in and around the vortex core. Consistent with the contours, peak stress levels in the core rise with blade-vortex separation while the region within which the stresses are elevated shrinks. The rise in stress levels with separation is most likely a consequence of coherent wandering motions, the motions becoming more important as the core becomes more organized and the velocity gradients within it increase.

Figures 3.49 to 3.52 show Z-wise velocity profiles through the blade tip vortex core for all values of  $\Delta$ . The z locations of the core centers are marked by the arrows in these plots. In the vicinity of the core these profiles are qualitatively very similar to those of the approach vortex. Quantitatively some small differences are apparent. The peak tangential velocity is  $33\pm 2\%U_{ref}$  compared to  $27\%U_{ref}$  in the approach vortex. The core radius is  $4.5\%c$  compared to  $3.8\%c$ , the rms amplitude of coherent core motions implied by the peak normal stresses in the core center  $0.8\%c$  compared to  $0.6\%c$  and, the peak axial velocity is  $11\pm 2\%$  compared to  $15\%$ . The ' $\pm$ ' sign here indicates the range of variations with  $\Delta$ . Most of these are small enough to be

a result of differences in the exact path of the profile through the vortex core. As is evidenced by the relatively large W component velocities seen in the core in some of the cases (especially  $\Delta/c=\pm 0.0625$ ) not all the profiles passed exactly through the core center.

In figure 3.50 regions where the profiles cut through parts of the surrounding blade wake may be seen (at  $z/c=-.9$  in figure 3.50a, for example). Comparing these regions clearly shows the increase in blade wake turbulence levels with  $\Delta$  observed in the grid measurements above. Between  $\Delta/c=-0.125$  and  $0.125$  the increase in both normal and shear-stress levels is as much as a factor of three.

### 3.5.3 Velocity autospectra

Autospectra normalized on  $U_{ref}$  and  $c$  are presented in figures 3.53 to 3.57. As indicated in part 'a' of these figures a majority of the spectra were measured either in parts of the vortex generator or blade wakes and thus are similar in form. All show inertial subranges in the U component near  $fc/U_{ref} = 5$  and peaks in the V or W components depending on the local orientation of the wakes. At higher frequencies  $fc/U_{ref} > 20$  the beginnings of a dissipation range can also be seen. While the blade and vortex generator wakes are very similar in shape they have different characteristic frequencies, defined by the location of the peak in the V or W spectrum. This difference is most clearly seen by comparing the W spectra measured at points A and I for  $\Delta/c=-0.125$  (figures 3.53f and g). The frequencies are  $fc/U_{ref}=1.8$  in the vortex generator wake and on  $fc/U_{ref}=2.8$  in the blade wake. The difference is smaller than at  $X/c=15.33$  because the frequency scale of a wake develops as the square root of the distance over which it has grown.

In contrast to the undisturbed vortex, spectral levels at nearly all frequencies are higher in the primary vortex core than in the surrounding flow (e.g. point H, figure 3.53). Except for  $\Delta/c=0.125$ , the core U spectra also show substantial inertial subranges suggesting the presence of a well developed energy cascade. Some of the V and W autospectra even show peaks like those seen in the surrounding blade wake (see point H in figure 3.54f, point E in figure 3.55d and point G in figure 3.56d). For  $\Delta/c=0.125$  the core spectra (figure 3.57 point H) lie somewhere between those seen at lower  $\Delta/c$  and in the approach vortex. No  $-5/3$  region is visible and spectral

levels at high frequencies  $fc/U_{ref} > 20$  are lower than in the immediately surrounding flow, although by not as much as in the approach vortex. The behavior of the core spectra at very low frequencies  $fc/U_{ref} < 2$  shows the degree to which core wandering contributed to the Reynolds stresses. For  $\Delta/c = 0.125$ ,  $-0.125$  and, to a lesser extent  $0.0625$  (figures 3.53, 3.57 and 3.56) low-frequency spectral levels rise much more than high-frequency spectral levels as the core center is approached, indicating core motions to be important in these cases. For  $\Delta/c = -0.0625$  and  $0$ , however, the increase in spectral levels at low and high frequencies is of the same magnitude. As already noted core wandering is likely to have been less important in these cases because the core was larger and the mean-velocity gradients within it weaker.

Parts c, e and g of these figures show the development of the velocity spectrum along the blade wake and into the blade tip vortex core. The increase in blade wake turbulence levels with  $\Delta$  appears to be accompanied by some change in the spectral shape, see point M in figures 3.53 and 3.57. At high frequencies  $fc/U_{ref} > 50$  spectral levels are almost the same at these two points. At low frequencies, however, spectral levels are as much as an order of magnitude lower at  $\Delta/c = -0.125$ . At low frequencies the spectra for  $\Delta/c = -0.125$  also have more rounded appearance and show no clear peak in either the V or W components. The implication is that with increasing  $\Delta$  this part of the blade wake becomes more organized and its large scale structure more important. Moving on into the blade tip vortex core (e.g. figures 3.53 and 3.54 points O and P) the velocity spectrum develops in much the same way it did in the approach vortex. Spectral levels at low frequencies increase dramatically due to core wandering. Spectral levels at high frequencies fall due to spin stabilization and a large dissipation range appears extending down to relatively low frequencies. Note that for  $\Delta/c = 0$  none of the spectrum measurement locations fell within the blade tip vortex core.

### 3.6 Flow downstream of the blade as a function of $x$ .

In this section we present measurements made at  $X/c = 22.6$  for  $\Delta/c = -0.0625$  and  $0.0625$  and use them along with the data presented above to discuss the streamwise development of the vortex downstream of the blade.

### 3.6.1 Velocity grids

Figures 3.58 through 3.65 show the velocity vectors and contours of turbulence quantities measured at  $X/c=22.6$ . The locations of the vortex cores are most clearly seen in the streamwise vorticity (figure 3.60). The core locations are listed in table 3.4 and plotted in figure 3.66 along with data from other streamwise stations. This figure reveals the rotation of the blade tip and primary vortices about each other and the approach of their cores. For  $\Delta/c=-0.0625$  (figure 3.66a) the line joining the vortex centers rotates some  $49^\circ$  and shortens from  $0.75c$  to  $0.64c$  between  $X/c=22.6$  and 30. For  $\Delta/c=0.0625$  (figure 3.66b) this line rotates only  $32^\circ$  and shortens from  $0.73c$  to  $0.72c$  over the same distance. These differences are probably due to the vorticity distribution around the primary vortex core. For  $\Delta/c=-0.0625$  (figure 3.60) this is considerably weaker and more spread out indicating a less organized core, much as at  $X/c=30$ . As illustrated by Rossow (1977) the vorticity distributions of vortex cores can exert a strong influence over how they interact.

The contours of vorticity and turbulence quantities reveal flows much more like those seen at  $X/c=30$  than at  $X/c=15.33$ . The vorticity contours show no sign of the region negative vorticity shed from the blade. The turbulence contours show the primary vortex core to be surrounded by the blade wake, apparently disconnected from the vortex generator wake. Between the primary and blade tip vortices, turbulence levels in the blade wake are a function of  $\Delta$ , increasing by about 30% between  $\Delta/c=-0.0625$  and  $0.0625$ . Overall turbulence levels are higher at this location than downstream, but this is simply because of the shorter distance over which the flows have developed.

Perhaps the clearest views of the streamwise development of these flows are given in figures 3.67 and 3.68. Here all the contours of turbulence kinetic energy measured between  $X/c=10$  and 30 in each flow are plotted together. This figure highlights the dramatic enlargement of the region of high turbulence levels around the vortex core as a consequence of its interaction with the blade. Also visible is the interaction between the vortex, blade wake and blade tip vortex, and the changes in blade wake turbulence levels with  $\Delta$ .

### 3.6.2 Velocity profiles

Z-wise profiles of mean velocities and Reynolds stresses measured through the primary vortex core for  $\Delta/c=\pm 0.0625$  figures 3.69 and 3.70. The arrows in these figures mark the core center locations. Detailed views of the core regions are shown in figures 3.71 and 3.72.

The core axial velocity deficit profiles are similar in form to those measured under the same conditions at  $X/c=30$ . The deficits are, however, larger by about 50% and confined to a smaller radius. Comparison with profiles measured at other streamwise locations (figures 3.73a and b) shows these differences to be part of the rapid diffusion of the core downstream of the blade. For  $\Delta/c=-0.0625$ , for example, the peak deficit is 19% at  $X/c=15.33$ , 10% at  $X/c=22.6$  and 6.3% at  $X/c=30$ . Despite this rapid change the axial velocity profiles retain a remarkably self-similar form, as illustrated in figure 3.74. This figure also shows close similarity among profiles measured at other blade-vortex separations and upstream of the blade.

As before the tangential velocity profiles in the core are obscured by the super-imposed velocity field of the blade tip vortex. Subtracting out that velocity field using the procedure described above gives the tangential velocity and circulation profiles shown in figures 3.75 to 3.78. These figures include tangential velocity profiles from other streamwise locations as well as our Betz's theory estimates and measurements for the approach vortex at  $X/c=10$ .

These figures show the rapid growth of the core and decay of the peak tangential velocity caused by the blade. For  $\Delta/c=-0.0625$   $v_{\theta 1}$  decays from  $27.2\%U_{ref}$  at  $X/c=10$  to  $19.4\%$  at  $X/c=15.33$  and then  $6.1\%$  and  $4.5\%$  at  $X/c=22.6$  and  $30$  respectively. A similar but slightly slower change is seen for  $\Delta/c=0.0625$ . Despite these variations, the tangential velocity profiles remain remarkably self similar, like those of axial velocity deficit, see figure 3.79. Figure 3.80 shows the corresponding variations of core radius and circulation (see also table 3.5). The effects of the blade on the core radius appear consistent with what was observed in the flow visualizations; i.e. in the immediate vicinity of the blade the interaction appears to have little effect on the core radius, it is only downstream, when the vortex encounters the blade wake that the core growth rate increases. For  $\Delta/c=-0.0625$  the radius initially falls slightly from its upstream value. It then begins a rapid growth, however, quadrupling its size by  $X/c=30$ . There is no sign

at this point that the growth has stopped. For  $\Delta/c=0.0625$  the rapid growth does not appear to begin until later (somewhere near  $X/c=22.6$ ), reducing the size of the core seen at  $X/c=30$ . Obviously more data is needed to establish a useable functional relationship between the parameters of the blade vortex interaction and the resulting core radius at a given streamwise station. However, a hint as to the form of such a relationship is apparent in the flow visualization results of figure 3.5. Replotted in figure 3.81 these data show an approximately inverse relationship between 'divergence angle of bubble stream marking the core' (hopefully indicative of average core growth rate) and  $\Delta$ .

Bearing in mind the rapid variations in peak tangential velocity and core radius, the core circulation (figure 3.80b) is remarkably constant downstream of the blade. In both cases it remains close to 16%. Along with the lack of variation in core circulation with  $\Delta$ , these results suggest the possibility of a simple method for accounting for the effects of the blade on core circulation in a calculation, viz. if the core passes closer than a certain distance from the blade, the core circulation is reduced by a fixed amount.

As before the agreement between the circulation and velocity profiles and the prediction from Betz's theory is very poor even at large radius. Changes in the circulation distribution of the vortex as it passes the blade and non-axisymmetry of the flow again seem to be the most likely explanations.

Figures 3.70b and 72b show the turbulence stress profiles in the core at  $X/c=22.6$ . For  $\Delta/c=0.0625$  peak stress levels in the core are substantially higher than for  $\Delta/c=-0.0625$  but are concentrated over a smaller region, consistent with what was seen at  $X/c=30$ . A comparison with core profiles measured at other locations shows a general reduction in peak levels downstream of the blade. For example, for  $\Delta/c=-0.0625$  the peak  $\overline{w^2}/U_{ref}^2$  is .009 at  $X/c=10$ , .0047 at  $X/c=15.325$ , .0013 at  $X/c=22.6$  and .0007 at  $X/c=30$ . In considering these numbers it should be remembered that almost all the normal stress at  $X/c=10$  was attributed to coherent vortex wandering motions, based on autospectra measured in the core. The reduction in peak stress levels with  $x$  therefore probably has more to do with the rapid diffusion of the core mean-velocity gradients than with true turbulence levels. In fact, spectral measurements presented above and

below suggest that true turbulence levels within the core may have been substantially larger at  $X/c=22.6$  and 30.

Figure 3.82 to 3.85 shows mean velocity and turbulence stress profiles through the blade tip vortex core at  $X/c=22.6$  for  $\Delta/c=-0.0625$  (profiles were not measured for  $\Delta/c=0.0625$ ). Qualitatively these are very like those of the blade tip vortex core at  $X/c=30$ . Quantitatively some small differences are apparent. The peak tangential velocity slightly higher, at  $36\%U_{ref}$ . The core radius and apparent rms amplitude of coherent core motions are a little smaller, at  $4.3\%c$  and  $0.56\%c$  respectively.

### 3.6.3 Velocity autospectra

Autospectra are presented in figures 3.86 and 3.87. As at other locations the majority of the spectra were measured either in parts of the vortex generator or blade wakes and thus are similar in form. All show inertial subranges in the U component near  $fc/U_{ref} = 5$  and peaks in the V or W components depending on the local orientation of the wakes. The characteristic frequencies of the blade and vortex generator wakes are most clearly seen in the W spectra measured inboard of the primary vortex core, at points A and I in both cases (figures 3.86f and g for  $\Delta/c=-0.0625$  and figures 3.87f and g for  $\Delta/c=0.0625$ ). The frequencies are  $fc/U_{ref}=2.3$  and  $3.5$  for the vortex generator and blade wakes respectively. These are, as one would expect, higher than the corresponding frequencies at  $X/c=30$ . The flow structure in and around the primary vortex core (points F, G and H figure 3.86, points E and F figure 3.87) is similar to that seen at  $X/c=30$ . Spectral levels at all measured frequencies are higher in the core center than in the surrounding flow and the spectra here show substantial inertial subranges suggesting the presence of a well developed energy cascade. The behavior of these core spectra at very low frequencies  $fc/U_{ref}<2$  shows the degree to which core wandering contributed to the Reynolds stresses. For  $\Delta/c=0.0625$  (figure 3.87) low-frequency spectral levels rise much more than high-frequency spectral levels as the core center is approached, indicating core motions to be important in this case. For  $\Delta/c=-0.0625$ , however, (figure 3.86) the increase in spectral levels at low and high



frequencies is of the same magnitude. Core wandering is likely to have been less important in this case

Those spectra measured in and around the blade tip vortex and wake are similar to those seen here at  $X/c=30$ . Approaching the core (points J to M figure 3.86, points M to O figure 3.87) the blade wake spectra show a gradual loss in energy at low frequencies, presumably because of the suppression of large scale structures in the straining and highly curved flowfield of the vortex. Entering the core (points N to P figure 3.86, and point P figure 3.87) spectral levels at low frequencies greatly increase because of coherent wandering motions. At high frequencies, however, spectral levels fall and a large dissipation region appears.

$\Delta/c$	$x/c$	Measurements
	10	a,c,e
-0.125	30	a,c,d,e
-0.0625	15.33	a,b,c,e
	22.6	a,b,c,d,e
	30	a,b,c,d,e
0	30	a,d,e
0.0625	22.6	a,c,e
	30	a,c,d,e
0.125	30	a,c,d,e

**Key:**

- a - Grid of mean velocity and turbulence stress measurements to show overall flow structure
- b - Refined grid in vicinity of primary vortex core
- c - Detailed z-wise profile through the primary vortex core
- d - Detailed z-wise profile through the blade tip vortex core
- e - Spectra in blade and vortex generator wakes and vortex cores

Table 3.1 Conditions, locations and types of velocity measurements made.

	Wake regions	Core edge	Core center
$U/U_{ref}$	0.015	0.015	0.014
$V/U_{ref}$	0.025	0.025	0.024
$W/U_{ref}$	0.025	0.024	0.023
$\overline{u^2}/U_{ref}^2$	$3.1 \times 10^{-6}$	$1.4 \times 10^{-5}$	$4.3 \times 10^{-5}$
$\overline{v^2}/U_{ref}^2$	$9.5 \times 10^{-6}$	$1.5 \times 10^{-5}$	$1.7 \times 10^{-4}$
$\overline{w^2}/U_{ref}^2$	$9.9 \times 10^{-6}$	$2.0 \times 10^{-5}$	$1.6 \times 10^{-4}$
$\overline{u'v'}/U_{ref}^2$	$4.3 \times 10^{-6}$	$1.4 \times 10^{-5}$	$1.2 \times 10^{-4}$
$\overline{v'w'}/U_{ref}^2$	$4.5 \times 10^{-6}$	$2.3 \times 10^{-5}$	$5.2 \times 10^{-5}$
$\overline{u'w'}/U_{ref}^2$	$2.9 \times 10^{-6}$	$8.5 \times 10^{-6}$	$1.0 \times 10^{-4}$

Table 3.2 Typical uncertainties in hot-wire measurements.

$\Delta/c$	1	2	3	4
-0.125	0.031	0.031	0.05	0.23
-0.063	0.031	0.047	0.08	1.50
0.0	0.016	0.031	-	3.15
0.063	0.023	0.031	-0.09	0.81
0.125	0.031	0.031	-0.05	0.41

Table 3.3. Table of flow properties compiled from flow visualizations of Rife et al. (1990) for cases in which hot-wire measurements were made. (1) maximum amplitude of core wandering in y direction (chords) (2) maximum amplitude of core wandering in z direction (chords) (3) total spanwise drift of vortex between leading and trailing edges of blade (chords) (4) Divergence angle of bubble stream marking vortex core after encountering blade (degrees).

(a) Primary vortex core

$\Delta/c$	$X/c$	$y/c$	$z/c$	$Y/c$	$Z/c$
-	10	0.0	0.0	0.18	-0.06
-0.125	30	-0.36	0.05	-0.18	0.36
-0.0625	15.33	0.02	0.04	0.33	0.02
	22.6	0.12	0.1	0.11	0.28
	30	-0.29	0.06	-0.18	0.36
0	30	0.01	0.16	0.07	0.40
0.0625	22.6	0.30	-0.03	0.23	0.15
	30	-0.07	0.10	0.11	0.41
0.125	30	0.05	0.16	0.11	0.40

Table 3.4 Relative and absolute locations of vortex core centers

**(b) Blade tip-vortex core**

$\Delta/c$	$X/c$	$y/c$	$z/c$	$Y/c$	$Z/c$
-0.125	30	-0.32	-0.64	-0.14	-0.33
-0.0625	22.6	-0.34	-0.49	-0.35	-0.31
	30	-0.28	-0.58	-0.17	-0.28
0	30	-0.24	-0.49	-0.18	-0.25
0.0625	22.6	-0.32	-0.42	-0.39	-0.24
	30	-0.38	-0.55	-0.20	-0.24
0.125	30	-0.32	-0.48	-0.26	-0.24

Table 3.4 Relative and absolute locations of vortex core centers

$\Delta/c$	$X/c$	$r_1/c$	$v_{\theta 1}/U_{ref}$	$\Gamma_1/\Gamma_0$	$(U_{ref}-U_0)/U_{ref}$
-	10	3.8%	27.2%	27.0%	15.3%
-0.125	30	6.6%	8.8%	15.1%	10.2%
-0.0625	15.33	3.1%	19.4%	15.7%	18.7%
	22.6	10%	6.1%	15.9%	10%
	30	14.5%	4.5%	17.1%	6.3%
0.0625	22.6	4.2%	13.2%	14.5%	14.7%
	30	9.3%	7.0%	17.0%	7.2%
0.125	30	5%	17.7%	23.0%	13.8%

Table 3.5 Parameters of the primary vortex core; core radius  $r_1/c$ , peak tangential velocity  $v_{\theta 1}/U_{ref}$ , core circulation  $\Gamma_1/\Gamma_0$ , axial velocity deficit  $(U_{ref}-U_0)/U_{ref}$ .

Blade leading edge

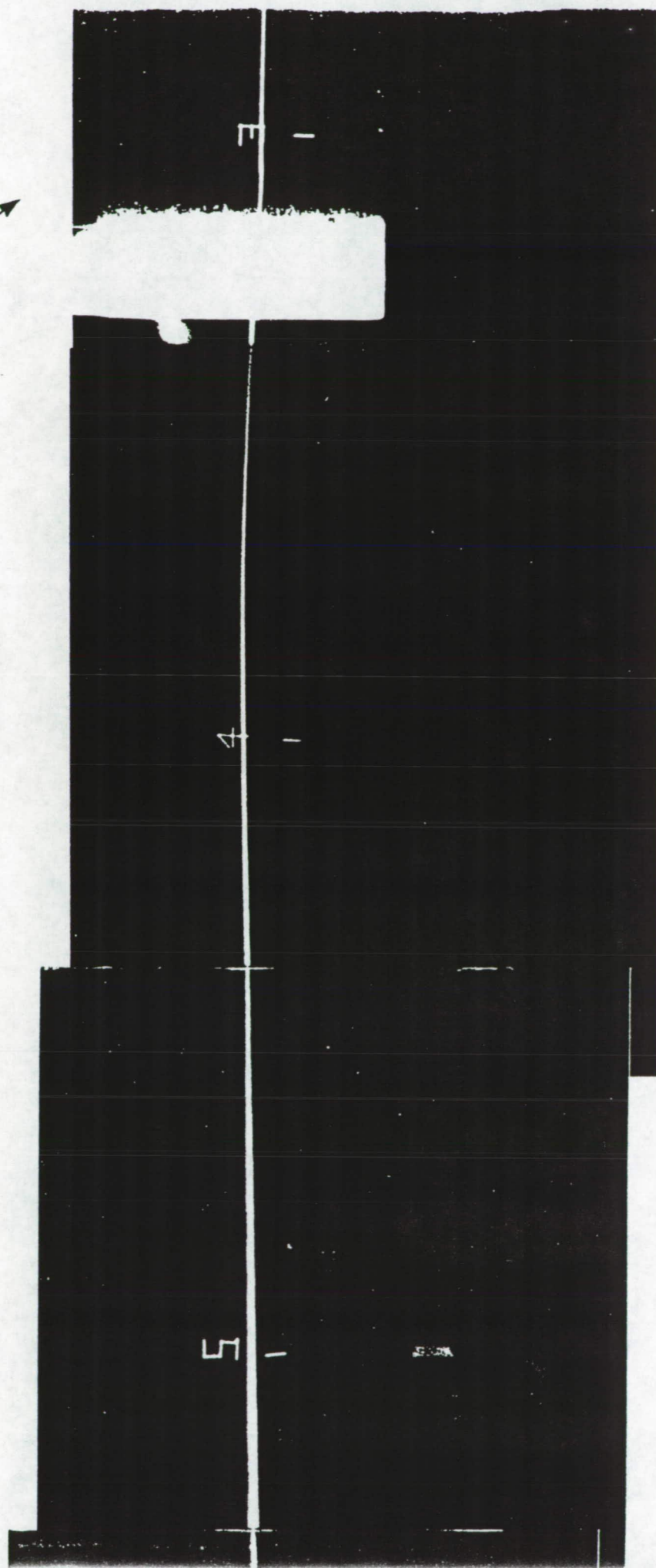


Figure 3.1 Helium-bubble flow visualization of perpendicular blade vortex interaction from Rife et al. (1993). Blade and vortex generator angle of attack =  $5^\circ$ ,  $Re_c = 260,000$ . Vortex passing pressure side of blade (a)  $\Delta/c = -0.125$ .



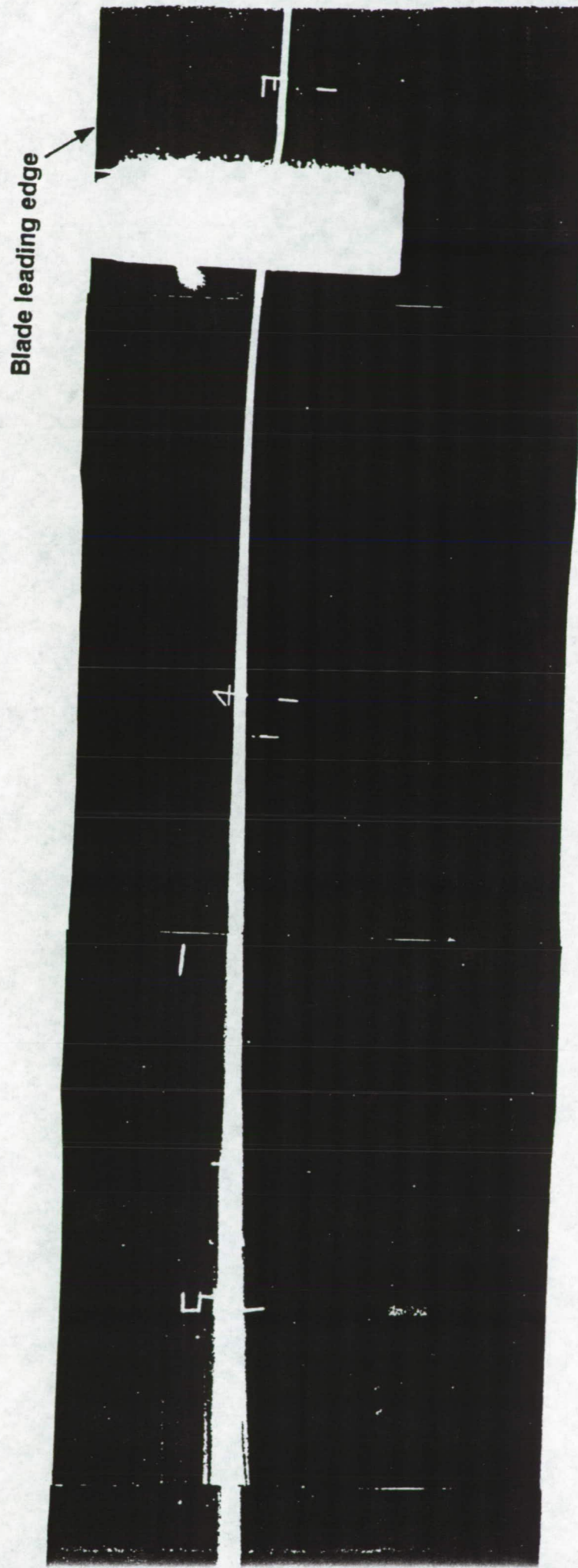


Figure 3.2 Helium-bubble flow visualization of perpendicular blade vortex interaction from Rife et al. (1993). Blade and vortex generator angle of attack =  $5^\circ$ ,  $Re_c = 260,000$ . Vortex passing pressure side of blade  $\Delta/c = -0.0625$ .

Blade leading edge

Figure 3.3 Helium-bubble flow visualization of perpendicular blade vortex interaction from Rife et al. (1993). Blade and vortex generator angle of attack =  $5^\circ$ ,  $Re_c = 260,000$ . Vortex passing suction side of blade  $\Delta c=0.125$ .



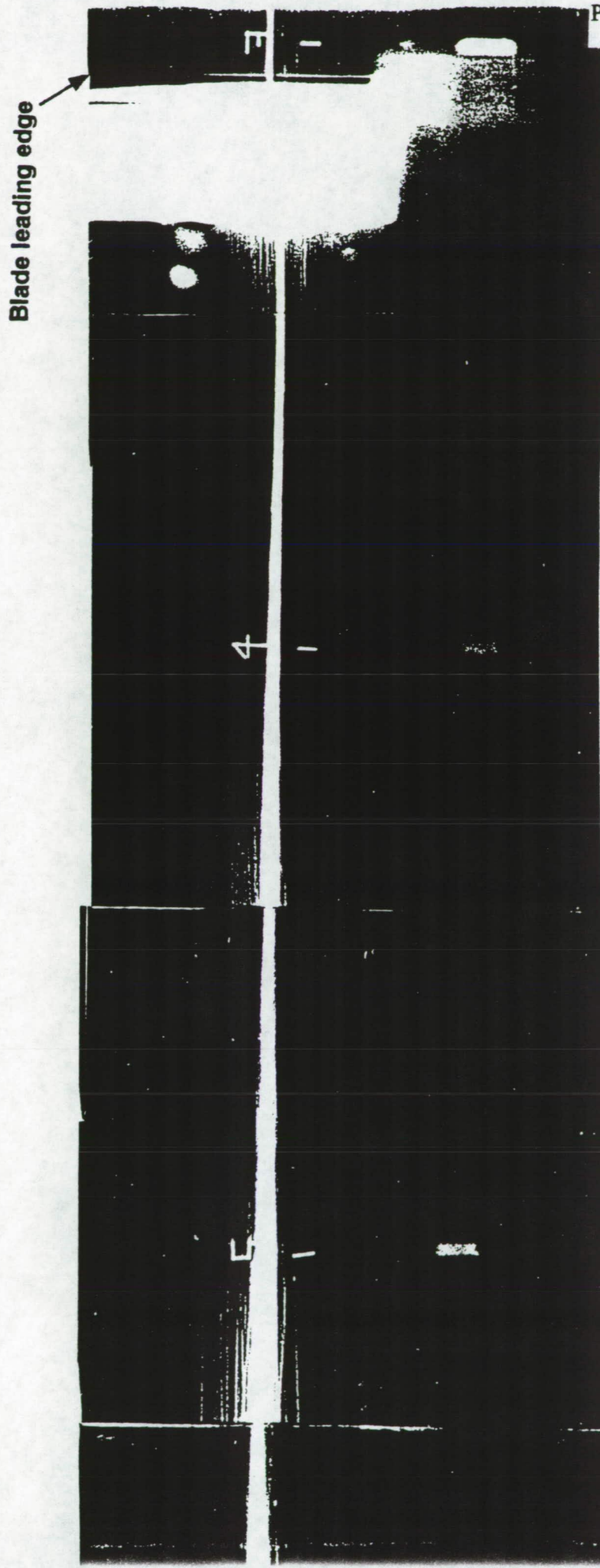
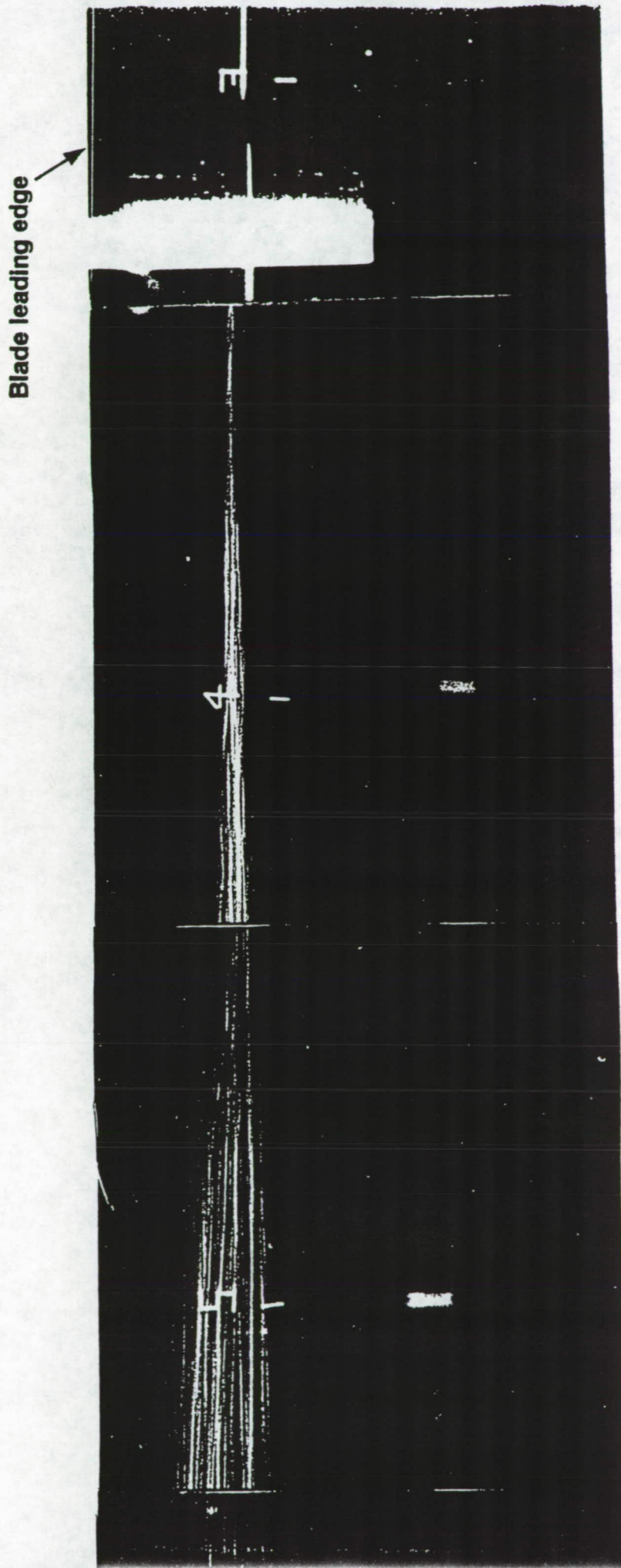


Figure 3.4 Helium-bubble flow visualization of perpendicular blade vortex interaction from Rife et al. (1993). Blade and vortex generator angle of attack =  $5^\circ$ ,  $Re_c = 260,000$ . Vortex passing suction side of blade  $\Delta/c=0.0625$ .



(a)

Figure 3.5 Helium-bubble flow visualization of perpendicular blade vortex interaction from Rife et al. (1993). Blade and vortex generator angle of attack =  $5^\circ$ .  $Re_c = 260,000$ . Vortex impinging on blade leading edge.  $\Delta c=0$ .

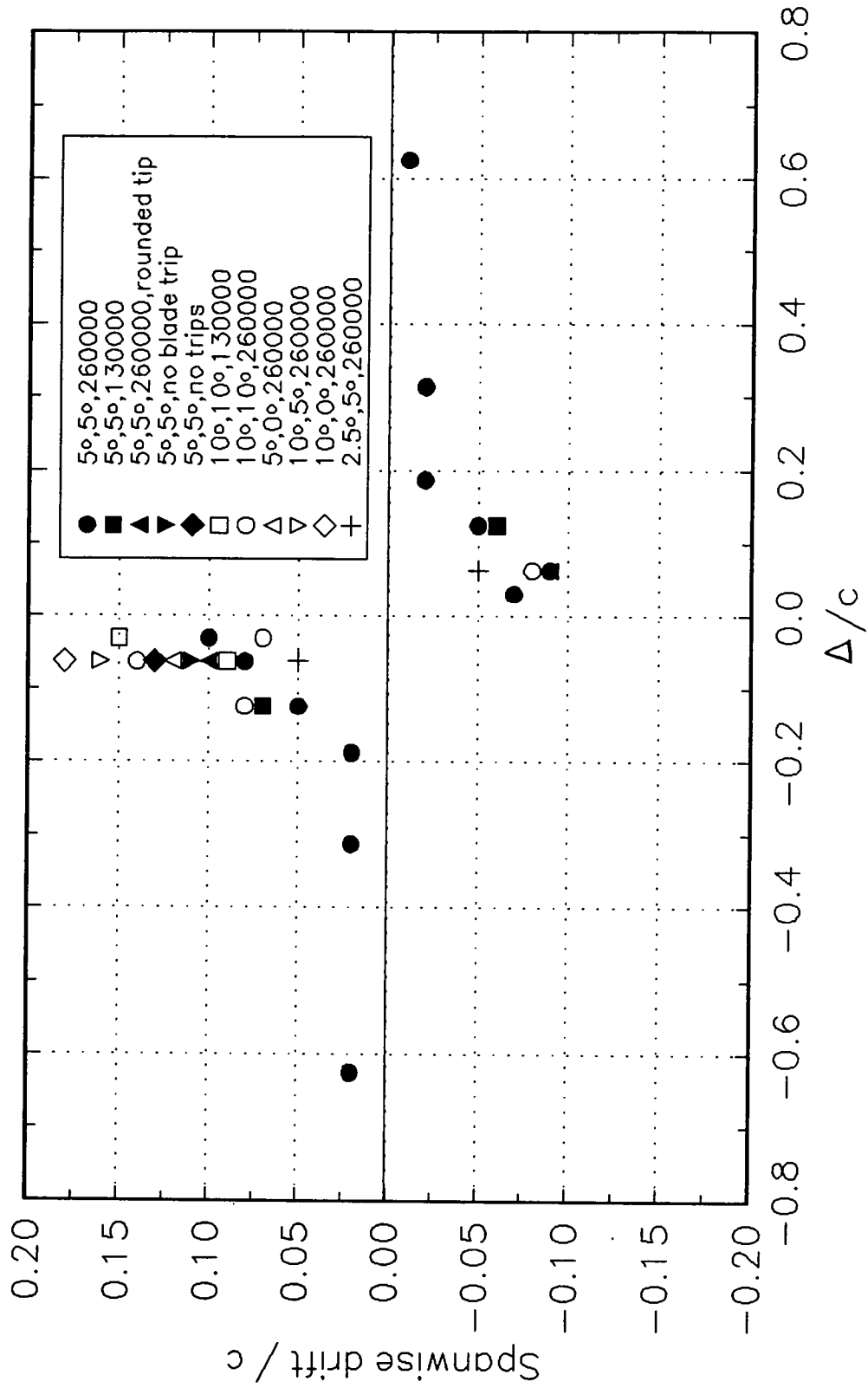


Figure 3.6 Spanwise drift of vortex between leading and trailing edges of blade as a function of blade-vortex separation  $\Delta/c$ . Numbers in legend are, respectively, angle of attack of vortex generator, angle of attack of blade, chord Reynolds number.

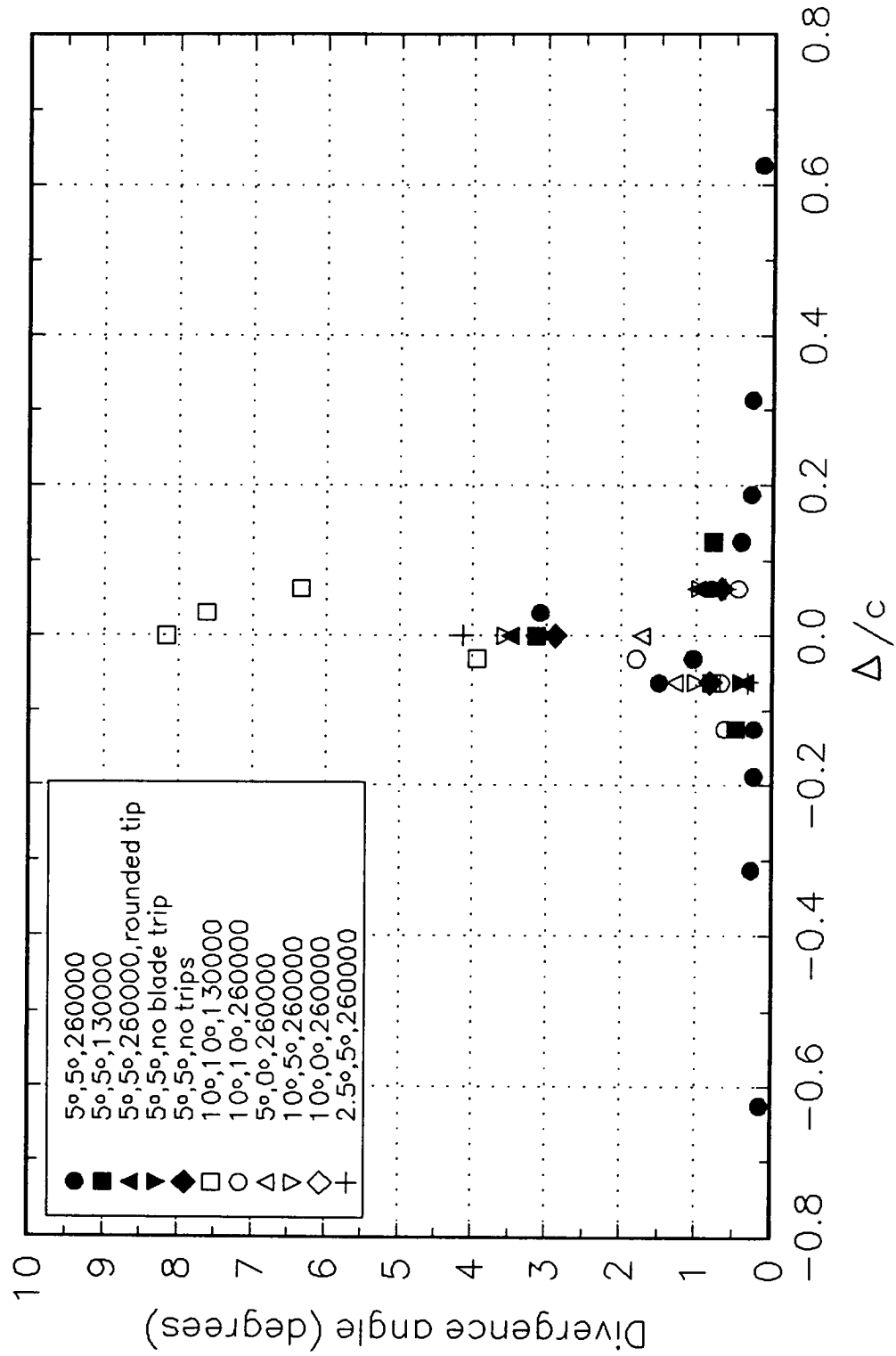


Figure 3.7 Divergence angle of bubble stream marking core as a function of blade-vortex separation  $\Delta/c$ . Numbers in legend are, respectively, angle of attack of vortex generator, angle of attack of blade, chord Reynolds number.

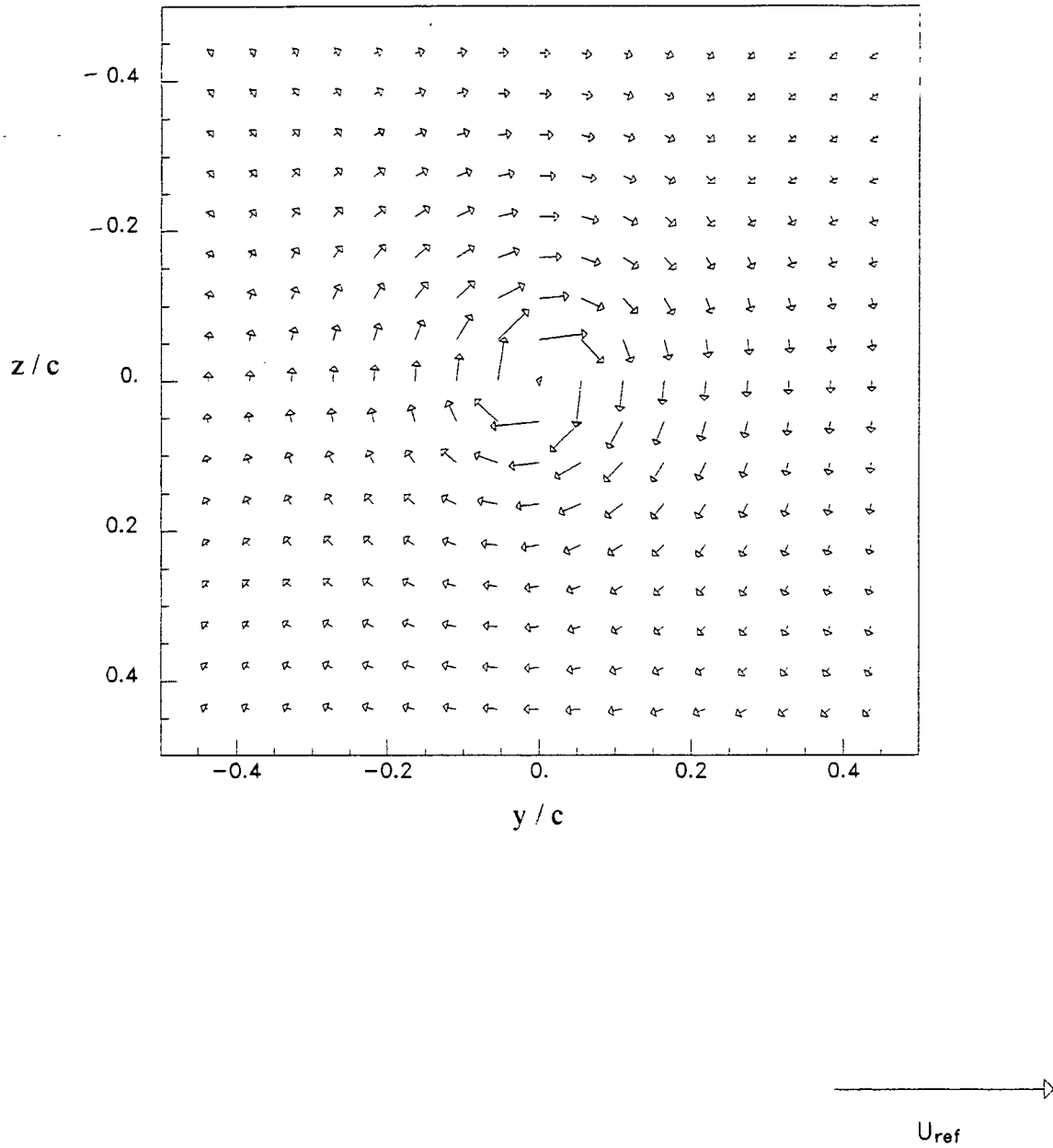


Figure 3.8 Mean cross-flow velocity vectors, approach vortex,  $X/c=10$ .



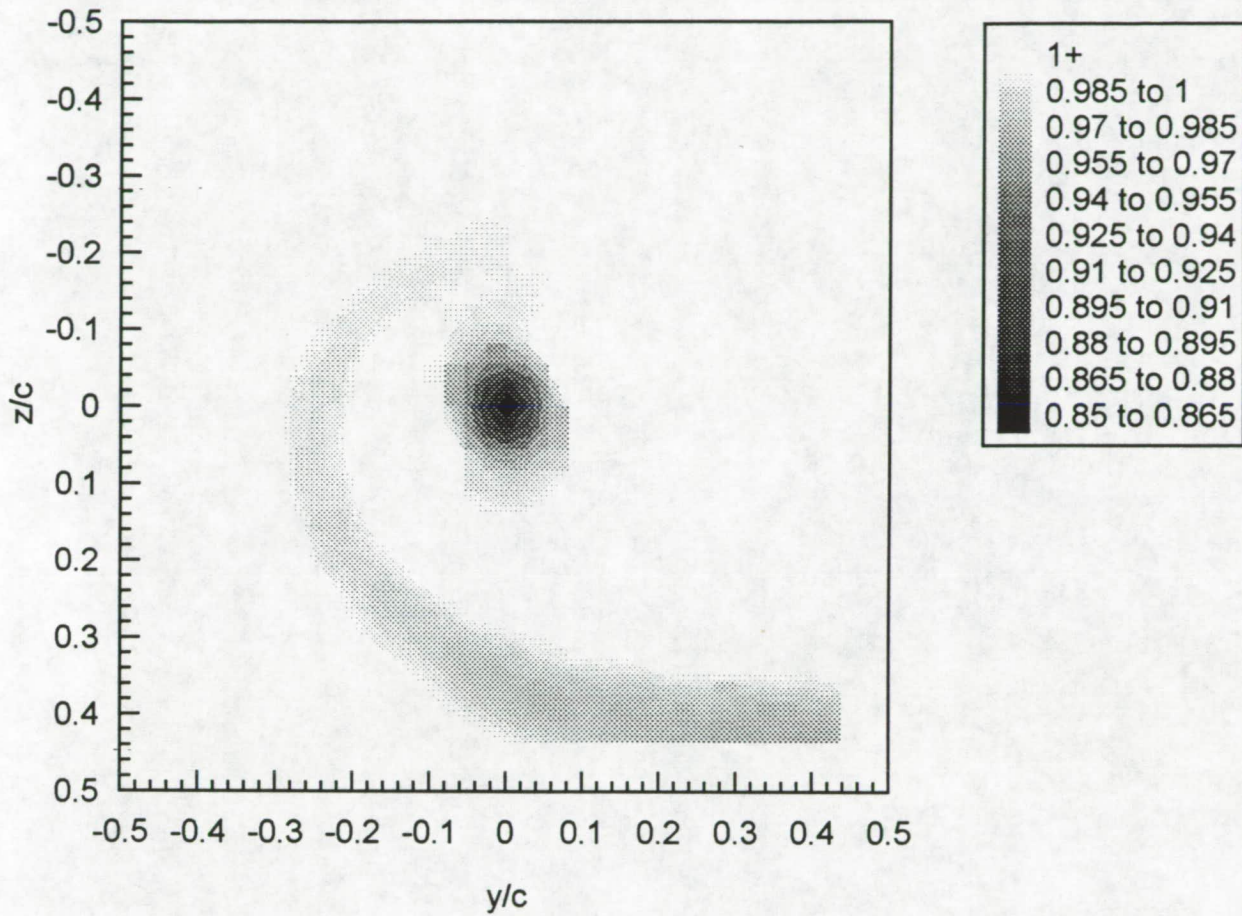


Figure 3.9 Contours of axial mean velocity  $U/U_{ref}$ , approach vortex,  $X/c=10$ .



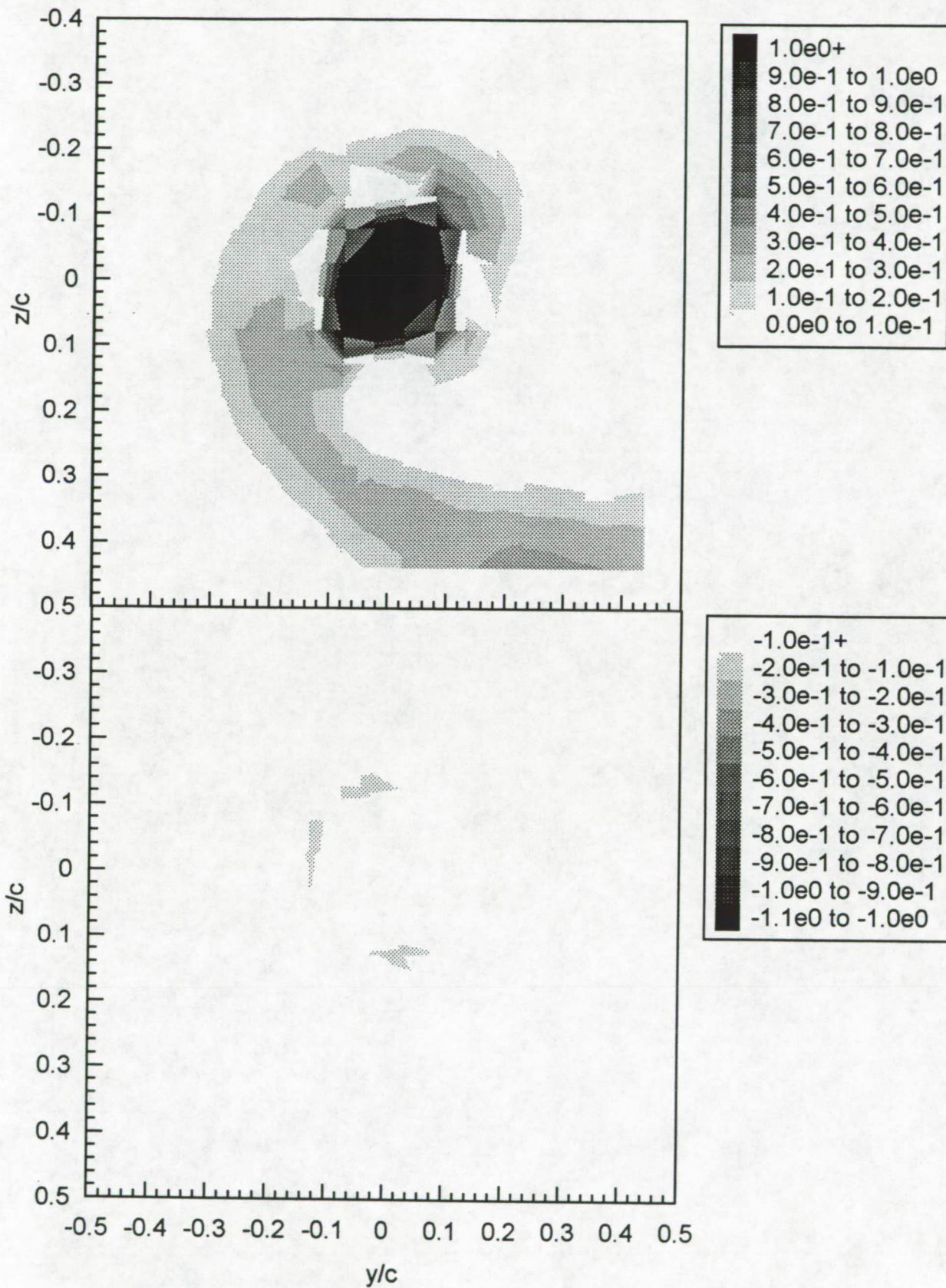


Figure 3.10 Contours of axial mean vorticity  $\omega_x c/U_{ref}$ , approach vortex,  $X/c=10$ . Upper figure - positive vorticity, lower figure - negative vorticity.



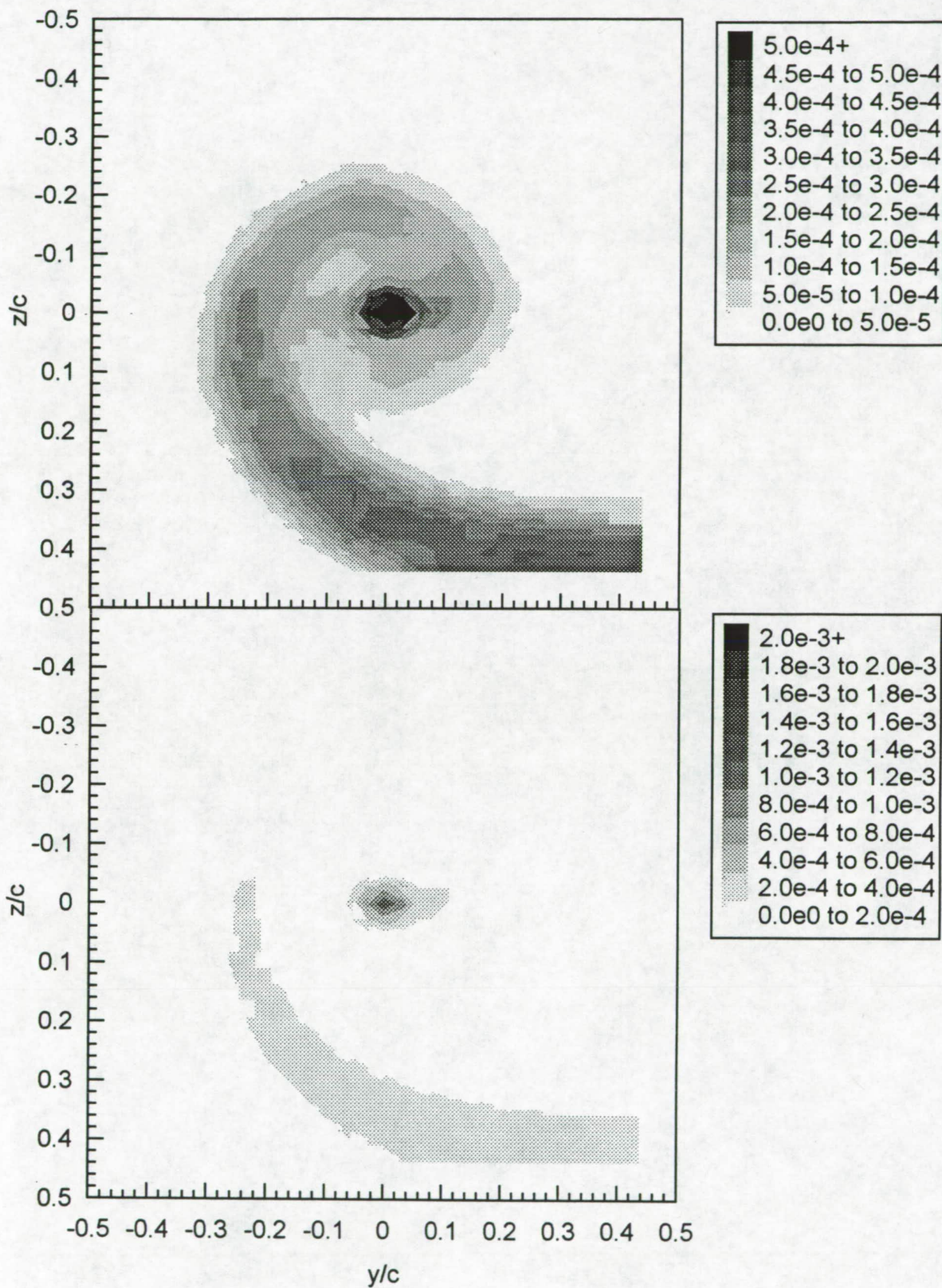


Figure 3.11 Contours of axial normal turbulence stress  $\overline{u'^2}/U_{ref}^2$ , approach vortex,  $X/c=10$ . Upper and lower figures show different contour ranges.



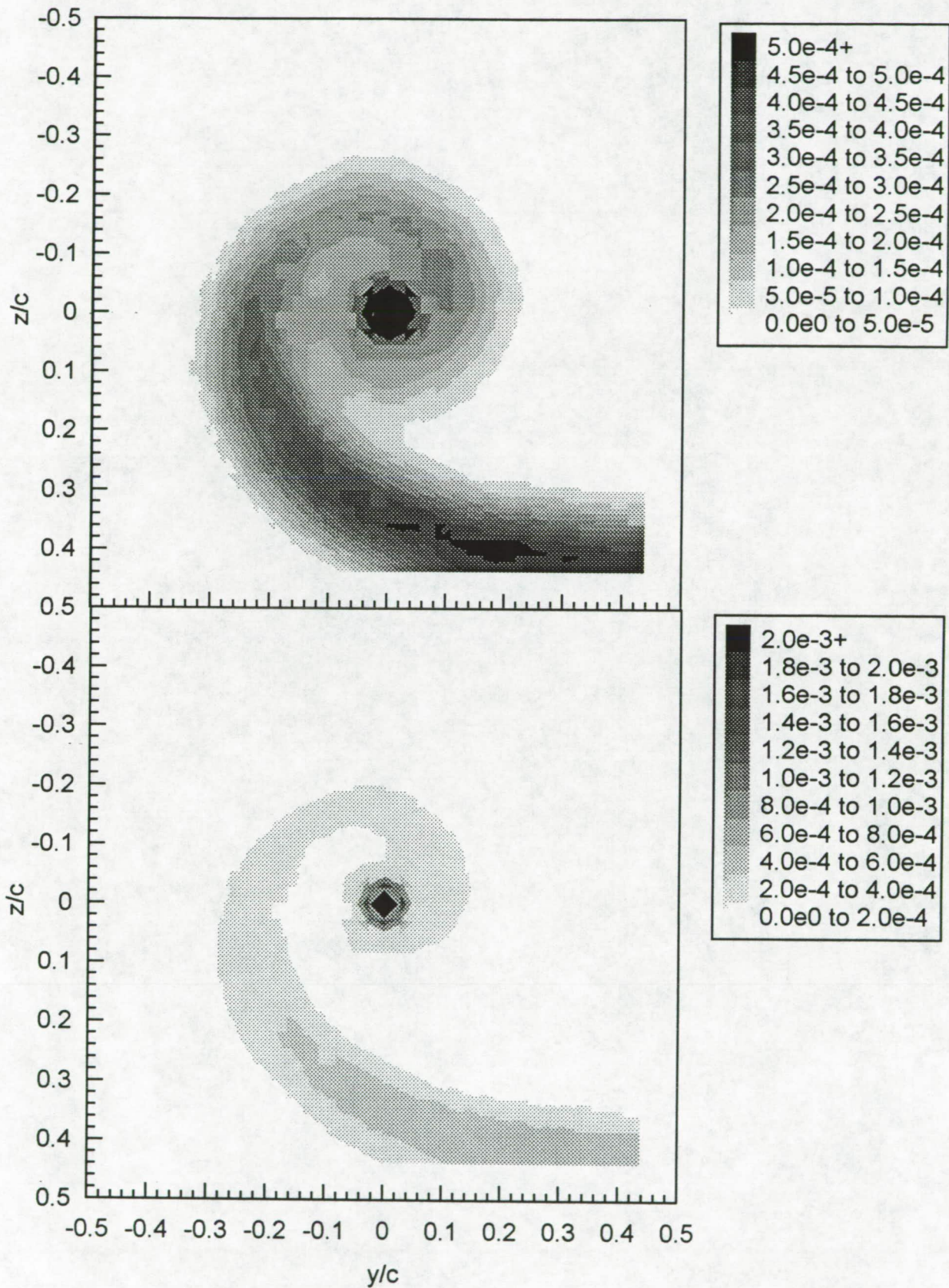


Figure 3.12 Contours of turbulence kinetic energy  $k/U_{ref}^2$ , approach vortex,  $X/c=10$ . Upper and lower figures show different contour ranges.

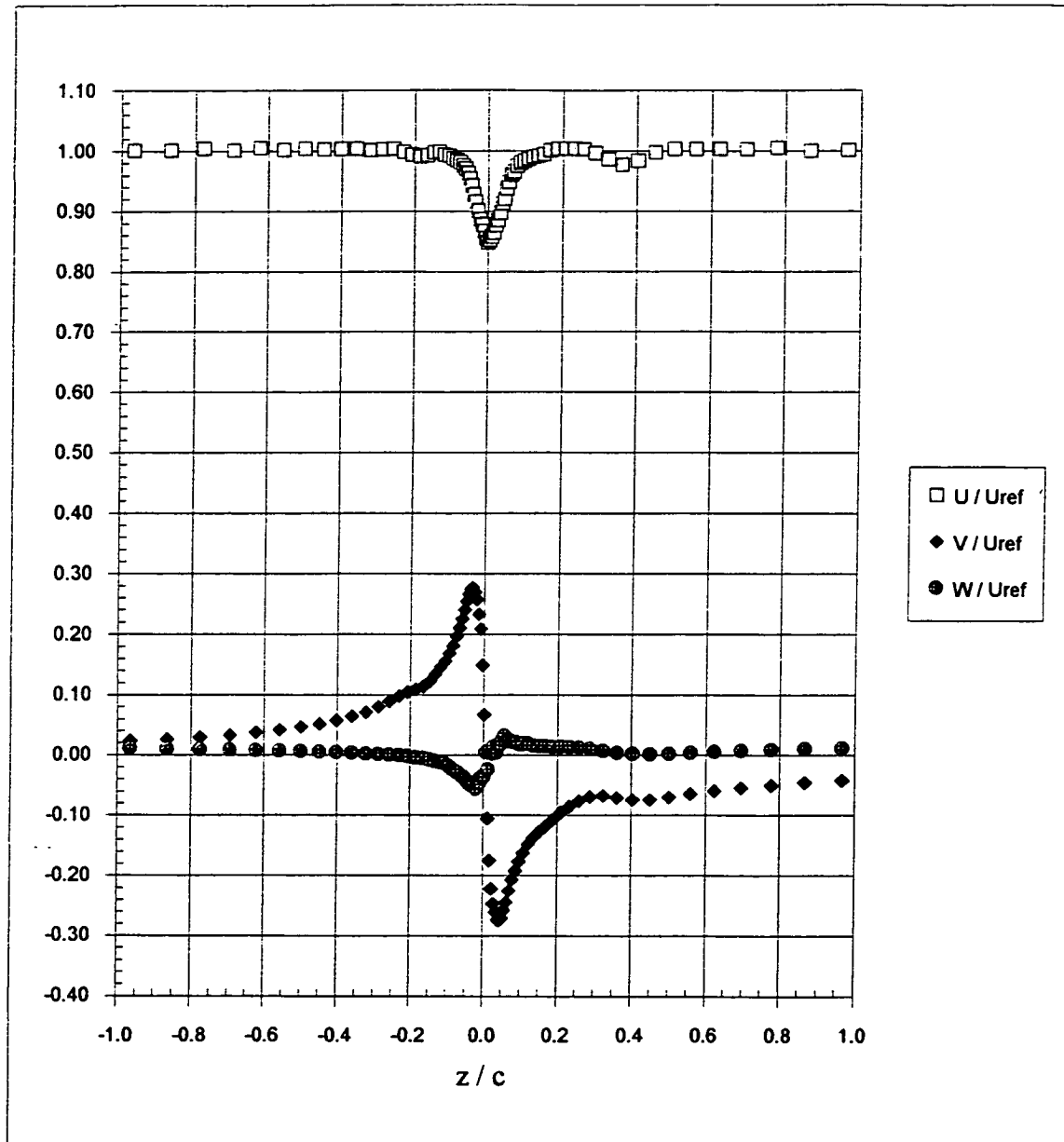


Figure 3.13 Velocity profiles along the line  $y/c=0$ , approach vortex,  $X/c=10$ . (a) Mean velocity.

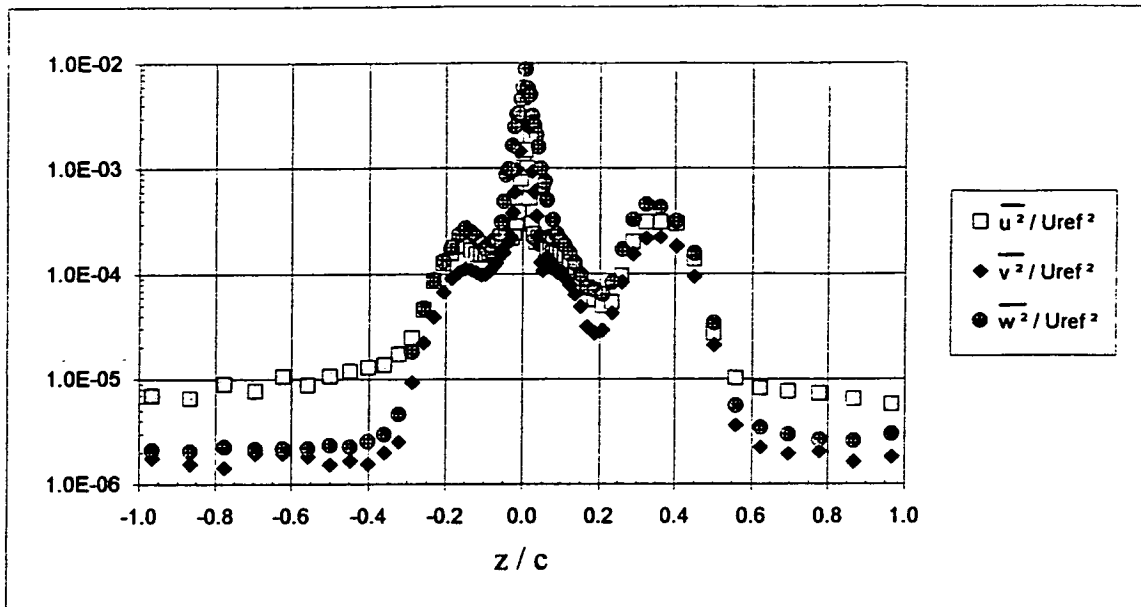


Figure 3.13 Velocity profiles along the line  $y/c=0$ , approach vortex,  $X/c=10$ . (b) Turbulence normal stresses.

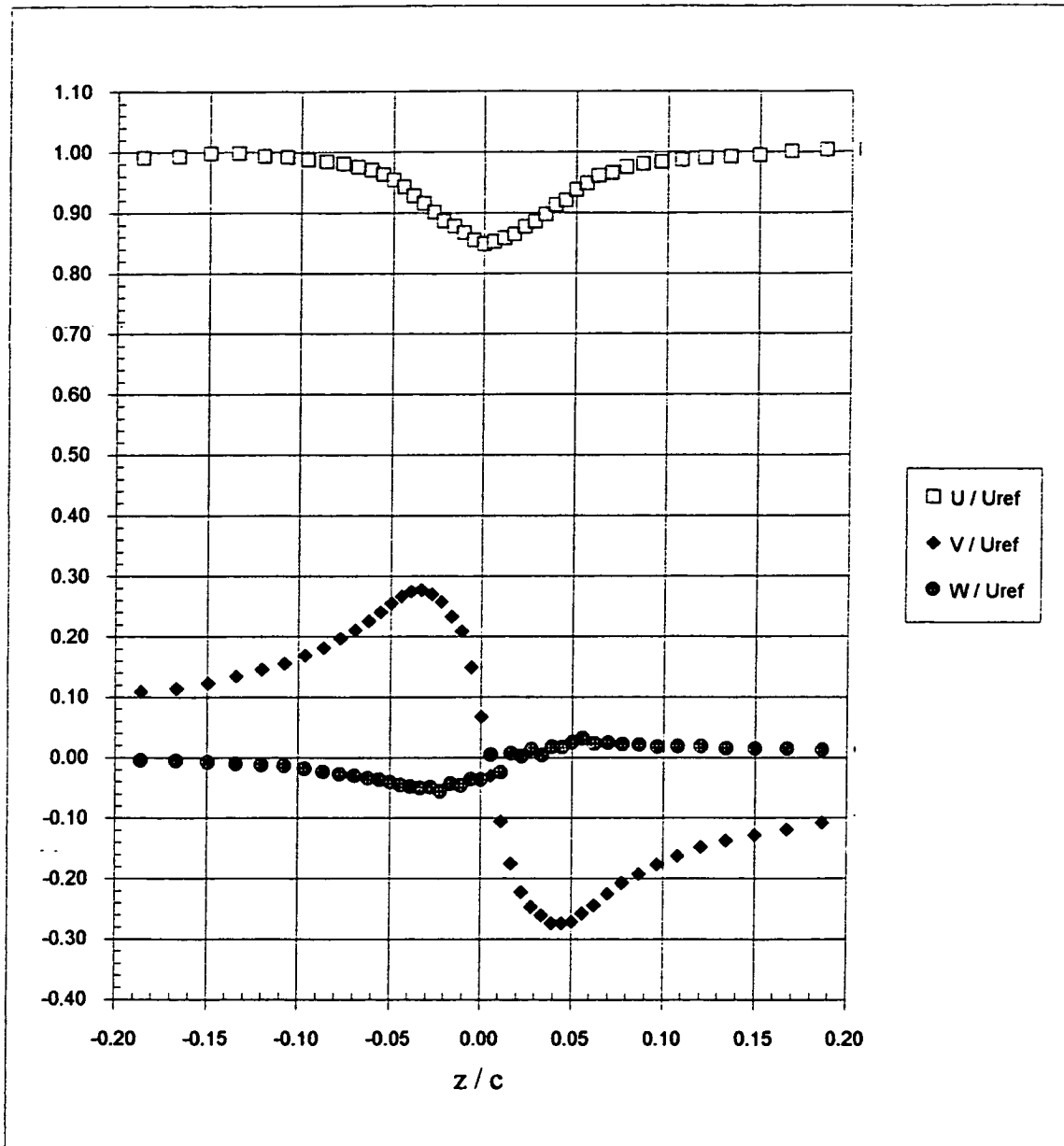


Figure 3.14 Core region velocity profiles along the line  $y/c=0$ , approach vortex,  $X/c=10$ . (a) Mean velocity.

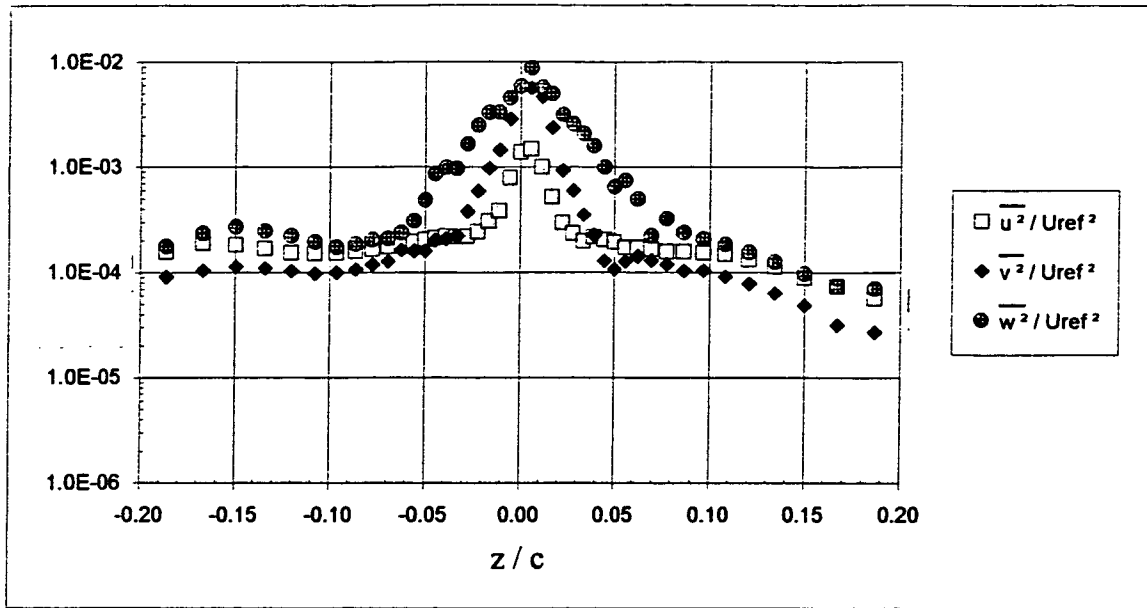


Figure 3.14 Core region velocity profiles along the line  $y/c=0$ , approach vortex,  $X/c=10$ . (b) Turbulence normal stresses.

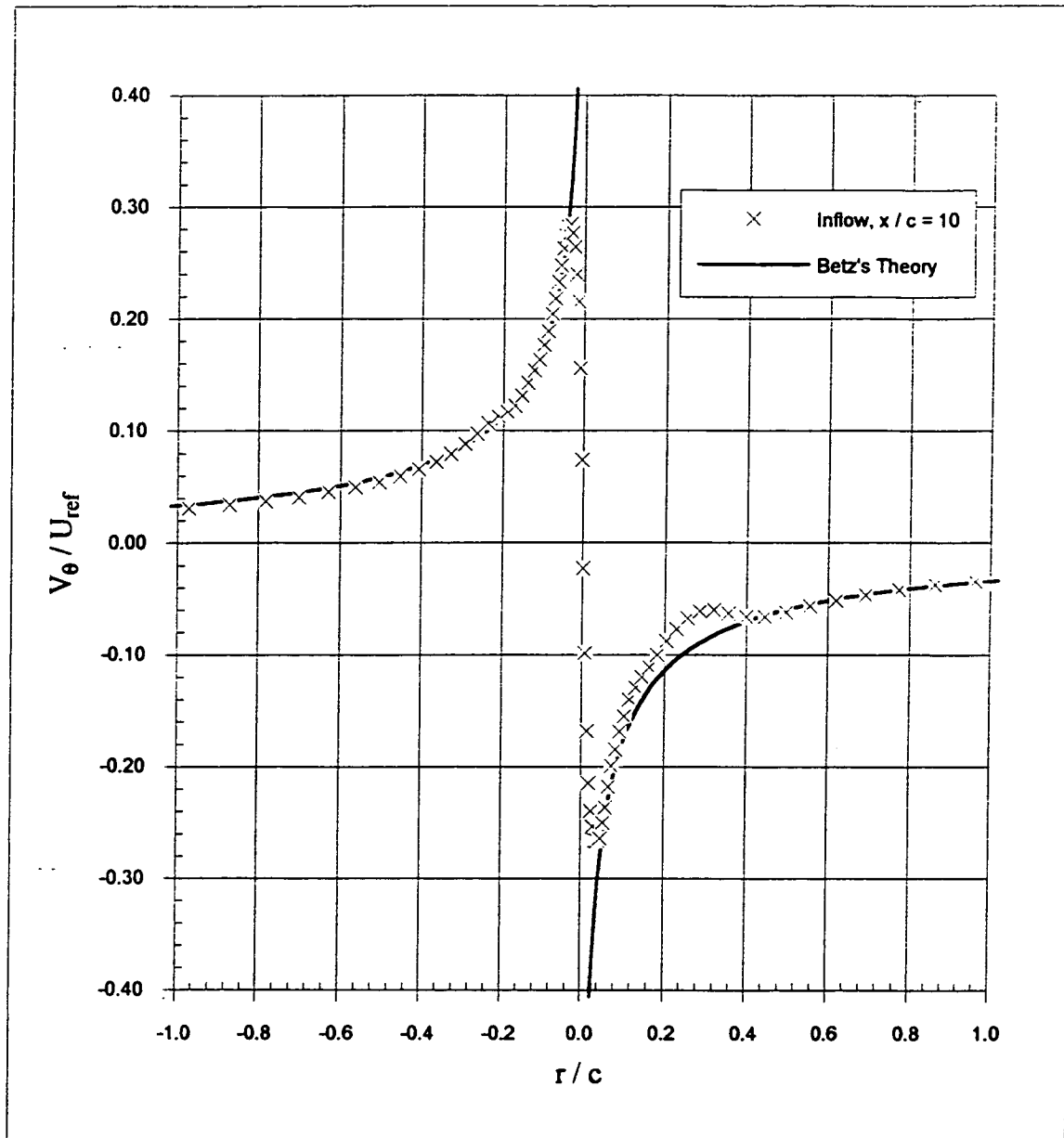


Figure 3.15 Comparison of measured mean tangential velocity profile at  $X/c=10$  and Betz's theory. (a) Whole vortex.



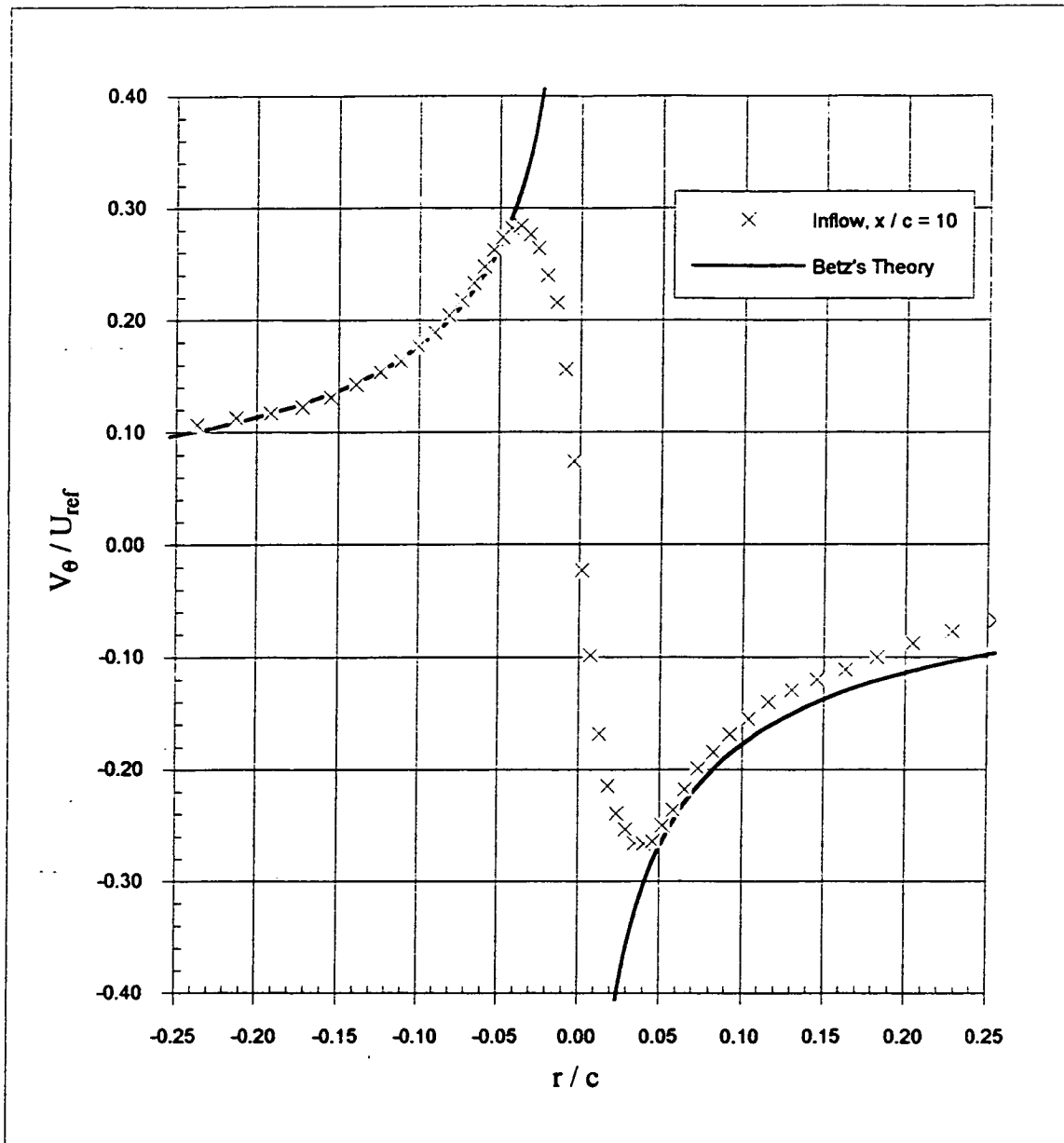


Figure 3.15 Comparison of measured mean tangential velocity profile at  $X/c=10$  and Betz's theory. (b) Core region.

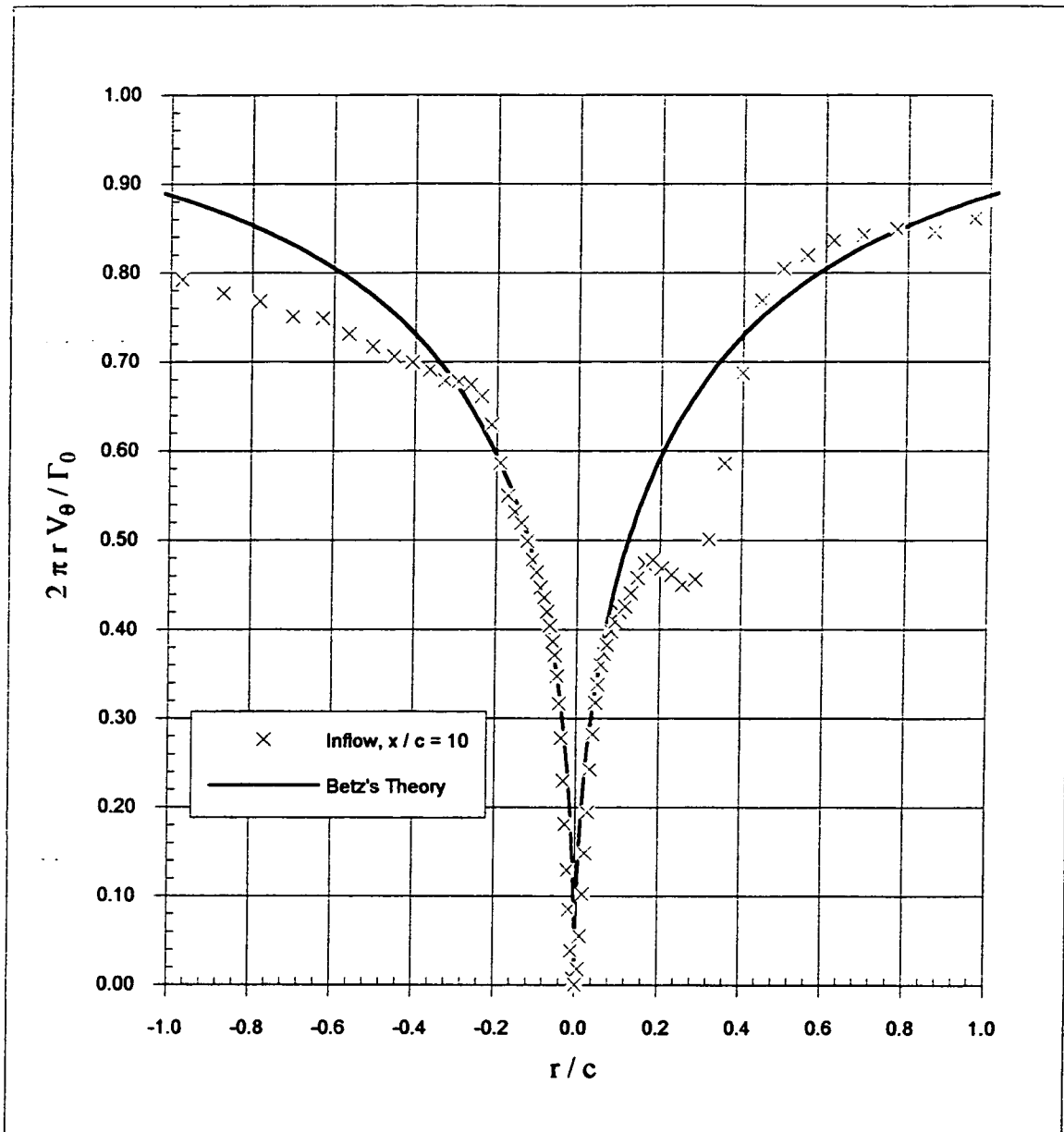


Figure 3.16 Comparison of circulation profile, estimated assuming axisymmetry, at  $X/c=10$  and Betz's theory. (a) Whole vortex.

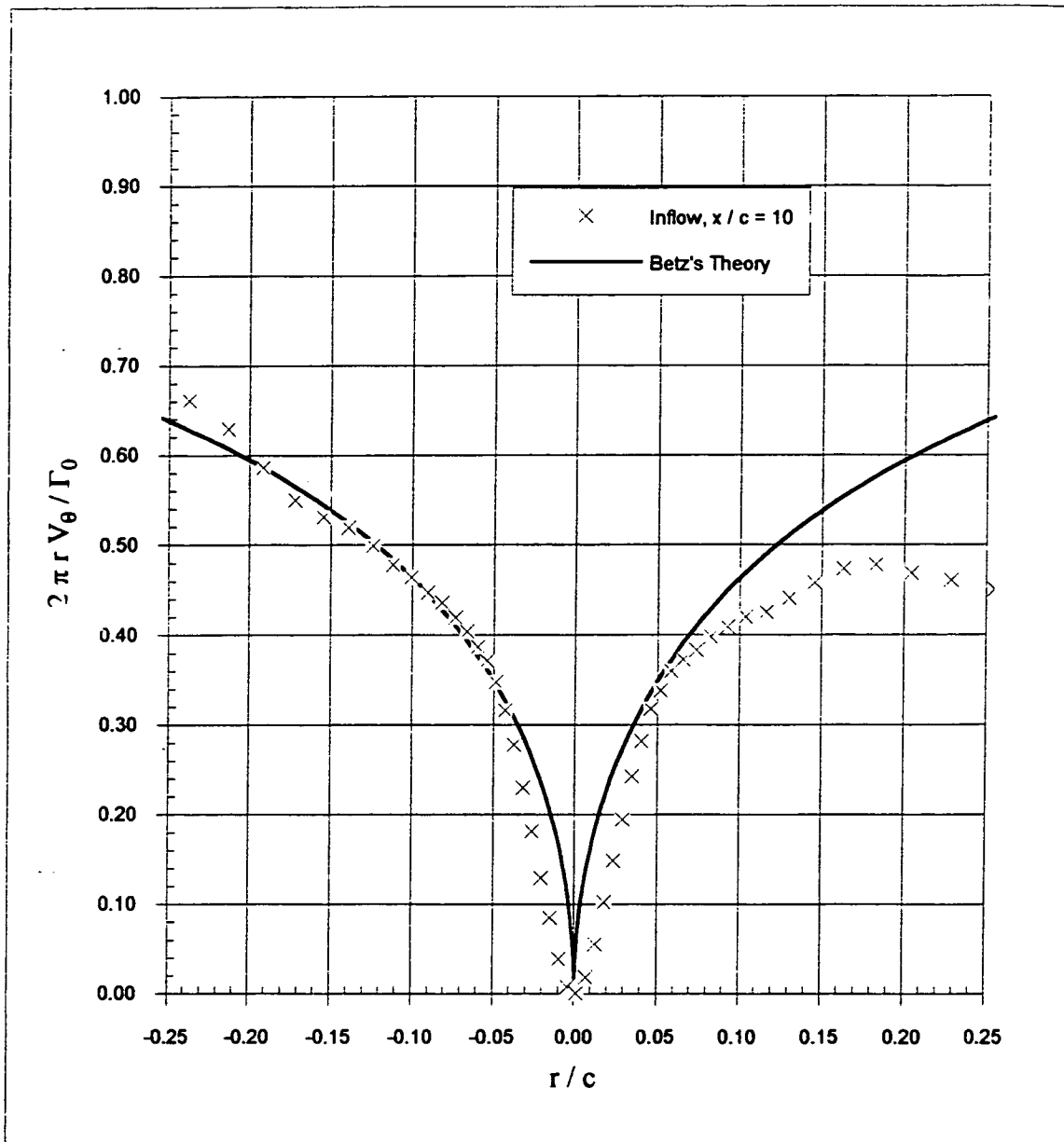


Figure 3.16 Comparison of circulation profile, estimated assuming axisymmetry, at  $X/c=10$  and Betz's theory. (b) Core region.

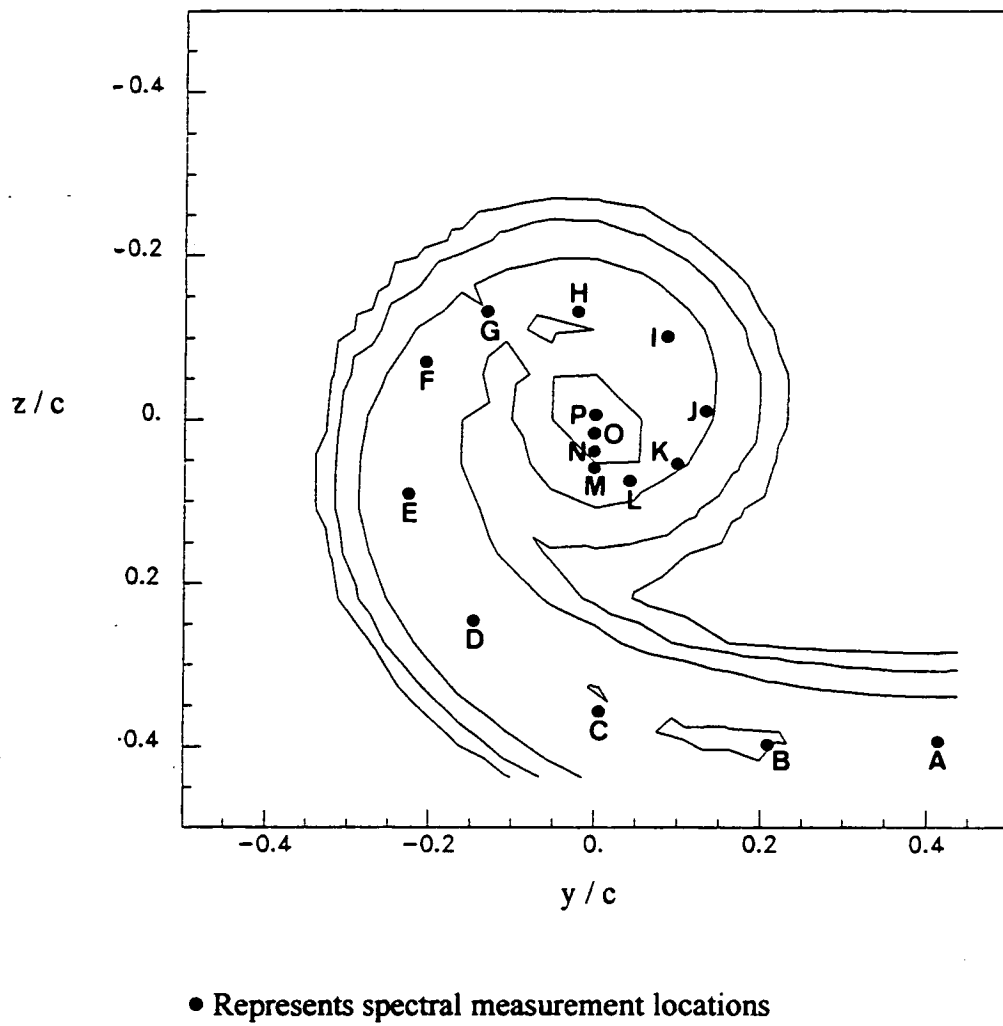
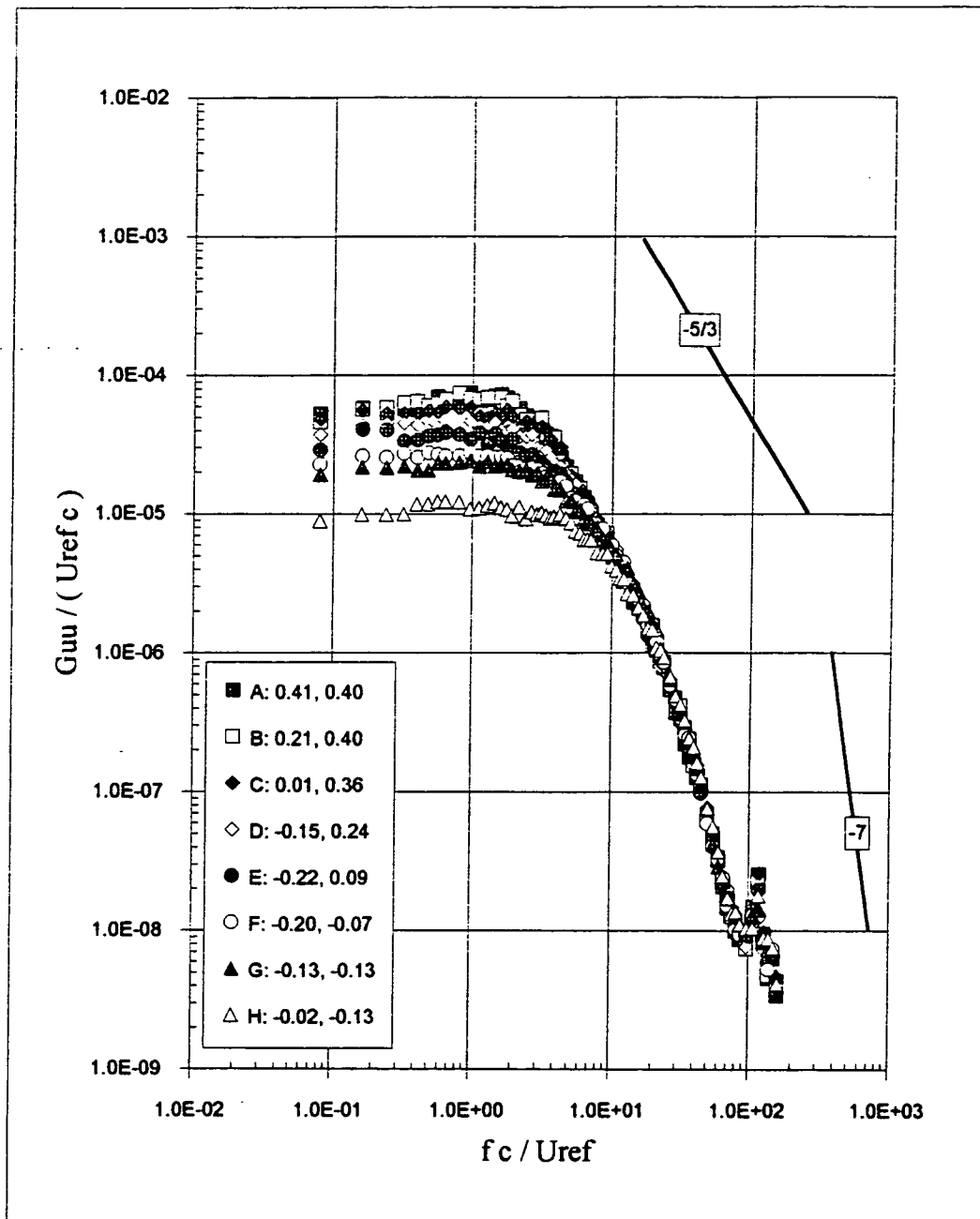
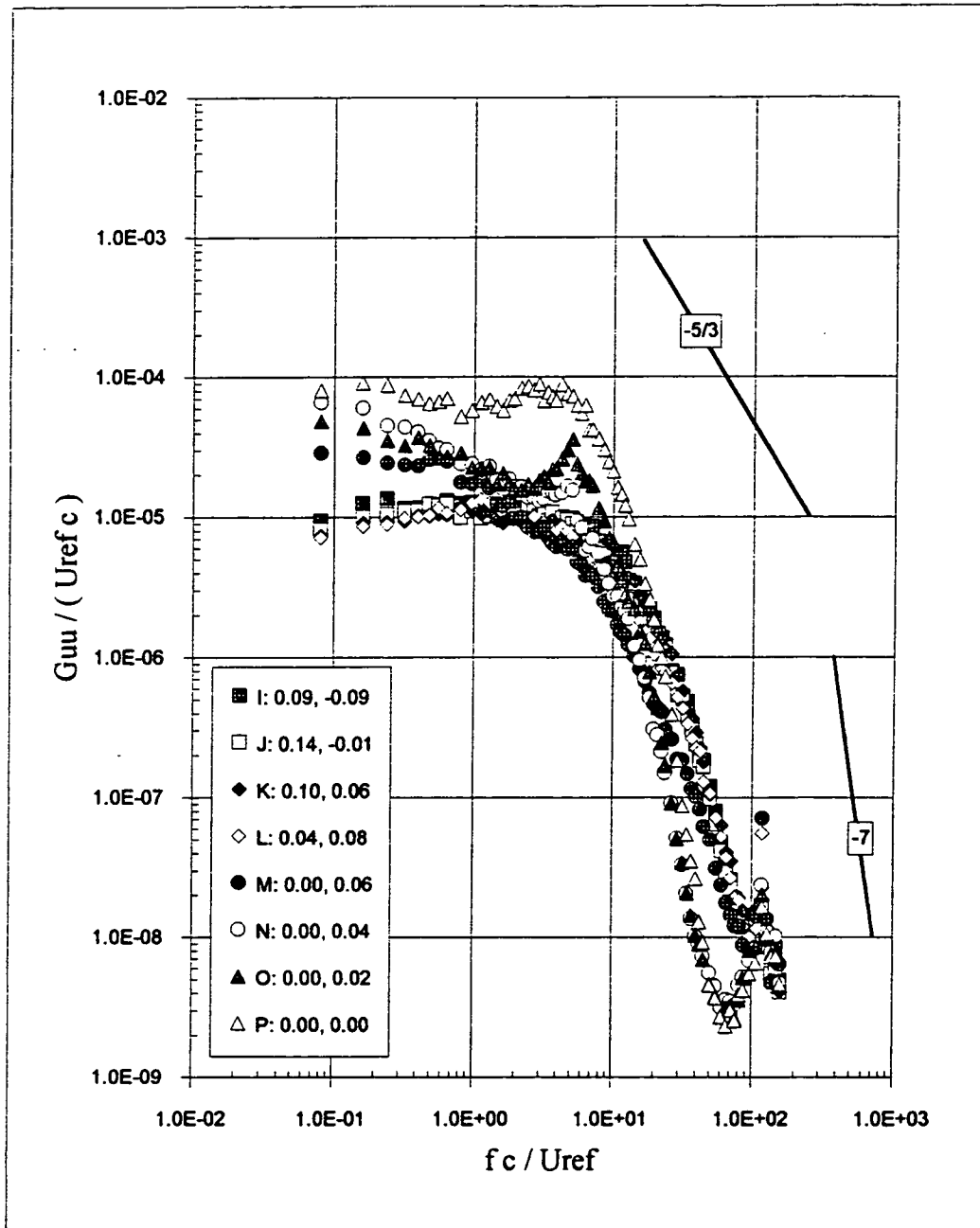


Figure 3.17 Velocity autospectra,  $X/c=10$ . (a) Locations of spectral measurements relative to turbulence kinetic energy contours.



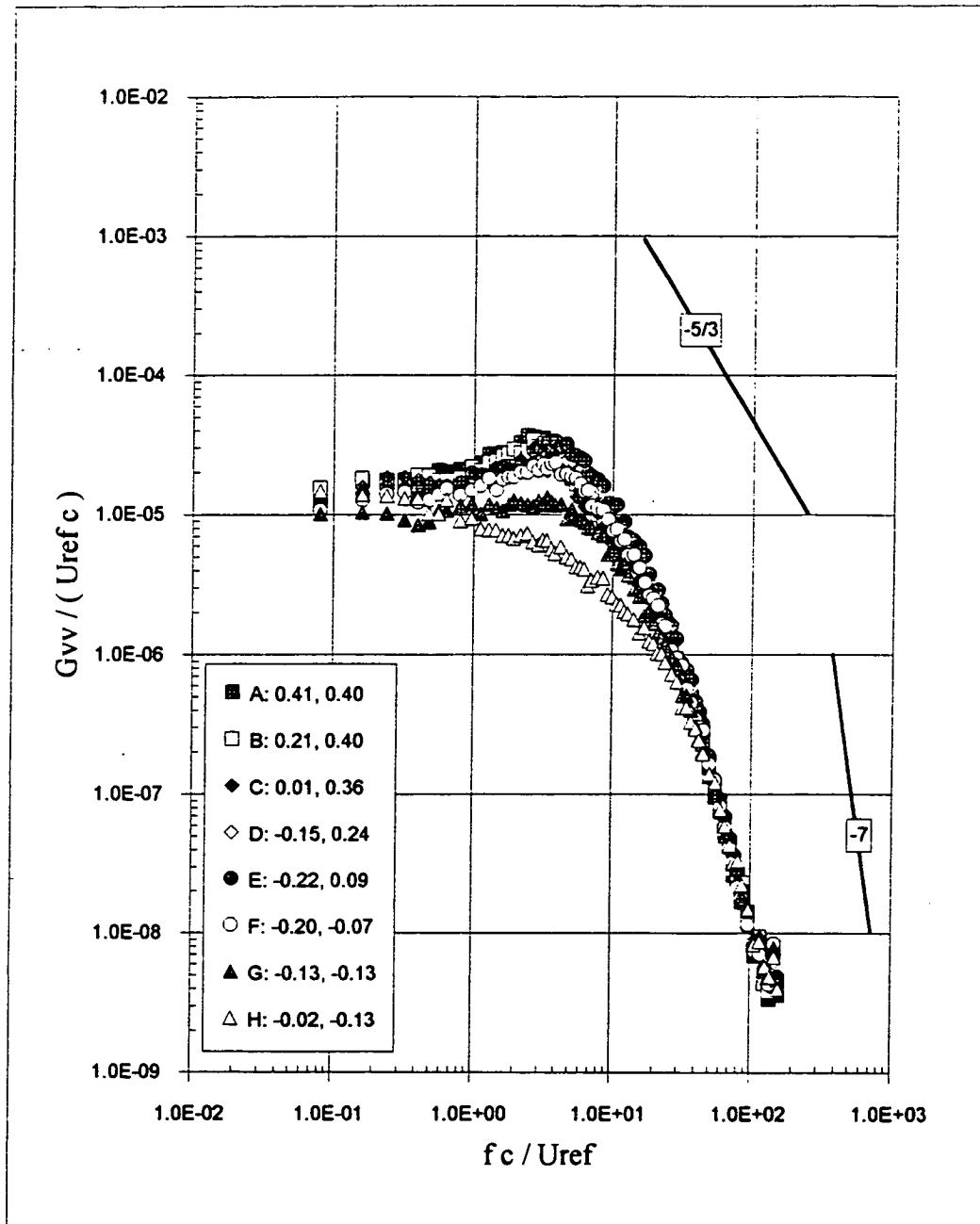
Numbers in legend represent the  $y/c$  and  $z/c$  locations respectively

Figure 3.17 Velocity autospectra at  $X/c=10$ . (b)  $G_{uu}$



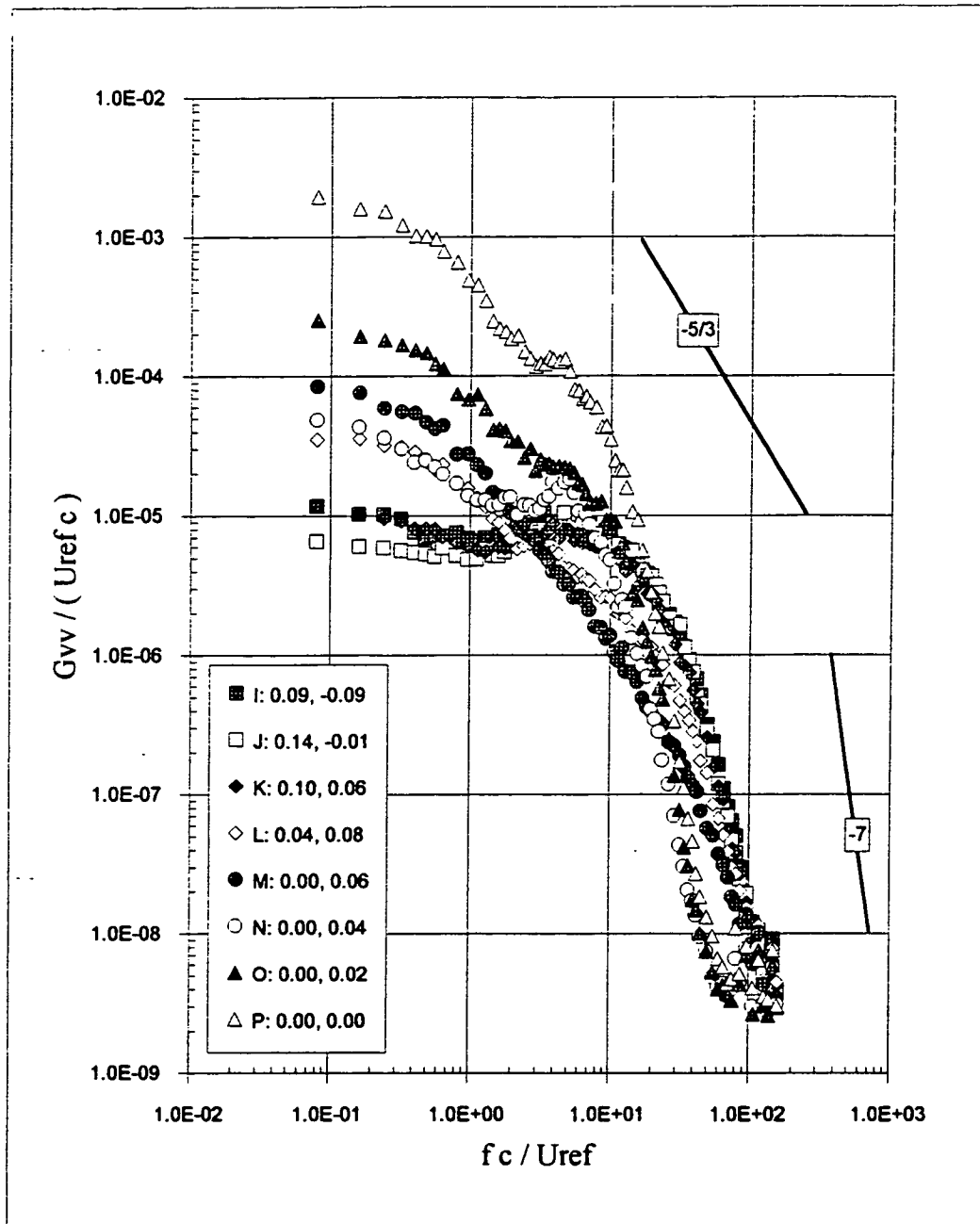
Numbers in legend represent the  $y/c$  and  $z/c$  locations respectively

Figure 3.17 Velocity autospectra at  $X/c=10$ . (c)  $G_{uu}$  contd.



Numbers in legend represent the  $y/c$  and  $z/c$  locations respectively

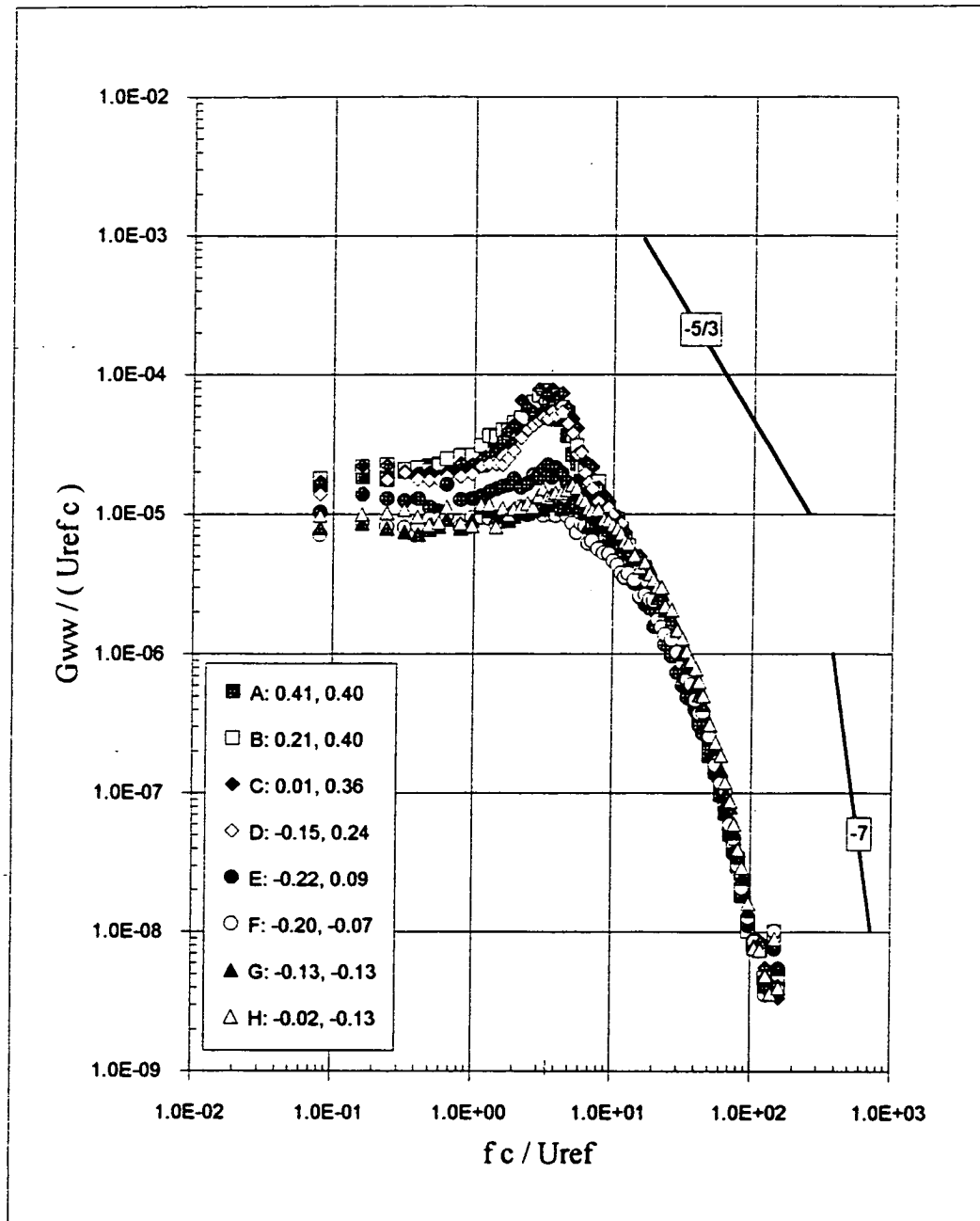
Figure 3.17 Velocity autospectra at  $X/c=10$ . (d)  $G_{vv}$



Numbers in legend represent the  $y/c$  and  $z/c$  locations respectively

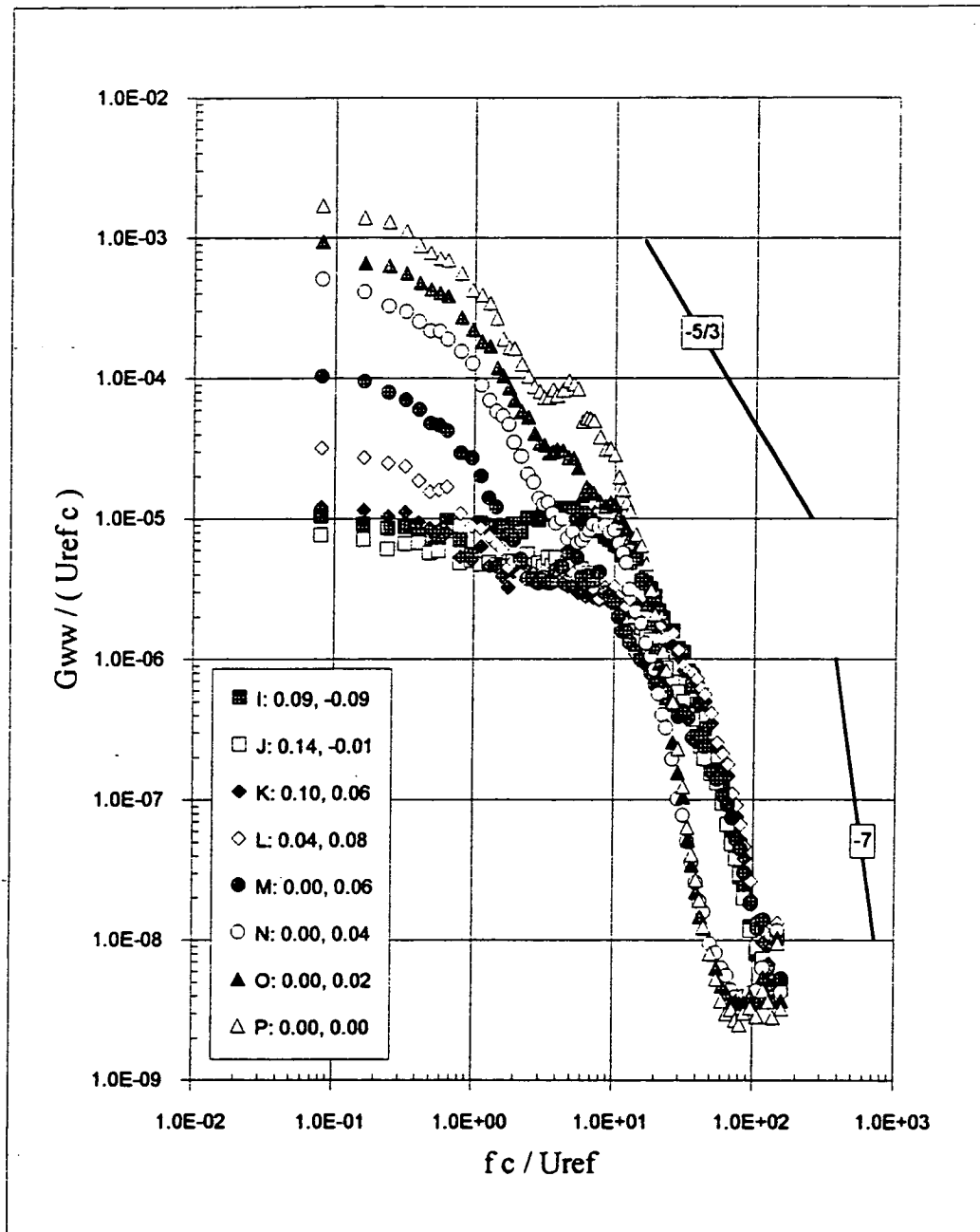
Figure 3.17 Velocity autospectra at  $X/c=10$ . (e)  $G_w$  contd.





Numbers in legend represent the  $y/c$  and  $z/c$  locations respectively

Figure 3.17 Velocity autospectra at  $X/c=10$ . (f)  $G_{ww}$



Numbers in legend represent the  $y / c$  and  $z / c$  locations respectively

Figure 3.17 Velocity autospectra at  $X/c=10$ . (g)  $G_{ww}$  contd.

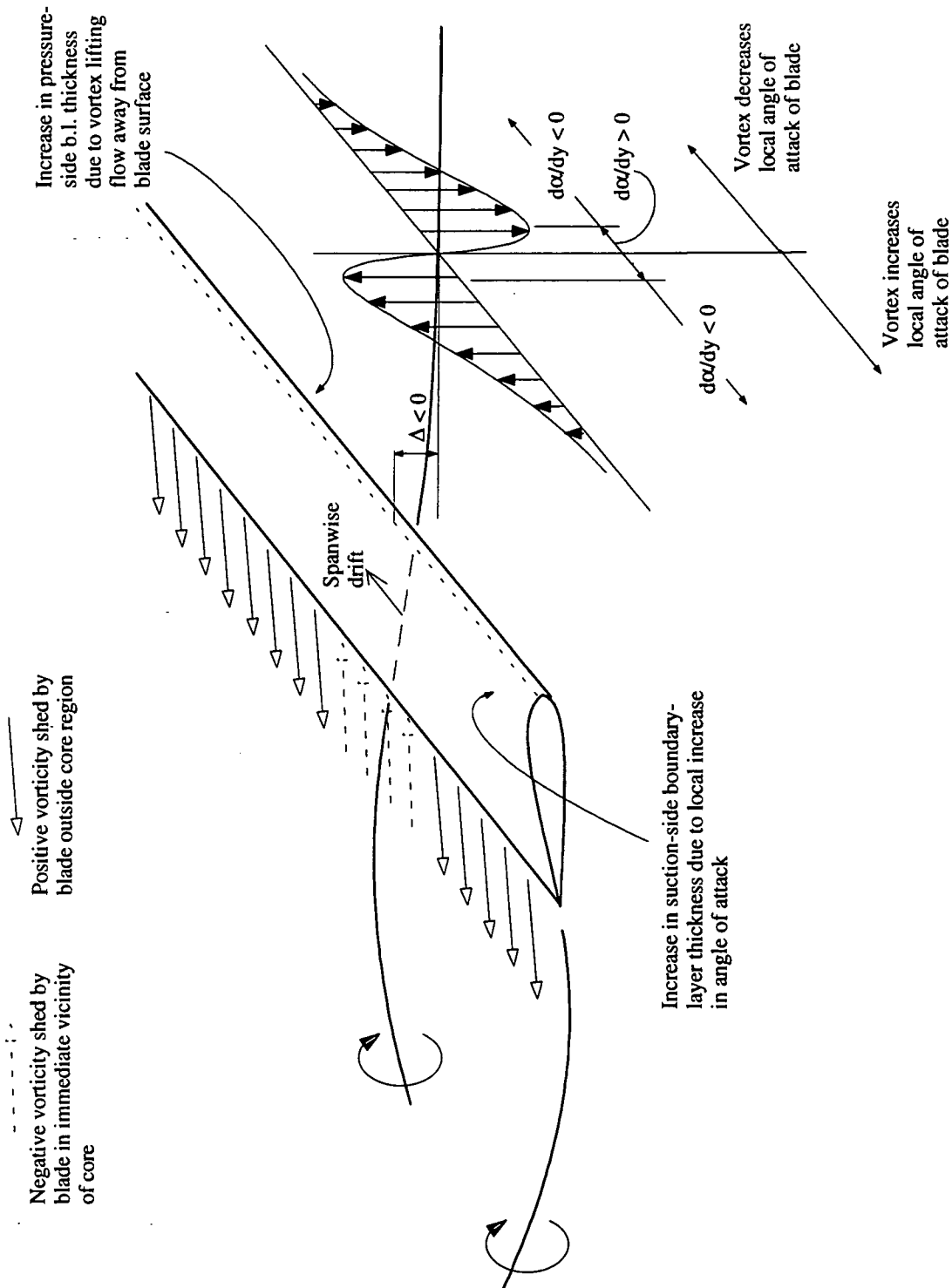


Figure 3.18 Expected flow structure with vortex passing to pressure side of blade

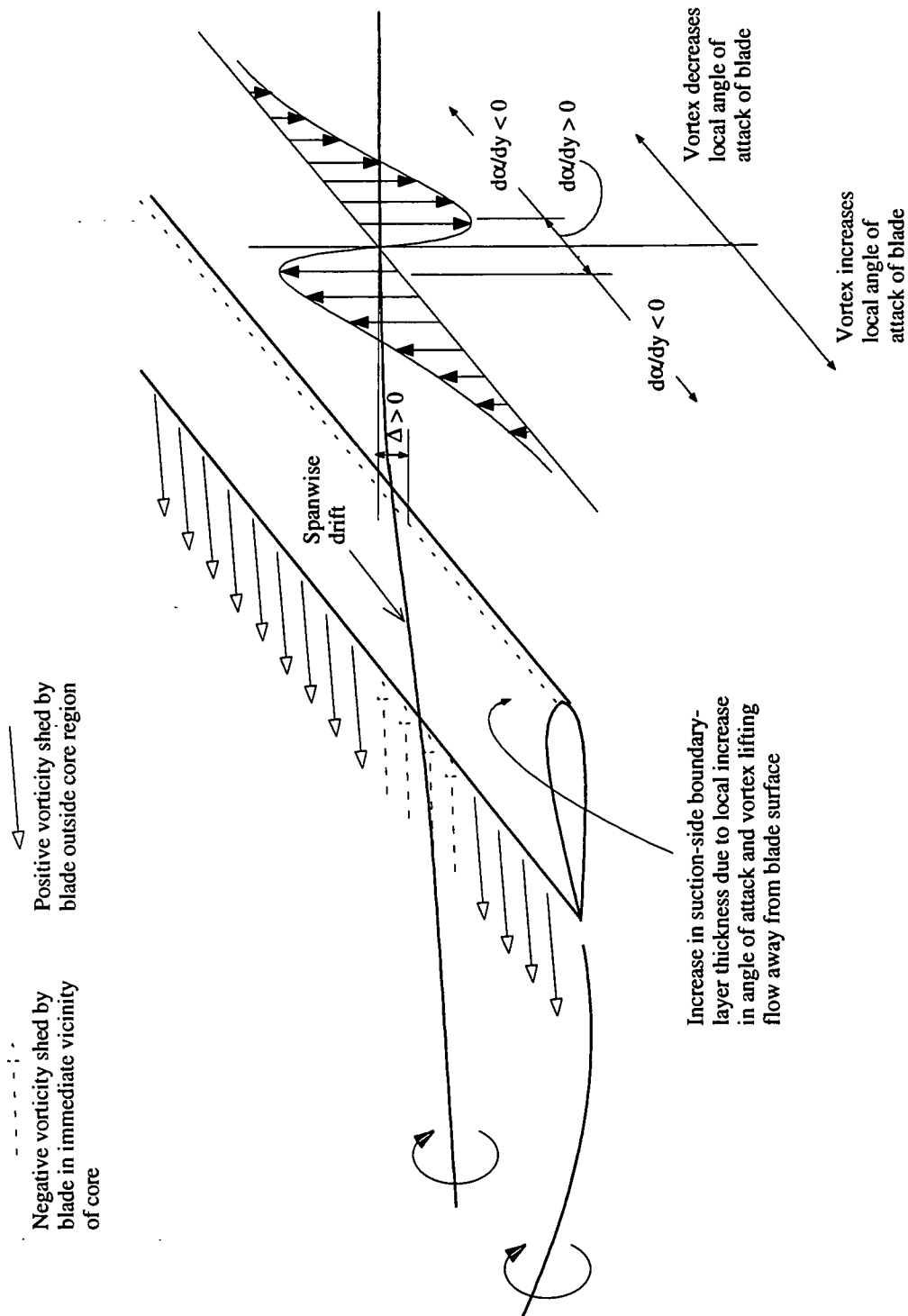


Figure 3.19 Expected flow structure with vortex passing to suction side of blade

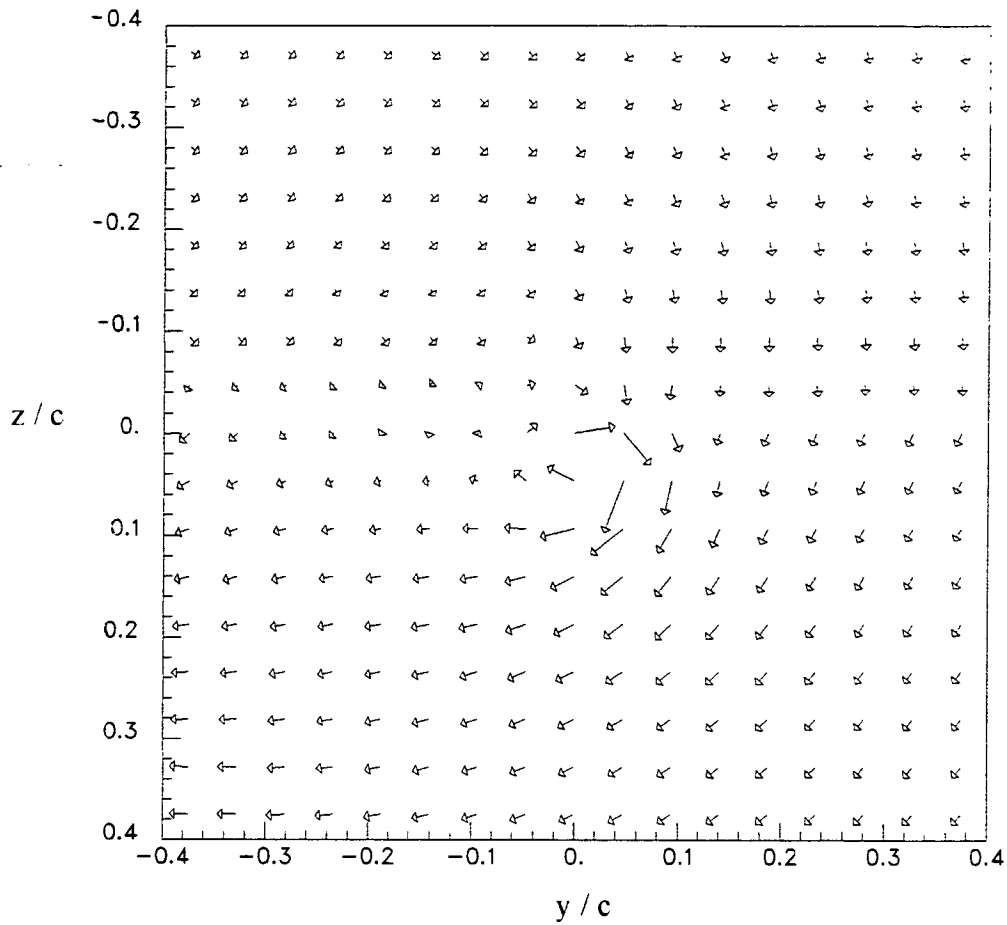


Figure 3.20 Mean cross-flow velocity vectors, vortex passing to pressure side of blade  $\Delta/c = -0.0625$ ,  $X/c=15.33$ . (a) Coarse grid.

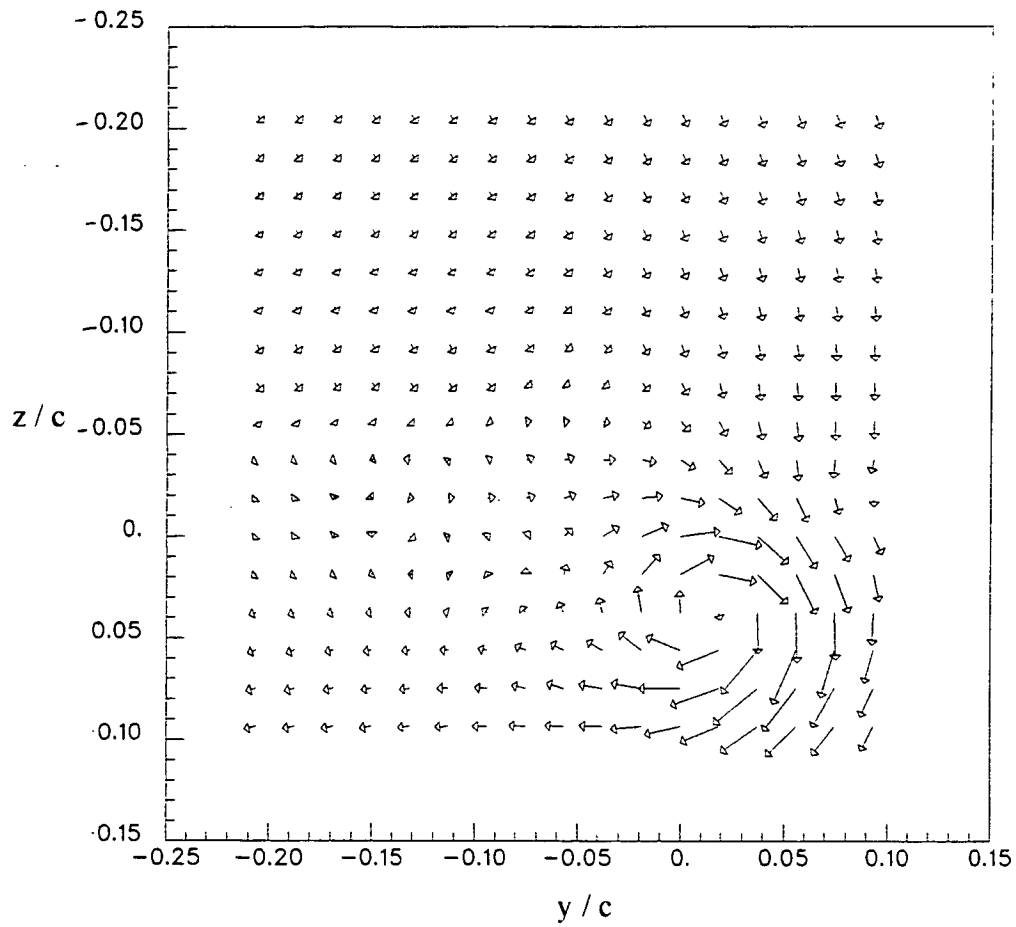


Figure 3.20 Mean cross-flow velocity vectors, vortex passing to pressure side of blade  $\Delta/c = -0.0625$ ,  $X/c=15.33$ . (b) Fine grid.

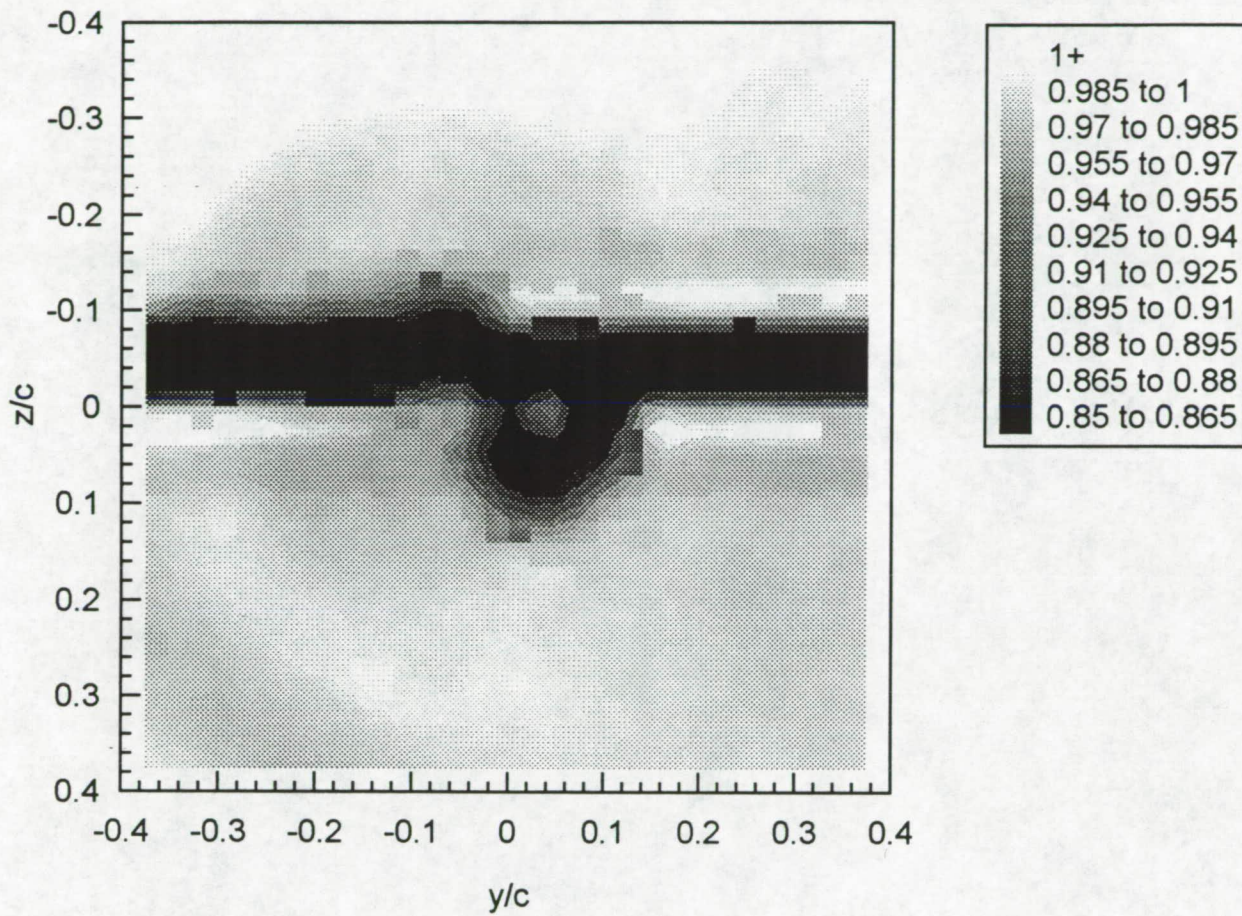


Figure 3.21 Contours of axial mean velocity  $U/U_{ref}$ , vortex passing to pressure side of blade  $\Delta/c = -0.0625$ ,  $X/c=15.33$ . (a) Coarse grid.



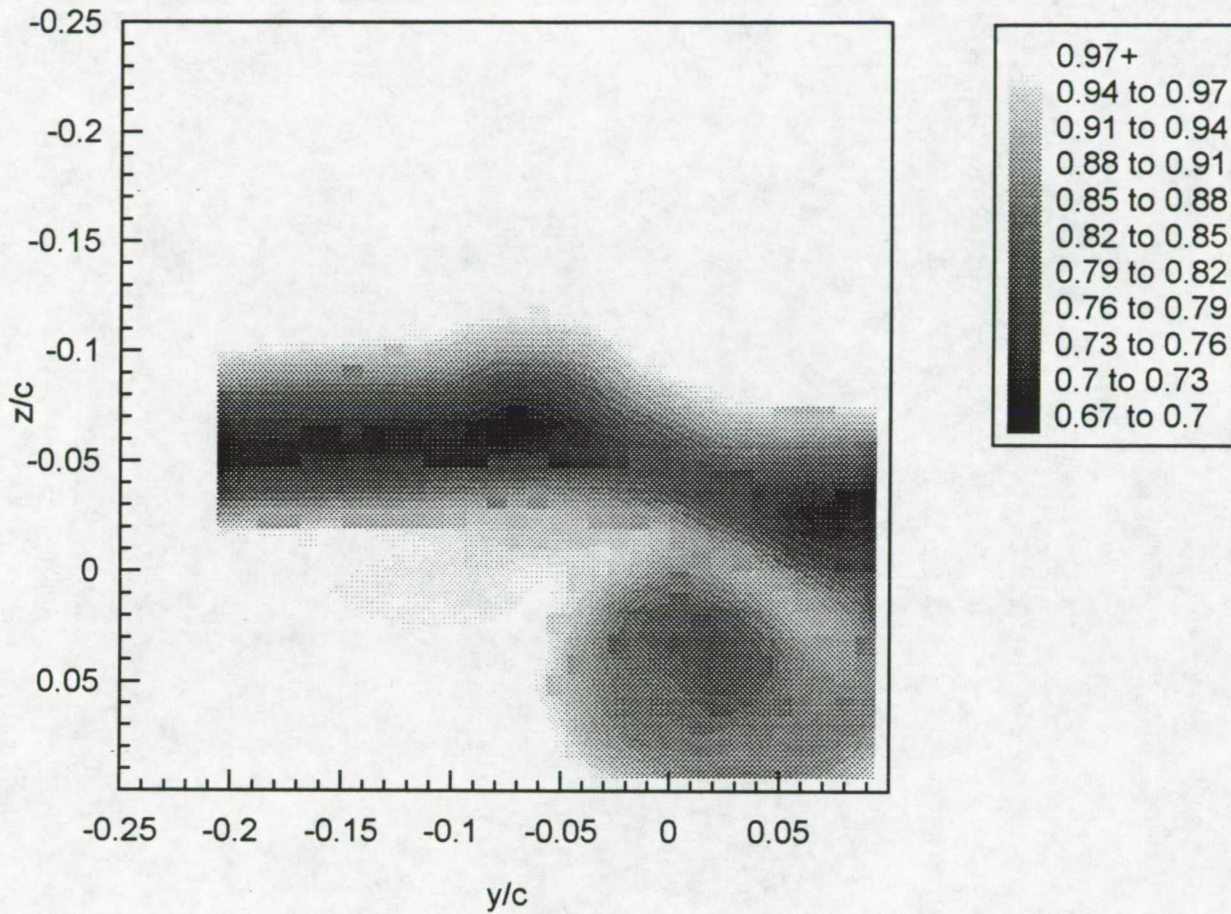


Figure 3.21 Contours of axial mean velocity  $U/U_{ref}$ , vortex passing to pressure side of blade  $\Delta/c = -0.0625$ ,  $X/c=15.33$ . (b) Fine grid.



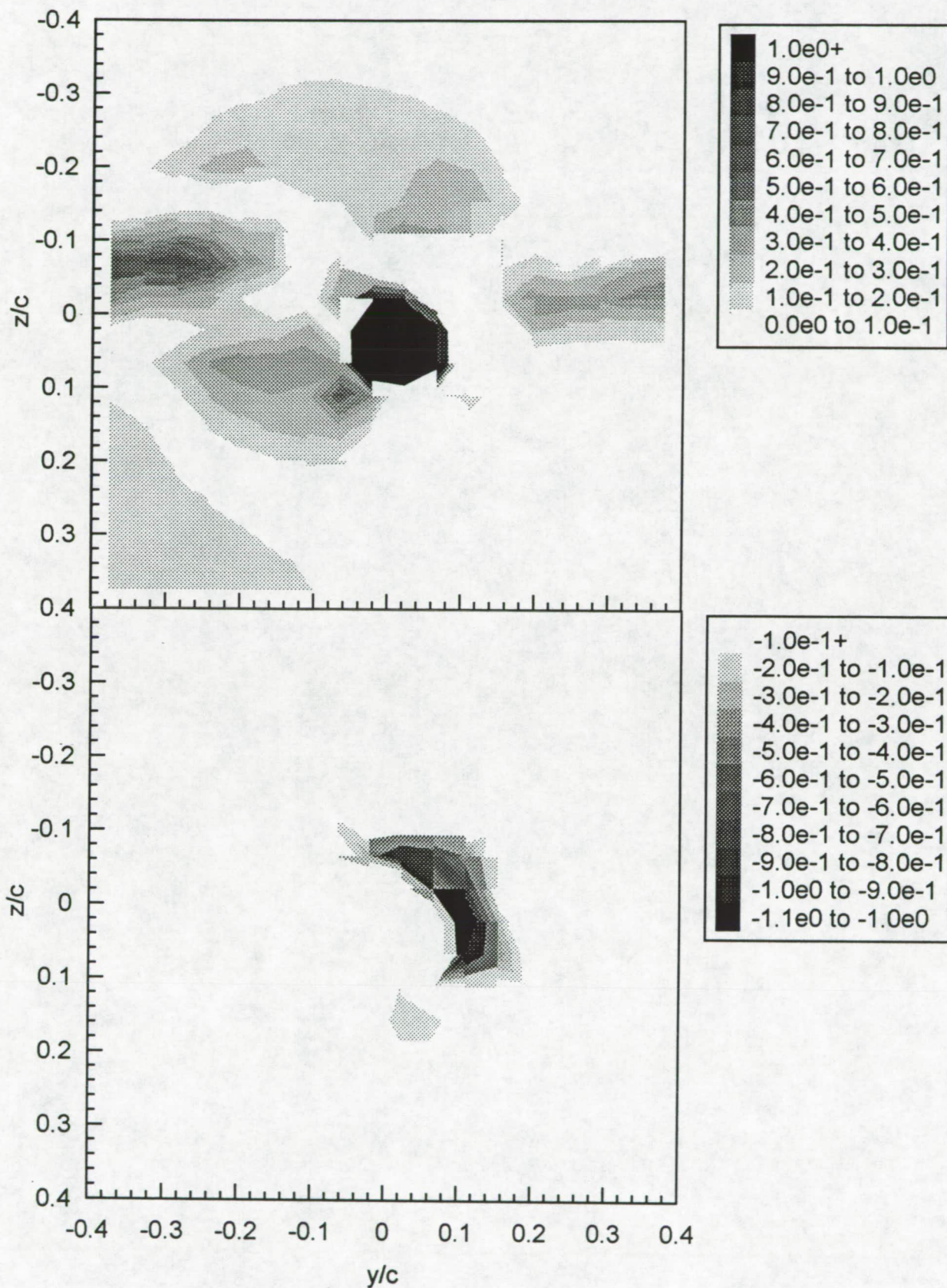


Figure 3.22 Contours of axial mean vorticity  $\omega_x c / U_{ref}$ , vortex passing to pressure side of blade  $\Delta/c = -0.0625$ ,  $X/c = 15.33$ . (a) Coarse grid. Upper figure - positive vorticity, lower figure - negative vorticity.



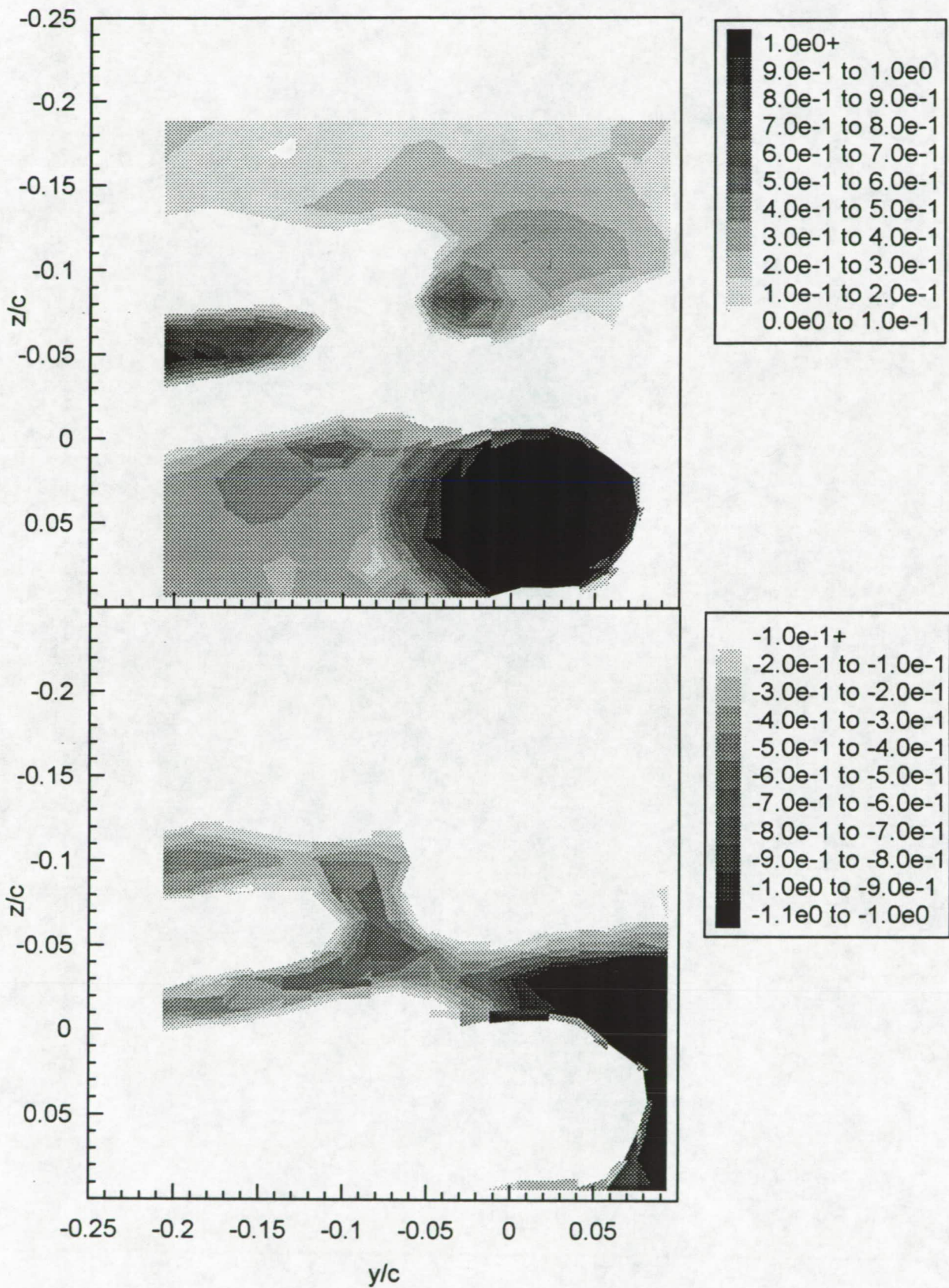


Figure 3.22 Contours of axial mean vorticity  $\omega_x c / U_{ref}$ , vortex passing to pressure side of blade  $\Delta/c = -0.0625$ ,  $X/c = 15.33$ . (b) Fine grid. Upper figure - positive vorticity, lower figure - negative vorticity.



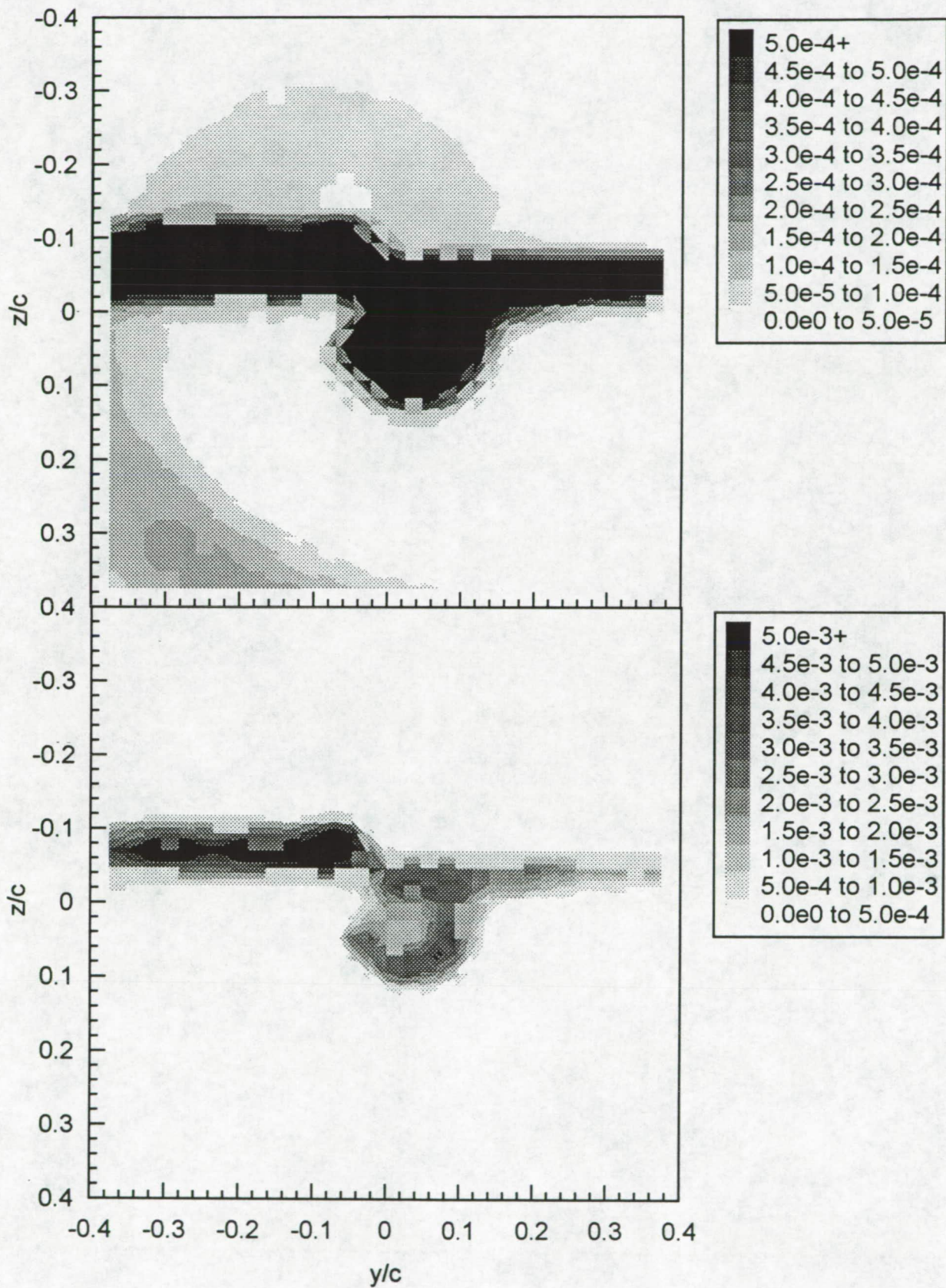


Figure 3.23 Contours of axial normal turbulence stress  $\overline{u'^2}/U_{ref}^2$ , vortex passing to pressure side of blade  $\Delta/c = -0.0625$ ,  $X/c=15.33$ . (a) Coarse grid. Upper and lower figures show different contour ranges.



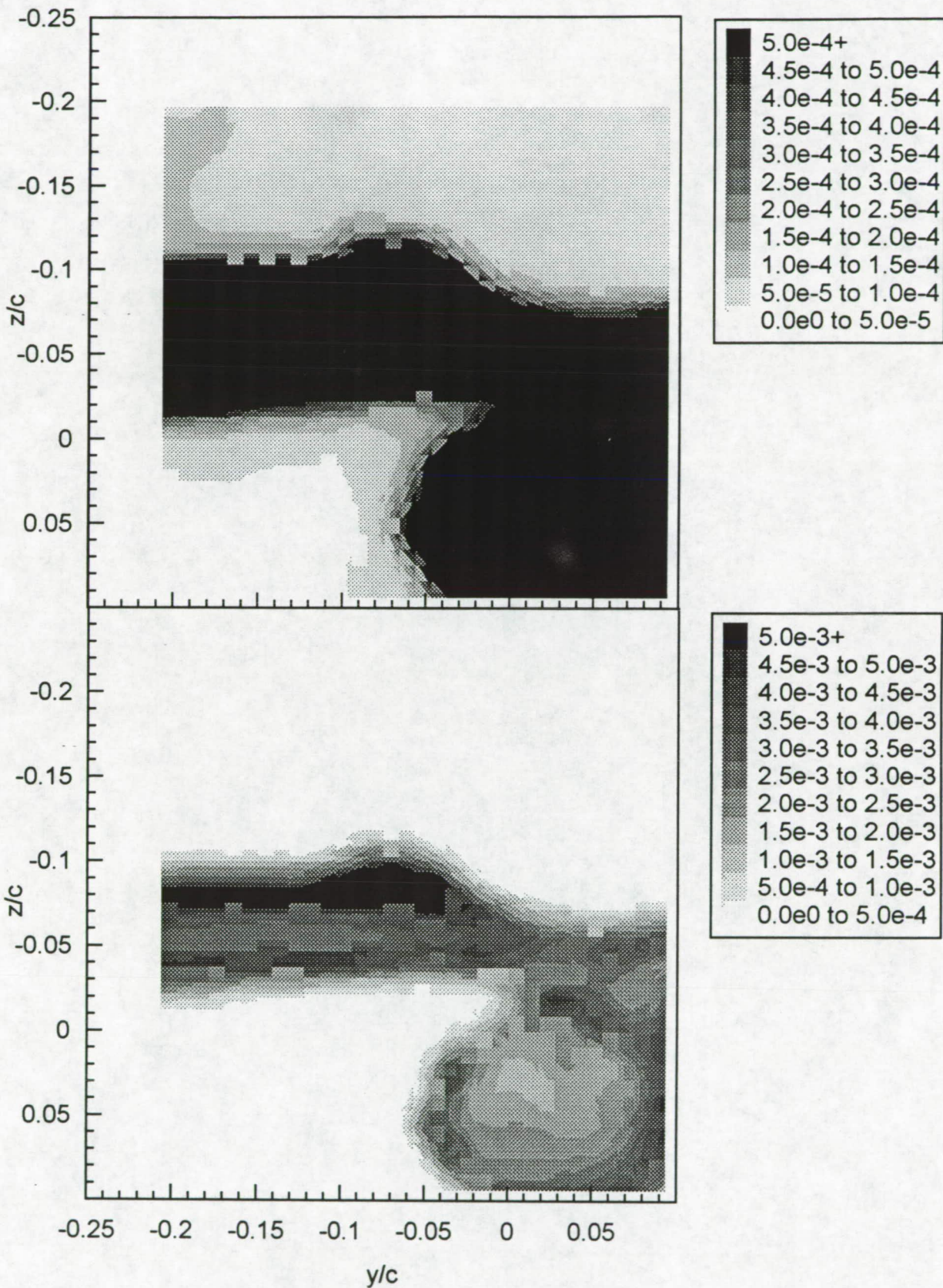


Figure 3.23 Contours of axial normal turbulence stress  $\overline{u'^2}/U_{ref}^2$ , vortex passing to pressure side of blade  $\Delta/c = -0.0625$ ,  $X/c=15.33$ . (b) Fine grid. Upper and lower figures show different contour ranges.



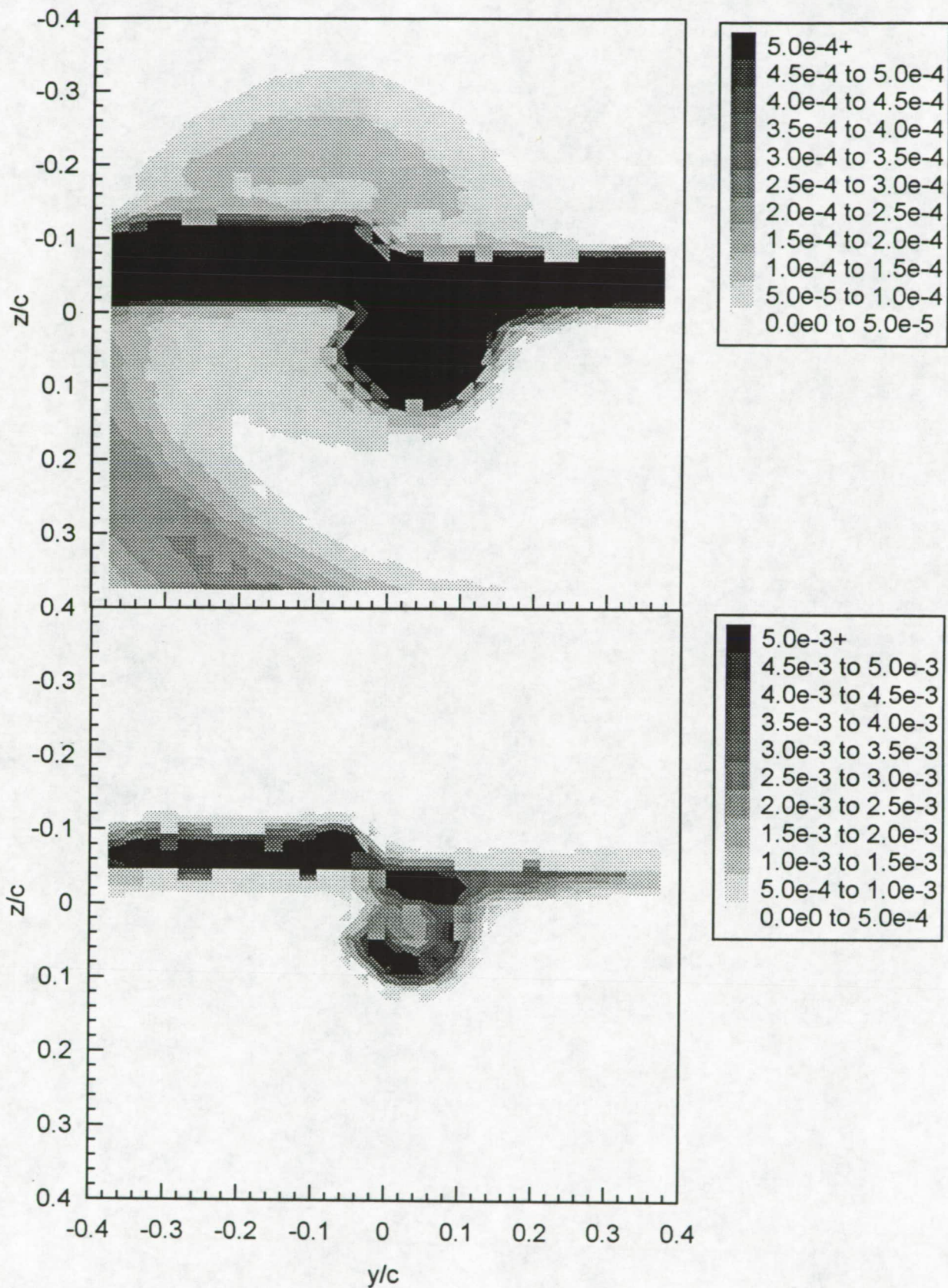


Figure 3.24 Contours of turbulence kinetic energy  $k/U_{ref}^2$ , vortex passing to pressure side of blade  $\Delta/c = -0.0625$ ,  $X/c=15.33$ . (a) Coarse grid. Upper and lower figures show different contour ranges.



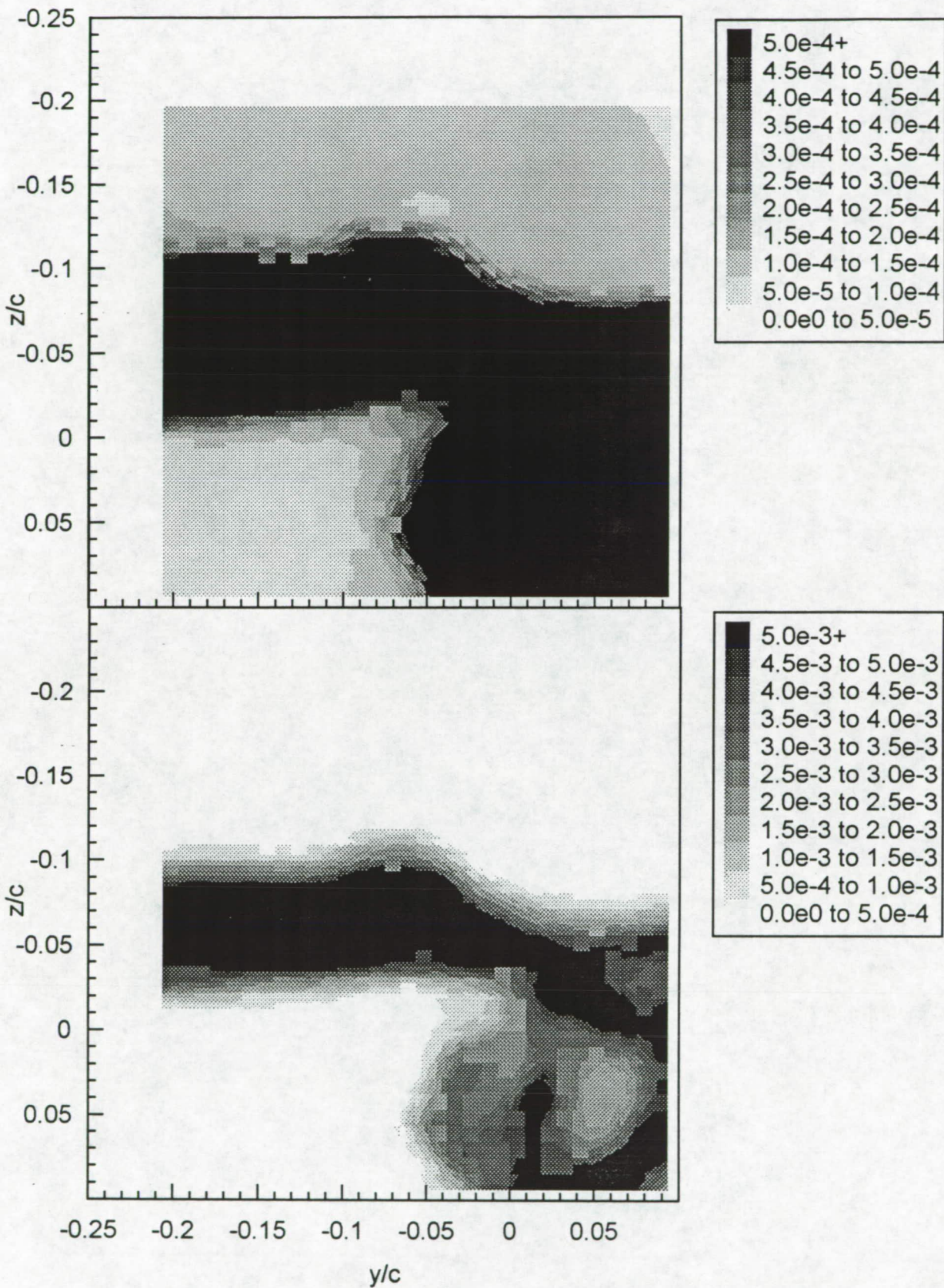


Figure 3.24 Contours of turbulence kinetic energy  $k/U_{ref}^2$ , vortex passing to pressure side of blade  $\Delta/c = -0.0625$ ,  $X/c=15.33$ . (b) Fine grid. Upper and lower figures show different contour ranges.



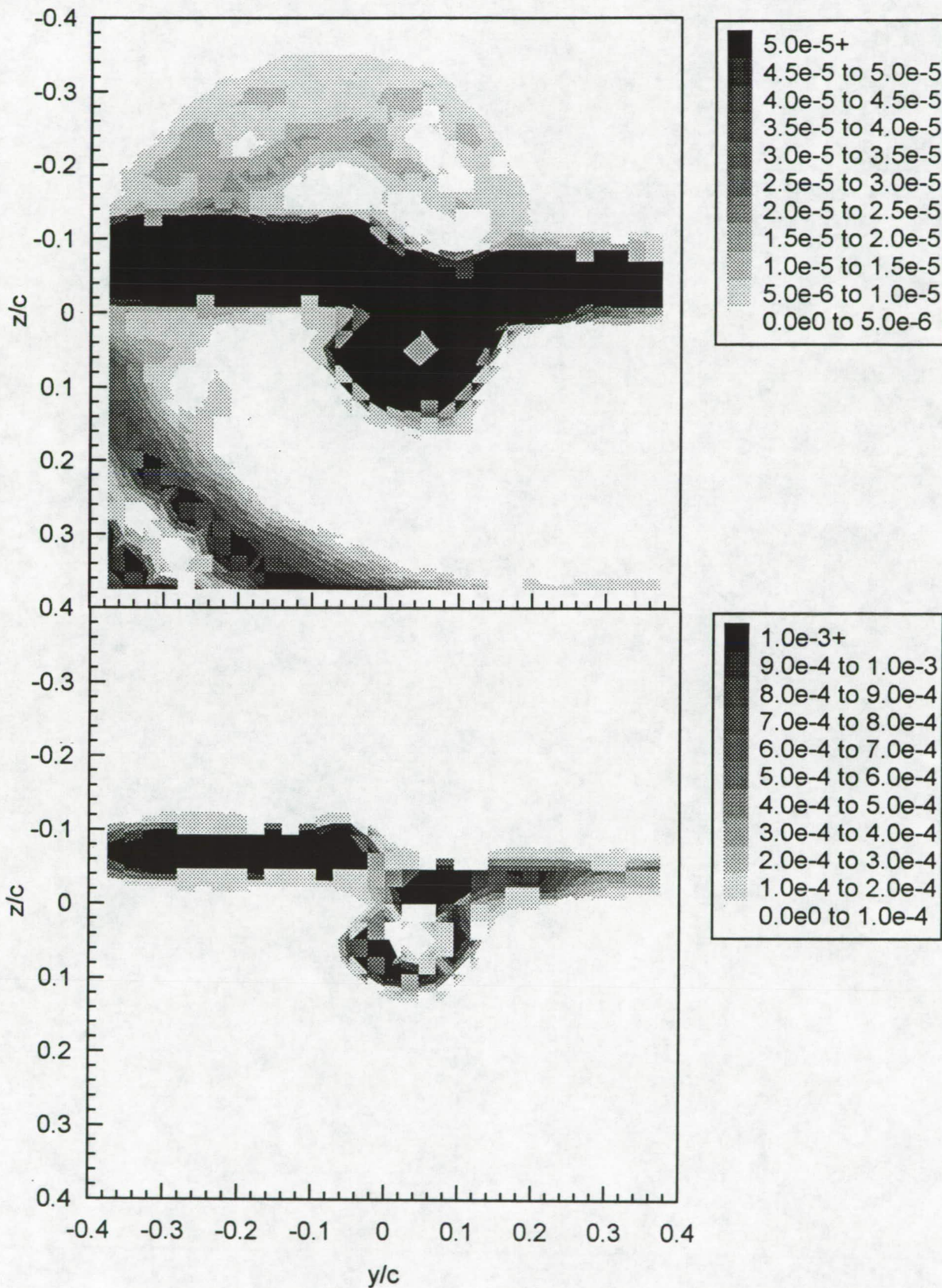


Figure 3.25 Contours of axial shear stress magnitude  $\tau_a/U_{ref}^2$ , vortex passing to pressure side of blade  $\Delta/c = -0.0625$ ,  $X/c=15.33$ . (a) Coarse grid. Upper and lower figures show different contour ranges.



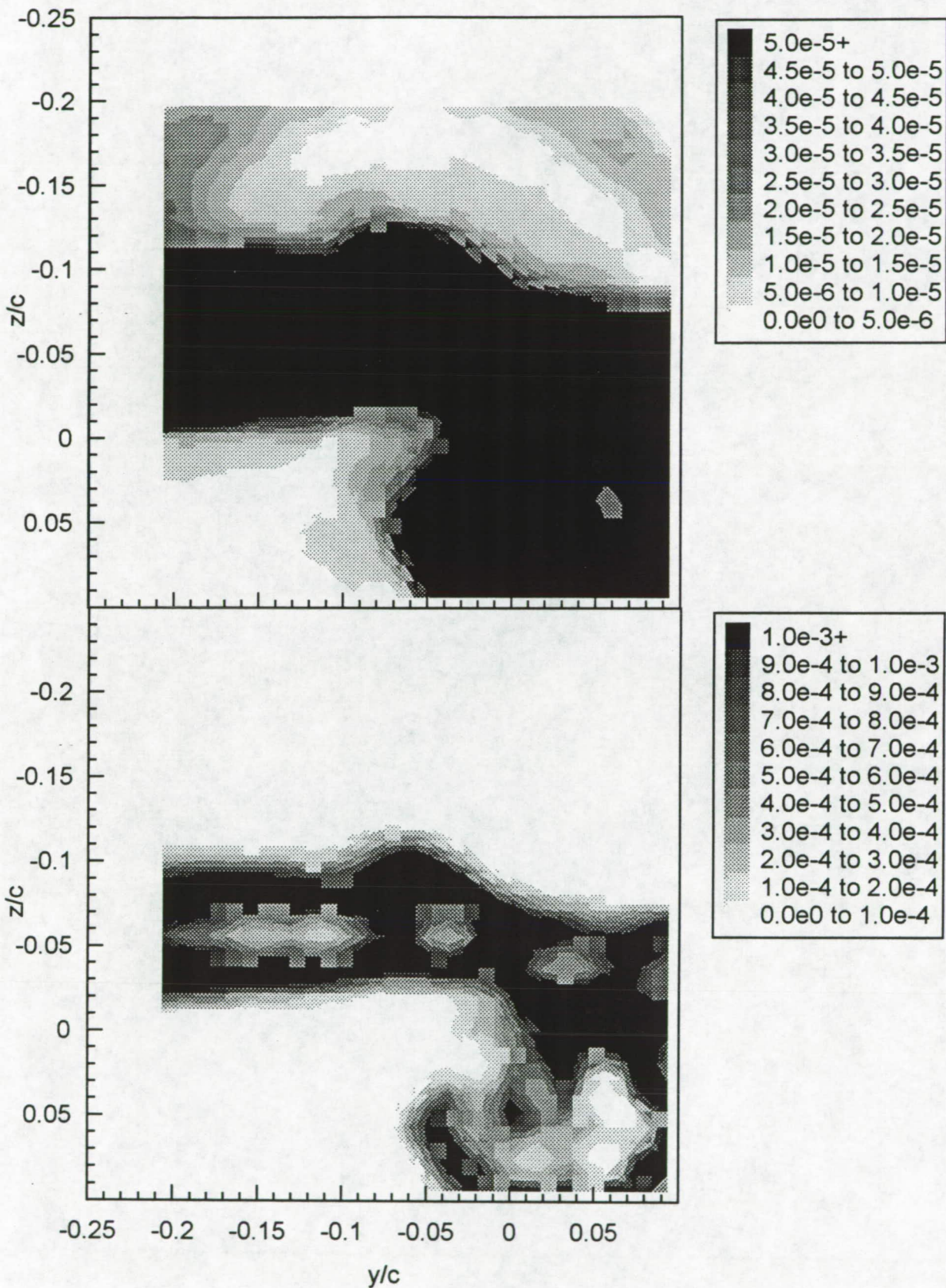


Figure 3.25 Contours of axial shear stress magnitude  $\tau_a/U_{ref}^2$ , vortex passing to pressure side of blade  $\Delta/c = -0.0625$ ,  $X/c=15.33$ . (b) Fine grid. Upper and lower figures show different contour ranges.



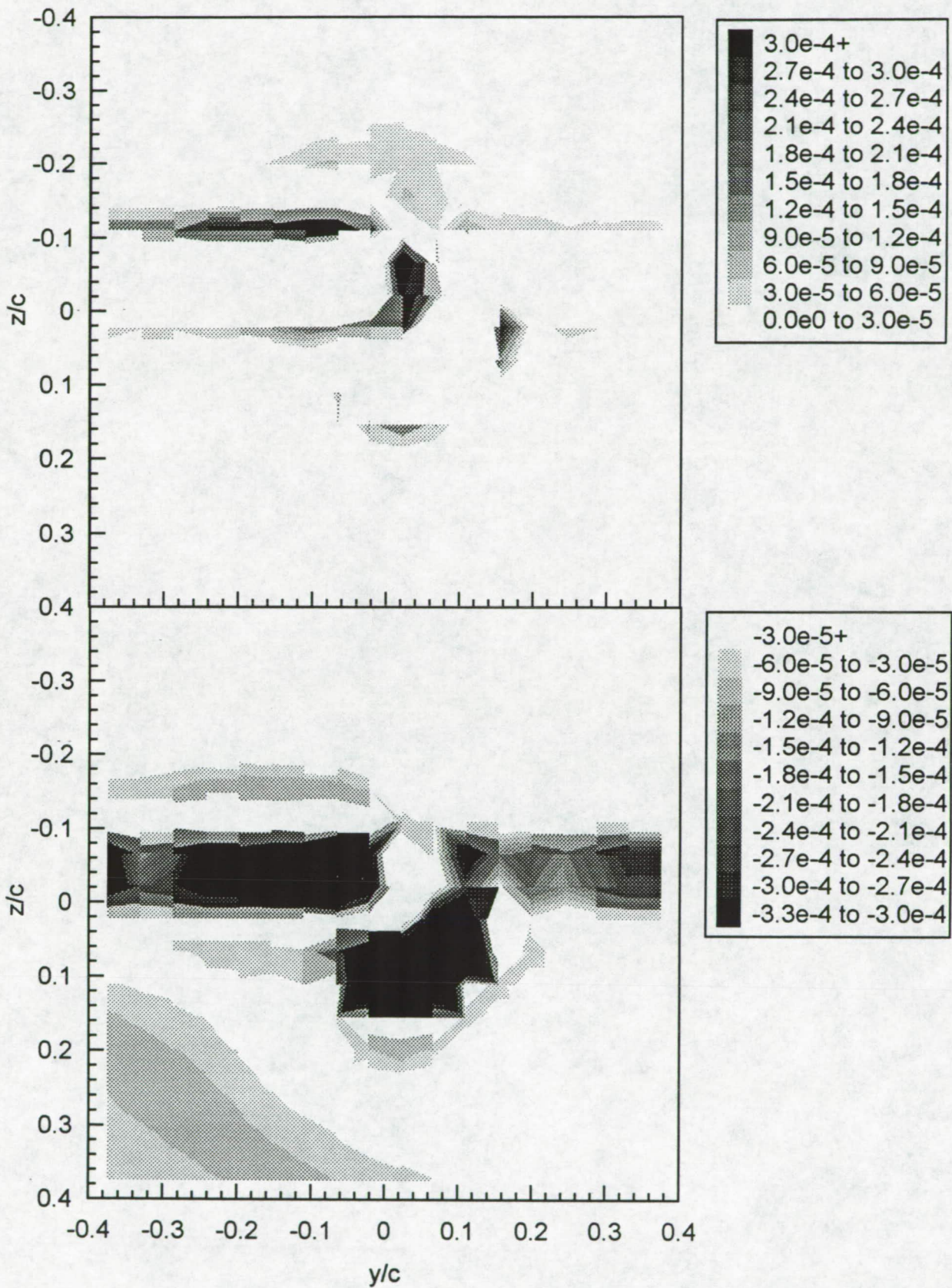


Figure 3.26 Contours of cross-flow shear stress  $\tau_c/U_{ref}^2$ , vortex passing to pressure side of blade  $\Delta/c = -0.0625$ ,  $X/c=15.33$ . (a) Coarse grid. Upper figure - positive stress, lower figure - negative stress.



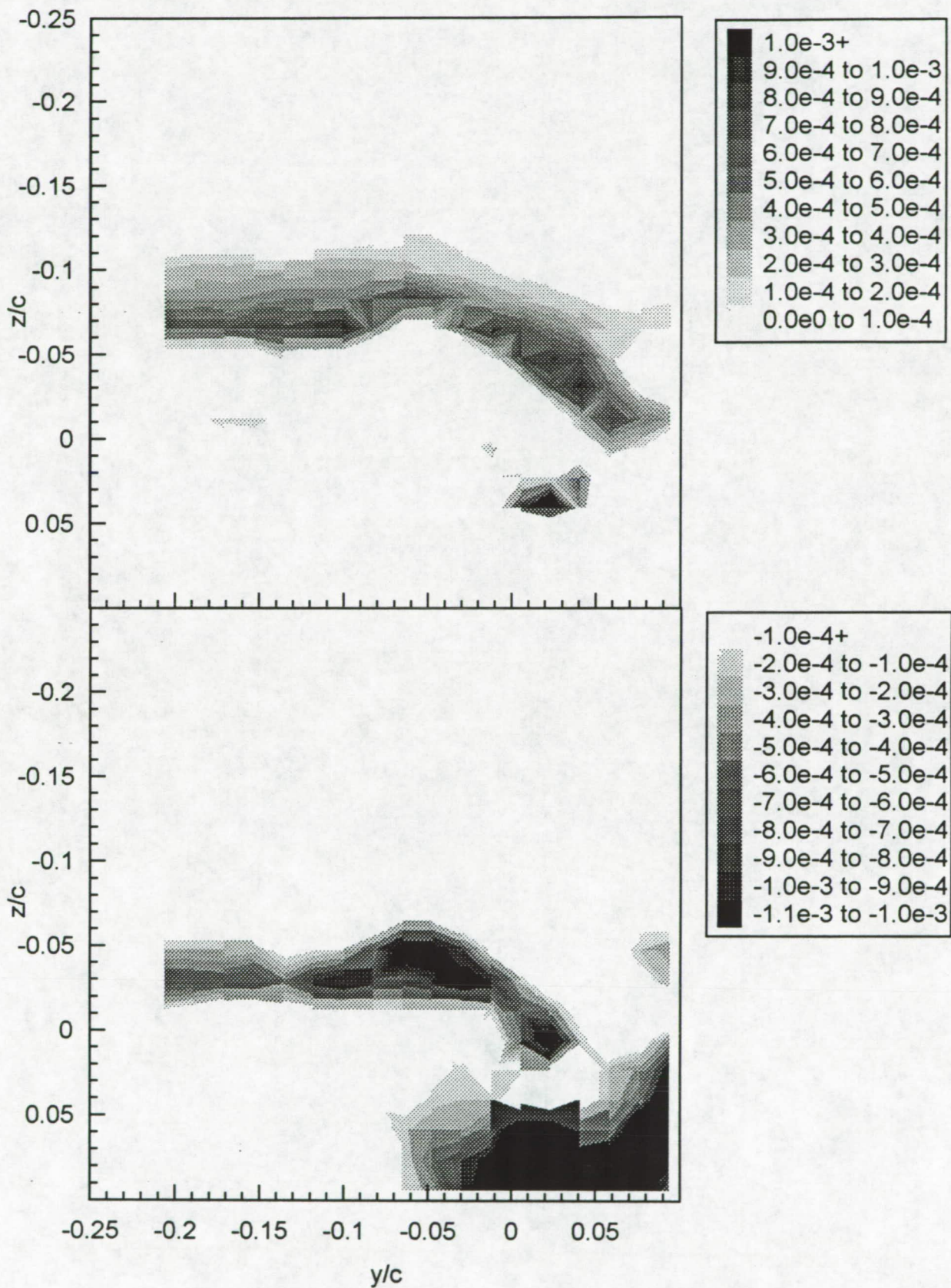


Figure 3.26 Contours of cross-flow shear stress  $\tau_c/U_{ref}^2$ , vortex passing to pressure side of blade  $\Delta/c = -0.0625$ ,  $X/c=15.33$ . (b) Fine grid. Upper figure - positive stress, lower figure - negative stress.



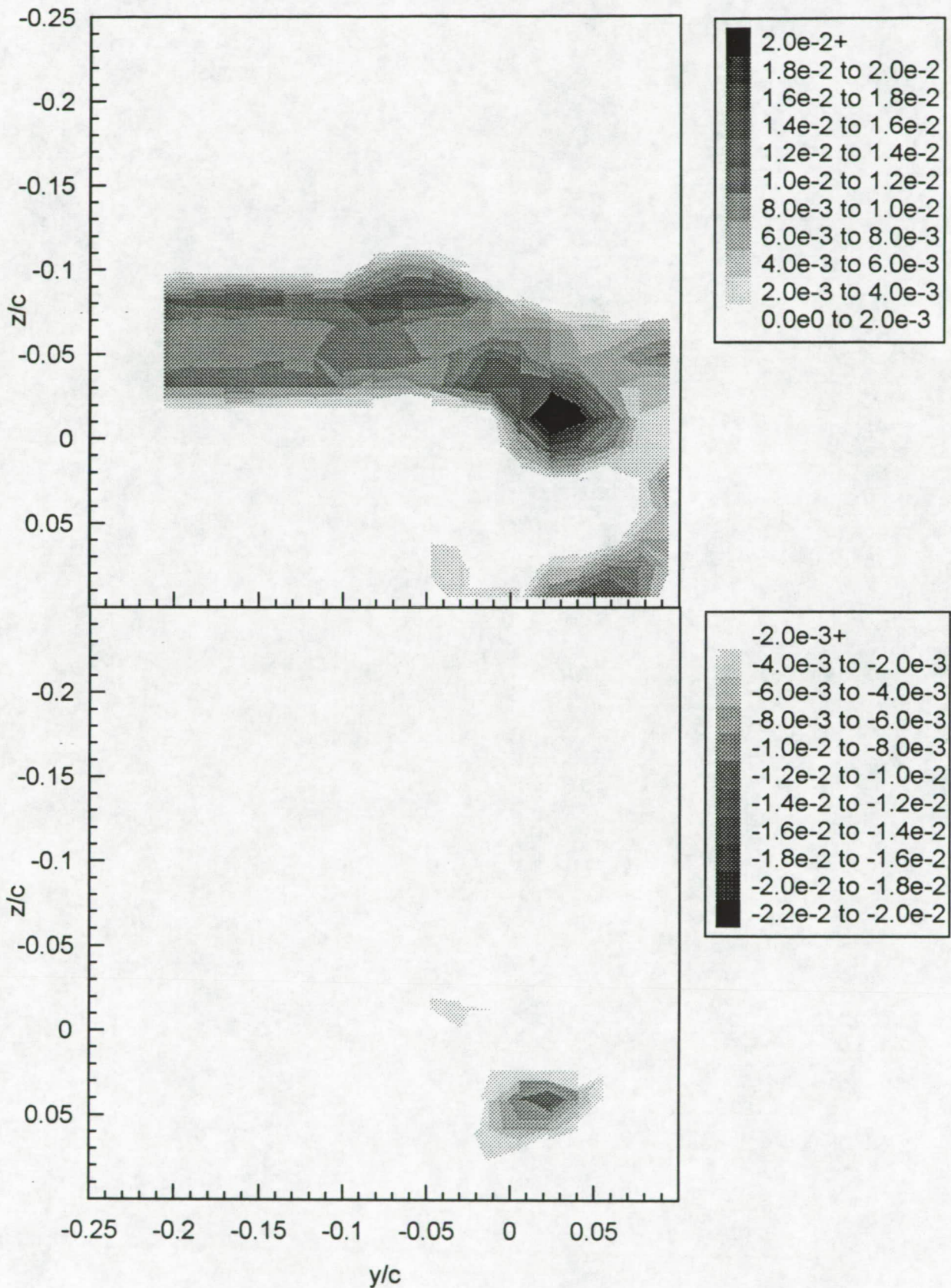


Figure 3.27 Contours of turbulence kinetic energy production  $Pc/U_{ref}^3$ , vortex passing to pressure side of blade  $\Delta/c = -0.0625$ ,  $X/c=15.33$ . Fine grid. Upper figure - positive production, lower figure - negative production.

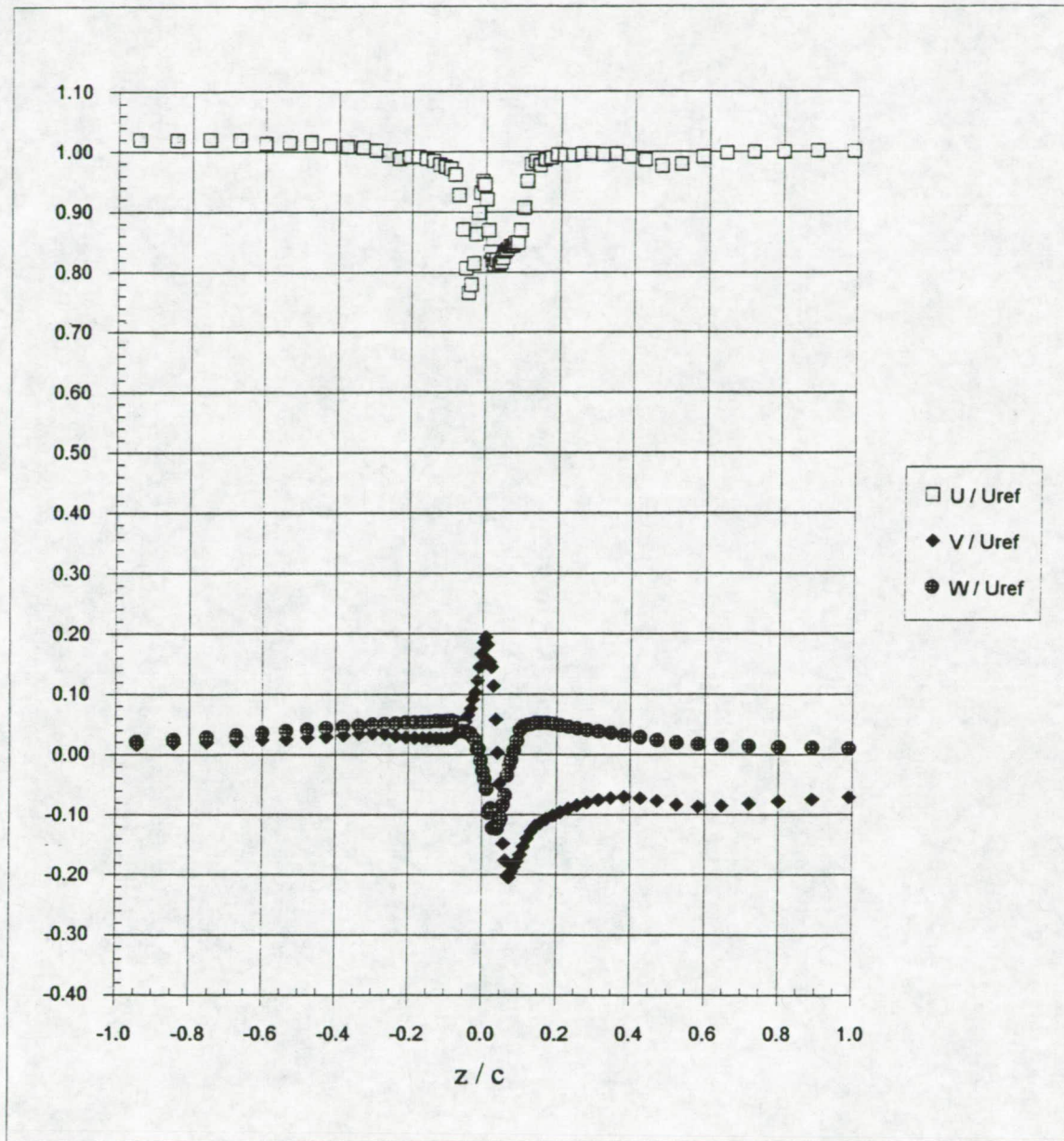


Figure 3.28 Velocity profiles along the line  $y/c=0$ ,  $\Delta/c = -0.0625$ ,  $X/c=15.33$ . (a) Mean velocity.



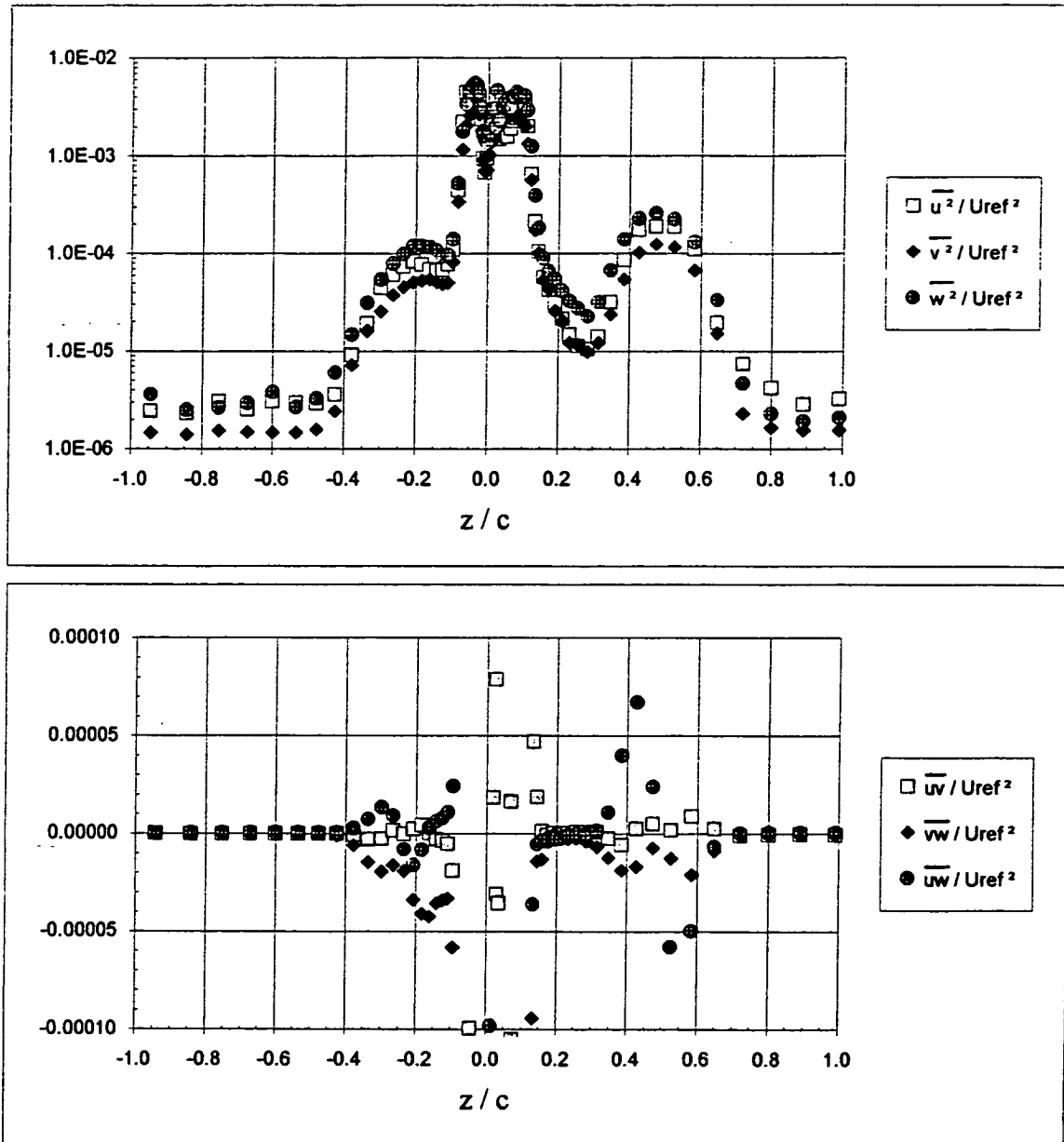


Figure 3.28 Velocity profiles along the line  $y/c=0$ ,  $\Delta/c = -0.0625$ ,  $X/c=15.33$ . (b) Turbulence stresses.

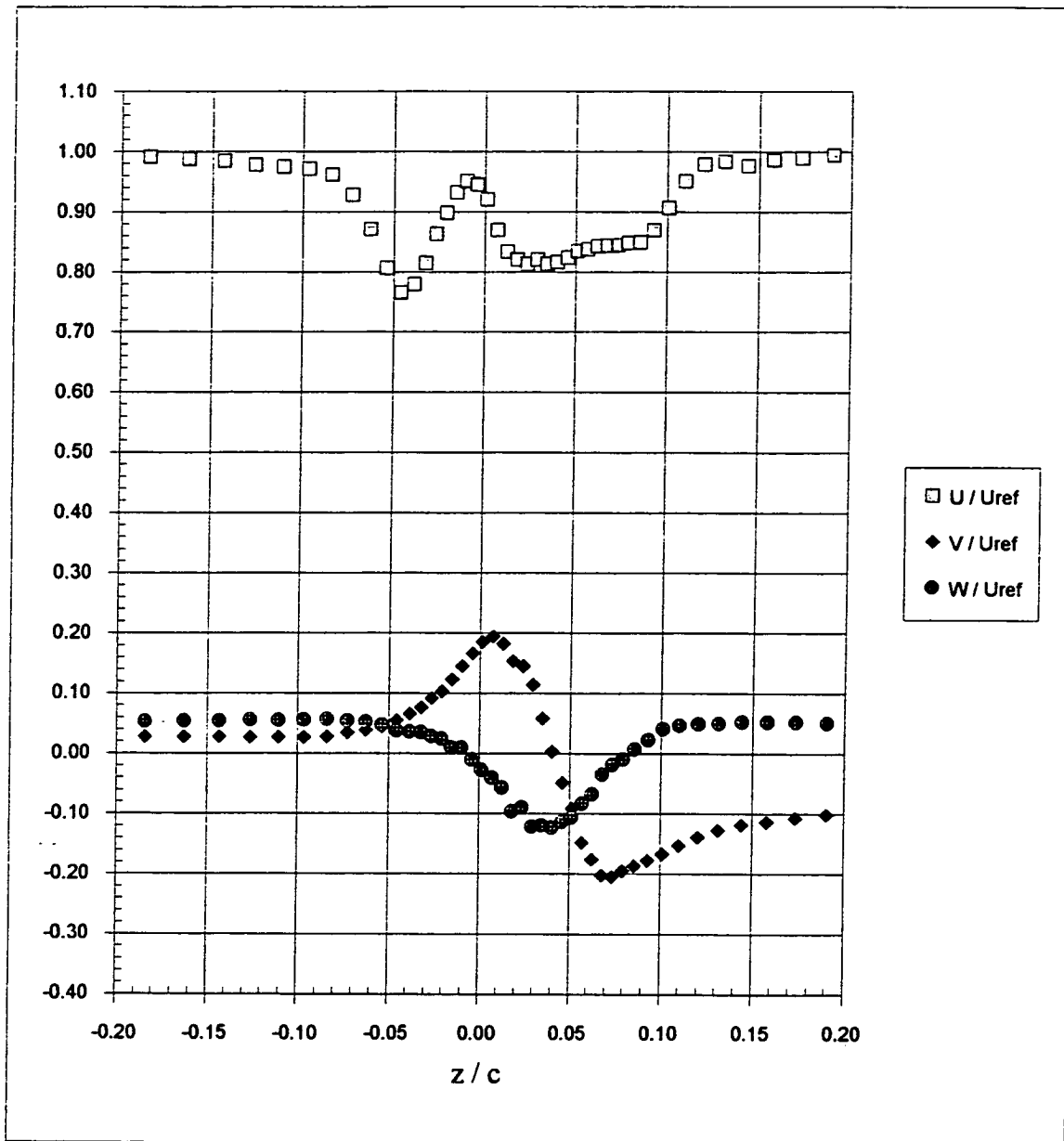


Figure 3.29 Velocity profiles along the line  $y/c=0$  in the vicinity of the primary vortex core,  $\Delta/c = -0.0625$ ,  $X/c=15.33$ . (a) Mean velocity.

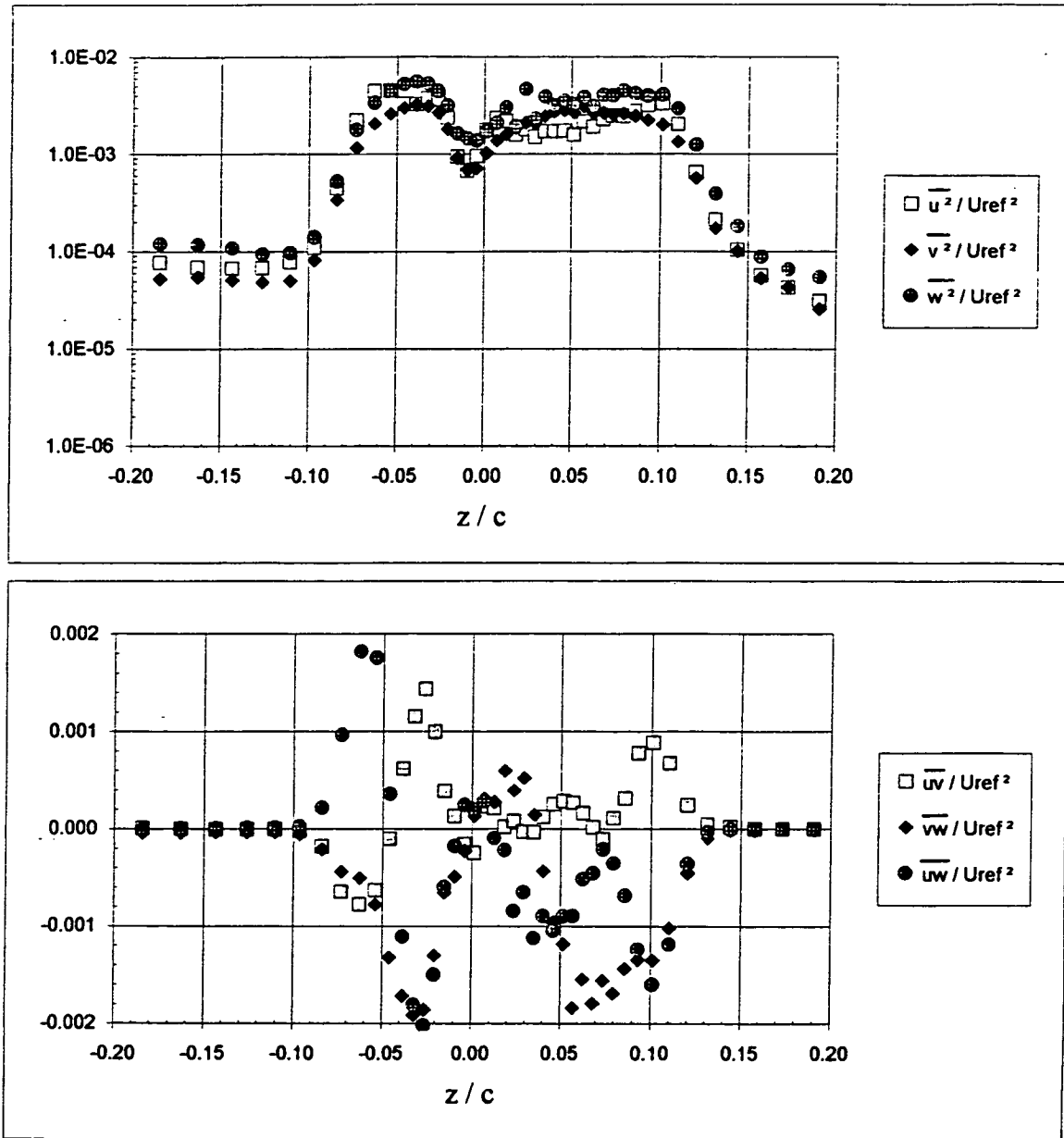
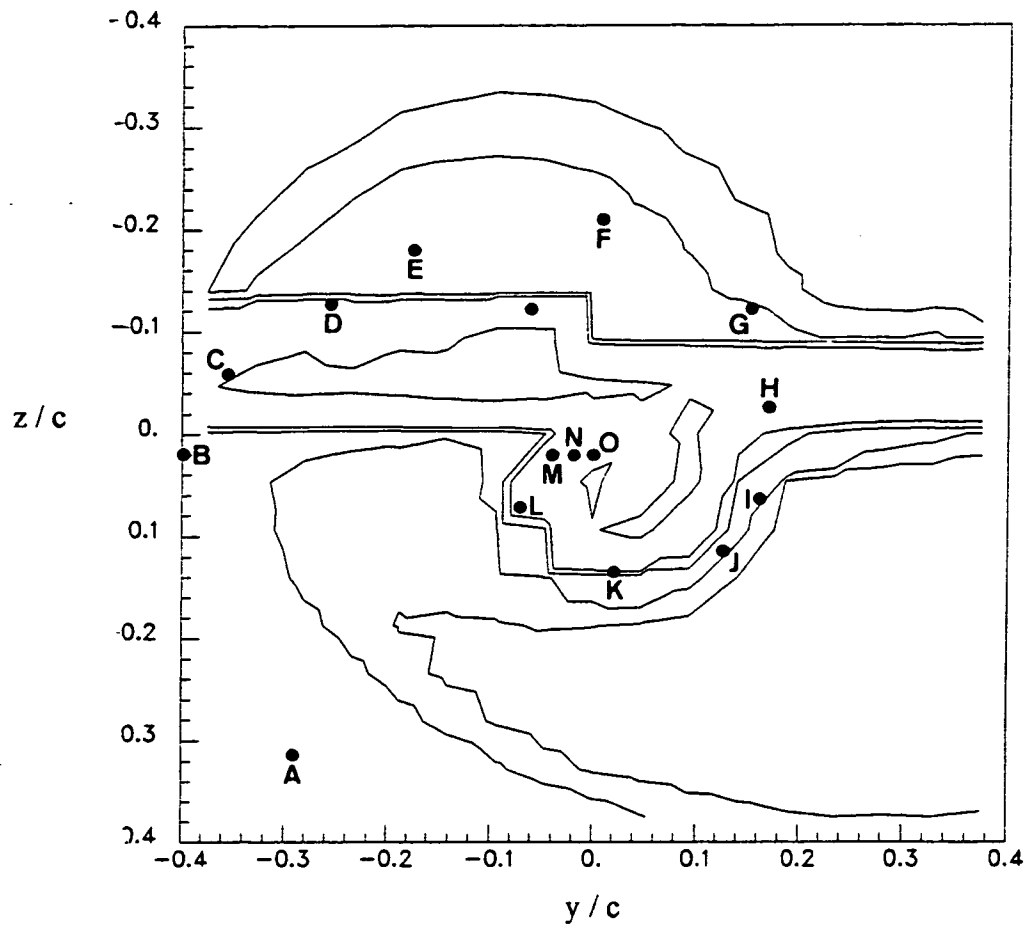


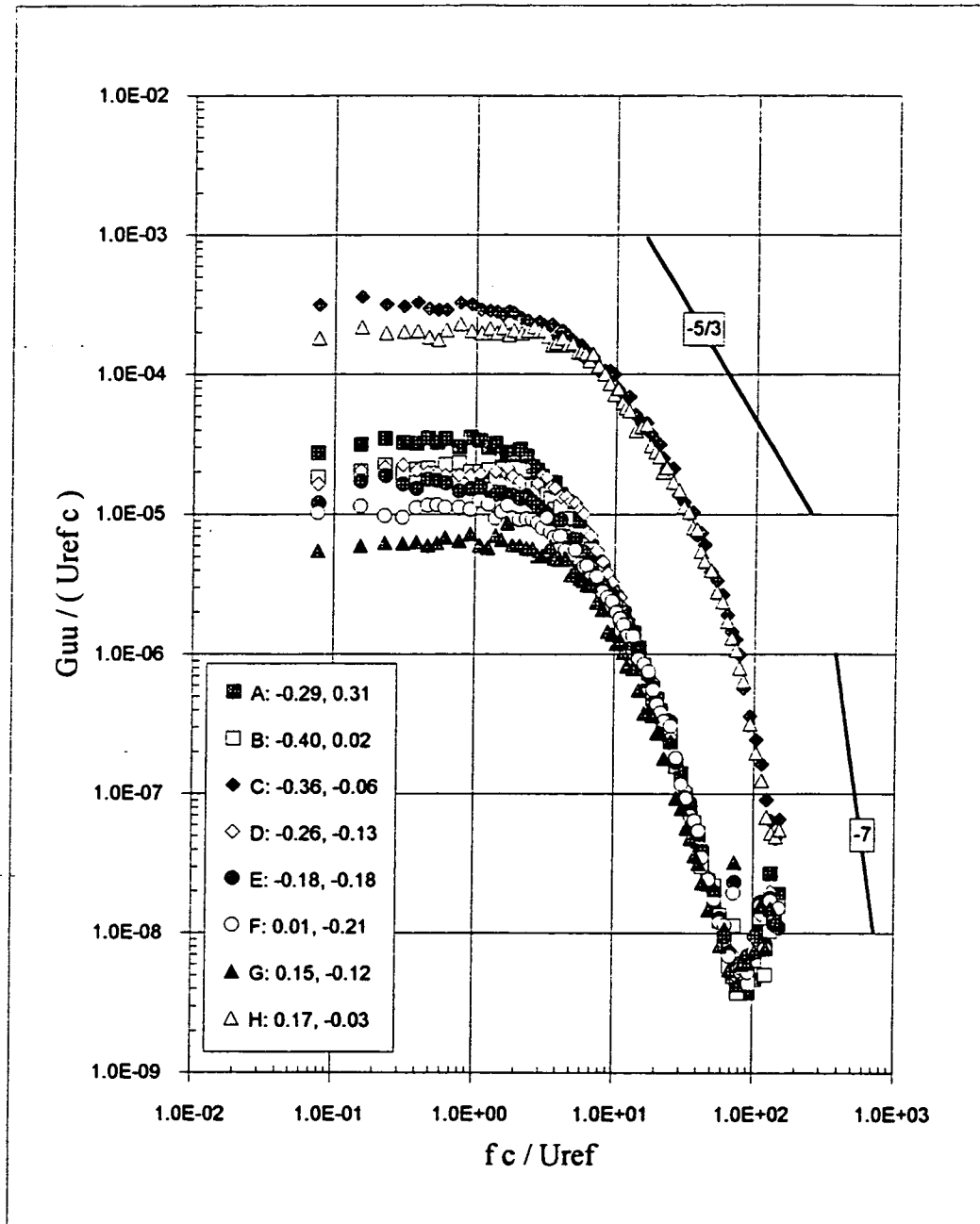
Figure 3.29 Velocity profiles along the line  $y/c=0$  in the vicinity of the primary vortex core,  $\Delta/c = -0.0625$ ,  $X/c=15.33$ . (b) Turbulence stresses.



• Represents spectral measurement locations

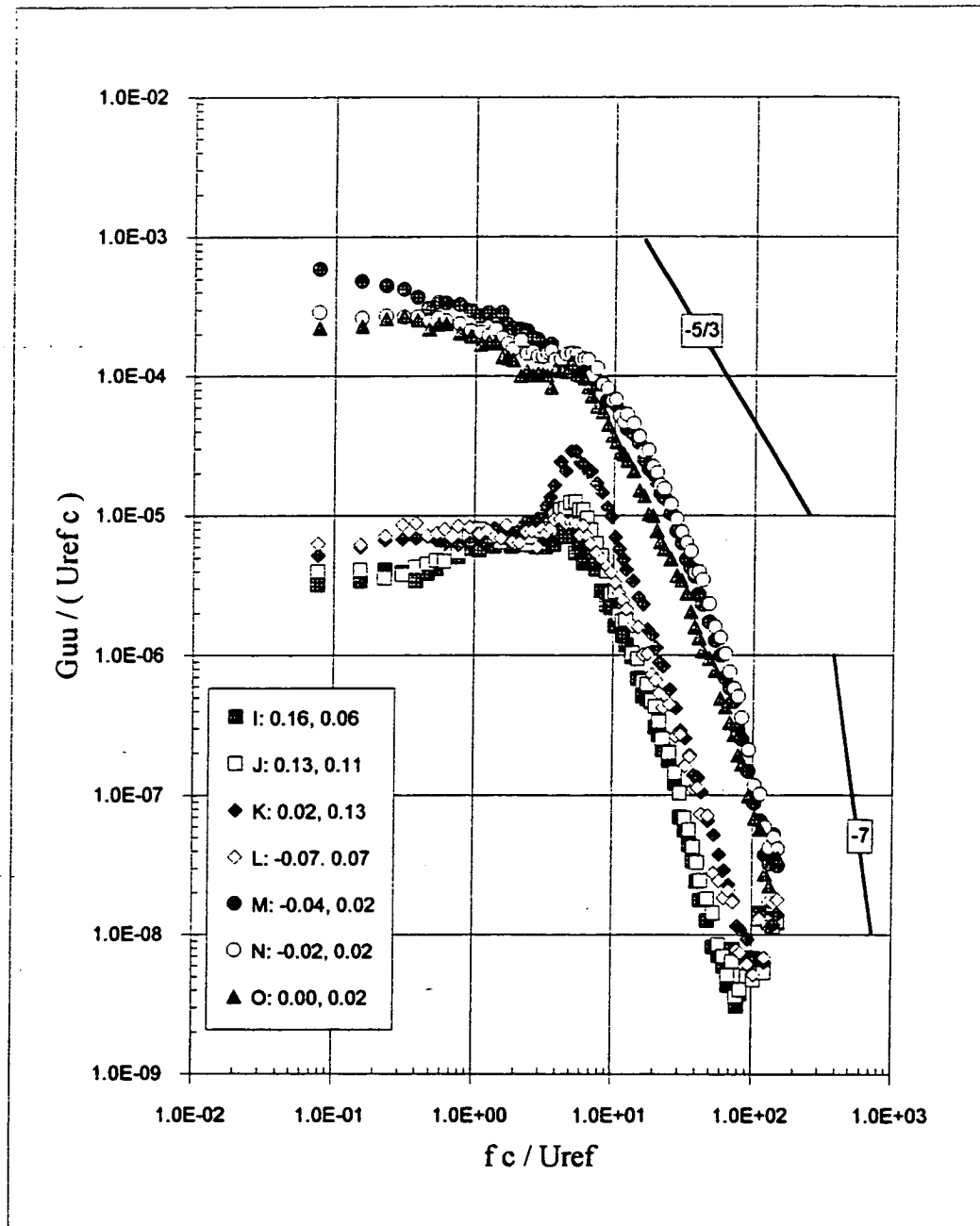
Figure 3.30 Velocity autospectra,  $X/c=15.33$ ,  $\Delta/c = -0.0625$ . (a) Locations of spectral measurements relative to turbulence kinetic energy contours.





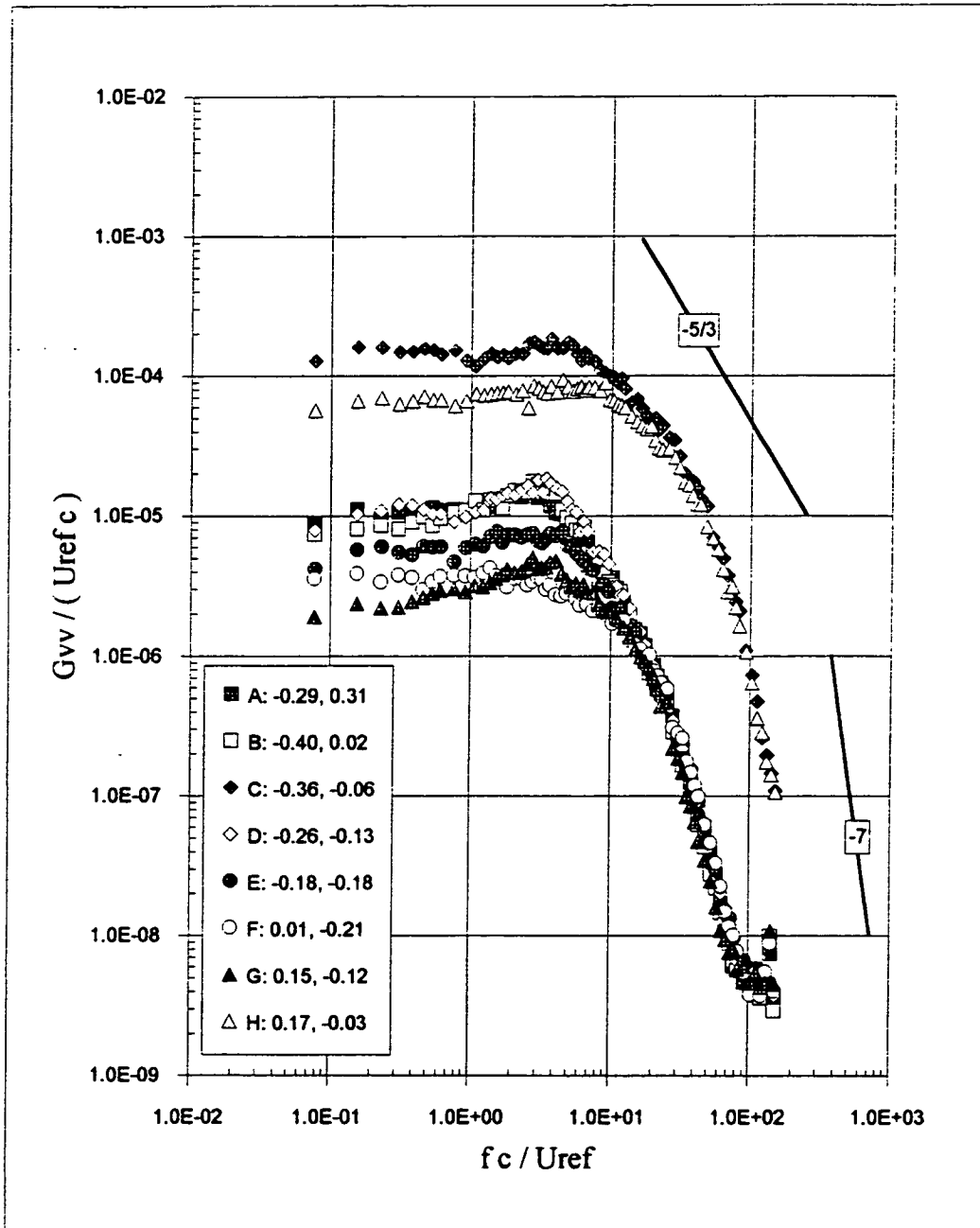
Numbers in legend represent the  $y / c$  and  $z / c$  locations respectively

Figure 3.30 Velocity autospectra at  $X/c=15.33$ ,  $\Delta/c = -0.0625$ . (b)  $G_{uu}$



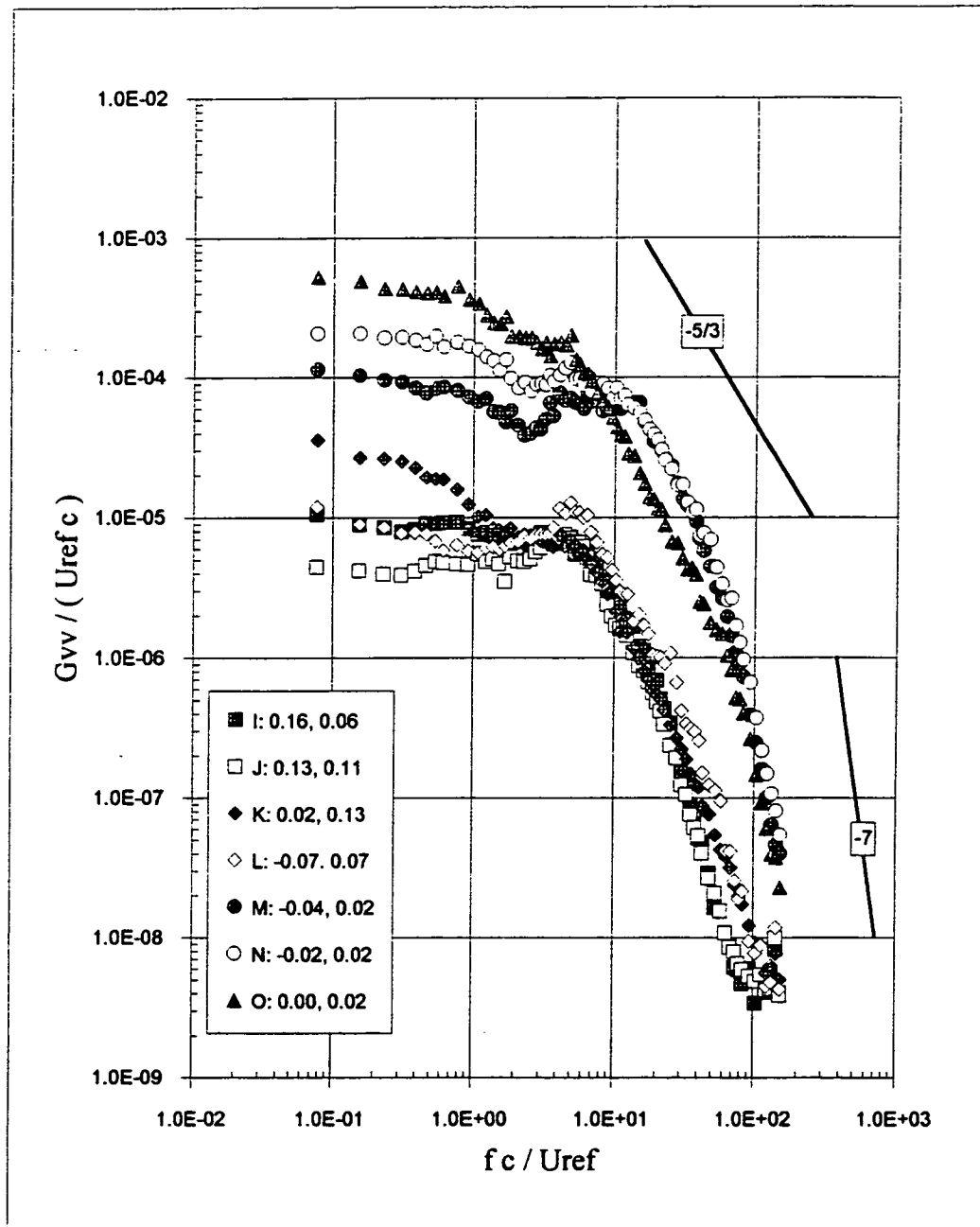
Numbers in legend represent the  $y/c$  and  $z/c$  locations respectively

Figure 3.30 Velocity autospectra at  $X/c=15.33$ ,  $\Delta/c = -0.0625$ . (c)  $G_{uu}$  contd.



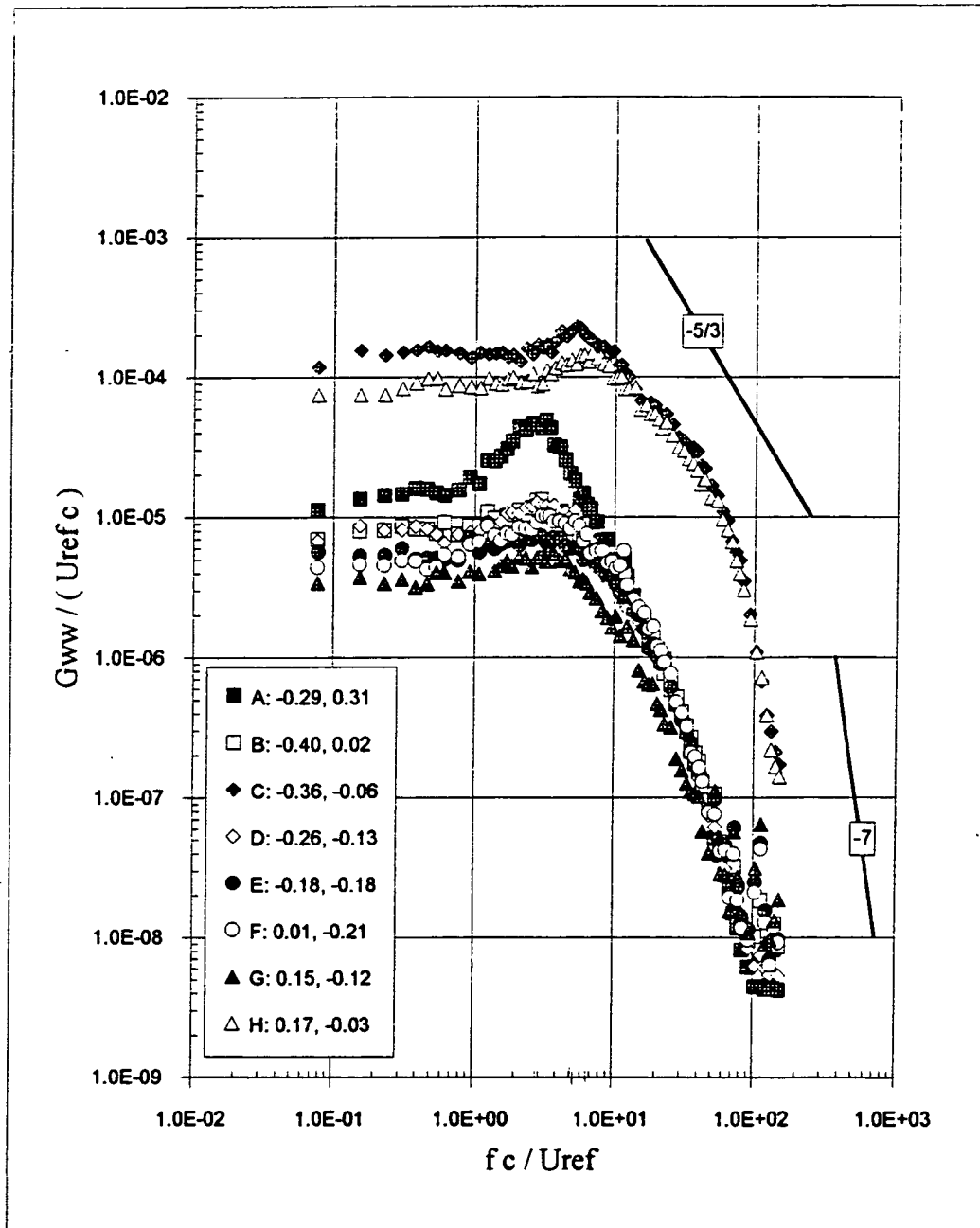
Numbers in legend represent the  $y / c$  and  $z / c$  locations respectively

Figure 3.30 Velocity autospectra at  $X/c=15.33$ ,  $\Delta/c = -0.0625$ . (d)  $G_{vw}$



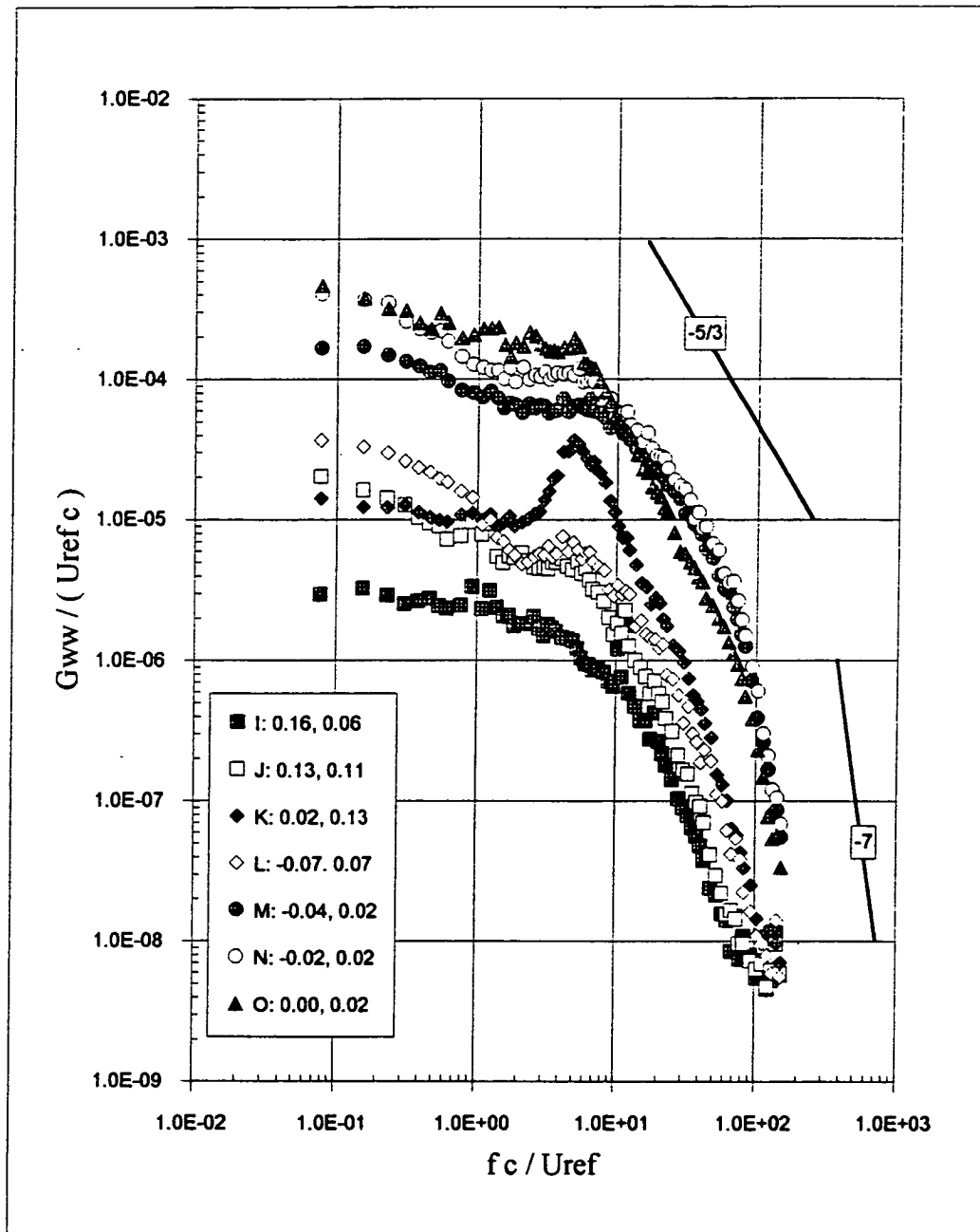
Numbers in legend represent the  $y / c$  and  $z / c$  locations respectively

Figure 3.30 Velocity autospectra at  $X/c=15.33$ ,  $\Delta/c = -0.0625$ . (e)  $G_{vv}$  contd.



Numbers in legend represent the  $y / c$  and  $z / c$  locations respectively

Figure 3.30 Velocity autospectra at  $X/c=15.33$ ,  $\Delta/c = -0.0625$ . (f)  $G_{ww}$



Numbers in legend represent the  $y/c$  and  $z/c$  locations respectively

Figure 3.30 Velocity autospectra at  $X/c=15.33$ ,  $\Delta/c = -0.0625$ . (g)  $G_{ww}$  contd.

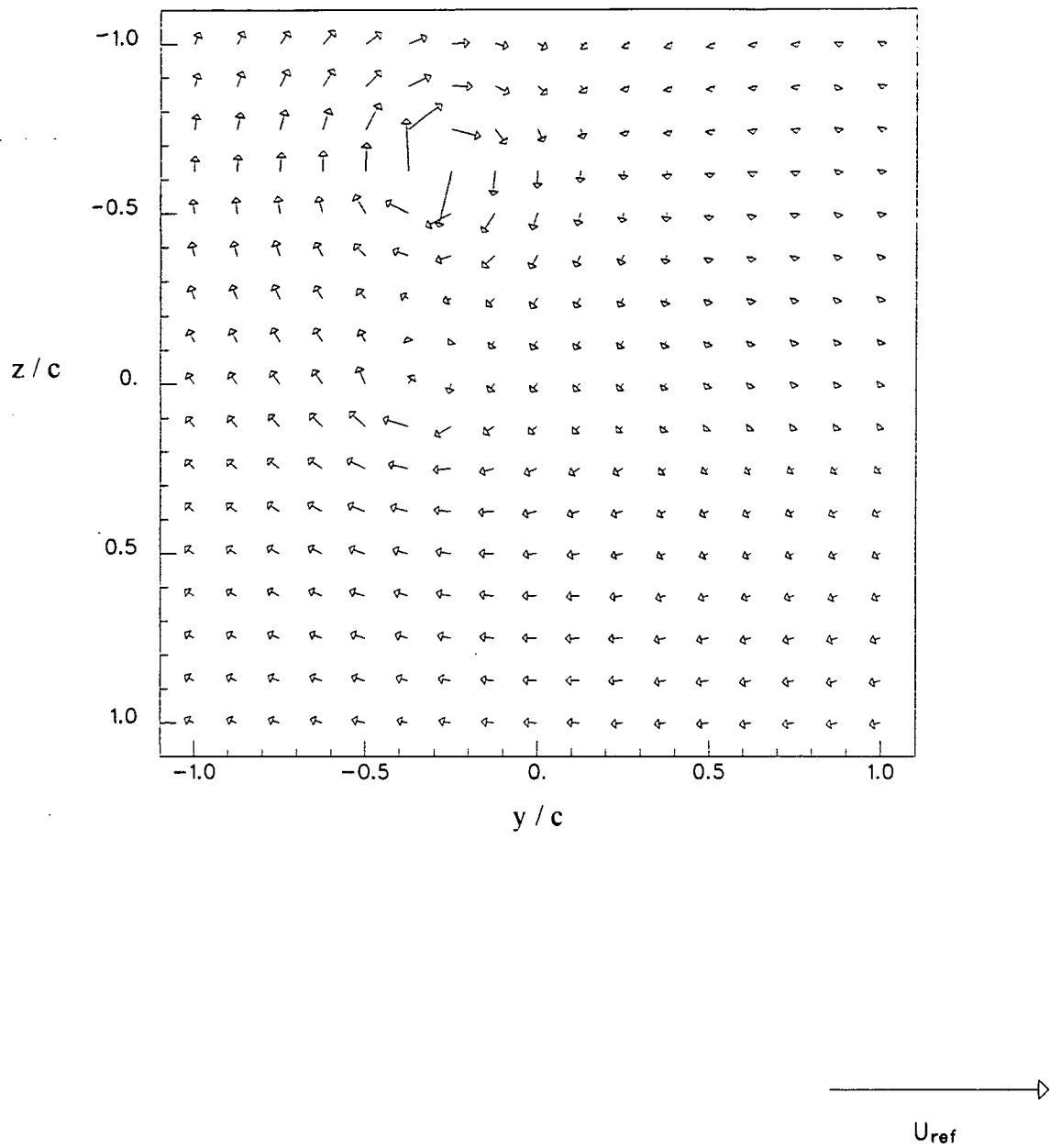


Figure 3.31 Mean cross-flow velocity vectors at  $X/c=30$ . (a)  $\Delta/c=-0.125$ .

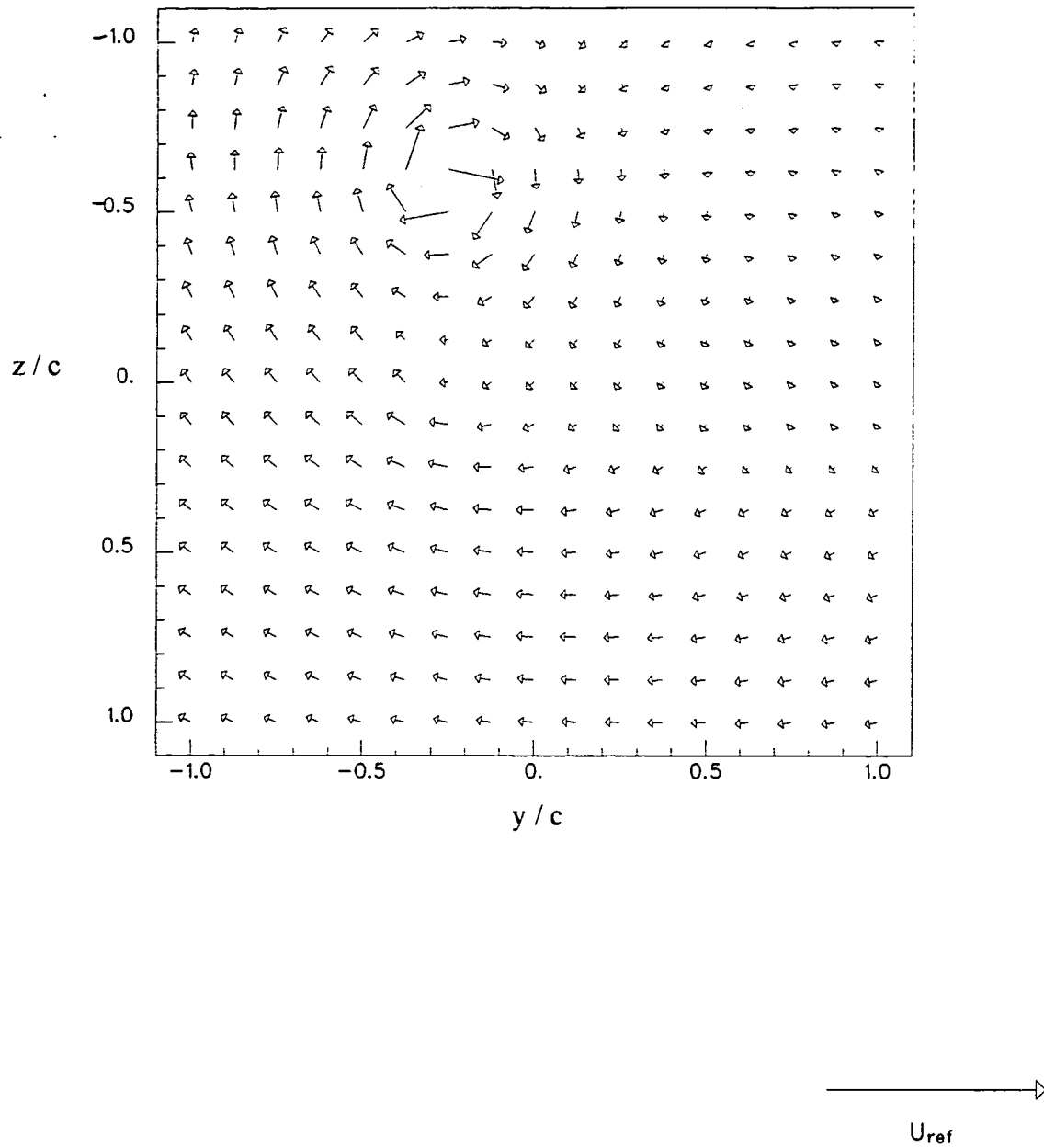


Figure 3.31 Mean cross-flow velocity vectors at  $X/c=30$ . (b)  $\Delta/c=-0.0625$ . (i) Coarse grid.



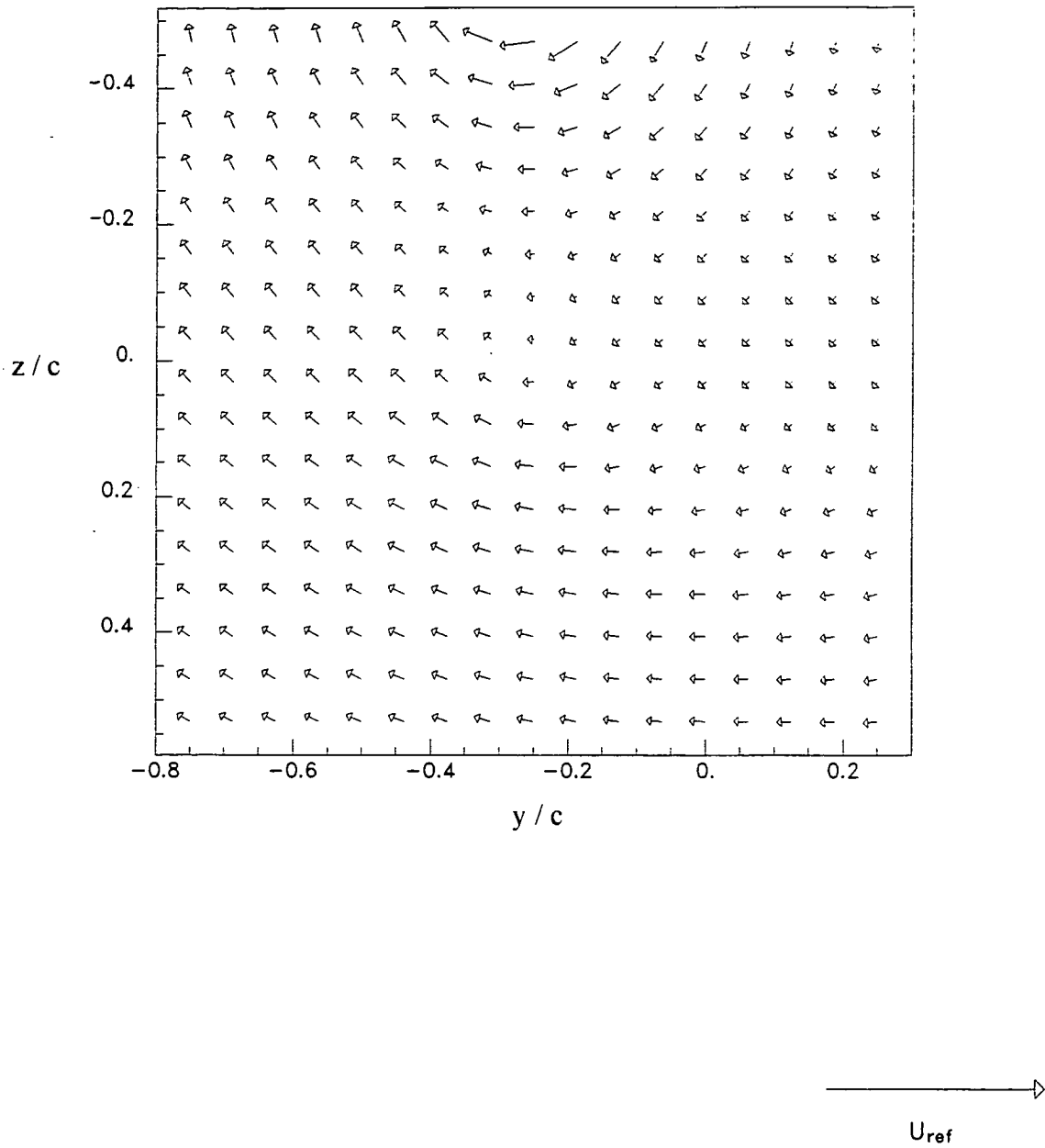


Figure 3.31 Mean cross-flow velocity vectors at  $X/c=30$ . (b)  $\Delta/c=-0.0625$ . (i) Fine grid.

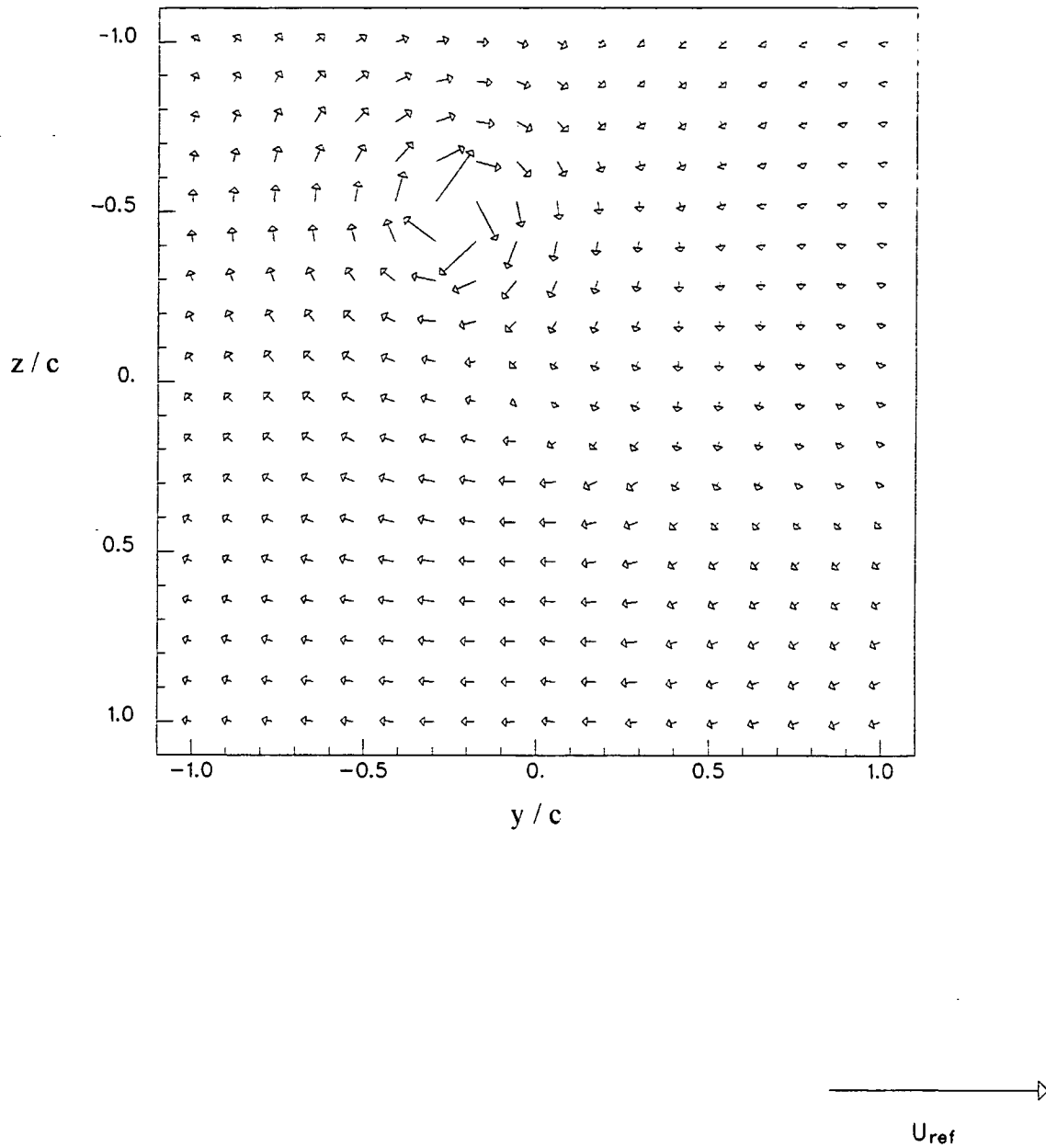


Figure 3.31 Mean cross-flow velocity vectors at  $X/c=30$ . (c)  $\Delta/c=0$ .

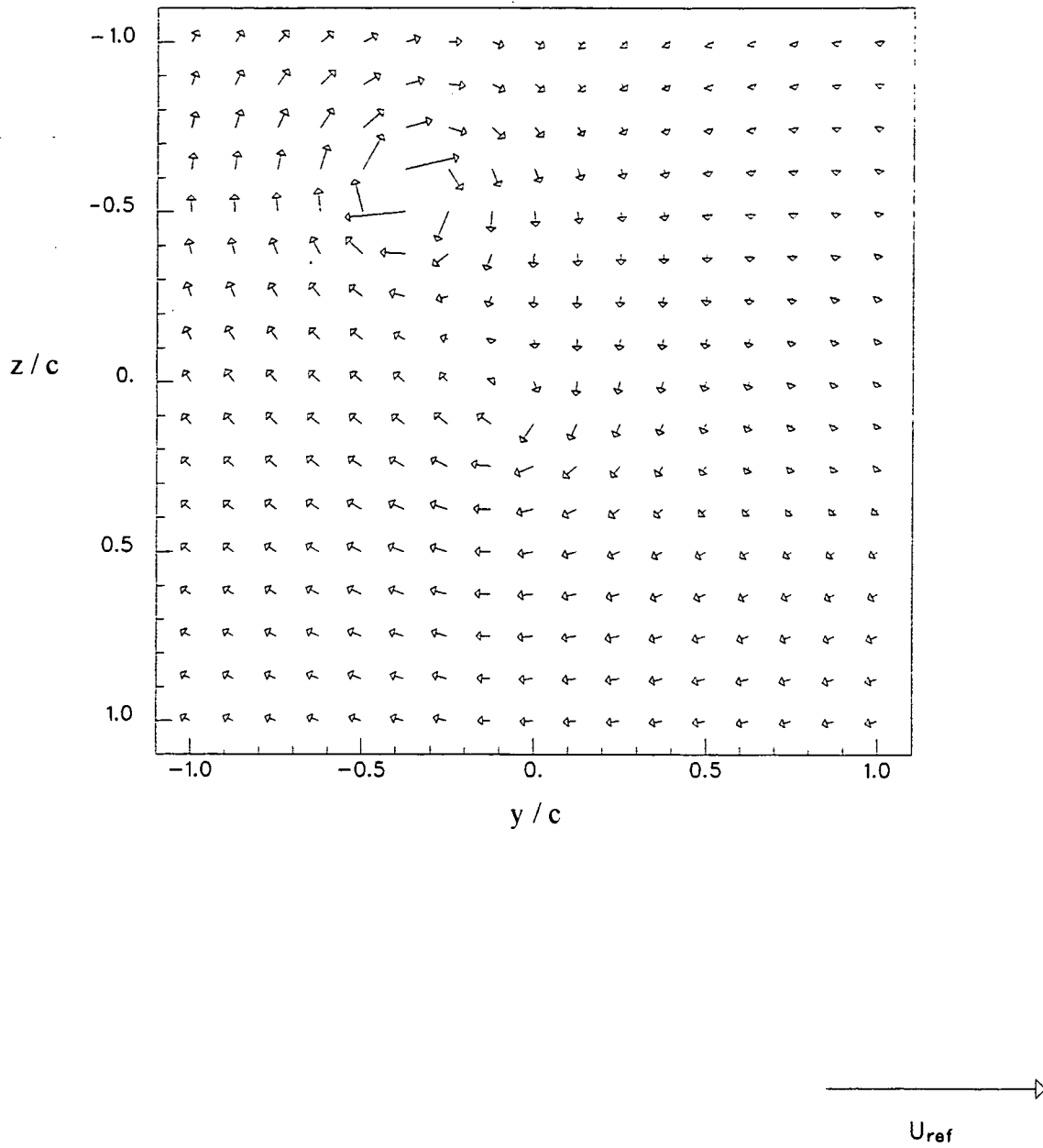


Figure 3.31 Mean cross-flow velocity vectors at  $X/c=30$ . (d)  $\Delta/c=0.0625$ .

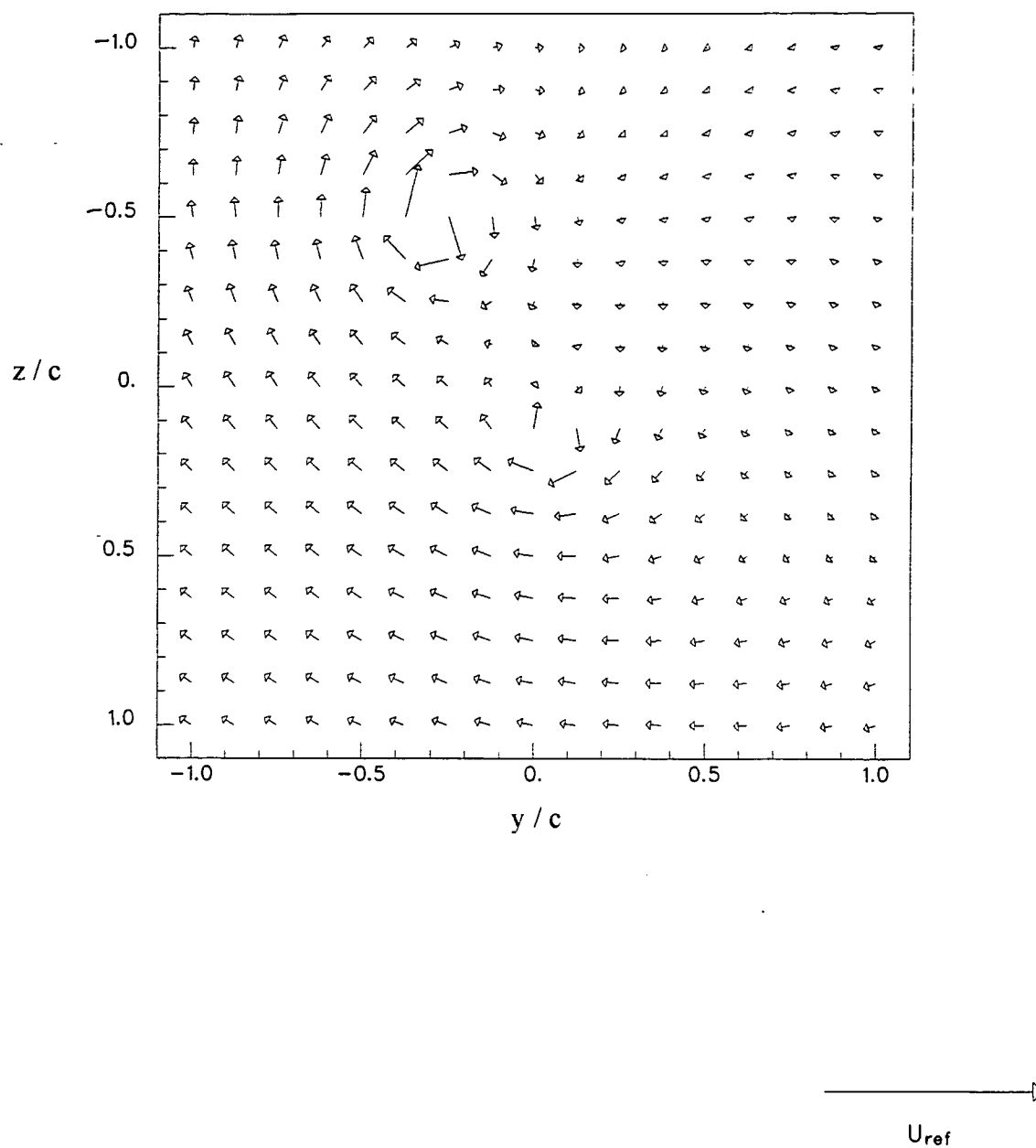


Figure 3.31 Mean cross-flow velocity vectors at  $X/c=30$ . (e)  $\Delta/c=0.125$ .

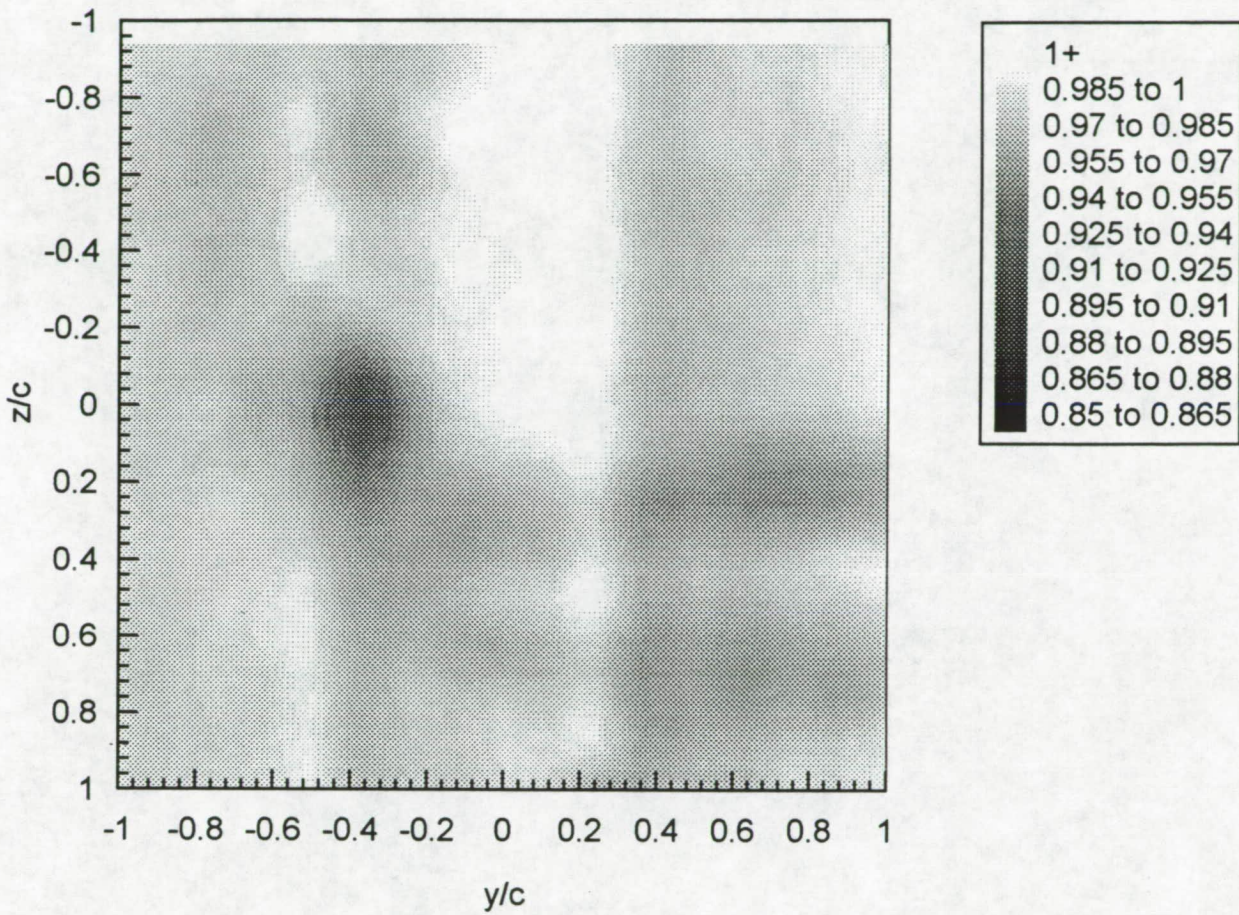


Figure 3.32 Contours of axial mean velocity  $U/U_{ref}$  at  $X/c=30$ . (a)  $\Delta/c=-0.125$ .



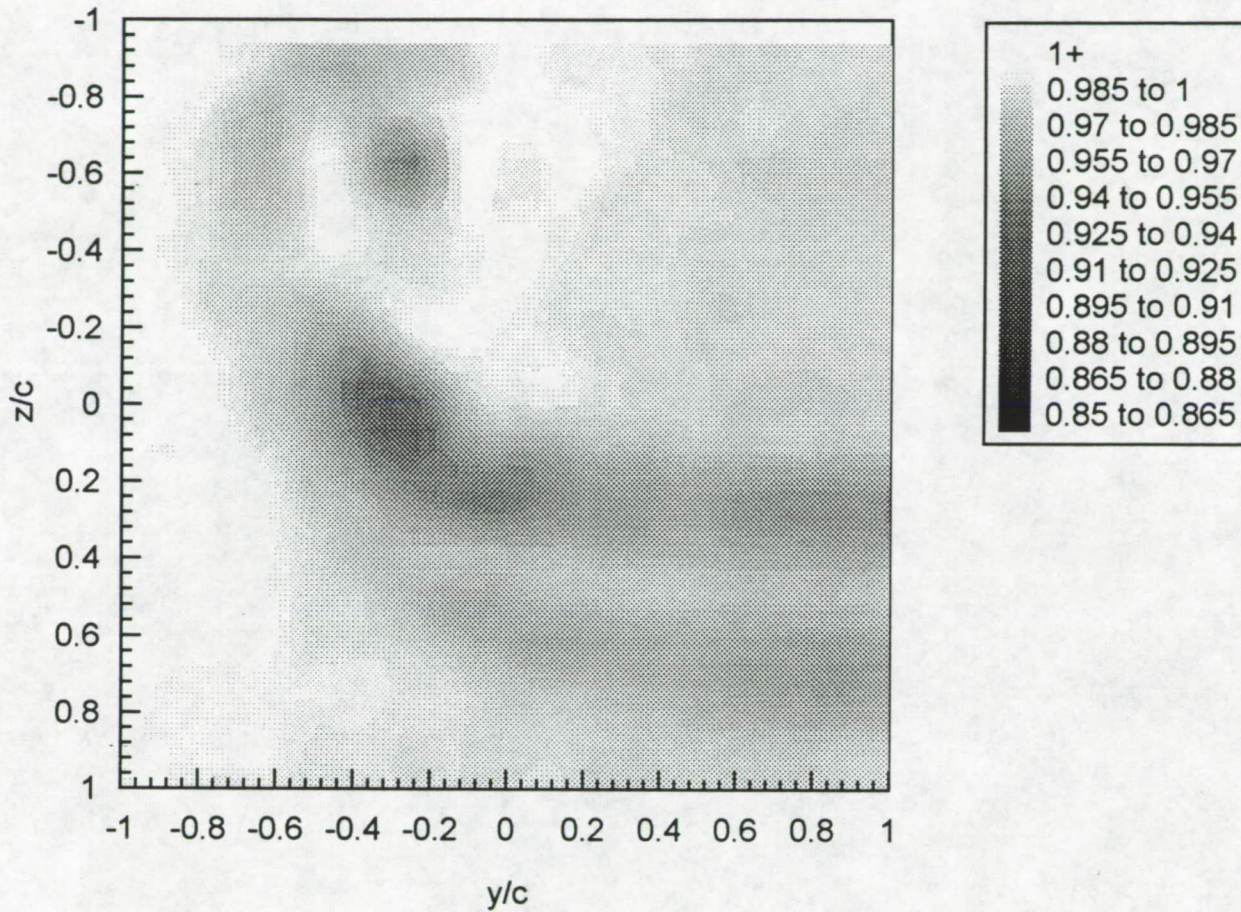


Figure 3.32 Contours of axial mean velocity  $U/U_{ref}$  at  $X/c=30$ . (b)  $\Delta/c=-0.0625$ . (i) Coarse grid.



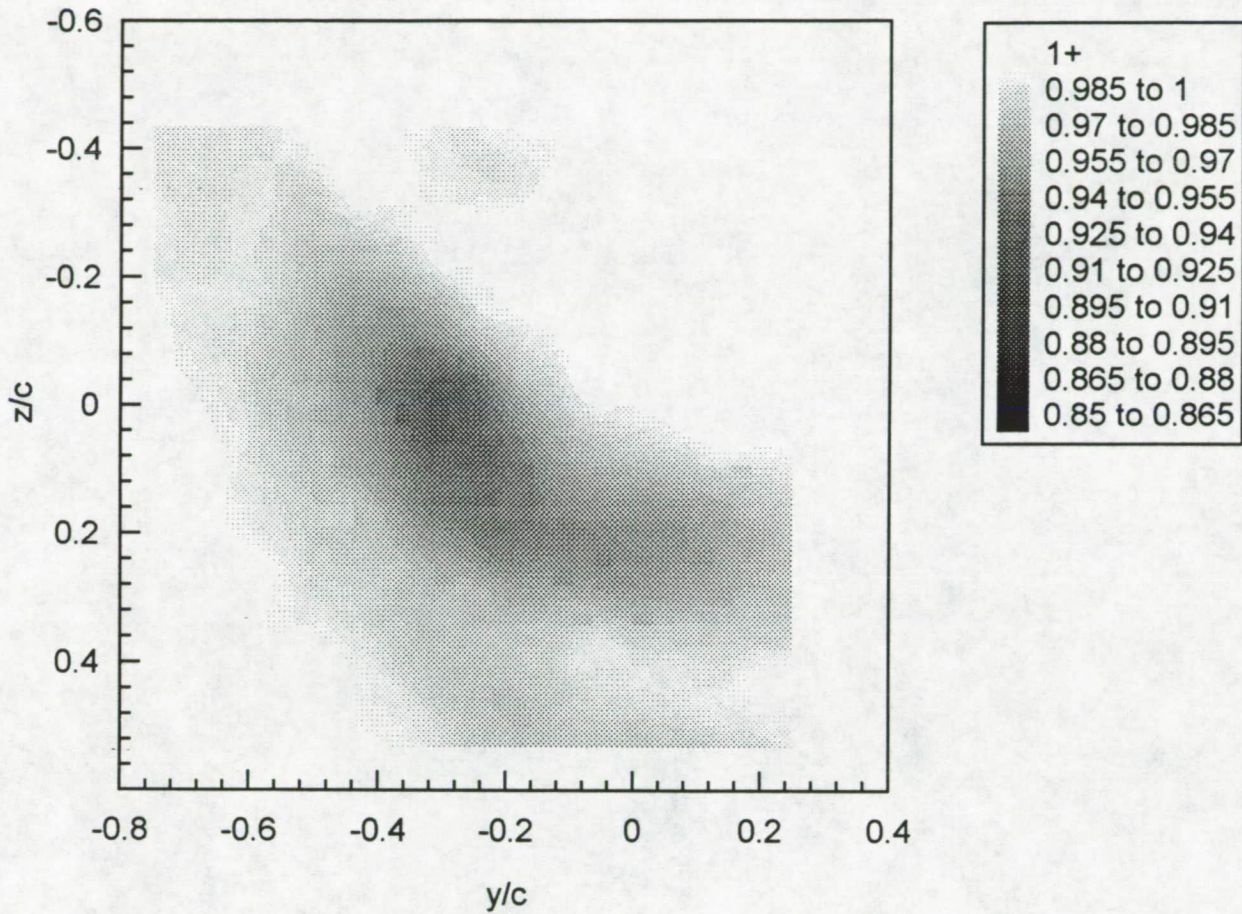


Figure 3.32 Contours of axial mean velocity  $U/U_{ref}$  at  $X/c=30$ . (b)  $\Delta/c=-0.0625$ . (i) Fine grid.



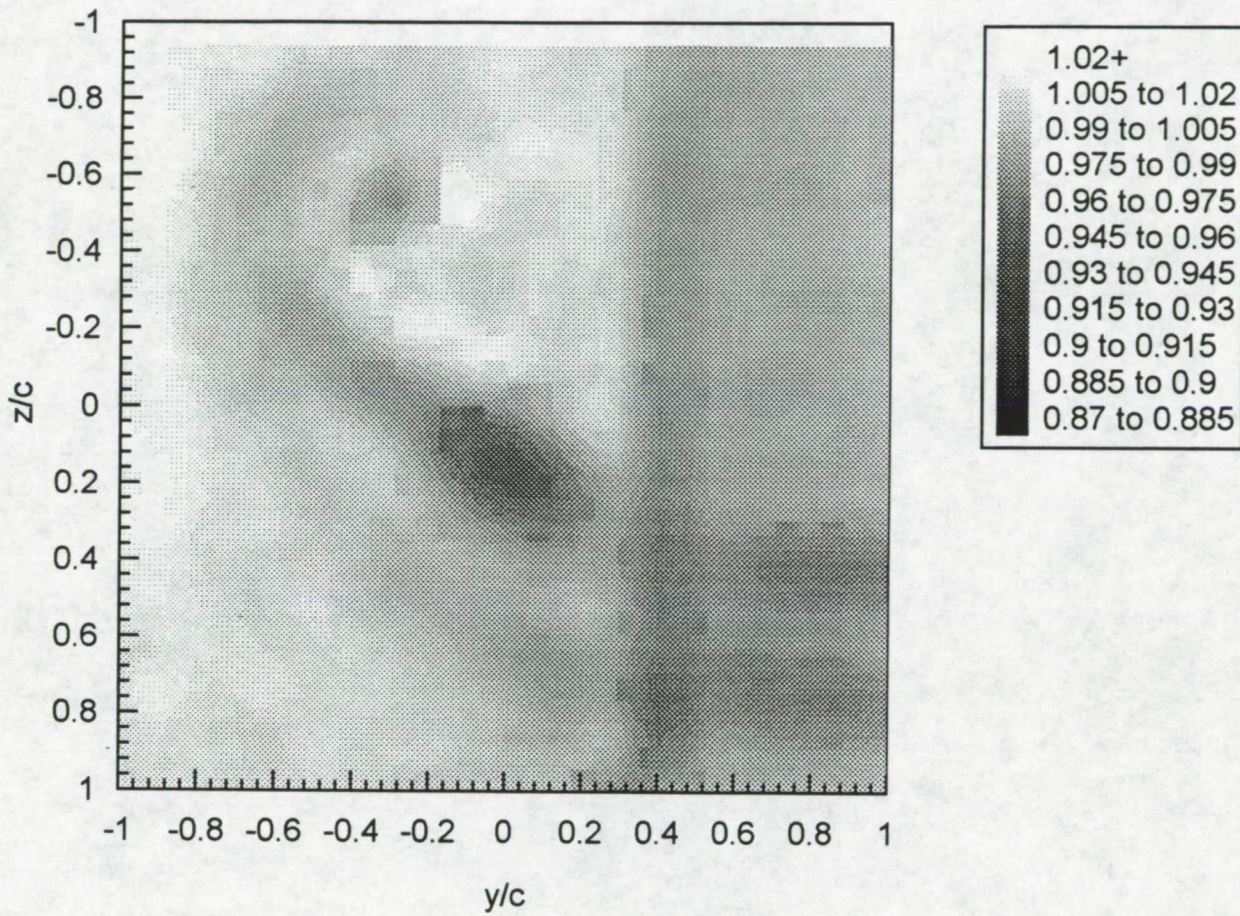


Figure 3.32 Contours of axial mean velocity  $U/U_{ref}$  at  $X/c=30$ . (c)  $\Delta/c=0$ .



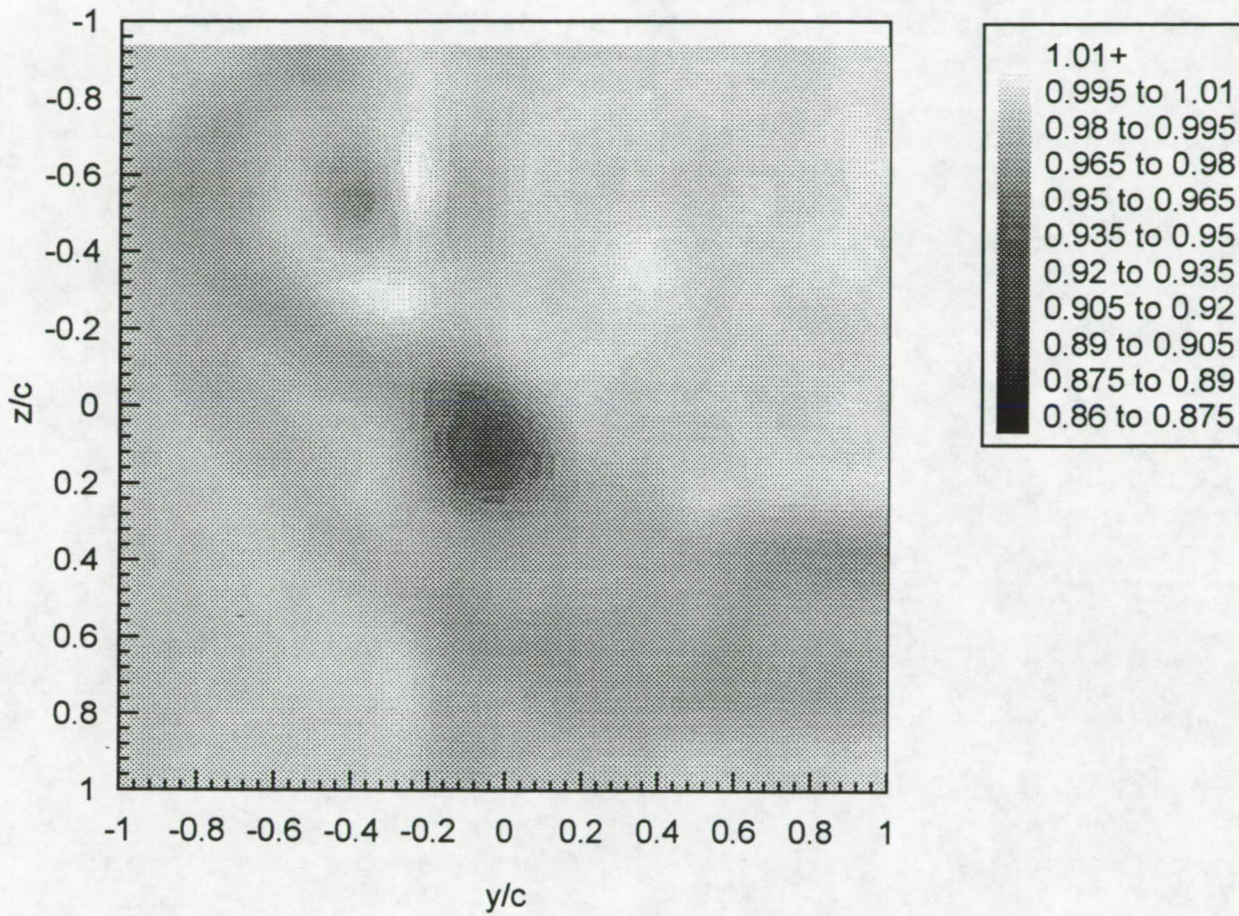


Figure 3.32 Contours of axial mean velocity  $U/U_{ref}$  at  $X/c=30$ . (d)  $\Delta/c=0.0625$ .



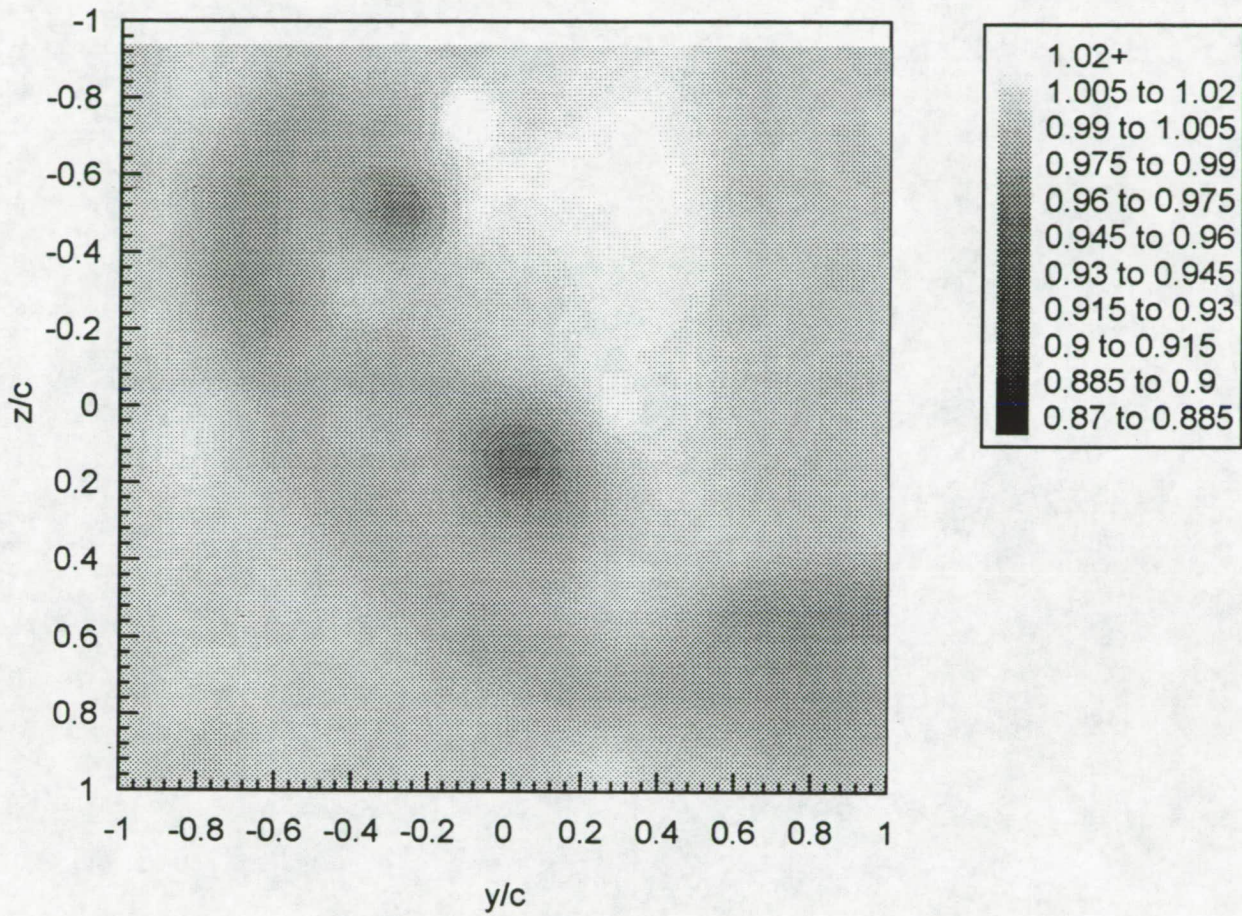


Figure 3.32 Contours of axial mean velocity  $U/U_{ref}$  at  $X/c=30$ . (e)  $\Delta/c=0.125$ .



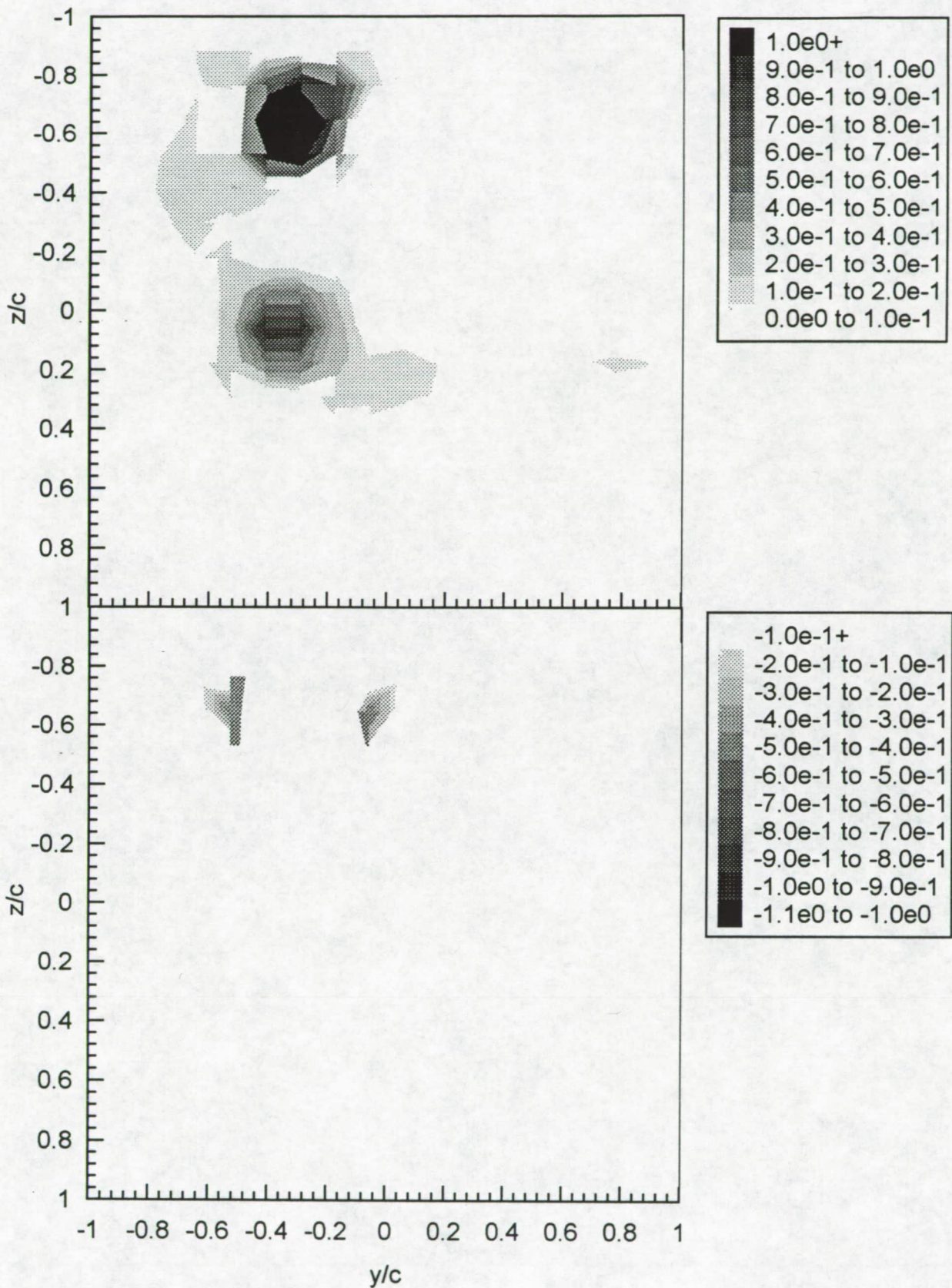


Figure 3.33 Contours of axial mean vorticity  $\omega_x c / U_{ref}$  at  $X/c = 30$ . (a)  $\Delta/c = -0.125$ . Upper figure - positive vorticity, lower figure - negative vorticity.



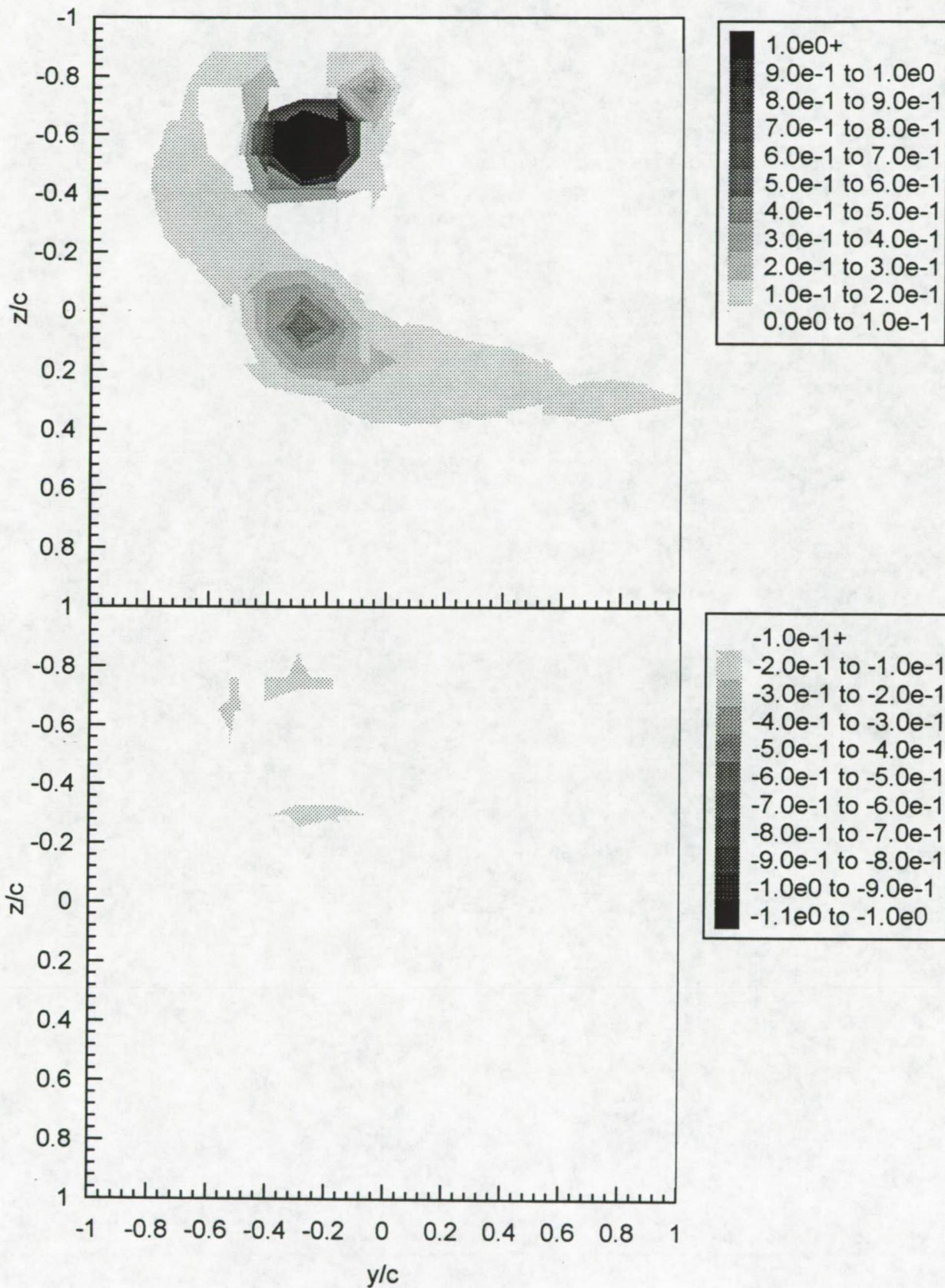


Figure 3.33 Contours of axial mean vorticity  $\omega_x c / U_{ref}$  at  $X/c = 30$ . (b)  $\Delta/c = -0.0625$ . (i) Coarse grid. Upper figure - positive vorticity, lower figure - negative vorticity.



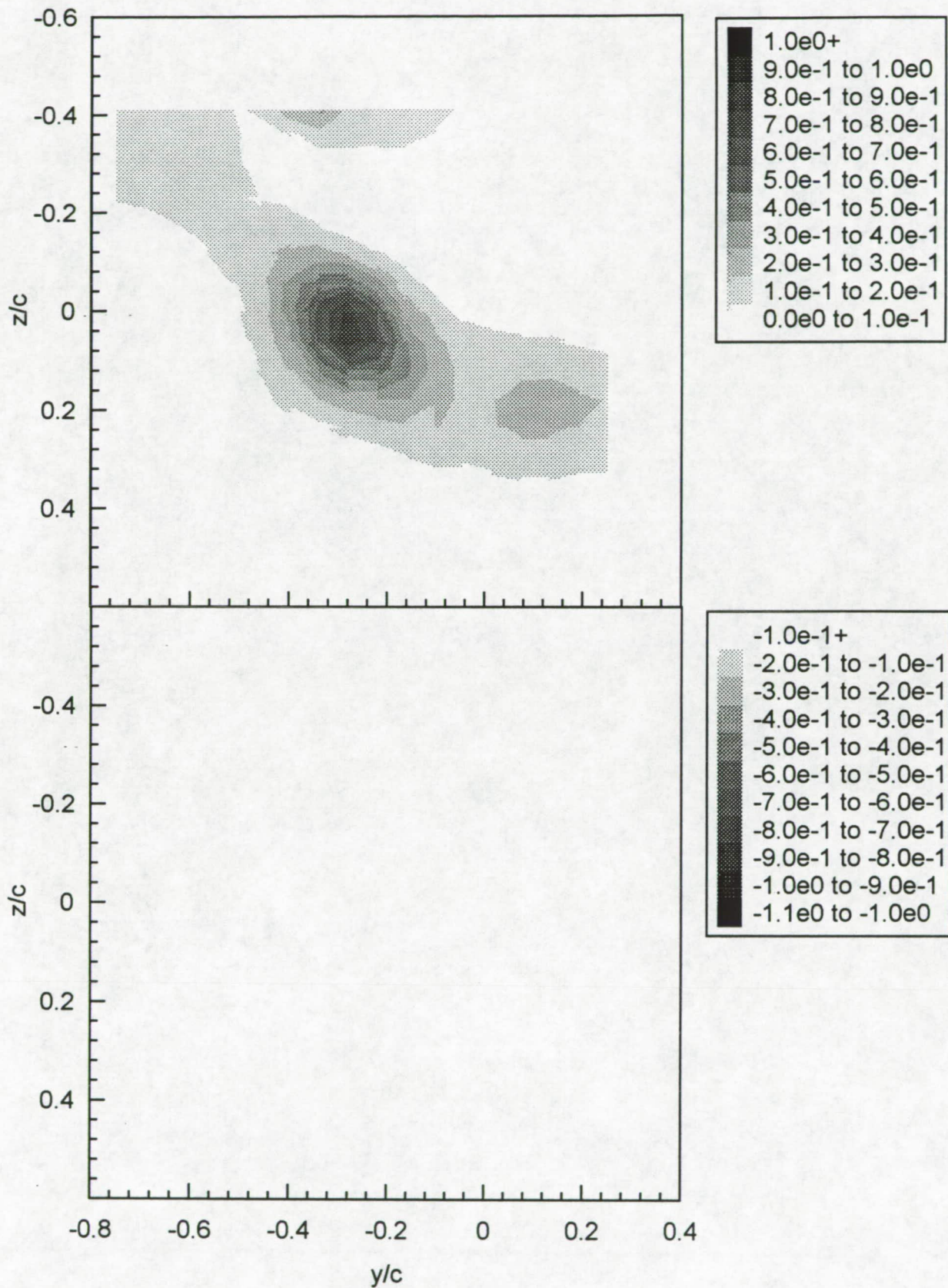


Figure 3.33 Contours of axial mean vorticity  $\omega_x c/U_{ref}$  at  $X/c=30$ . (b)  $\Delta/c=-0.0625$ . (i) Fine grid. Upper figure - positive vorticity, lower figure - negative vorticity.



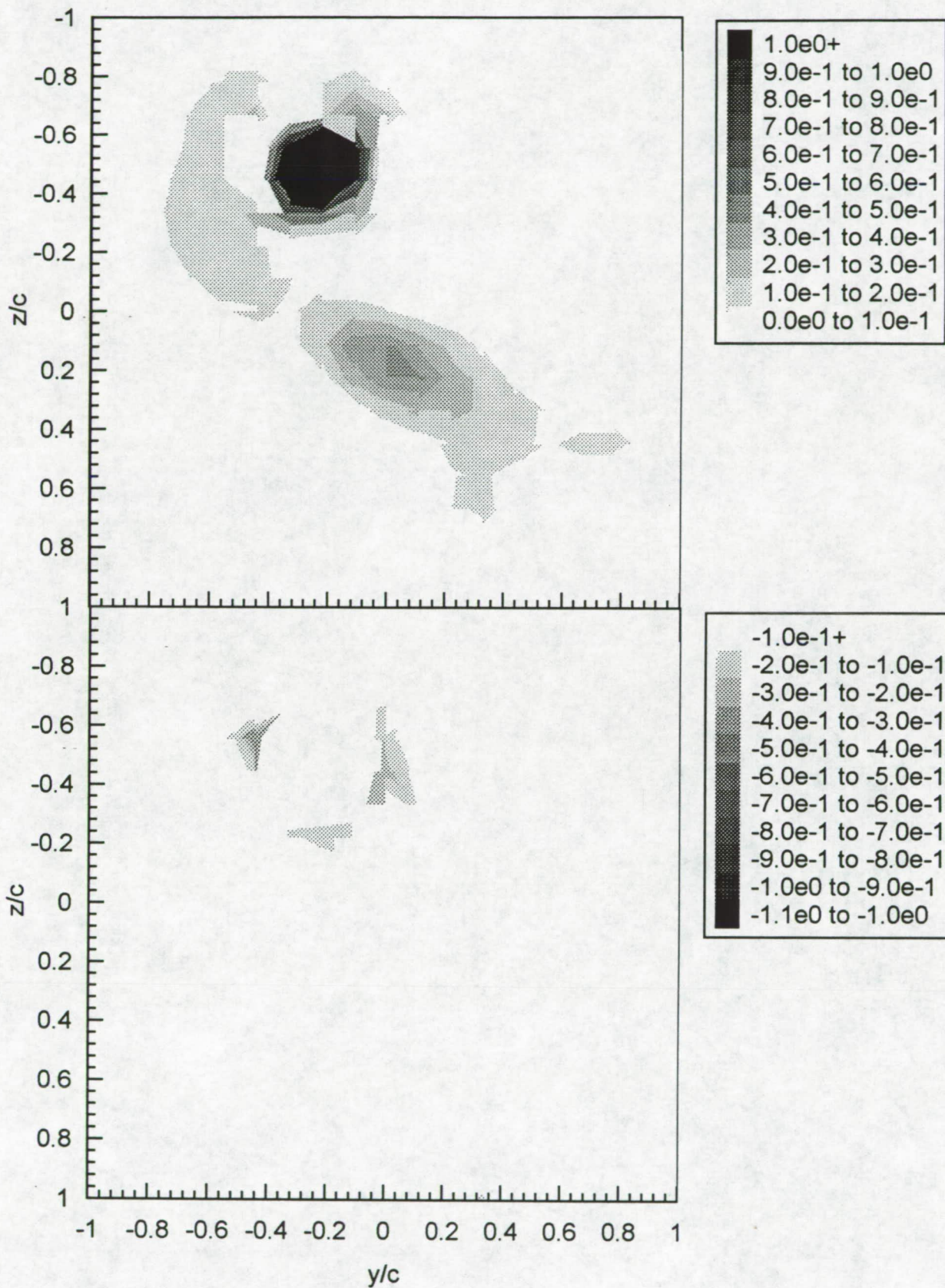


Figure 3.33 Contours of axial mean vorticity  $\omega_x c / U_{ref}$  at  $X/c = 30$ . (c)  $\Delta/c = 0$ . Upper figure - positive vorticity, lower figure - negative vorticity.



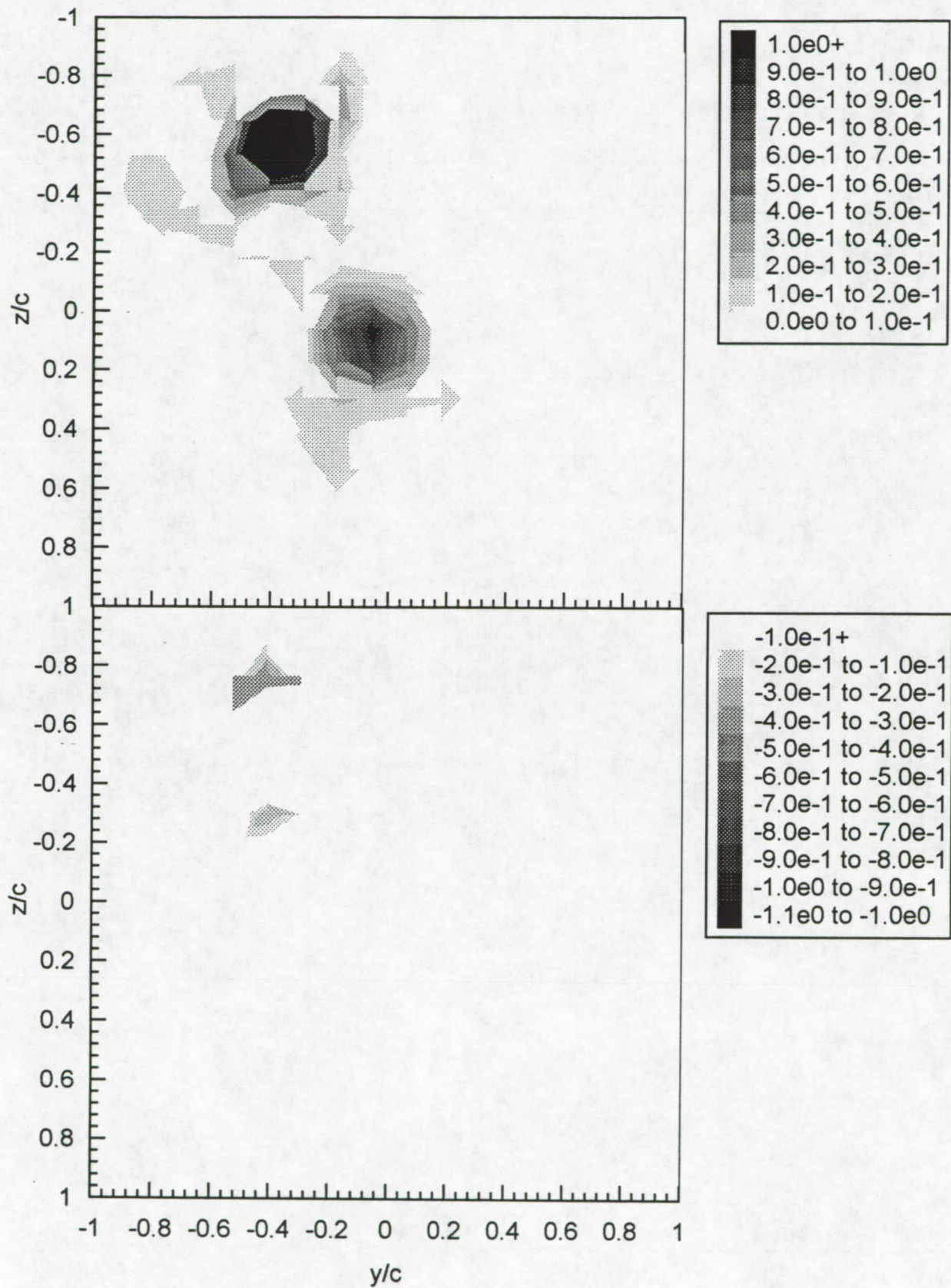


Figure 3.33 Contours of axial mean vorticity  $\omega_x c / U_{ref}$  at  $X/c = 30$ . (d)  $\Delta/c = 0.0625$ . Upper figure - positive vorticity, lower figure - negative vorticity.

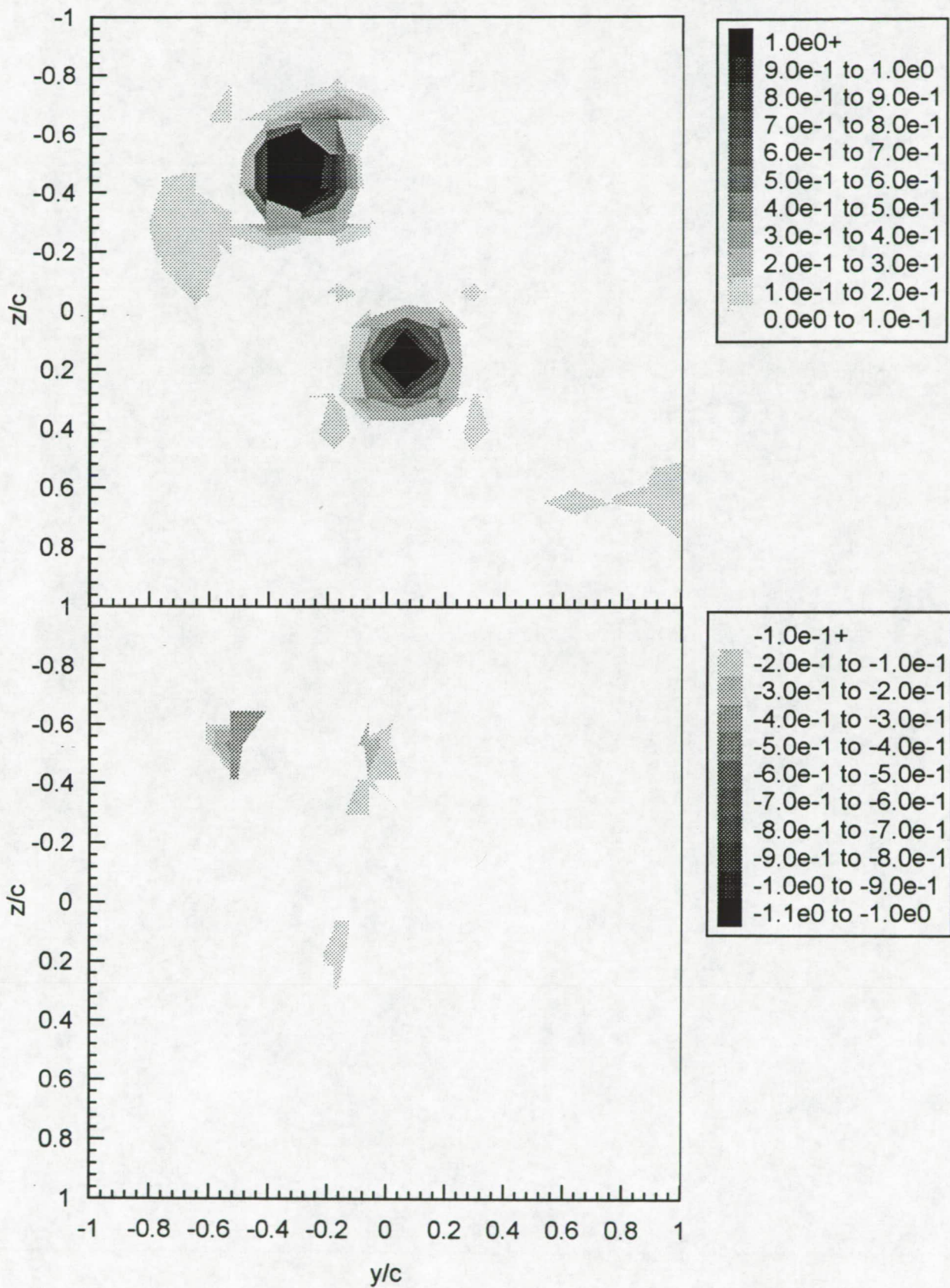


Figure 3.33 Contours of axial mean vorticity  $\omega_x c / U_{ref}$  at  $X/c = 30$ . (e)  $\Delta/c = 0.125$ . Upper figure - positive vorticity, lower figure - negative vorticity.



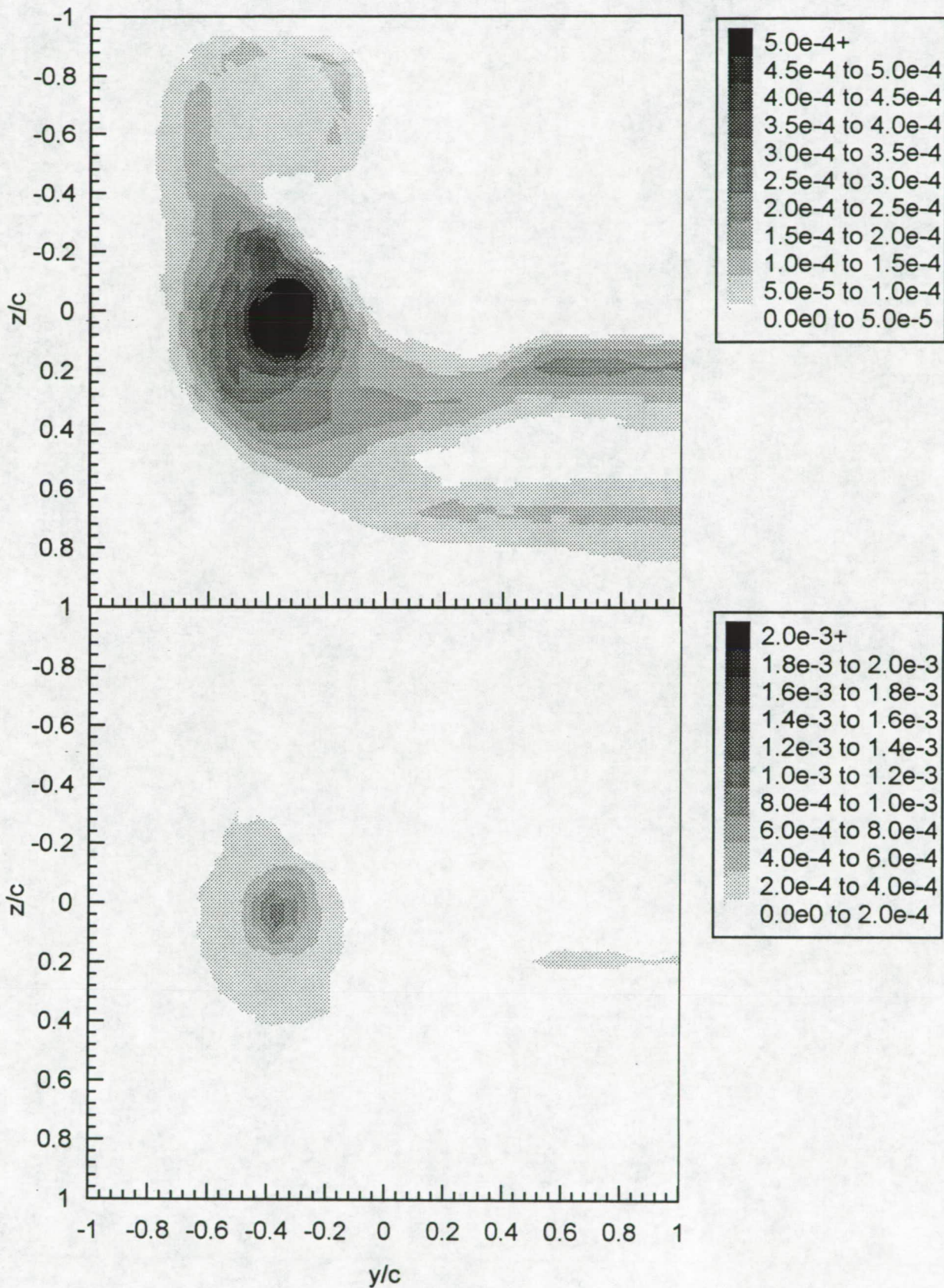


Figure 3.34 Contours of axial normal turbulence stress  $\overline{u'^2}/U_{ref}^2$  at  $X/c=30$ . (a)  $\Delta/c=-0.125$ . Upper and lower figures show different contour ranges.



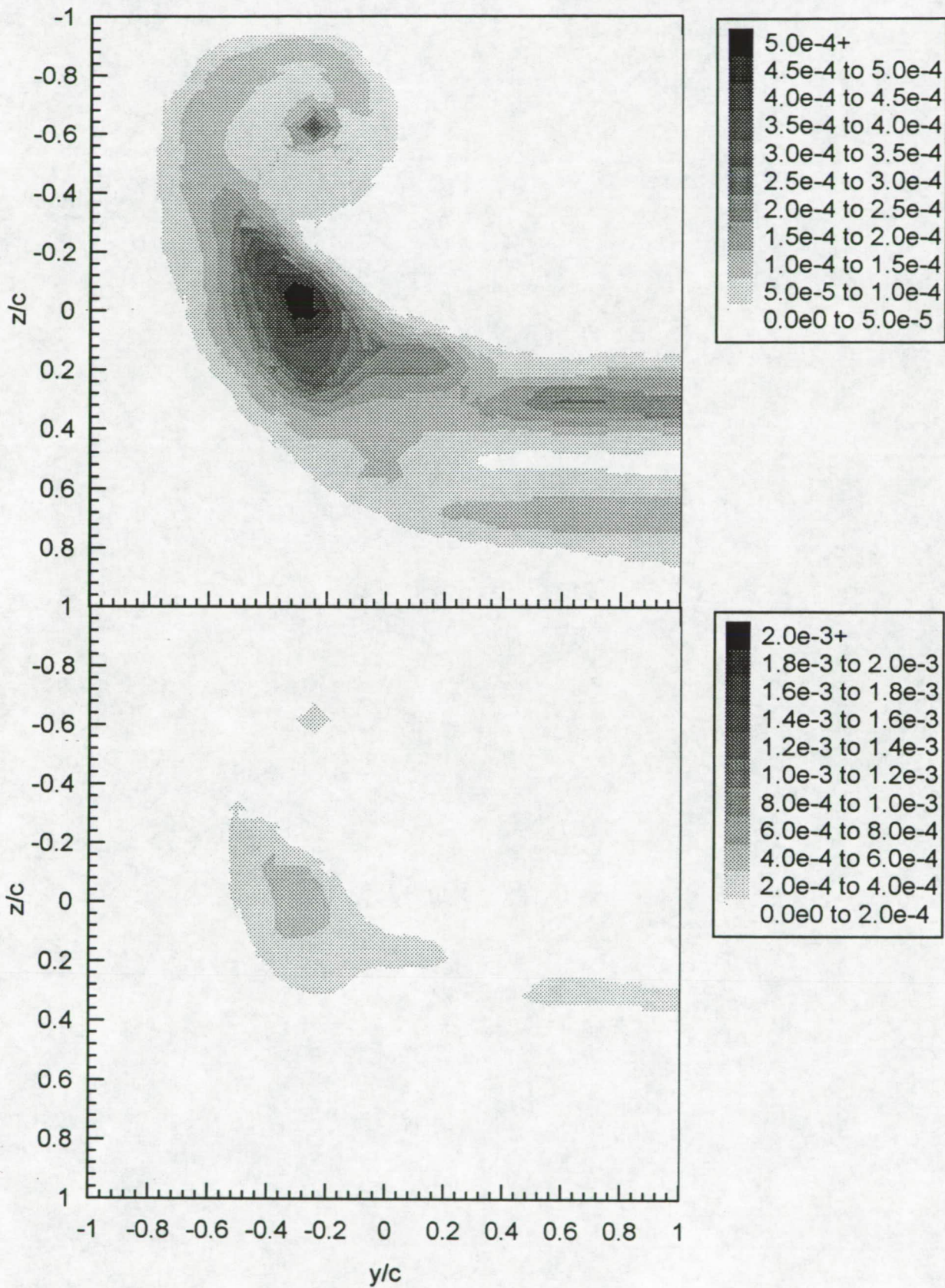


Figure 3.34 Contours of axial normal turbulence stress  $\overline{u'^2}/U_{ref}^2$  at  $X/c=30$ . (b)  $\Delta/c=-0.0625$ .  
(i) Coarse grid. Upper and lower figures show different contour ranges.



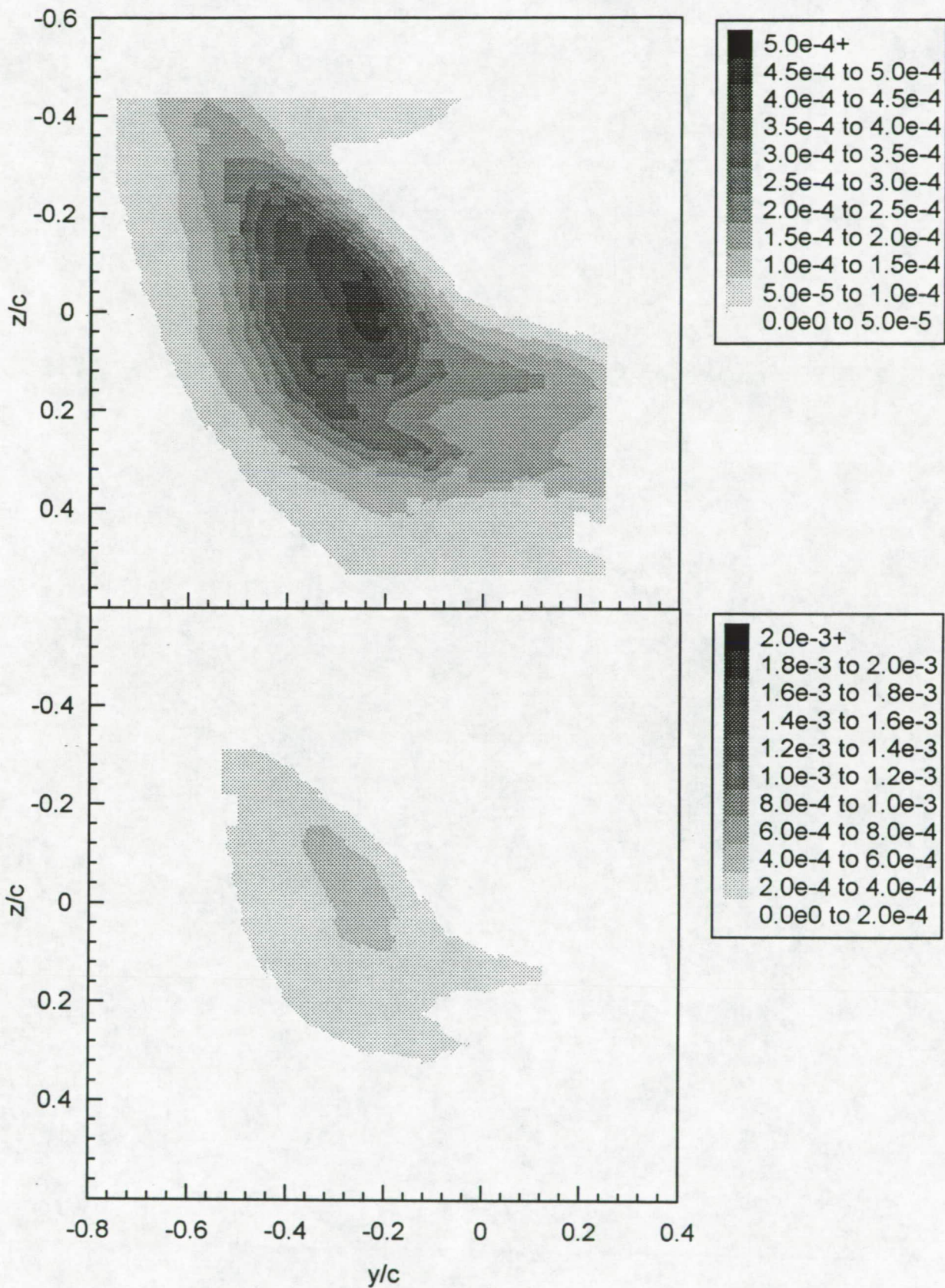


Figure 3.34 Contours of axial normal turbulence stress  $\overline{u'^2}/U_{ref}^2$  at  $X/c=30$ . (b)  $\Delta/c=-0.0625$ . (i) Fine grid. Upper and lower figures show different contour ranges.



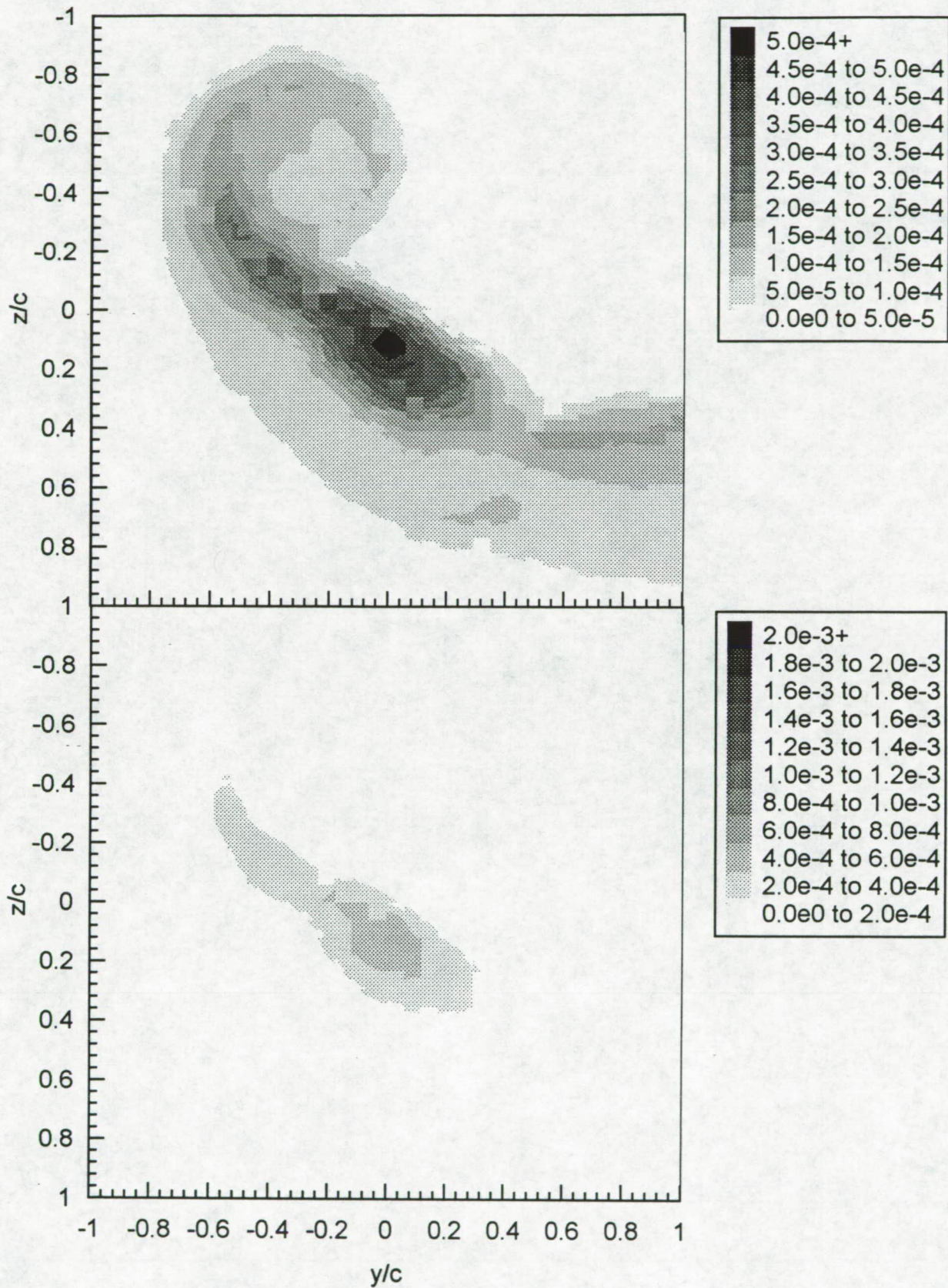


Figure 3.34 Contours of axial normal turbulence stress  $\overline{u'^2}/U_{ref}^2$  at  $X/c=30$ . (c)  $\Delta/c=0$ . Upper and lower figures show different contour ranges.



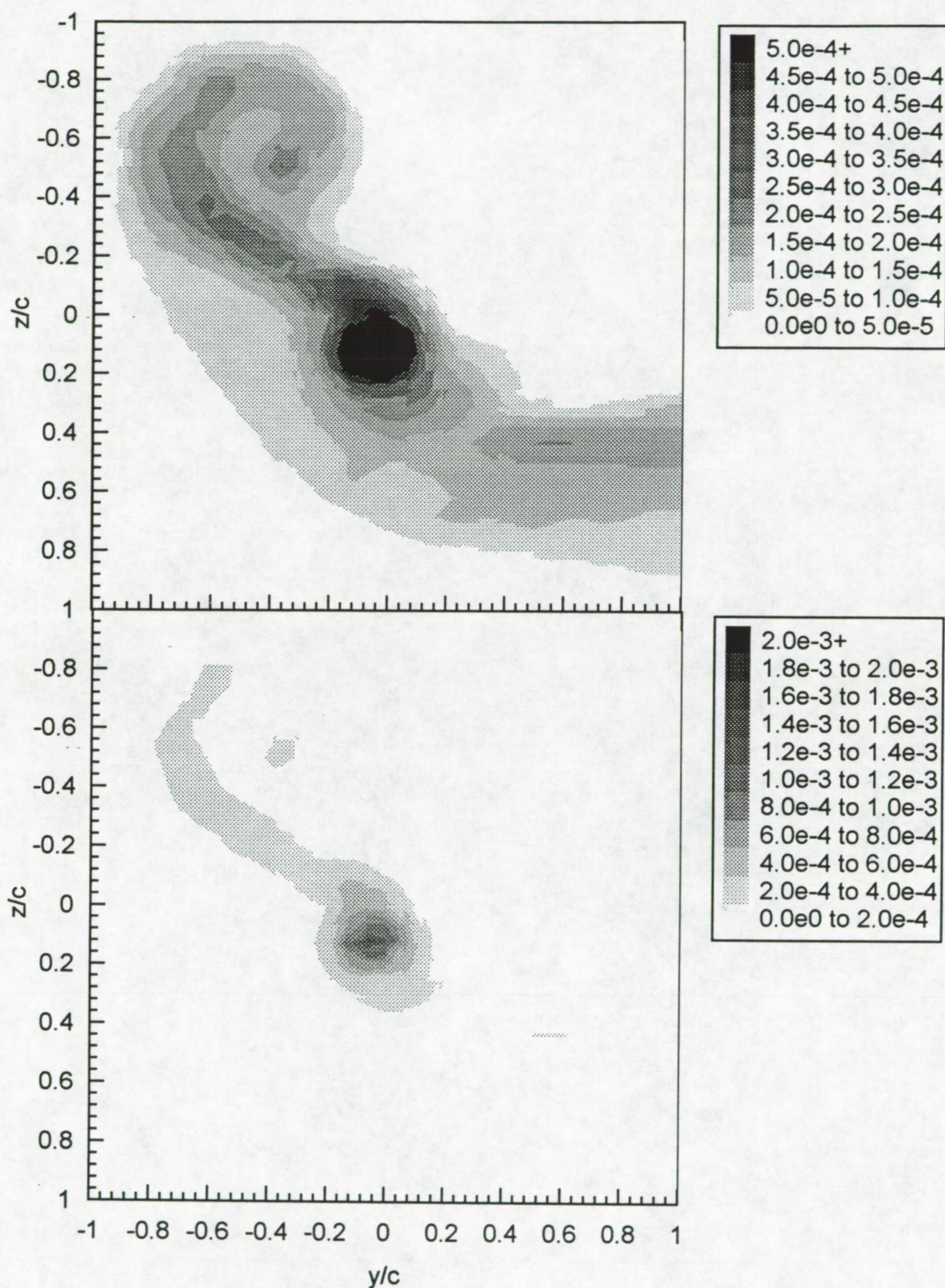


Figure 3.34 Contours of axial normal turbulence stress  $\overline{u'^2}/U_{ref}^2$  at  $X/c=30$ . (d)  $\Delta/c=0.0625$ . Upper and lower figures show different contour ranges.



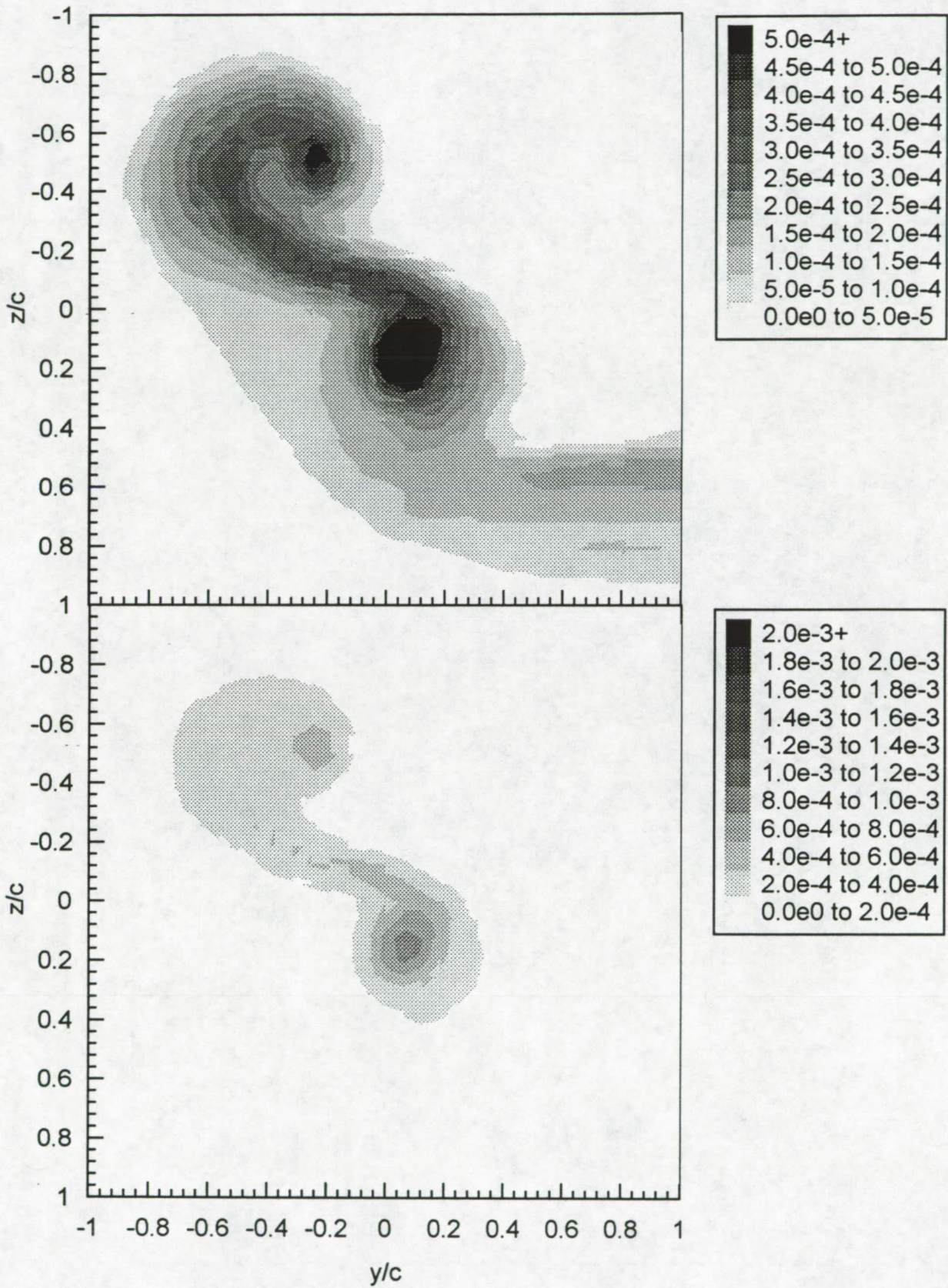


Figure 3.34 Contours of axial normal turbulence stress  $\overline{u'^2}/U_{ref}^2$  at  $X/c=30$ . (e)  $\Delta/c=0.125$ . Upper and lower figures show different contour ranges.



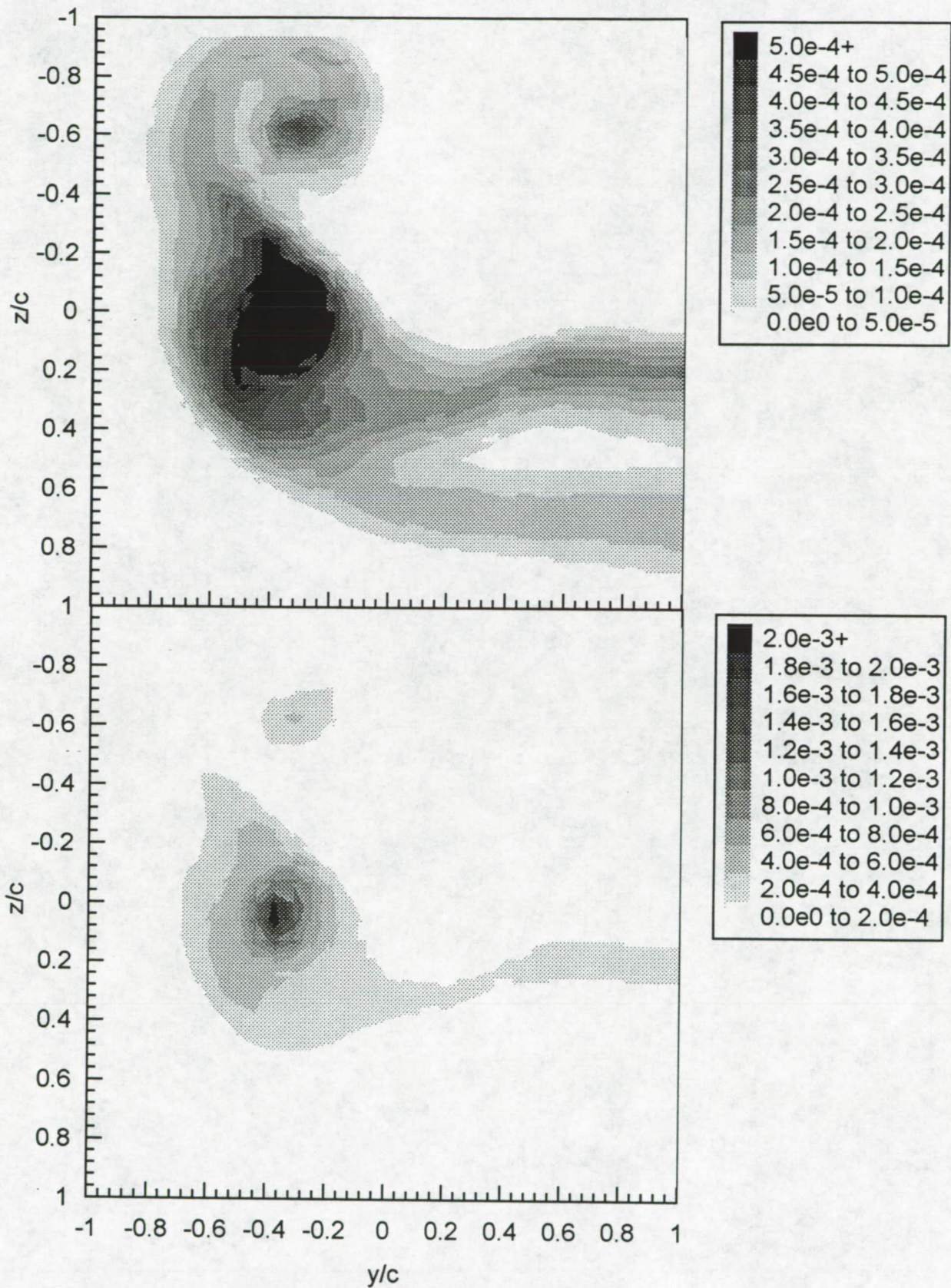


Figure 3.35 Contours of turbulence kinetic energy  $k/U_{ref}^2$  at  $X/c=30$ . (a)  $\Delta/c=-0.125$ . Upper and lower figures show different contour ranges.



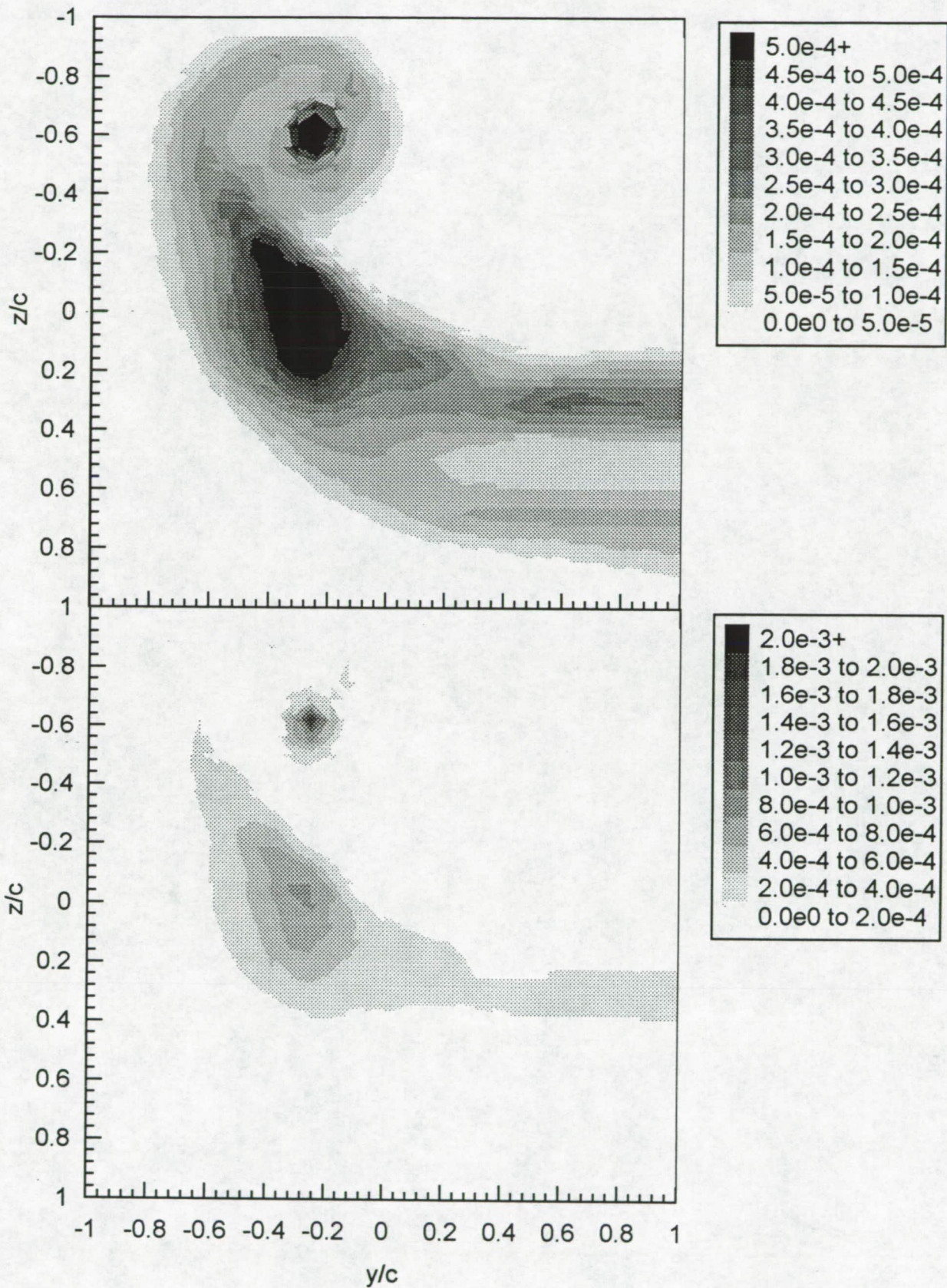


Figure 3.35 Contours of turbulence kinetic energy  $k/U_{ref}^2$  at  $X/c=30$ . (b)  $\Delta/c=-0.0625$ . (i) Coarse grid. Upper and lower figures show different contour ranges.



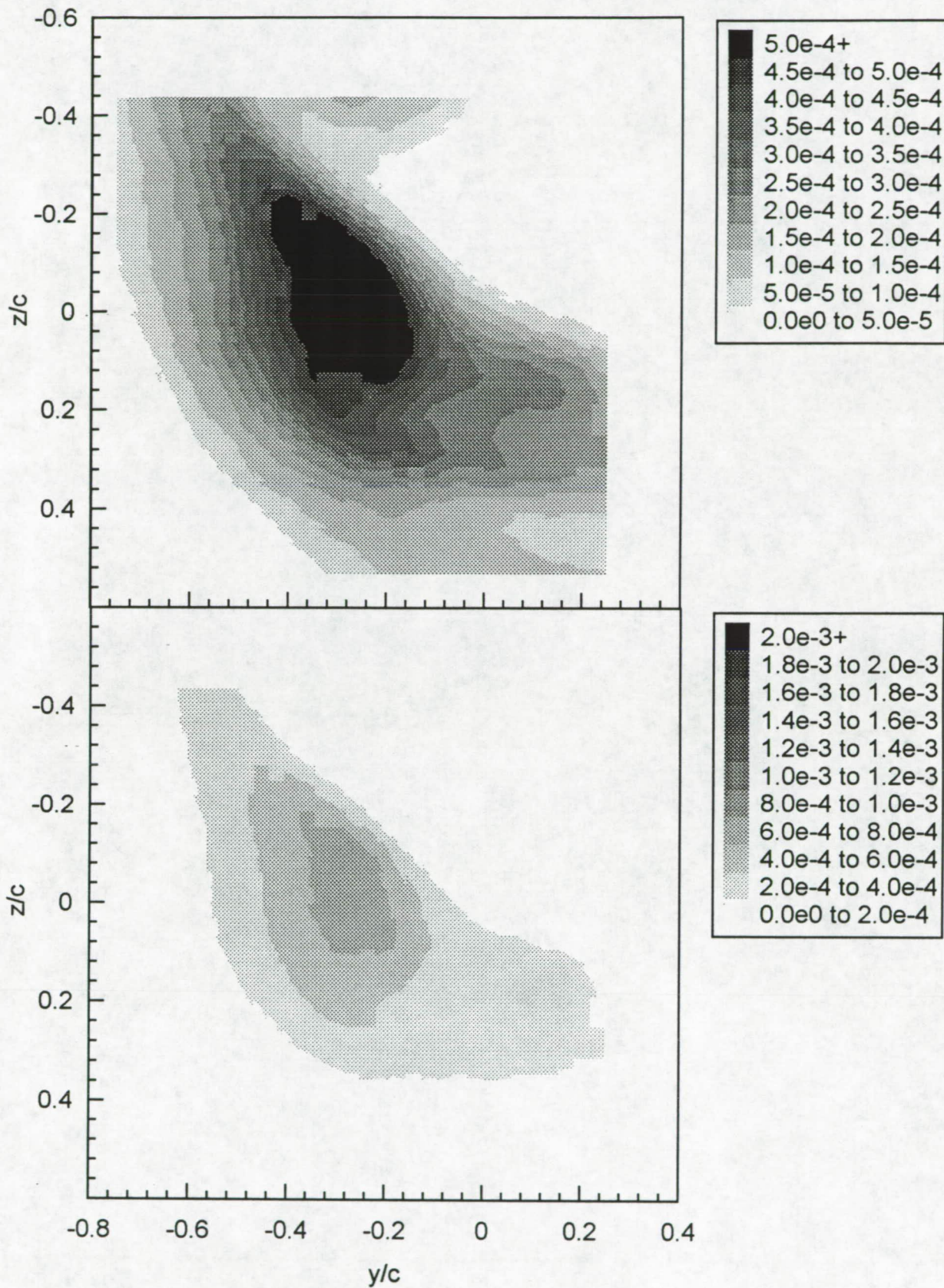


Figure 3.35 Contours of turbulence kinetic energy  $k/U_{ref}^2$  at  $X/c=30$ . (b)  $\Delta/c=-0.0625$ . (i) Fine grid. Upper and lower figures show different contour ranges.



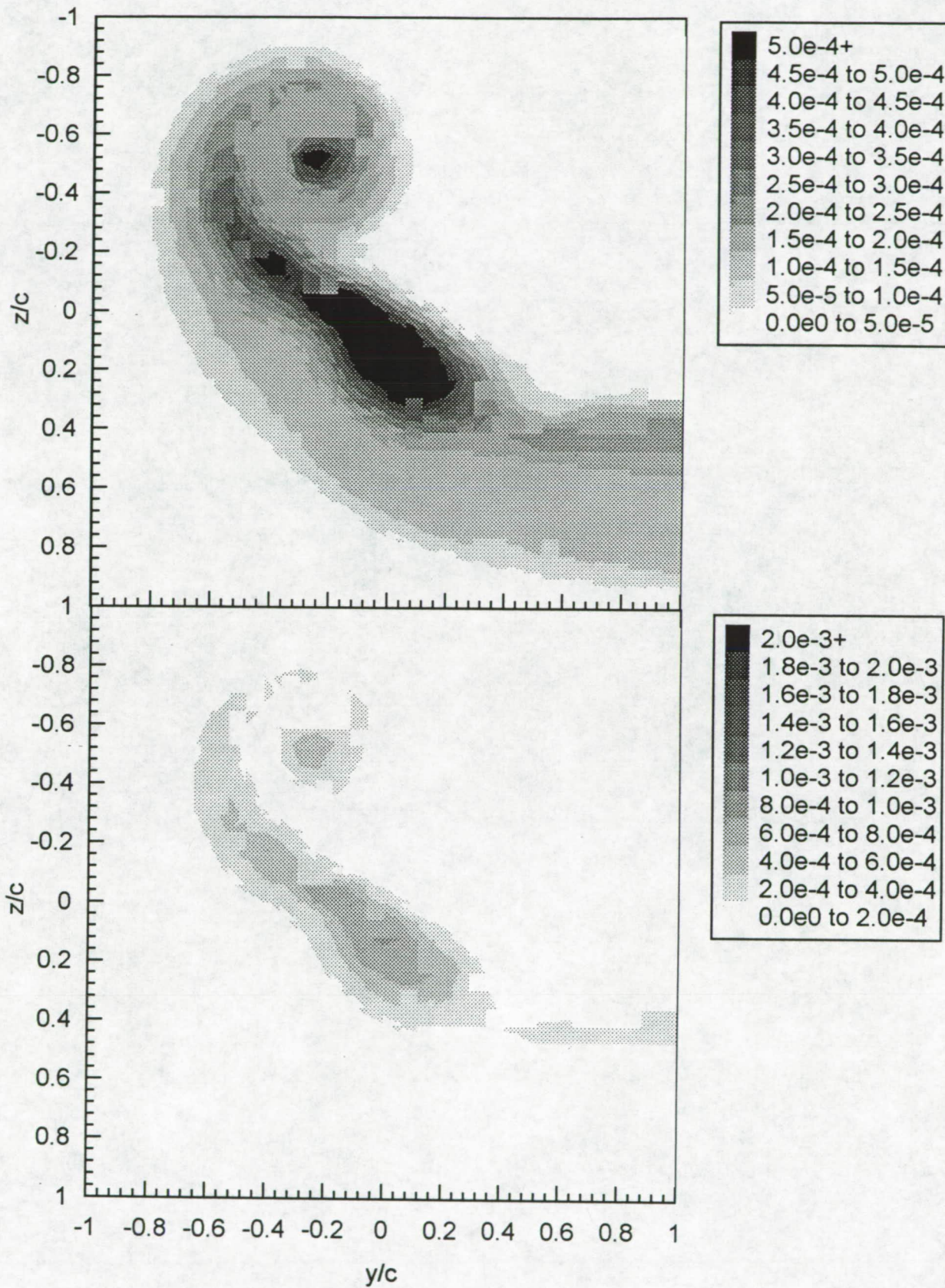


Figure 3.35 Contours of turbulence kinetic energy  $k/U_{ref}^2$  at  $X/c=30$ . (c)  $\Delta/c=0$ . Upper and lower figures show different contour ranges.



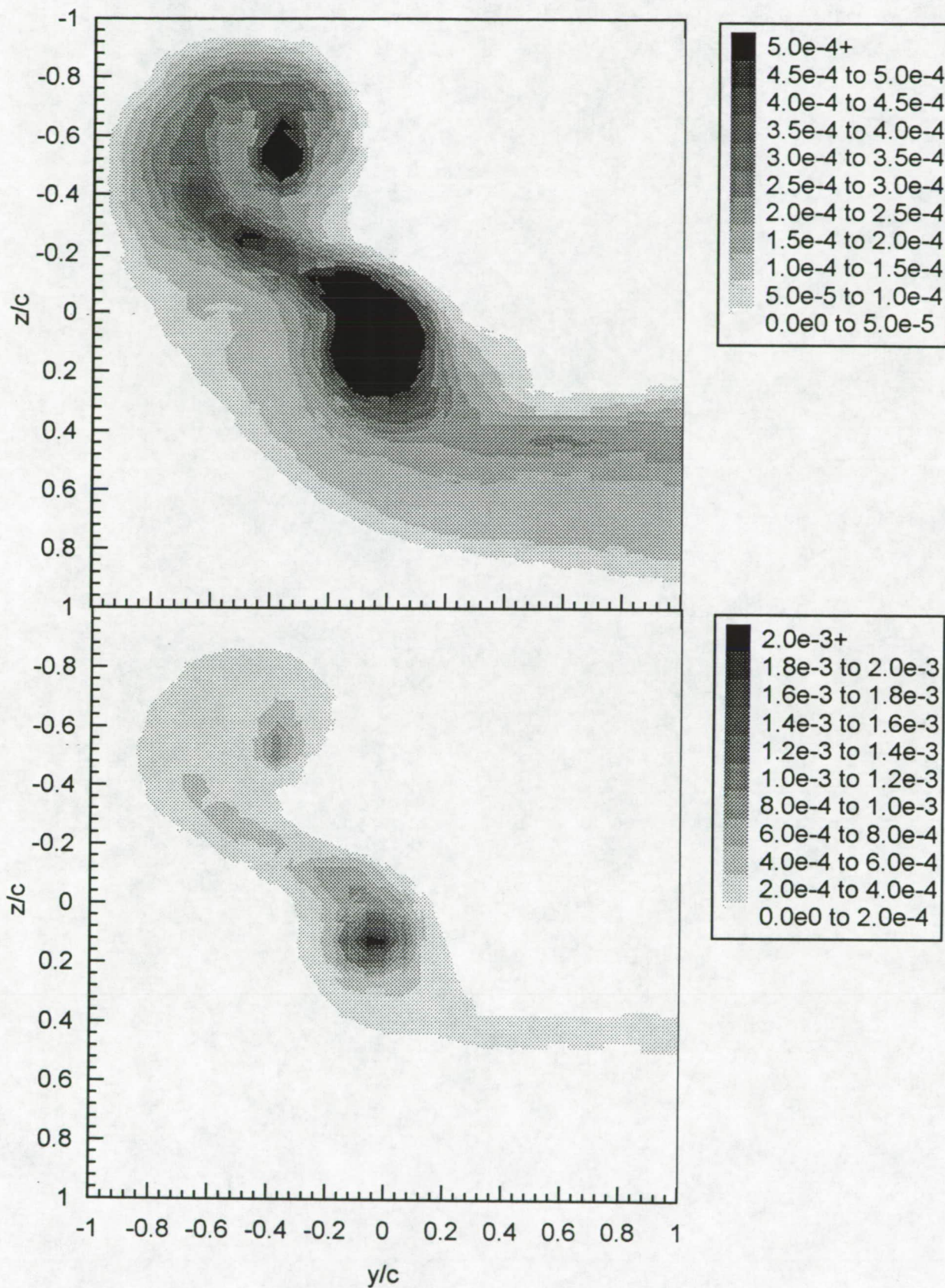


Figure 3.35 Contours of turbulence kinetic energy  $k/U_{ref}^2$  at  $X/c=30$ . (d)  $\Delta/c=0.0625$ . Upper and lower figures show different contour ranges.



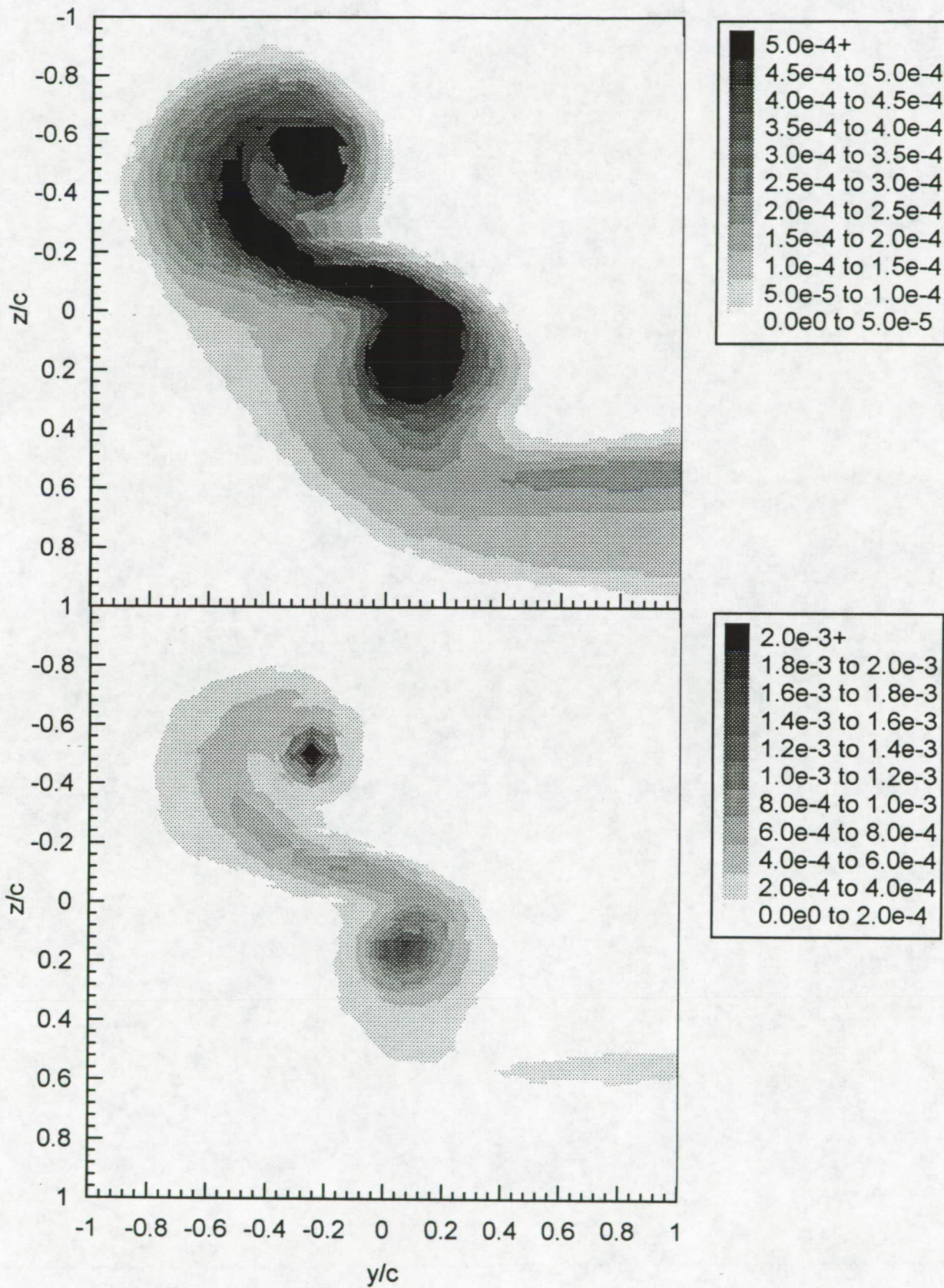


Figure 3.35 Contours of turbulence kinetic energy  $k/U_{ref}^2$  at  $X/c=30$ . (e)  $\Delta/c=0.125$ . Upper and lower figures show different contour ranges.



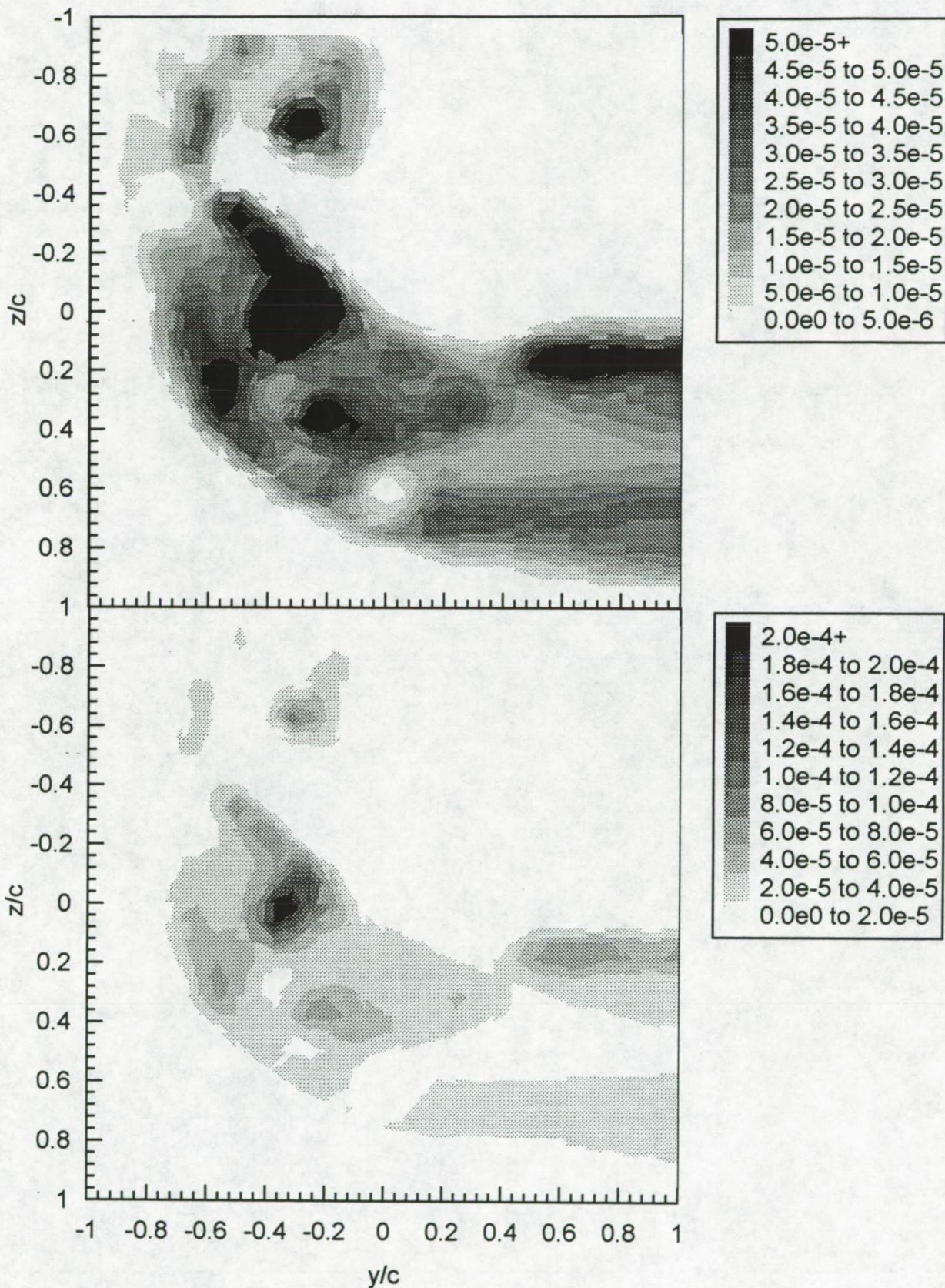


Figure 3.36 Contours of axial shear stress magnitude  $\tau_a/U_{ref}^2$  at  $X/c=30$ . (a)  $\Delta/c=-0.125$ . Upper and lower figures show different contour ranges.



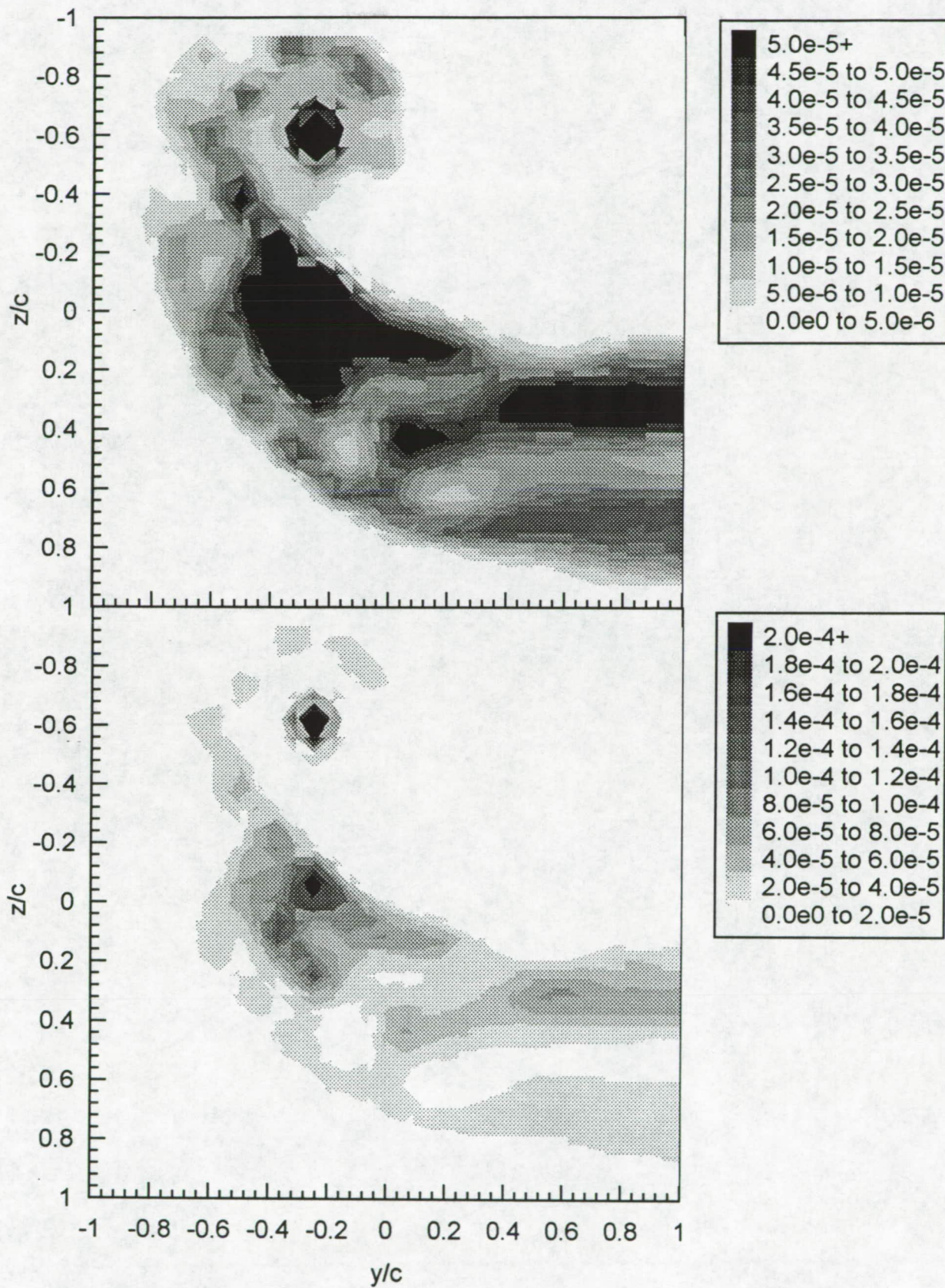


Figure 3.36 Contours of axial shear stress magnitude  $\tau_a/U_{ref}^2$  at  $X/c=30$ . (b)  $\Delta/c=-0.0625$ . (i) Coarse grid. Upper and lower figures show different contour ranges.



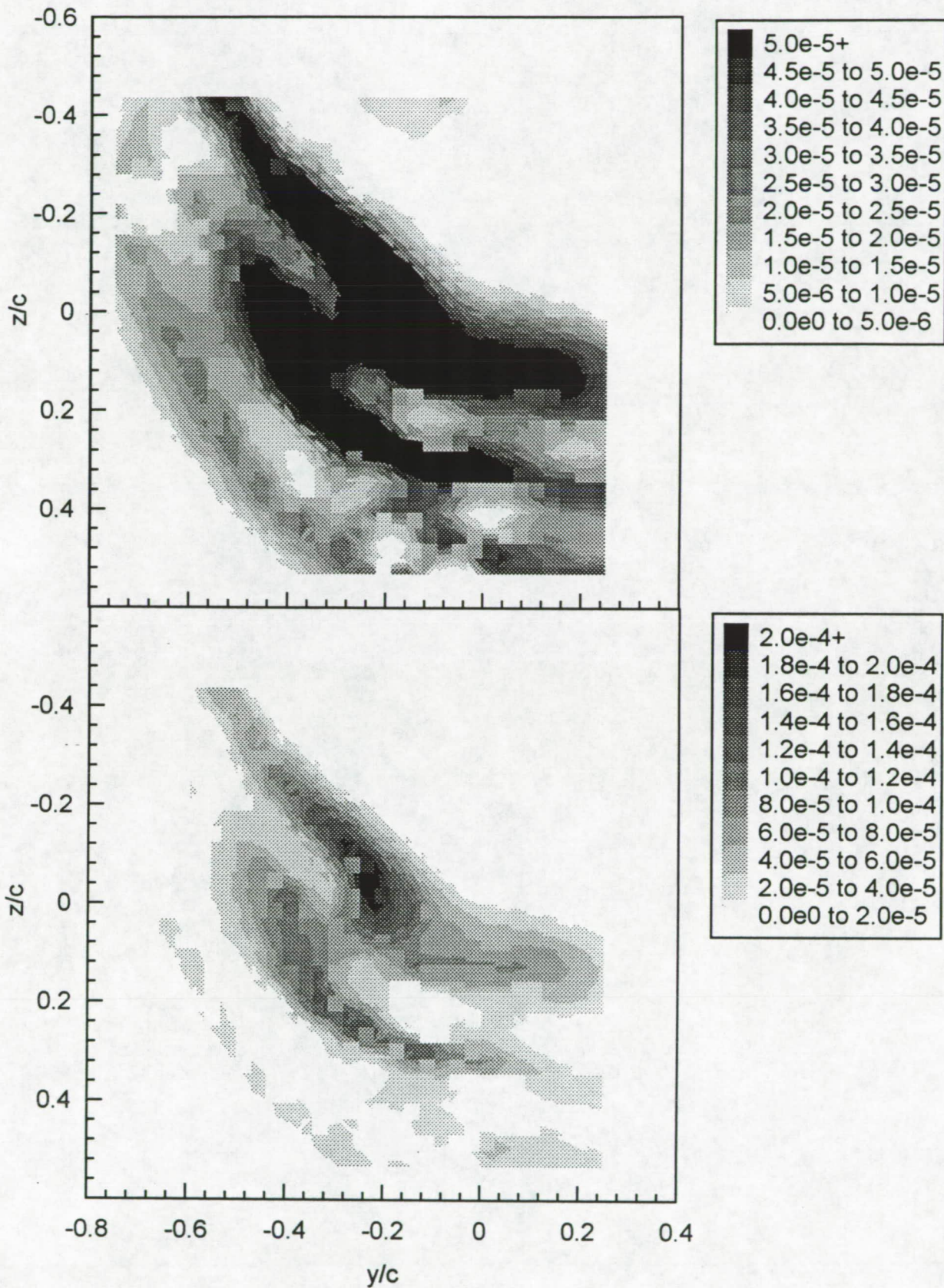


Figure 3.36 Contours of axial shear stress magnitude  $\tau_a/U_{ref}^2$  at  $X/c=30$ . (b)  $\Delta/c=-0.0625$ . (i) Fine grid. Upper and lower figures show different contour ranges.



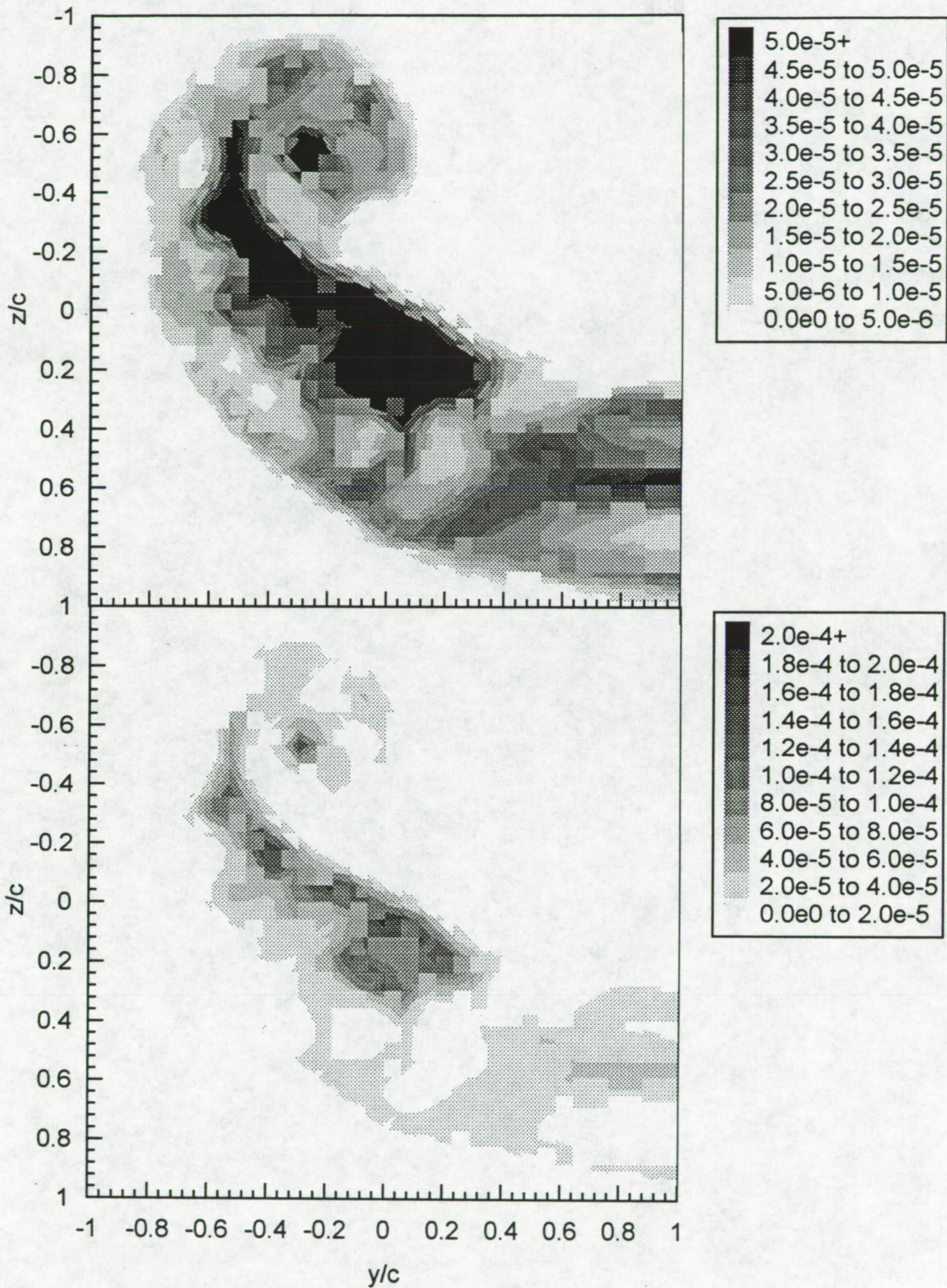


Figure 3.36 Contours of axial shear stress magnitude  $\tau_a/U_{ref}^2$  at  $X/c=30$ . (c)  $\Delta/c=0$ . Upper and lower figures show different contour ranges.



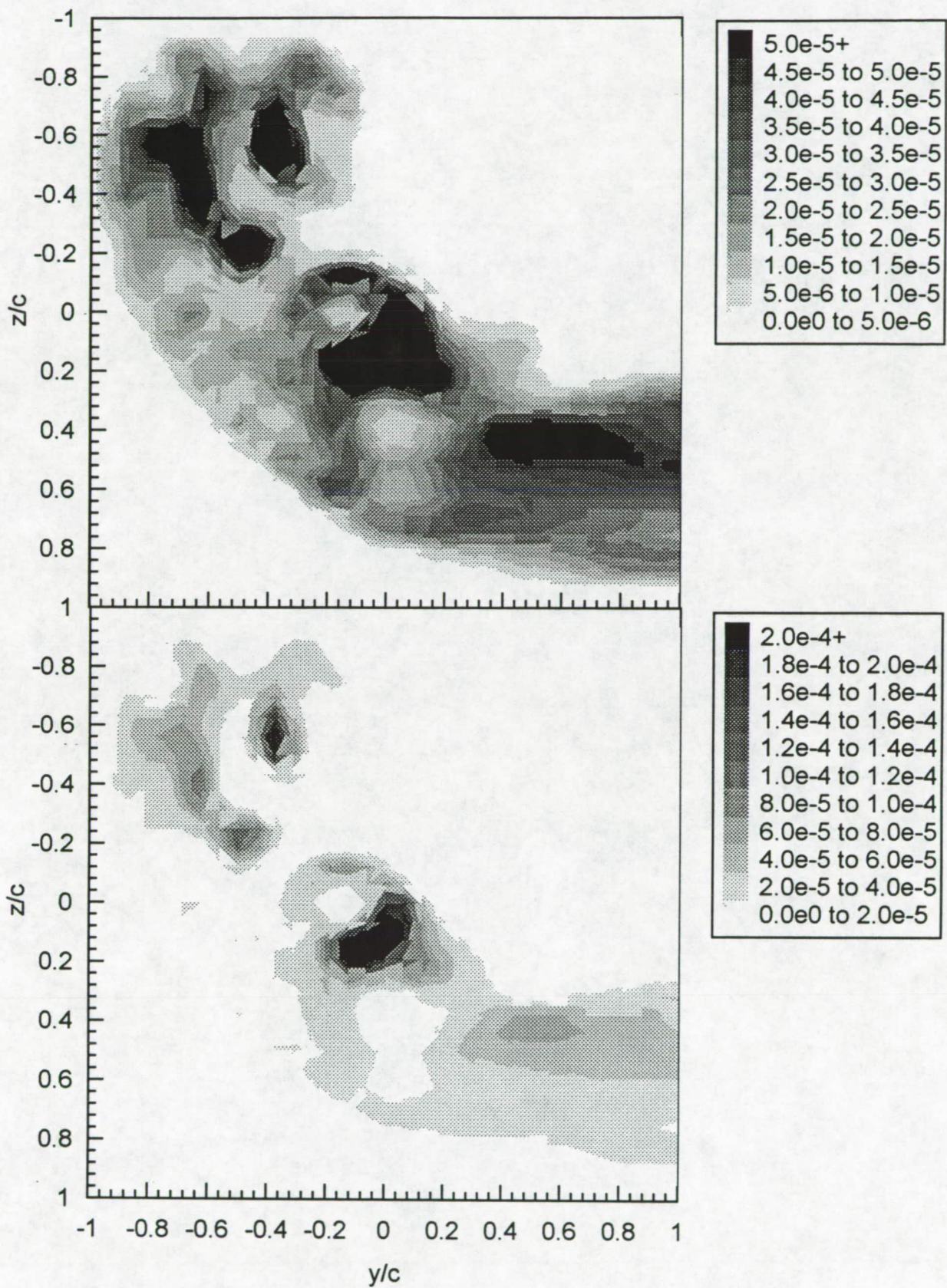


Figure 3.36 Contours of axial shear stress magnitude  $\tau_a/U_{ref}^2$  at  $X/c=30$ . (d)  $\Delta/c=0.0625$ . Upper and lower figures show different contour ranges.



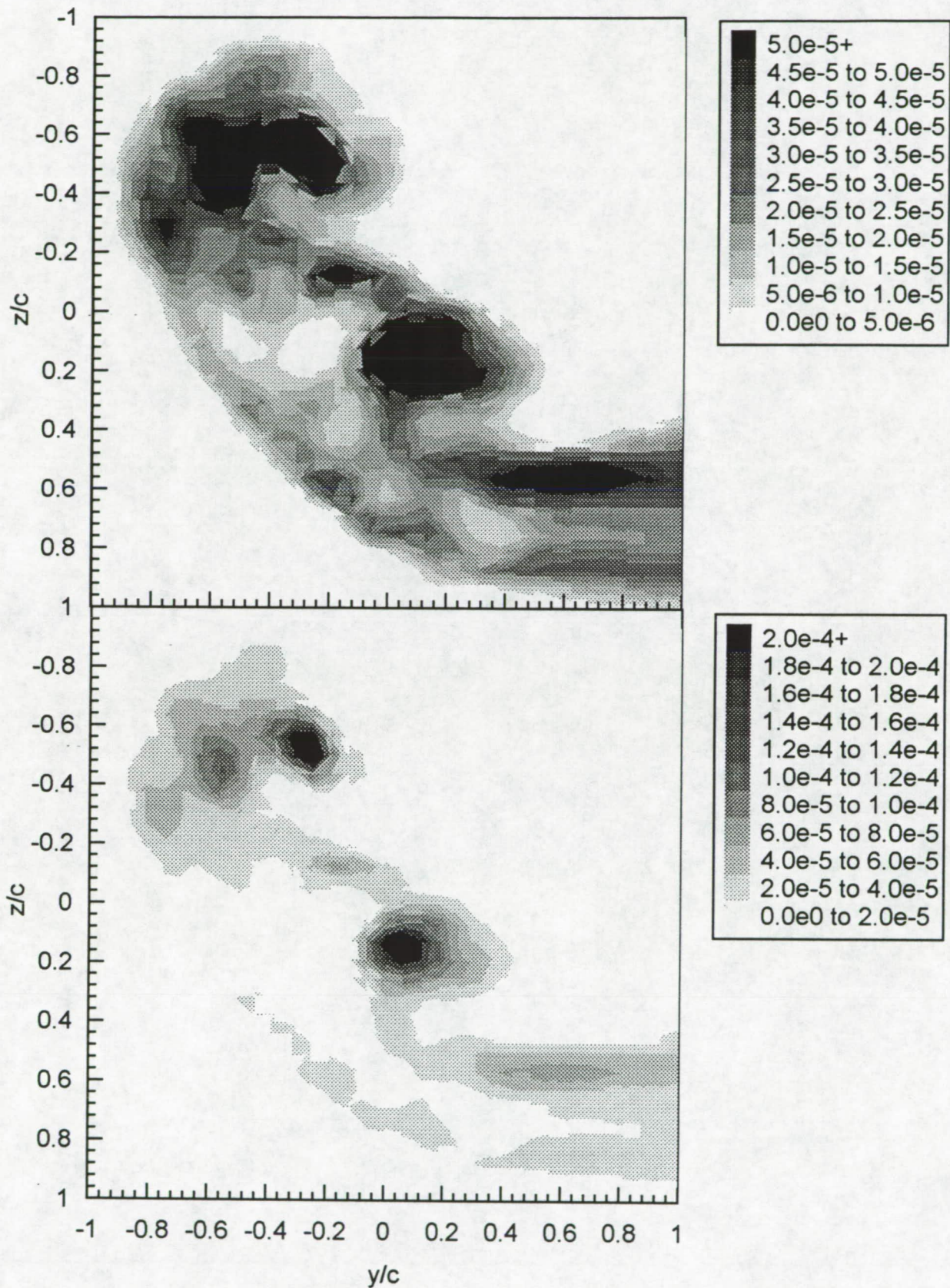


Figure 3.36 Contours of axial shear stress magnitude  $\tau_a/U_{ref}^2$  at  $X/c=30$ . (e)  $\Delta/c=0.125$ . Upper and lower figures show different contour ranges.



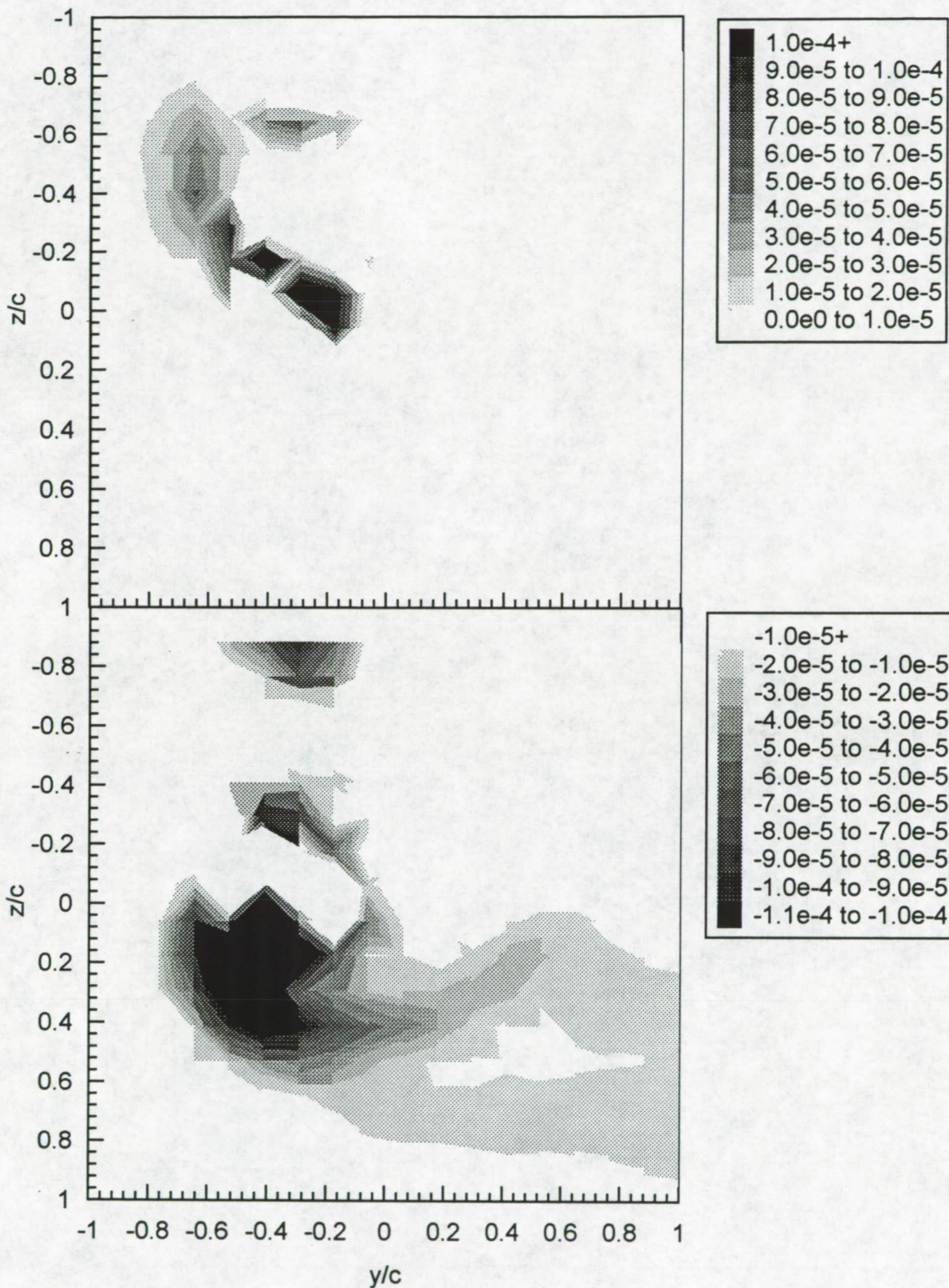


Figure 3.37 Contours of crossflow shear stress  $\tau_c/U_{ref}^2$  at  $X/c=30$ . (a)  $\Delta/c=-0.125$ . Upper figure - positive stress, lower figure - negative stress.



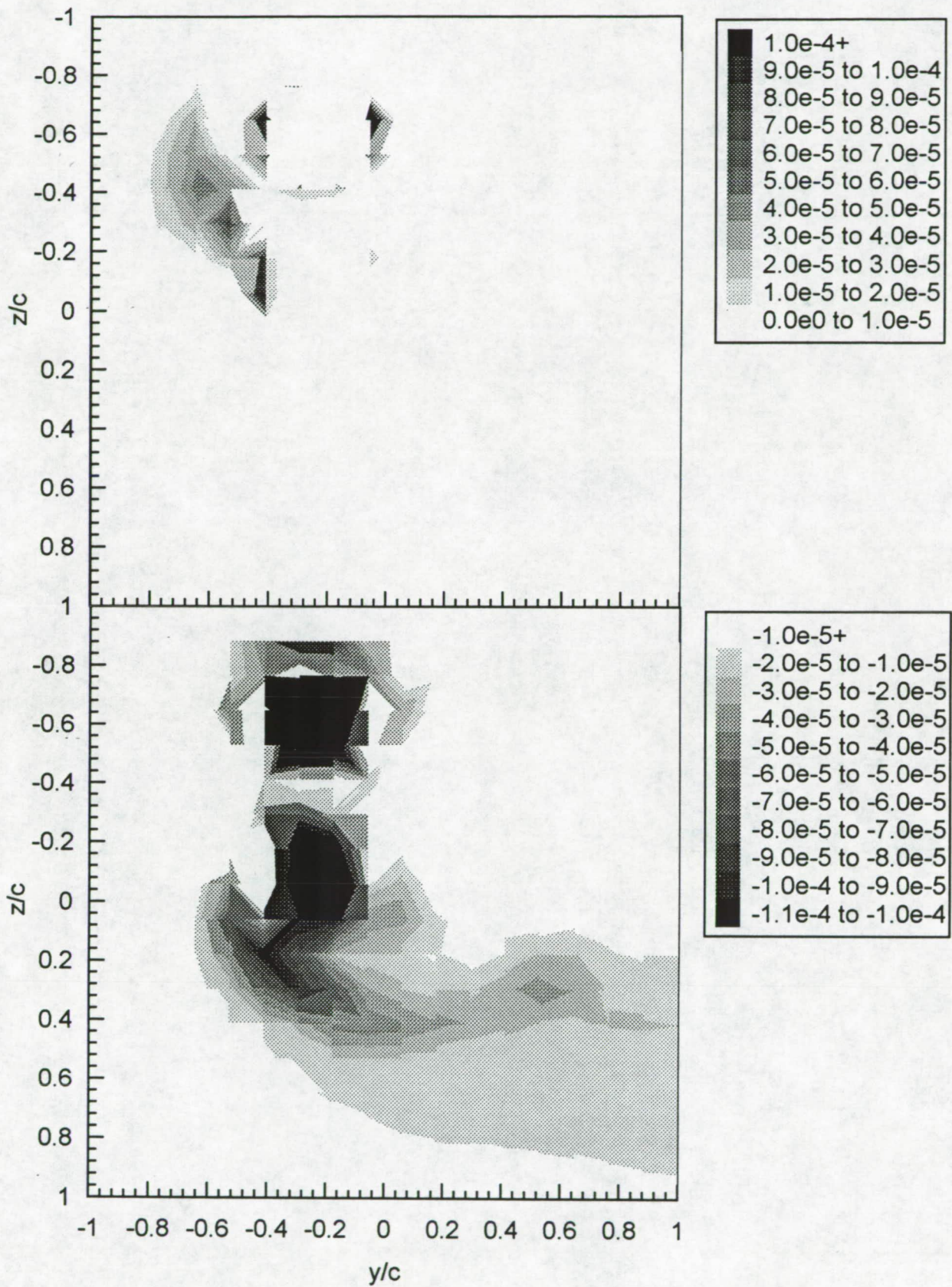


Figure 3.37 Contours of crossflow shear stress  $\tau_c/U_{ref}^2$  at  $X/c=30$ . (b)  $\Delta/c=-0.0625$ . (i) Coarse grid. Upper figure - positive stress, lower figure - negative stress.



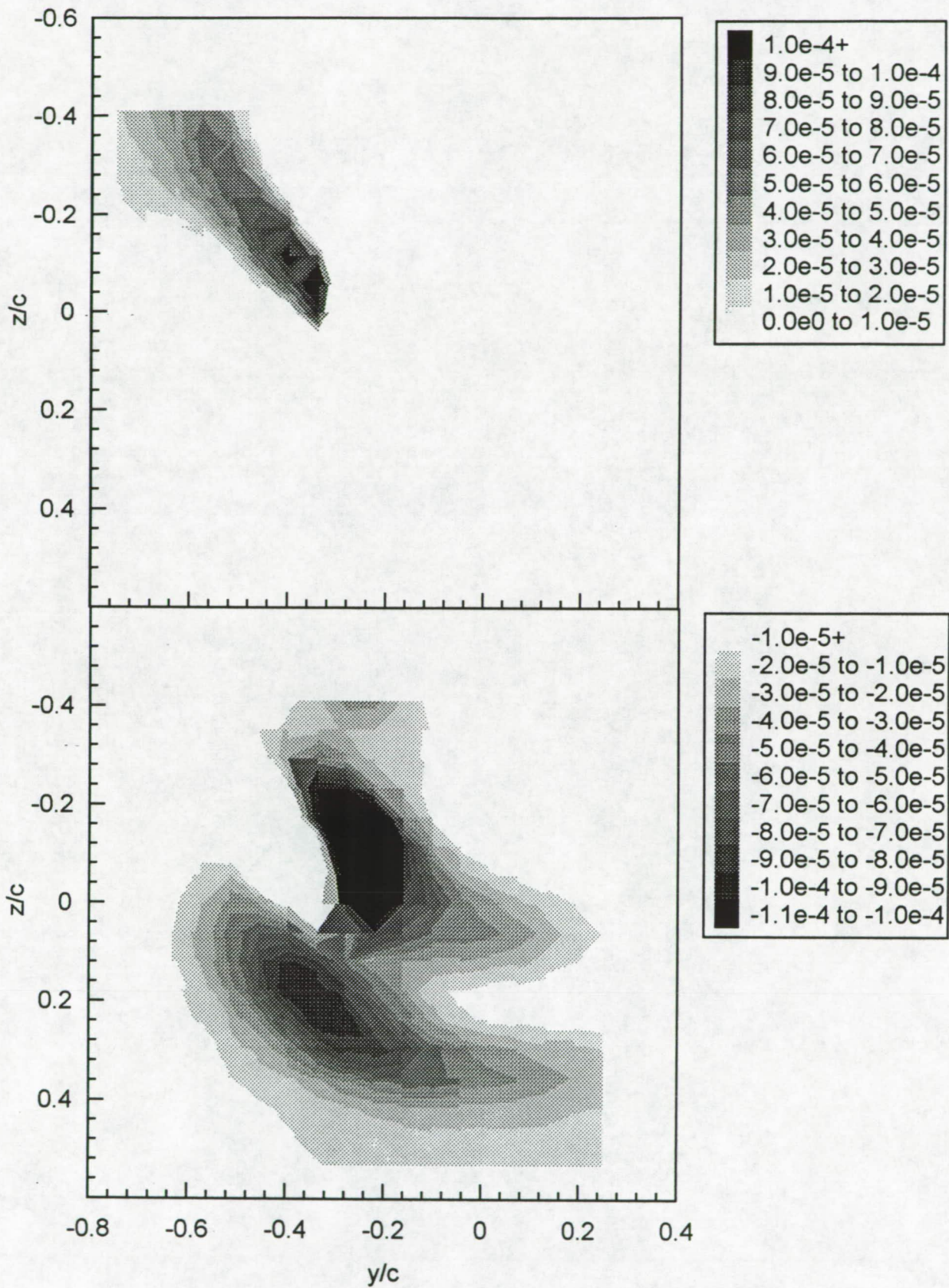


Figure 3.37 Contours of crossflow shear stress  $\tau_c/U_{ref}^2$  at  $X/c=30$ . (b)  $\Delta/c=-0.0625$ . (i) Fine grid. Upper figure - positive stress, lower figure - negative stress.



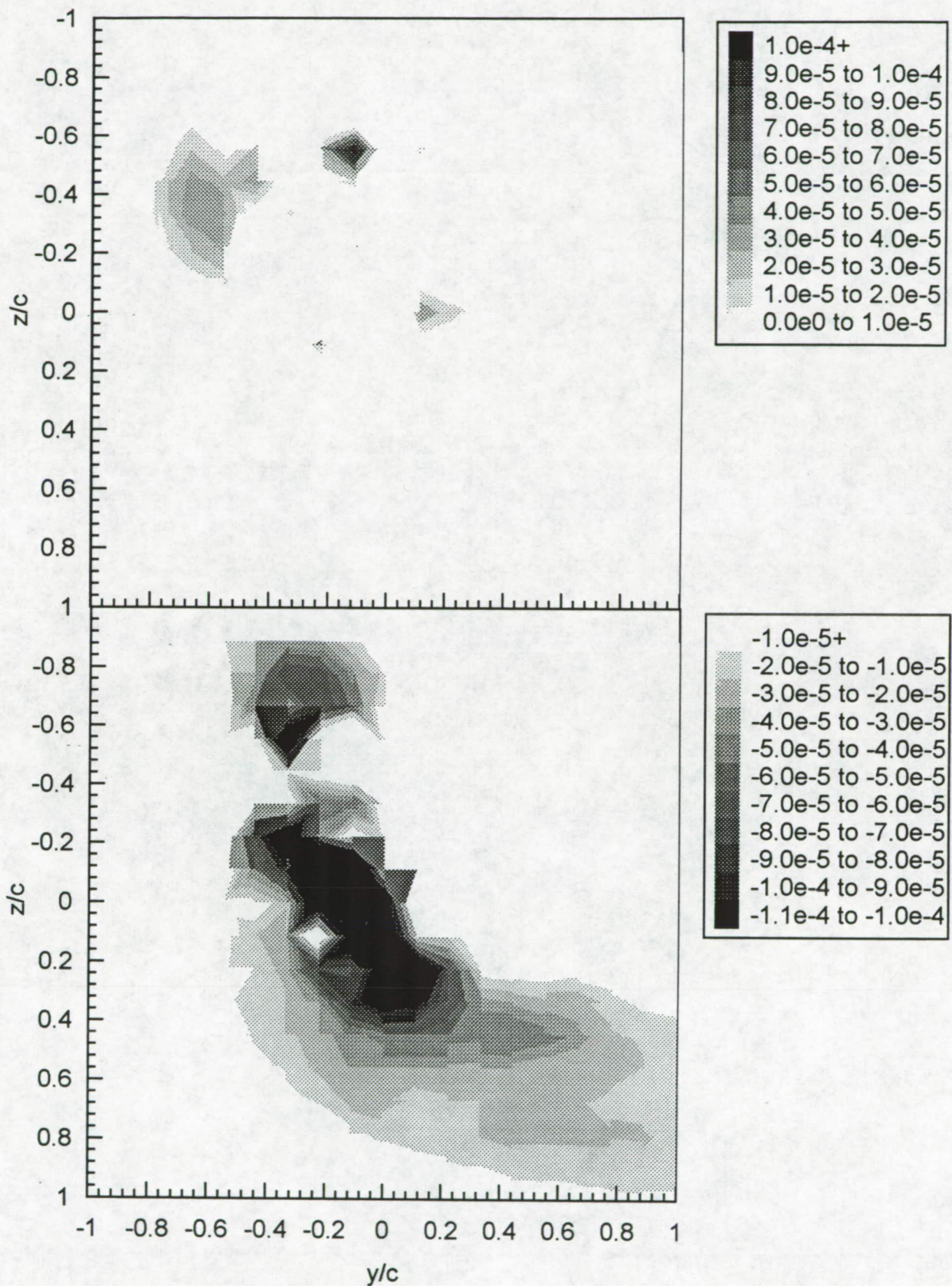


Figure 3.37 Contours of crossflow shear stress  $\tau_c/U_{ref}^2$  at  $X/c=30$ . (c)  $\Delta/c=0$ . Upper figure - positive stress, lower figure - negative stress.



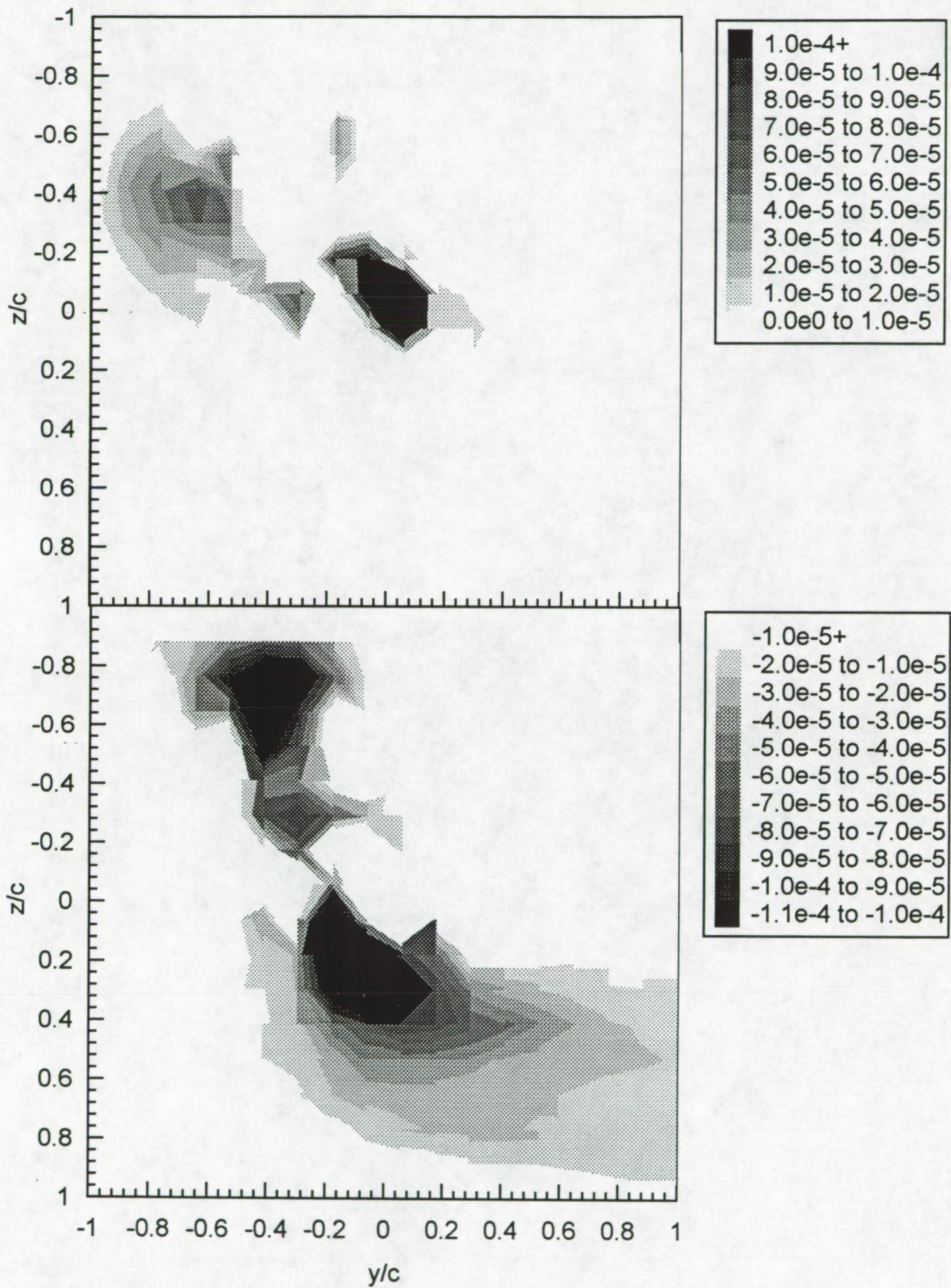


Figure 3.37 Contours of crossflow shear stress  $\tau_c/U_{ref}^2$  at  $X/c=30$ . (d)  $\Delta/c=0.0625$ . Upper figure - positive stress, lower figure - negative stress.



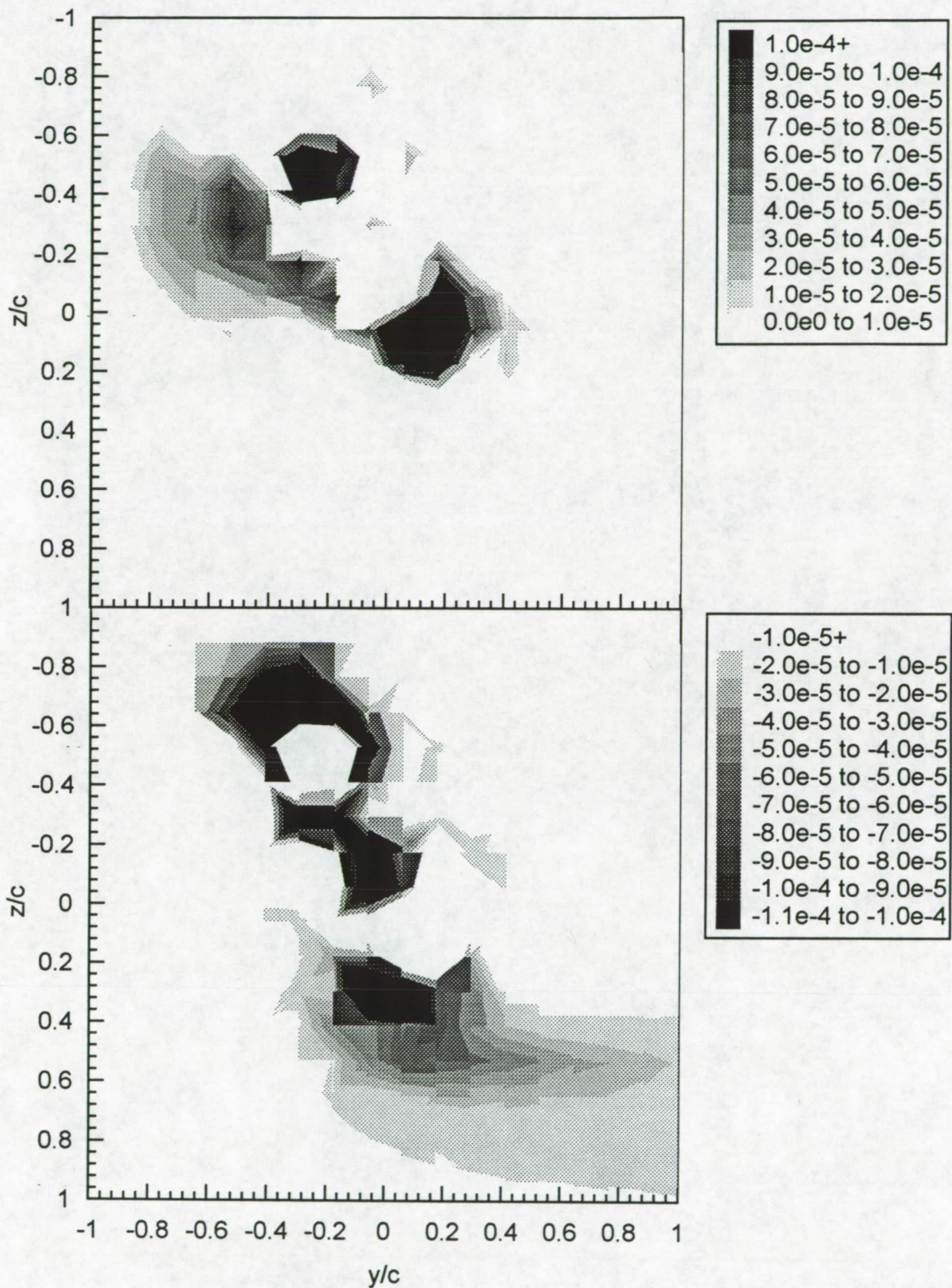


Figure 3.37 Contours of crossflow shear stress  $\tau_c/U_{ref}^2$  at  $X/c=30$ . (e)  $\Delta/c=0.125$ . Upper figure - positive stress, lower figure - negative stress.



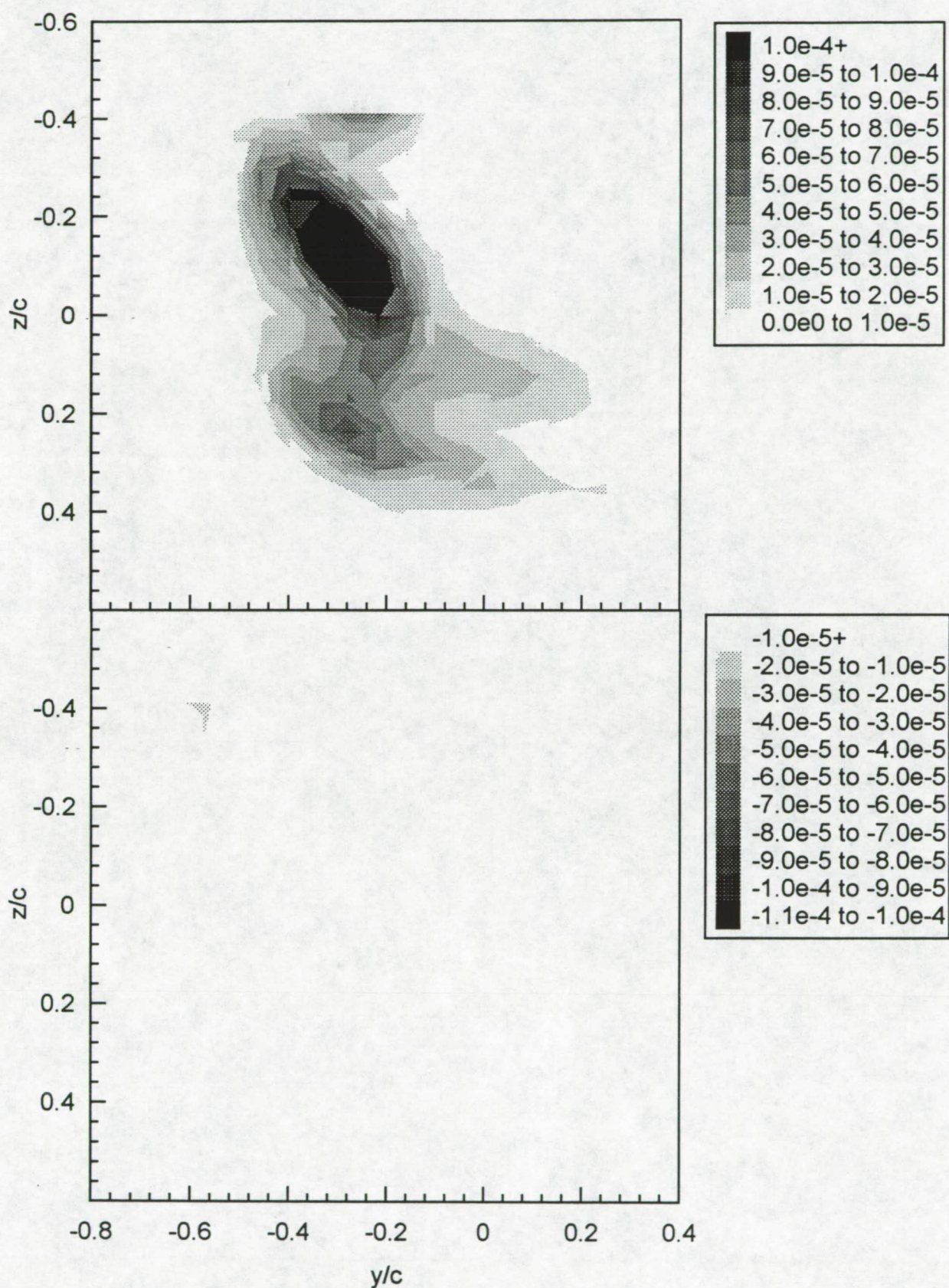


Figure 3.38 Contours of turbulence kinetic energy production  $Pc/U_{ref}^3$  at  $X/c=30$ .  $\Delta/c=-0.0625$ . Fine grid. Upper figure - positive production, lower figure - negative production.

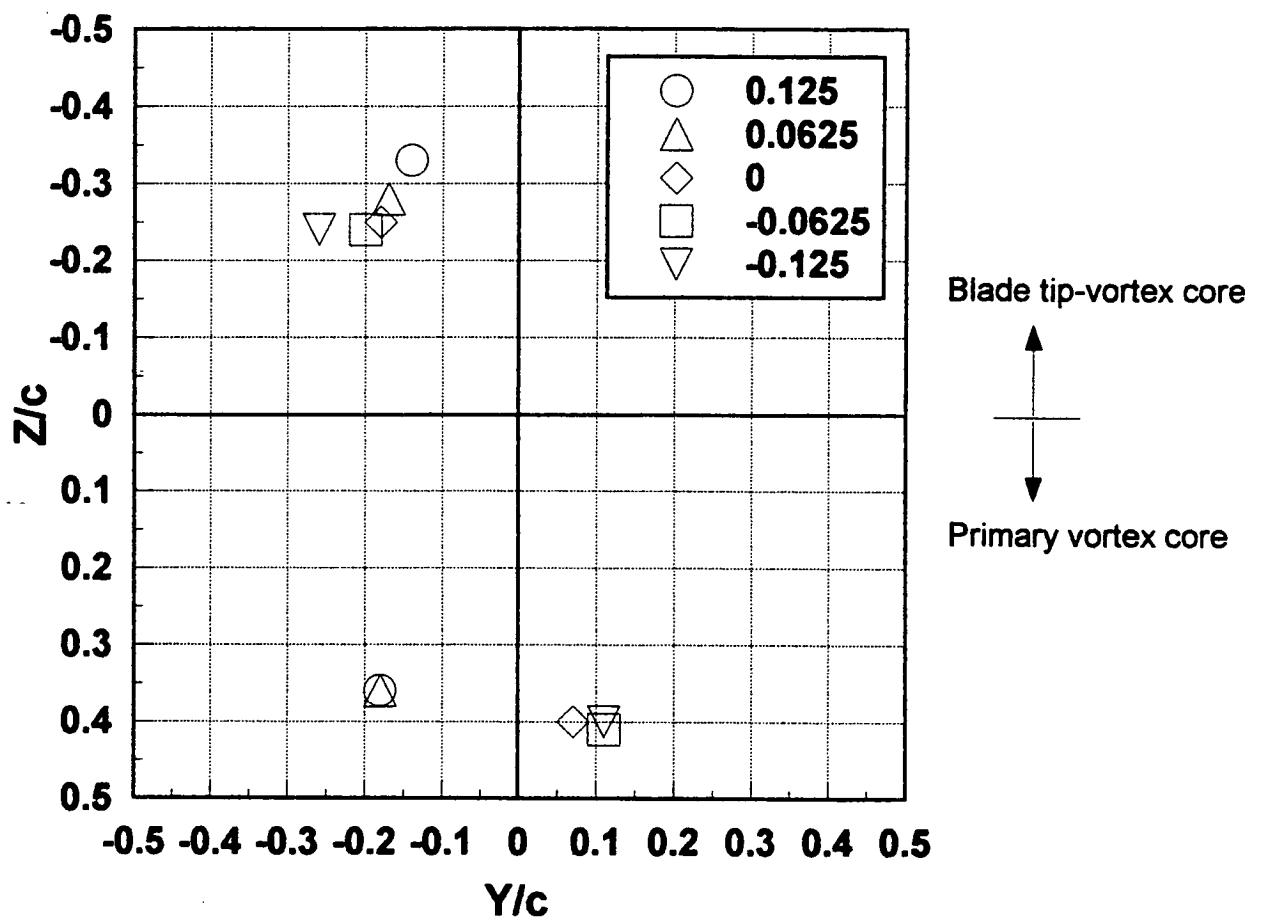


Figure 3.39 Absolute locations of the vortex cores at  $X/c=30$  as functions of  $\Delta/c$ . Values of  $\Delta/c$  listed in legend

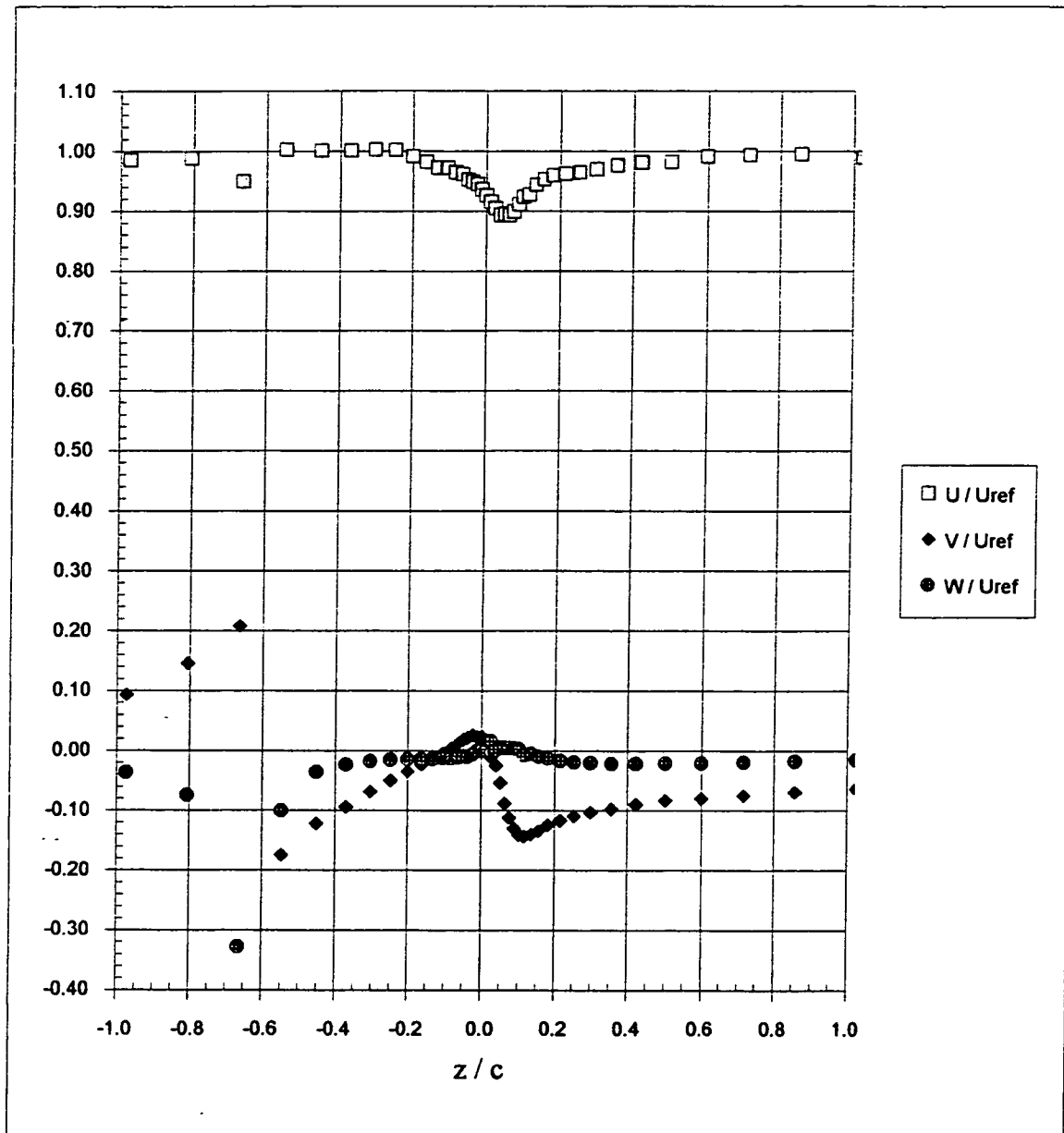


Figure 3.40 Mean velocity profiles through the primary vortex core at  $X/c=30$ . (a)  $\Delta/c=-0.125$ .



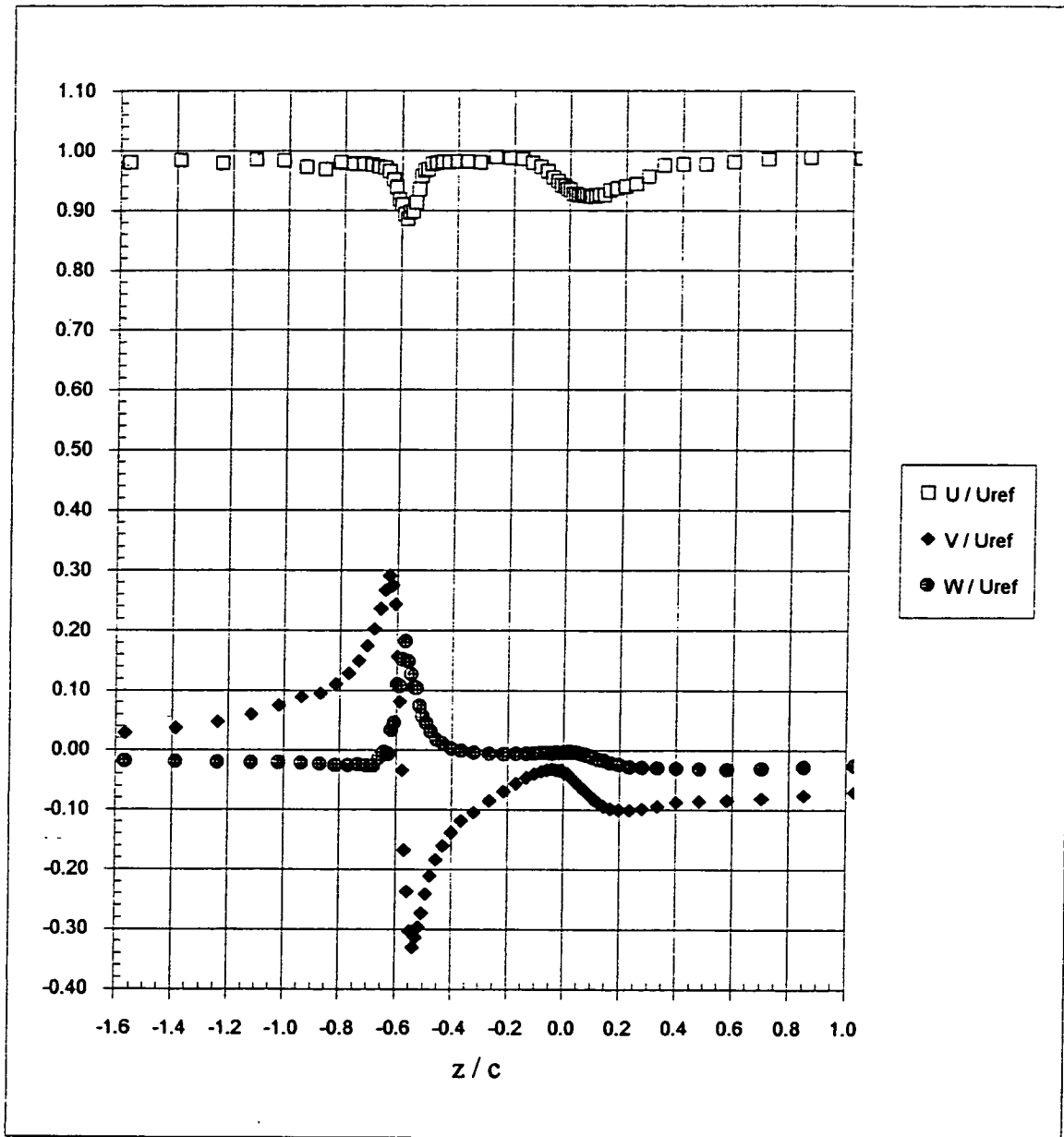


Figure 3.40 Mean velocity profiles through the primary vortex core at  $X/c=30$ . (b)  $\Delta c=-0.0625$ .

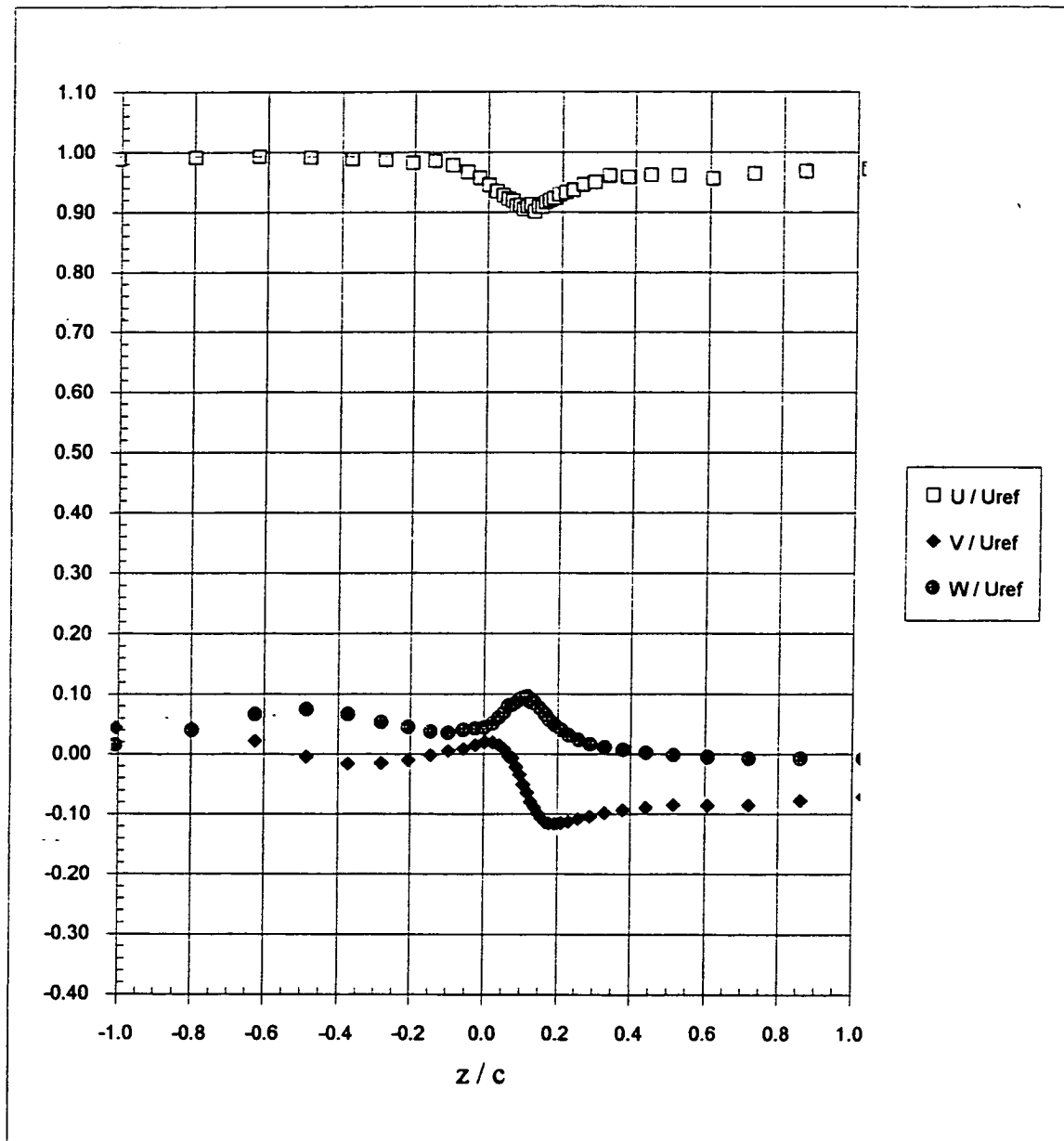


Figure 3.40 Mean velocity profiles through the primary vortex core at  $X/c=30$ . (c)  $\Delta/c=0.0625$ .

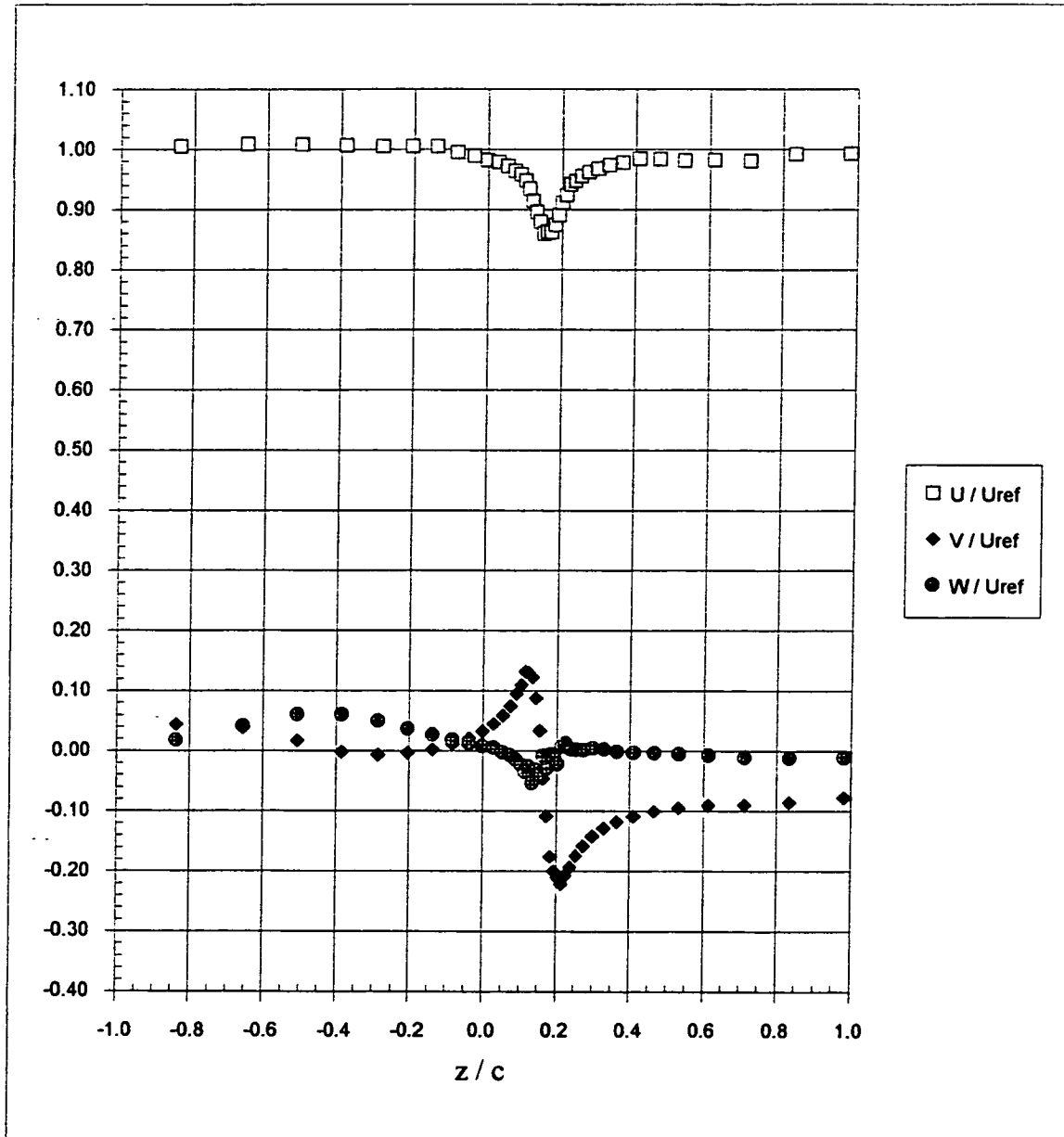


Figure 3.40 Mean velocity profiles through the primary vortex core at  $X/c=30$ . (d)  $\Delta/c=0.125$ .

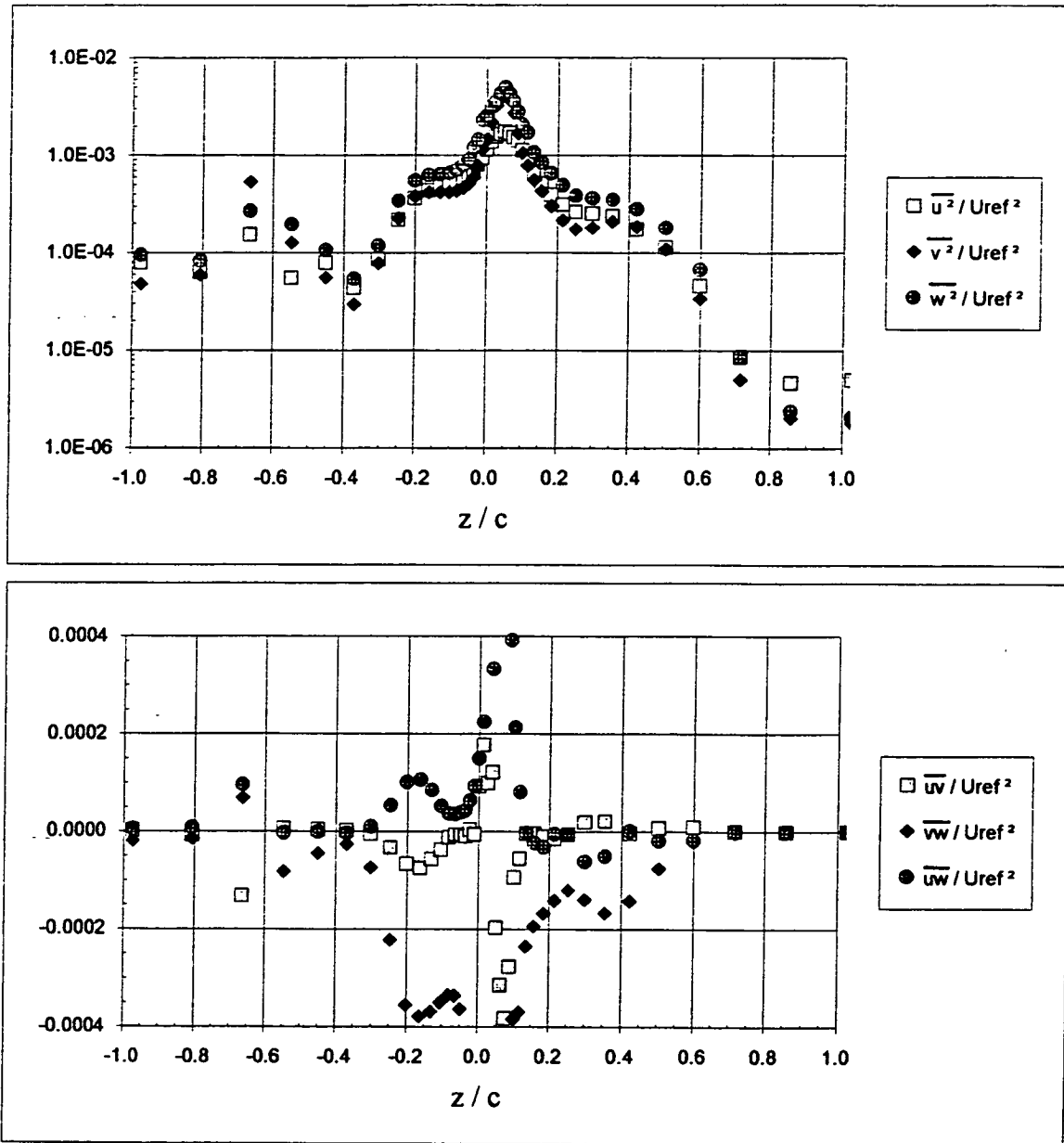


Figure 3.41 Turbulence stress profiles through the primary vortex core at  $X/c=30$ . (a)  $\Delta/c=-0.125$ .



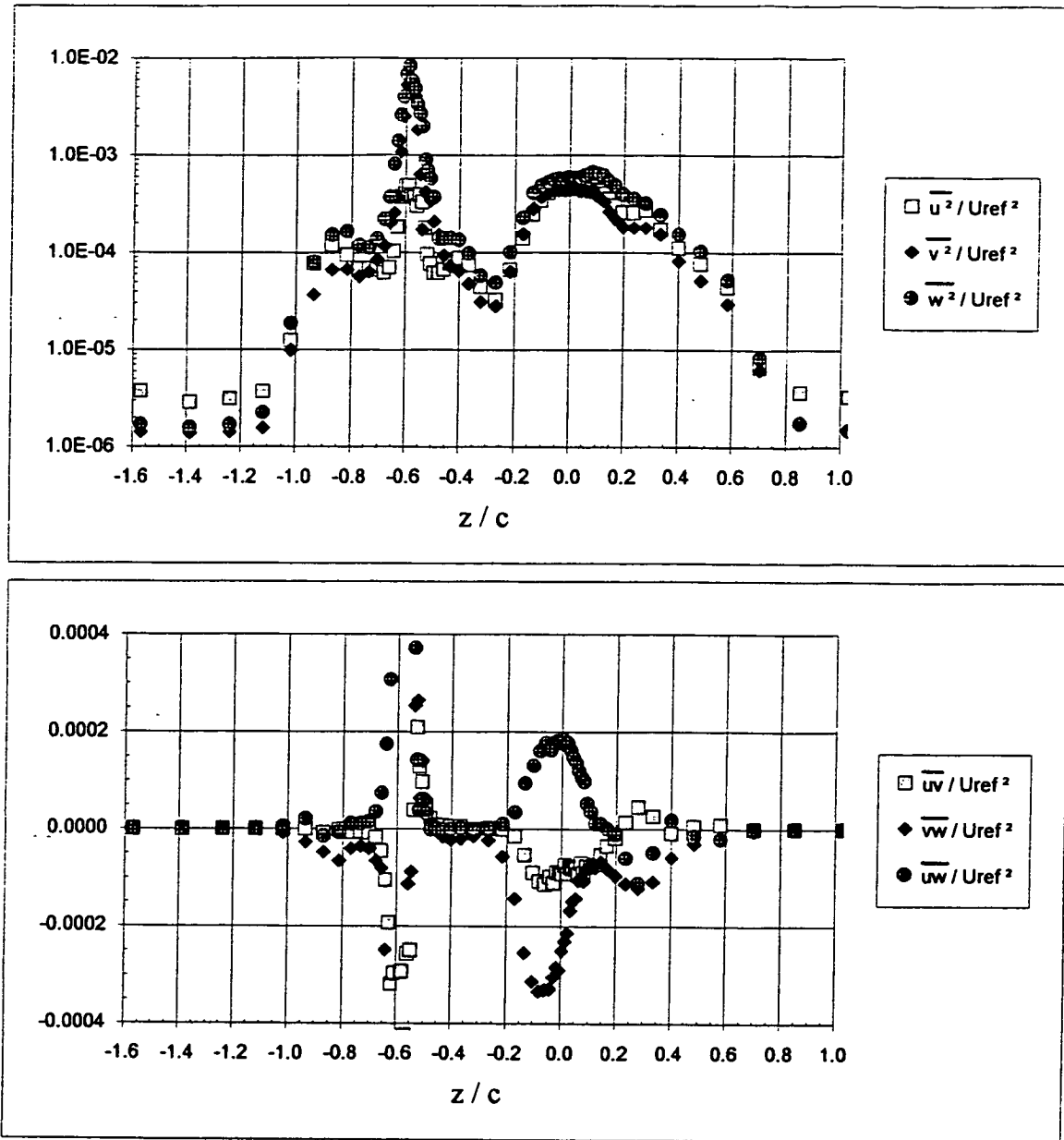


Figure 3.41 Turbulence stress profiles through the primary vortex core at  $X/c=30$ . (b)  $\Delta/c=-0.0625$ .

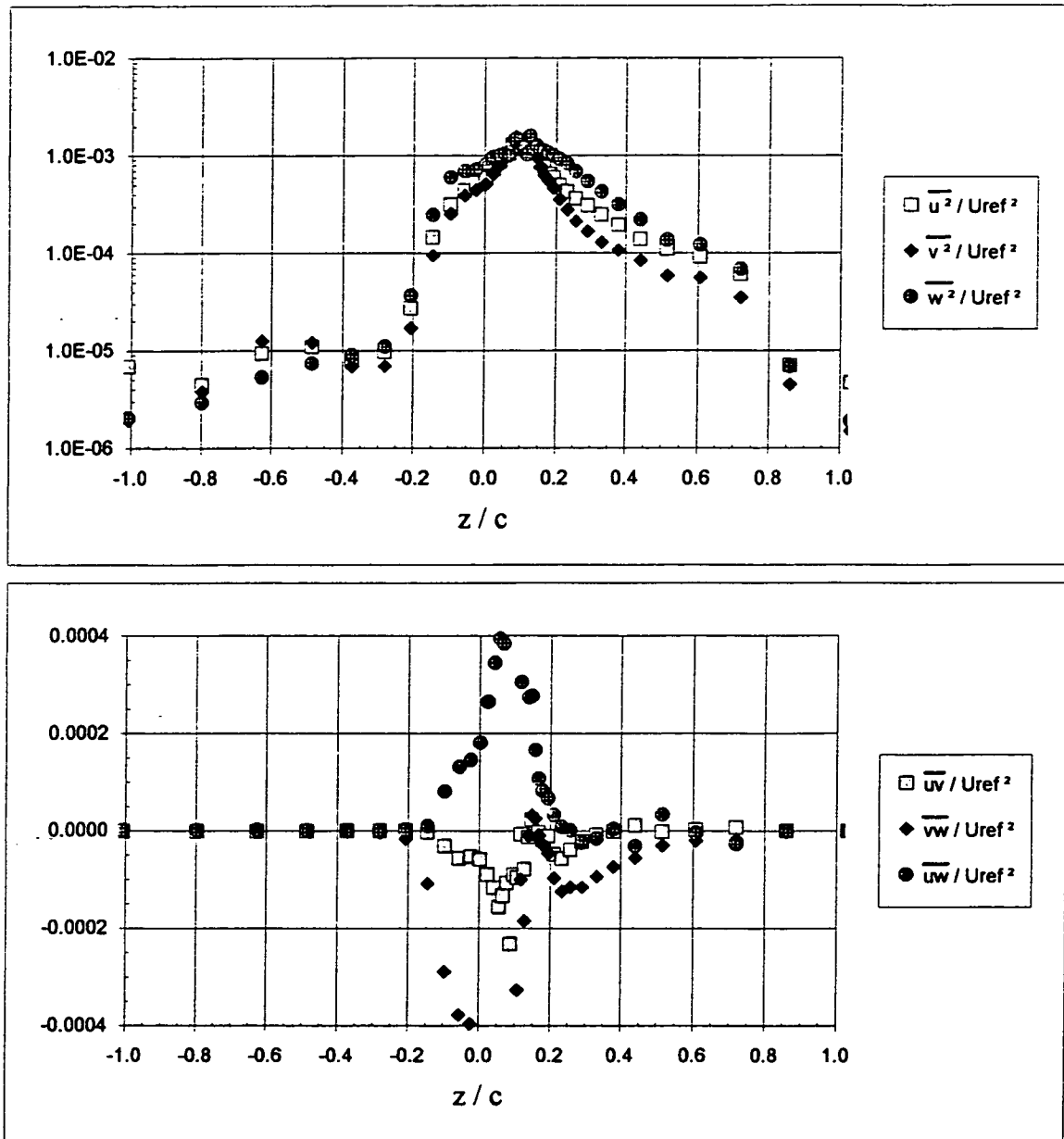


Figure 3.41 Turbulence stress profiles through the primary vortex core at  $X/c=30$ . (c)  $\Delta/c=0.0625$ .

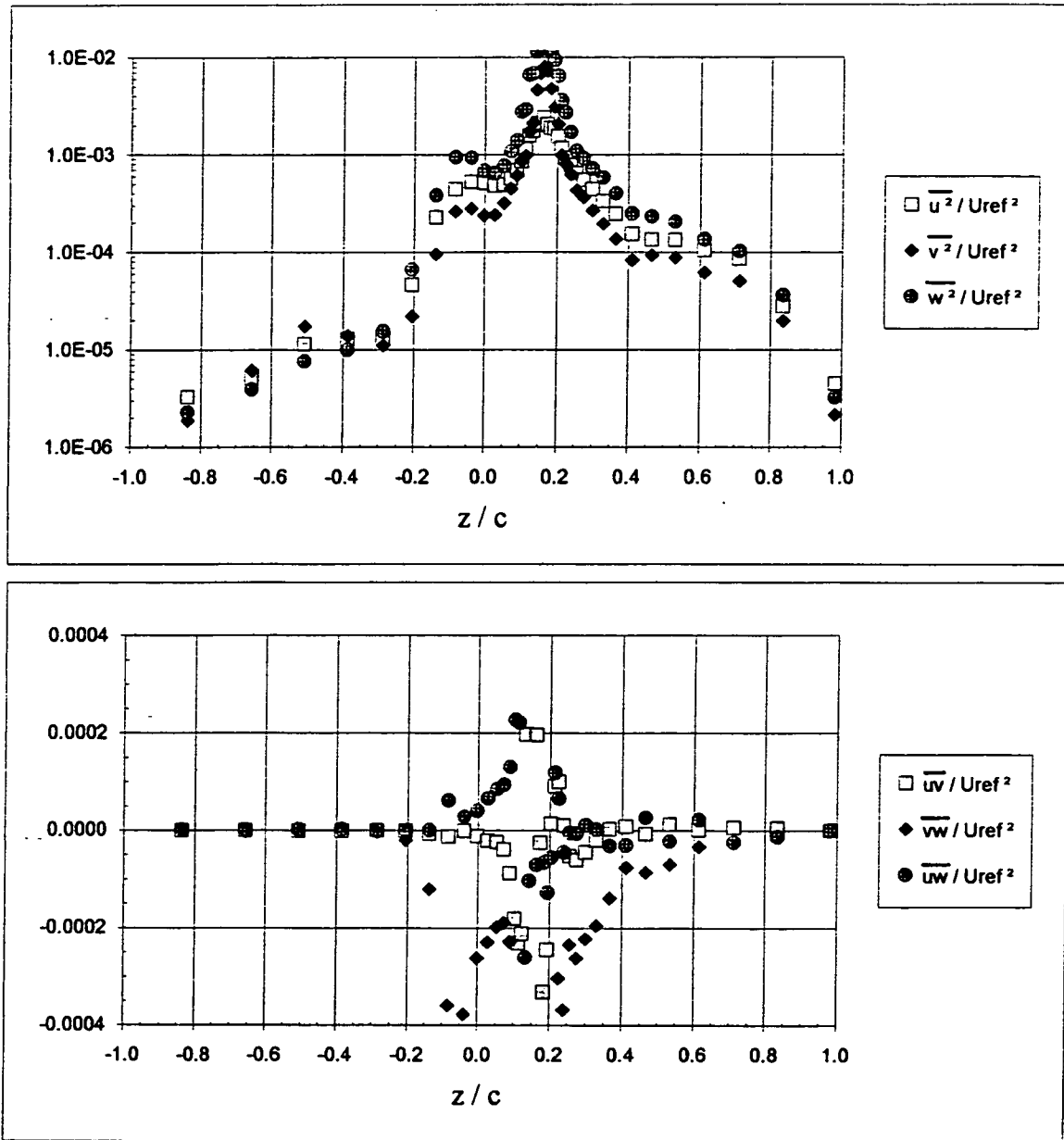


Figure 3.41 Turbulence stress profiles through the primary vortex core at  $X/c=30$ . (d)  $\Delta/c=0.125$ .

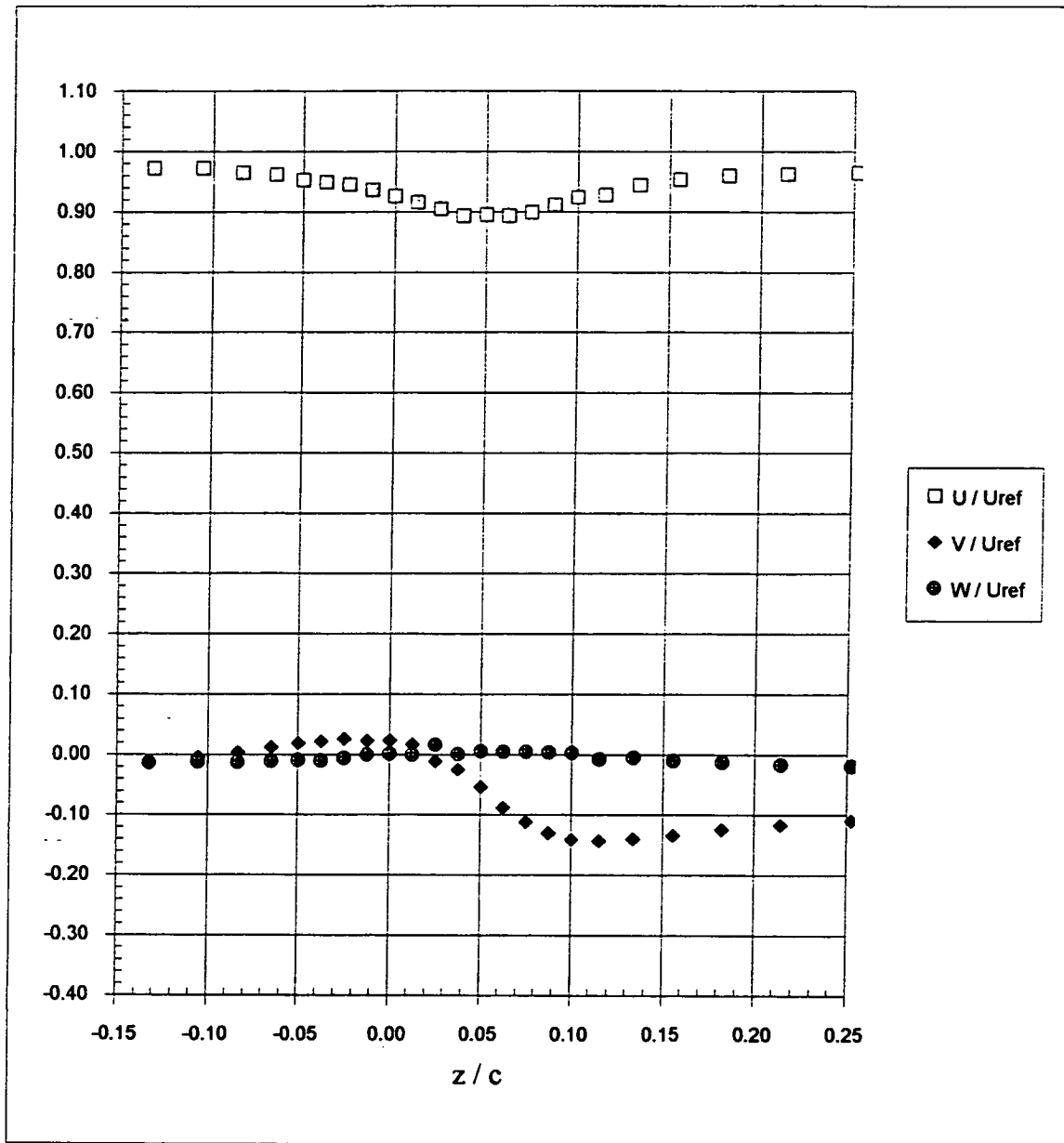


Figure 3.42 Mean velocity profiles in the vicinity of the primary vortex core at  $X/c=30$ . (a)  $\Delta/c=-0.125$ .



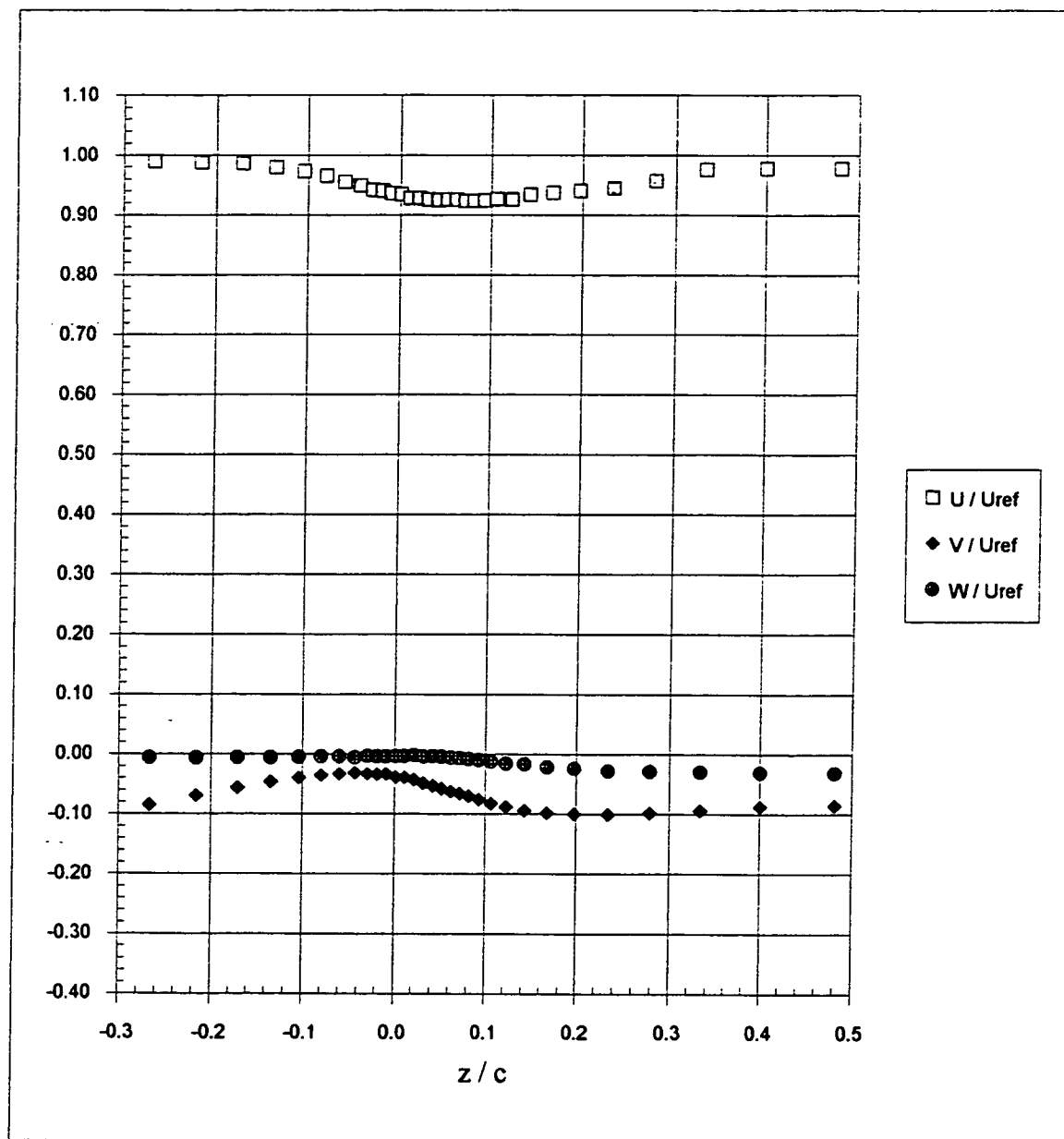


Figure 3.42 Mean velocity profiles in the vicinity of the primary vortex core at  $X/c=30$ . (b)  $\Delta/c=-0.0625$ .

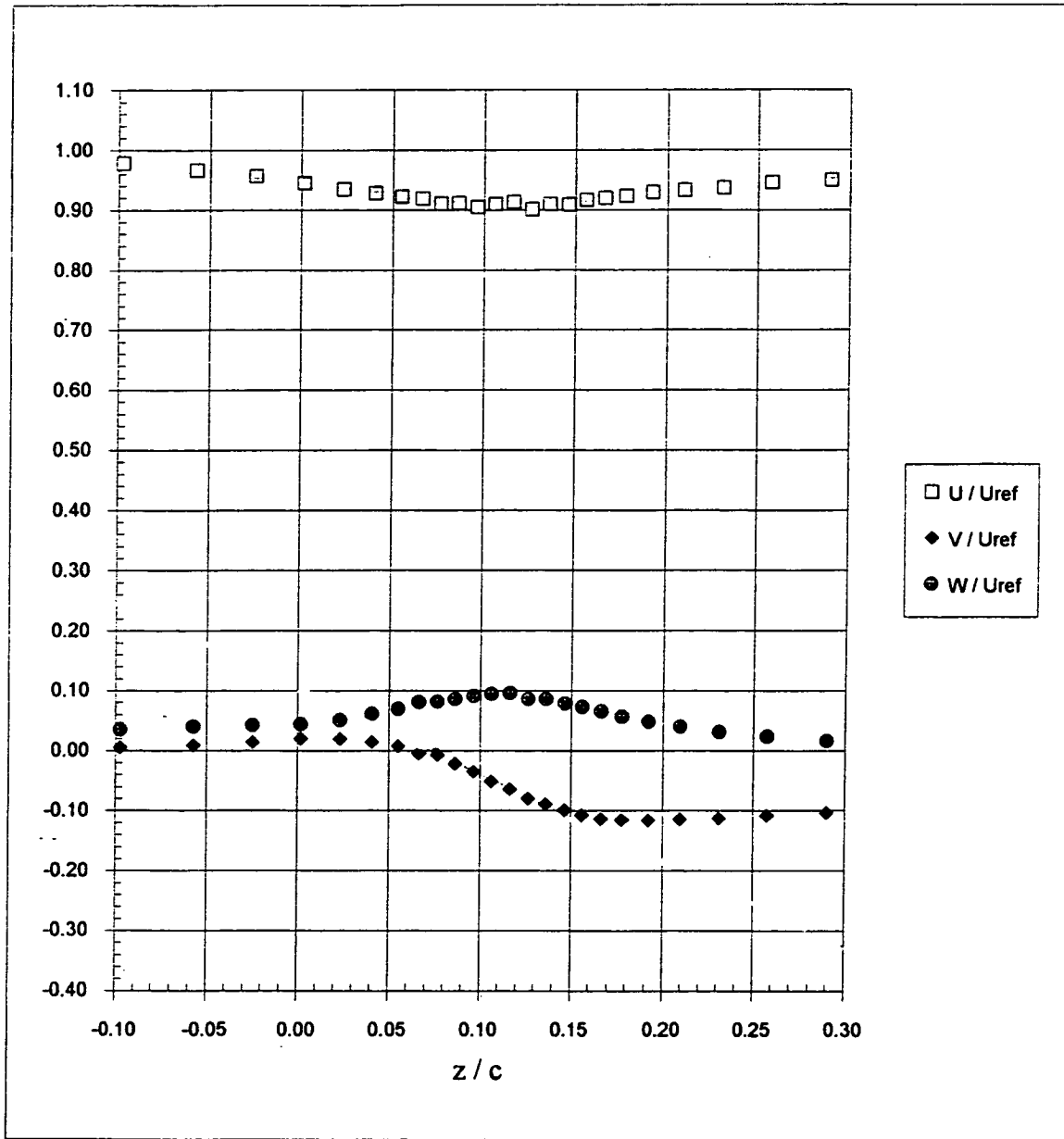


Figure 3.42 Mean velocity profiles in the vicinity of the primary vortex core at  $X/c=30$ . (c)  $\Delta/c=0.0625$ .

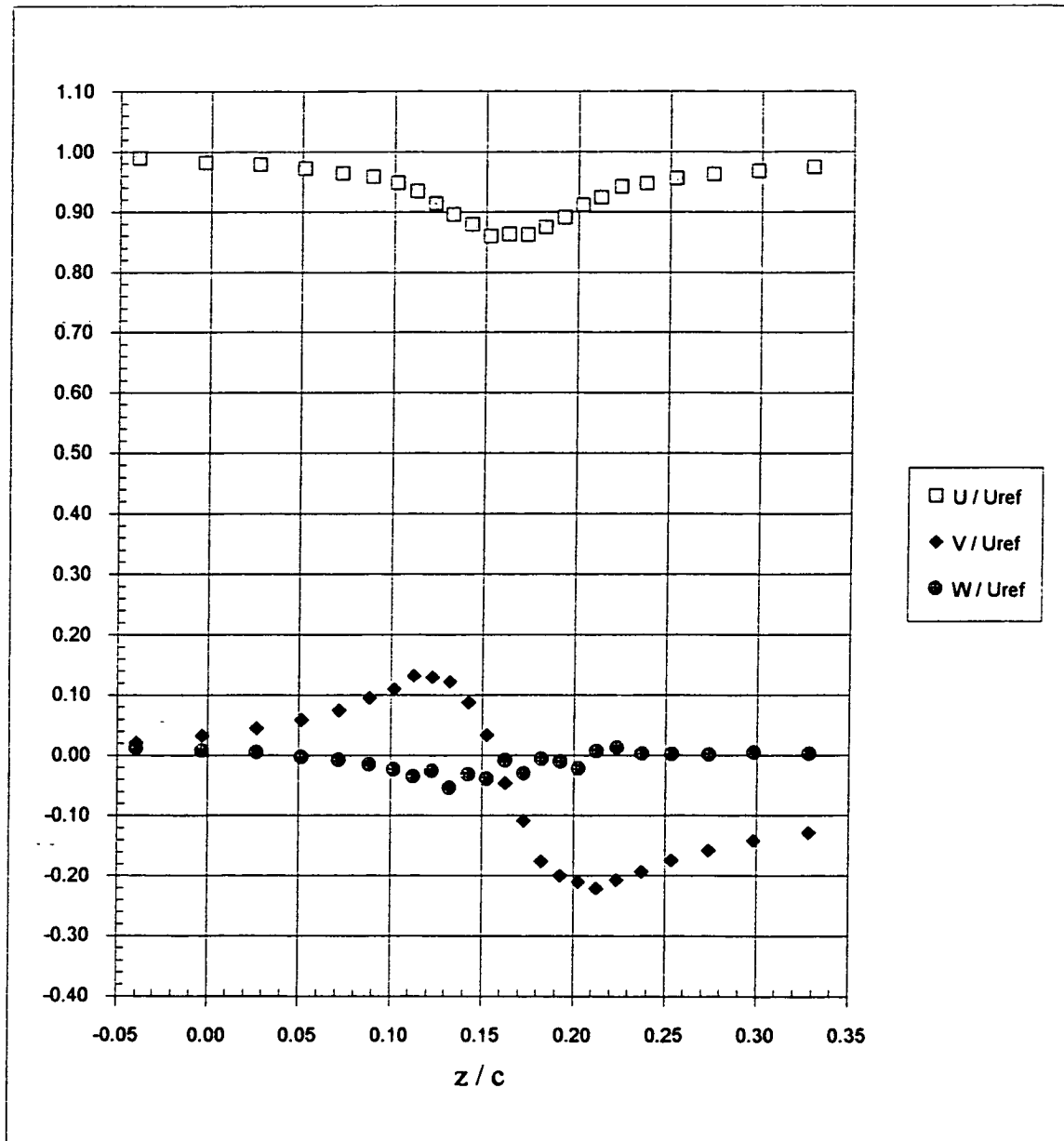


Figure 3.42 Mean velocity profiles in the vicinity of the primary vortex core at  $X/c=30$ . (d)  $\Delta/c=0.125$ .

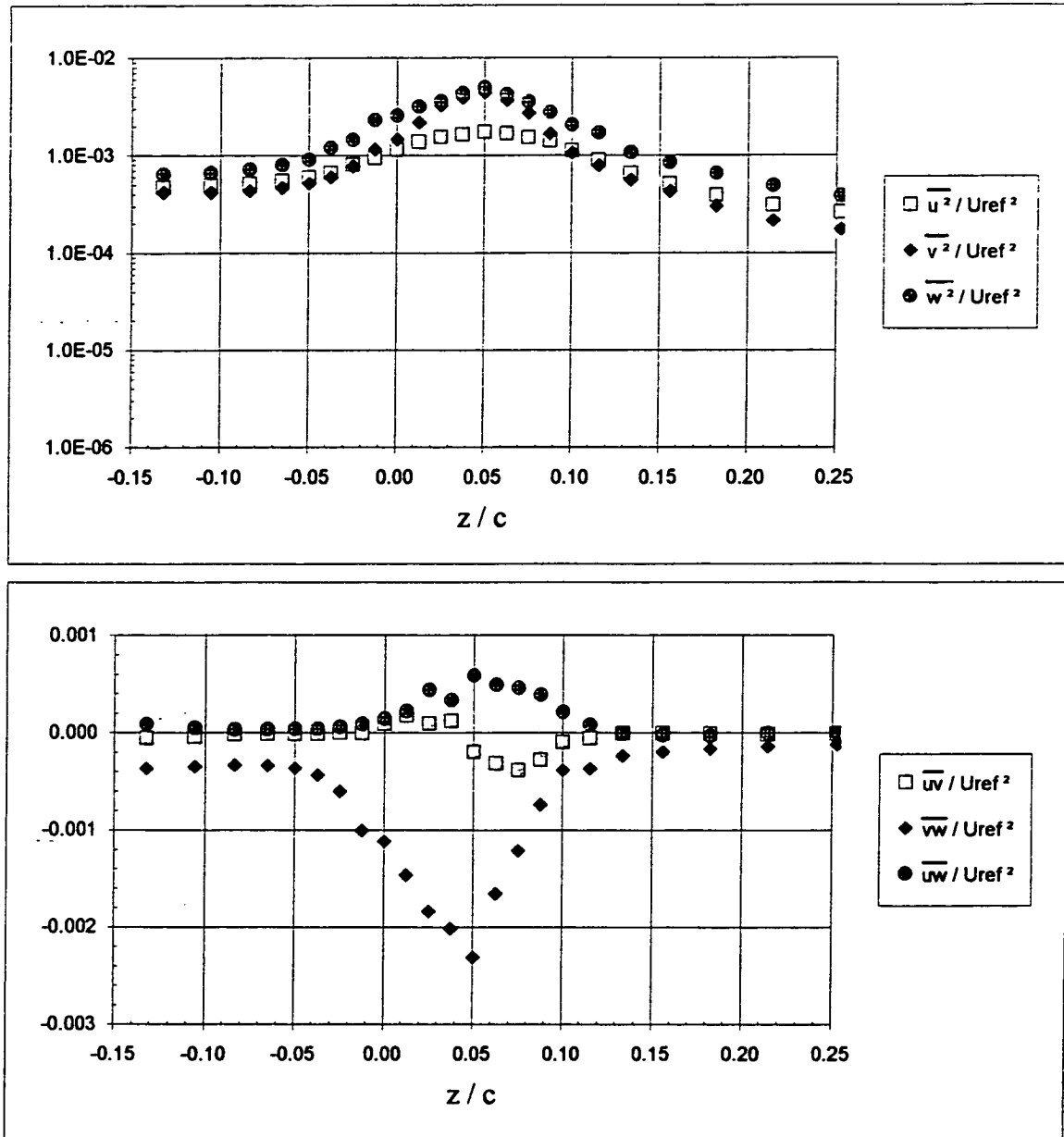


Figure 3.43 Turbulence stress profiles in the vicinity of the primary vortex core at  $X/c=30$ .  
(a)  $\Delta/c=-0.125$ .



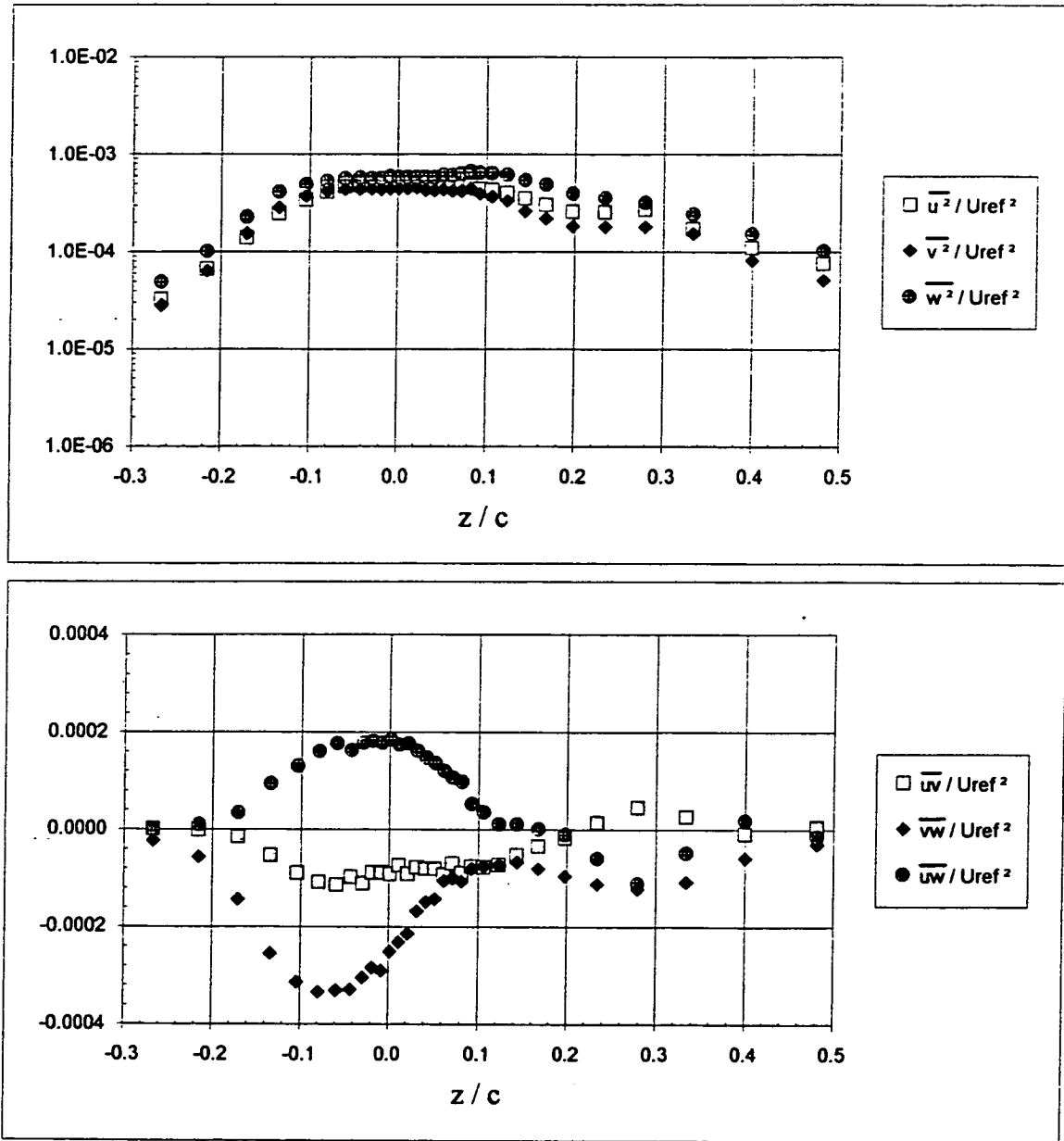


Figure 3.43 Turbulence stress profiles in the vicinity of the primary vortex core at  $X/c=30$ .  
(b)  $\Delta/c=-0.0625$ .

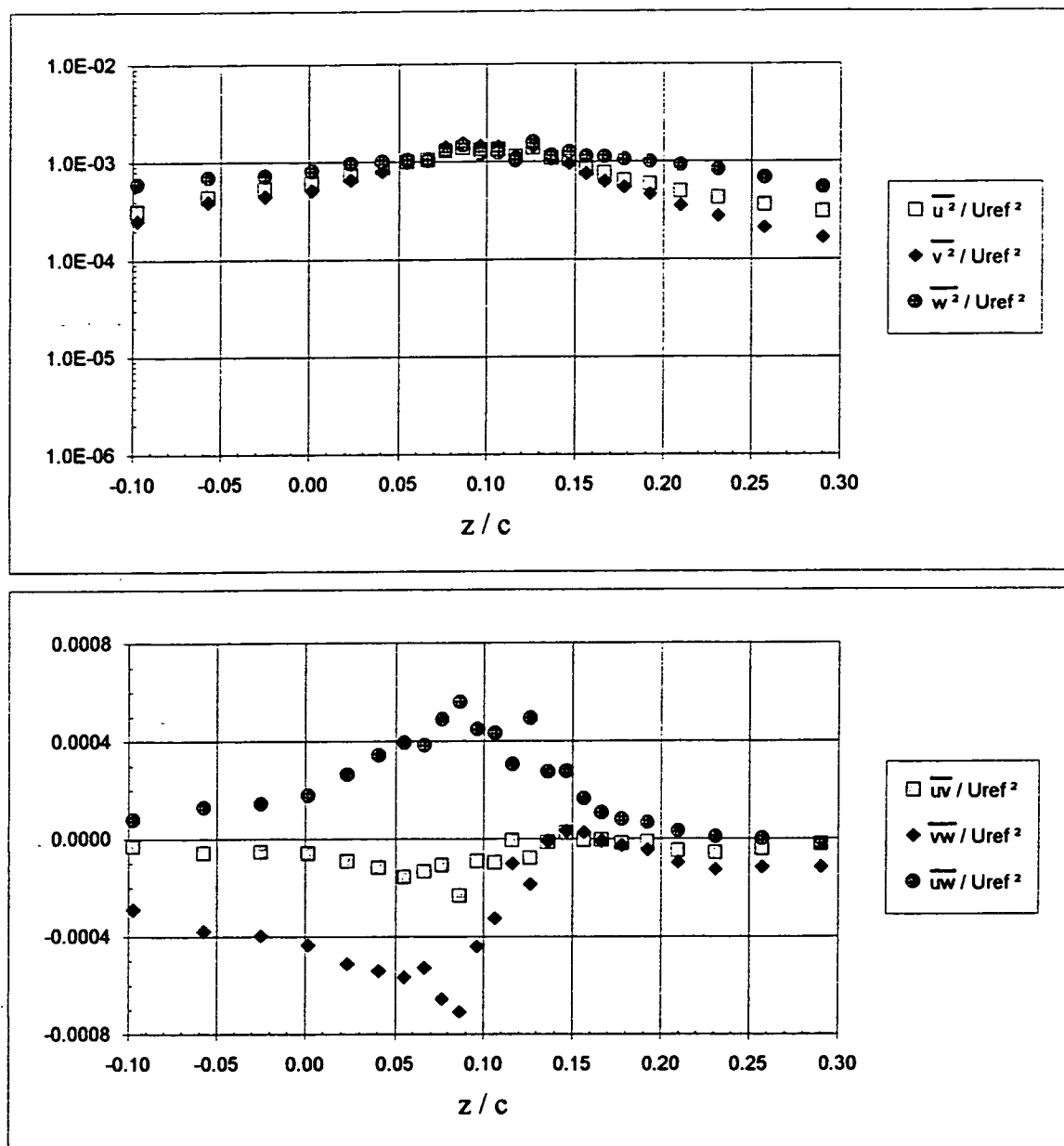


Figure 3.43 Turbulence stress profiles in the vicinity of the primary vortex core at  $X/c=30$ .  
(c)  $\Delta c=0.0625$ .

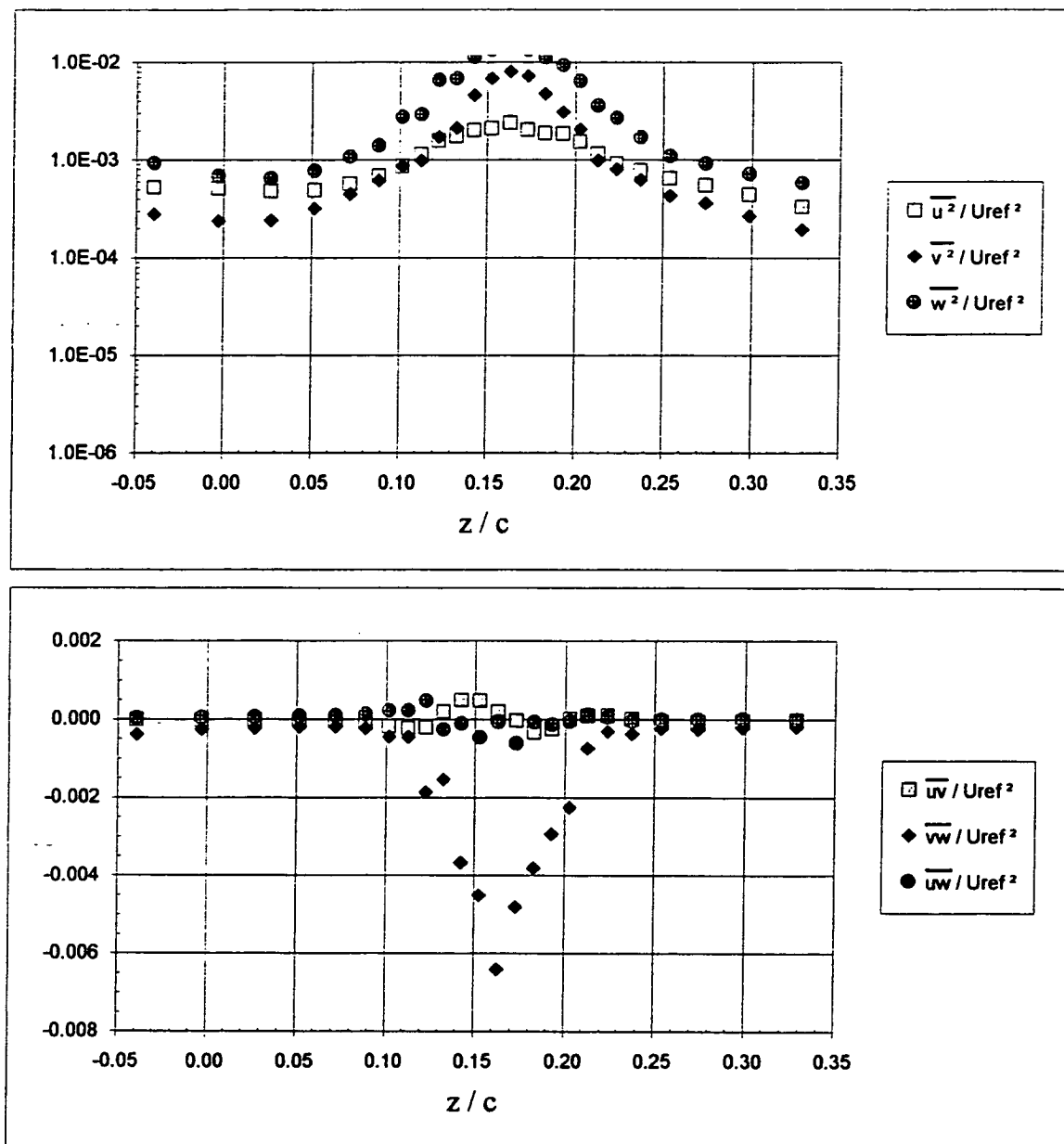


Figure 3.43 Turbulence stress profiles in the vicinity of the primary vortex core at  $X/c=30$ .  
(d)  $\Delta/c=0.125$ .

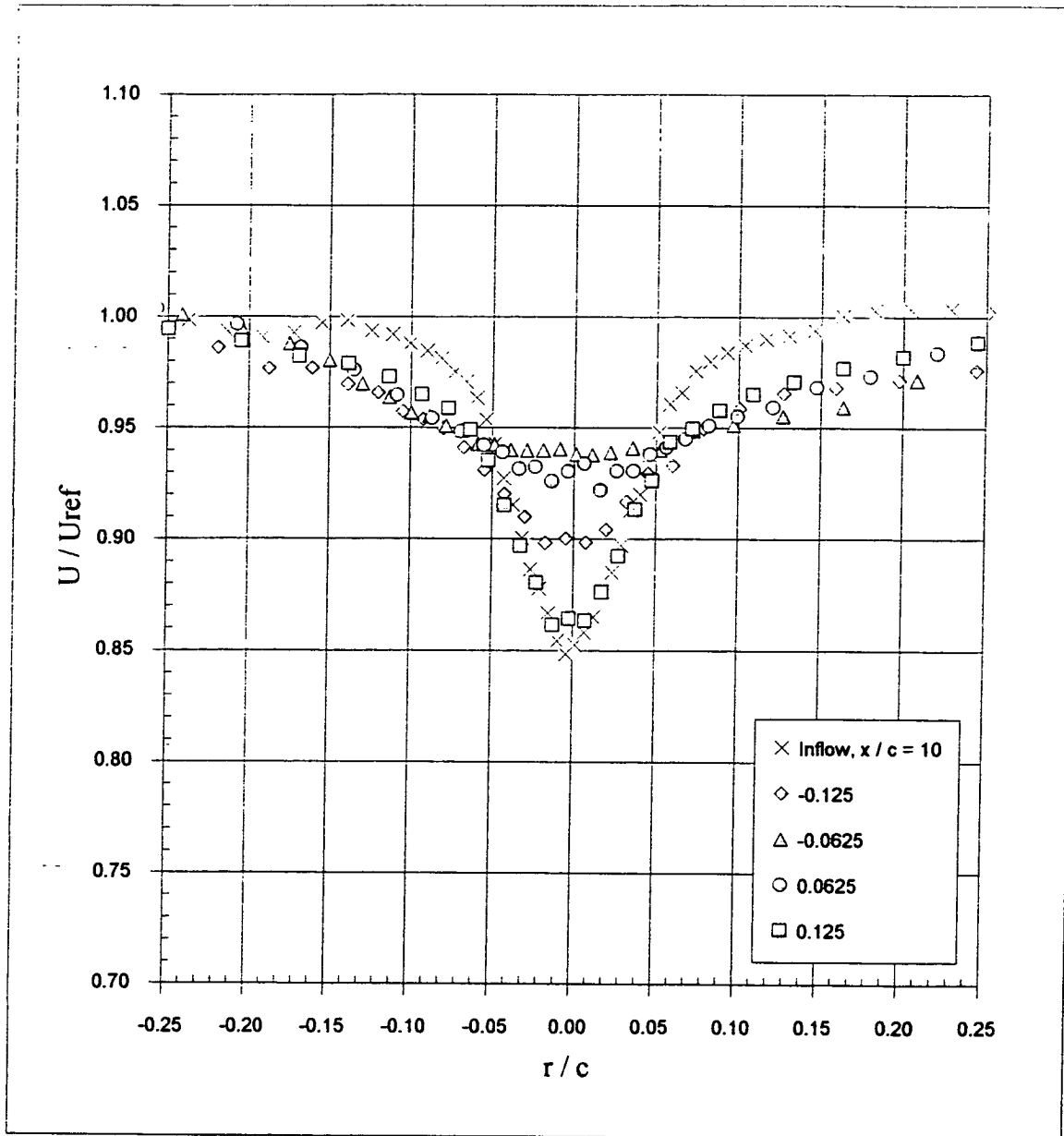


Figure 3.44 Axial velocity deficit profiles in the primary vortex core at  $X/c=30$  as a function of  $\Delta/c$ . Core axial velocity profile at  $X/c=10$  included for comparison.



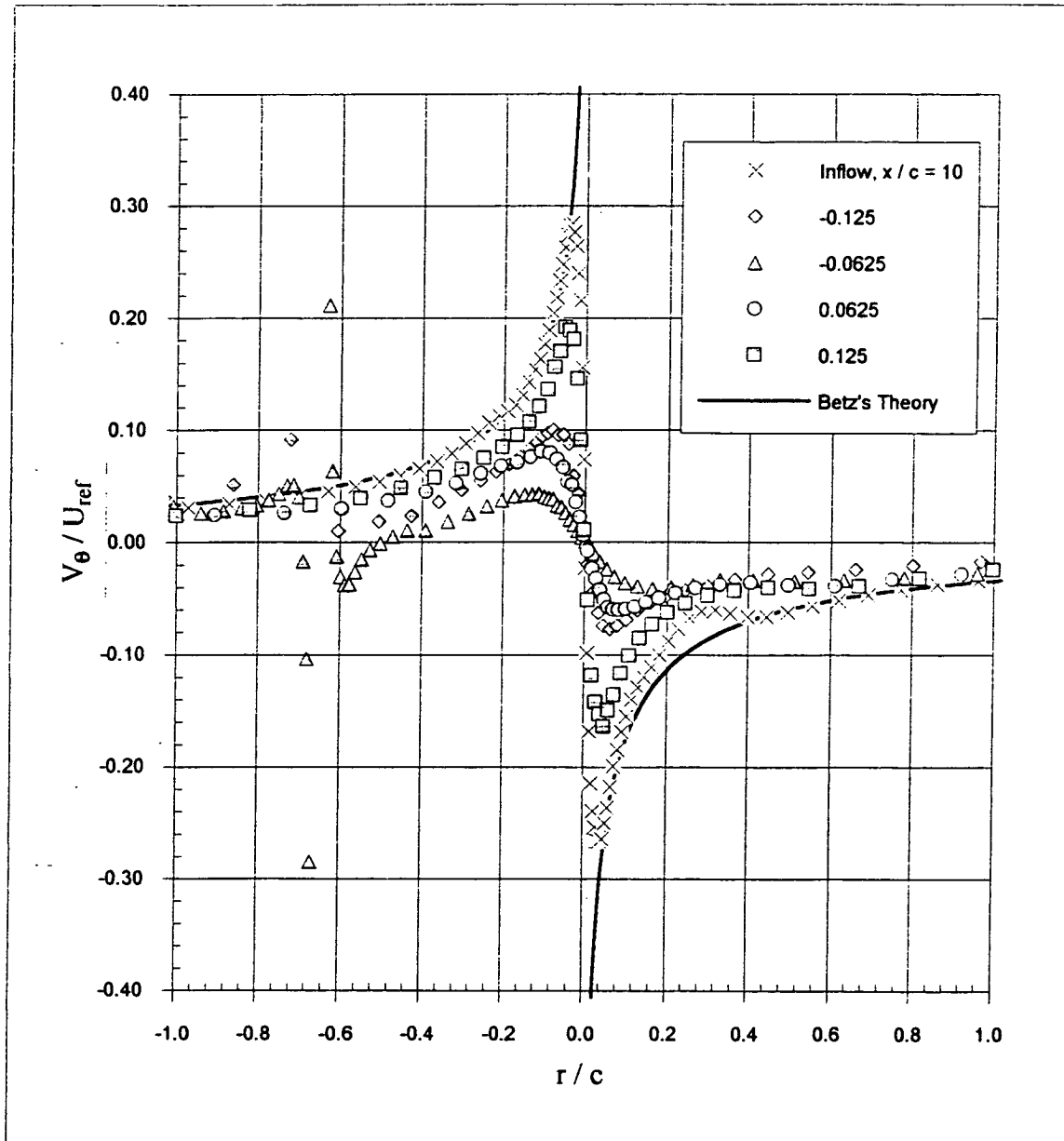


Figure 3.45 Tangential velocity profiles for the primary vortex at  $X/c=30$  as a function of  $\Delta/c$  after subtracting effects of blade tip vortex. Note that 'r' is radial distance from core center. (a) Whole profile.

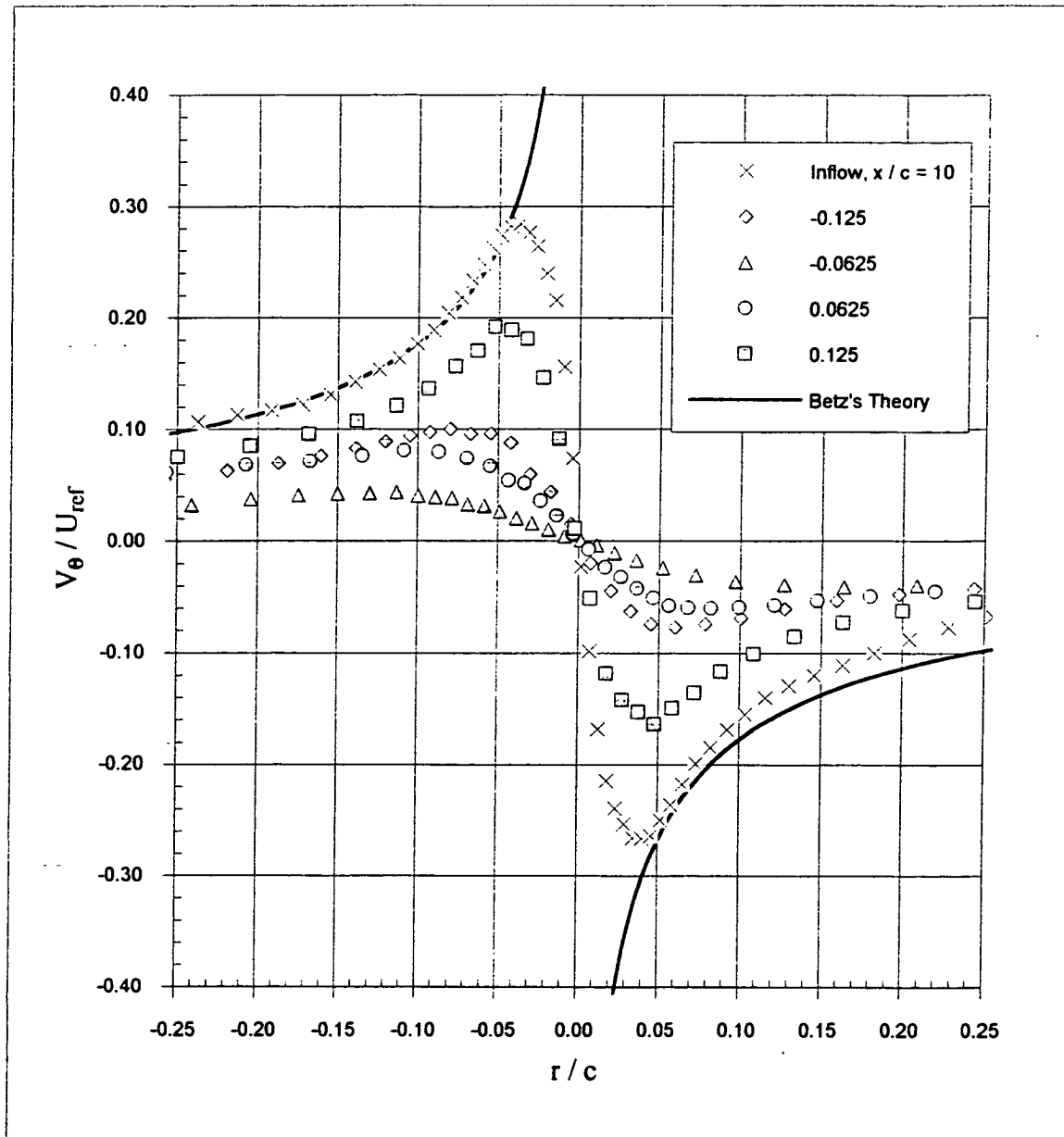


Figure 3.45 Tangential velocity profiles for the primary vortex at  $X/c=30$  as a function of  $\Delta/c$  after subtracting effects of blade tip vortex. Note that 'r' is radial distance from core center. (b) Core region.

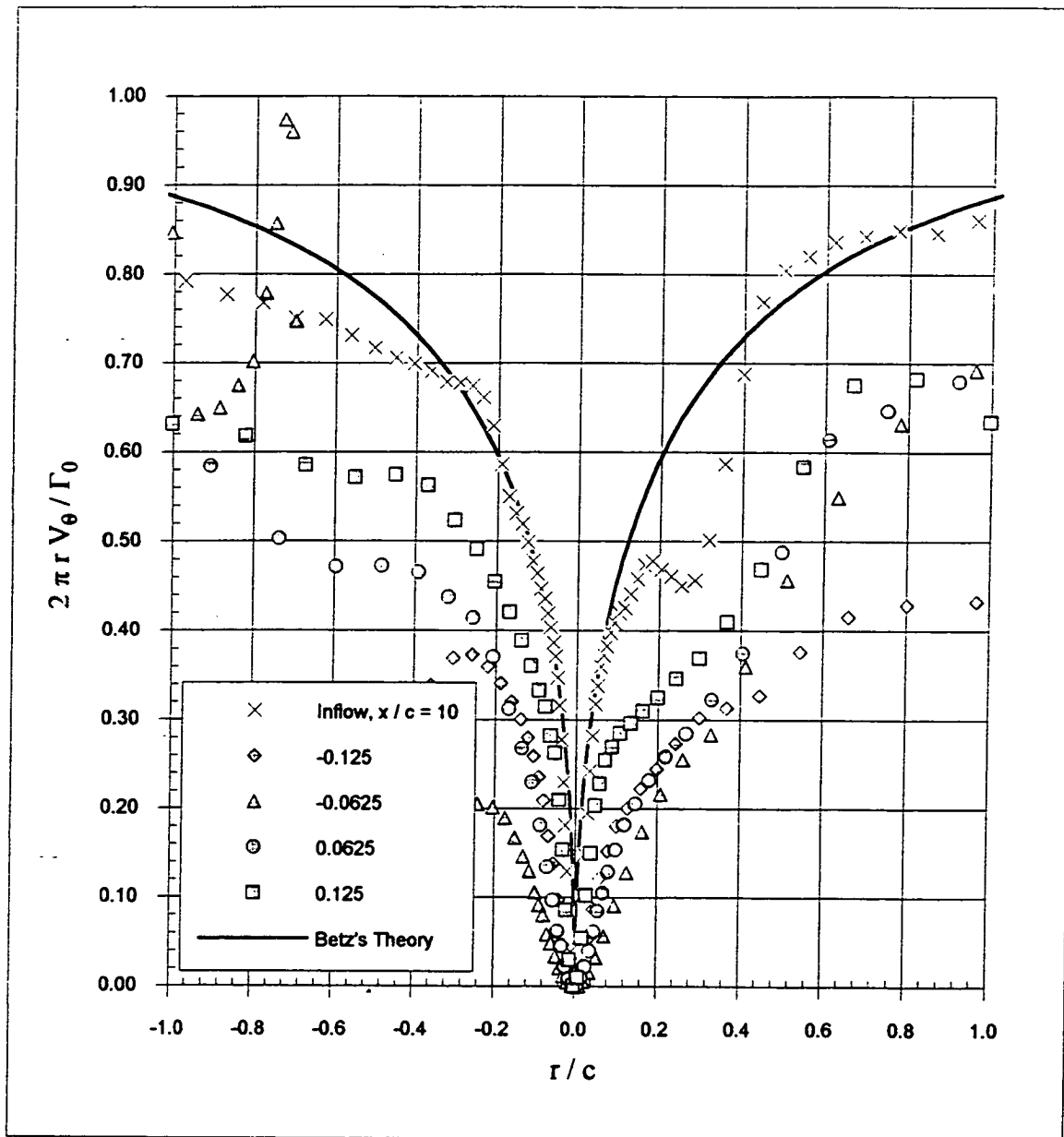


Figure 3.46 Circulation profiles for the primary vortex at  $X/c=30$  as a function of  $\Delta/c$  after subtracting effects of blade tip vortex. Note that 'r' is radial distance from core center. (a) Whole profile.





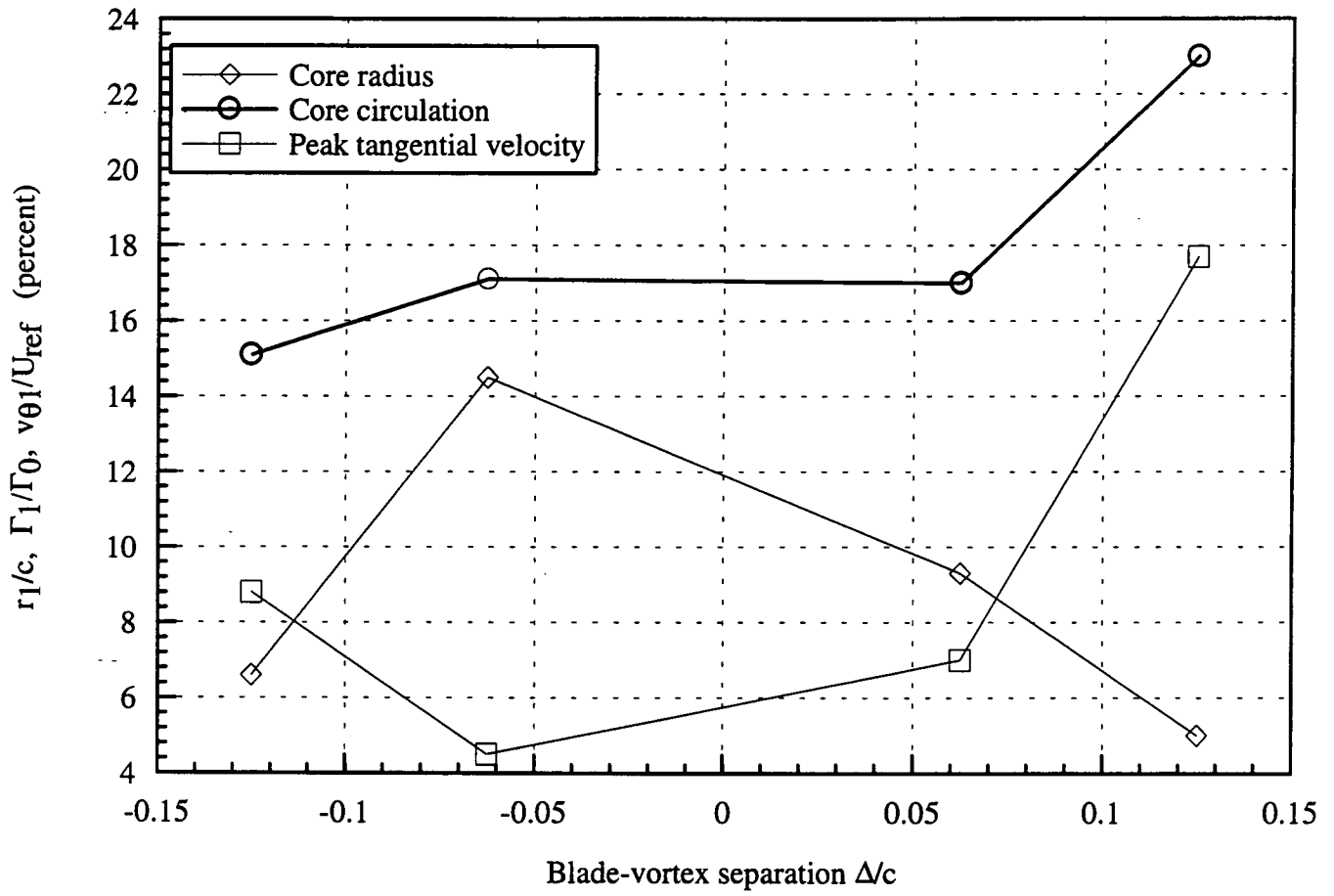


Figure 3.47 Variation of parameters of the primary vortex core with  $\Delta/c$  at  $X/c=30$ .

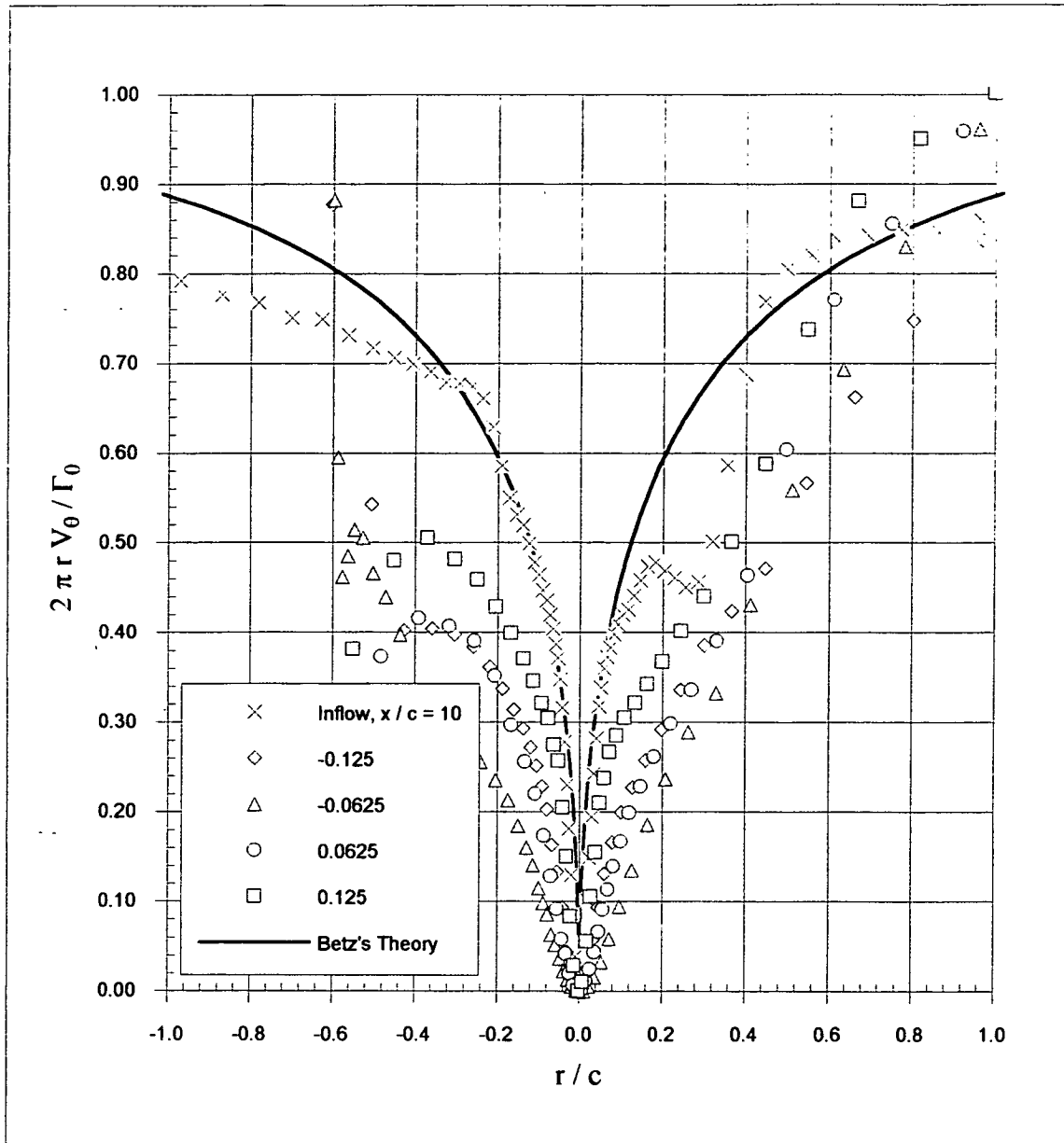


Figure 3.48 Circulation profiles for the primary vortex at  $X/c=30$  as a function of  $\Delta/c$  after subtracting effects of blade tip vortex taking the blade angle of attack as  $7^\circ$ . Note that 'r' is radial distance from core center. (a) Whole profile.

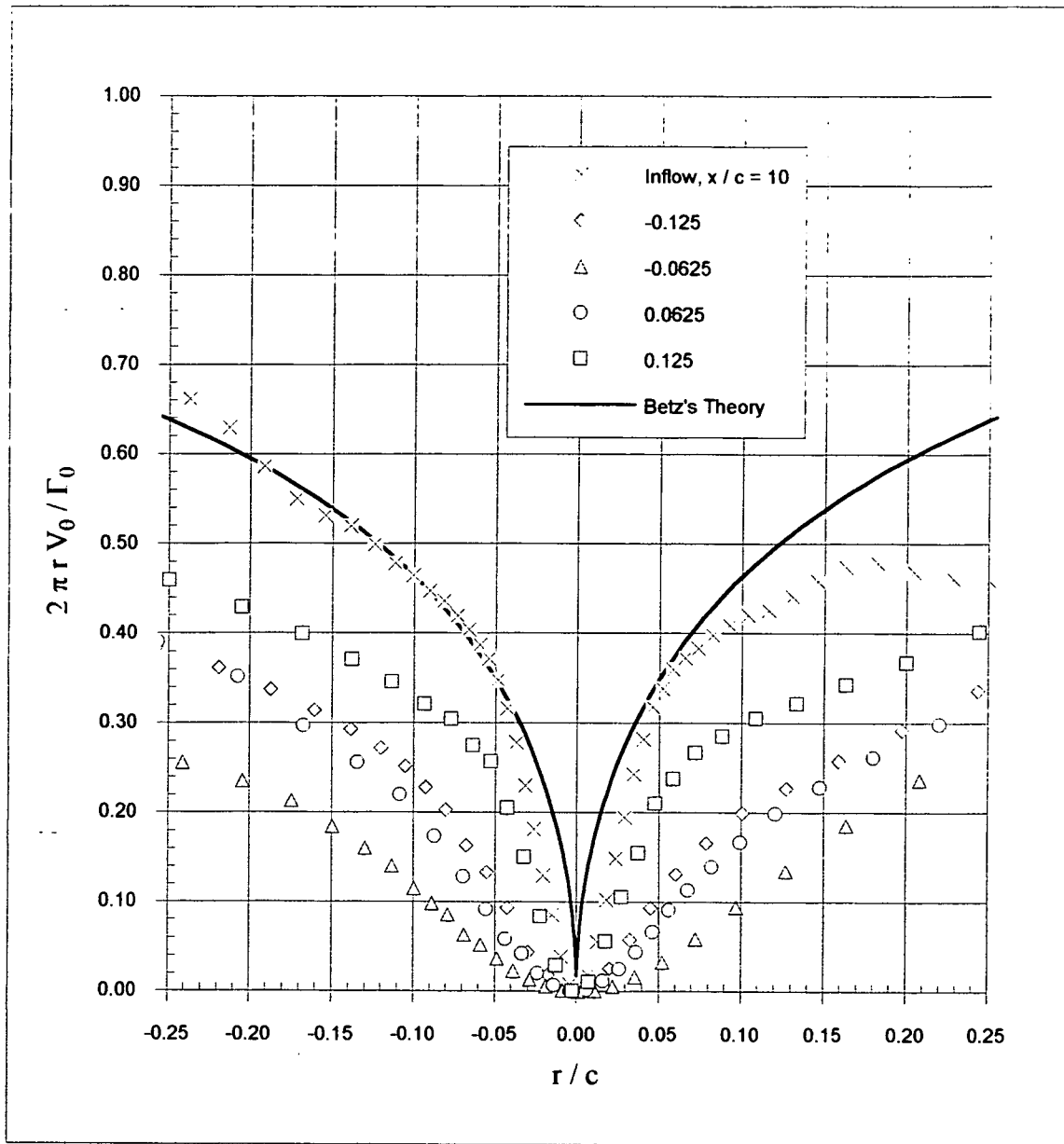


Figure 3.48 Circulation profiles for the primary vortex at  $X/c=30$  as a function of  $\Delta/c$  after subtracting effects of blade tip vortex taking the blade angle of attack as  $7^\circ$ . Note that 'r' is radial distance from core center. (b) Core region.

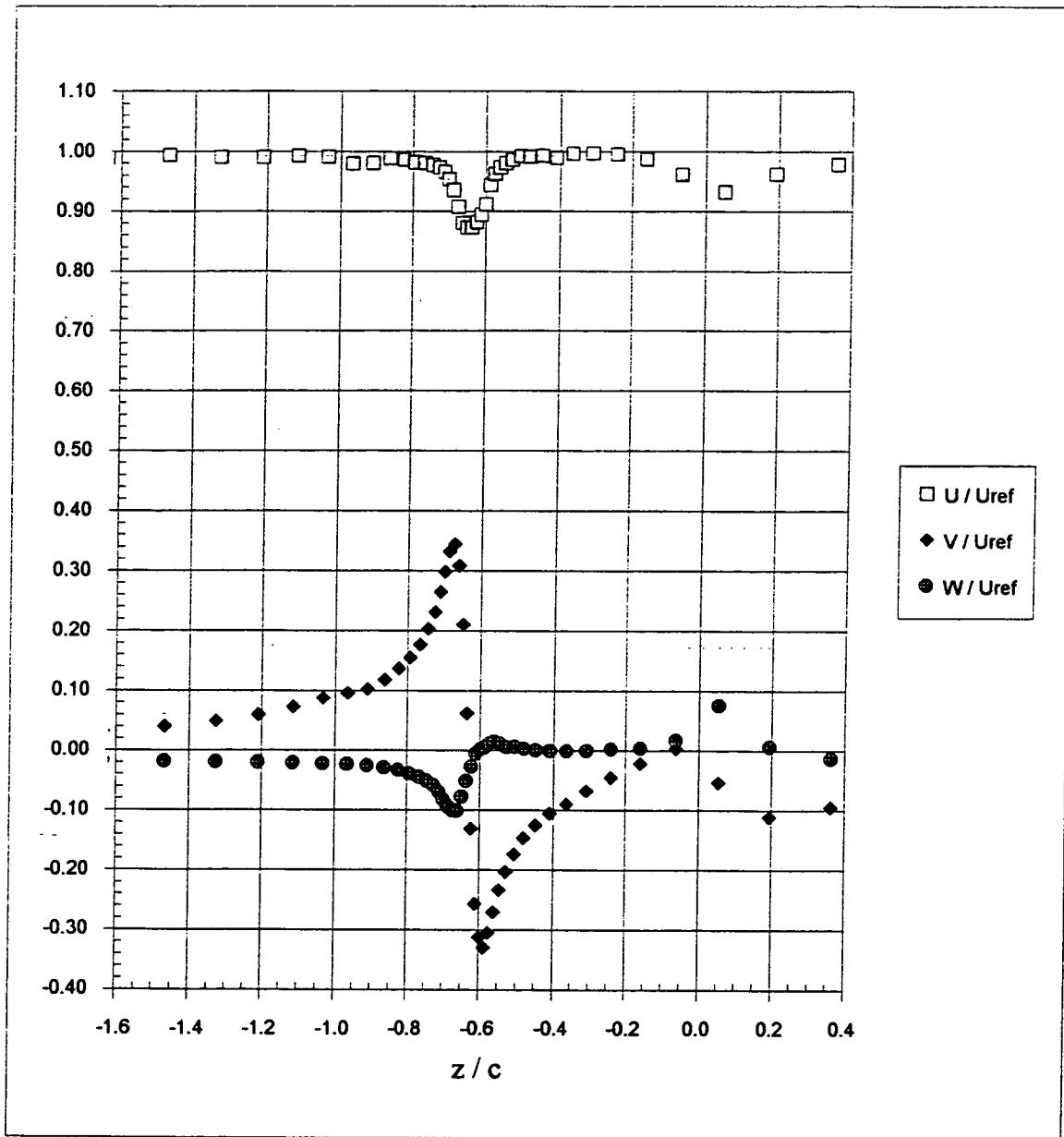


Figure 3.49 Mean velocity profiles through the blade tip vortex core at  $X/c=30$ . (a)  $\Delta/c=-0.125$ .



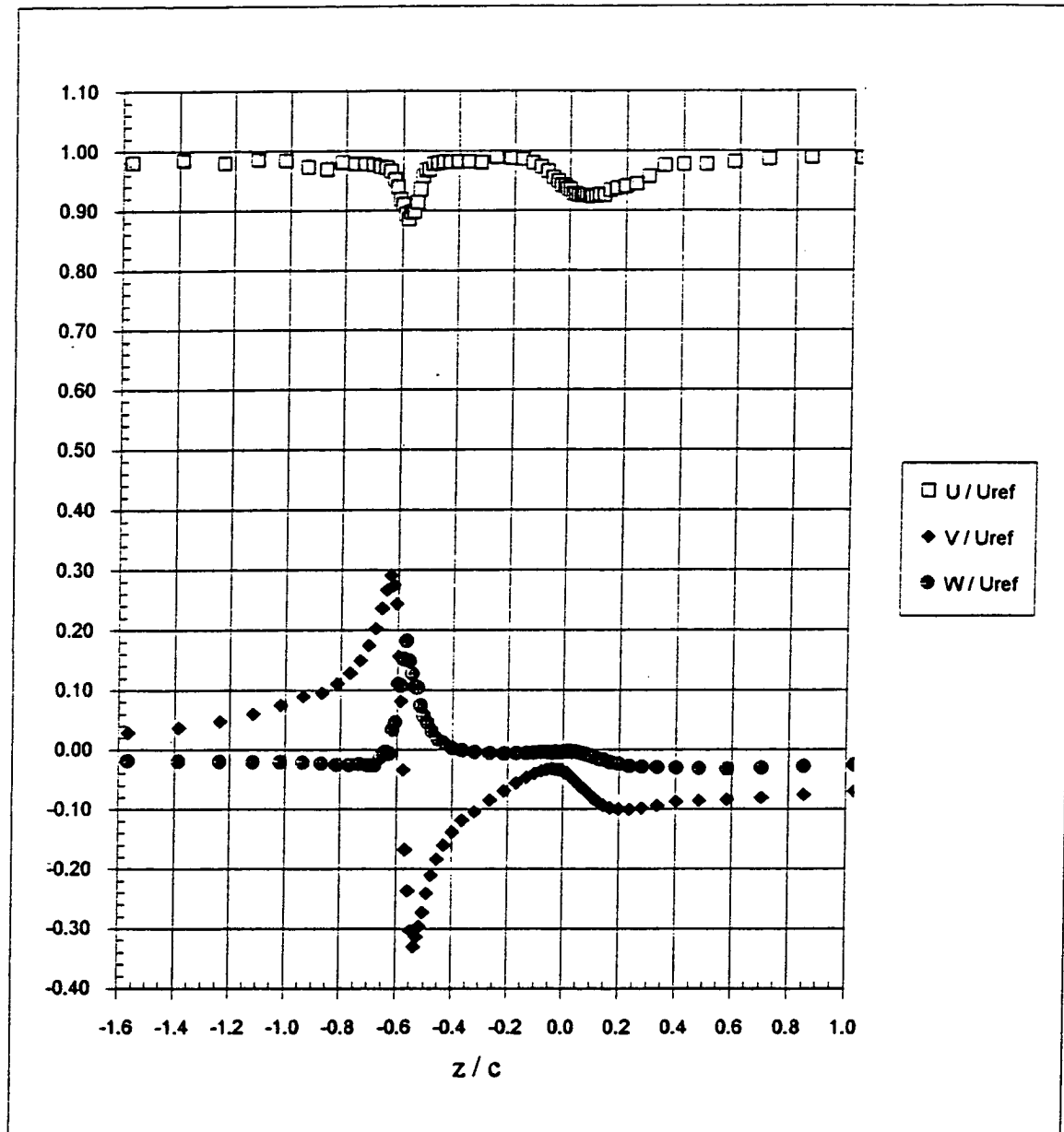


Figure 3.49 Mean velocity profiles through the blade tip vortex core at  $X/c=30$ . (b)  $\Delta/c=-0.0625$ .

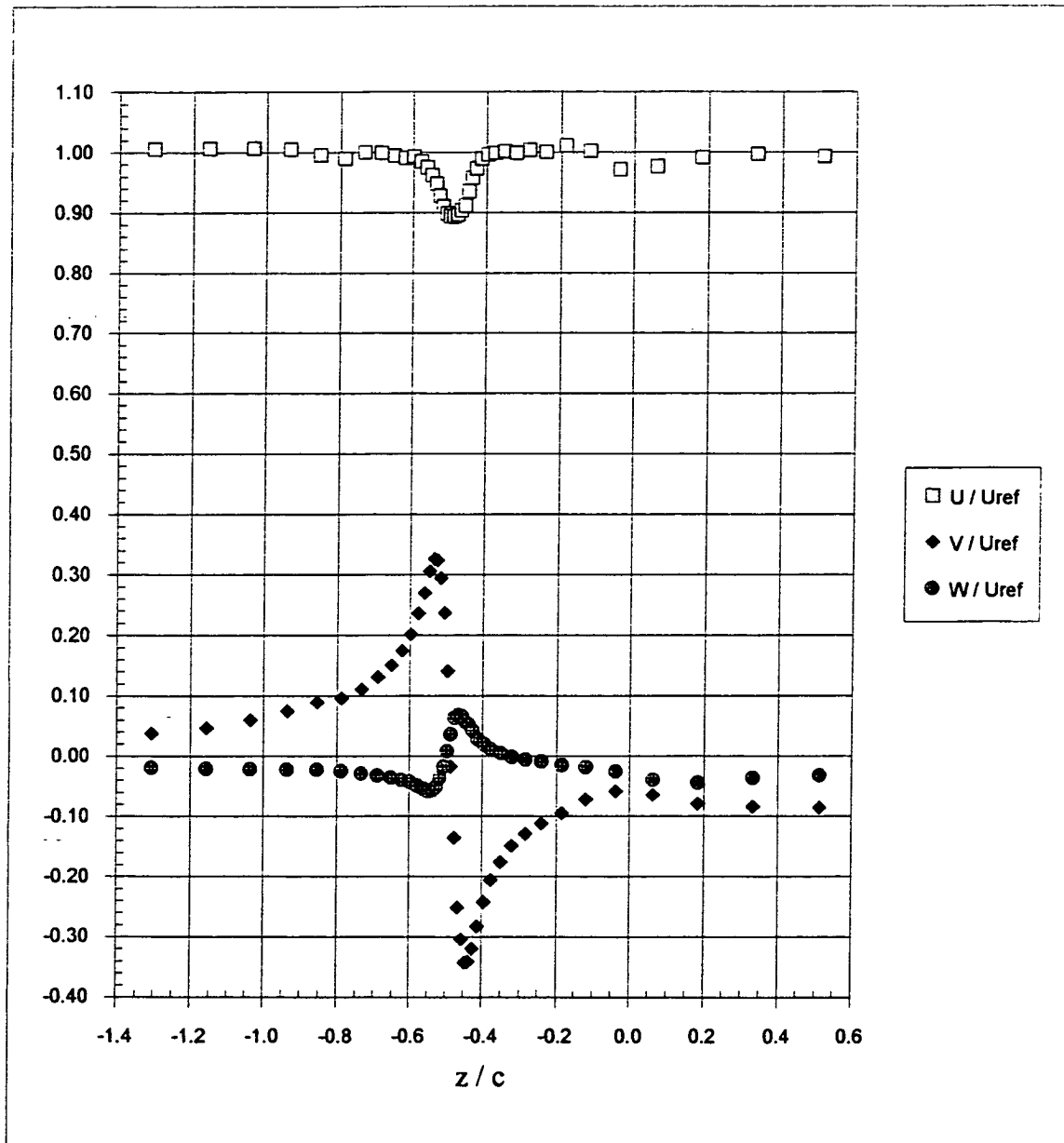


Figure 3.49 Mean velocity profiles through the blade tip vortex core at  $X/c=30$ . (c)  $\Delta/c=0$ .

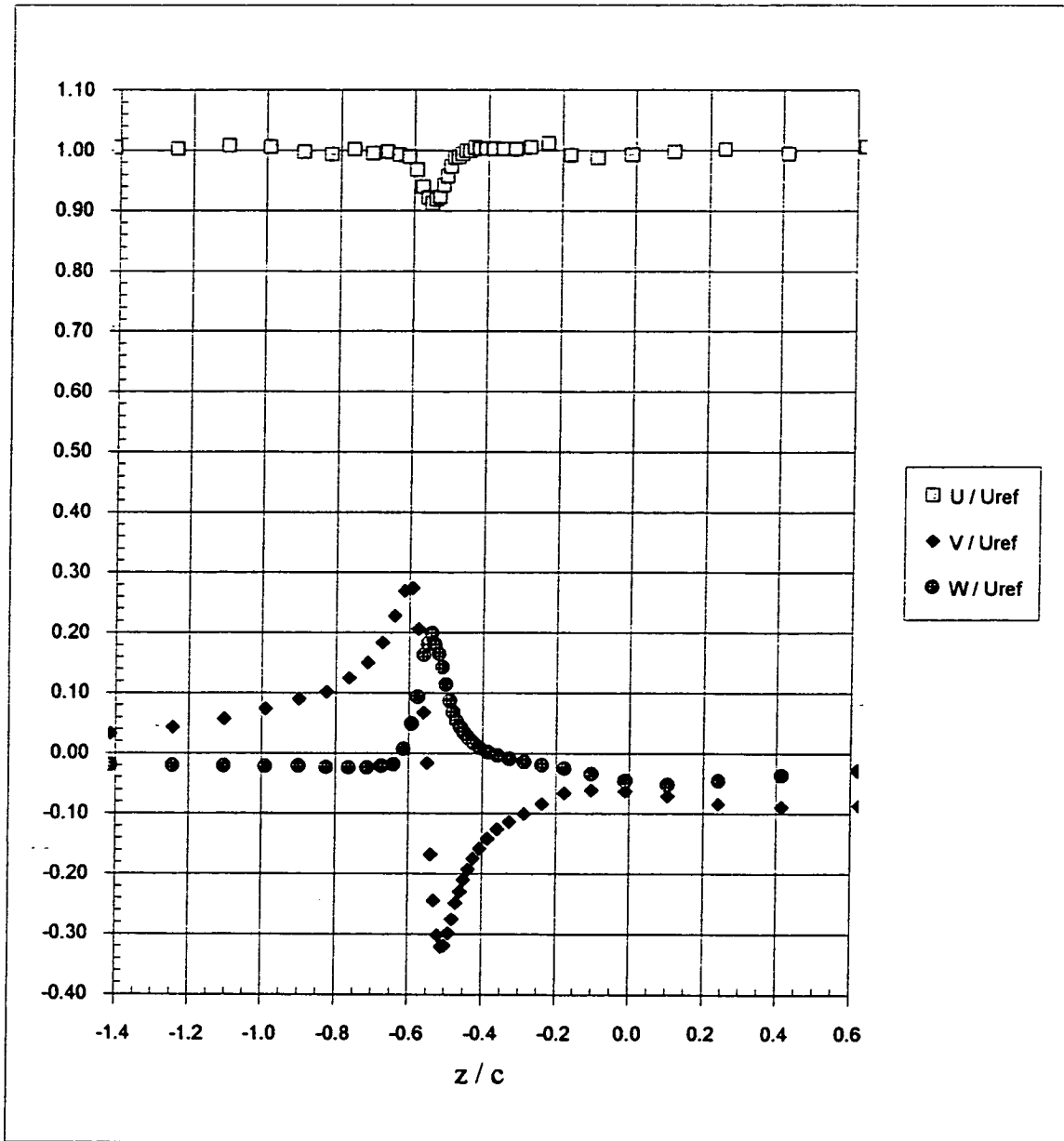


Figure 3.49 Mean velocity profiles through the blade tip vortex core at  $X/c=30$ . (d)  $\Delta/c=0.0625$ .

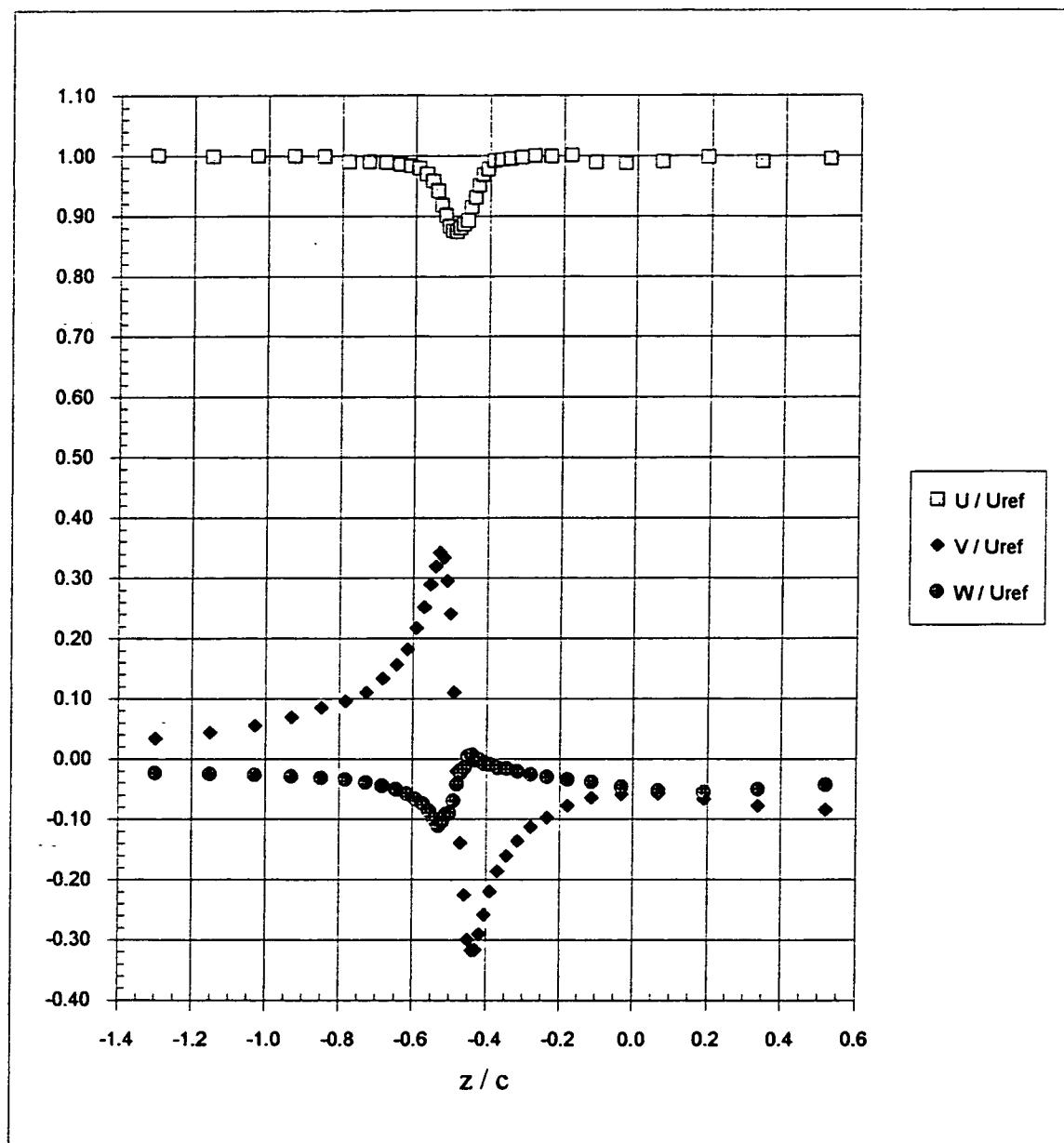


Figure 3.49 Mean velocity profiles through the blade tip vortex core at  $X/c=30$ . (e)  $\Delta/c=0.125$ .



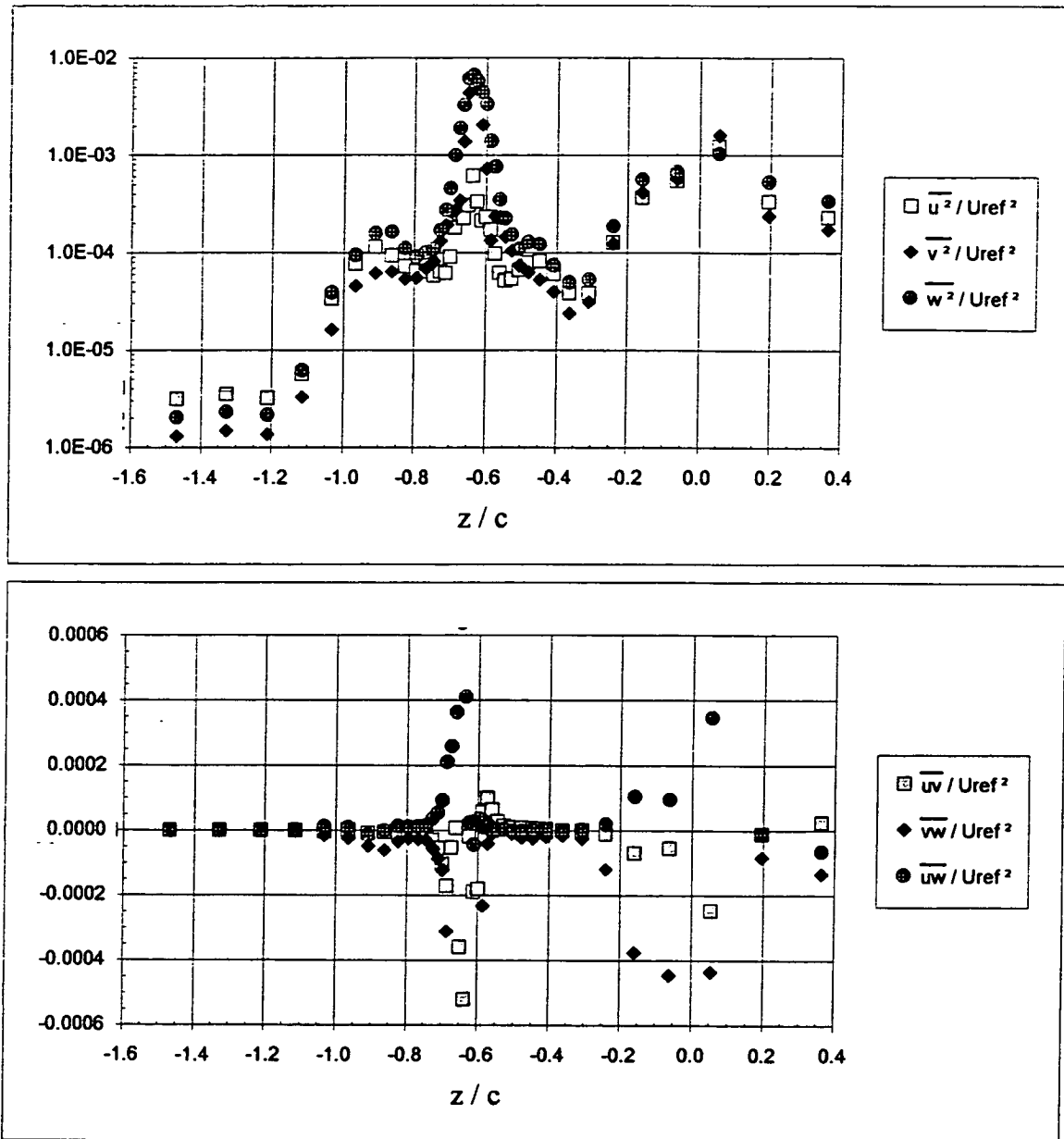


Figure 3.50 Turbulence stress profiles through the blade tip vortex core at  $X/c=30$ . (a)  $\Delta/c=-0.125$ .

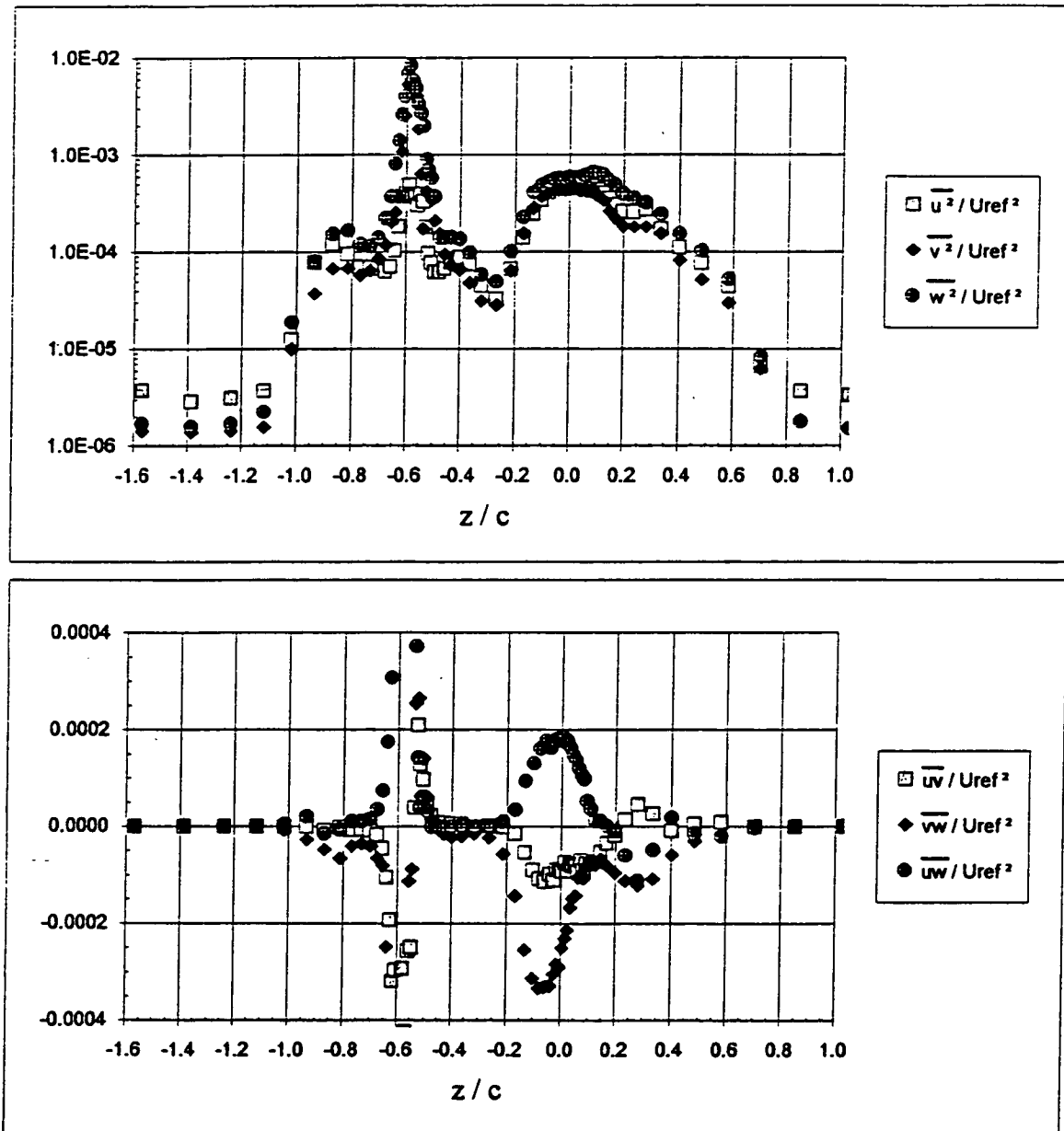


Figure 3.50 Turbulence stress profiles through the blade tip vortex core at  $X/c=30$ . (b)  $\Delta/c=-0.0625$ .

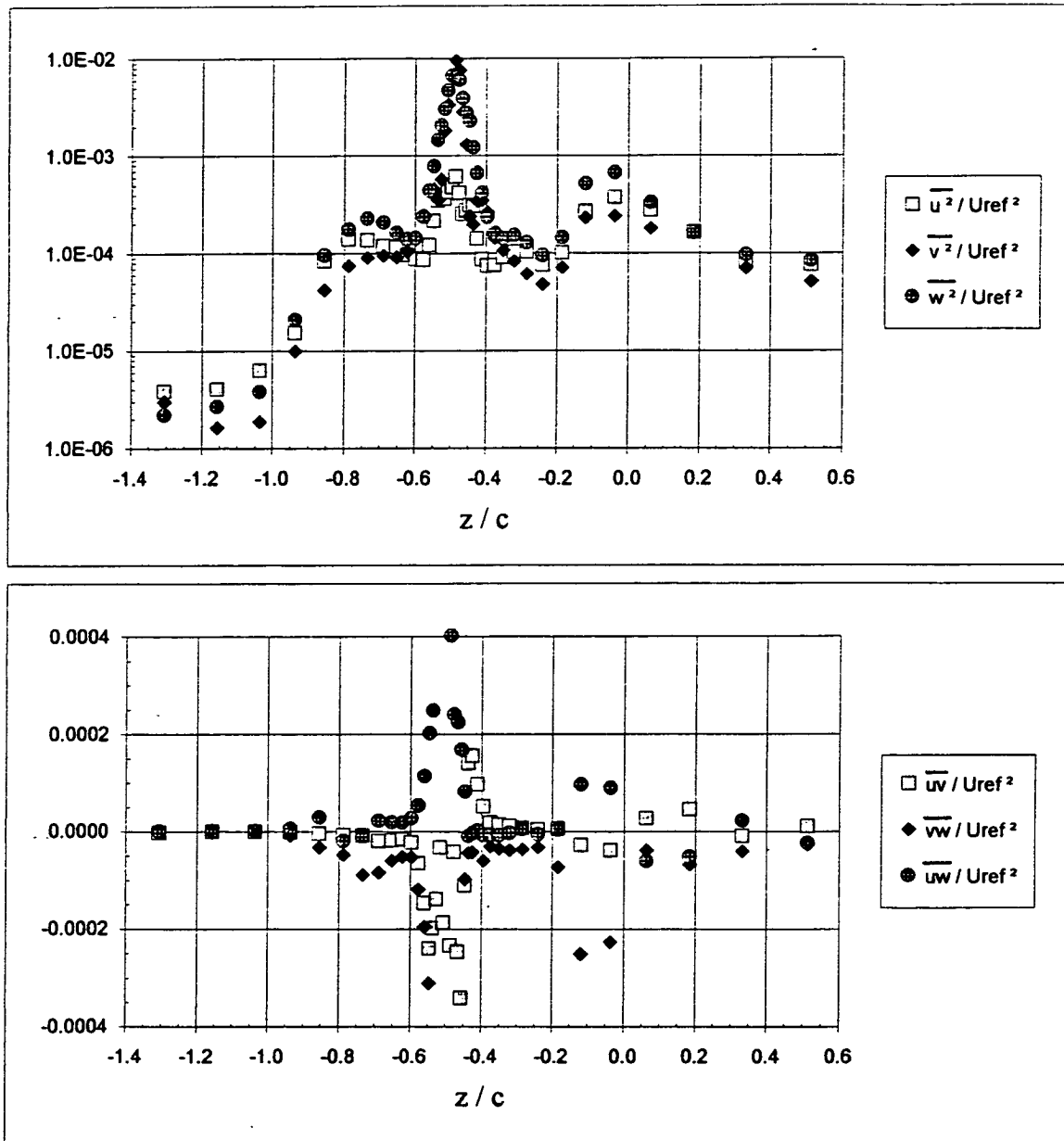


Figure 3.50 Turbulence stress profiles through the blade tip vortex core at  $X/c=30$ . (c)  $\Delta/c=0$ .

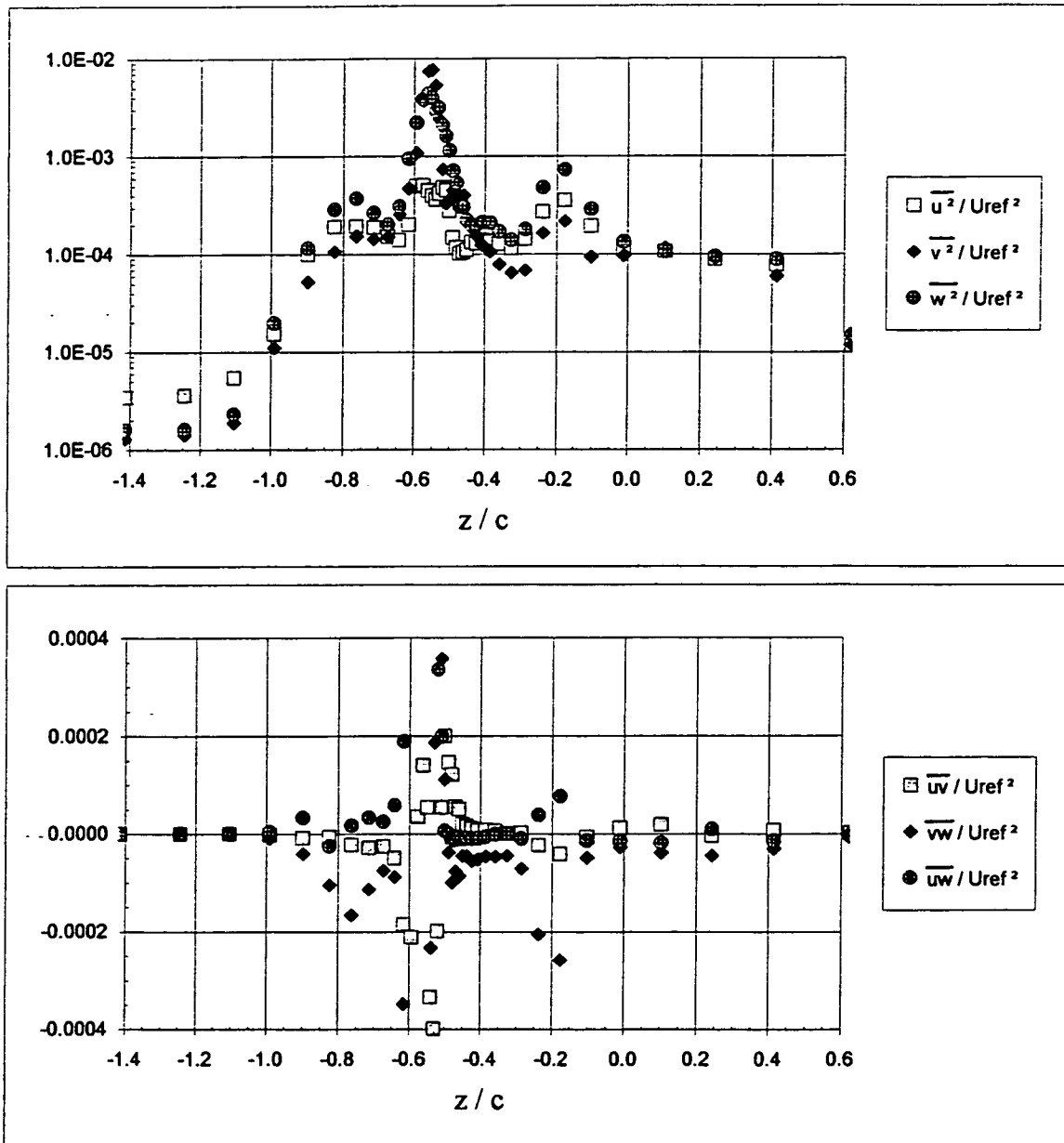


Figure 3.50 Turbulence stress profiles through the blade tip vortex core at  $X/c=30$ . (d)  $\Delta/c=0.0625$ .



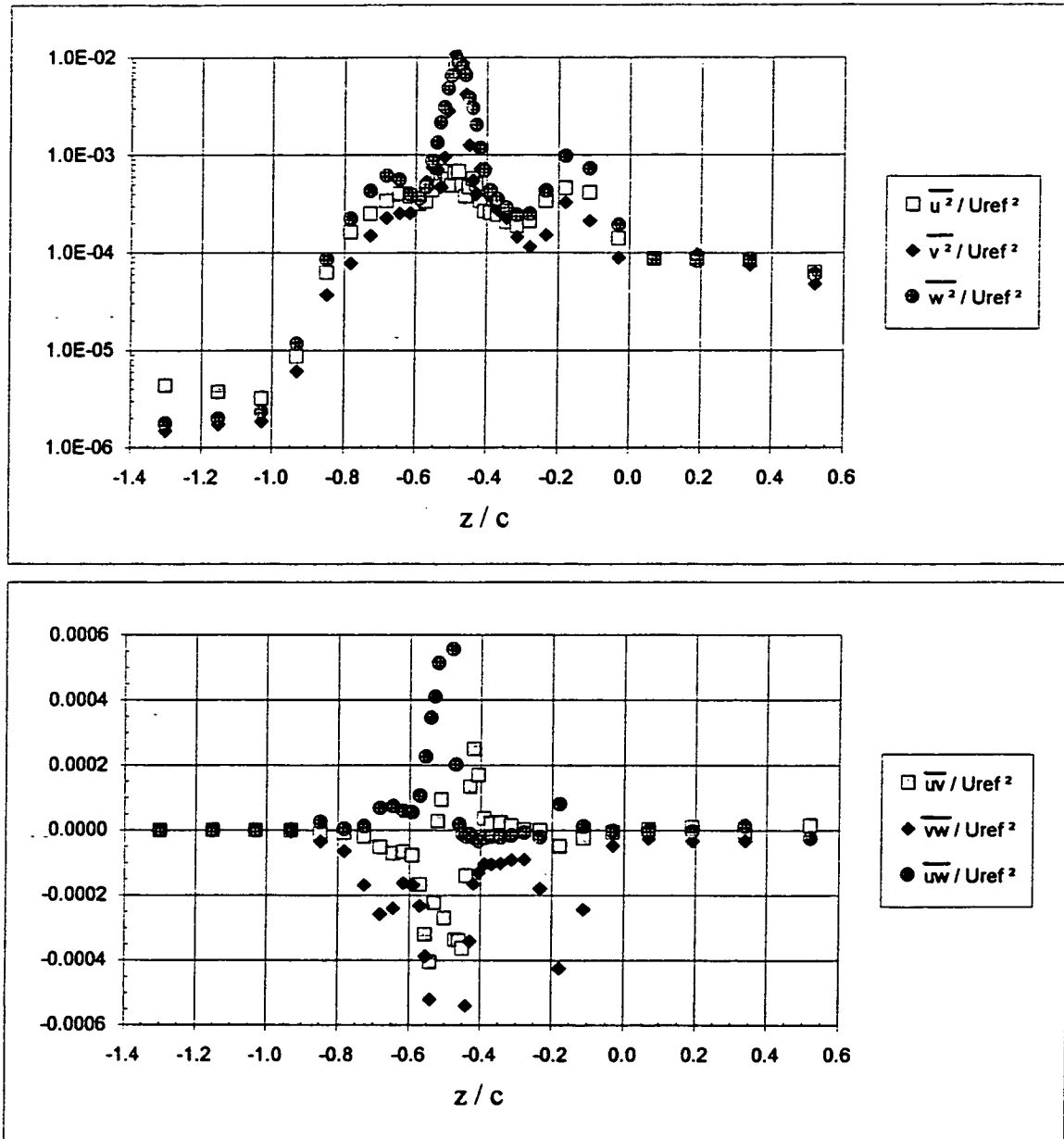


Figure 3.50 Turbulence stress profiles through the blade tip vortex core at  $X/c=30$ . (e)  $\Delta/c=0.125$ .

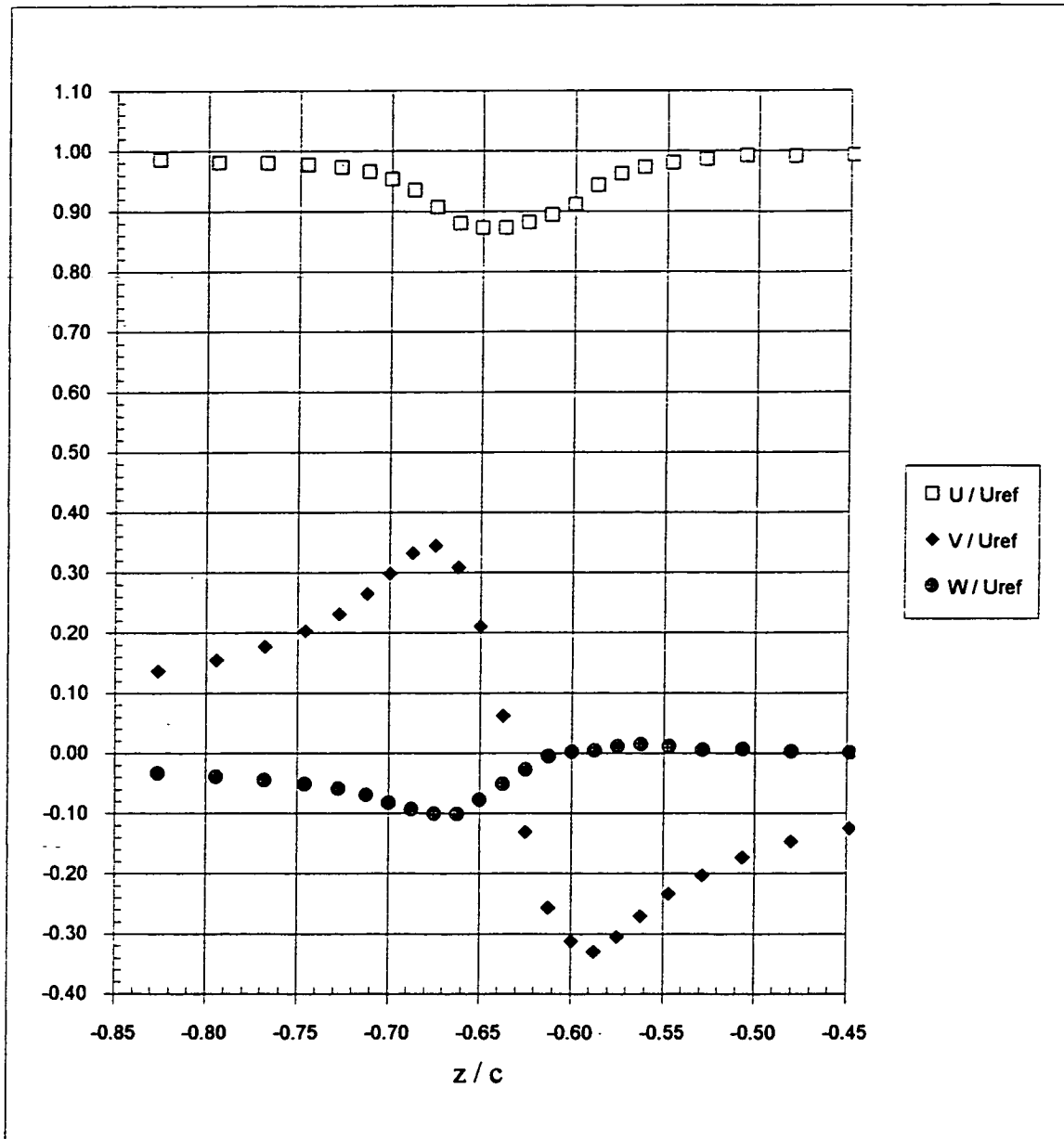


Figure 3.51 Mean velocity profiles in the vicinity of the blade tip vortex core at  $X/c=30$ . (a)  $\Delta/c=-0.125$ .

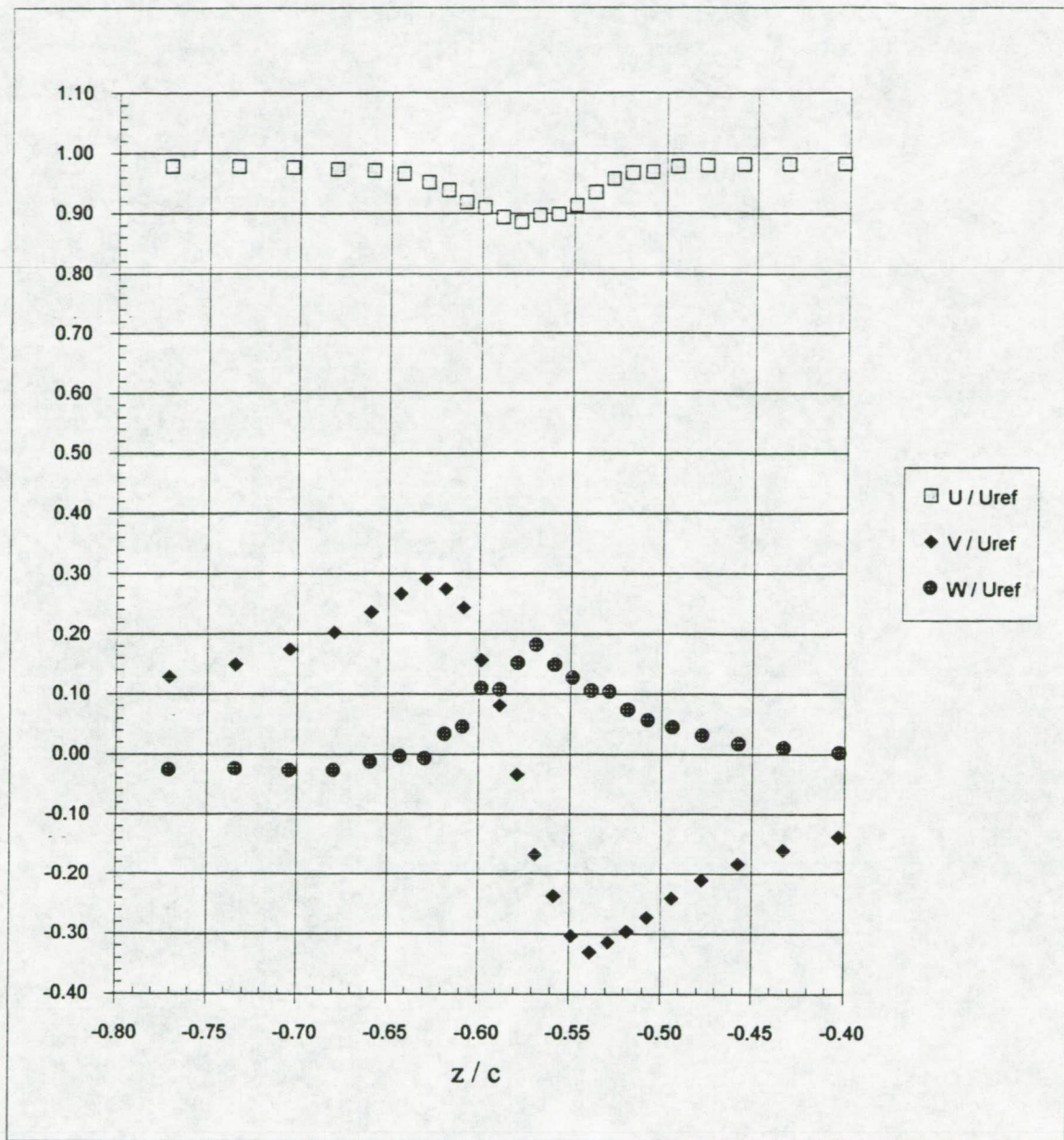


Figure 3.51 Mean velocity profiles in the vicinity of the blade tip vortex core at  $X/c=30$ .  
(b)  $\Delta/c=-0.0625$ .

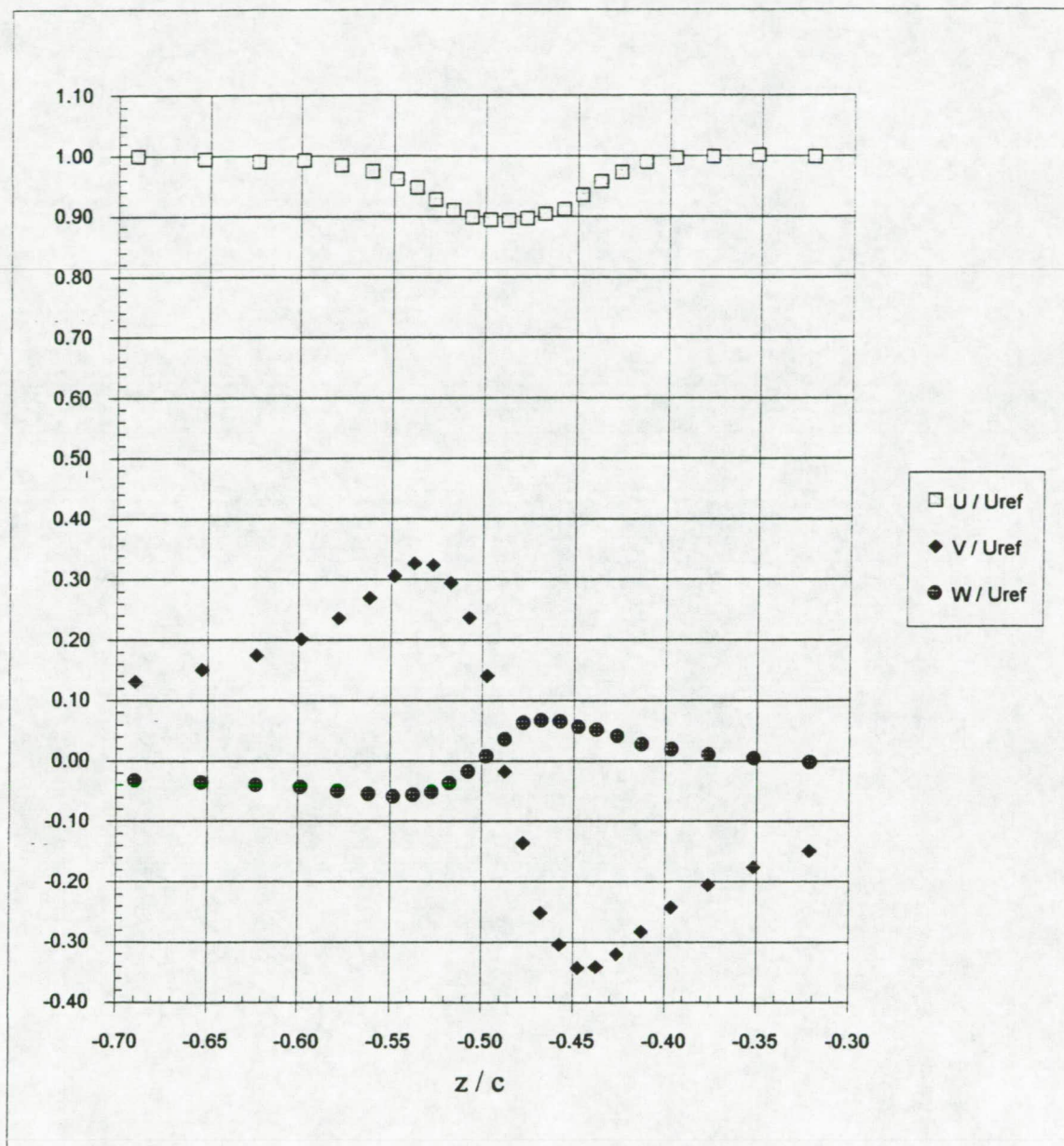


Figure 3.51 Mean velocity profiles in the vicinity of the blade tip vortex core at  $X/c=30$ . (c)  $\Delta/c=0$ .



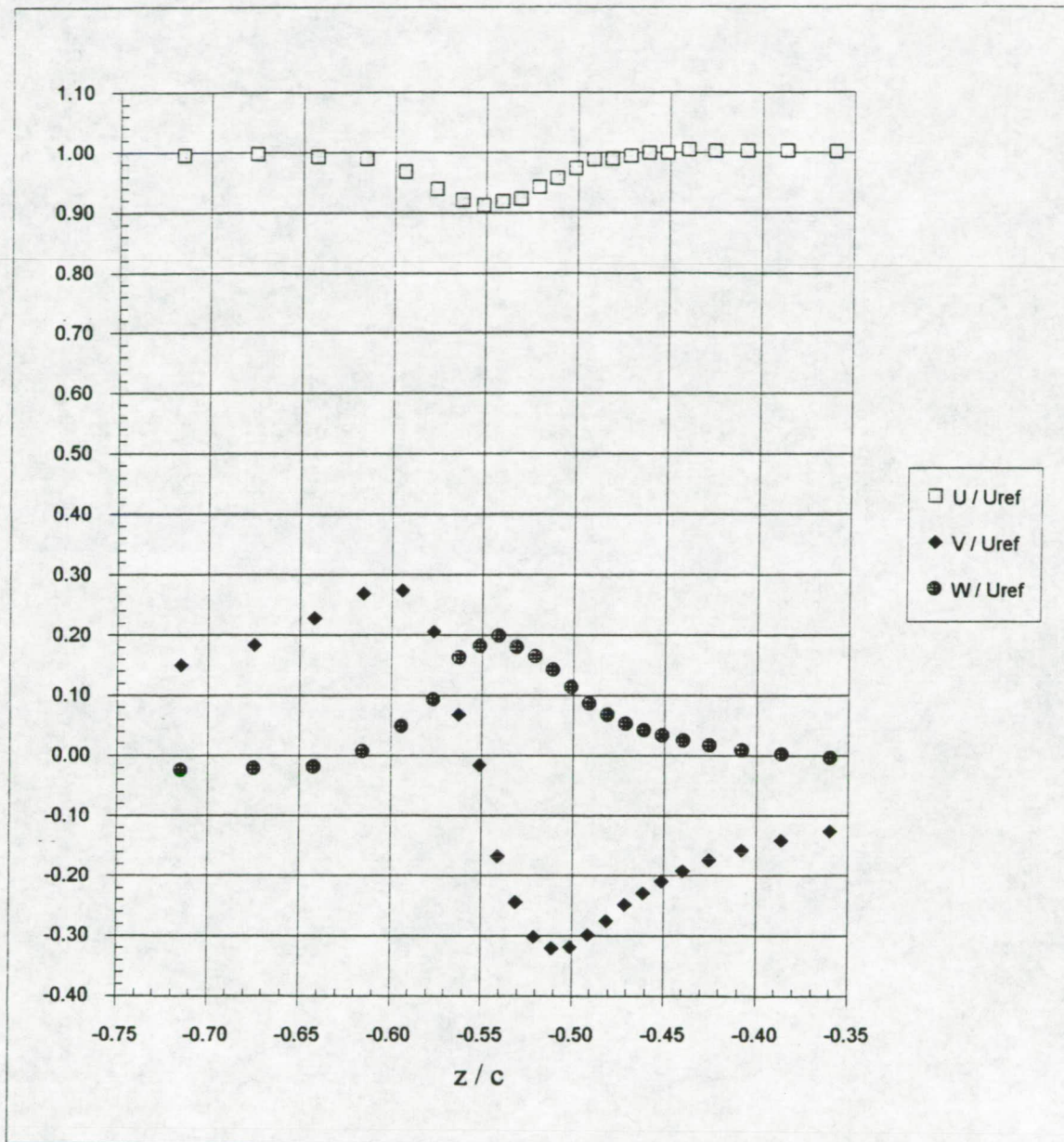


Figure 3.51 Mean velocity profiles in the vicinity of the blade tip vortex core at  $X/c=30$ .  
(d)  $\Delta/c=0.0625$ .

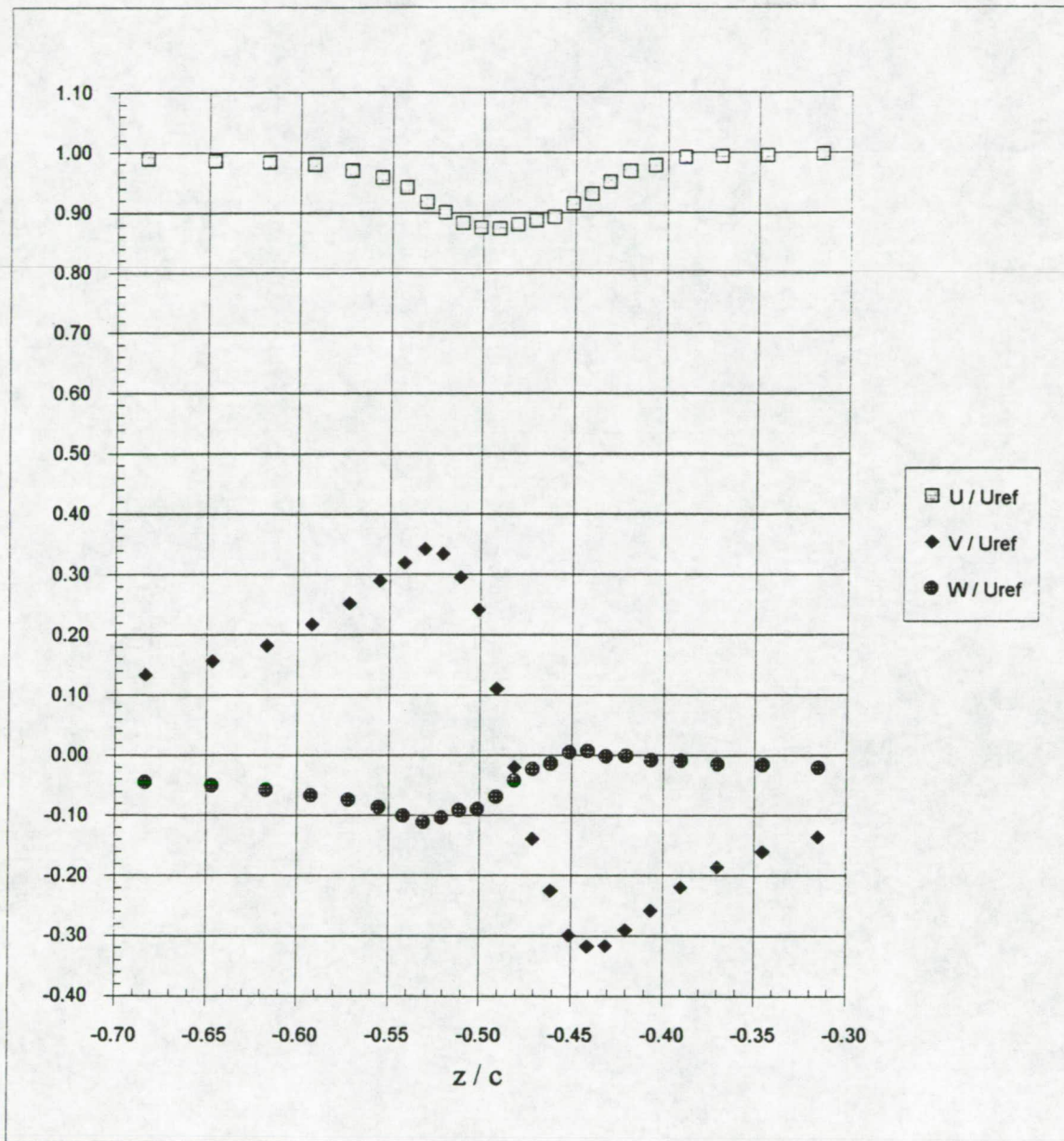


Figure 3.51 Mean velocity profiles in the vicinity of the blade tip vortex core at  $X/c=30$ . (e)  $\Delta/c=0.125$ .



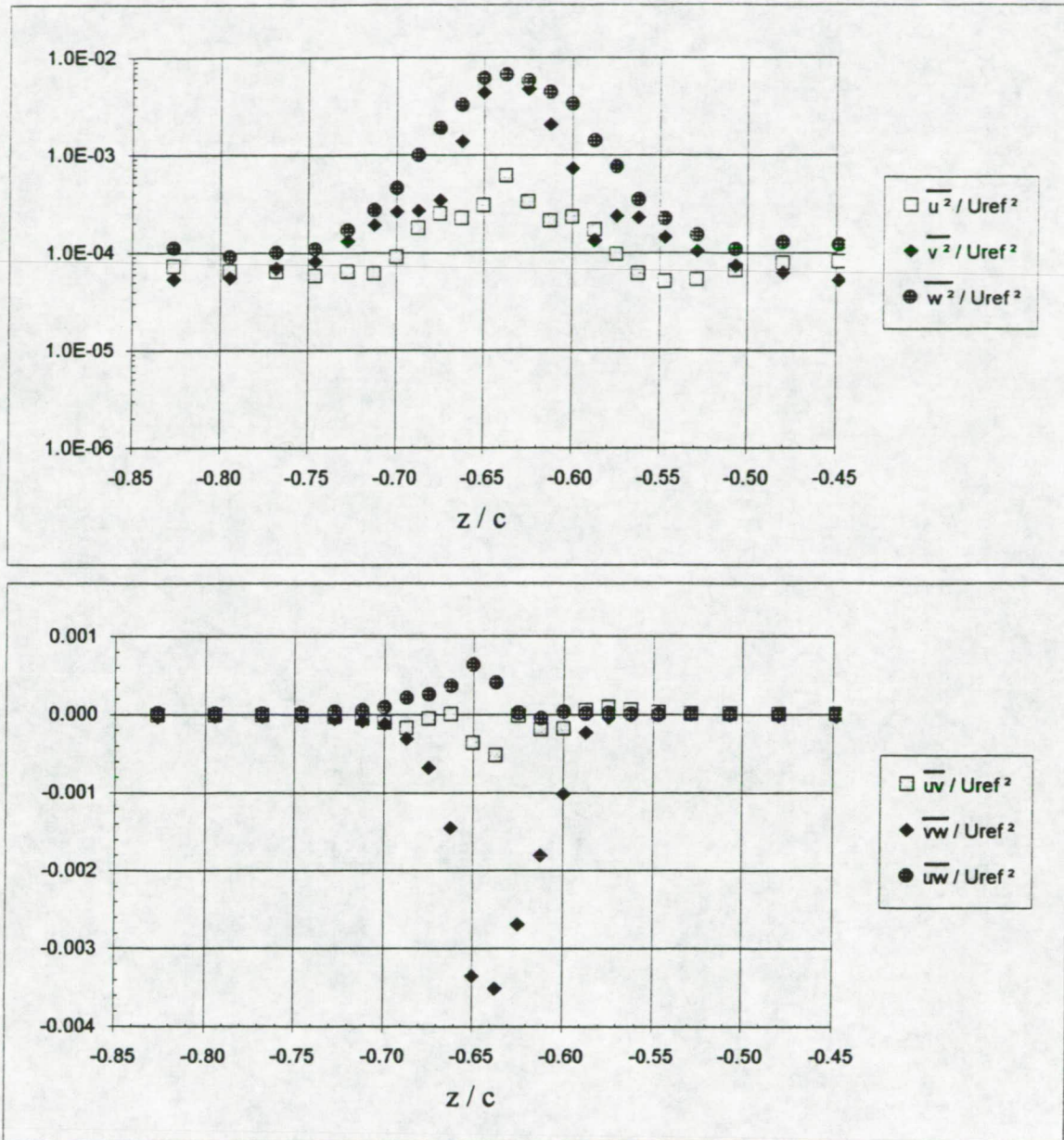


Figure 3.52 Turbulence stress profiles in the vicinity of the blade tip vortex core at  $X/c=30$ .  
(a)  $\Delta/c=-0.125$ .

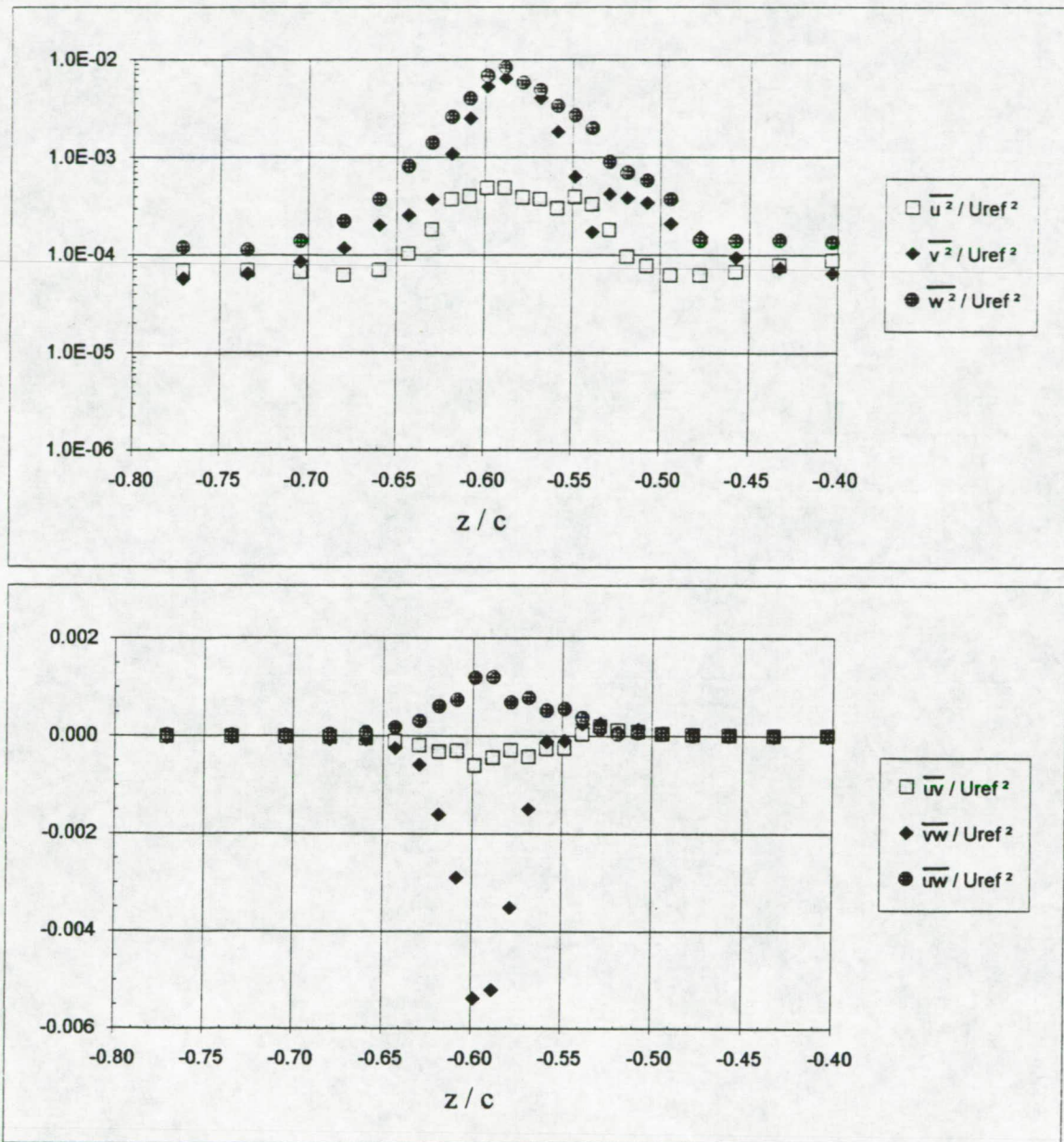


Figure 3.52 Turbulence stress profiles in the vicinity of the blade tip vortex core at  $X/c=30$ .  
 (b)  $\Delta/c=-0.0625$ .



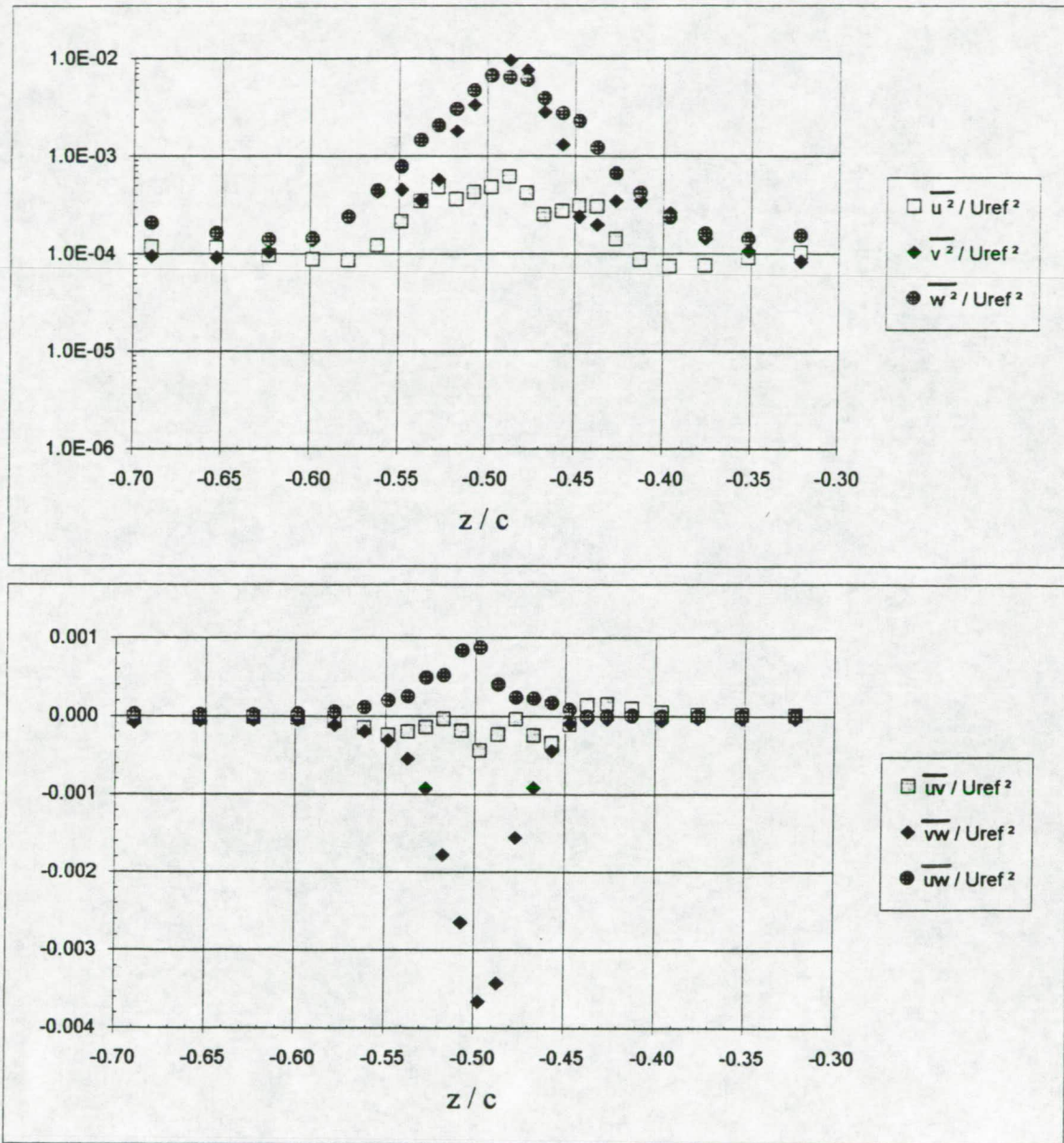


Figure 3.52 Turbulence stress profiles in the vicinity of the blade tip vortex core at  $X/c=30$ .  
(c)  $\Delta/c=0$ .

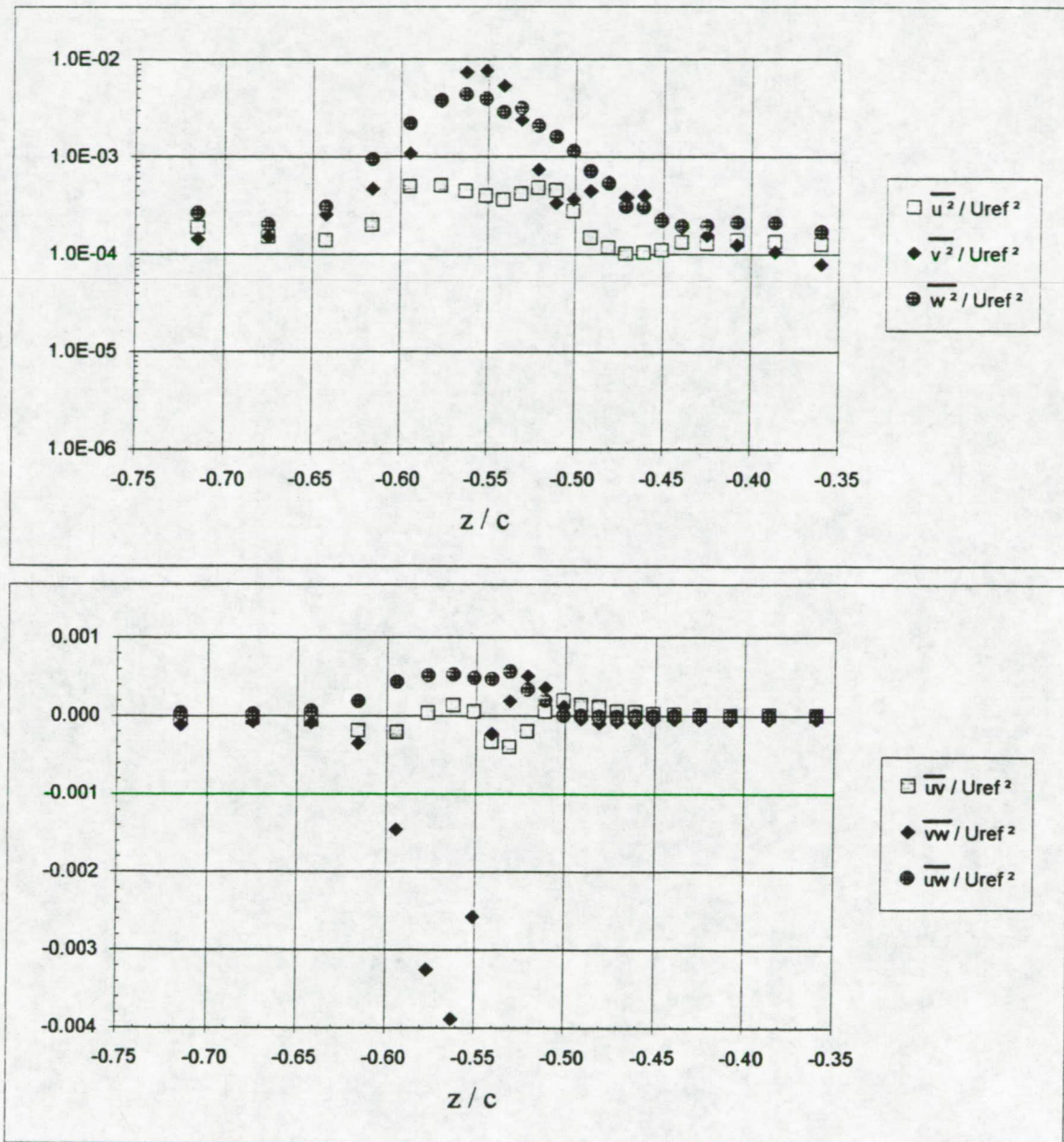


Figure 3.52 Turbulence stress profiles in the vicinity of the blade tip vortex core at  $X/c=30$ .  
(d)  $\Delta/c=0.0625$ .



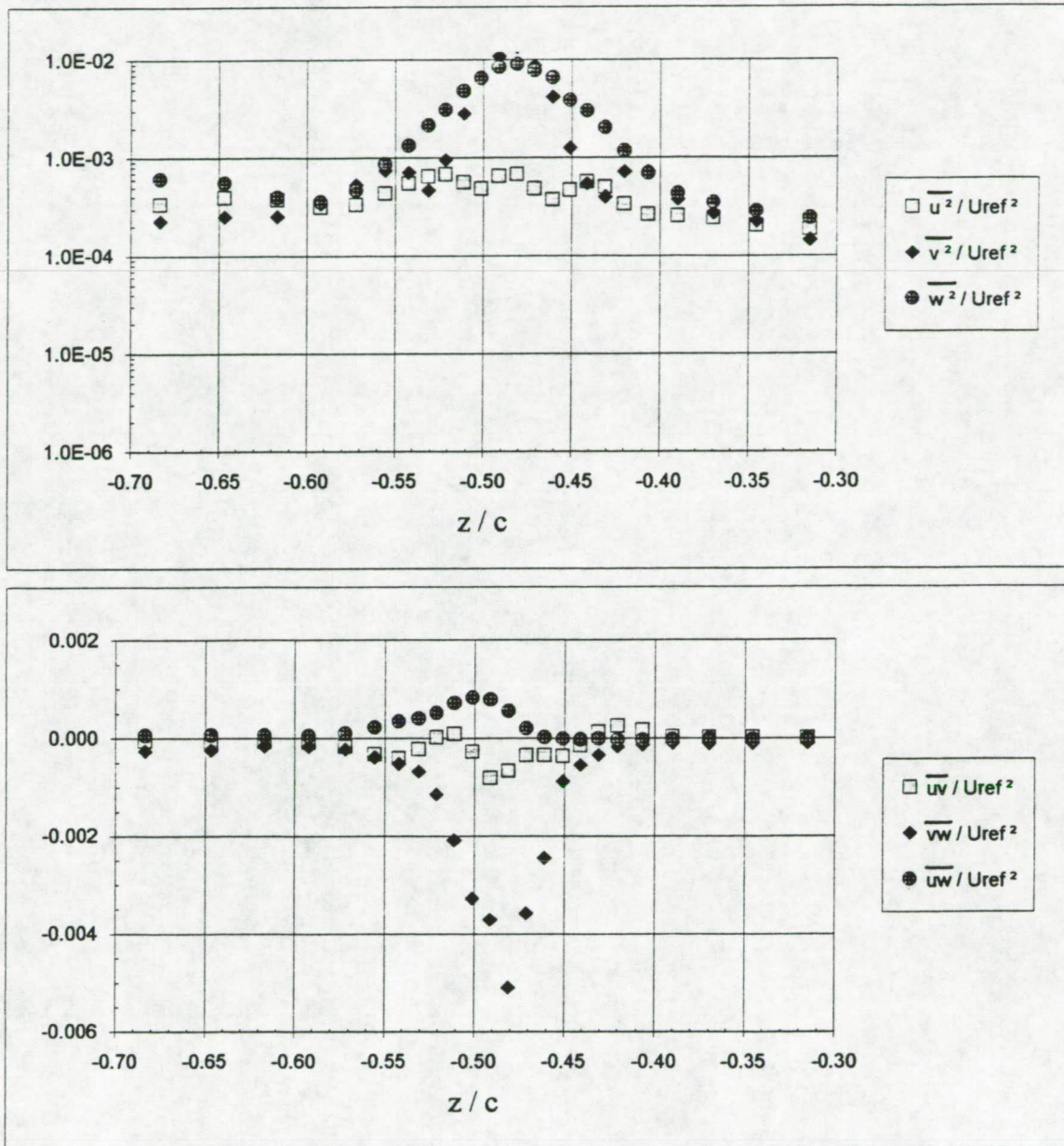
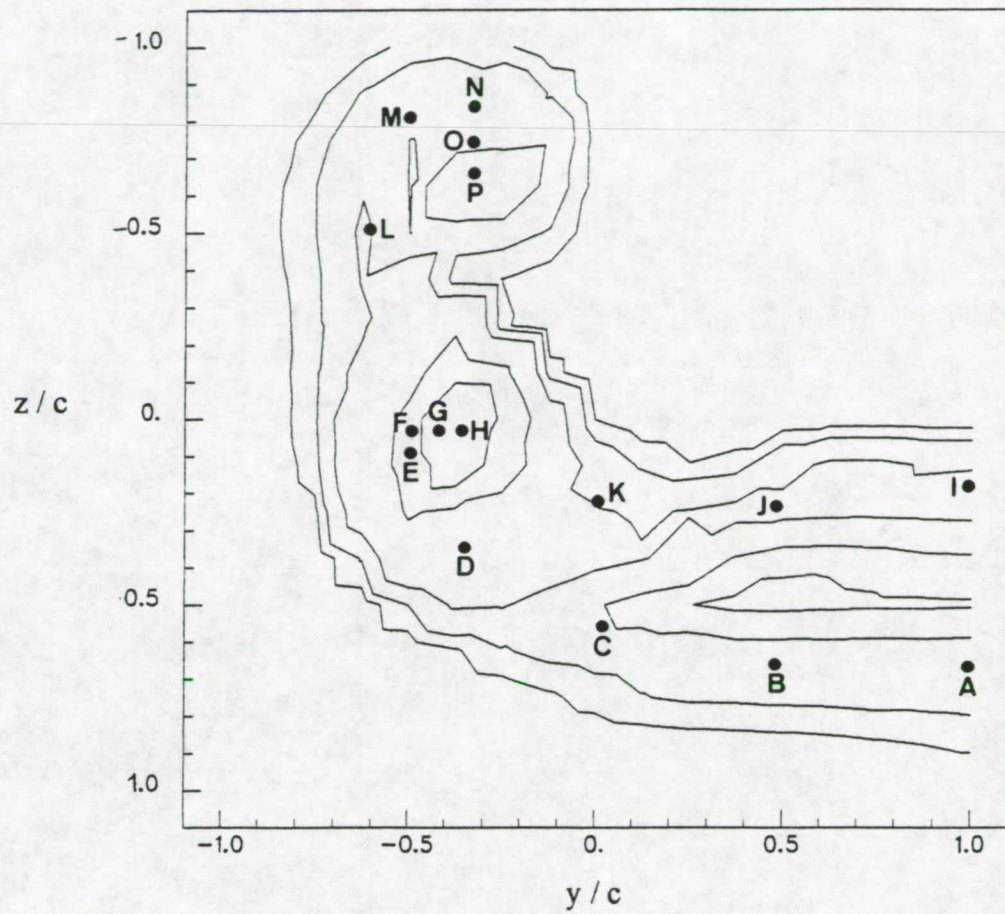


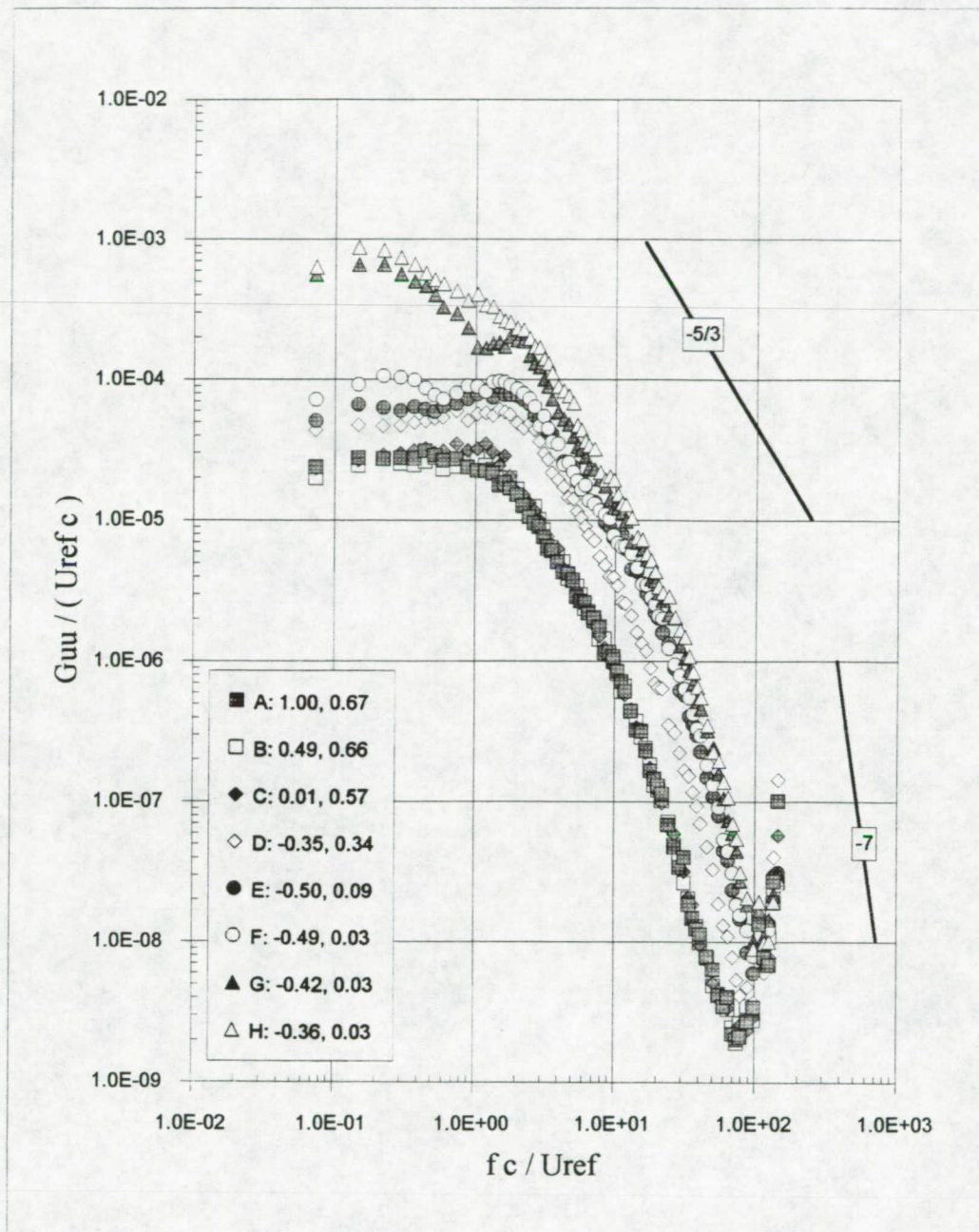
Figure 3.52 Turbulence stress profiles in the vicinity of the blade tip vortex core at  $X/c=30$ .  
(e)  $\Delta/c=0.125$ .



• Represents spectral measurement locations

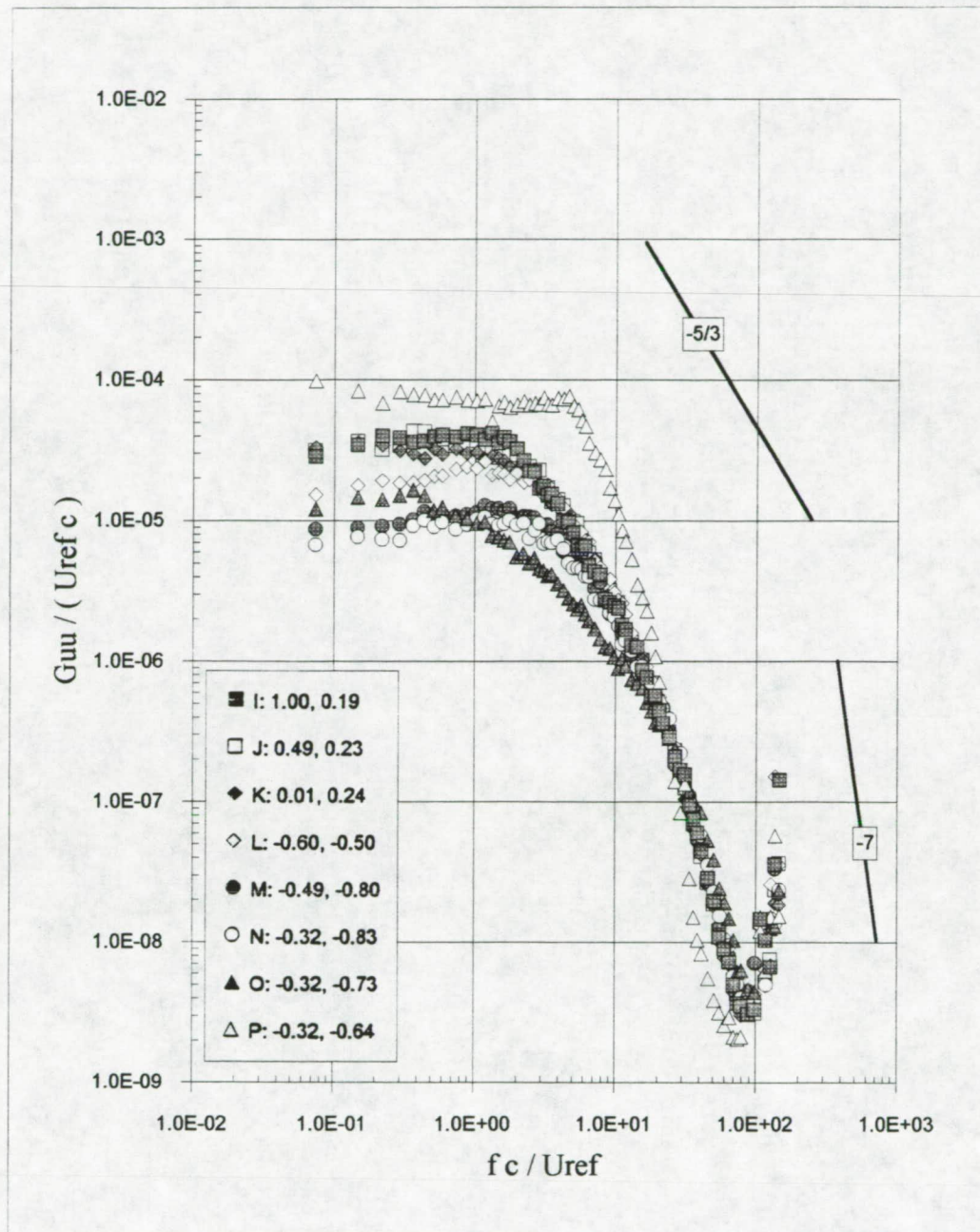
Figure 3.53 Velocity autospectra,  $X/c=30$ ,  $\Delta/c = -0.125$ . (a) Locations of spectral measurements relative to turbulence kinetic energy contours.





Numbers in legend represent the  $y/c$  and  $z/c$  locations respectively

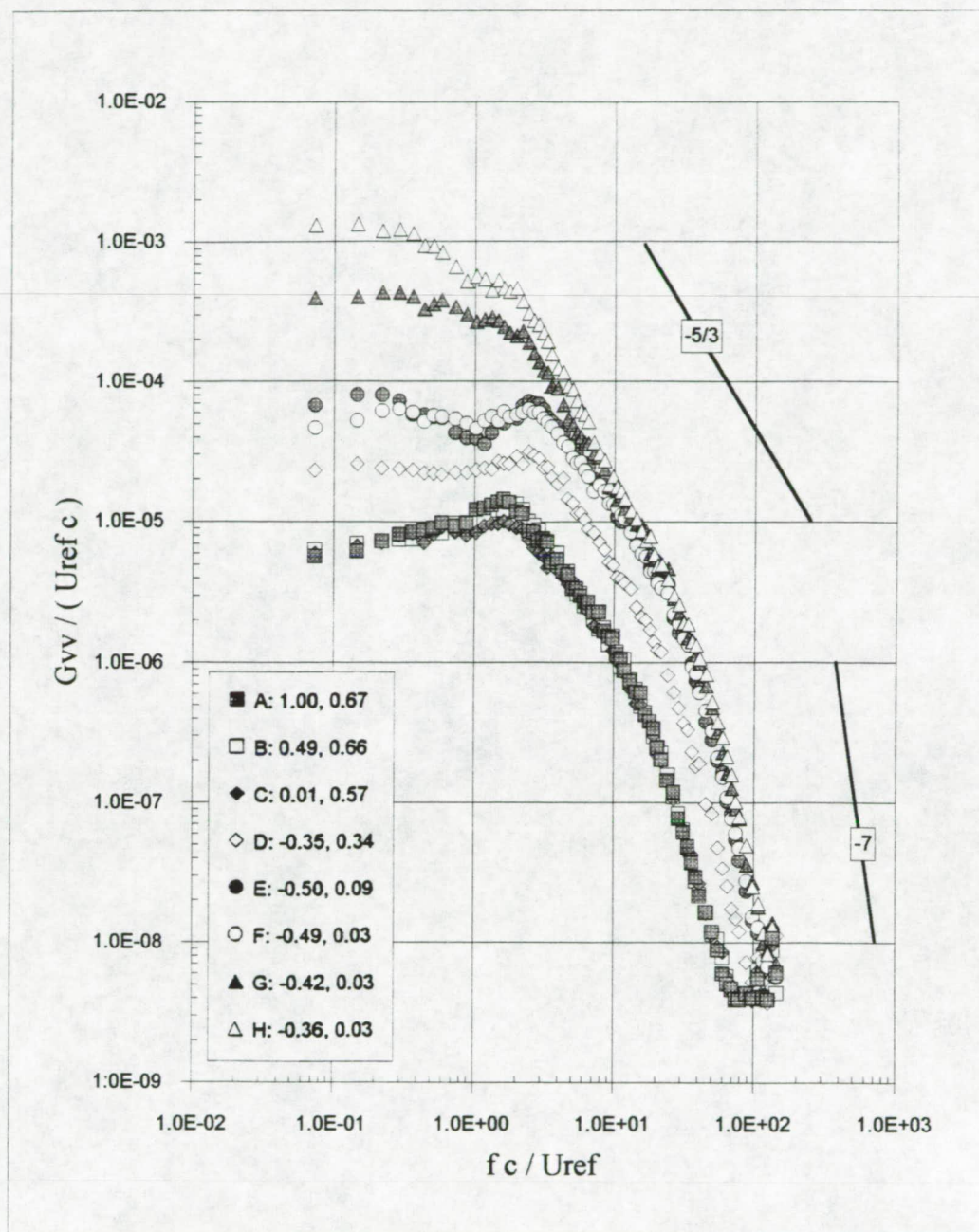
Figure 3.53 Velocity autospectra at  $X/c=30$ ,  $\Delta/c = -0.125$ . (b)  $G_{uu}$



Numbers in legend represent the  $y/c$  and  $z/c$  locations respectively

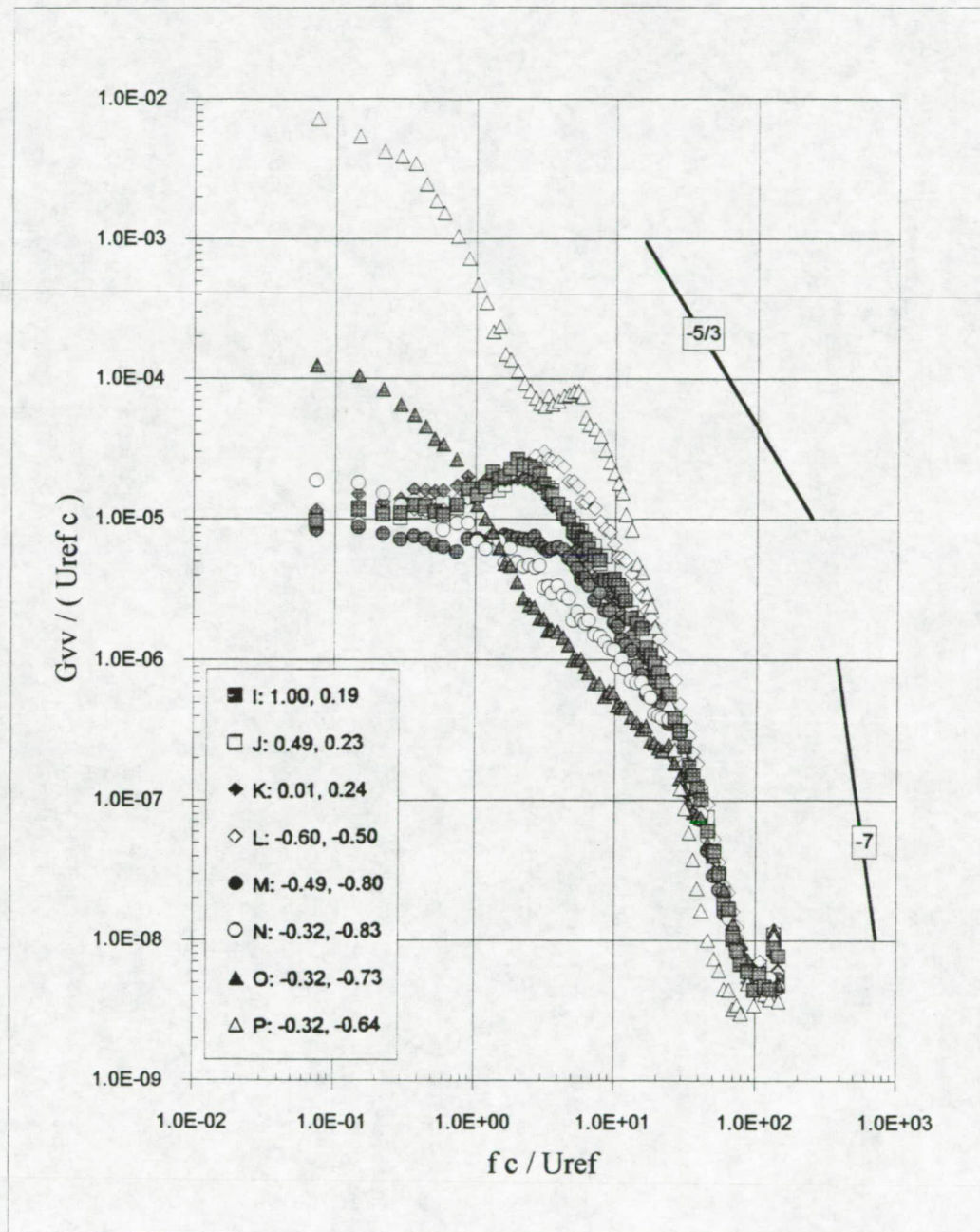
Figure 3.53 Velocity autospectra at  $X/c=30$ ,  $\Delta/c = -0.125$ . (c)  $G_{uu}$  contd.





Numbers in legend represent the  $y/c$  and  $z/c$  locations respectively

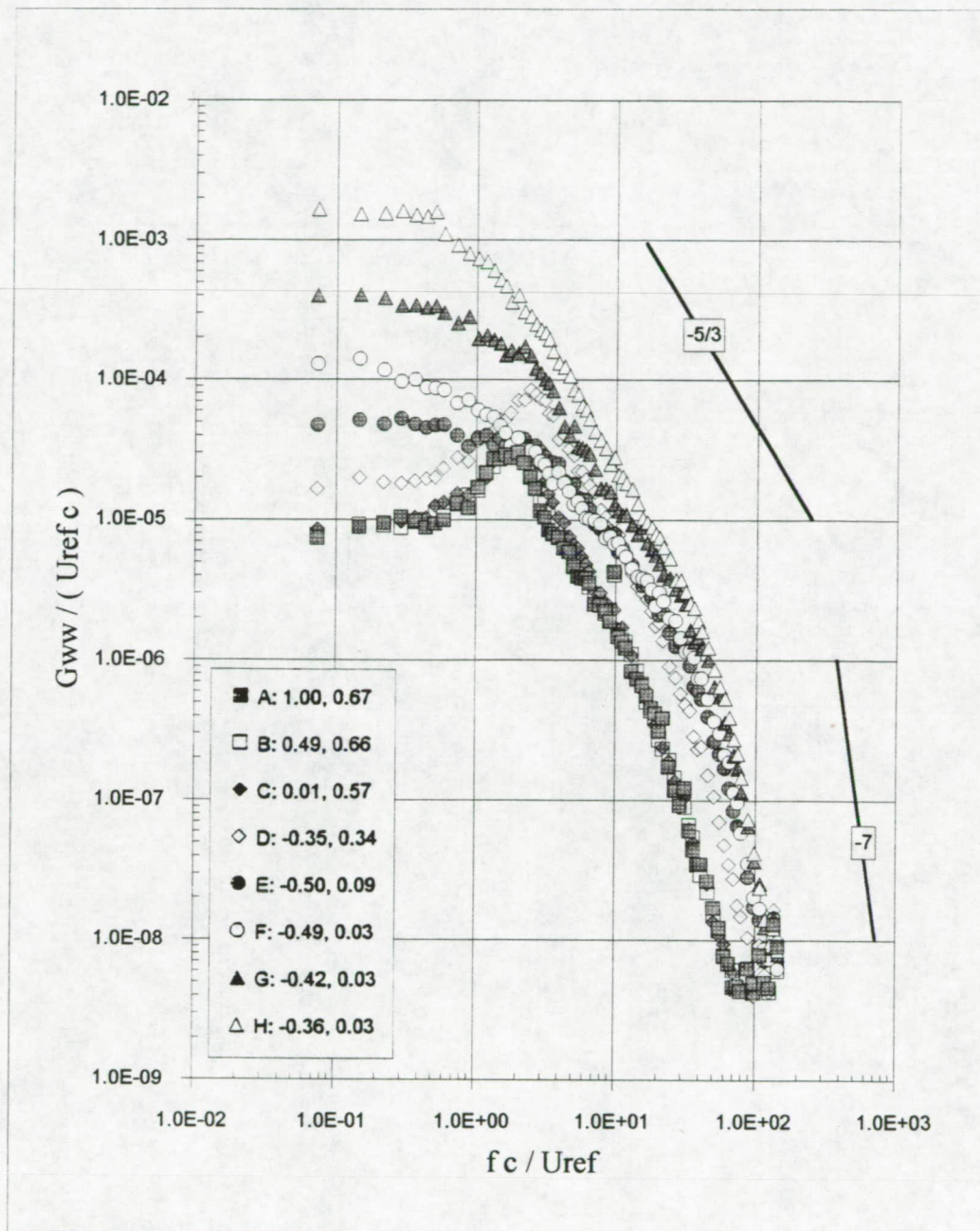
Figure 3.53 Velocity autospectra at  $X/c=30$ ,  $\Delta/c = -0.125$ . (d)  $G_{vv}$



Numbers in legend represent the  $y / c$  and  $z / c$  locations respectively

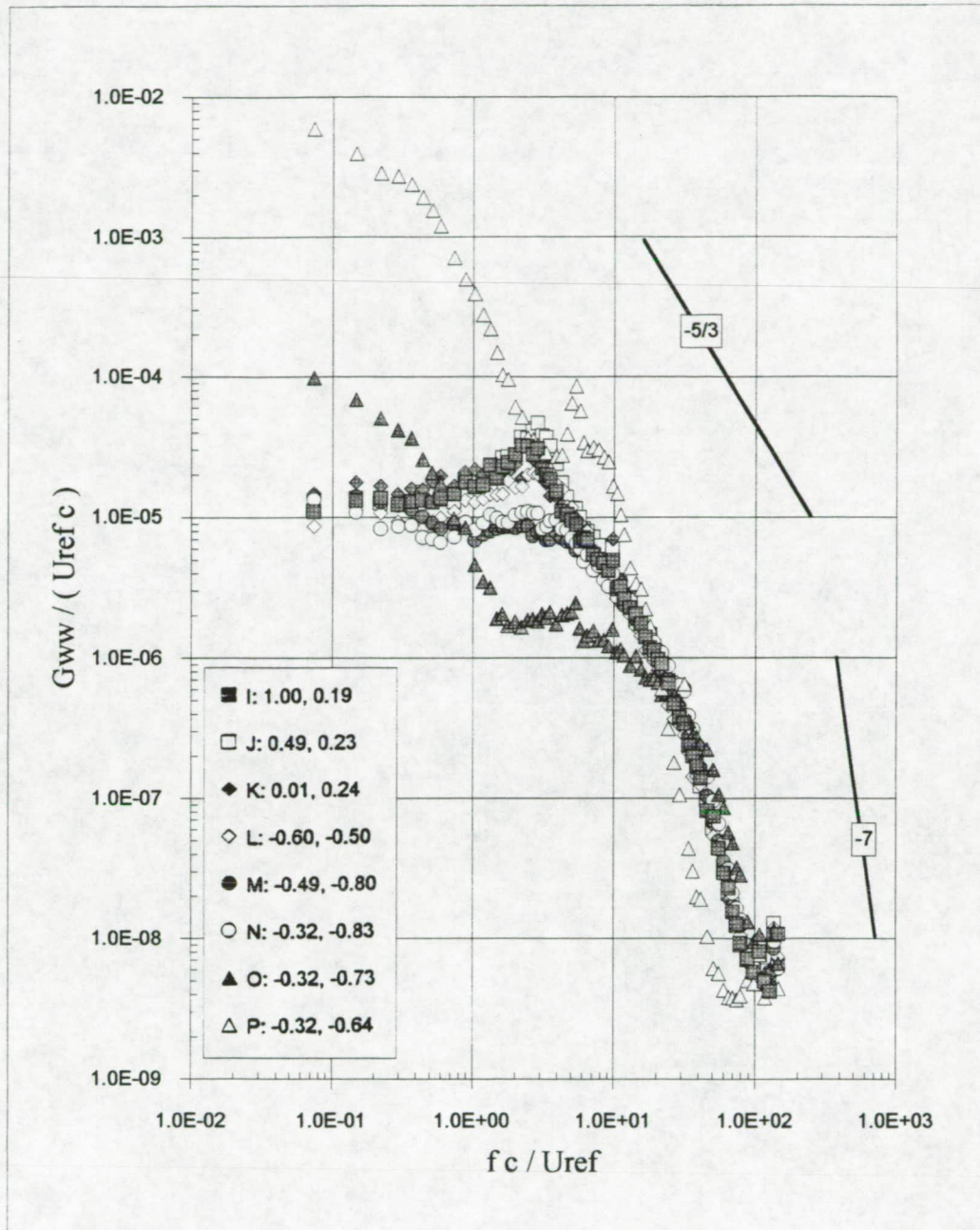
Figure 3.53 Velocity autospectra at  $X/c=30$ ,  $\Delta/c = -0.125$ . (e)  $G_{vv}$  contd.





Numbers in legend represent the  $y / c$  and  $z / c$  locations respectively

Figure 3.53 Velocity autospectra at  $X/c=30$ ,  $\Delta/c = -0.125$ . (f)  $G_{ww}$



Numbers in legend represent the  $y/c$  and  $z/c$  locations respectively

Figure 3.53 Velocity autospectra at  $X/c=30$ ,  $\Delta/c = -0.125$ . (g)  $G_{ww}$  contd.



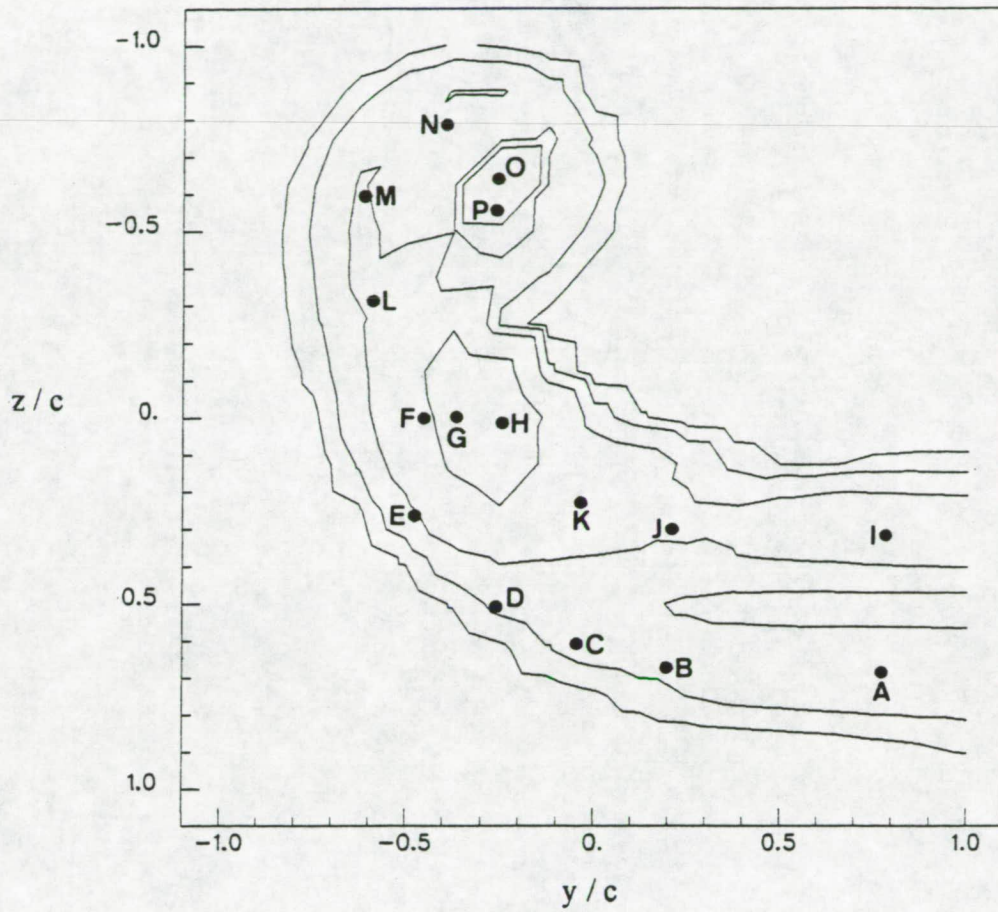
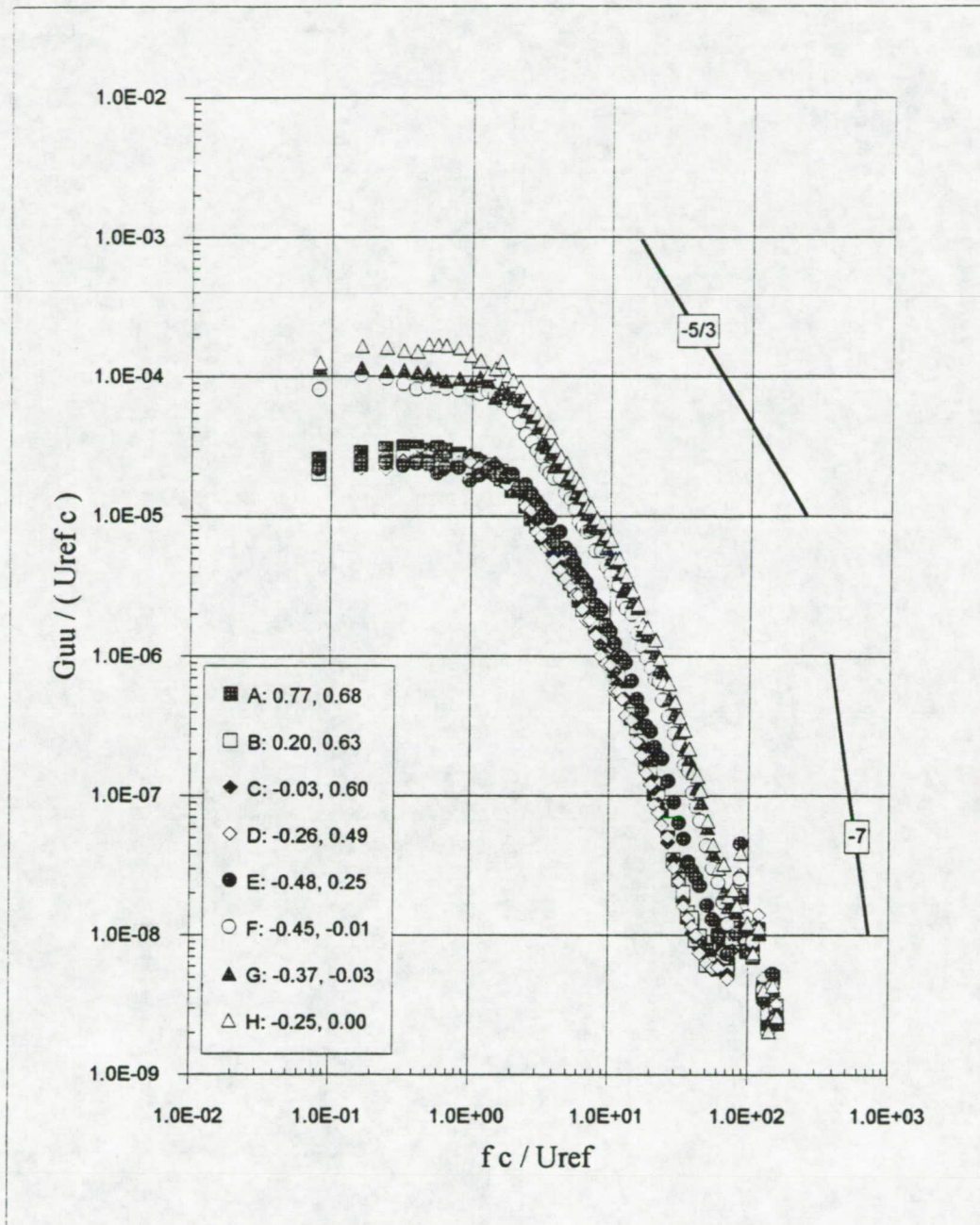


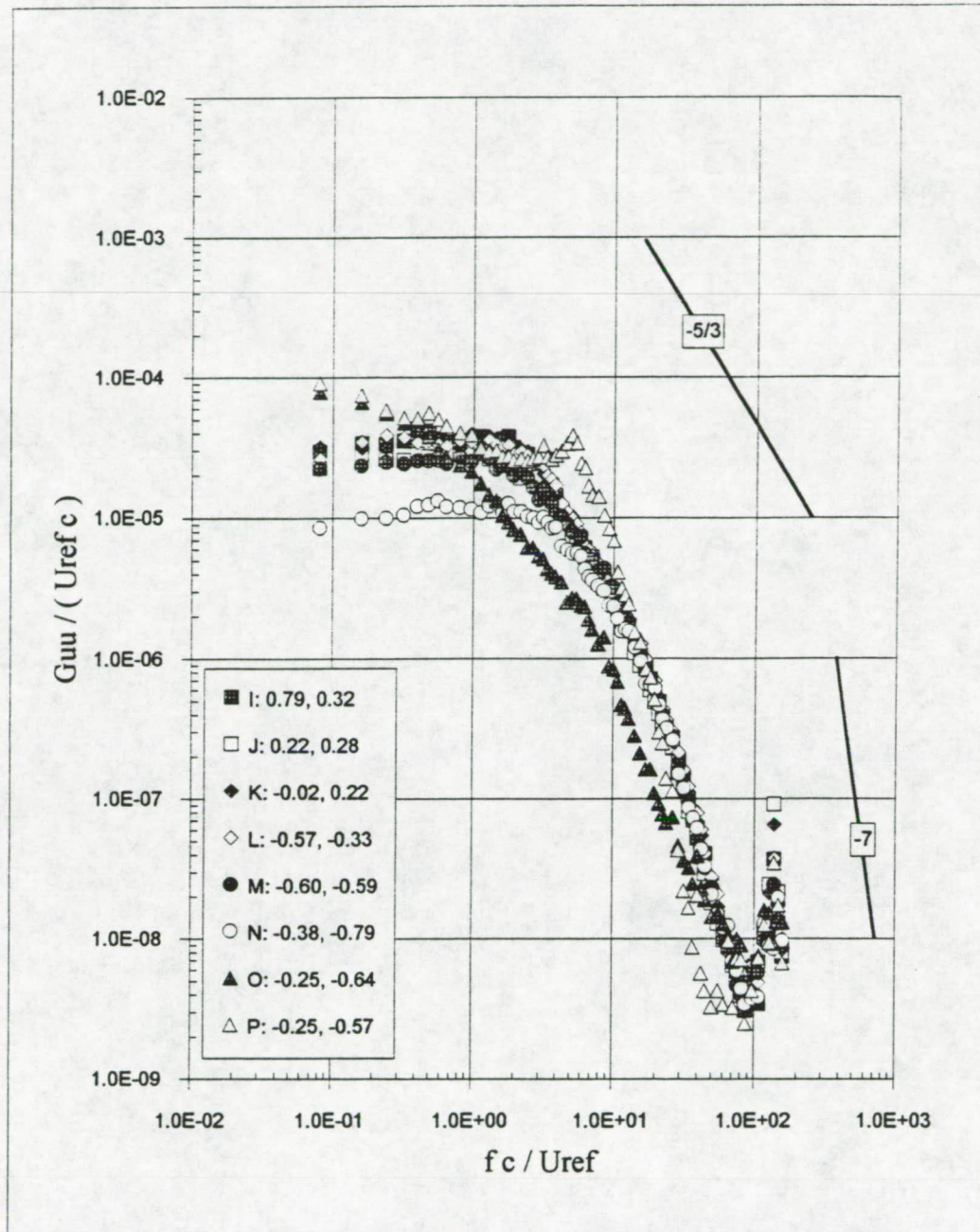
Figure 3.54 Velocity autospectra,  $X/c=30$ ,  $\Delta/c = -0.0625$ . (a) Locations of spectral measurements relative to turbulence kinetic energy contours.



Numbers in legend represent the  $y / c$  and  $z / c$  locations respectively

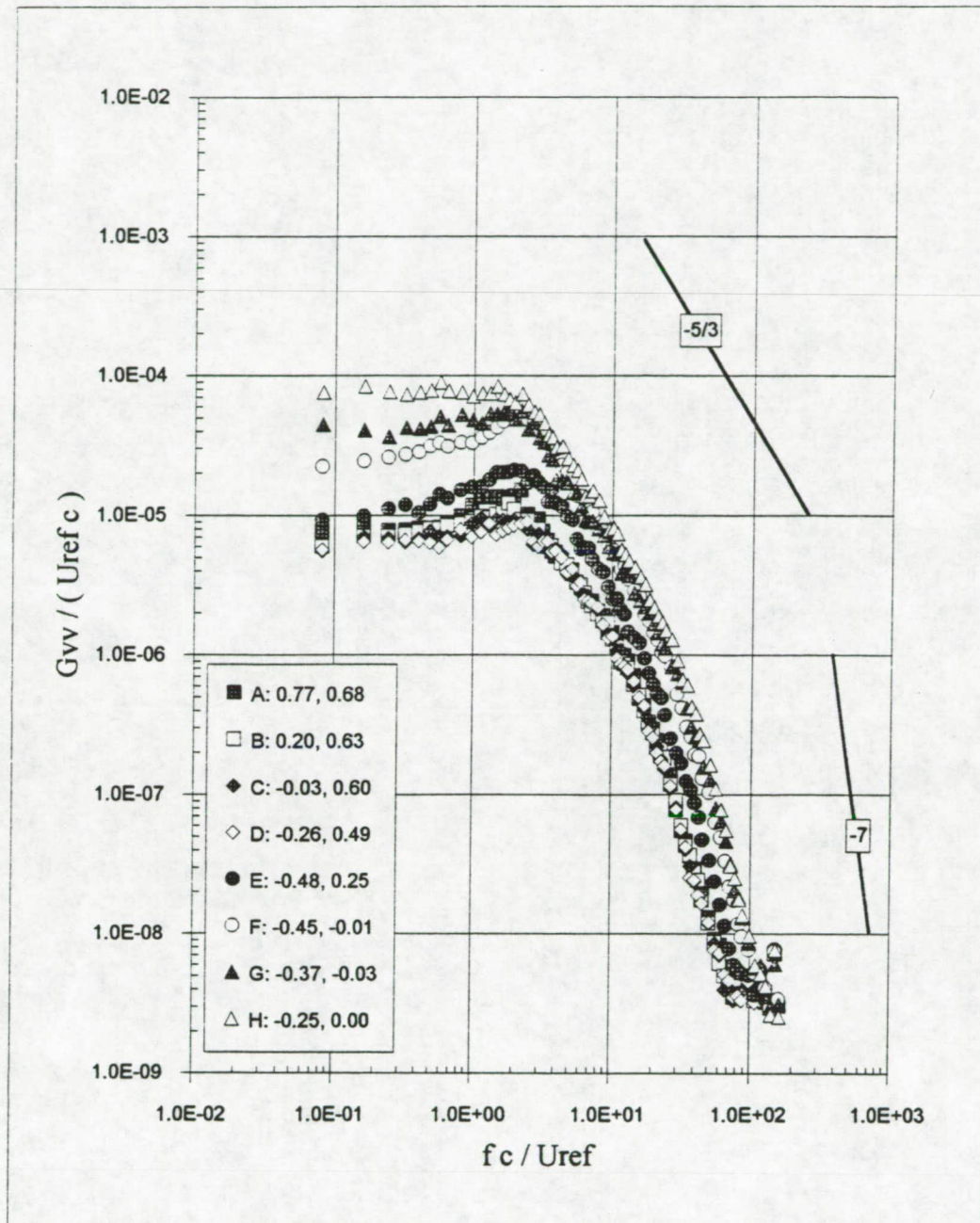
Figure 3.54 Velocity autospectra at  $X/c=30$ ,  $\Delta/c = -0.0625$ . (b)  $G_{uu}$





Numbers in legend represent the  $y/c$  and  $z/c$  locations respectively

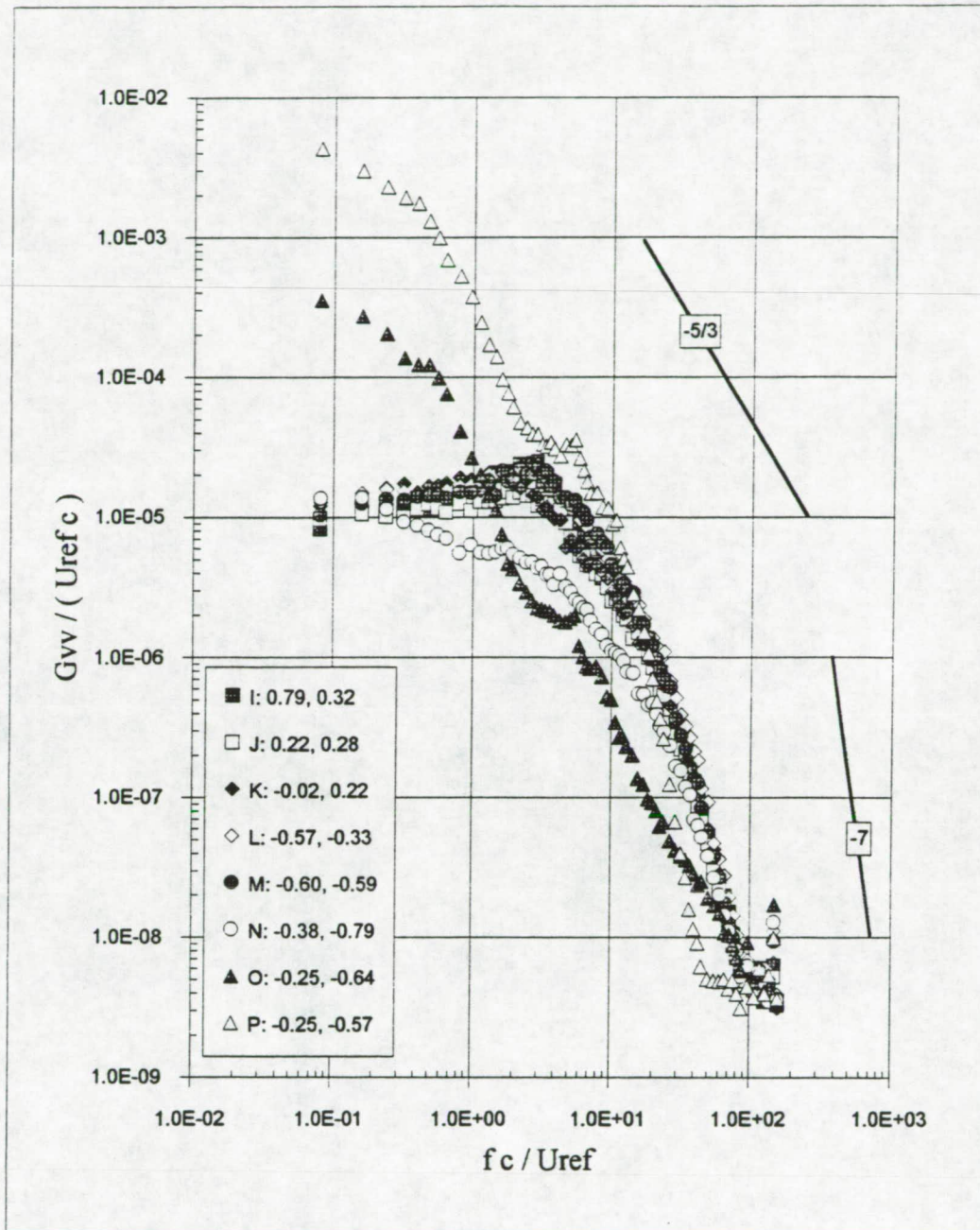
Figure 3.54 Velocity autospectra at  $X/c=30$ ,  $\Delta/c = -0.0625$ . (c)  $G_{uu}$  contd.



Numbers in legend represent the  $y/c$  and  $z/c$  locations respectively

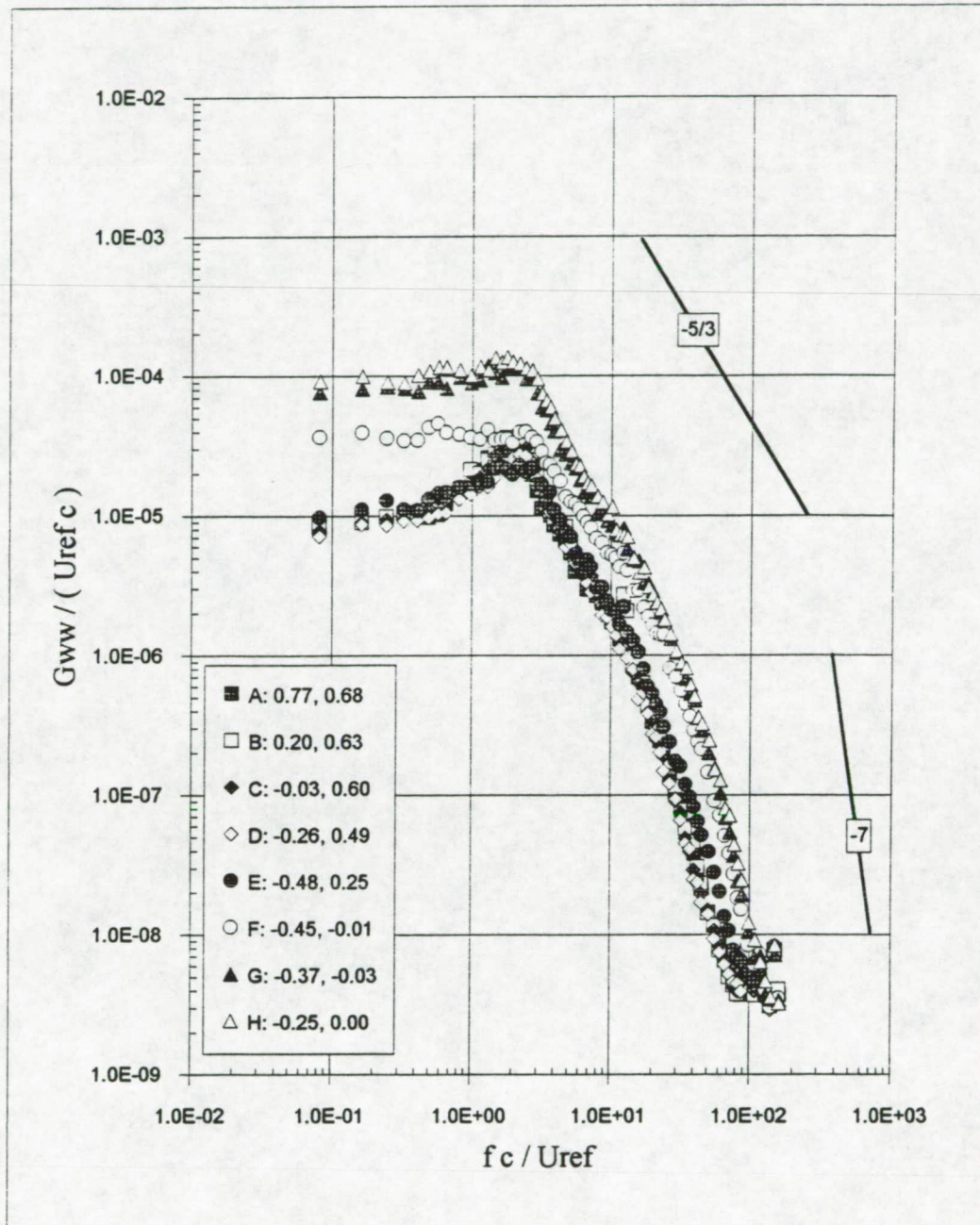
Figure 3.54 Velocity autospectra at  $X/c=30$ ,  $\Delta/c = -0.0625$ . (d)  $G_{vv}$





Numbers in legend represent the  $y / c$  and  $z / c$  locations respectively

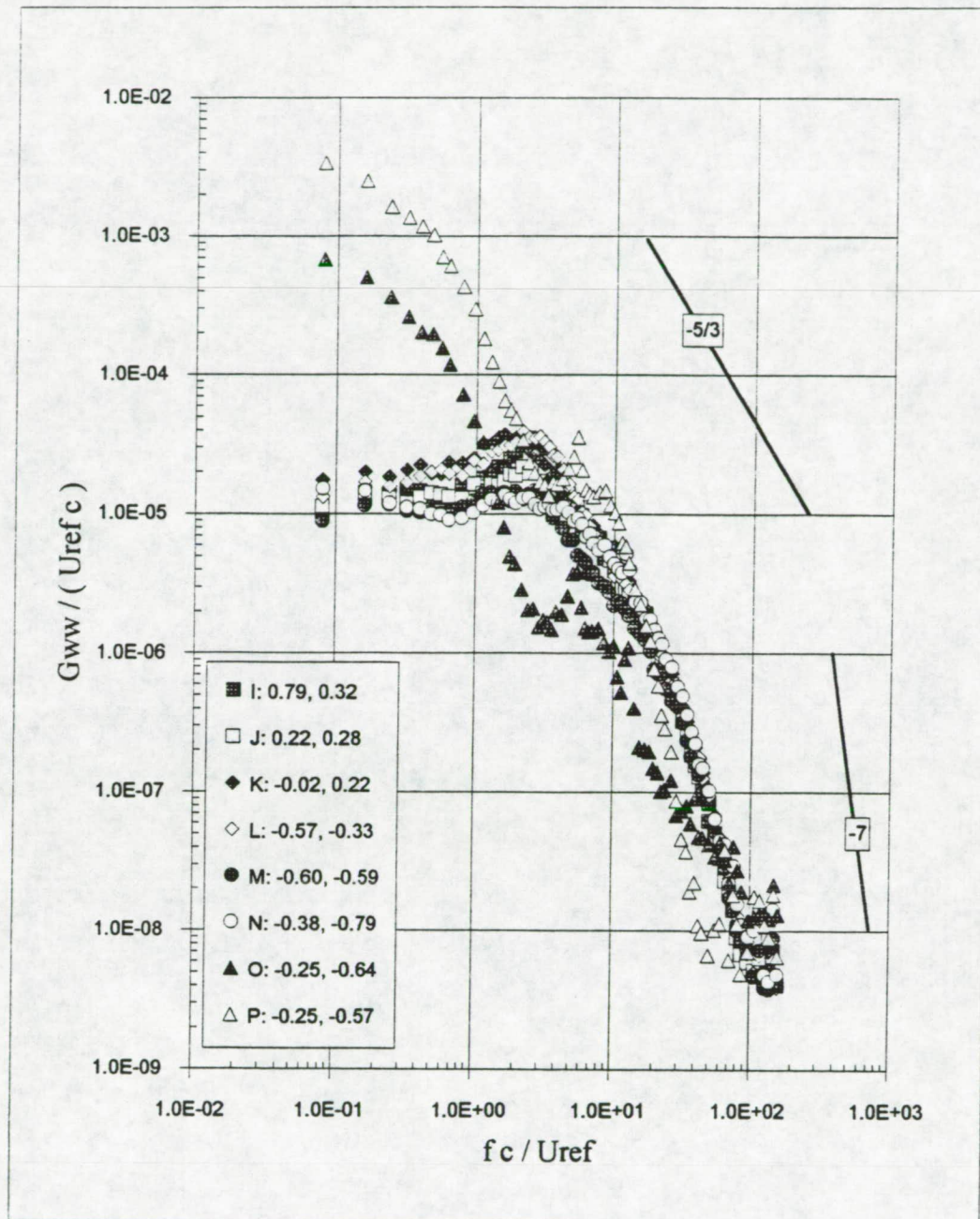
Figure 3.54 Velocity autospectra at  $X/c=30$ ,  $\Delta/c = -0.0625$ . (e)  $G_{vv}$  contd.



Numbers in legend represent the  $y/c$  and  $z/c$  locations respectively

Figure 3.54 Velocity autospectra at  $X/c=30$ ,  $\Delta/c = -0.0625$ . (f)  $G_{ww}$





Numbers in legend represent the  $y/c$  and  $z/c$  locations respectively

Figure 3.54 Velocity autospectra at  $X/c=30$ ,  $\Delta/c = -0.0625$ . (g)  $G_{ww}$  contd.

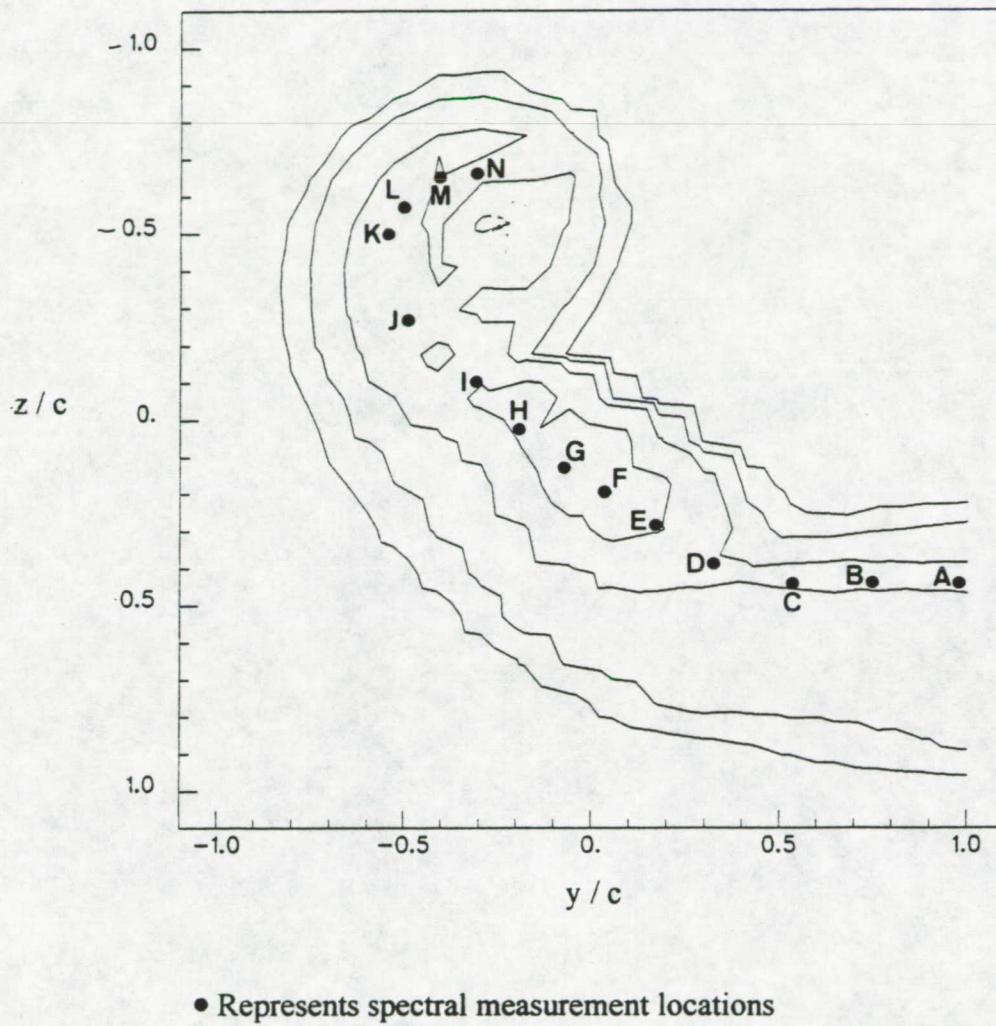
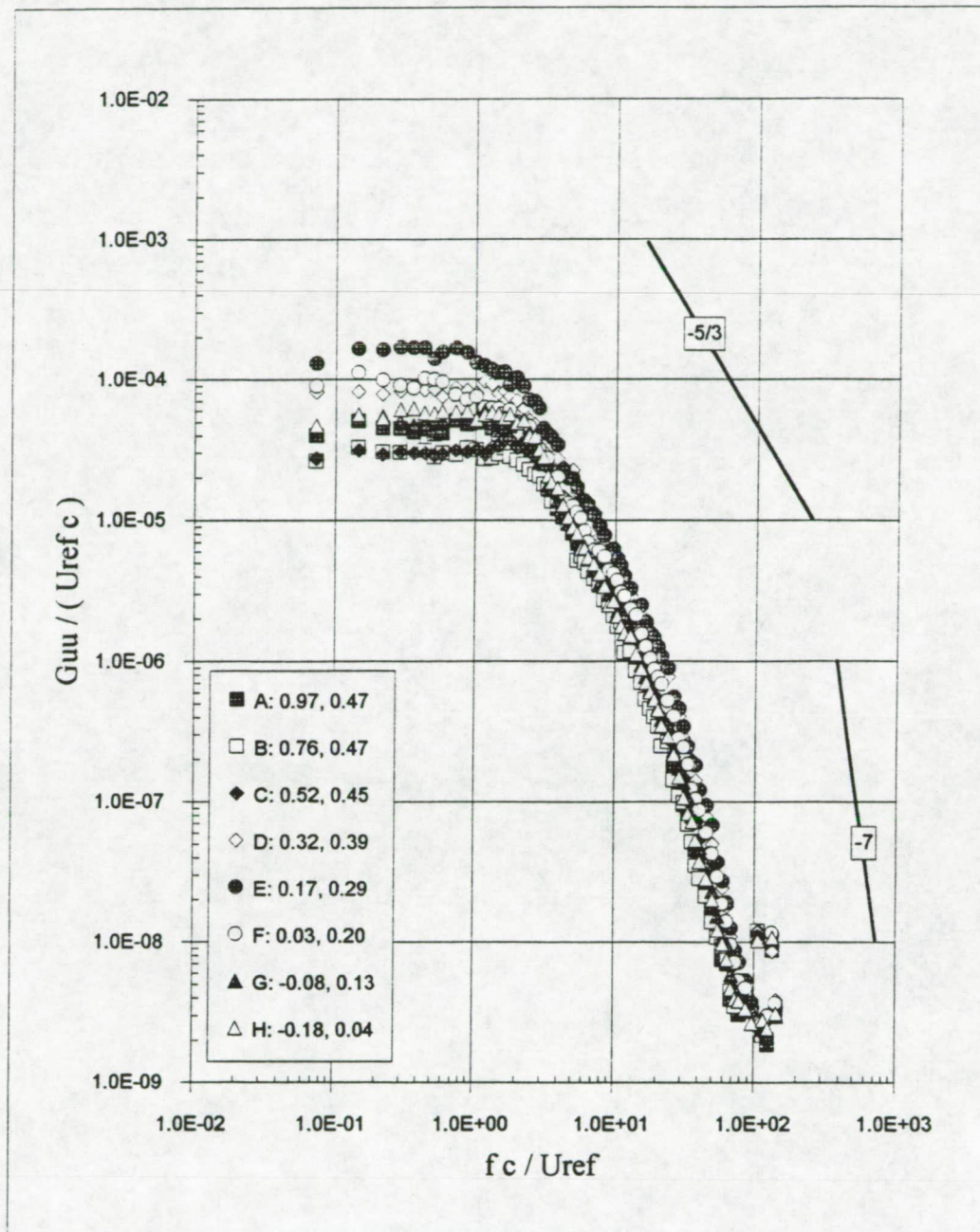


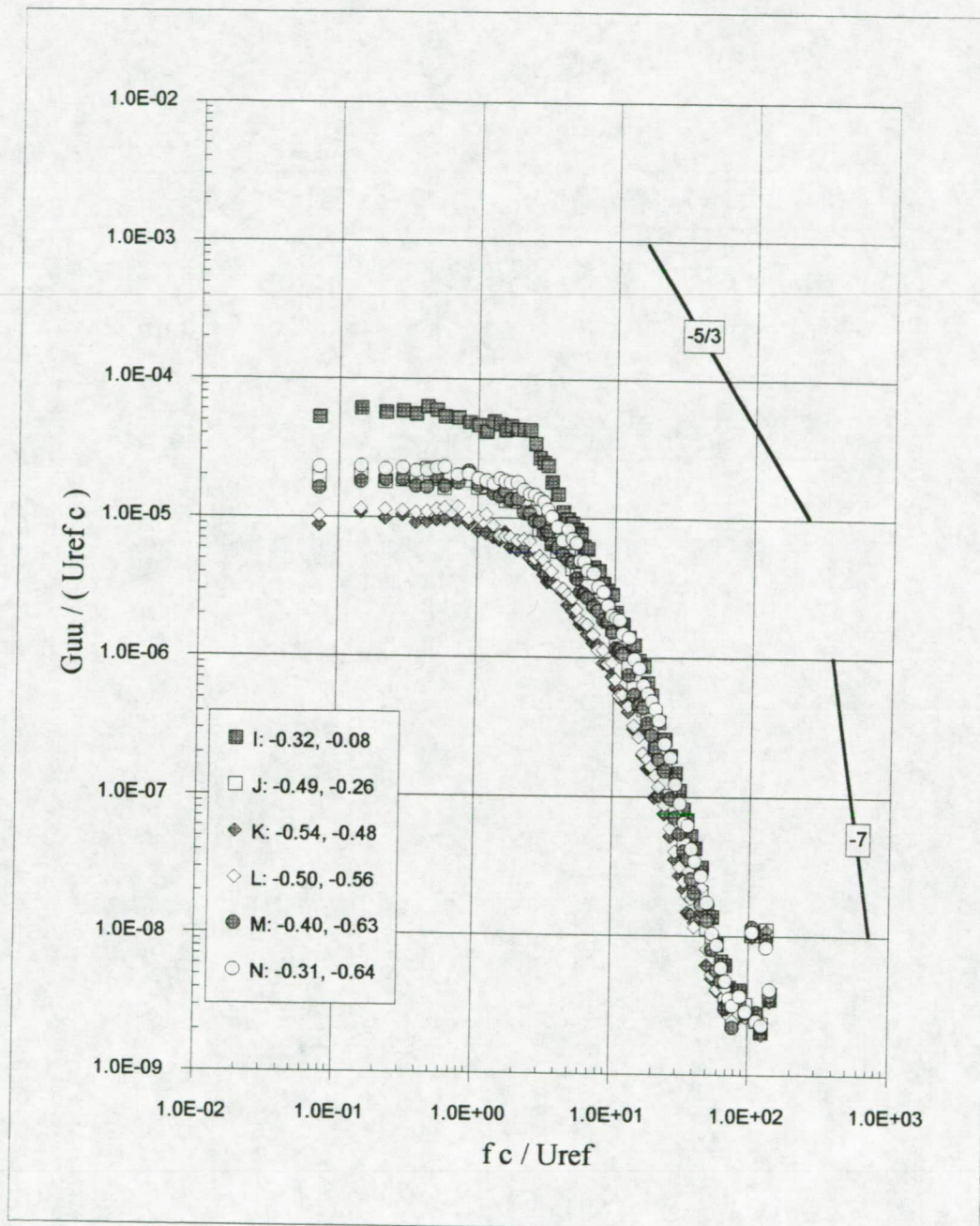
Figure 3.55 Velocity autospectra,  $X/c=30$ ,  $\Delta/c = 0$ . (a) Locations of spectral measurements relative to turbulence kinetic energy contours.





Numbers in legend represent the  $y / c$  and  $z / c$  locations respectively

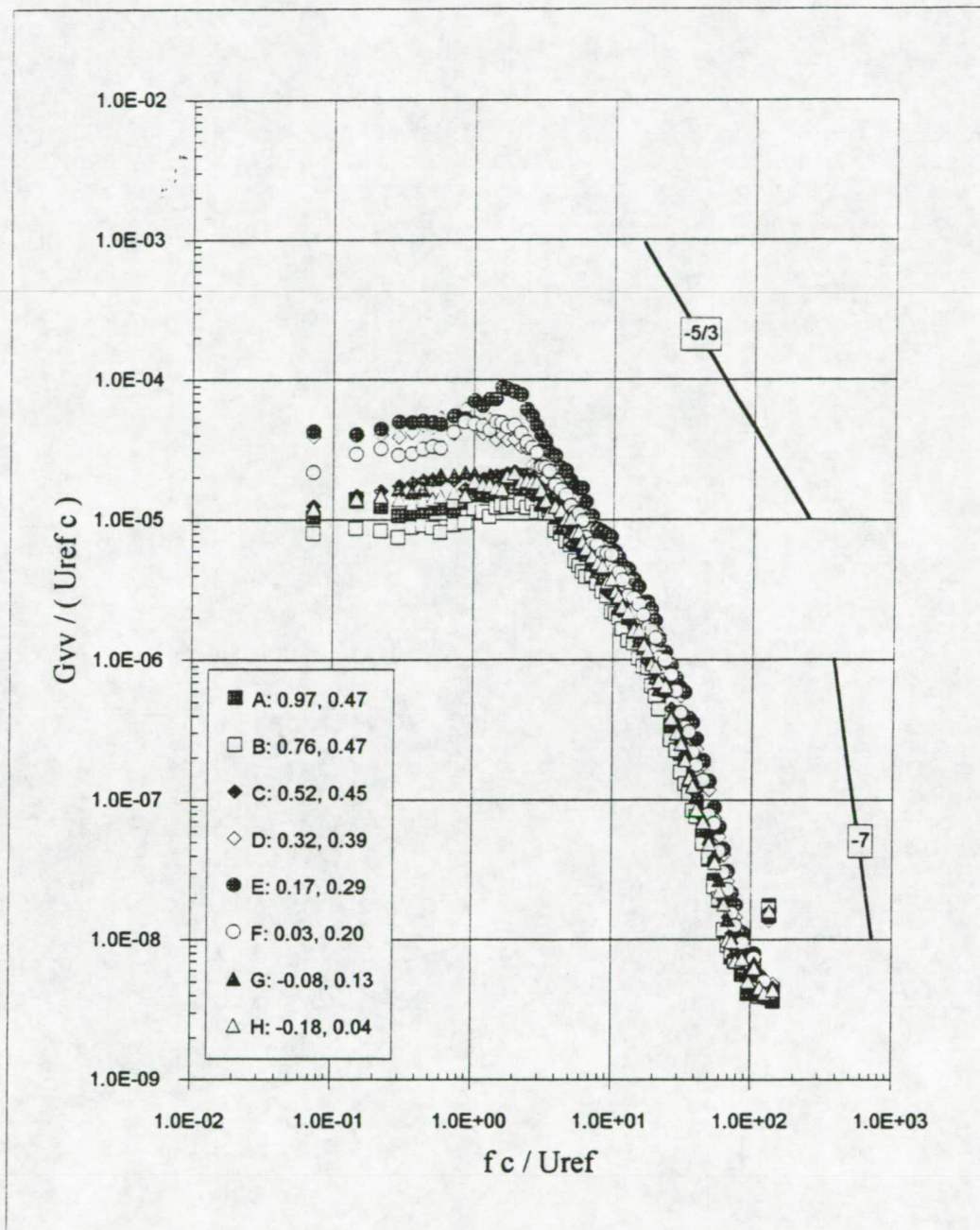
Figure 3.55 Velocity autospectra at  $X/c=30$ ,  $\Delta/c = 0$ . (b)  $G_{uu}$



Numbers in legend represent the  $y / c$  and  $z / c$  locations respectively

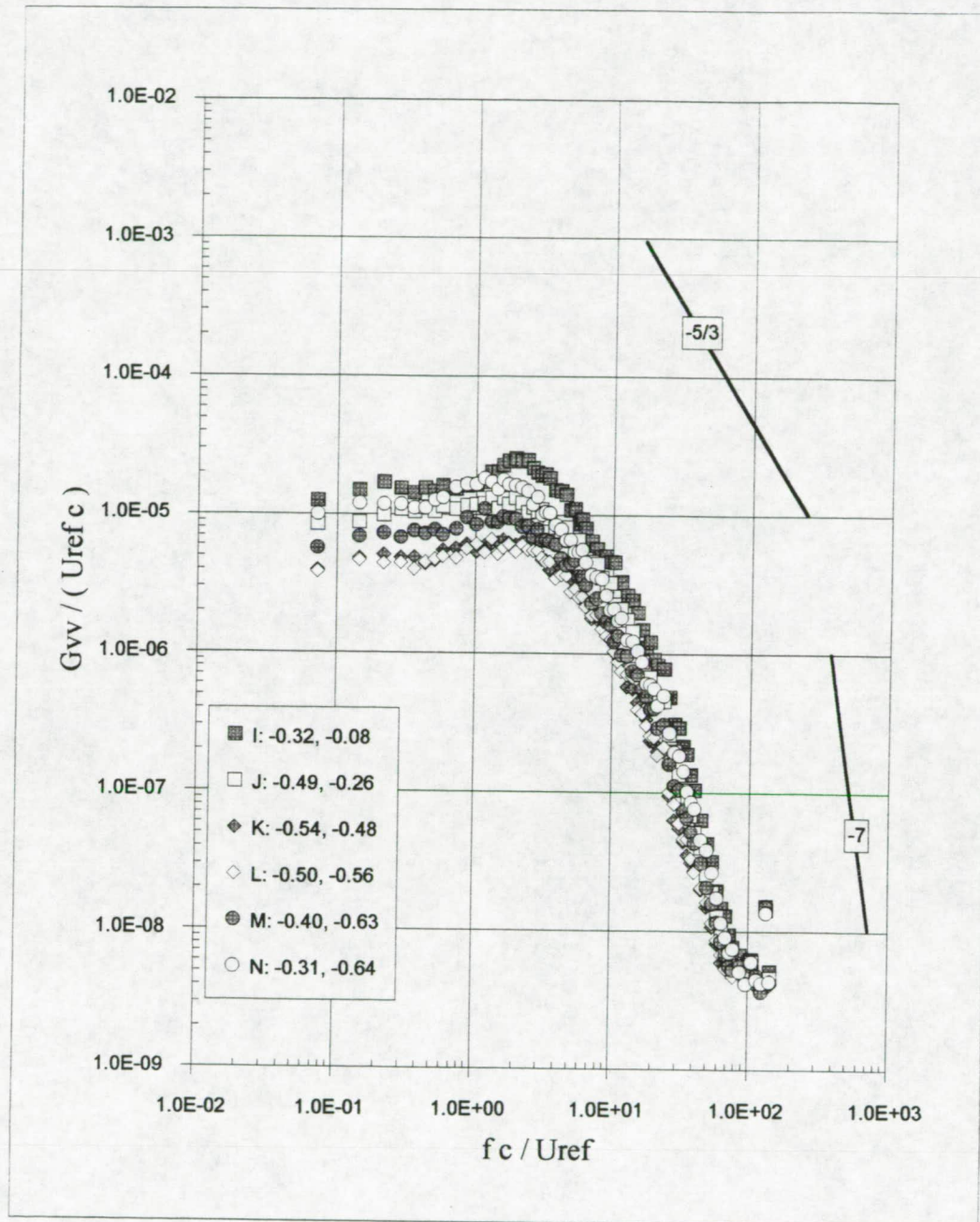
Figure 3.55 Velocity autospectra at  $X/c=30$ ,  $\Delta/c = 0$ . (c)  $G_{uu}$  contd.





Numbers in legend represent the  $y/c$  and  $z/c$  locations respectively

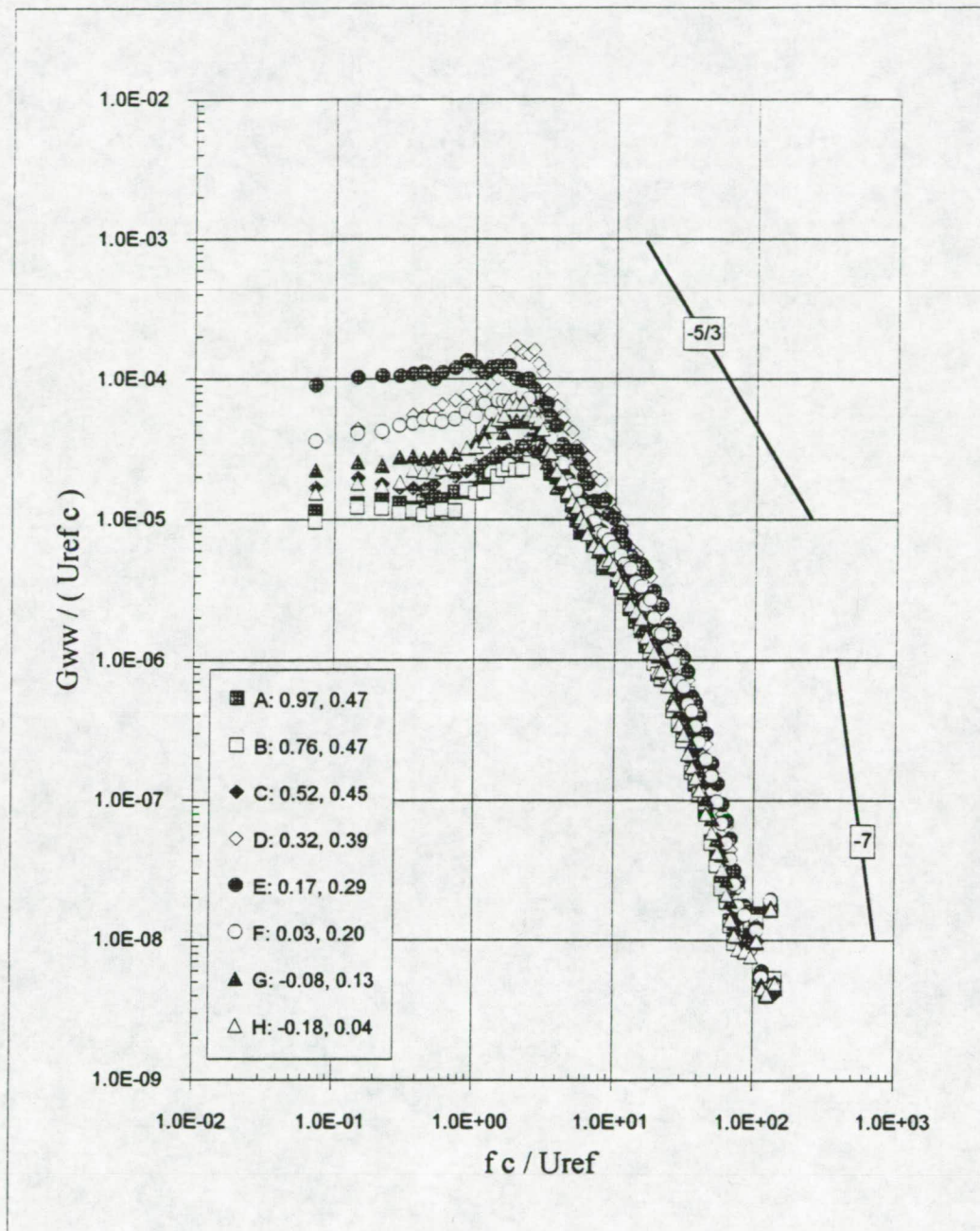
Figure 3.55 Velocity autospectra at  $X/c=30$ ,  $\Delta/c = 0$ . (d)  $G_{vv}$



Numbers in legend represent the  $y/c$  and  $z/c$  locations respectively

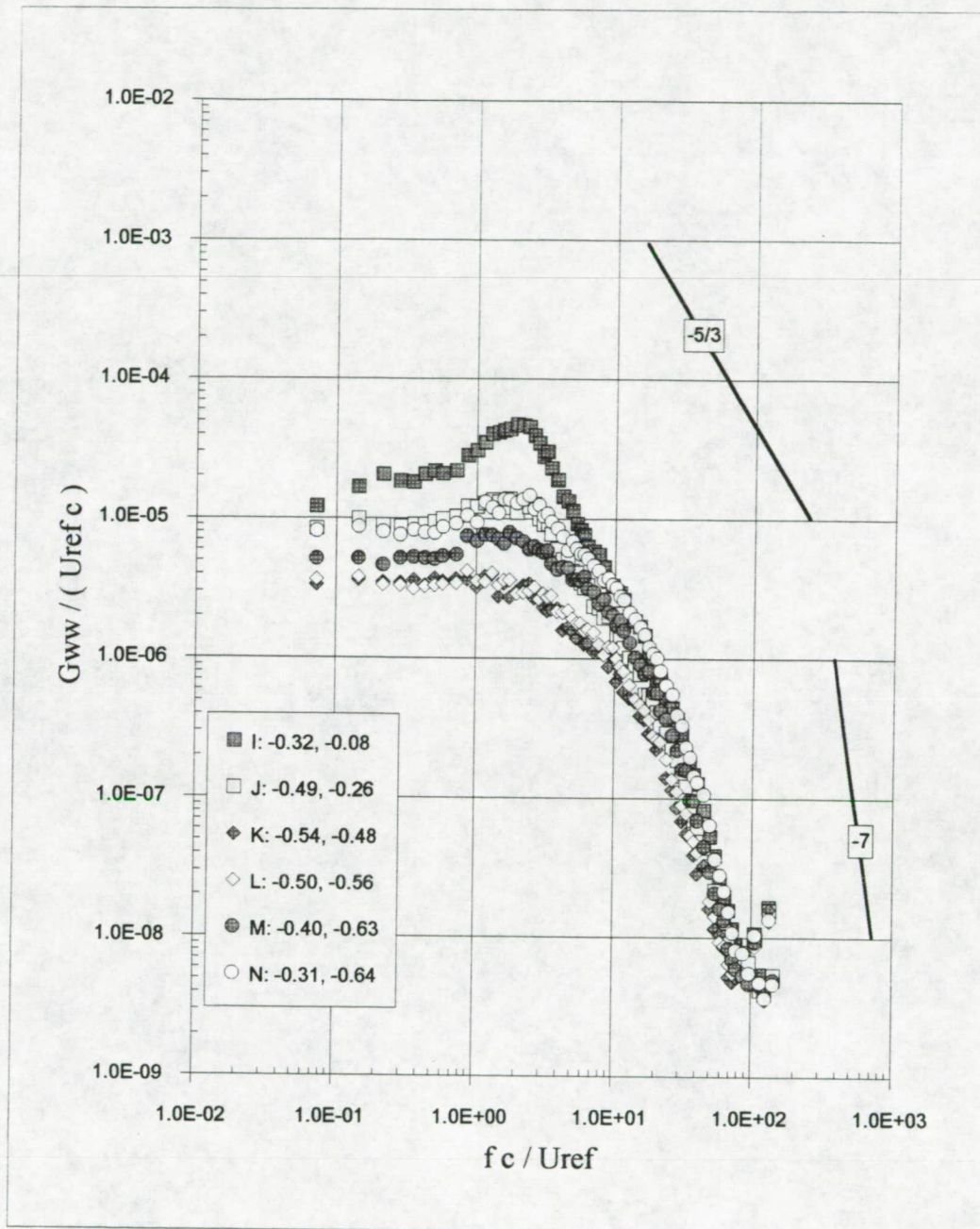
Figure 3.55 Velocity autospectra at  $X/c=30$ ,  $\Delta/c = 0$ . (e)  $G_{vv}$  contd.





Numbers in legend represent the  $y / c$  and  $z / c$  locations respectively

Figure 3.55 Velocity autospectra at  $X/c=30$ ,  $\Delta/c = 0$ . (f)  $G_{ww}$



Numbers in legend represent the  $y / c$  and  $z / c$  locations respectively

Figure 3.55 Velocity autospectra at  $X/c=30$ ,  $\Delta/c = 0$ . (g)  $G_{ww}$  contd.



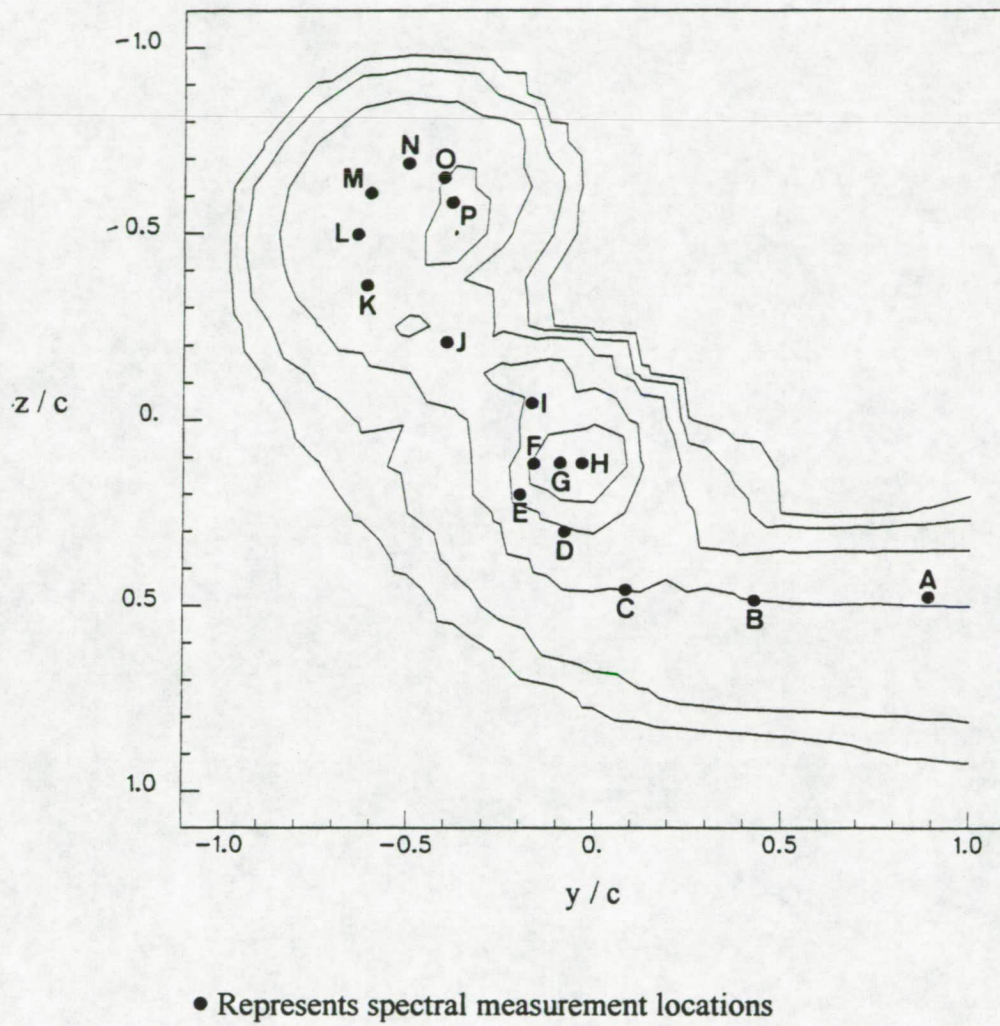
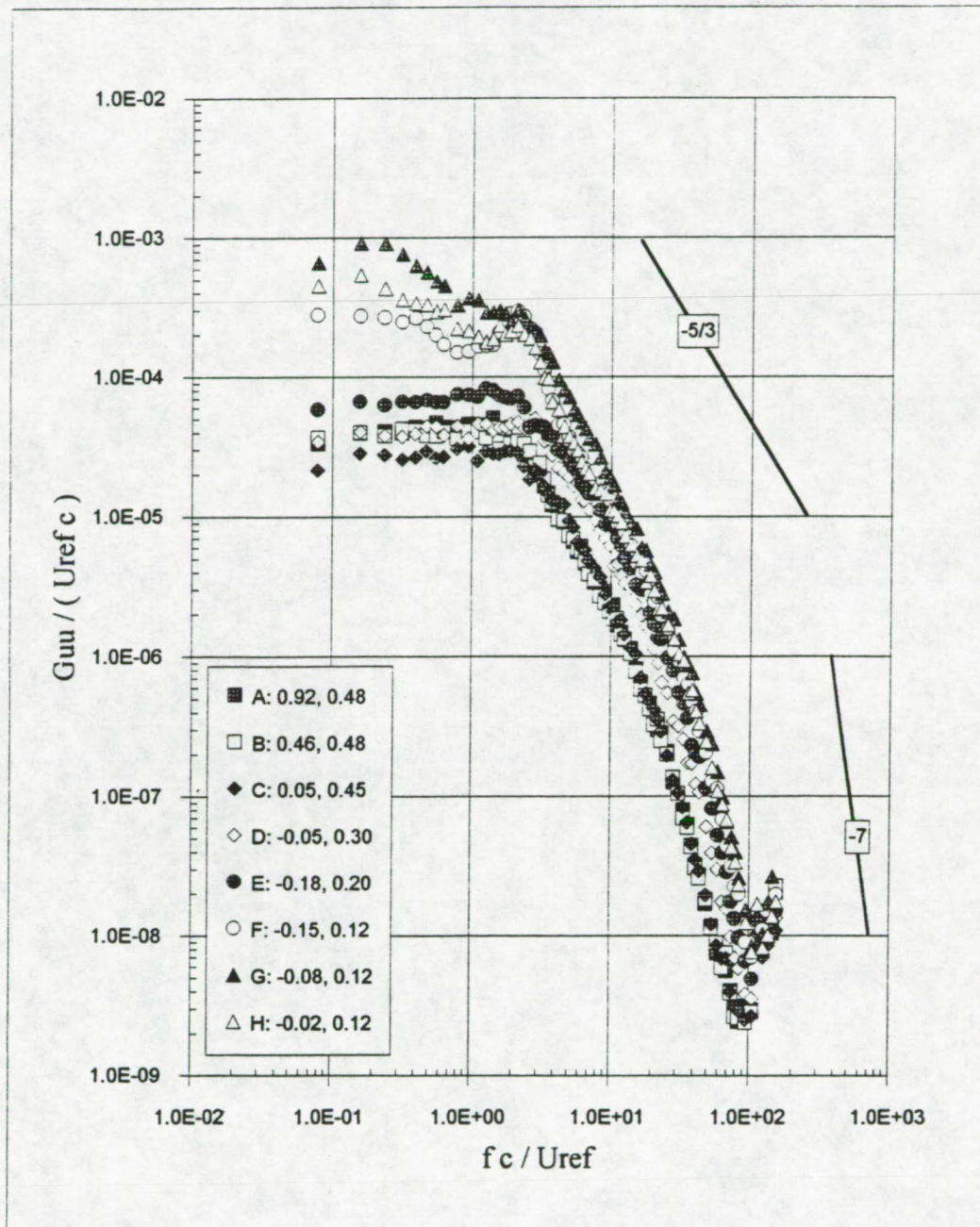


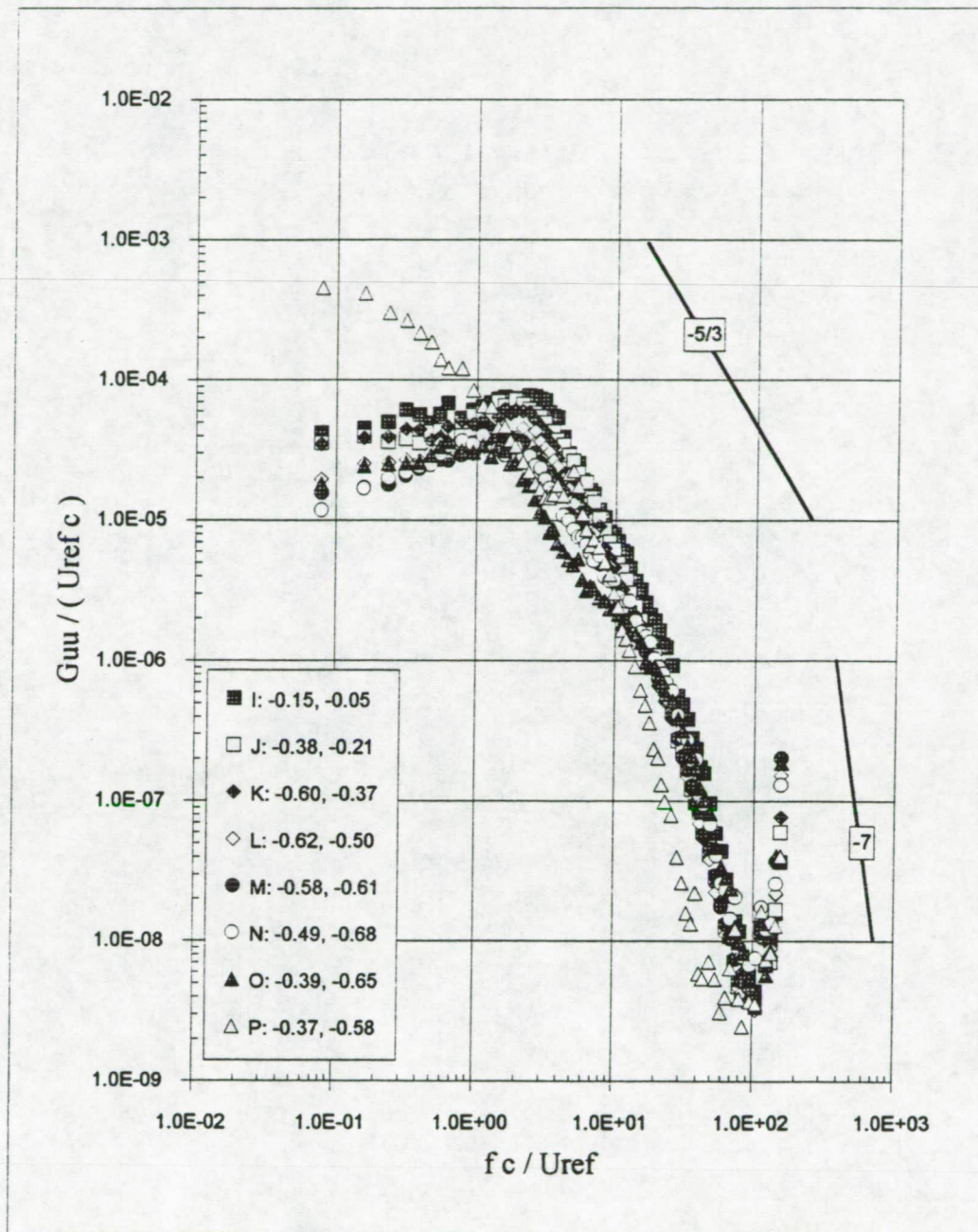
Figure 3.56 Velocity autospectra,  $X/c=30$ ,  $\Delta/c = 0.0625$ . (a) Locations of spectral measurements relative to turbulence kinetic energy contours.



Numbers in legend represent the  $y/c$  and  $z/c$  locations respectively

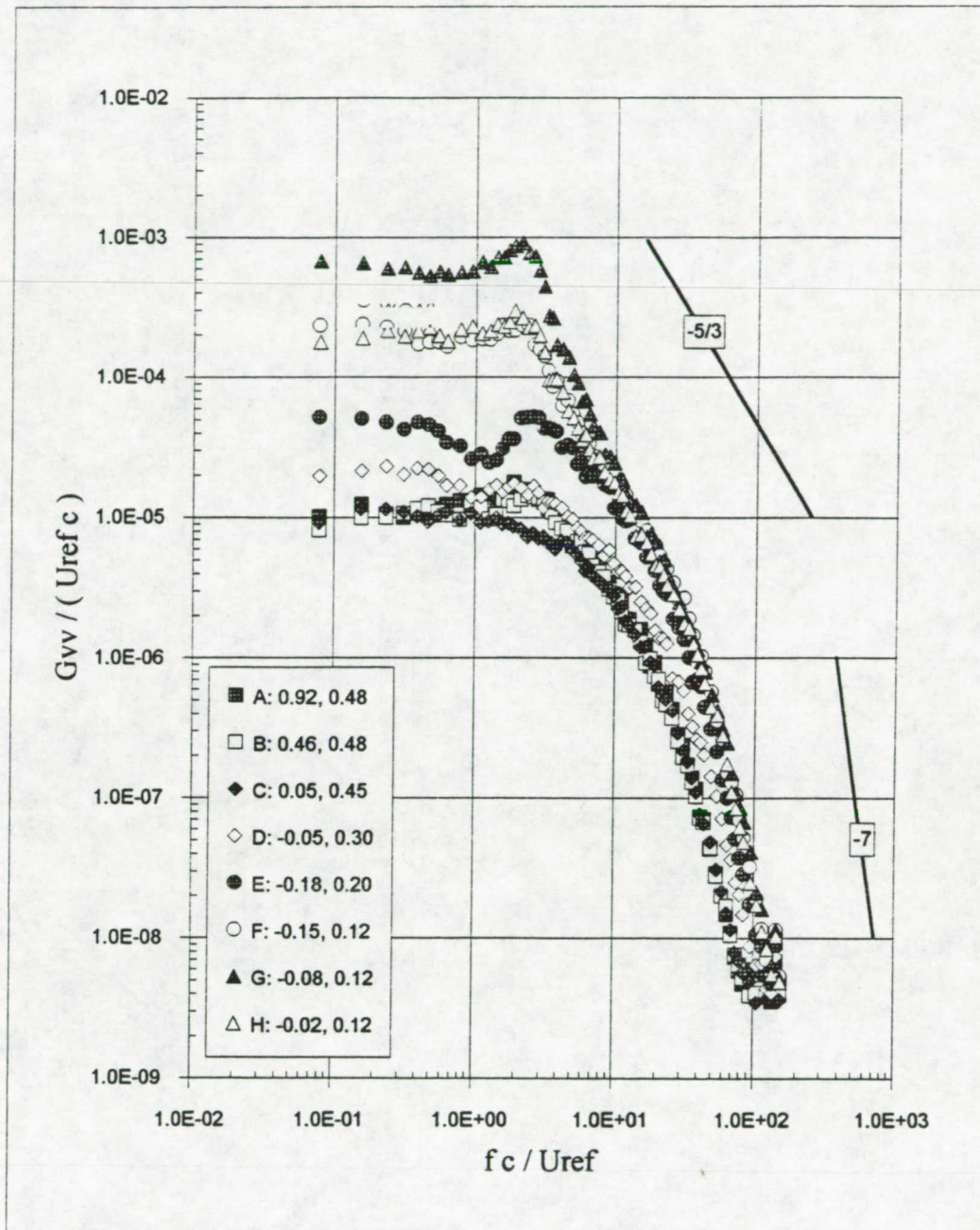
Figure 3.56 Velocity autospectra at  $X/c=30$ ,  $\Delta/c = 0.0625$ . (b)  $G_{uu}$





Numbers in legend represent the  $y/c$  and  $z/c$  locations respectively

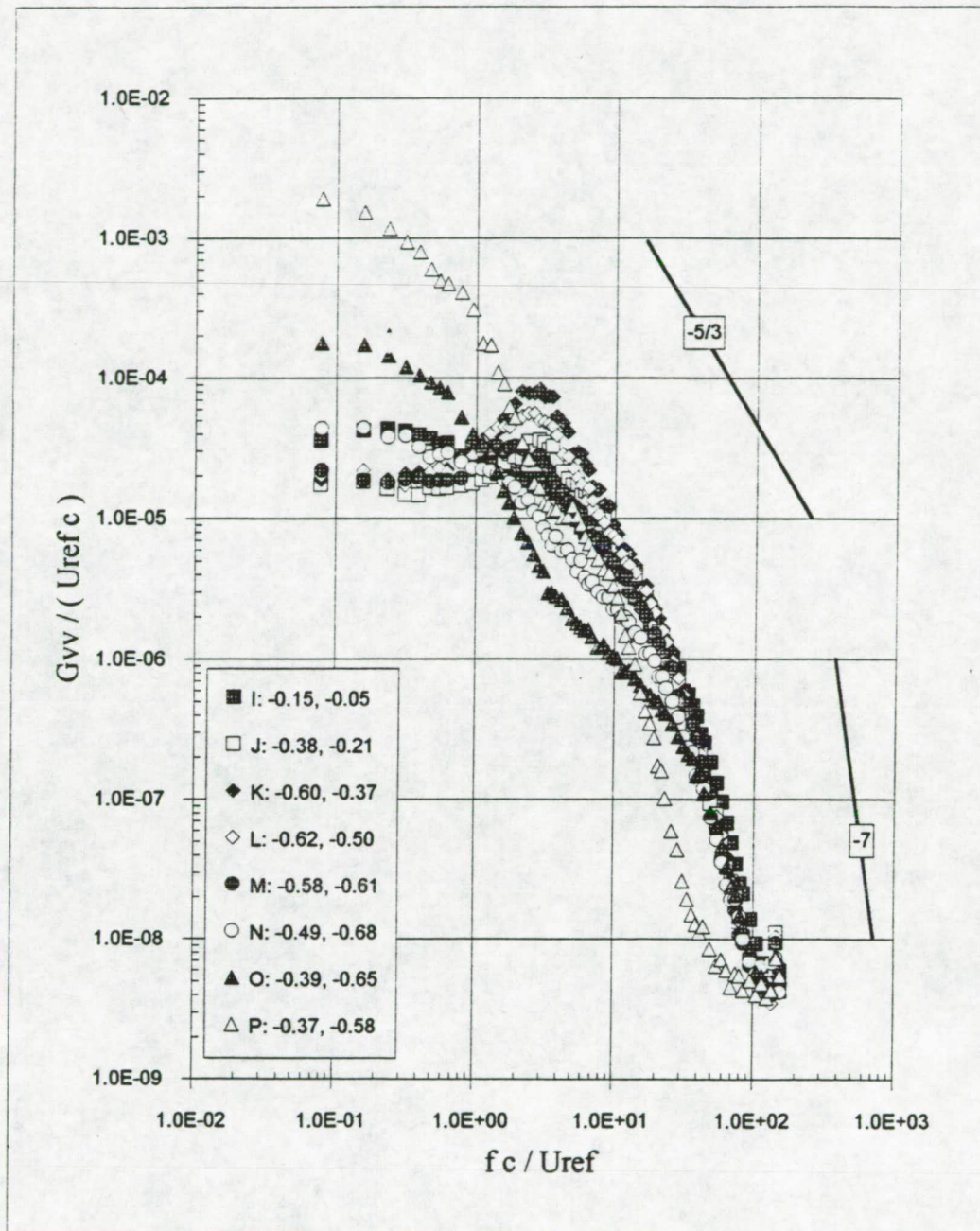
Figure 3.56 Velocity autospectra at  $X/c=30$ ,  $\Delta/c = 0.0625$ . (c)  $G_{uu}$  contd.



Numbers in legend represent the  $y/c$  and  $z/c$  locations respectively

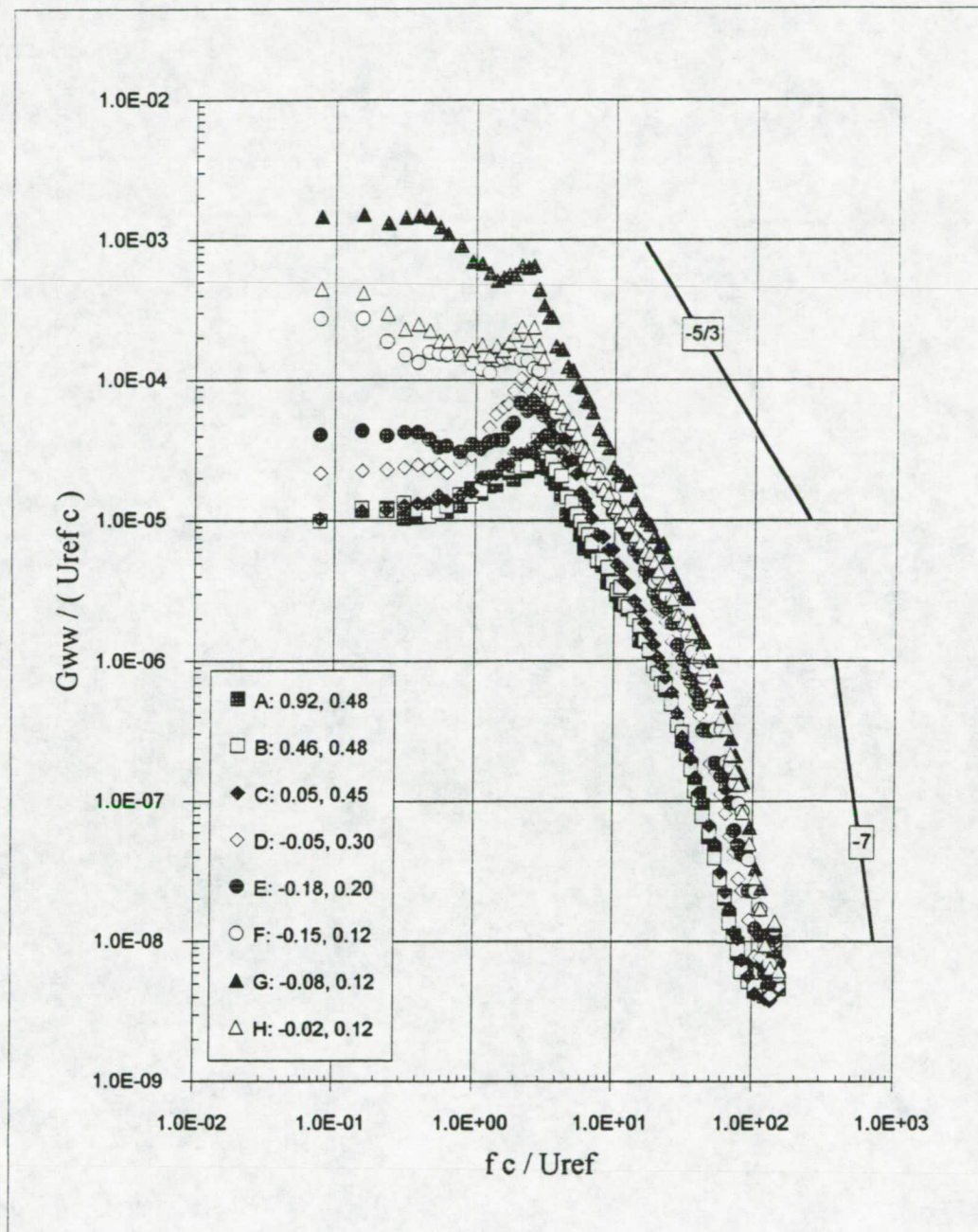
Figure 3.56 Velocity autospectra at  $X/c=30$ ,  $\Delta/c = 0.0625$ . (d)  $G_{vv}$





Numbers in legend represent the  $y / c$  and  $z / c$  locations respectively

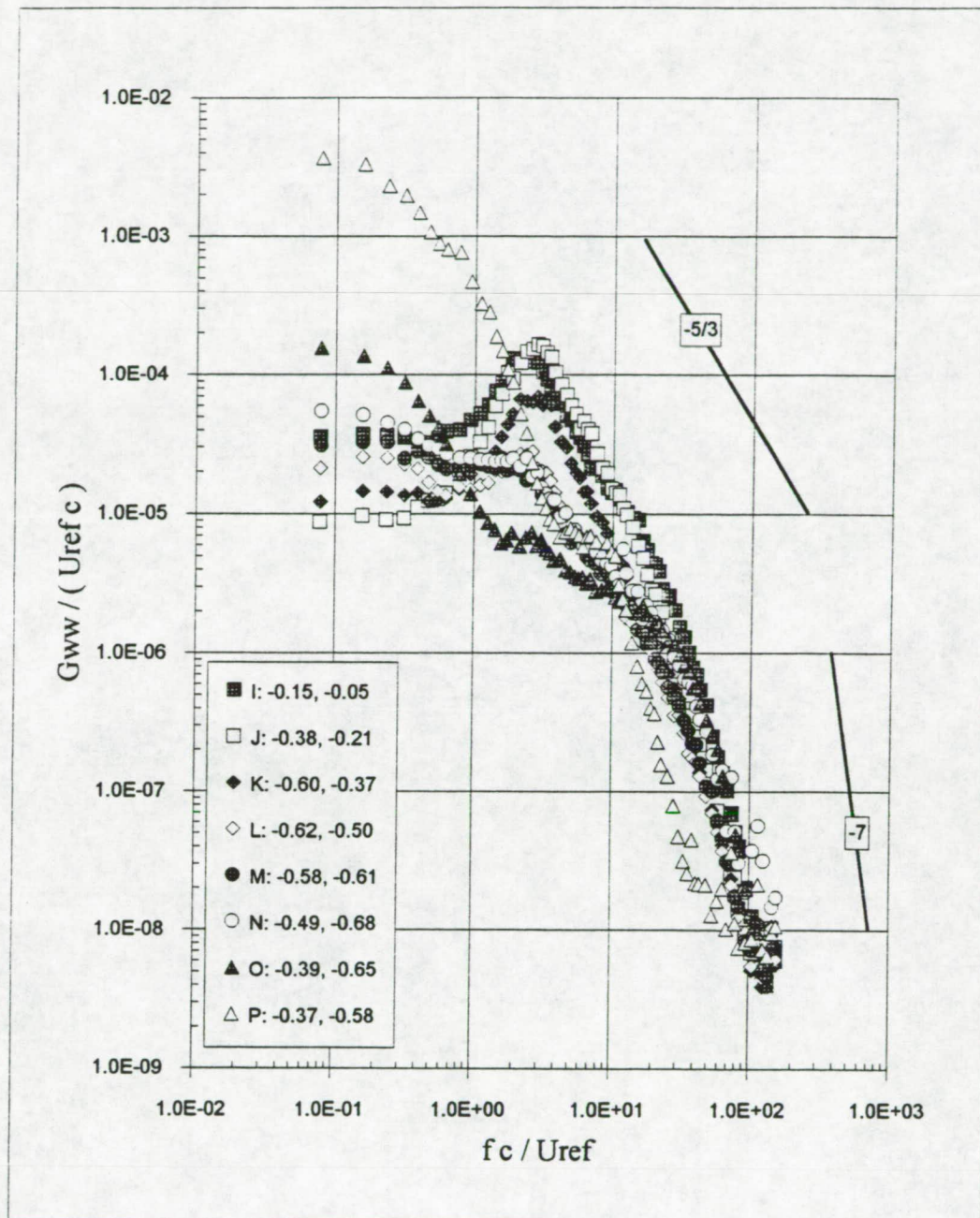
Figure 3.56 Velocity autospectra at  $X/c=30$ ,  $\Delta/c = 0.0625$ . (e)  $G_{vv}$  contd.



Numbers in legend represent the  $y / c$  and  $z / c$  locations respectively

Figure 3.56 Velocity autospectra at  $X/c=30$ ,  $\Delta/c = 0.0625$ . (f)  $G_{ww}$





Numbers in legend represent the  $y/c$  and  $z/c$  locations respectively

Figure 3.56 Velocity autospectra at  $X/c=30$ ,  $\Delta/c = 0.0625$ . (g)  $G_{ww}$  contd.

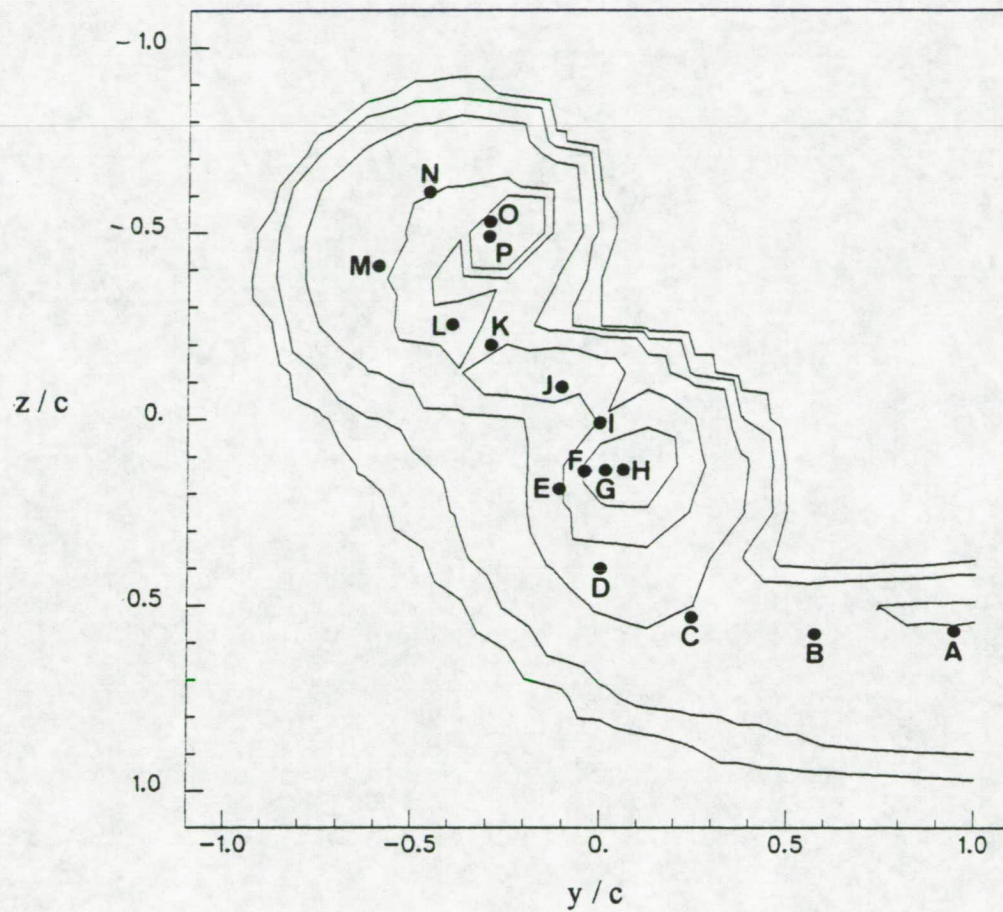
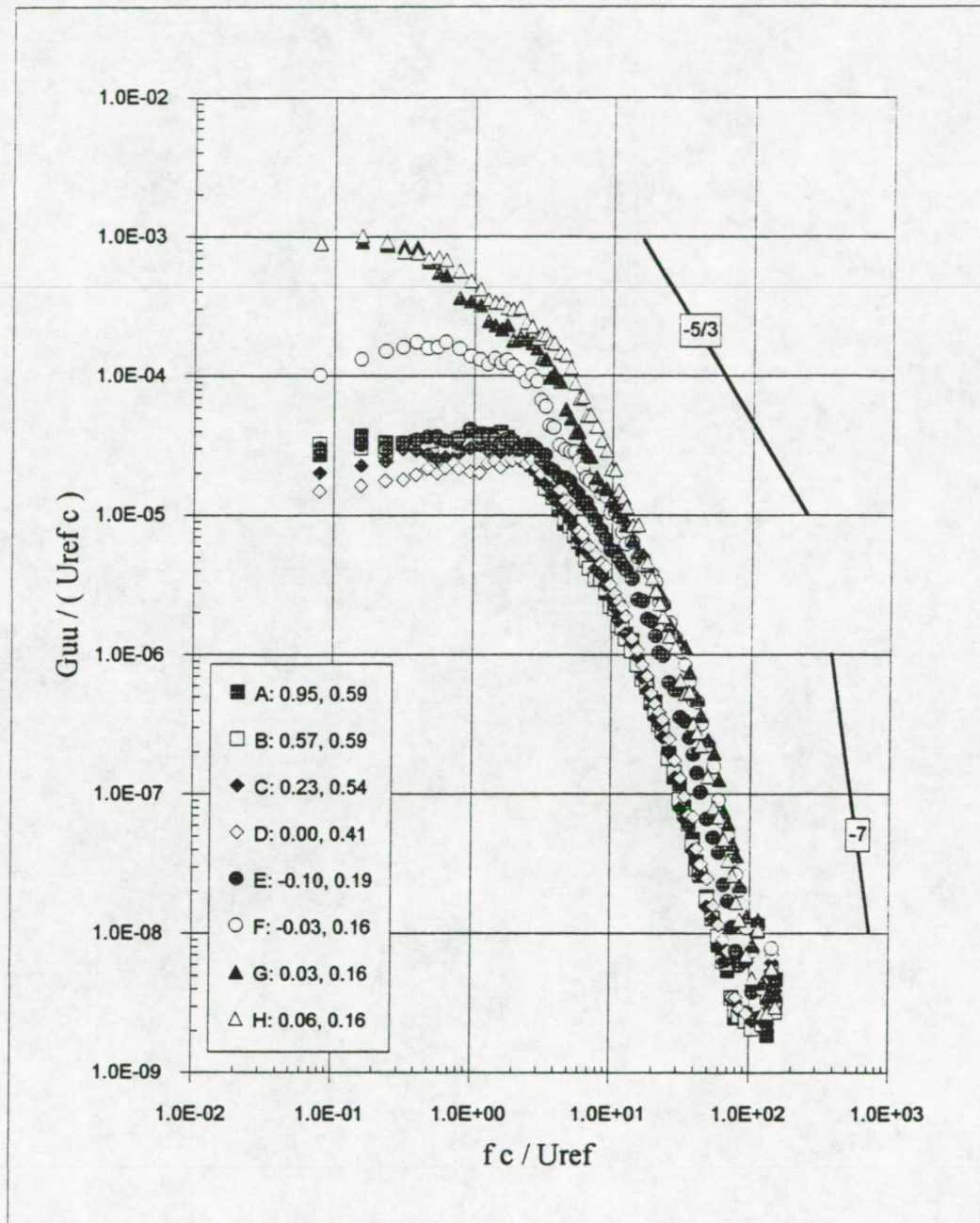


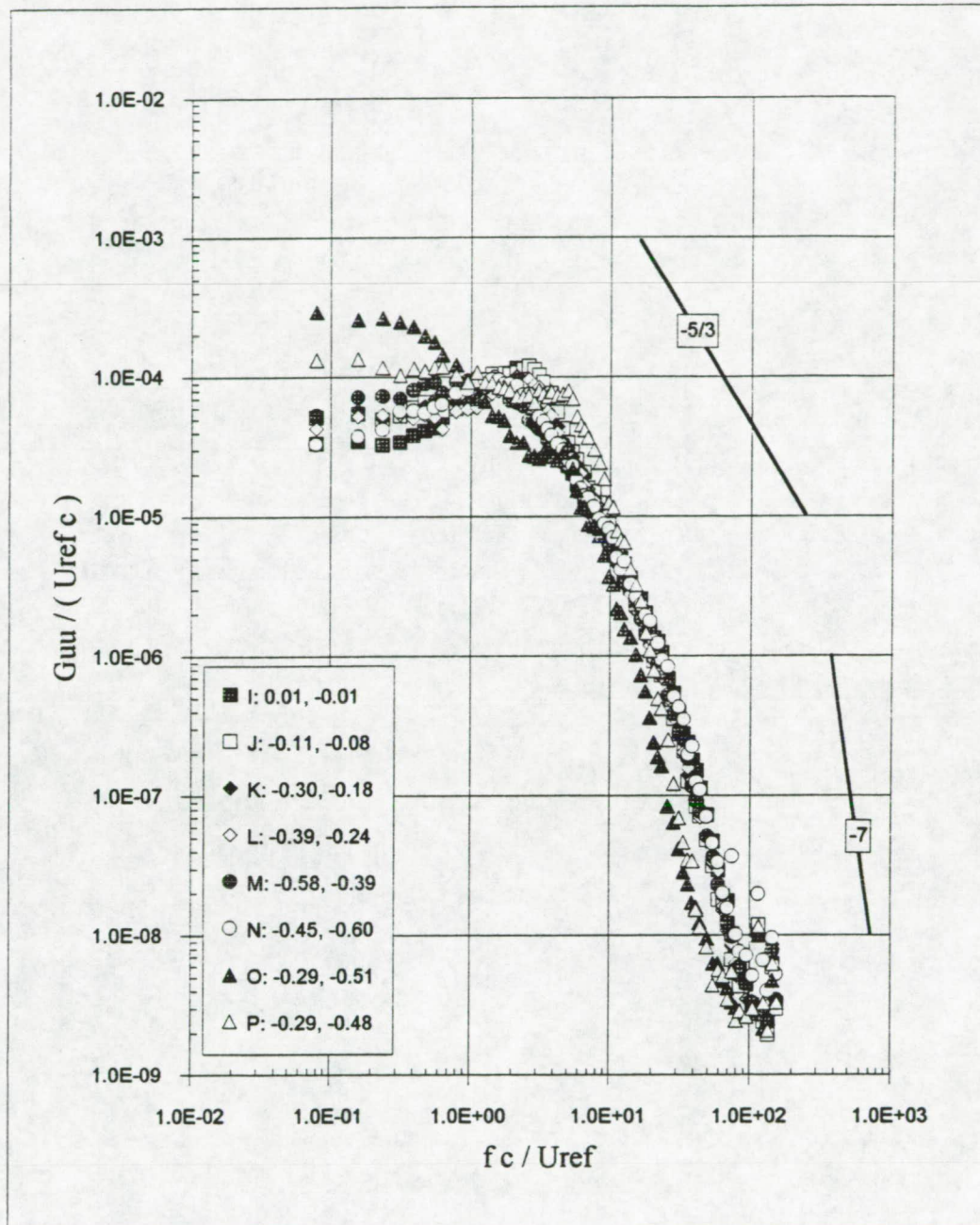
Figure 3.57 Velocity autospectra,  $X/c=30$ ,  $\Delta/c = 0.125$ . (a) Locations of spectral measurements relative to turbulence kinetic energy contours.





Numbers in legend represent the  $y/c$  and  $z/c$  locations respectively

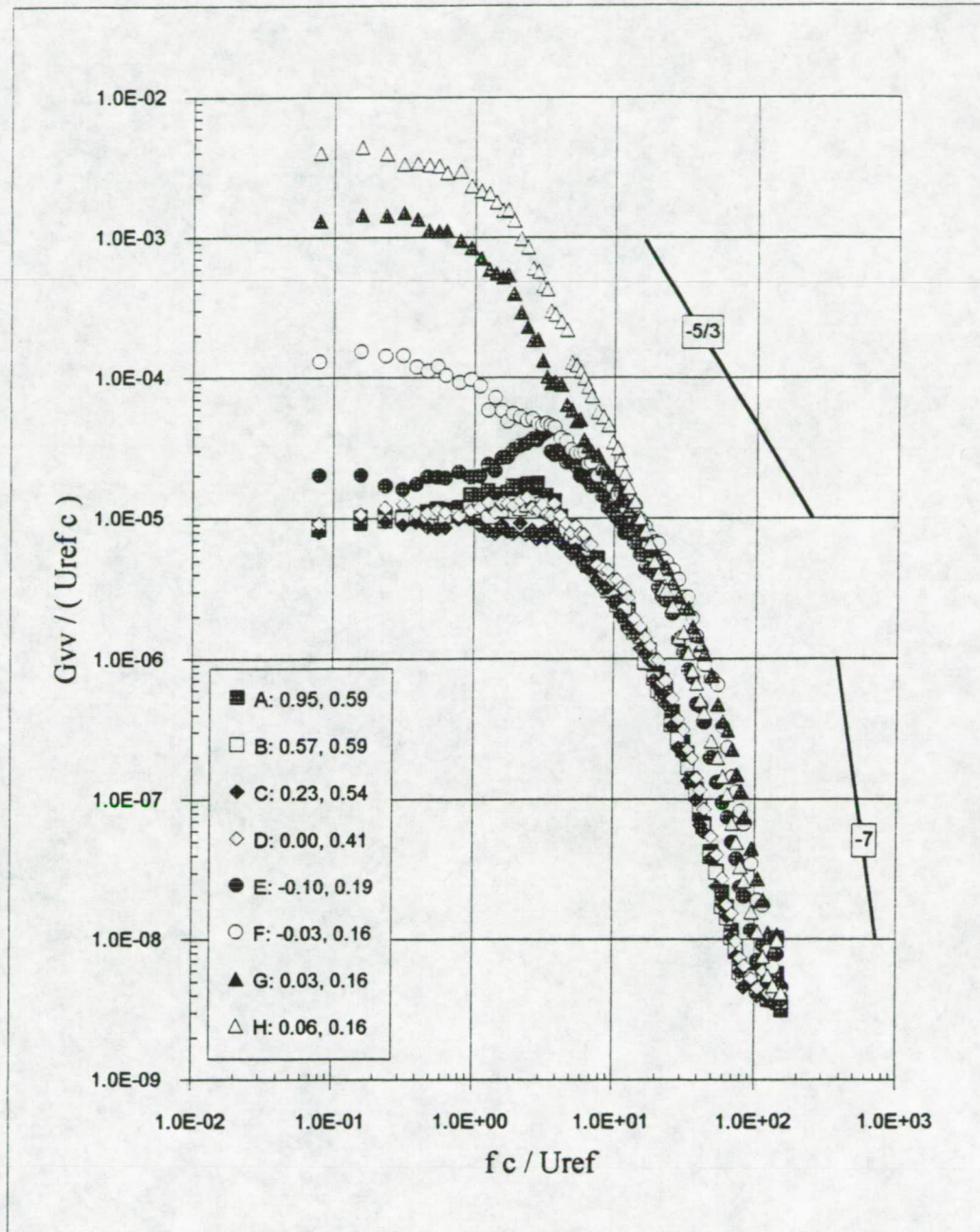
Figure 3.57 Velocity autospectra at  $X/c=30$ ,  $\Delta/c = 0.125$ . (b)  $G_{uu}$



Numbers in legend represent the  $y/c$  and  $z/c$  locations respectively

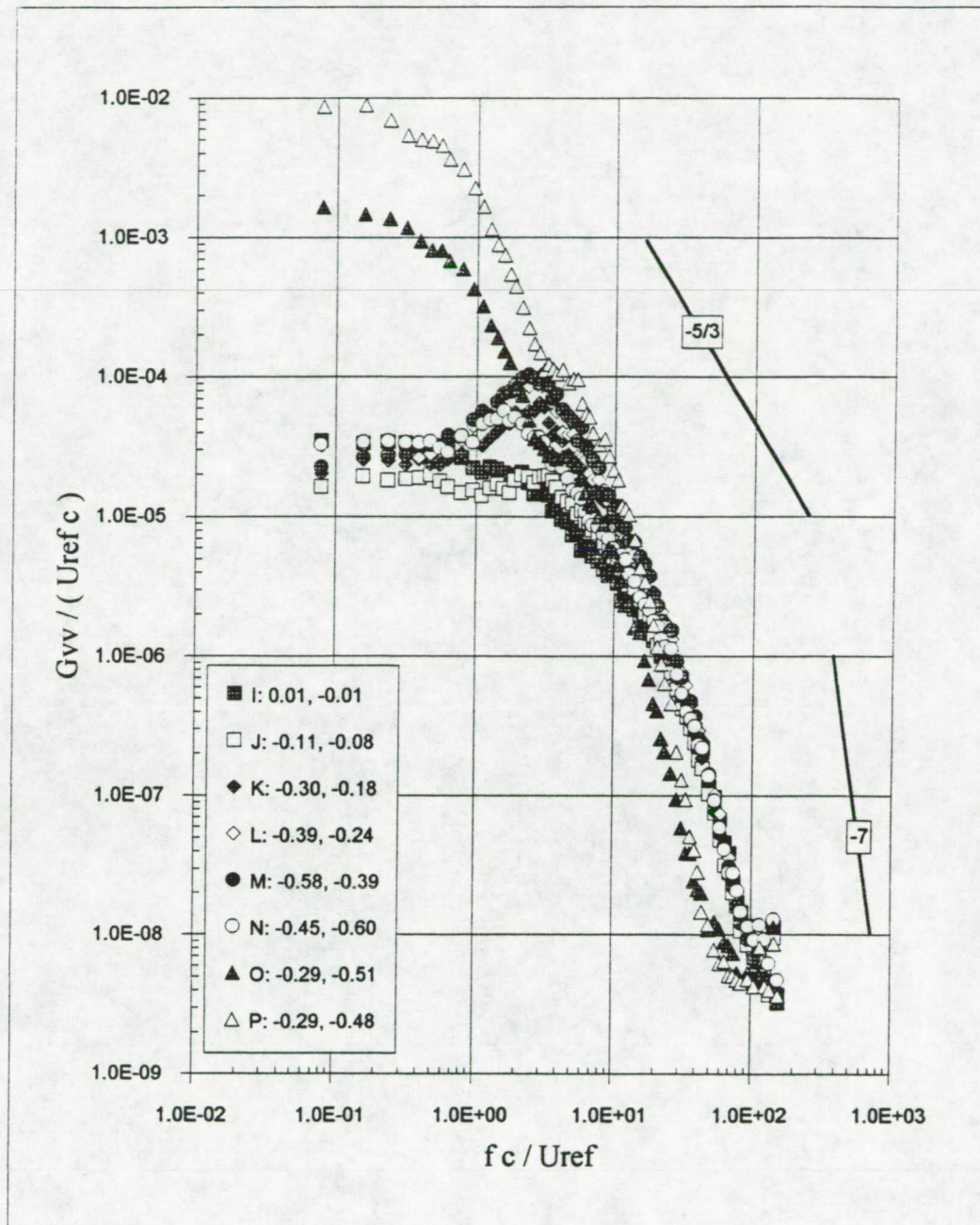
Figure 3.57 Velocity autospectra at  $X/c=30$ ,  $\Delta/c = 0.125$ . (c)  $G_{uu}$  contd.





Numbers in legend represent the  $y/c$  and  $z/c$  locations respectively

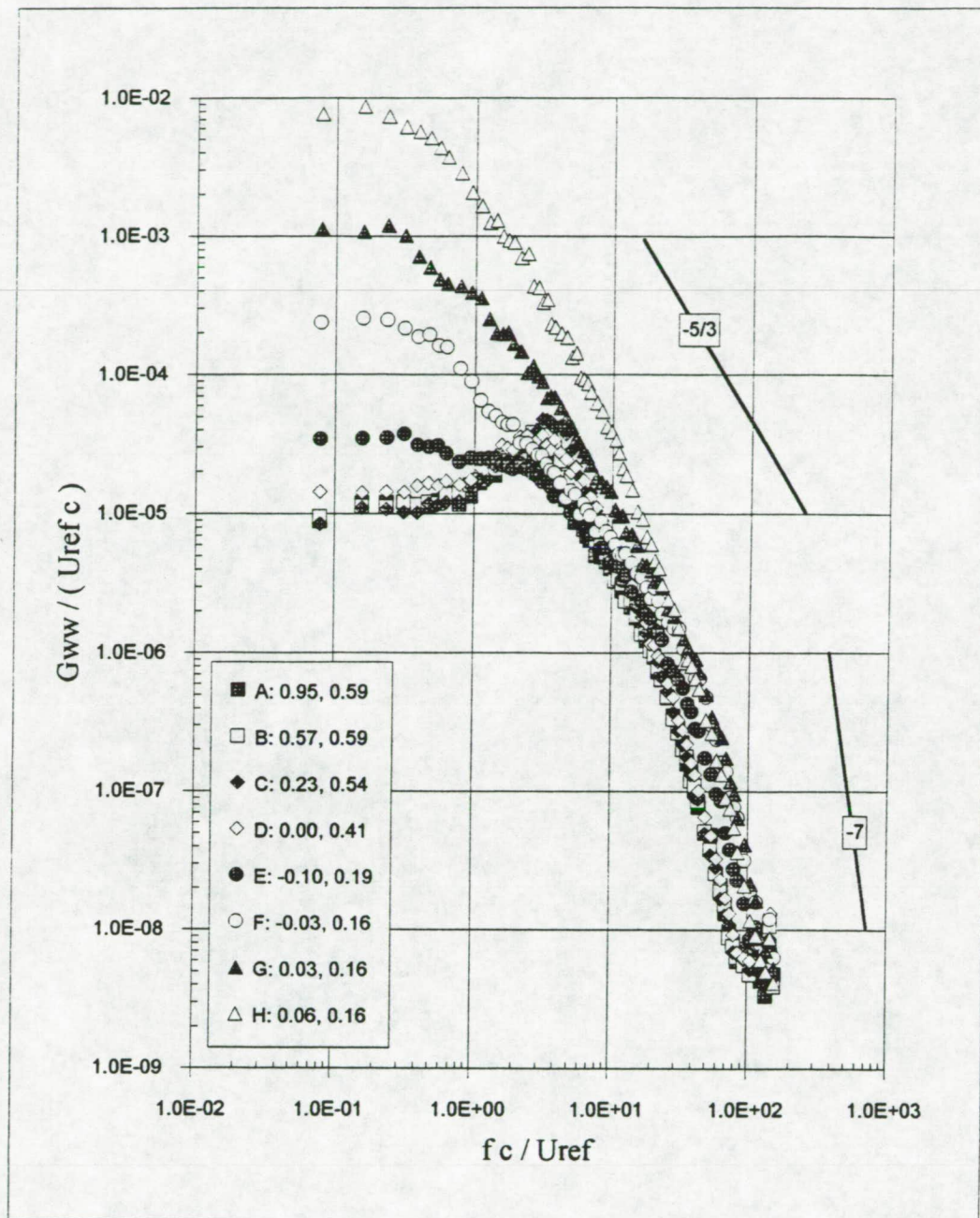
Figure 3.57 Velocity autospectra at  $X/c=30$ ,  $\Delta/c = 0.125$ . (d)  $G_{vv}$



Numbers in legend represent the  $y / c$  and  $z / c$  locations respectively

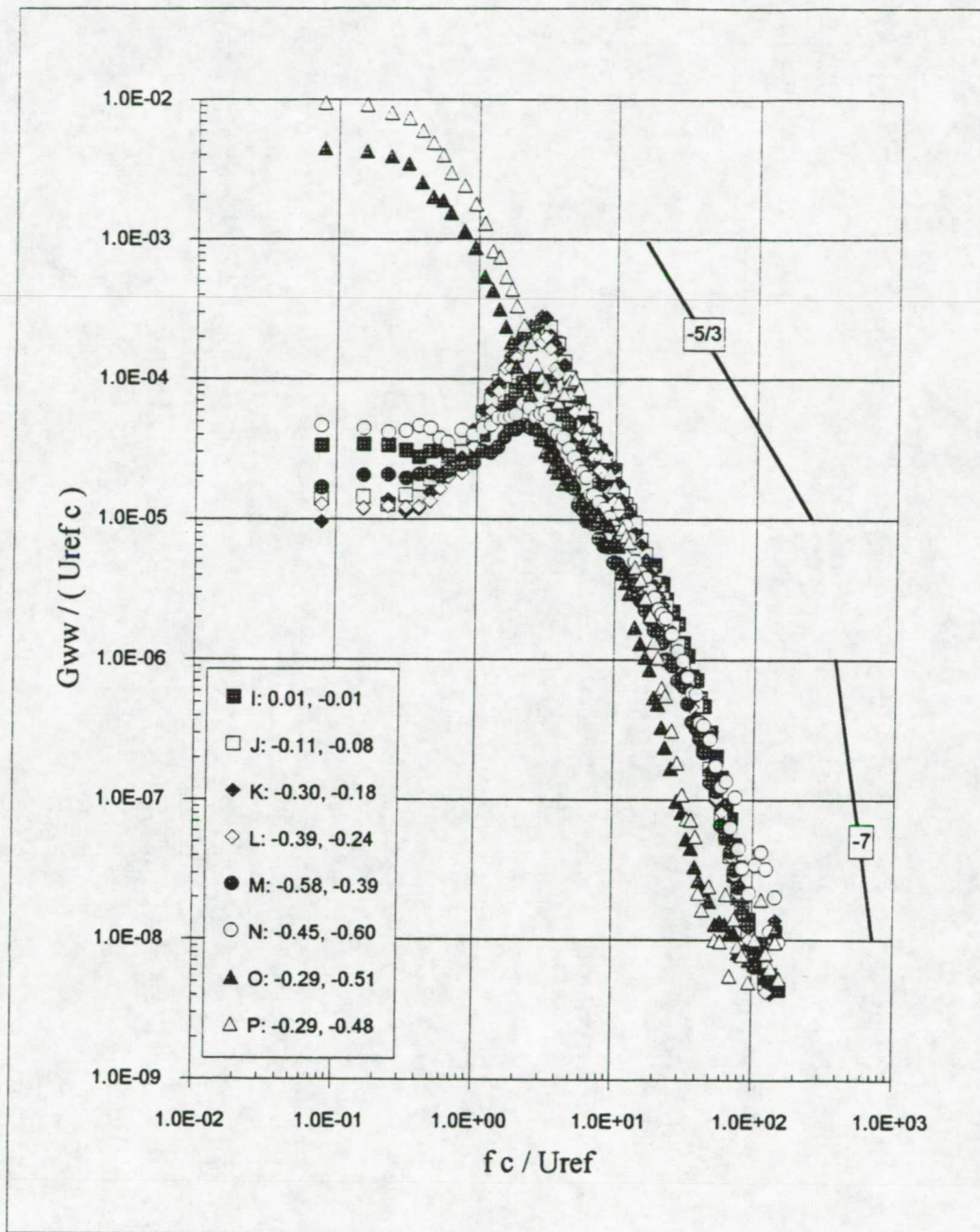
Figure 3.57 Velocity autospectra at  $X/c=30$ ,  $\Delta/c = 0.125$ . (e)  $G_{vv}$  contd.





Numbers in legend represent the  $y/c$  and  $z/c$  locations respectively

Figure 3.57 Velocity autospectra at  $X/c=30$ ,  $\Delta/c = 0.125$ . (f)  $G_{ww}$



Numbers in legend represent the  $y/c$  and  $z/c$  locations respectively

Figure 3.57 Velocity autospectra at  $X/c=30$ ,  $\Delta/c = 0.125$ . (g)  $G_{ww}$  contd.



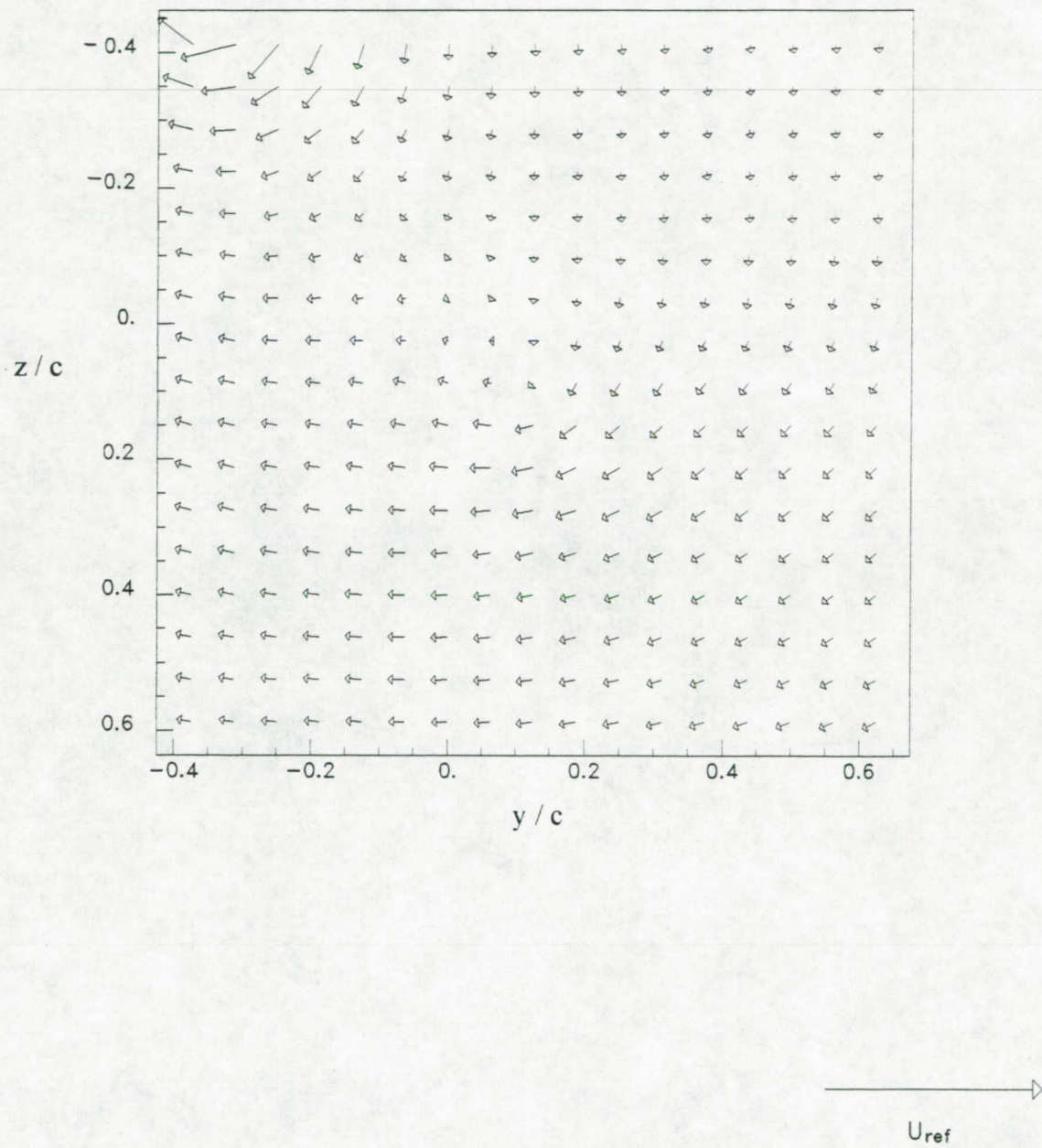


Figure 3.58 Mean cross-flow velocity vectors at  $X/c=22.6$ . (a)  $\Delta/c=-0.0625$ . (i) Coarse grid.



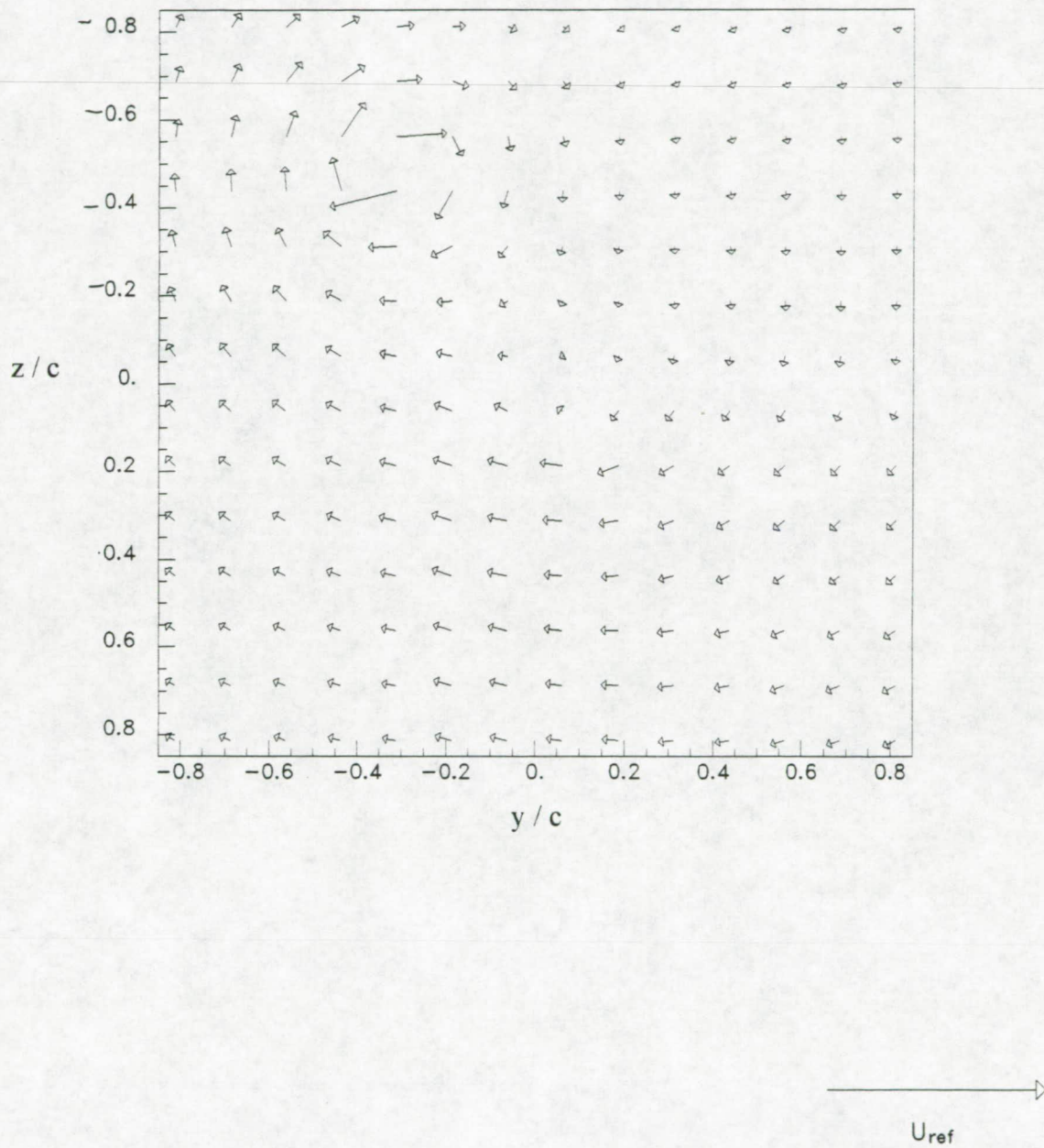


Figure 3.58 Mean cross-flow velocity vectors at  $X/c=22.6$ . (a)  $\Delta/c=-0.0625$ . (i) Fine grid.

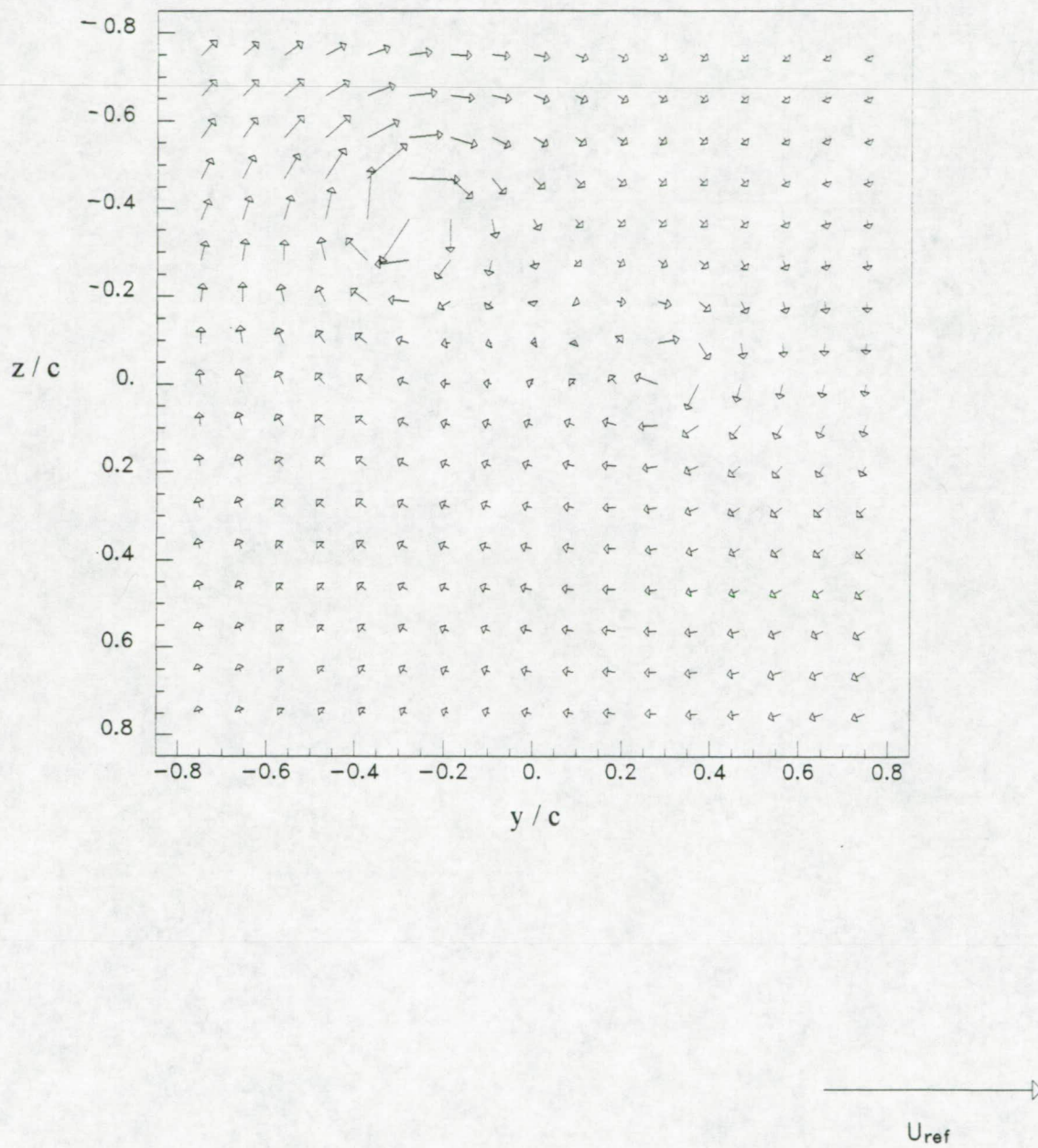


Figure 3.58 Mean cross-flow velocity vectors at  $X/c=22.6$ . (b)  $\Delta/c=0.0625$ .



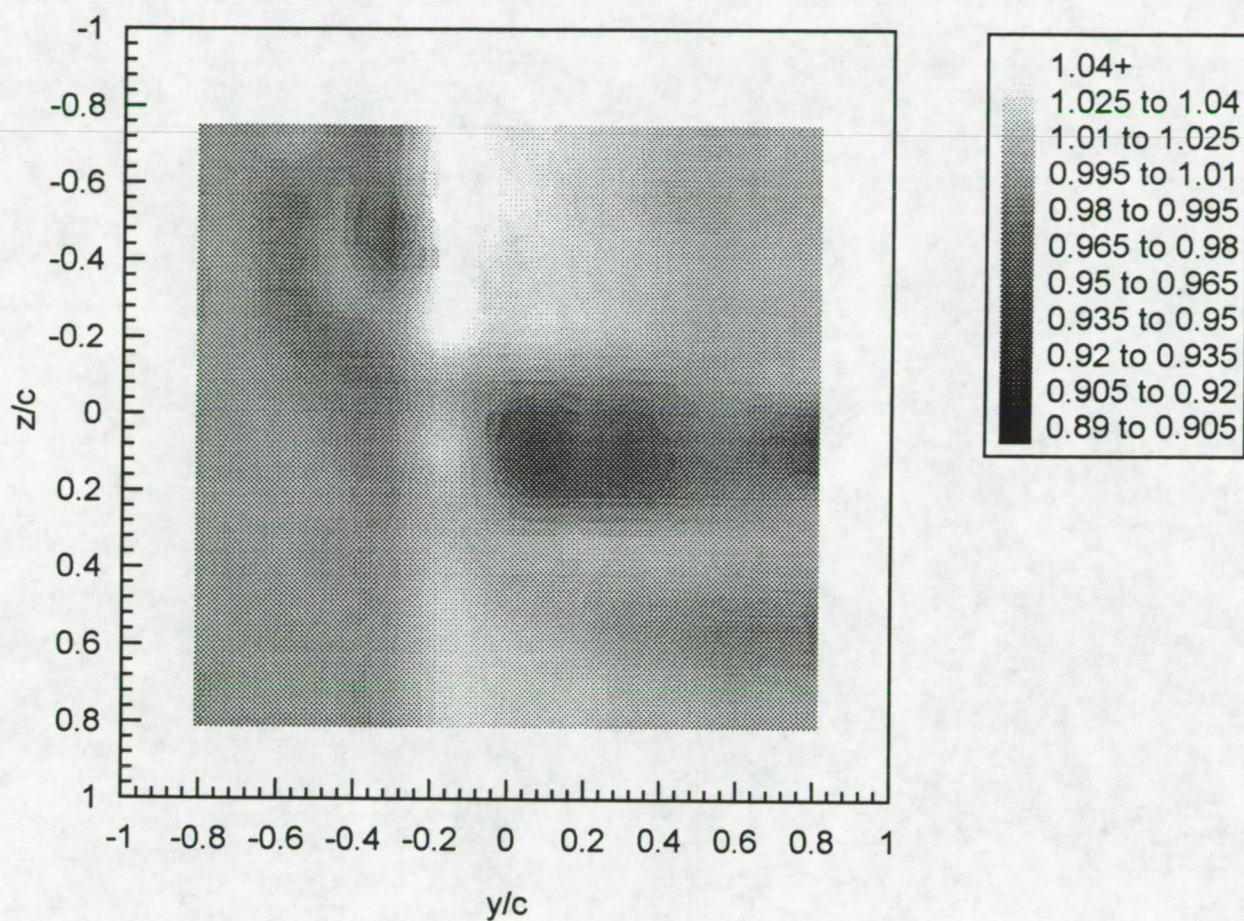


Figure 3.59 Contours of axial mean velocity  $U/U_{ref}$  at  $X/c=22.6$ . (a)  $\Delta/c=-0.0625$ . (i) Coarse grid.



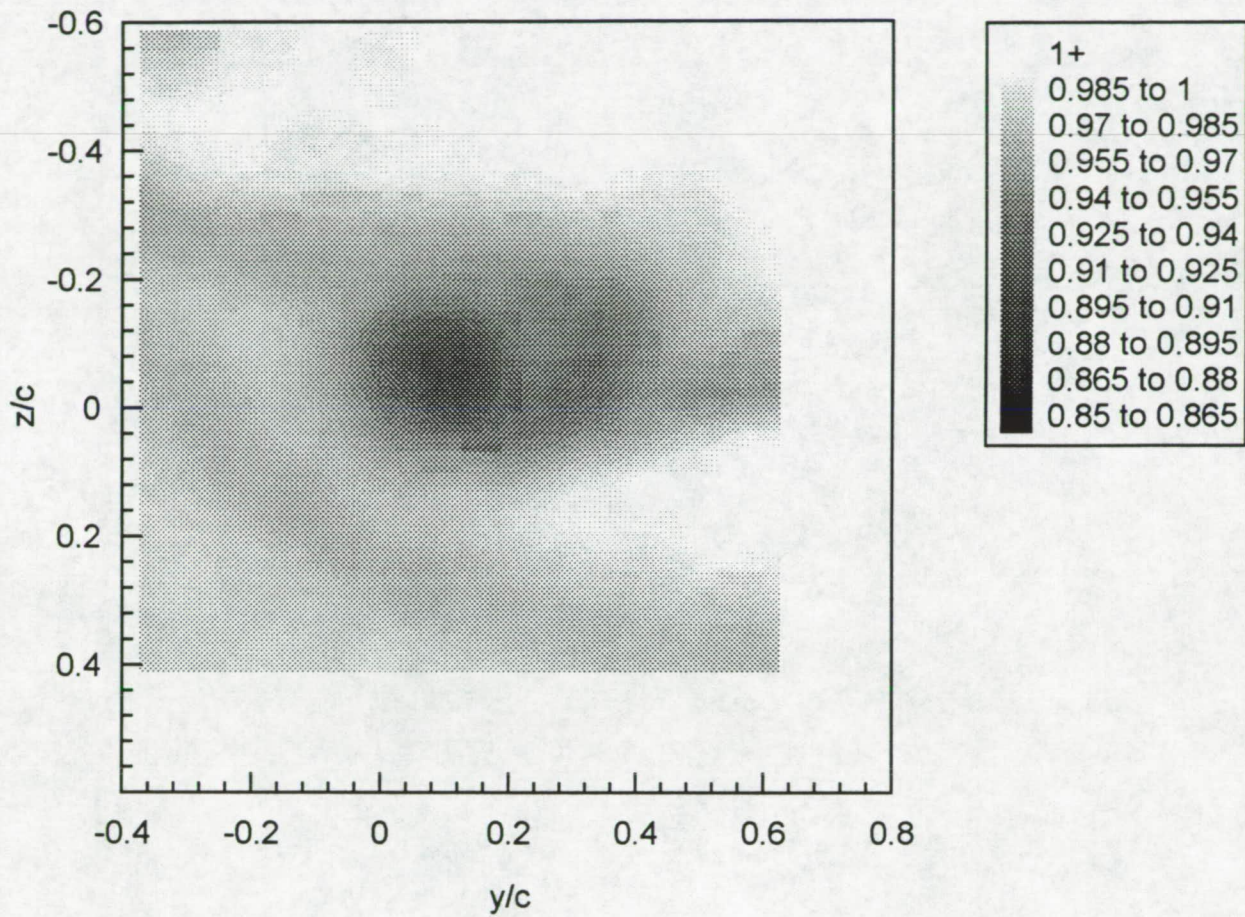


Figure 3.59 Contours of axial mean velocity  $U/U_{ref}$  at  $X/c=22.6$ . (a)  $\Delta/c=-0.0625$ . (i) Fine grid.



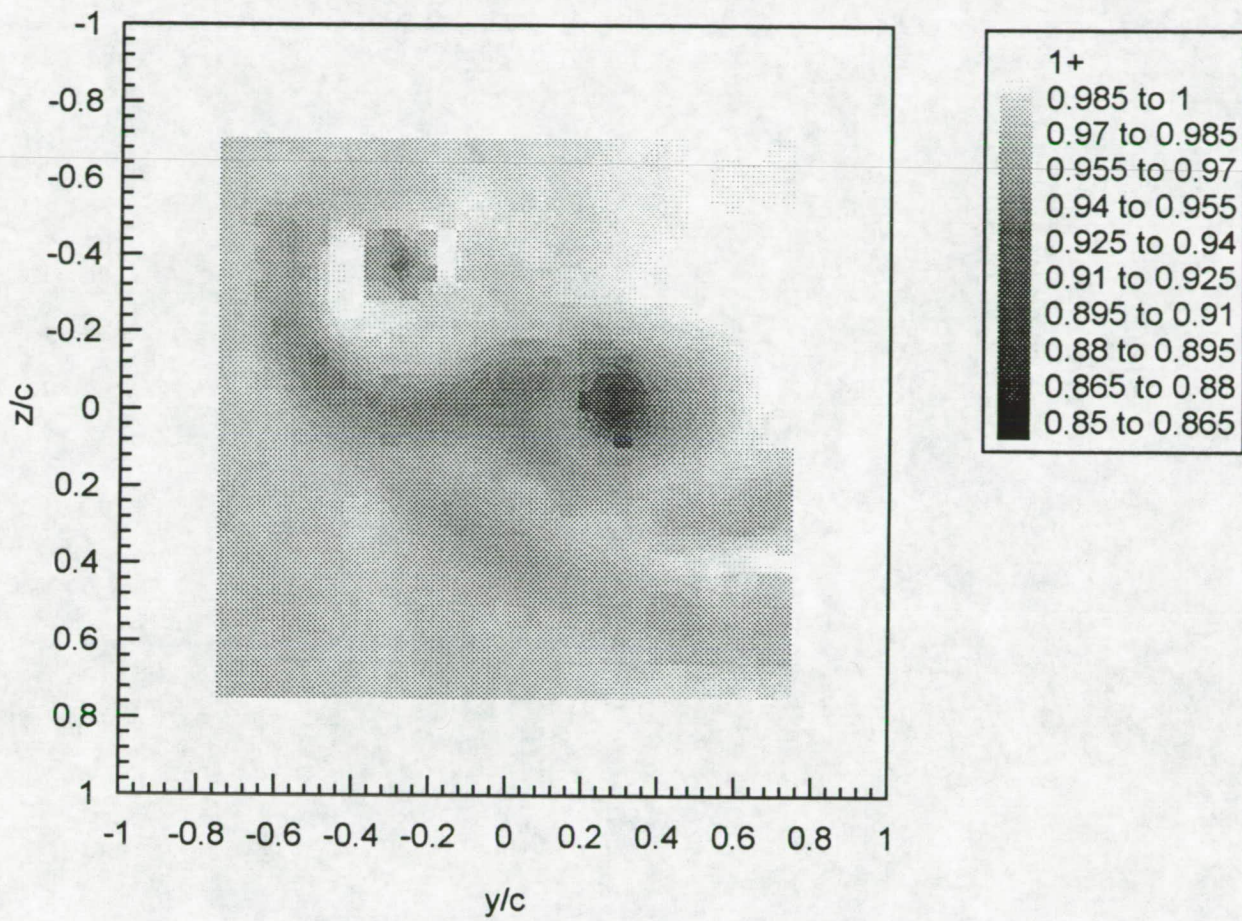


Figure 3.59 Contours of axial mean velocity  $U/U_{ref}$  at  $X/c=22.6$ . (b)  $\Delta/c=0.0625$ .



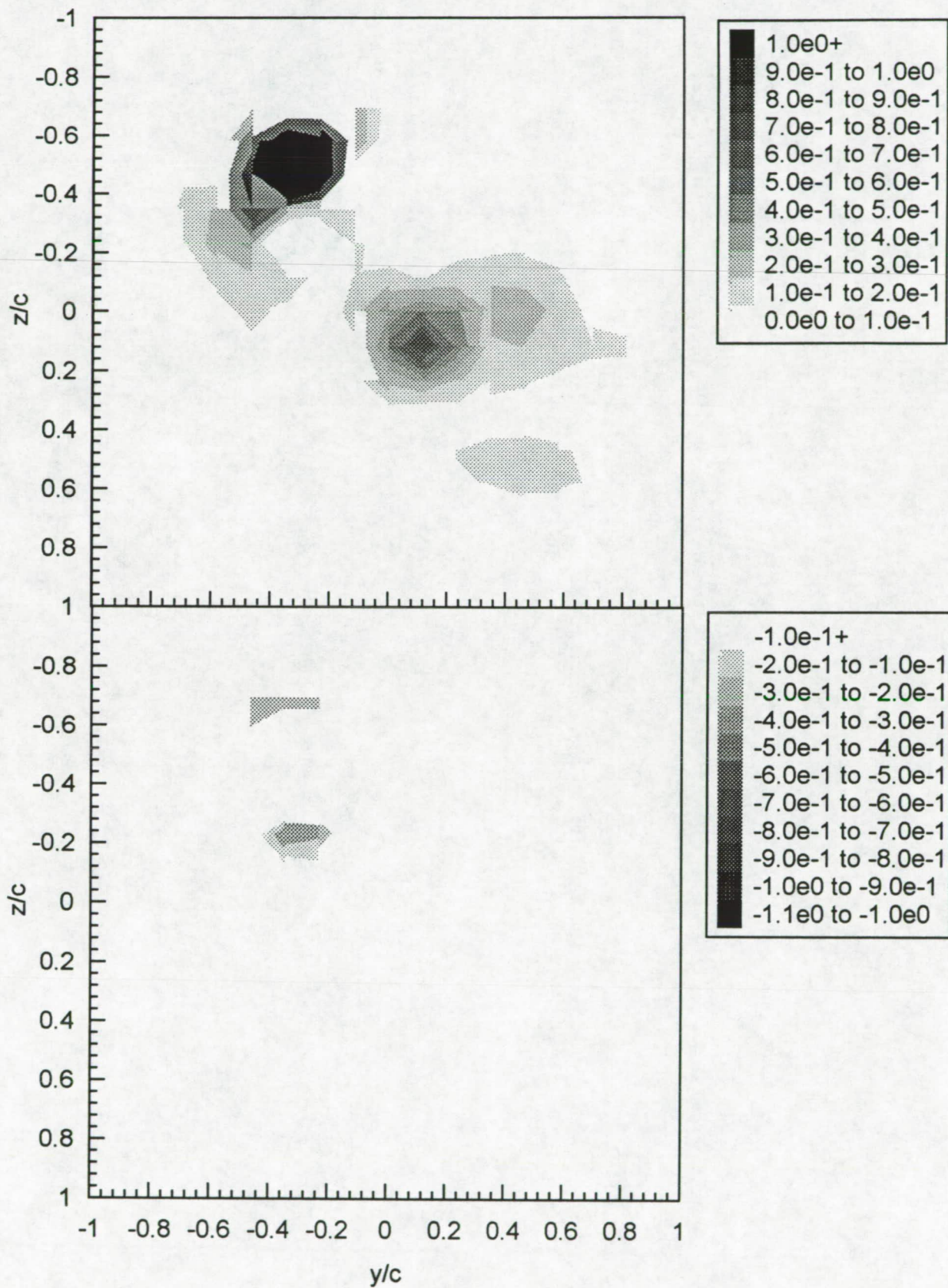


Figure 3.60 Contours of axial mean vorticity  $\omega_x c / U_{ref}$  at  $X/c = 22.6$ . (a)  $\Delta/c = -0.0625$ . (i) Coarse grid. Upper figure - positive vorticity, lower figure - negative vorticity.



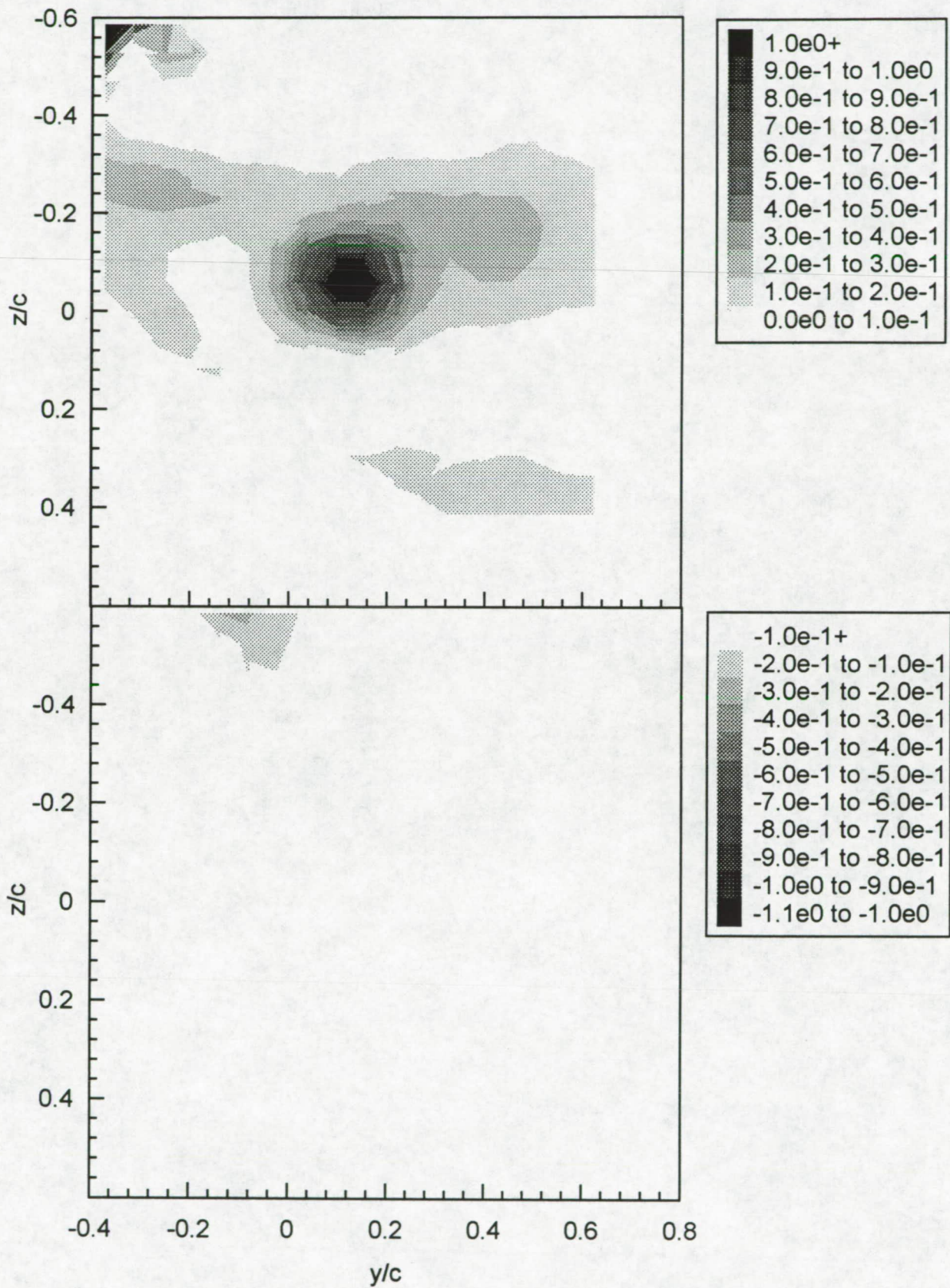


Figure 3.60 Contours of axial mean vorticity  $\omega_x c / U_{ref}$  at  $X/c = 22.6$ . (a)  $\Delta/c = -0.0625$ . (i) Fine grid. Upper figure - positive vorticity, lower figure - negative vorticity.



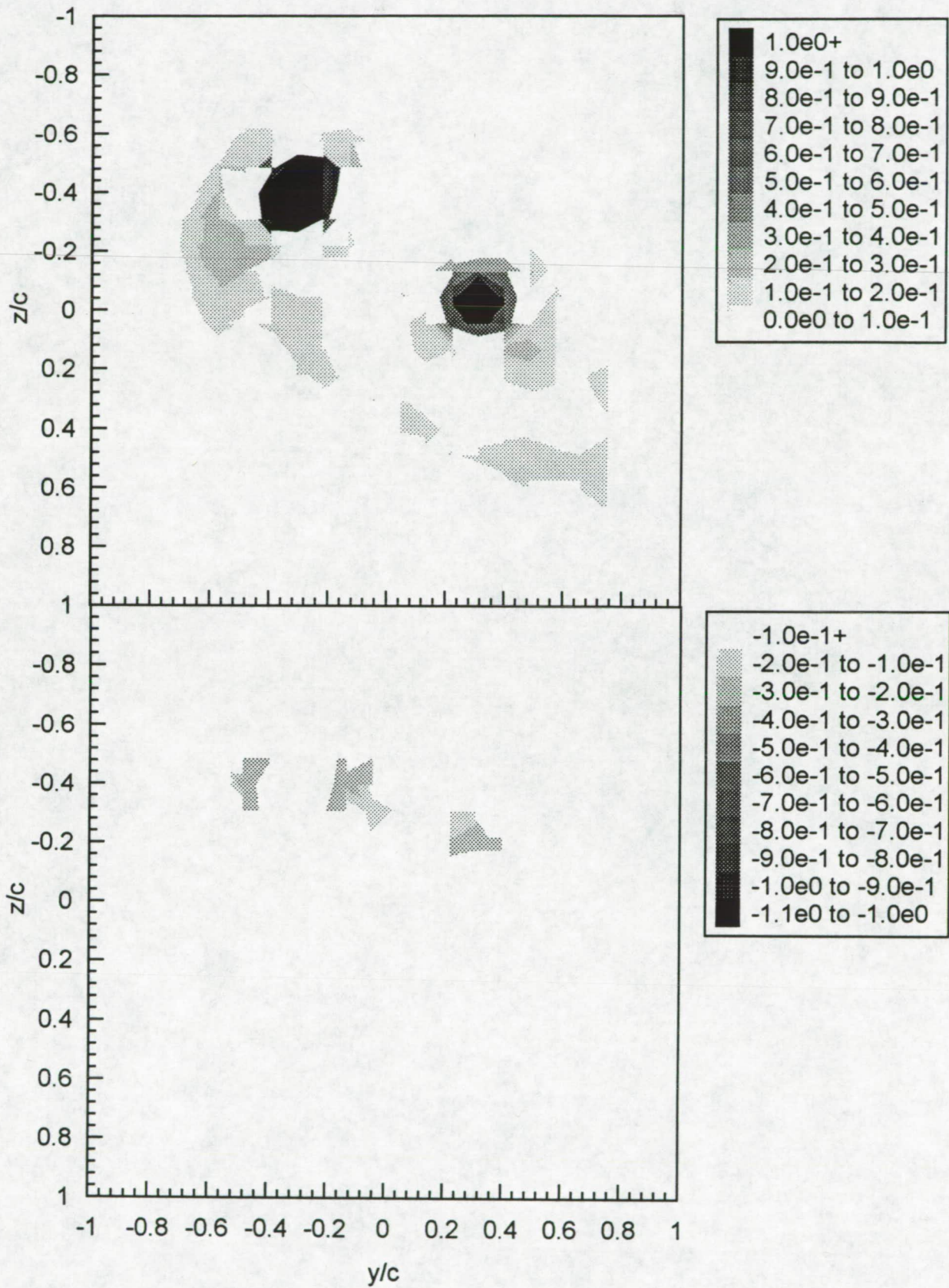


Figure 3.60 Contours of axial mean vorticity  $\omega_x c/U_{ref}$  at  $X/c=22.6$ . (b)  $\Delta/c=0.0625$ . Upper figure - positive vorticity, lower figure - negative vorticity.



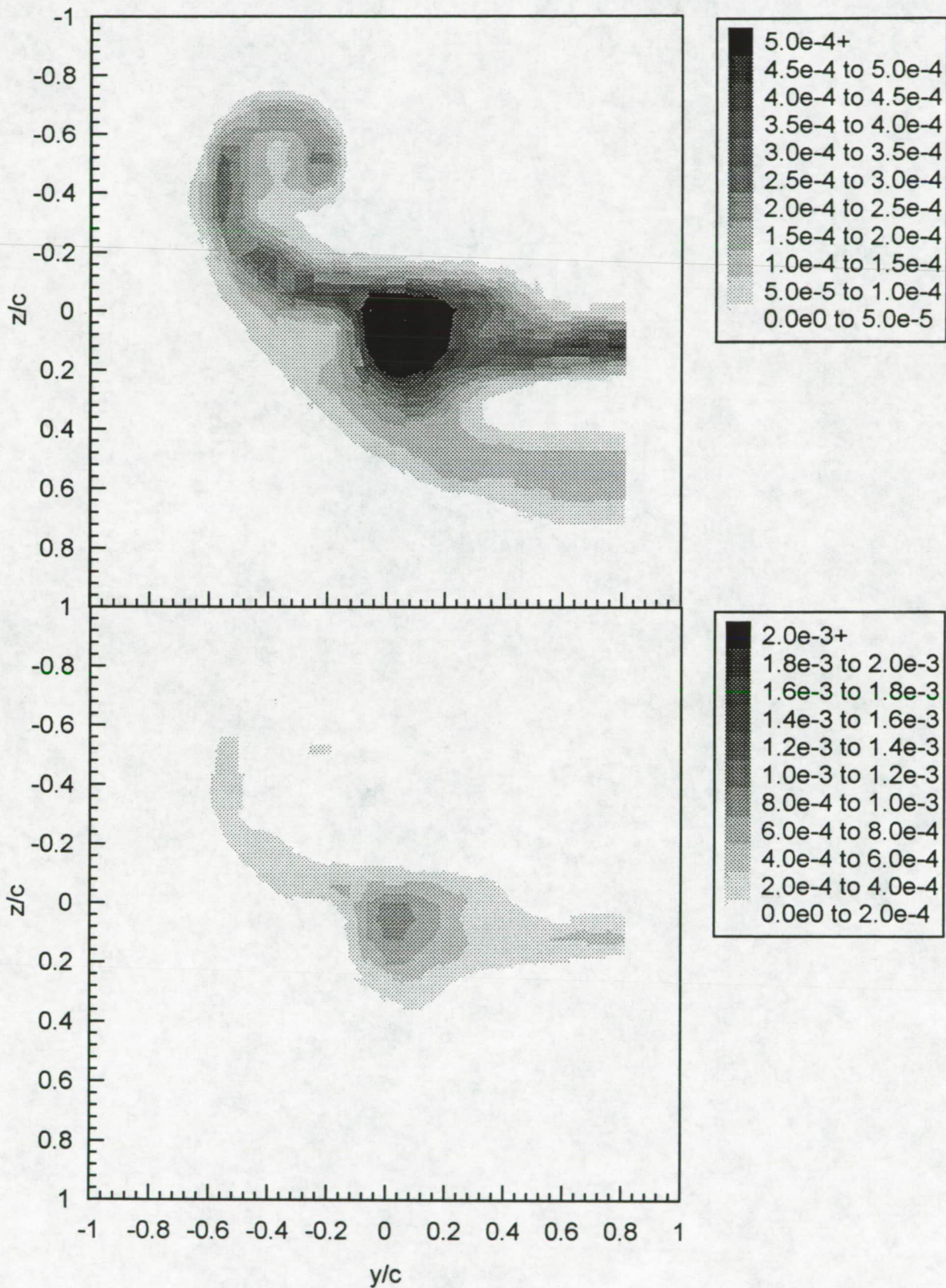


Figure 3.61 Contours of axial normal turbulence stress  $\overline{u'^2}/U_{ref}^2$  at  $X/c=22.6$ . (a)  $\Delta/c=-0.0625$ . (i) Coarse grid. Upper and lower figures show different contour ranges.



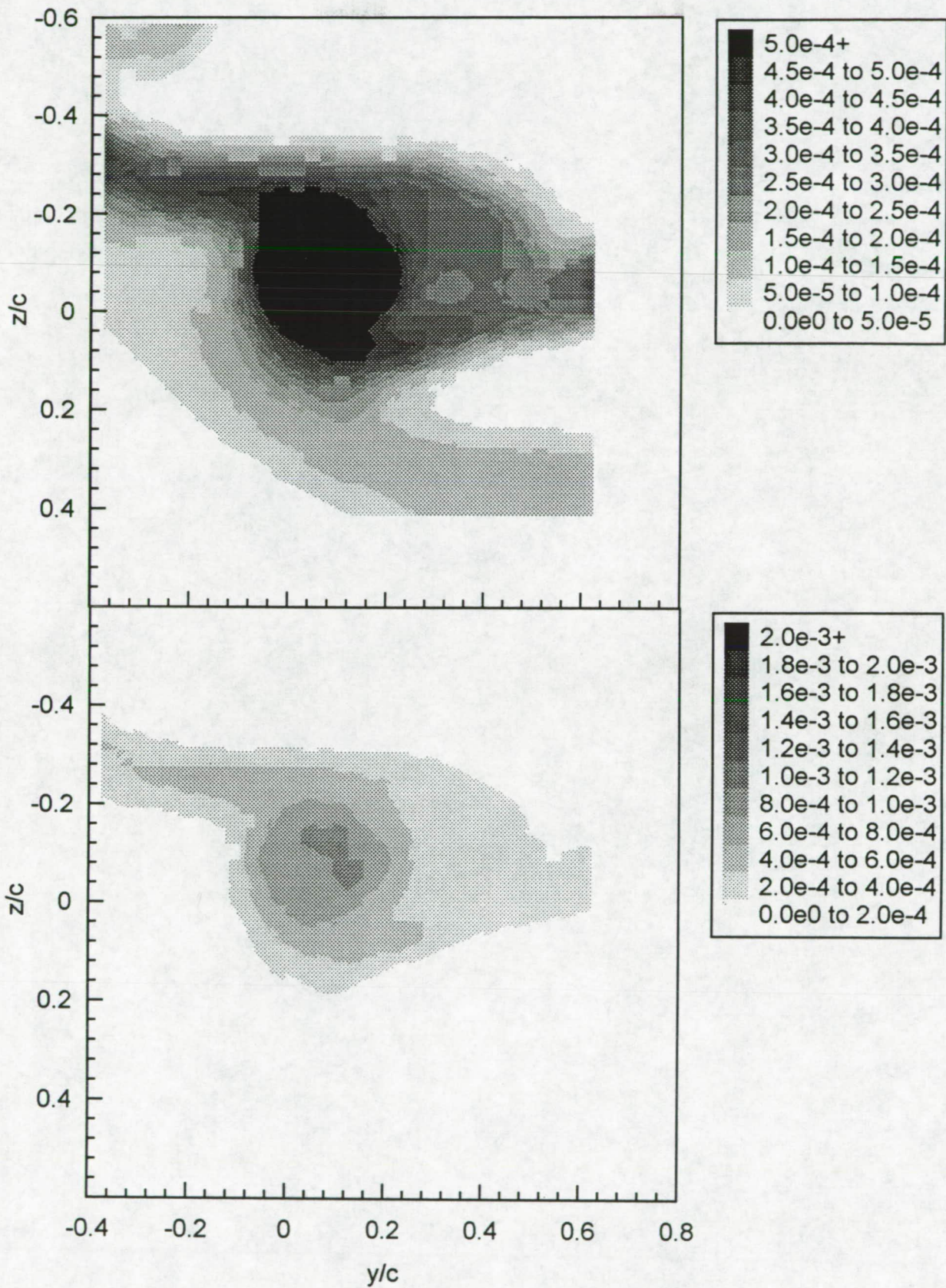


Figure 3.61 Contours of axial normal turbulence stress  $\overline{u'^2}/U_{ref}^2$  at  $X/c=22.6$ . (a)  $\Delta/c=-0.0625$ . (i) Fine grid. Upper and lower figures show different contour ranges.



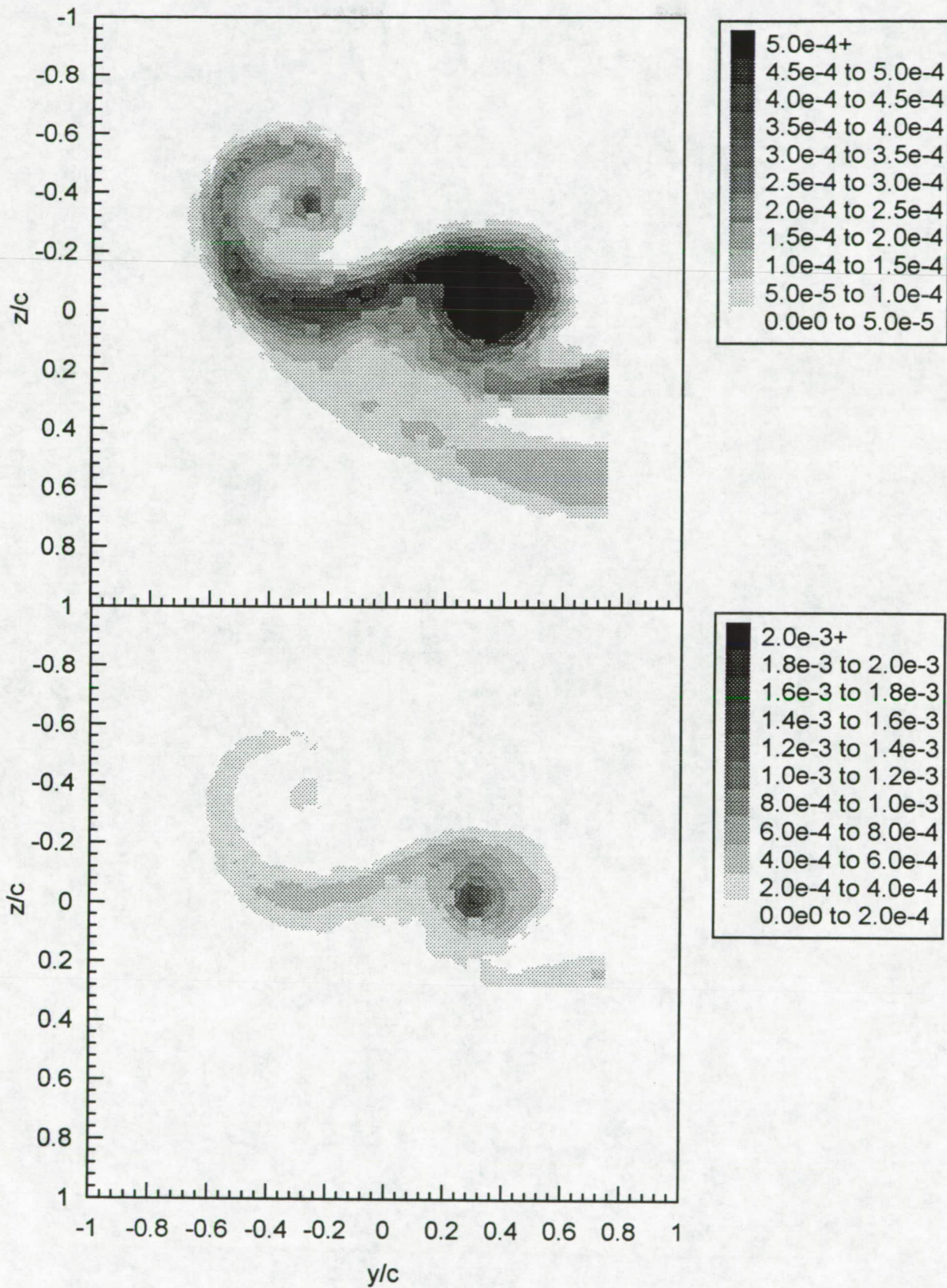


Figure 3.61 Contours of axial normal turbulence stress  $\overline{u'^2}/U_{ref}^2$  at  $X/c=22.6$ . (b)  $\Delta/c=0.0625$ . Upper and lower figures show different contour ranges.



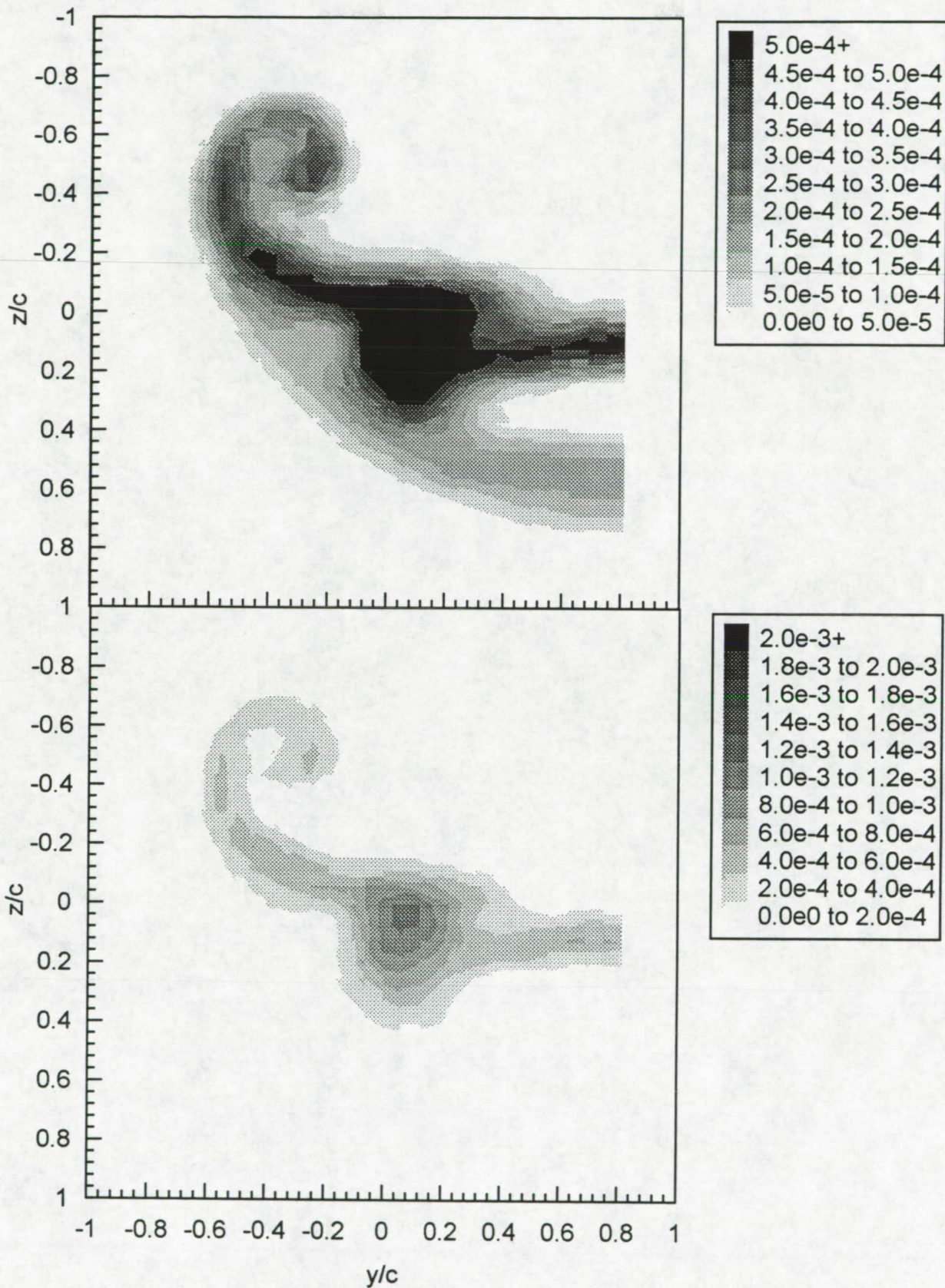


Figure 3.62 Contours of turbulence kinetic energy  $k/U_{ref}^2$  at  $X/c=22.6$ . (a)  $\Delta/c=-0.0625$ . (i) Coarse grid. Upper and lower figures show different contour ranges.



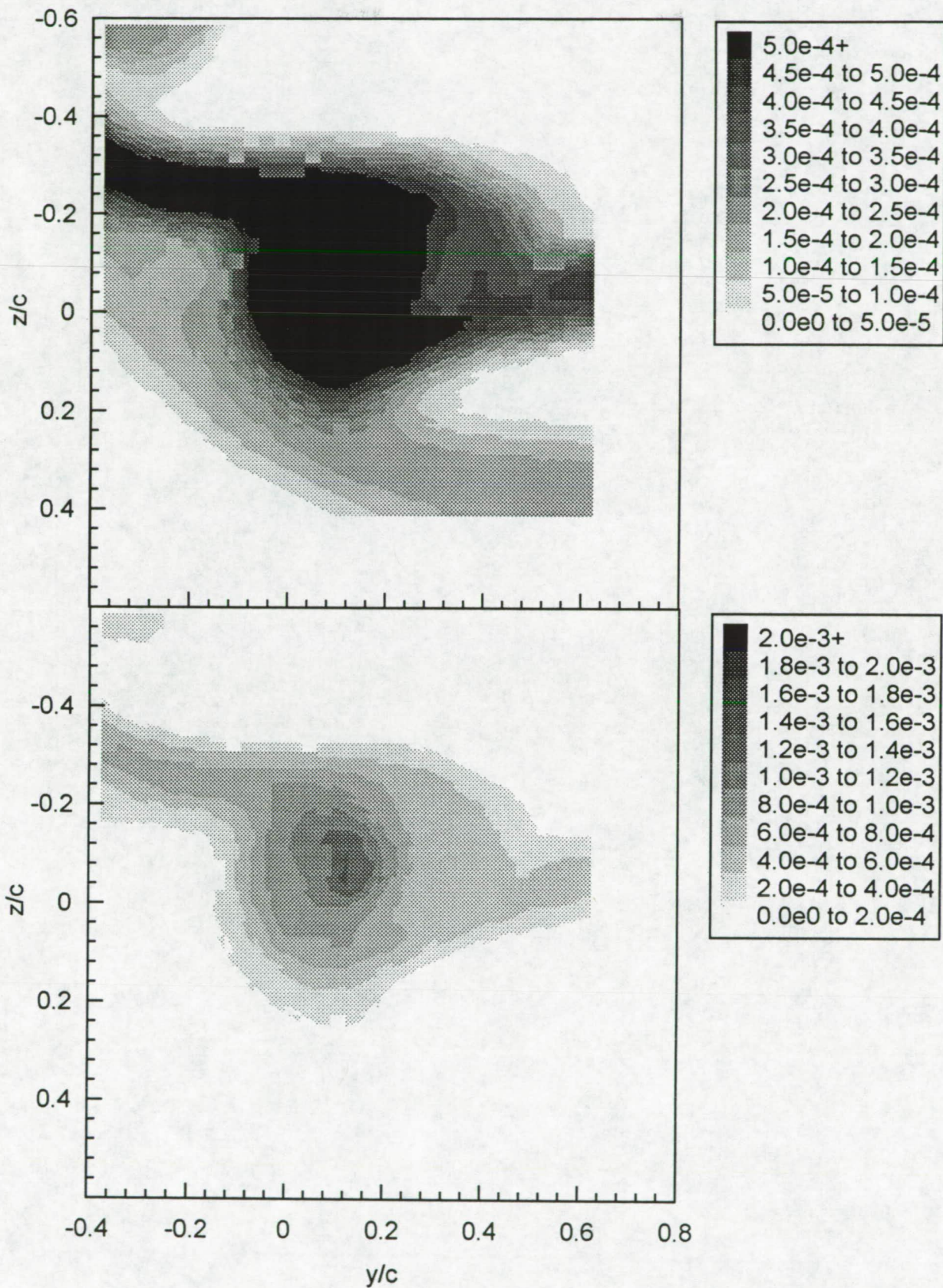


Figure 3.62 Contours of turbulence kinetic energy  $k/U_{ref}^2$  at  $X/c=22.6$ . (a)  $\Delta/c=-0.0625$ . (i) Fine grid. Upper and lower figures show different contour ranges.



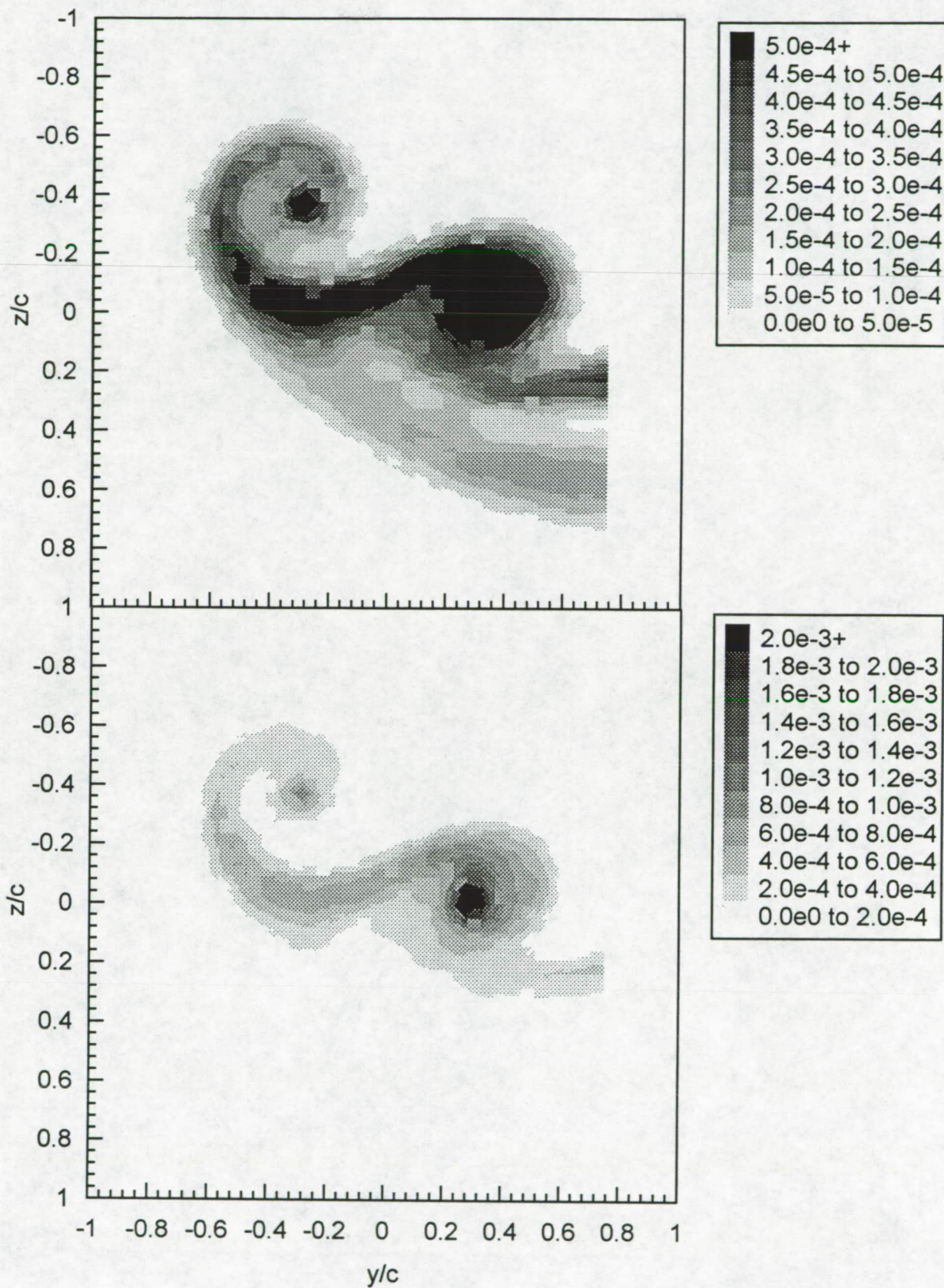


Figure 3.62 Contours of turbulence kinetic energy  $k/U_{ref}^2$  at  $X/c=22.6$ . (b)  $\Delta/c=0.0625$ . Upper and lower figures show different contour ranges.



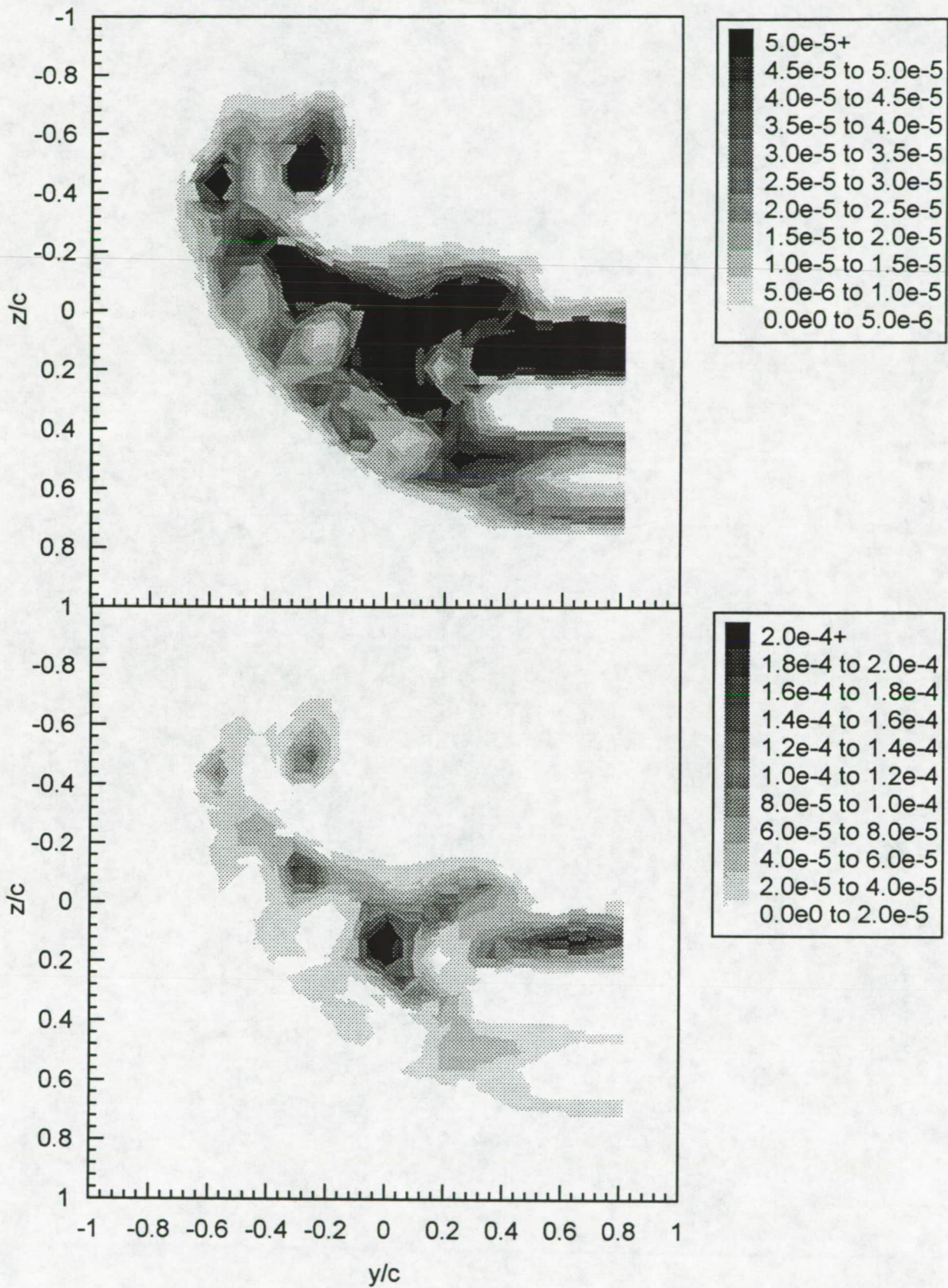


Figure 3.63 Contours of axial shear stress magnitude  $\tau_a/U_{ref}^2$  at  $X/c=22.6$ . (a)  $\Delta/c=-0.0625$ . (i) Coarse grid. Upper and lower figures show different contour ranges.



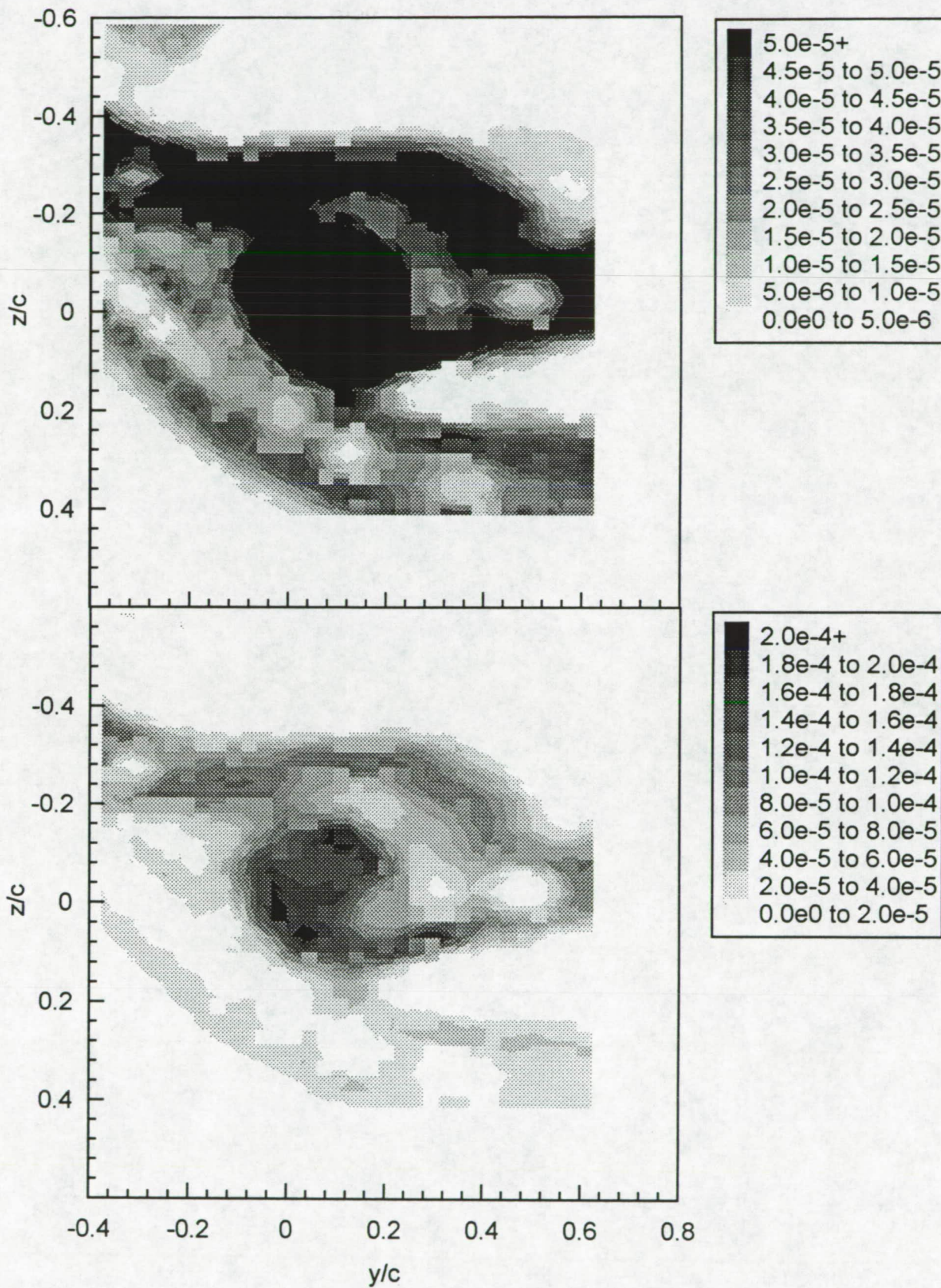


Figure 3.63 Contours of axial shear stress magnitude  $\tau_a/U_{ref}^2$  at  $X/c=22.6$ . (a)  $\Delta/c=-0.0625$ . (i) Fine grid. Upper and lower figures show different contour ranges.



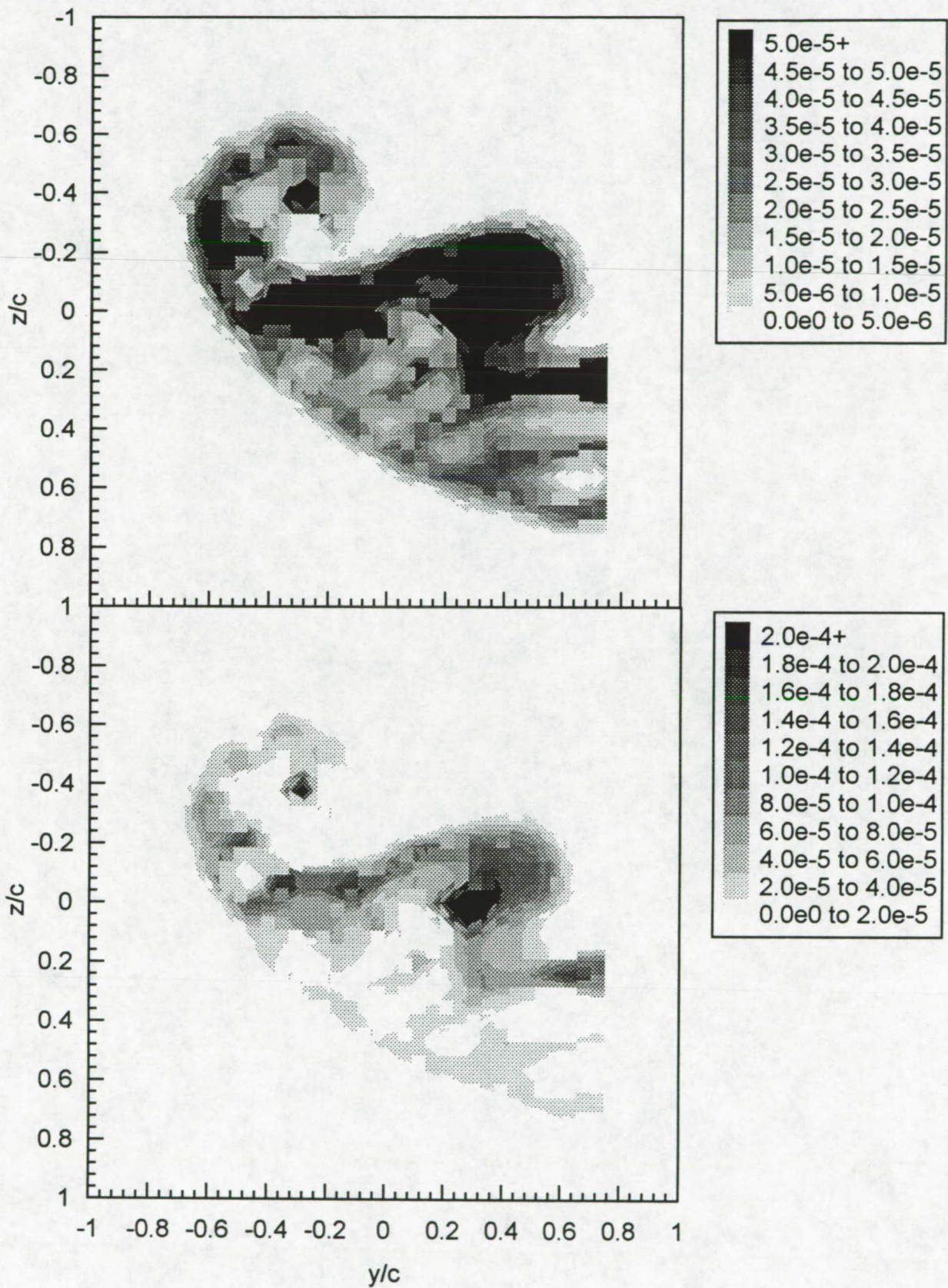


Figure 3.63 Contours of axial shear stress magnitude  $\tau_a/U_{ref}^2$  at  $X/c=22.6$ . (b)  $\Delta/c=0.0625$ . Upper and lower figures show different contour ranges.



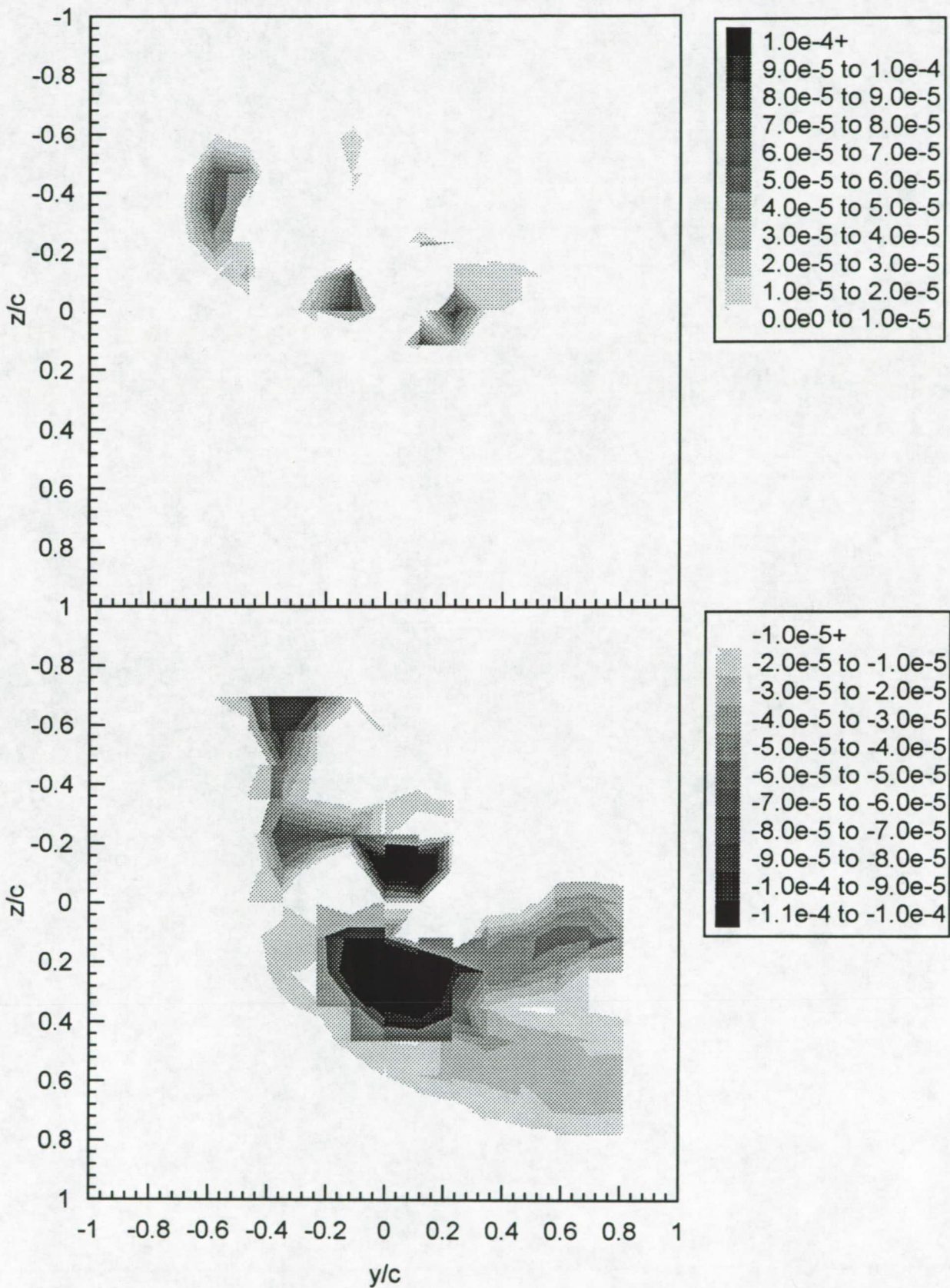


Figure 3.64 Contours of crossflow shear stress  $\tau_c/U_{ref}^2$  at  $X/c=22.6$ . (a)  $\Delta/c=-0.0625$ . (i) Coarse grid. Upper figure - positive stress, lower figure - negative stress.



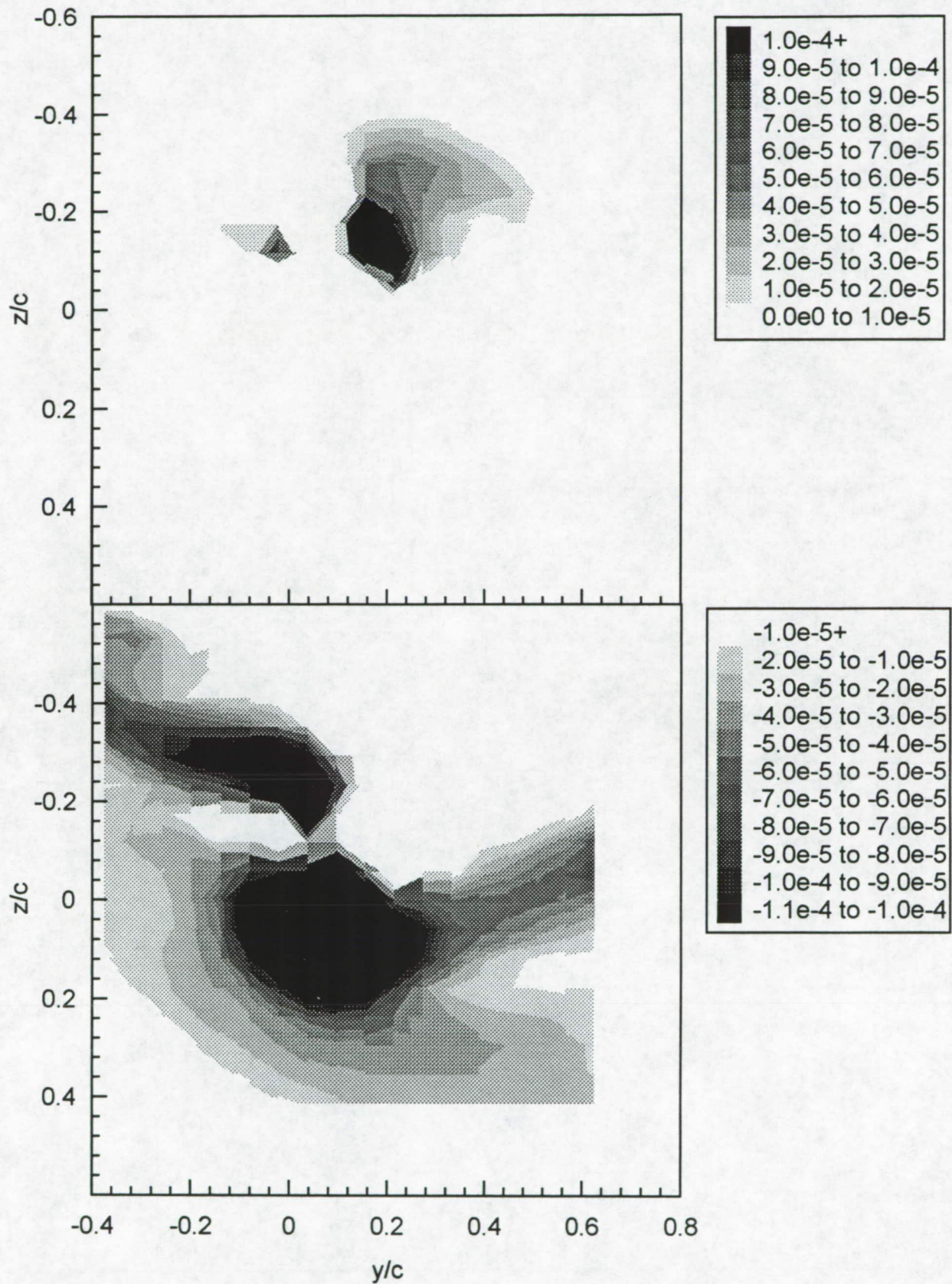


Figure 3.64 Contours of crossflow shear stress  $\tau_c/U_{ref}^2$  at  $X/c=22.6$ . (a)  $\Delta/c=-0.0625$ . (i) Fine grid. Upper figure - positive stress, lower figure - negative stress.



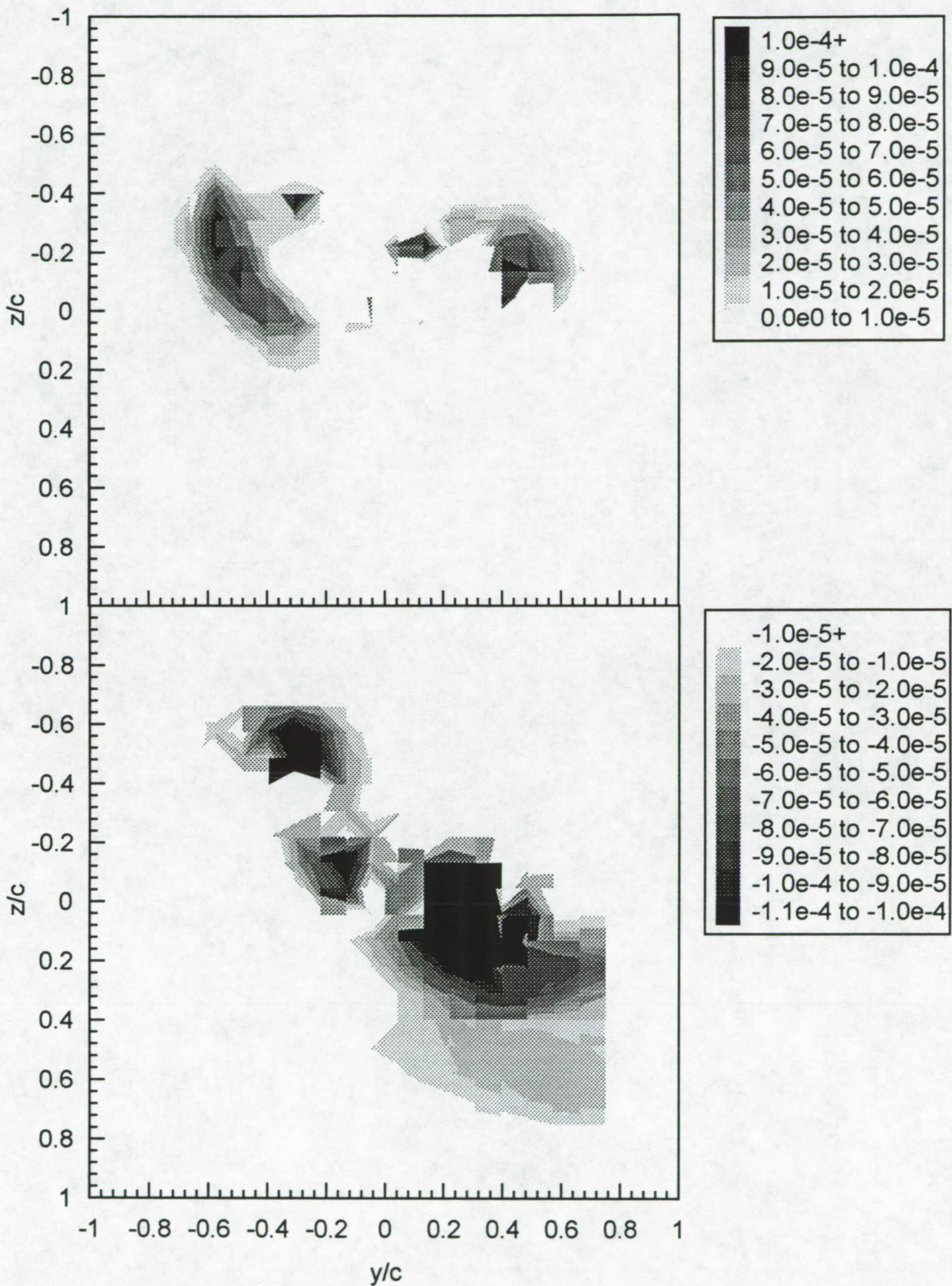


Figure 3.64 Contours of crossflow shear stress  $\tau_c/U_{ref}^2$  at  $X/c=22.6$ . (b)  $\Delta/c=0.0625$ . Upper figure - positive stress, lower figure - negative stress.



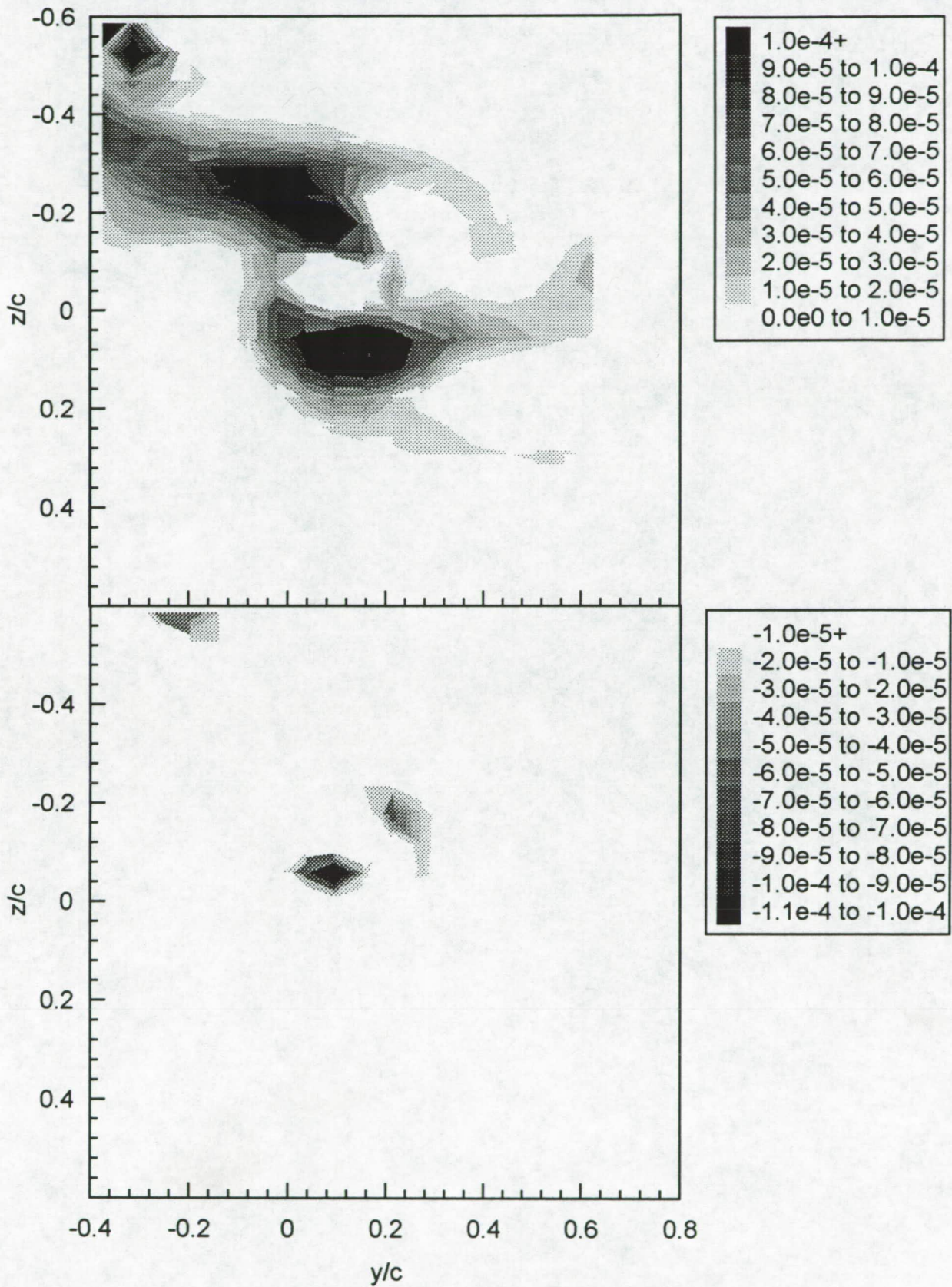


Figure 3.65 Contours of turbulence kinetic energy production  $Pc/U_{ref}^3$  at  $X/c=22.6$ .  $\Delta/c=-0.0625$ . Fine grid. Upper figure - positive production, lower figure - negative production.



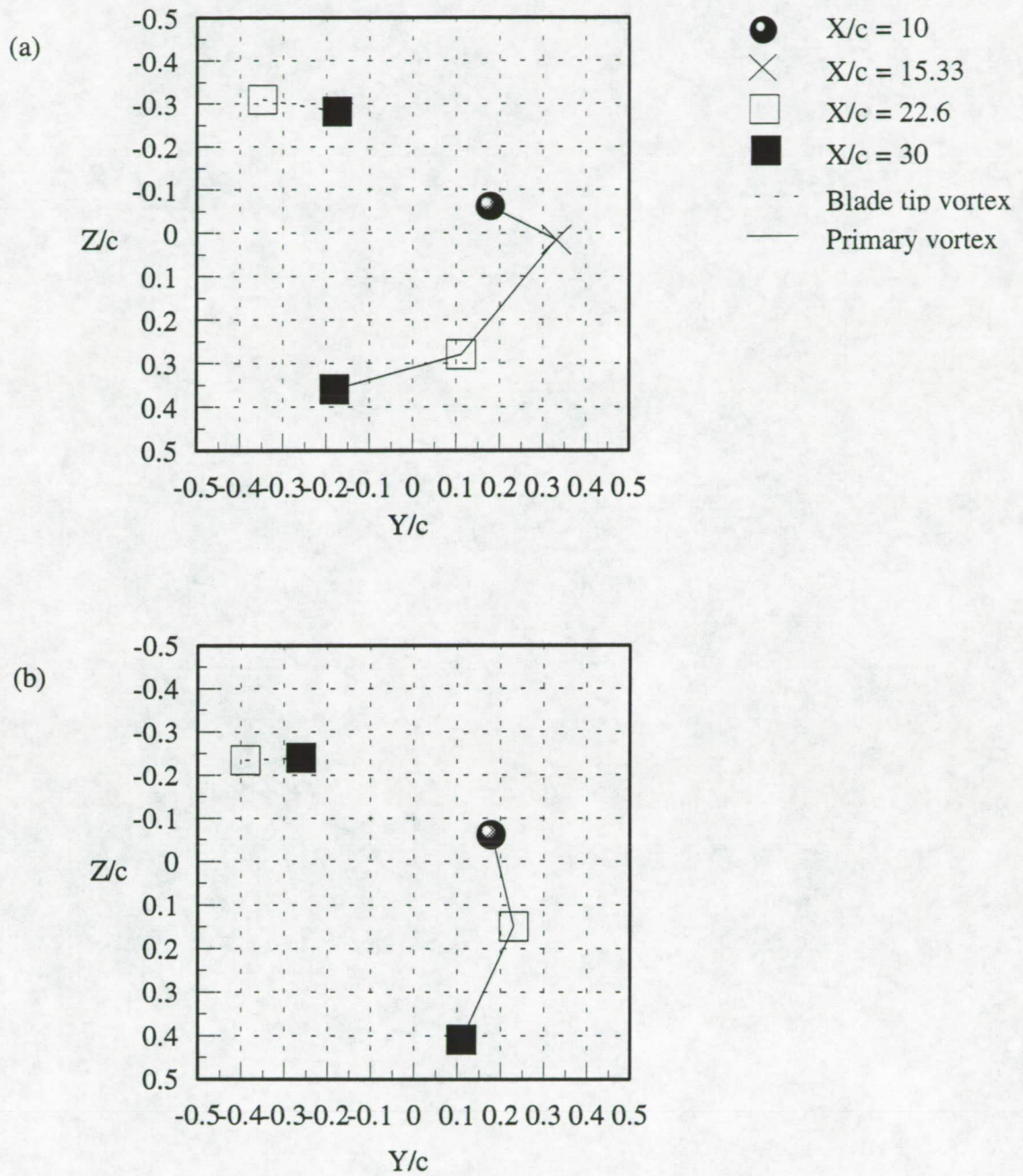


Figure 3.66 Locations of the primary and blade tip vortex centers as functions of  $X$   
 (a)  $\Delta/c = -0.0625$ , (b)  $\Delta/c = 0.0625$ .

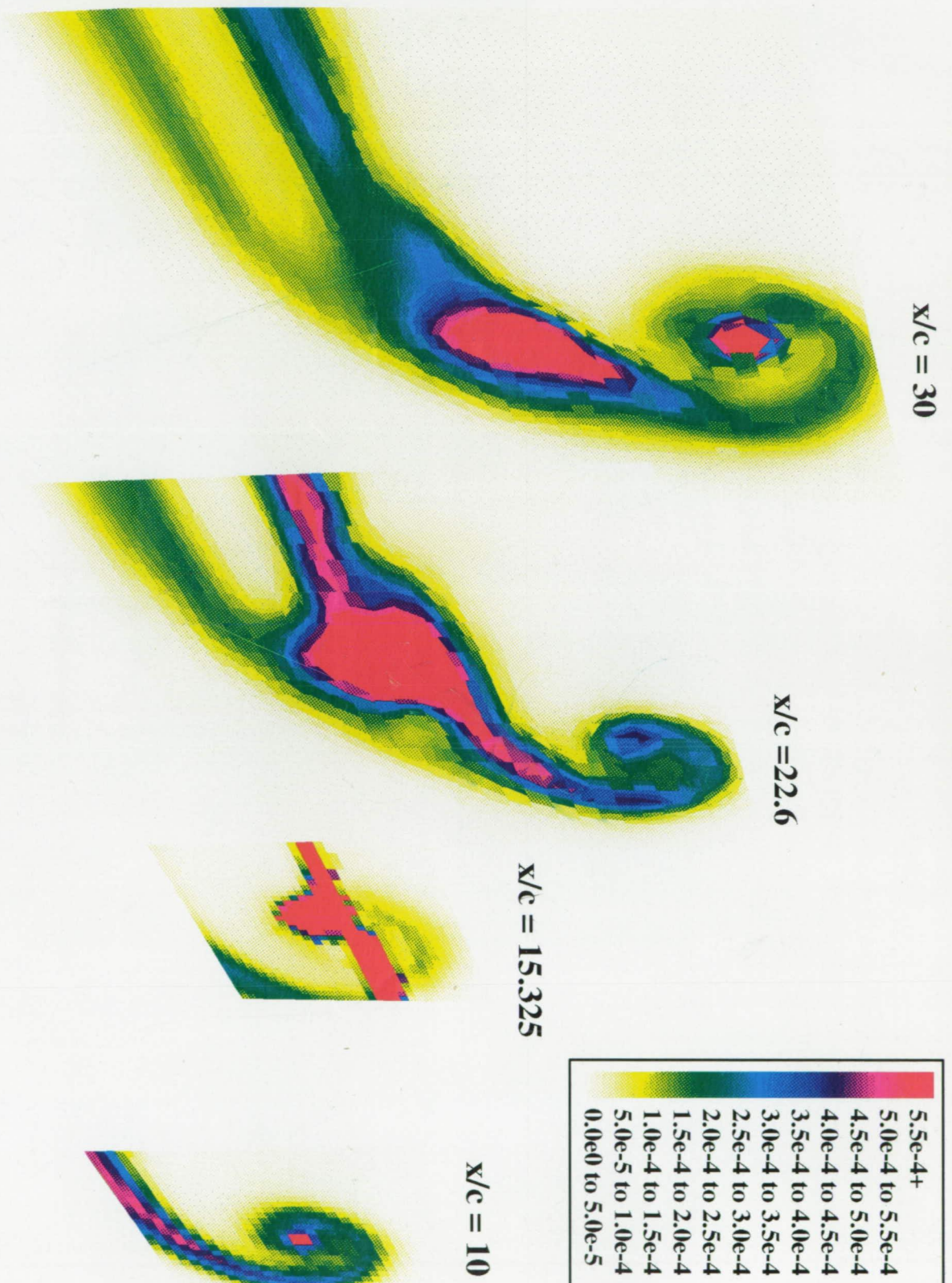


Figure 3.67 Contours of turbulence kinetic energy for all streamwise locations,  $Mc=0.0625$



$x/c = 30$

$x/c = 22.6$



$x/c = 10$

Figure 3.68 Contours of turbulence kinetic energy for all streamwise locations,  $Mc=0.0625$ .



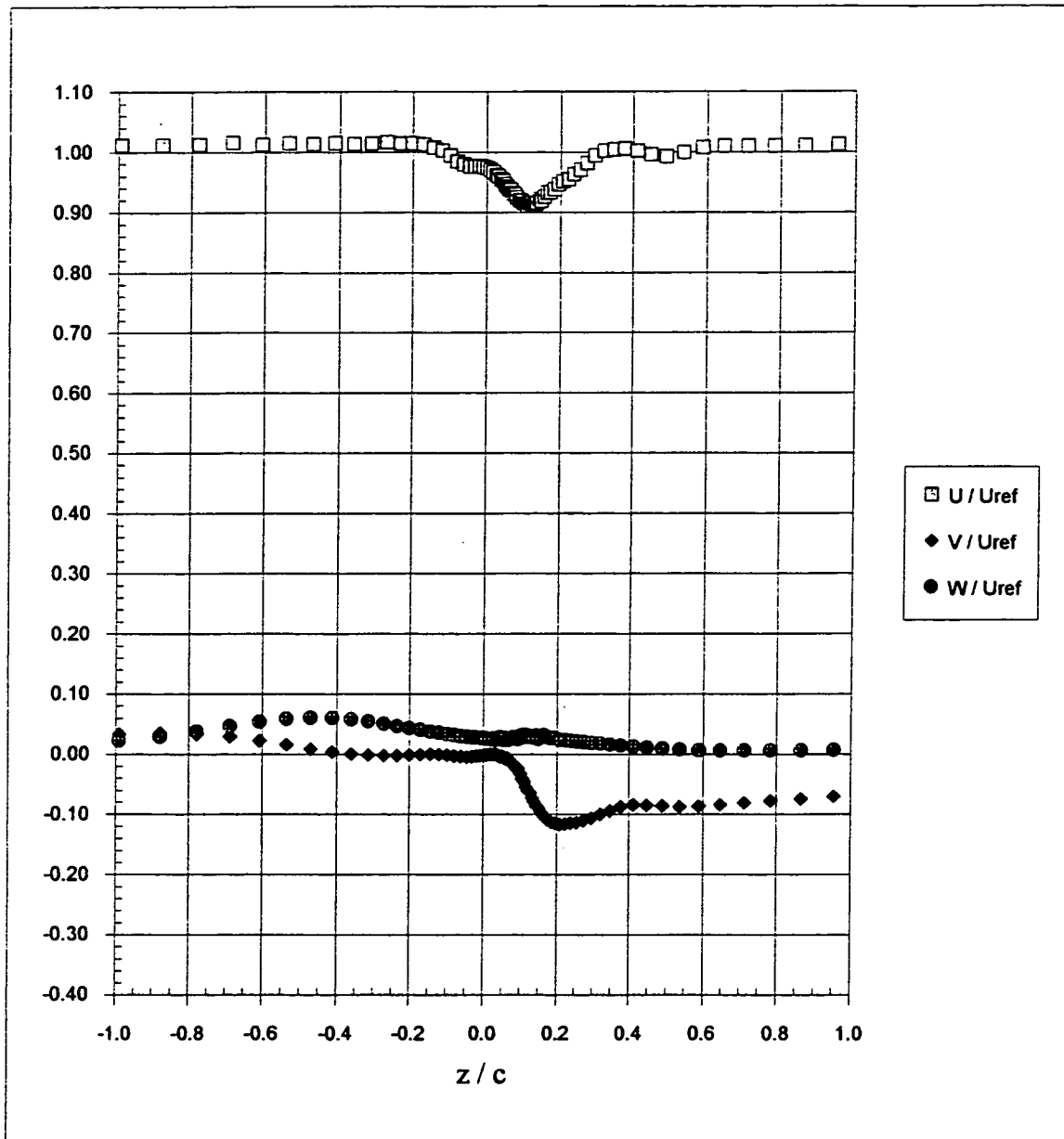


Figure 3.69 Mean velocity profiles through the primary vortex core at  $X/c=22.6$ . (a)  $\Delta/c=-0.0625$ .

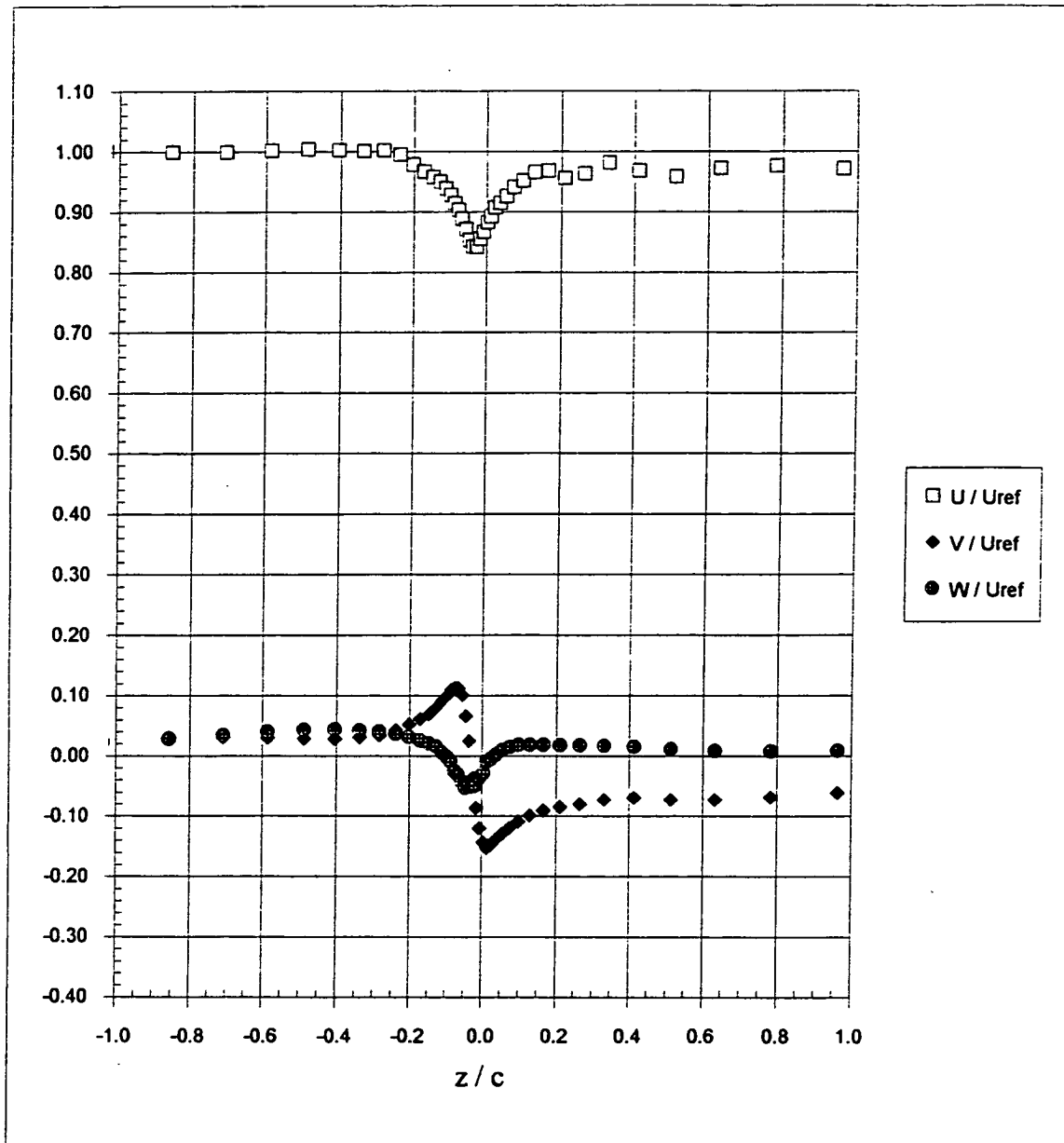


Figure 3.69 Mean velocity profiles through the primary vortex core at  $X/c=22.6$ . (b)  $\Delta/c=0.0625$ .

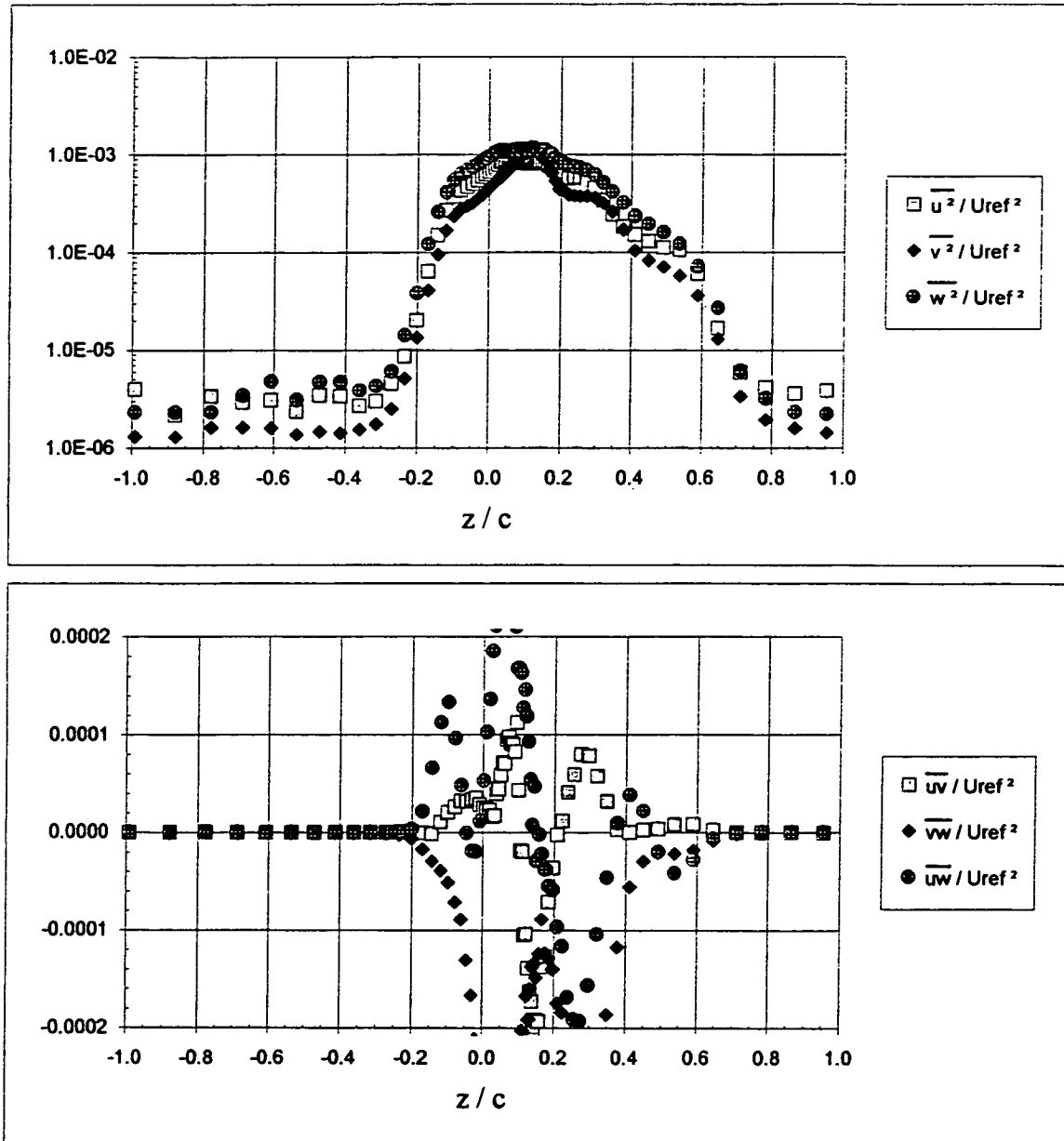


Figure 3.70 Turbulence stress profiles through the primary vortex core at  $X/c=22.6$ . (a)  $\Delta/c=-0.0625$ .



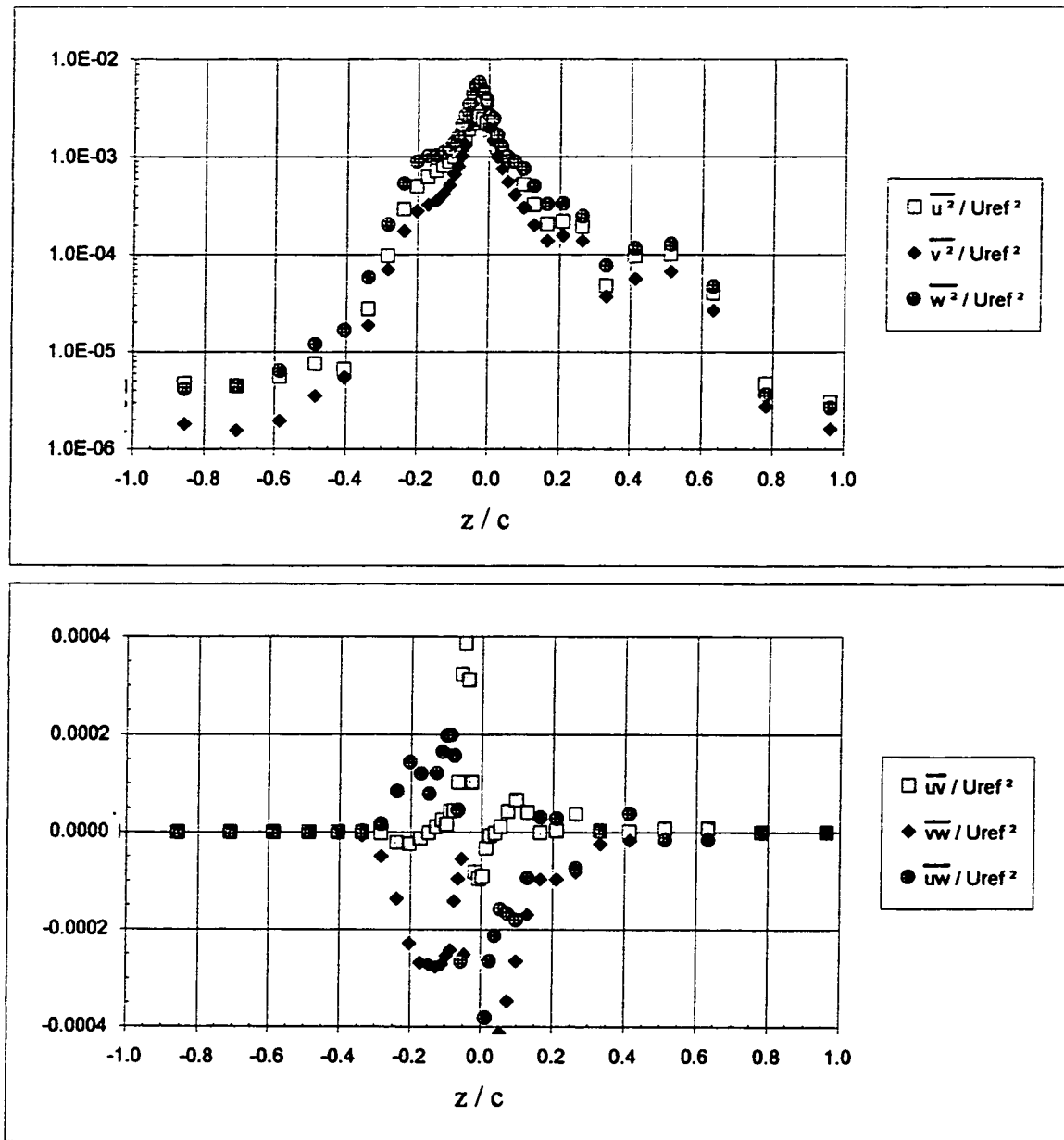


Figure 3.70 Turbulence stress profiles through the primary vortex core at  $X/c=22.6$ . (b)  $\Delta/c=0.0625$ .

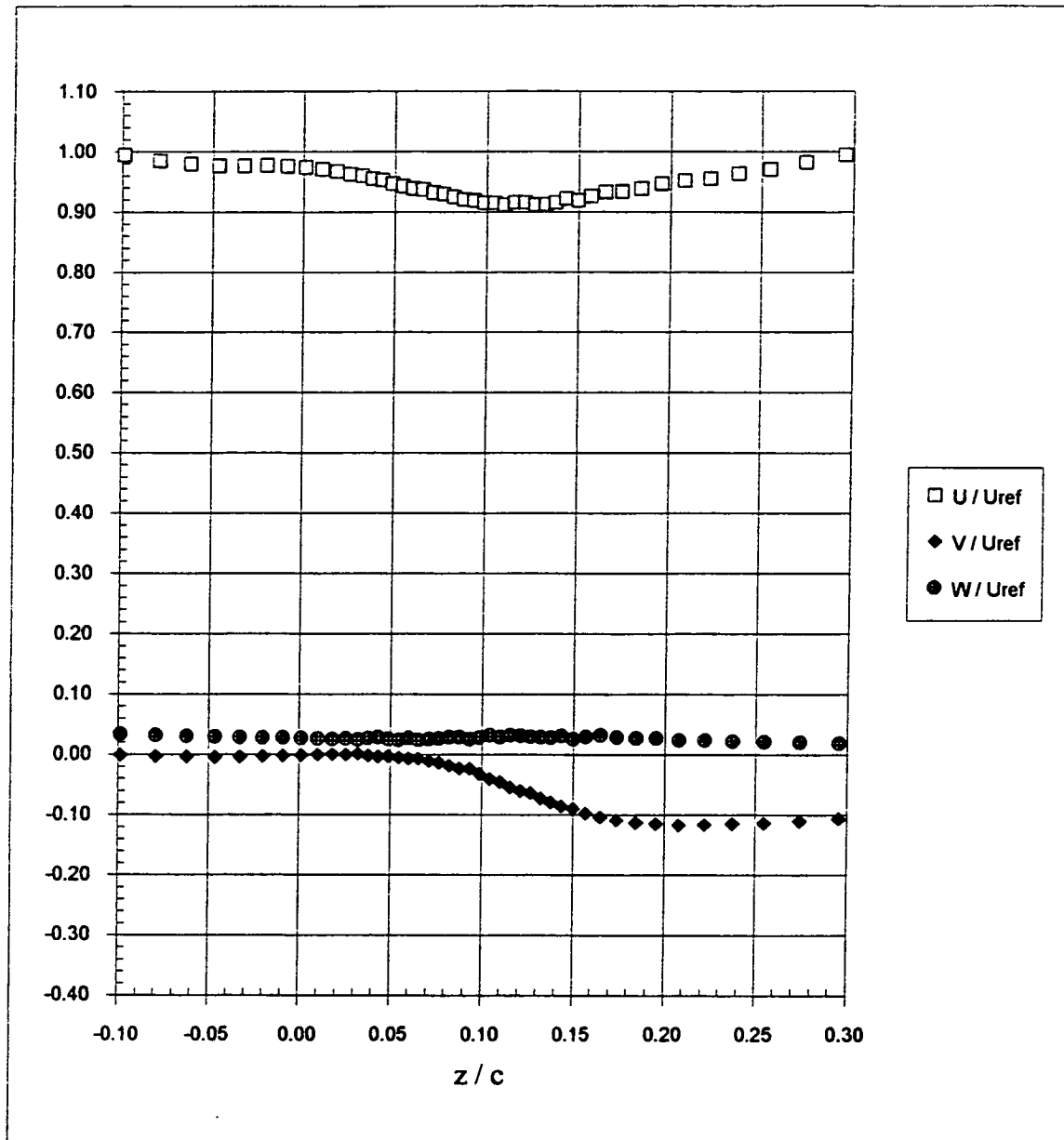


Figure 3.71 Mean velocity profiles in the vicinity of the primary vortex core at  $X/c=22.6$ .  
(a)  $\Delta/c=-0.0625$ .

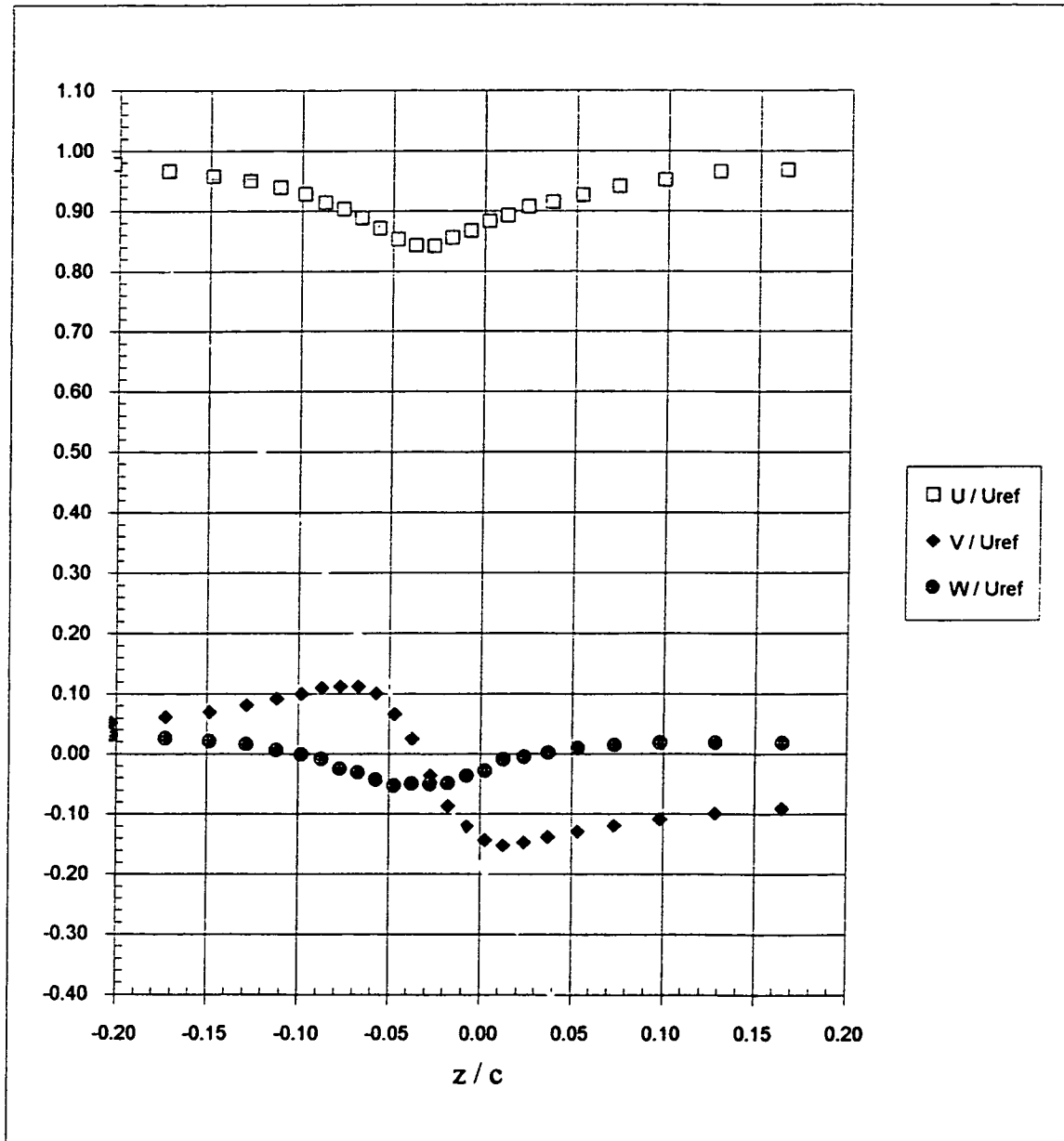


Figure 3.71 Mean velocity profiles in the vicinity of the primary vortex core at  $X/c=22.6$ .  
(b)  $\Delta/c=0.0625$ .



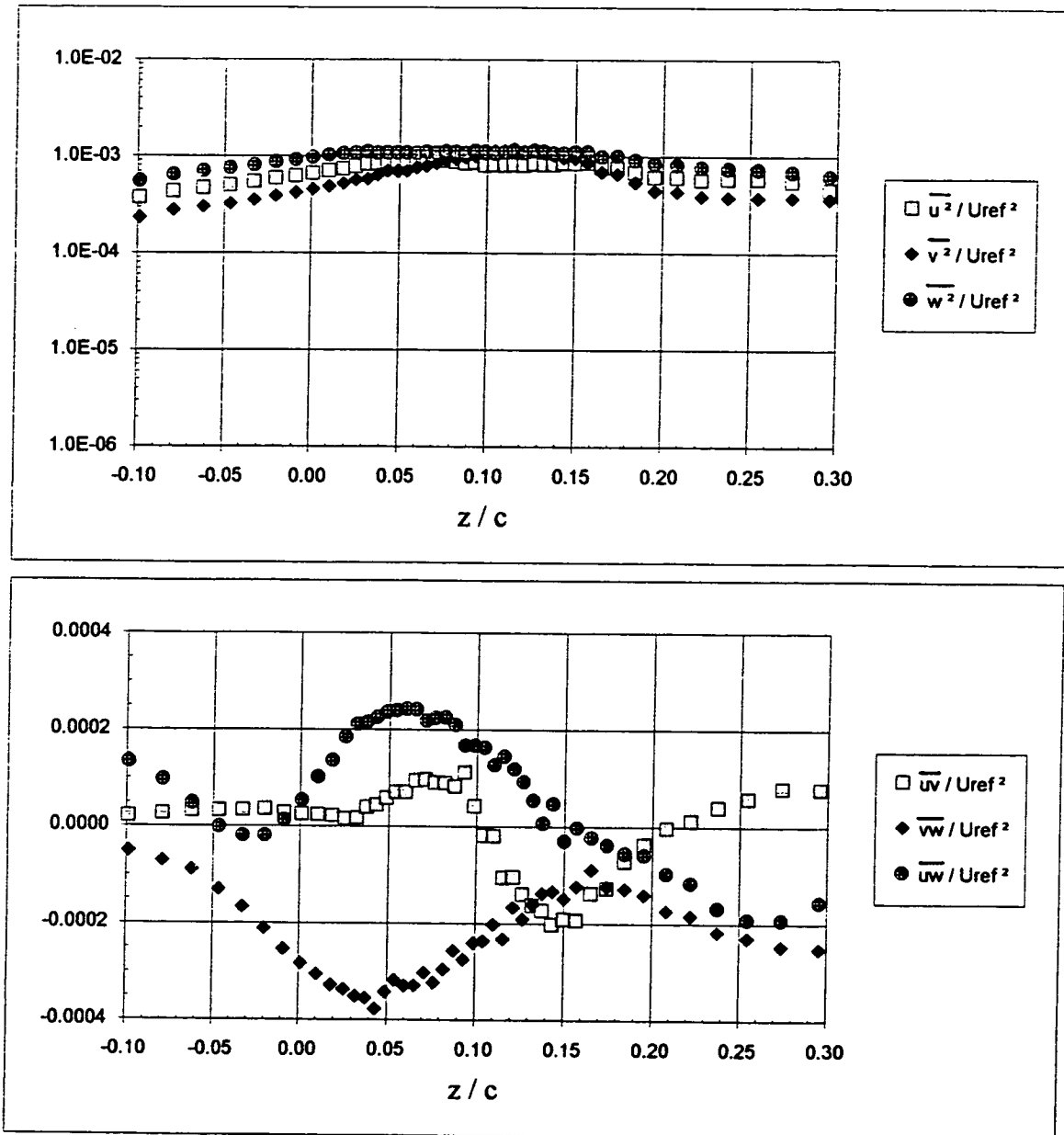


Figure 3.72 Turbulence stress profiles in the vicinity of the primary vortex core at  $X/c=22.6$ . (a)  $\Delta/c=-0.0625$ .

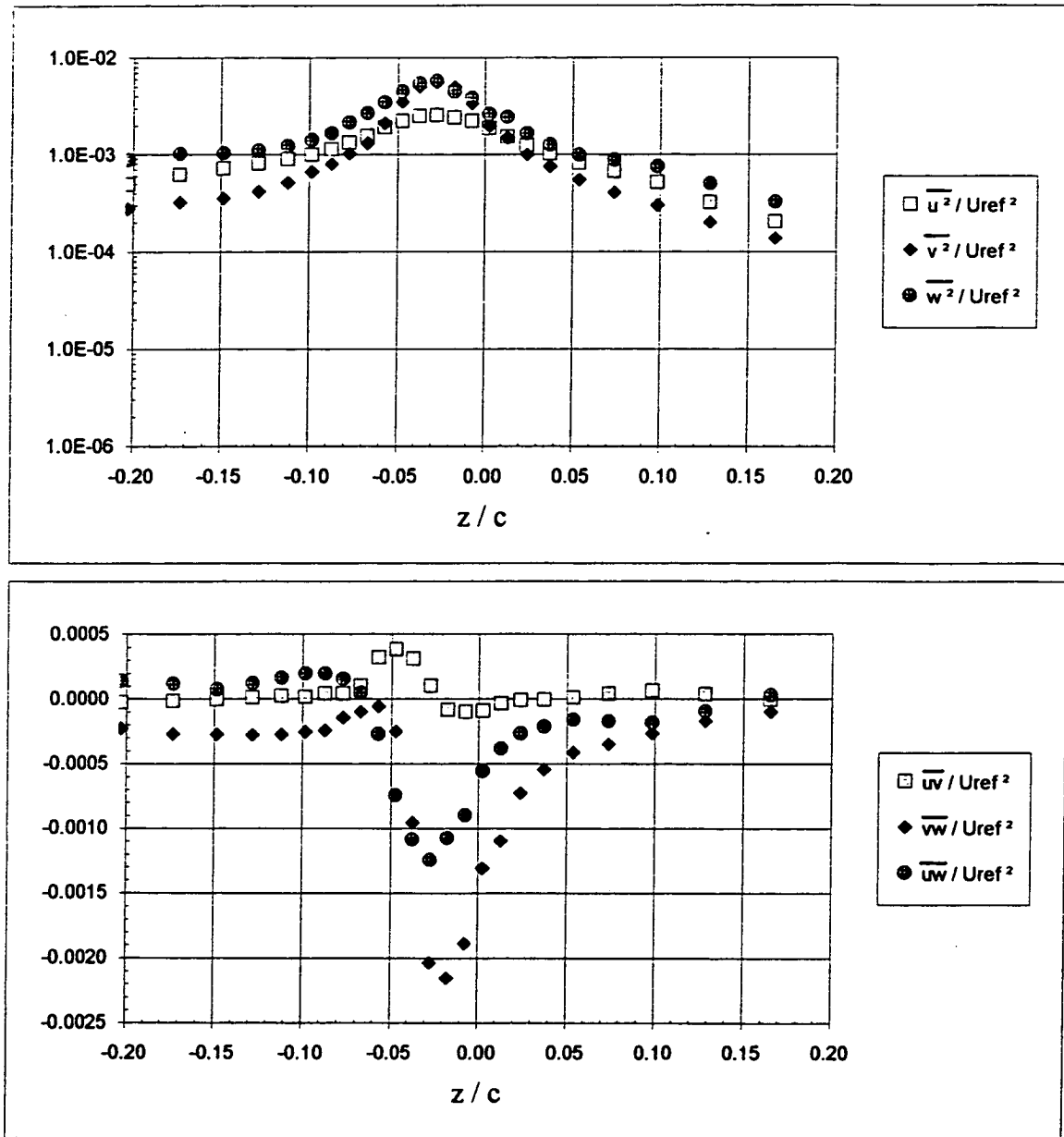


Figure 3.72 Turbulence stress profiles in the vicinity of the primary vortex core at  $X/c=22.6$ . (b)  $\Delta/c=0.0625$ .

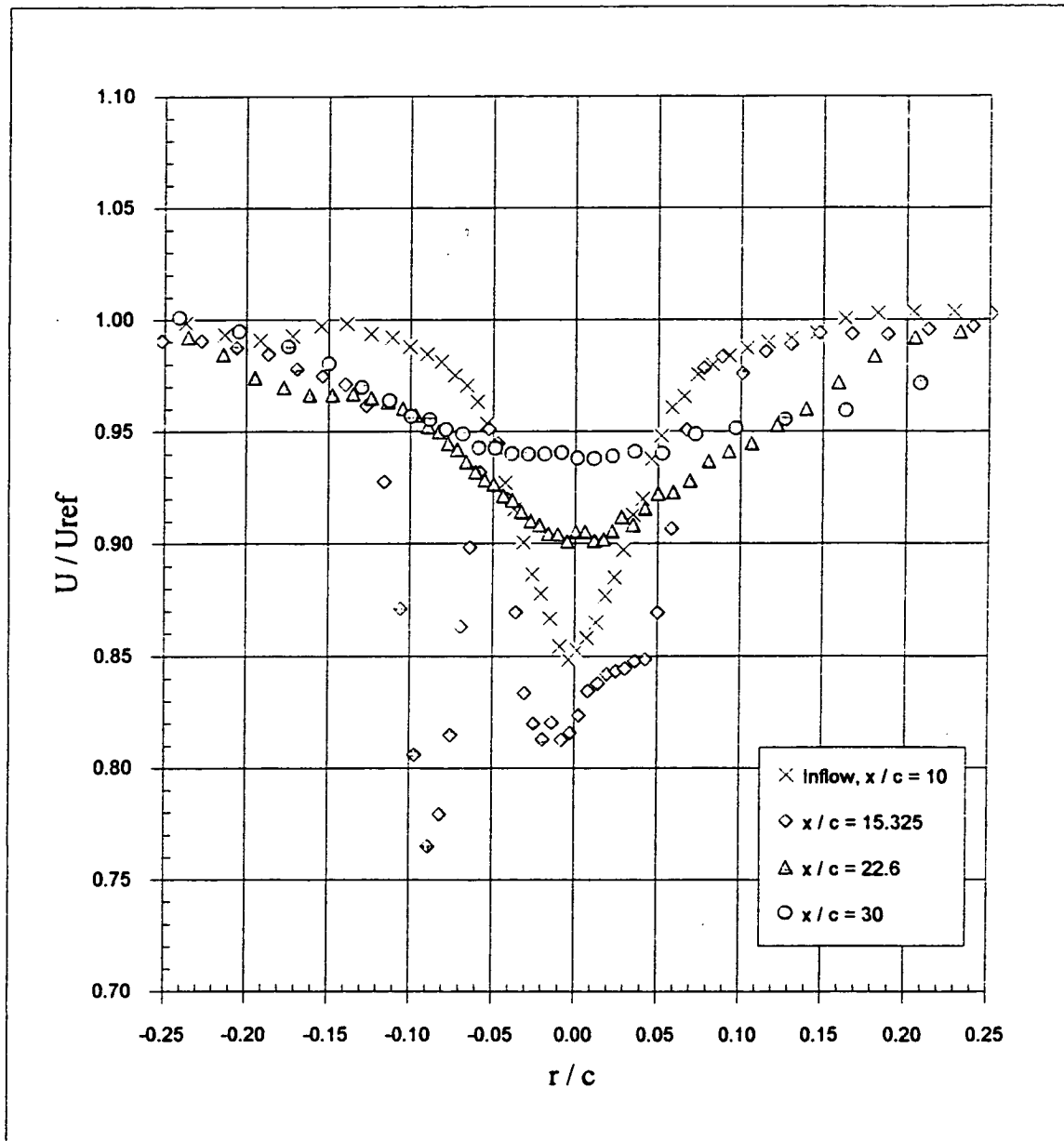


Figure 3.73 Development of the core axial velocity profile with  $X$ . Note that ' $r$ ' represents radial distance from the core center. (a)  $\Delta/c = -0.0625$ .



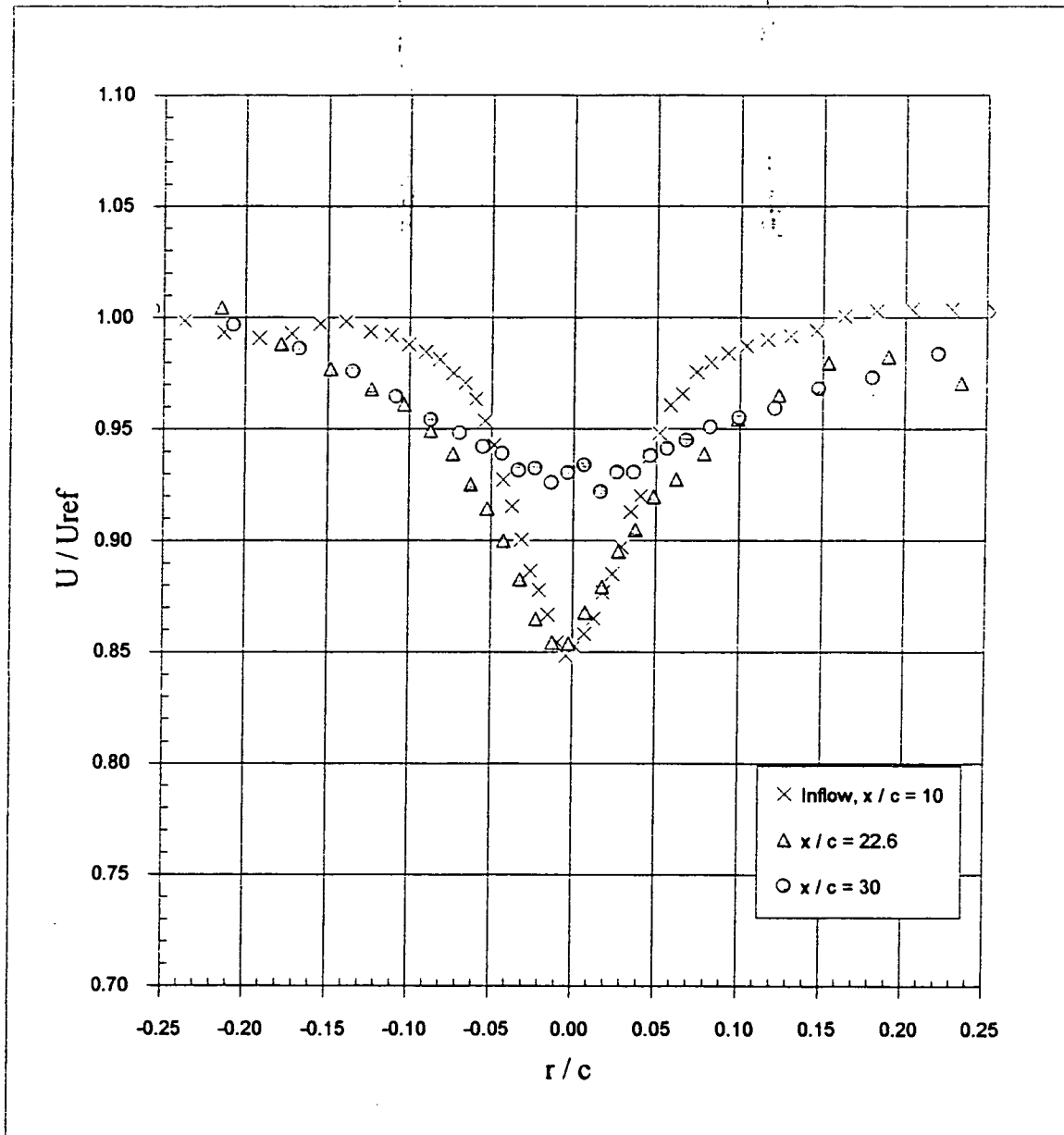


Figure 3.73 Development of the core axial velocity profile with  $X$ . Note that ' $r$ ' represents radial distance from the core center. (b)  $\Delta/c=0.0625$ .

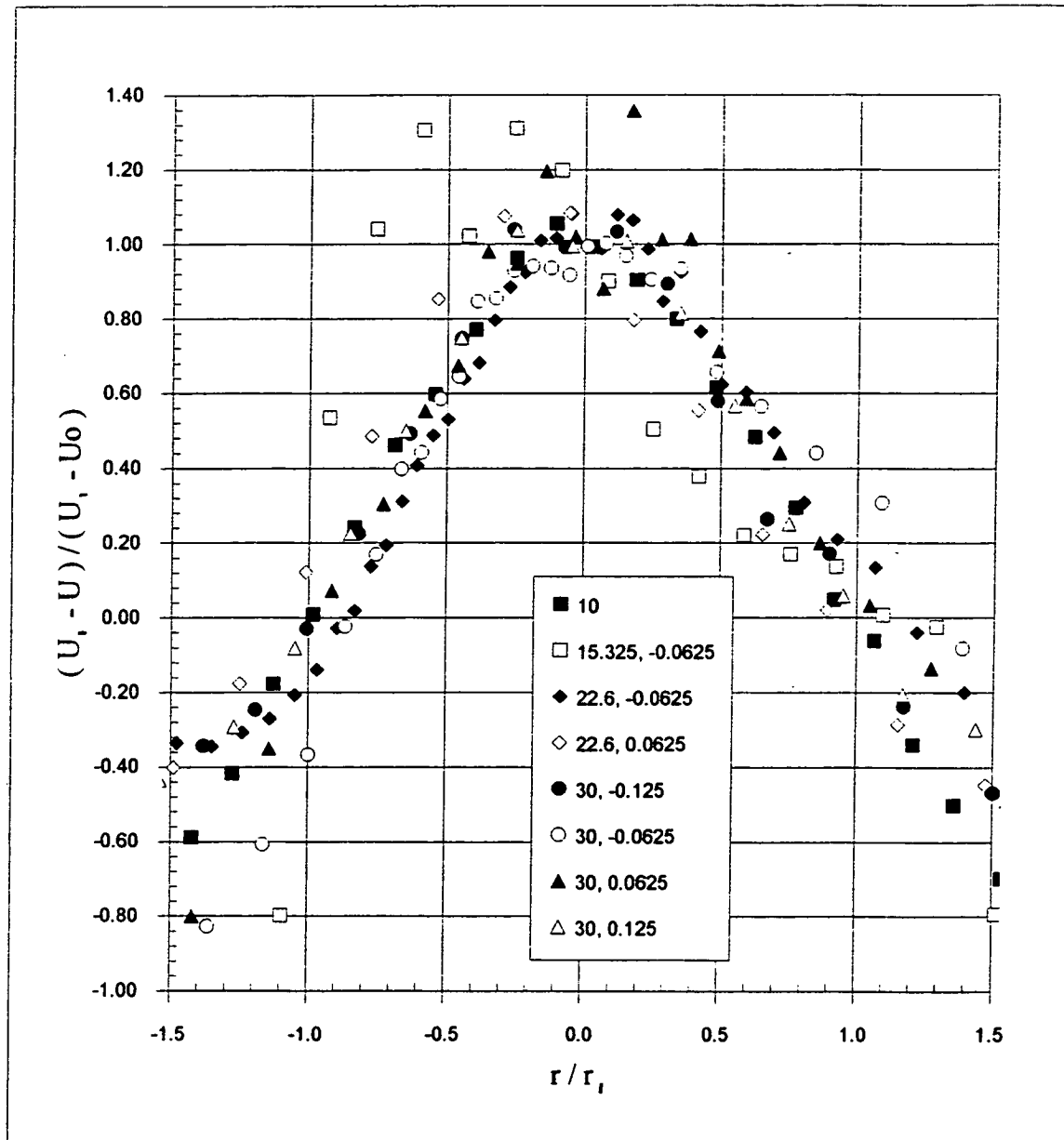


Figure 3.74 All core axial velocity profiles normalized on axial velocity at core center  $U_0$ , at core edge  $U_i$  and on core radius  $r_i$ . Note that 'r' represents radial distance from the core center. Numbers in legend are respectively  $X/c$  and  $\Delta/c$ .

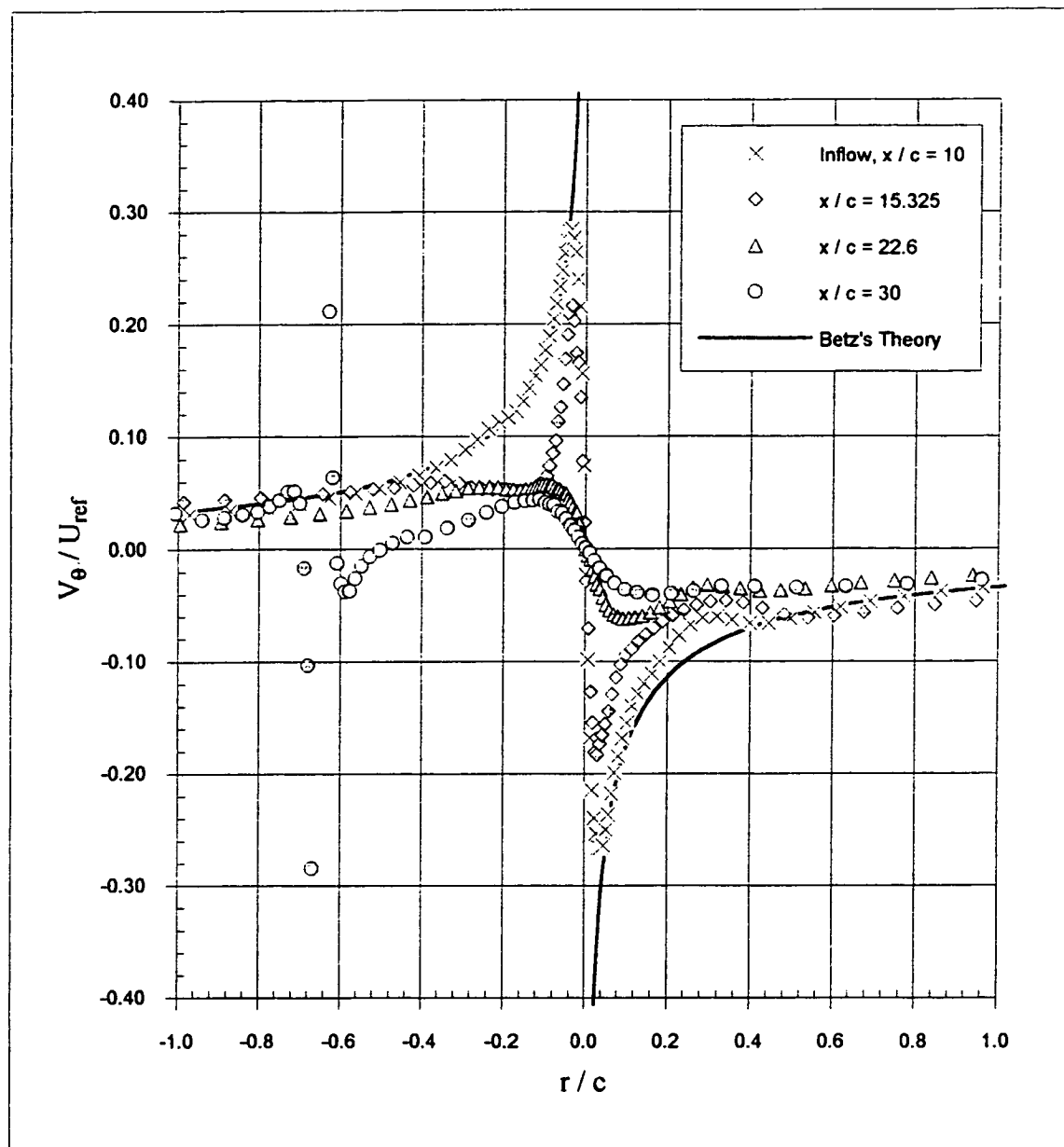


Figure 3.75 Tangential velocity profiles for  $\Delta/c = -0.0625$  as a function of  $X/c$  after subtracting effects of blade tip vortex. Note that 'r' is radial distance from core center. (a) Whole profile.



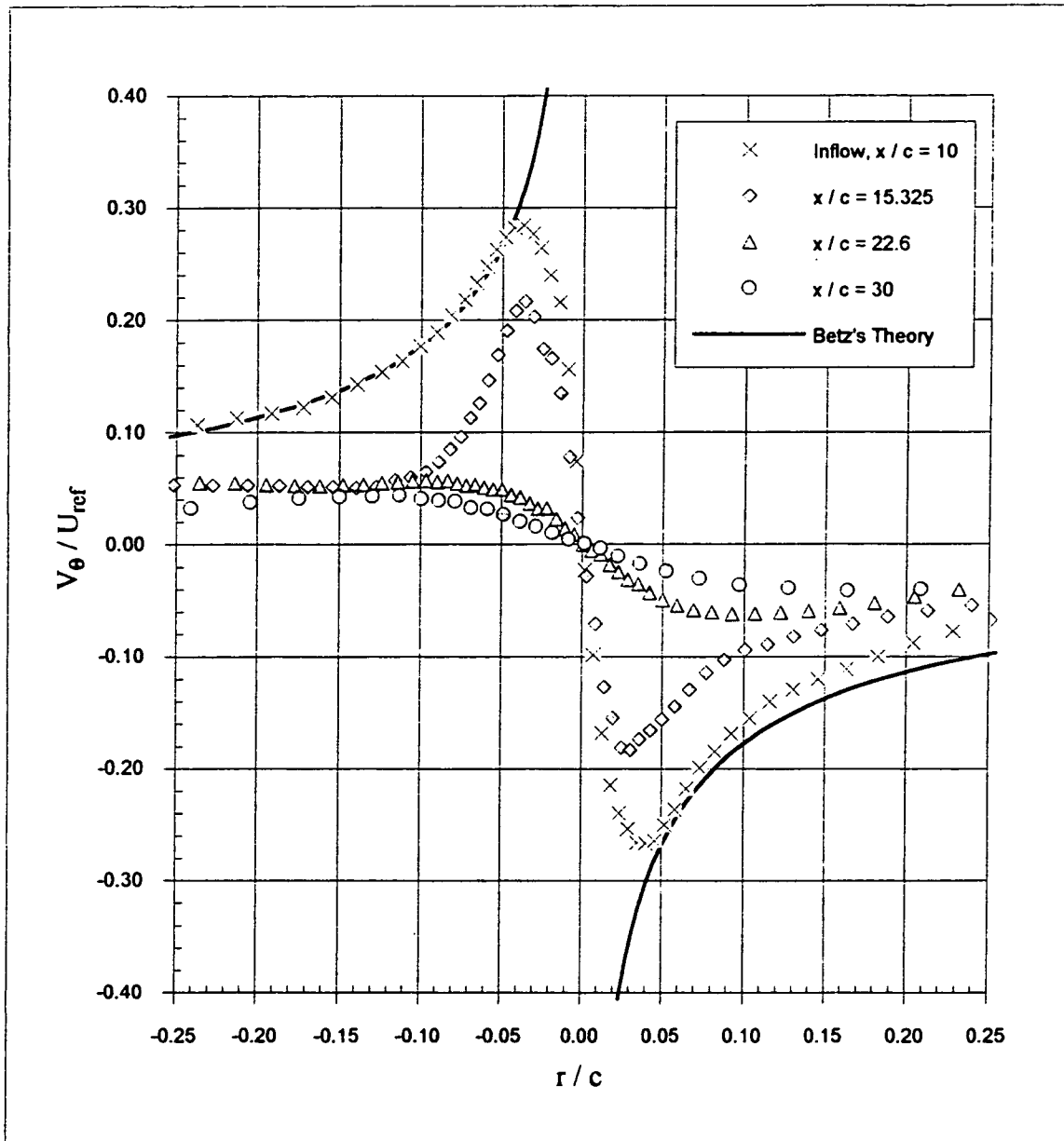


Figure 3.75 Tangential velocity profiles for  $\Delta/c = -0.0625$  as a function of  $X/c$  after subtracting effects of blade tip vortex. Note that 'r' is radial distance from core center. (b) Core region.

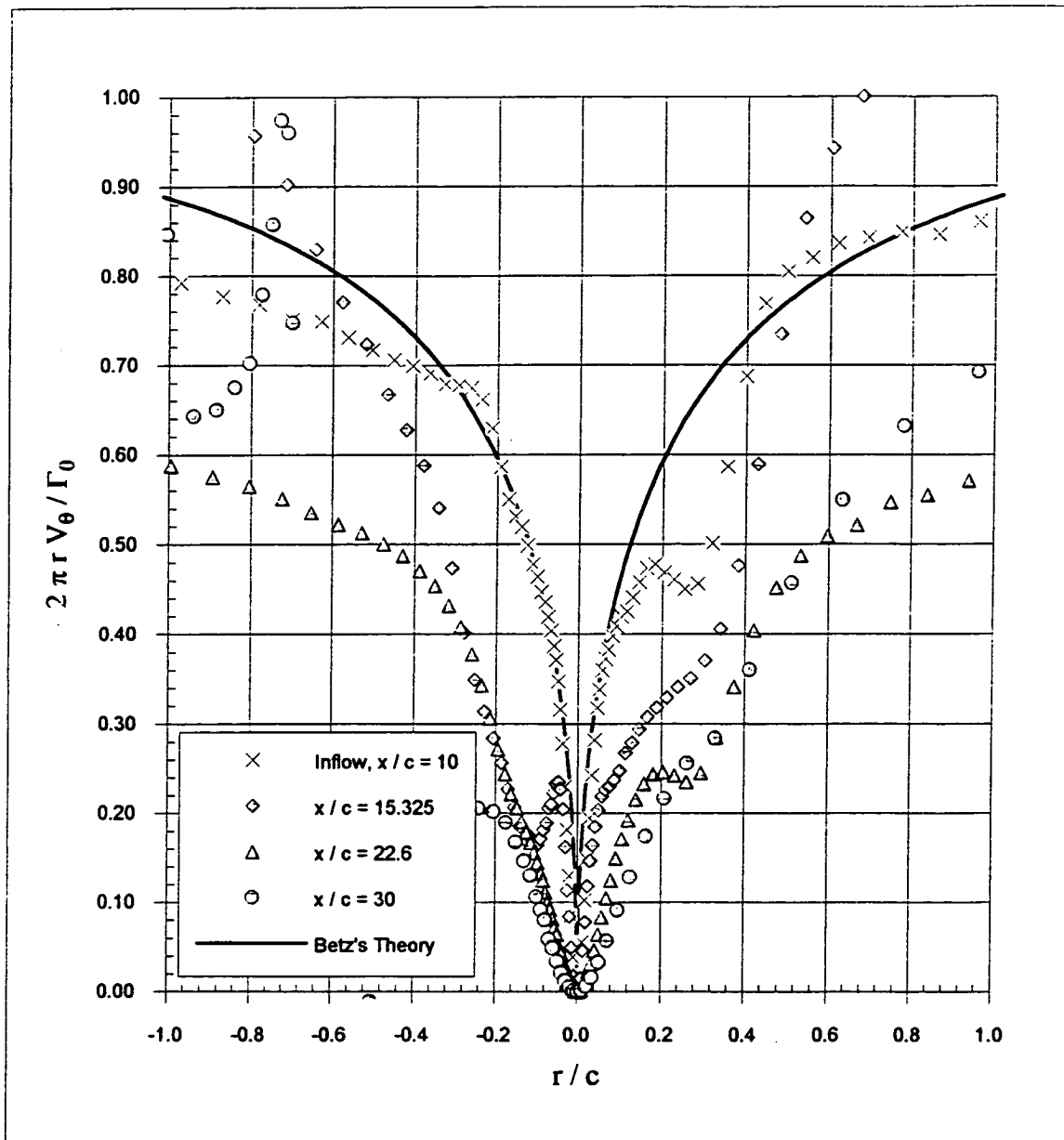


Figure 3.76 Circulation profiles for  $\Delta/c = -0.0625$  as a function of  $X/c$  after subtracting effects of blade tip vortex. Note that 'r' is radial distance from core center. (a) Whole profile.

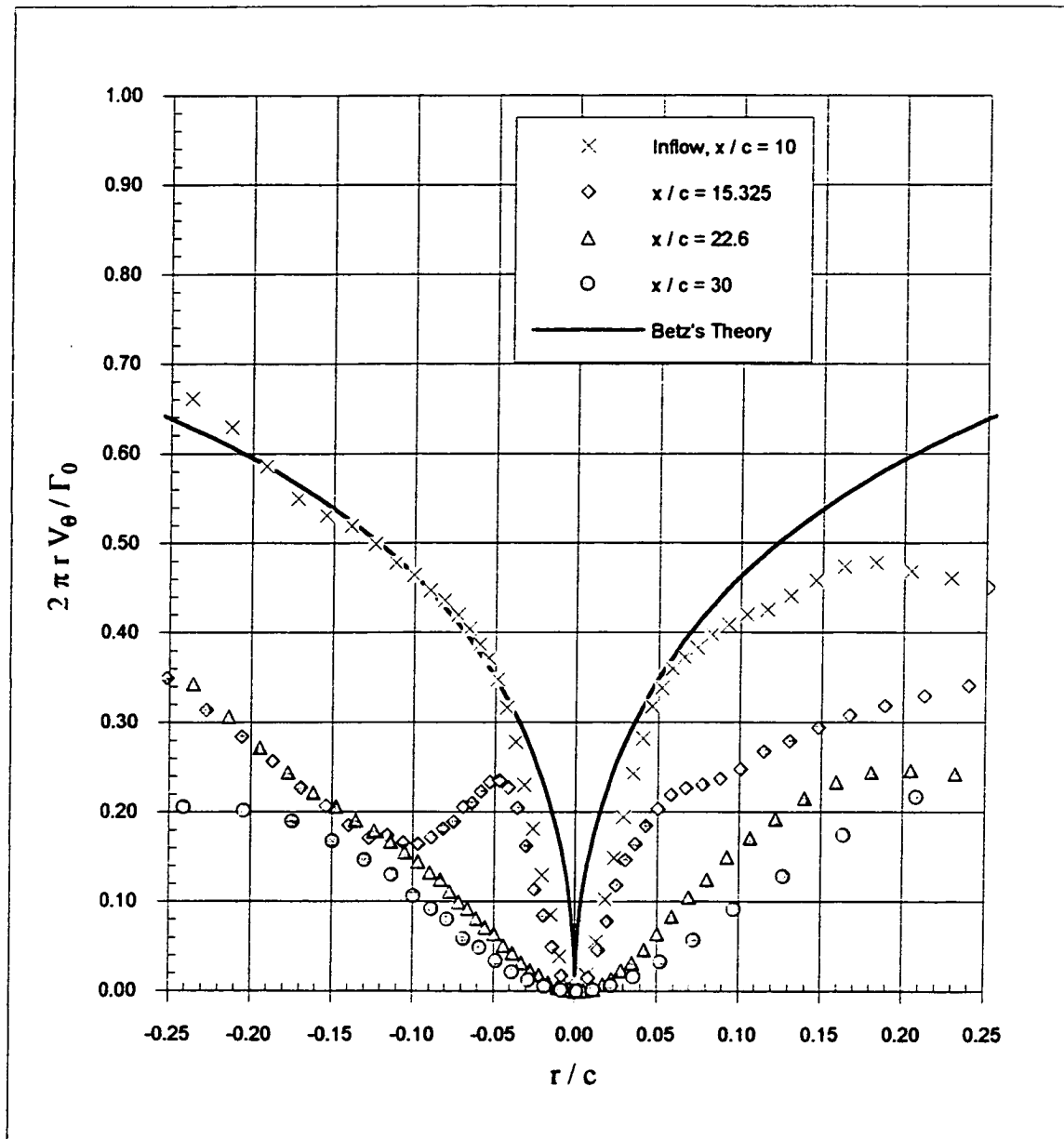


Figure 3.76 Circulation profiles for  $\Delta/c = -0.0625$  as a function of  $X/c$  after subtracting effects of blade tip vortex. Note that 'r' is radial distance from core center. (b) Core region.



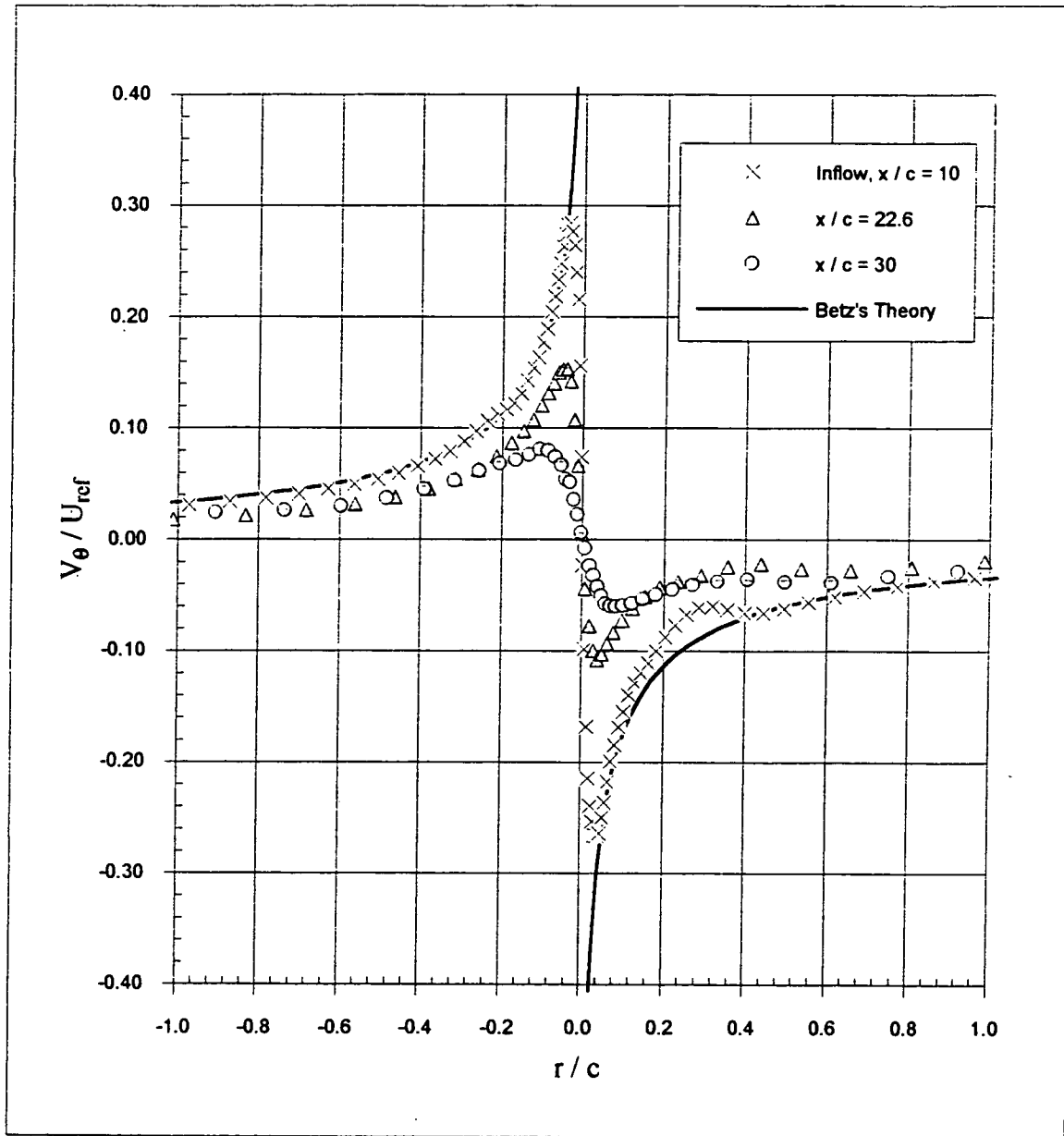


Figure 3.77 Tangential velocity profiles for  $\Delta/c=0.0625$  as a function of  $X/c$  after subtracting effects of blade tip vortex. Note that 'r' is radial distance from core center. (a) Whole profile.

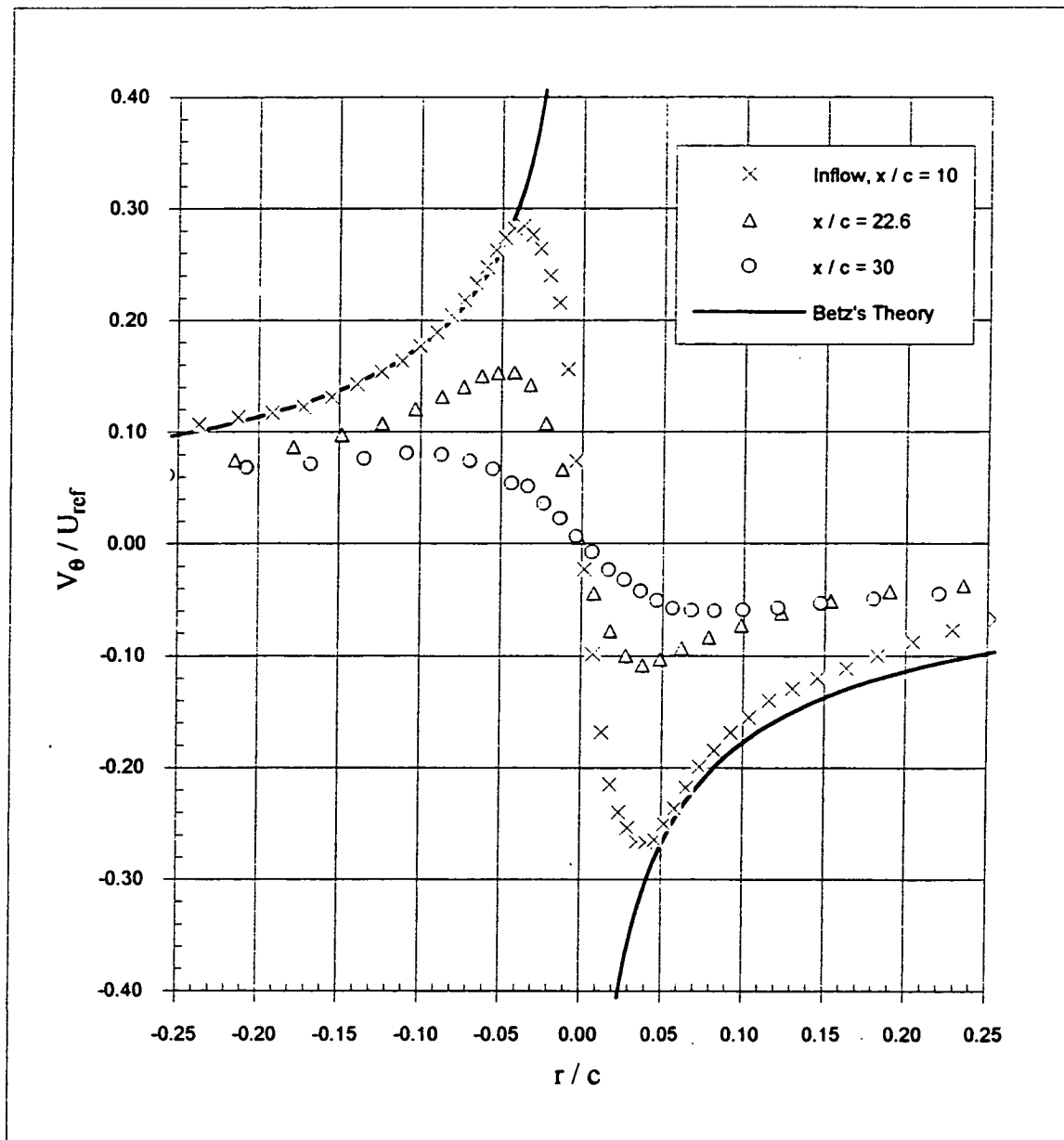


Figure 3.77 Tangential velocity profiles for  $\Delta/c=0.0625$  as a function of  $X/c$  after subtracting effects of blade tip vortex. Note that 'r' is radial distance from core center. (b) Core region.

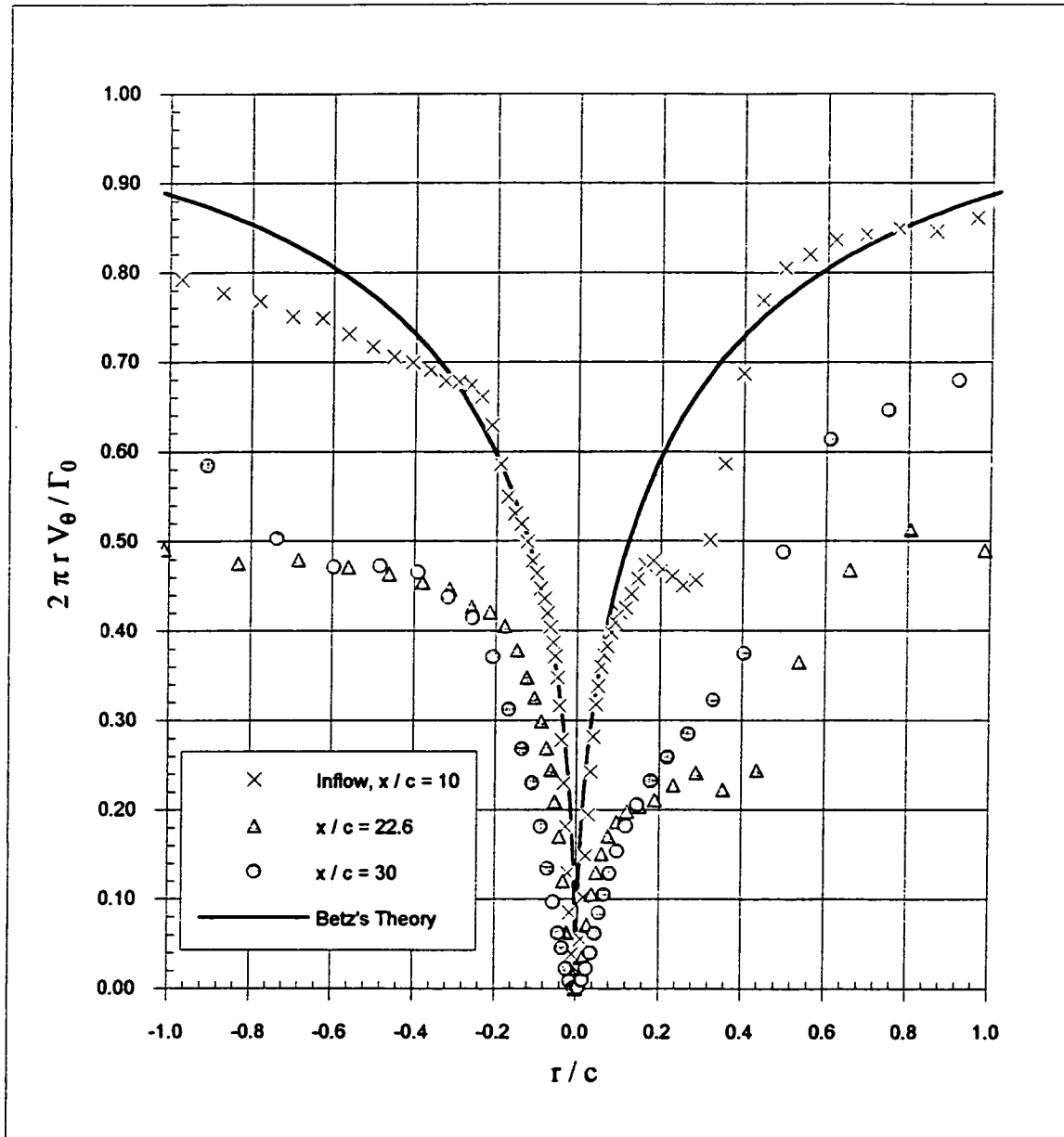


Figure 3.78 Circulation profiles for  $\Delta/c=0.0625$  as a function of  $X/c$  after subtracting effects of blade tip vortex. Note that 'r' is radial distance from core center. (a) Whole profile.



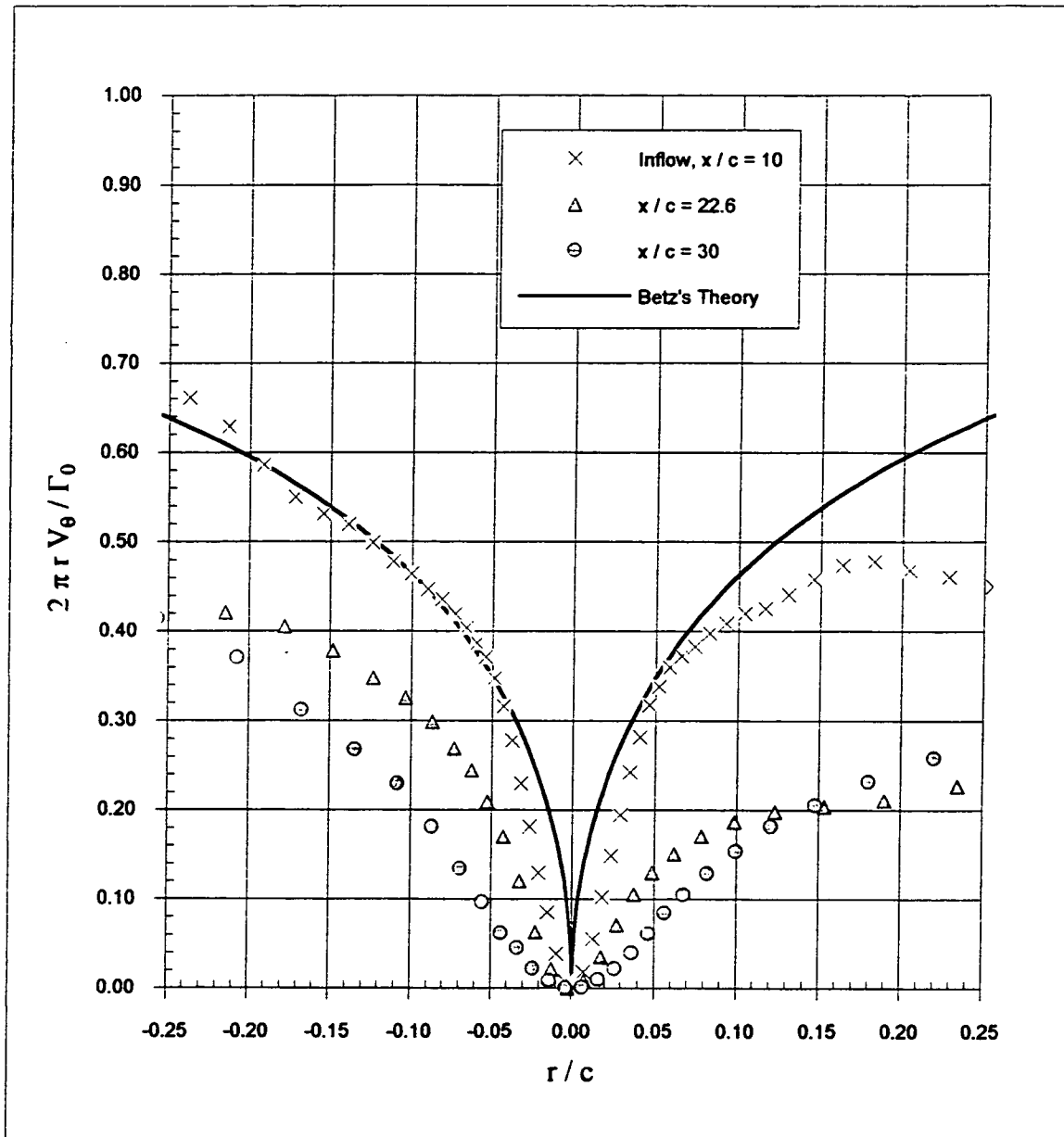


Figure 3.78 Circulation profiles for  $\Delta/c=0.0625$  as a function of  $X/c$  after subtracting effects of blade tip vortex. Note that 'r' is radial distance from core center. (b) Core region.

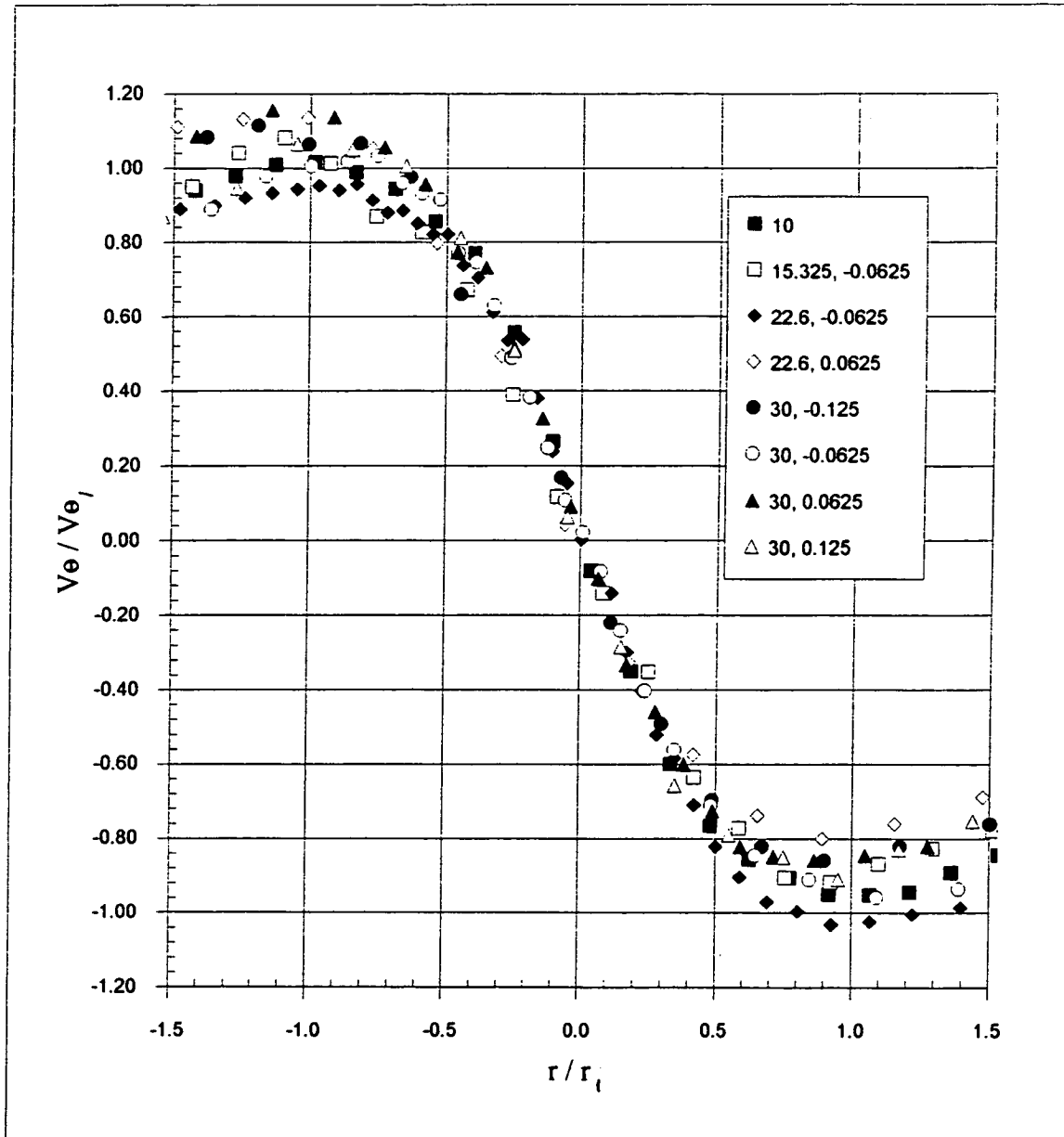


Figure 3.79 All core tangential velocity profiles normalized on peak tangential velocity  $v_{\theta 1}$  and on core radius  $r_1$ . Note that 'r' represents radial distance from the core center. Numbers in legend are respectively  $X/c$  and  $\Delta/c$ .

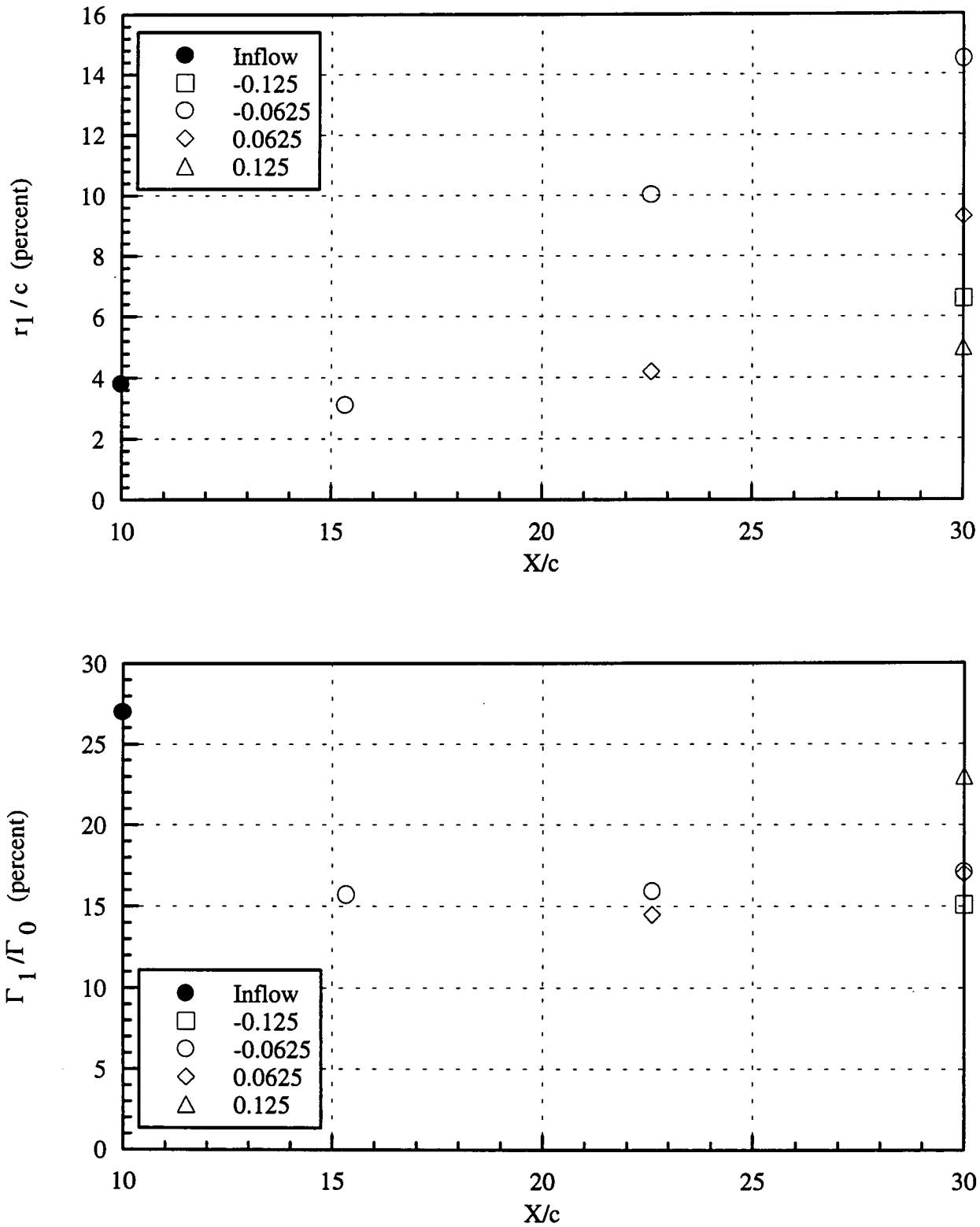


Figure 3.80 Variation of parameters of primary vortex core with  $X$ . (a) Core radius, (b) core circulation. Numbers in legends refer to blade-vortex separation  $\Delta/c$ .



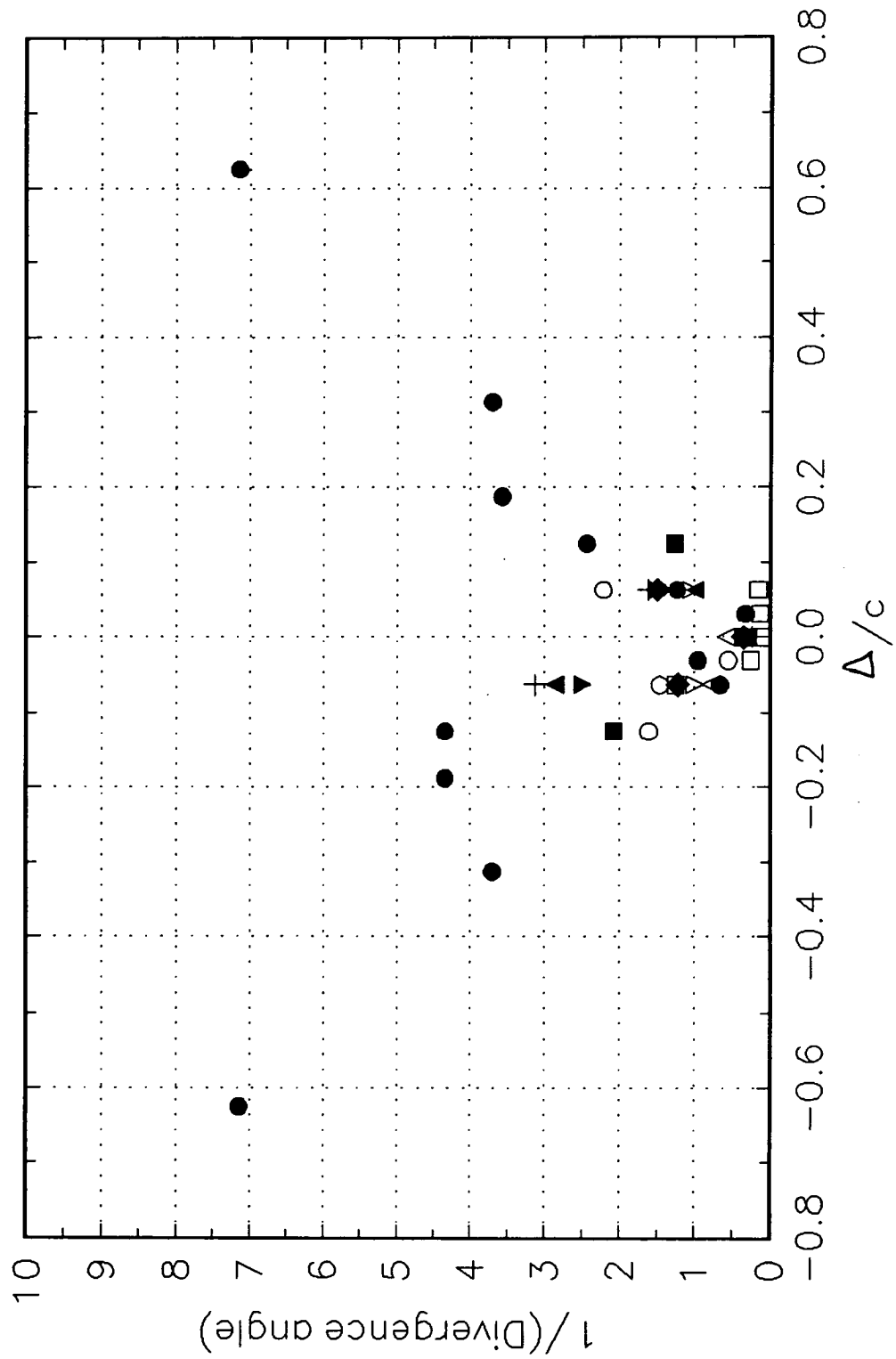


Figure 3.81 Reciprocal of divergence angle of bubble stream marking core plotted vs. blade-vortex separation  $\Delta/c$ . Numbers in legend are, respectively, angle of attack of vortex generator, angle of attack of blade, chord Reynolds number.

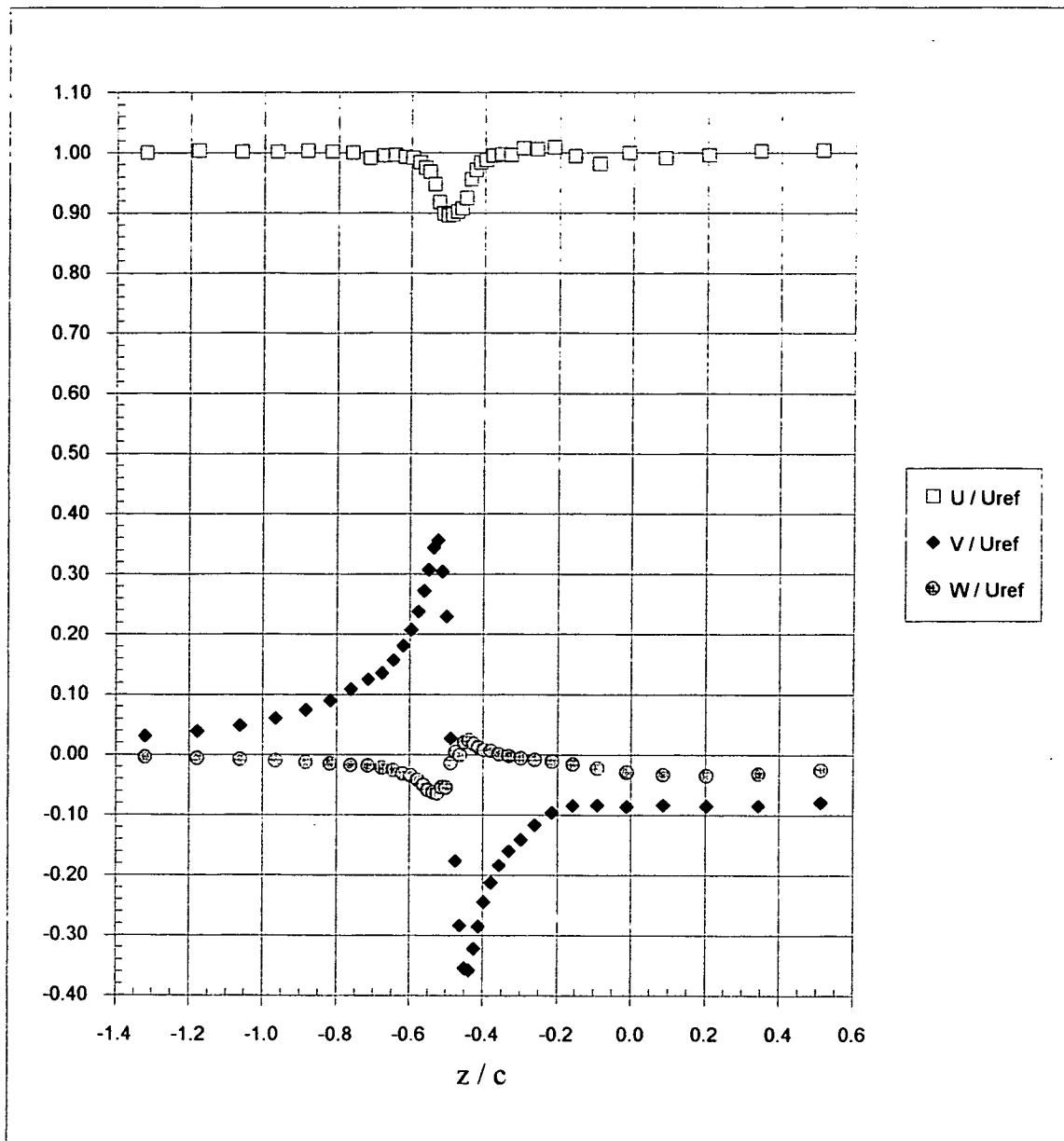


Figure 3.82 Mean velocity profiles through the blade tip vortex core at  $X/c=22.6$ .  $\Delta/c=-0.0625$ .

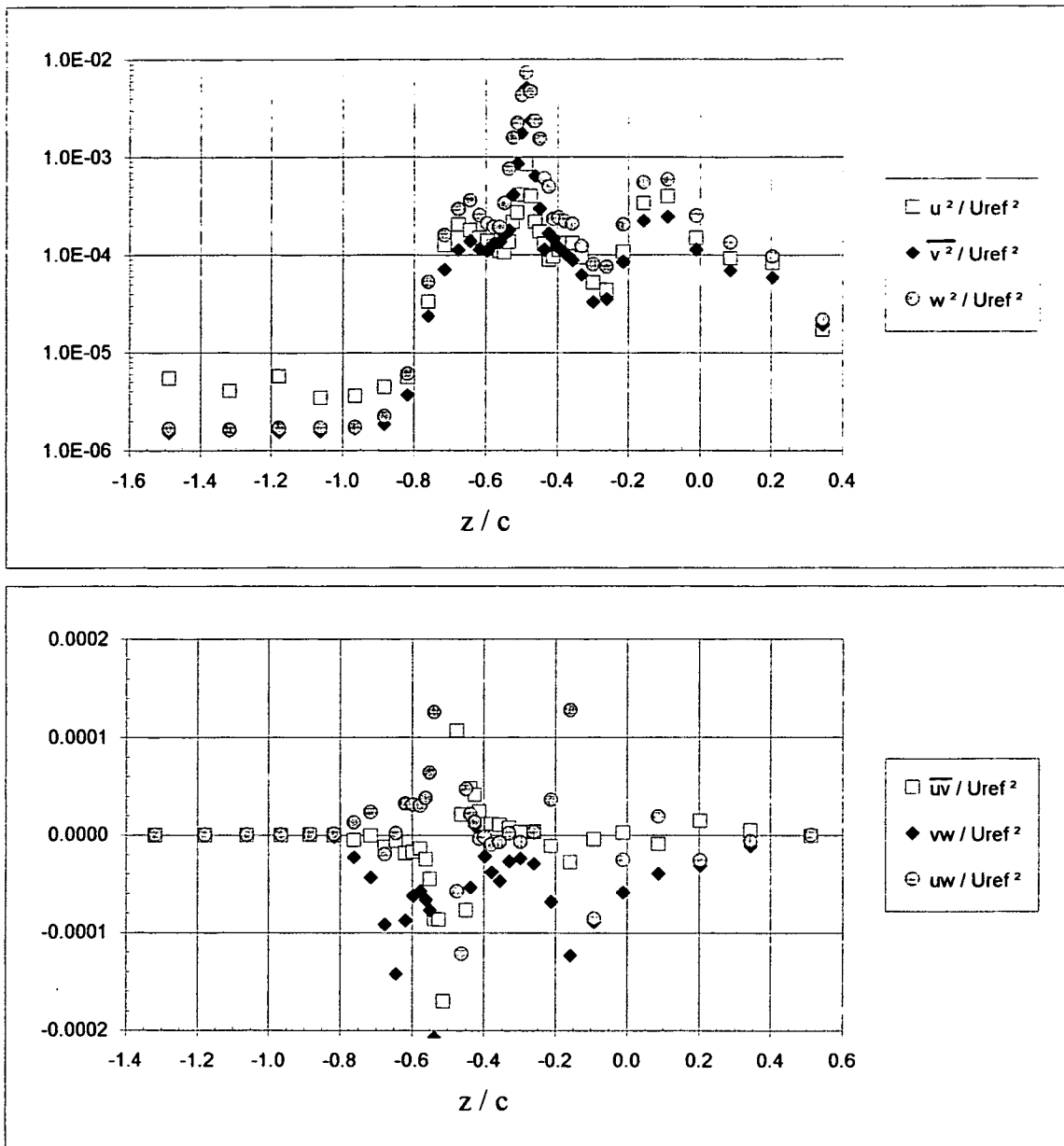


Figure 3.83 Turbulence stress profiles through the blade tip vortex core at  $X/c=22.6$ .  $\Delta/c=-0.0625$ .



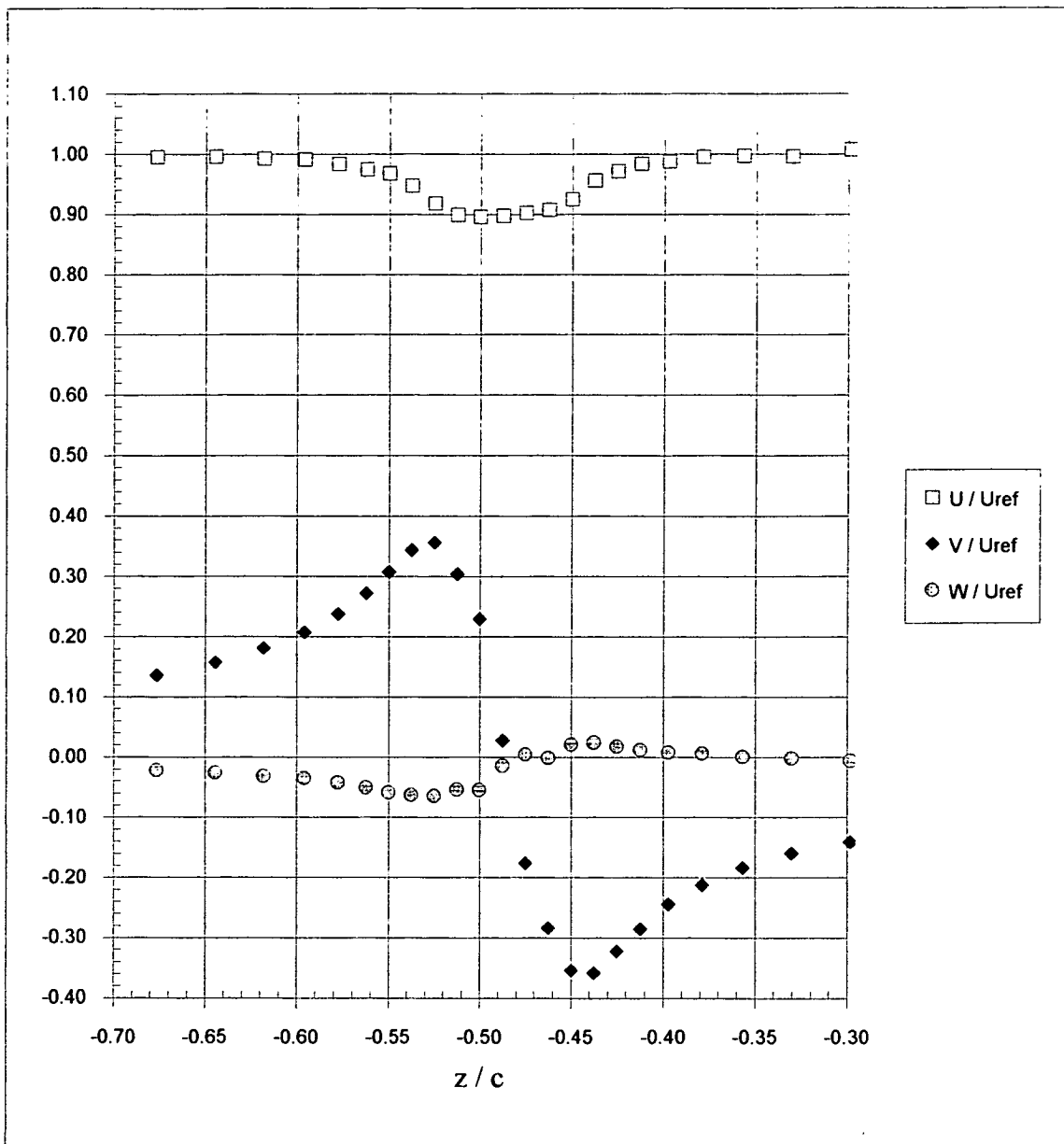


Figure 3.84 Mean velocity profiles in the vicinity of the blade tip vortex core at  $X/c=22.6$ .  $\Delta/c=-0.0625$ .

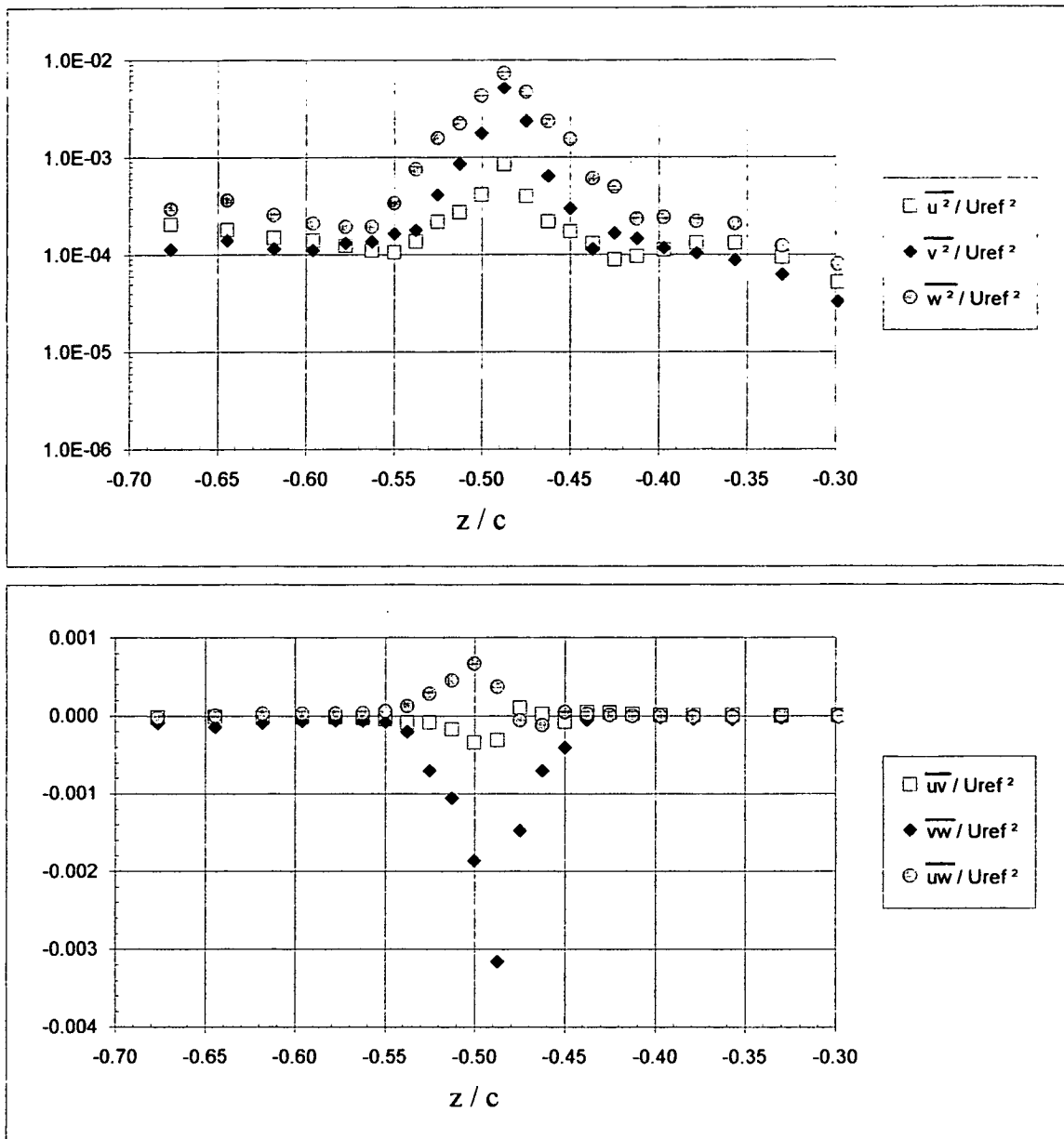
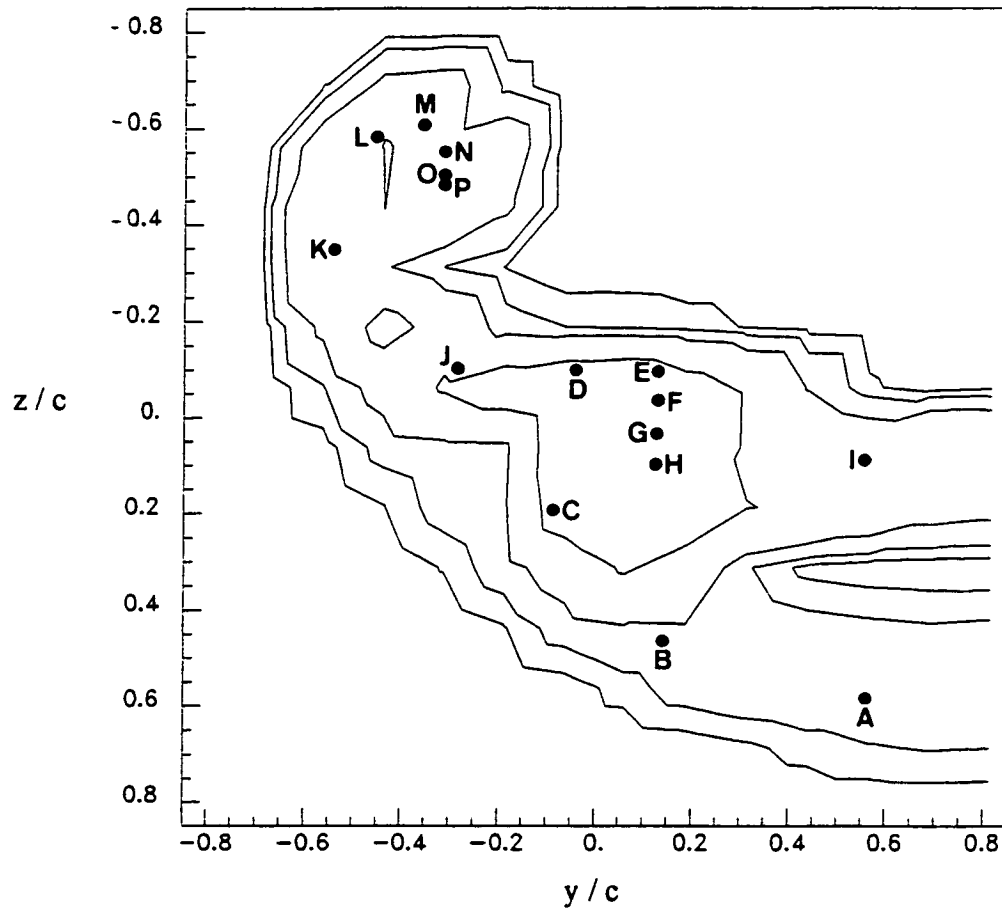


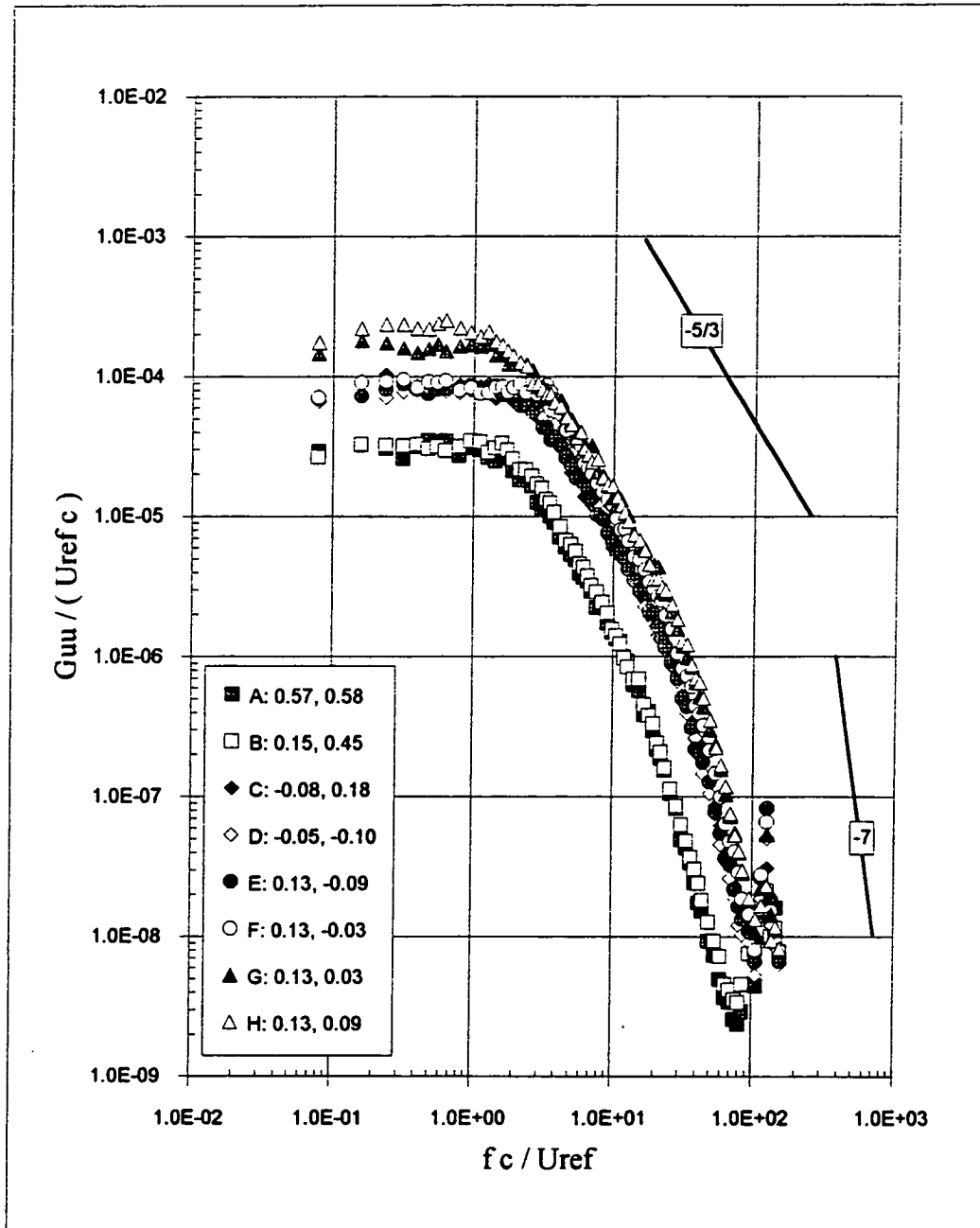
Figure 3.85 Turbulence stress profiles in the vicinity of the blade tip vortex core at  $X/c=22.6$ ,  $\Delta/c=-0.0625$ .



• Represents spectral measurement locations

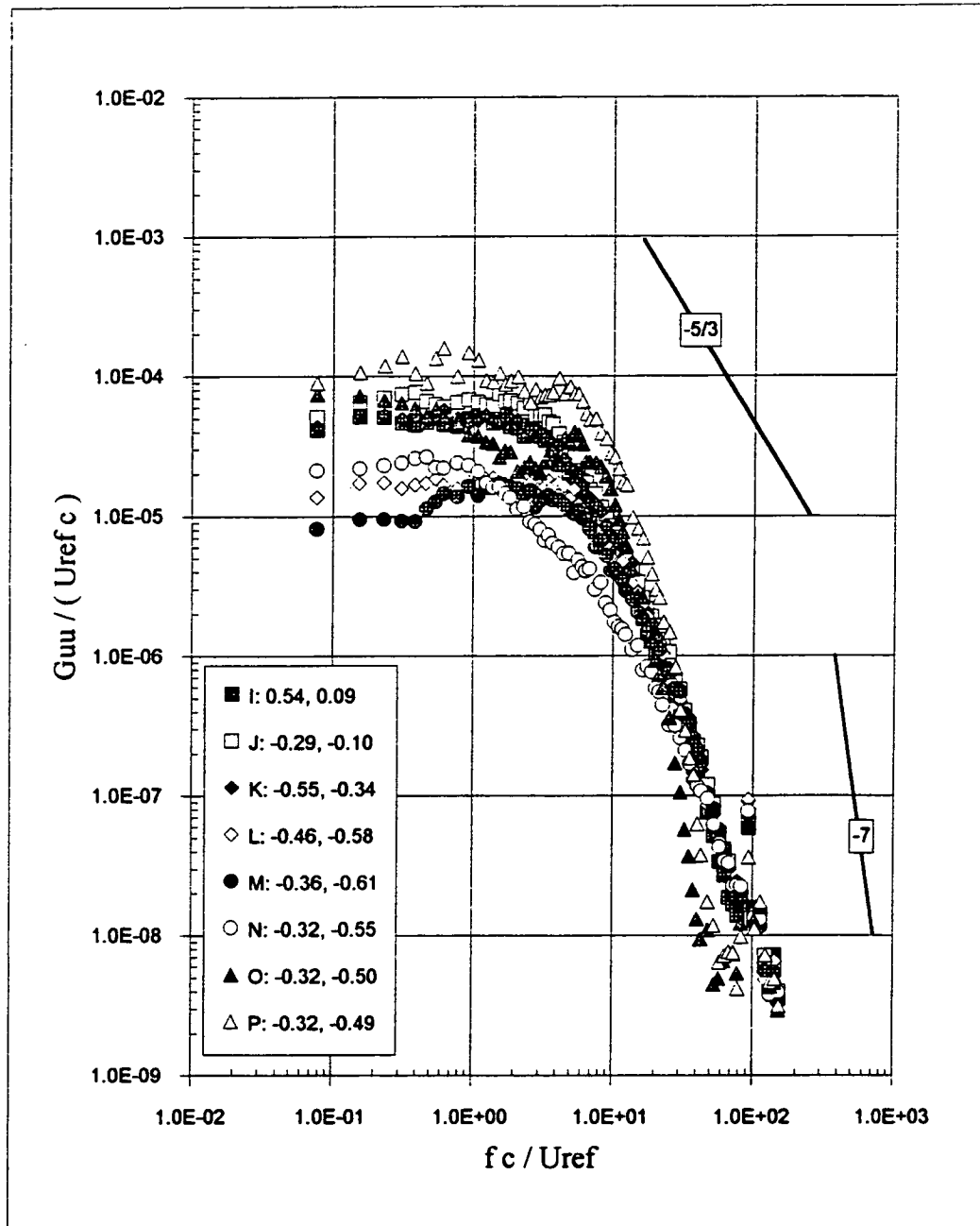
Figure 3.86 Velocity autospectra,  $X/c=22.6$ ,  $\Delta/c = -0.0625$ . (a) Locations of spectral measurements relative to turbulence kinetic energy contours.





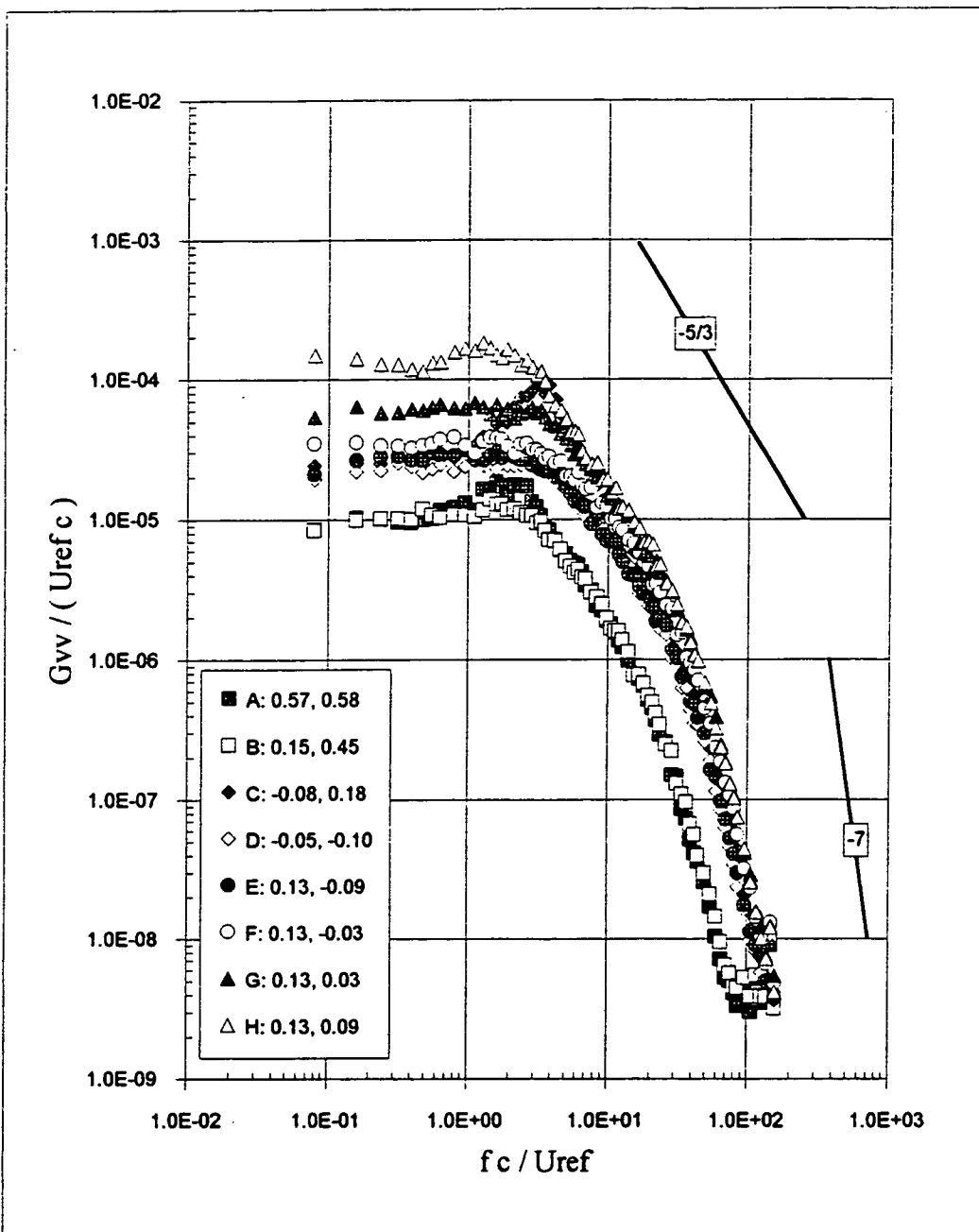
Numbers in legend represent the  $y / c$  and  $z / c$  locations respectively

Figure 3.86 Velocity autospectra at  $X/c=22.6$ ,  $\Delta/c = -0.0625$ . (b)  $G_{uu}$



Numbers in legend represent the  $y/c$  and  $z/c$  locations respectively

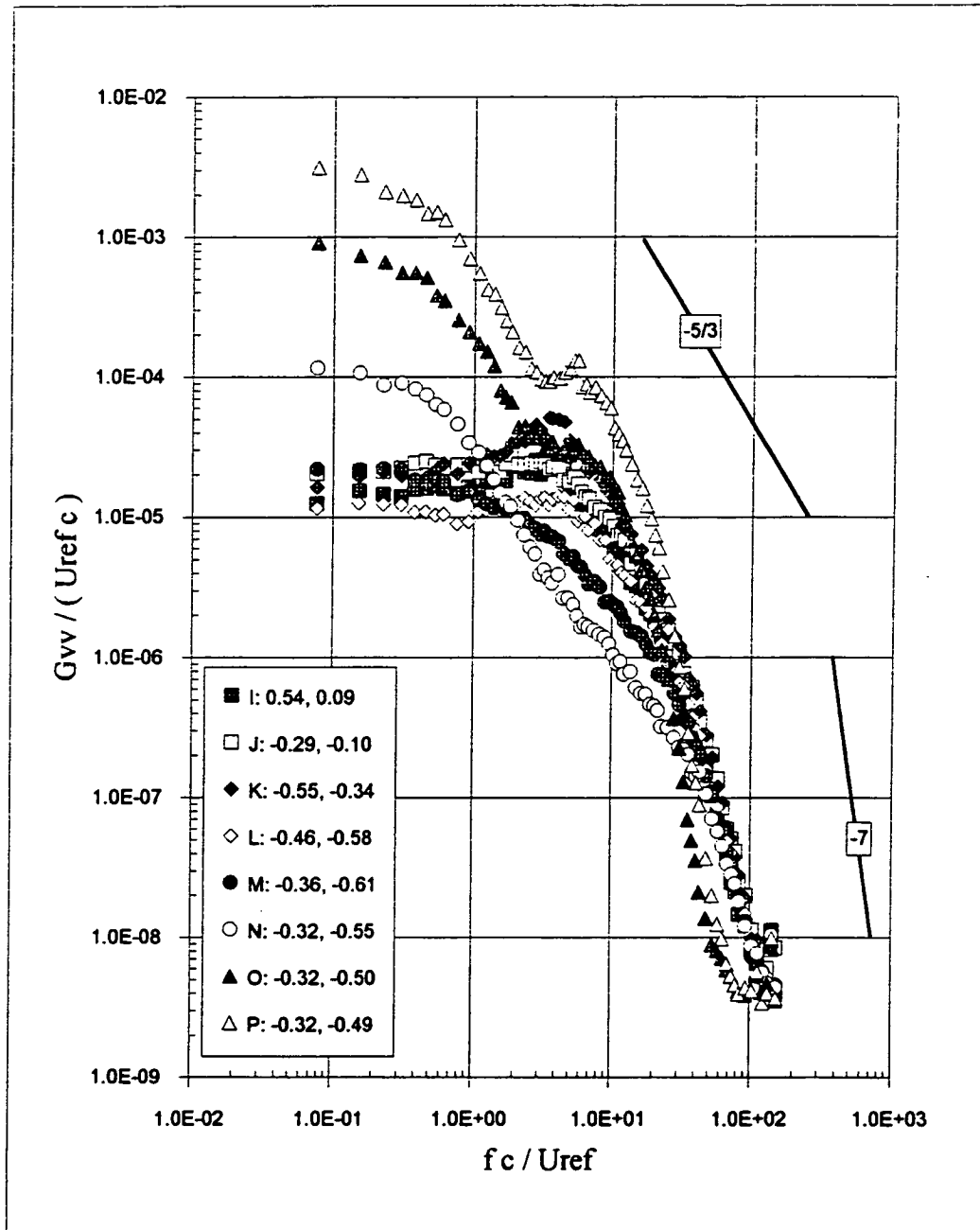
Figure 3.86 Velocity autospectra at  $X/c=22.6$ ,  $\Delta/c = -0.0625$ . (c)  $G_{uu}$  contd.



Numbers in legend represent the  $y/c$  and  $z/c$  locations respectively

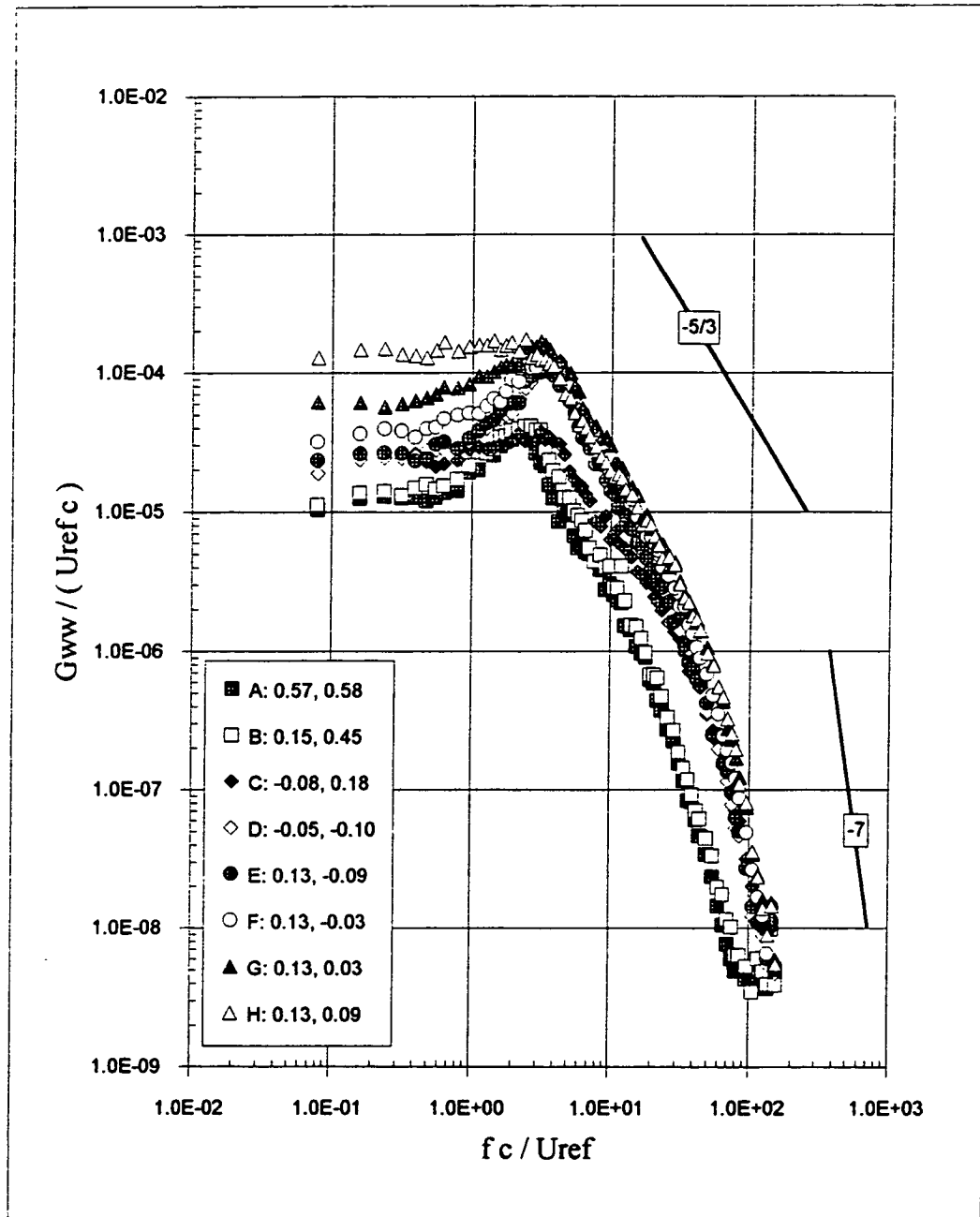
Figure 3.86 Velocity autospectra at  $X/c=22.6$ ,  $\Delta/c = -0.0625$ . (d)  $G_w$





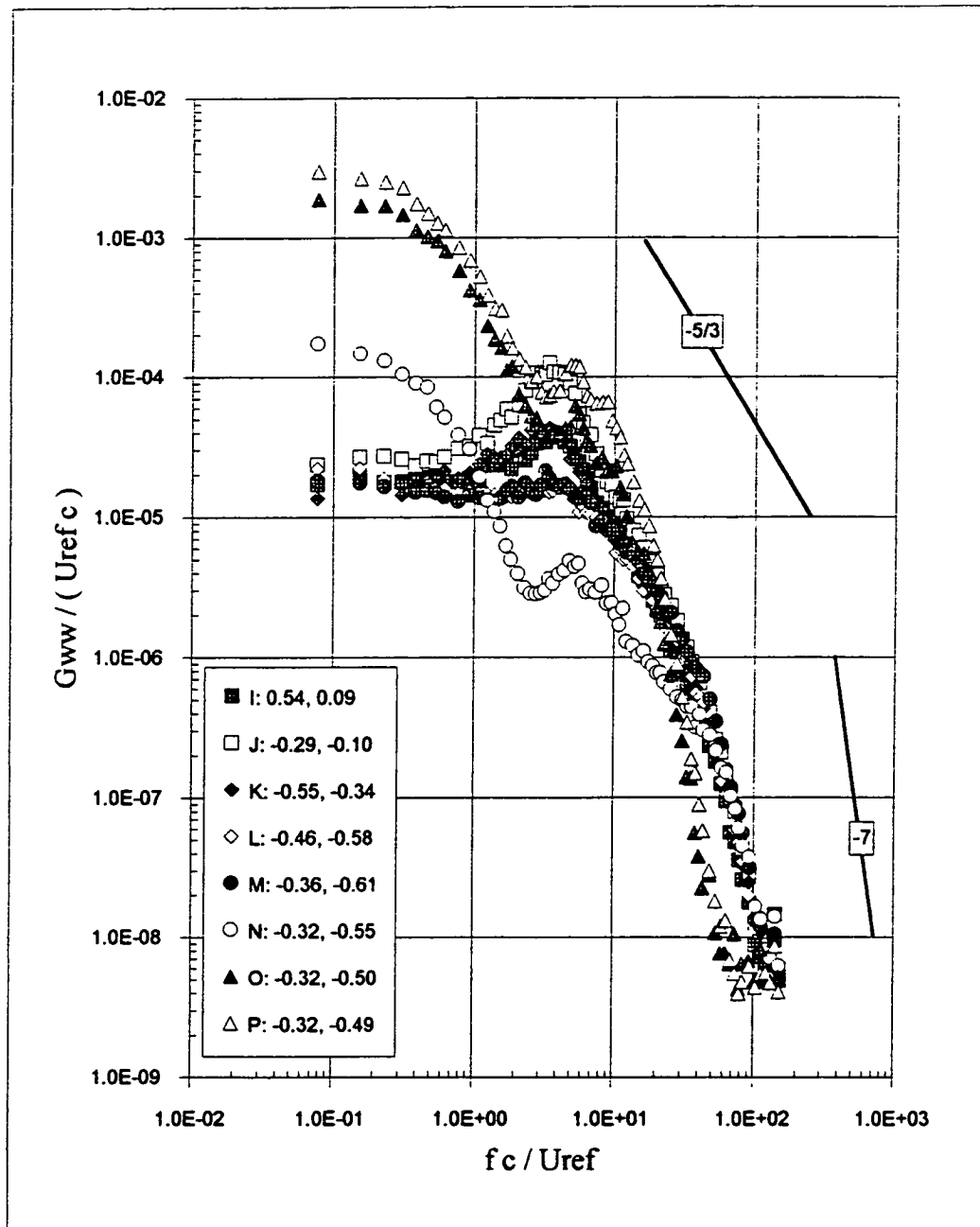
Numbers in legend represent the  $y/c$  and  $z/c$  locations respectively

Figure 3.86 Velocity autospectra at  $X/c=22.6$ ,  $\Delta/c = -0.0625$ . (e)  $G_w$  contd.



Numbers in legend represent the  $y / c$  and  $z / c$  locations respectively

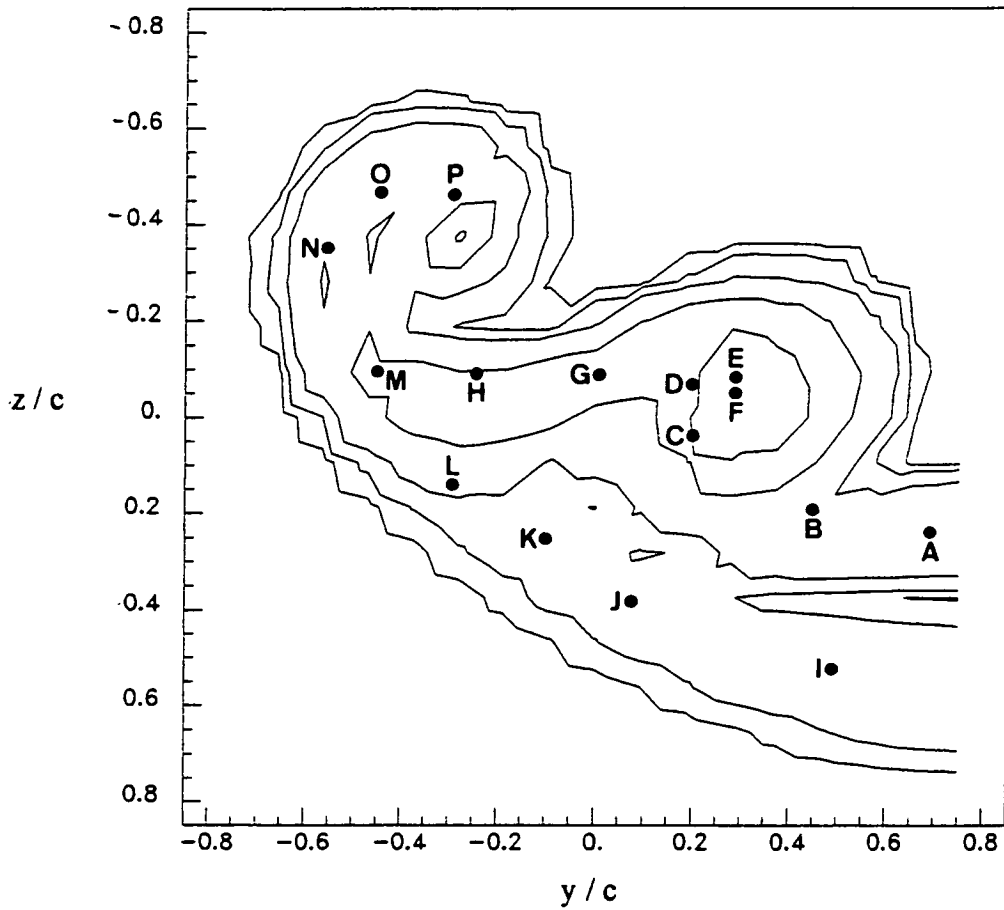
Figure 3.86 Velocity autospectra at  $X/c=22.6$ ,  $\Delta/c = -0.0625$ . (f)  $G_{ww}$



Numbers in legend represent the  $y/c$  and  $z/c$  locations respectively

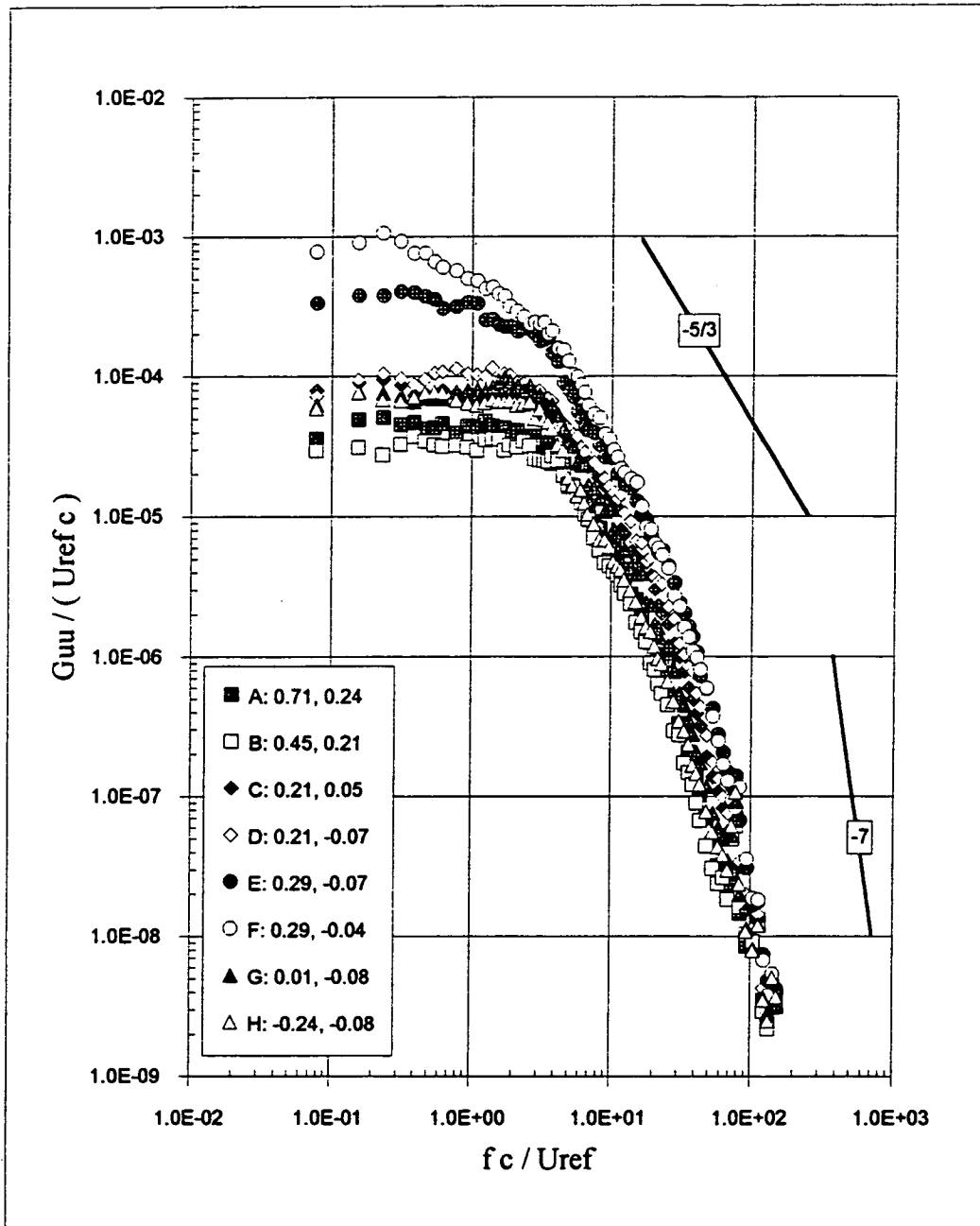
Figure 3.86 Velocity autospectra at  $X/c=22.6$ ,  $\Delta/c = -0.0625$ . (g)  $G_{ww}$  contd.





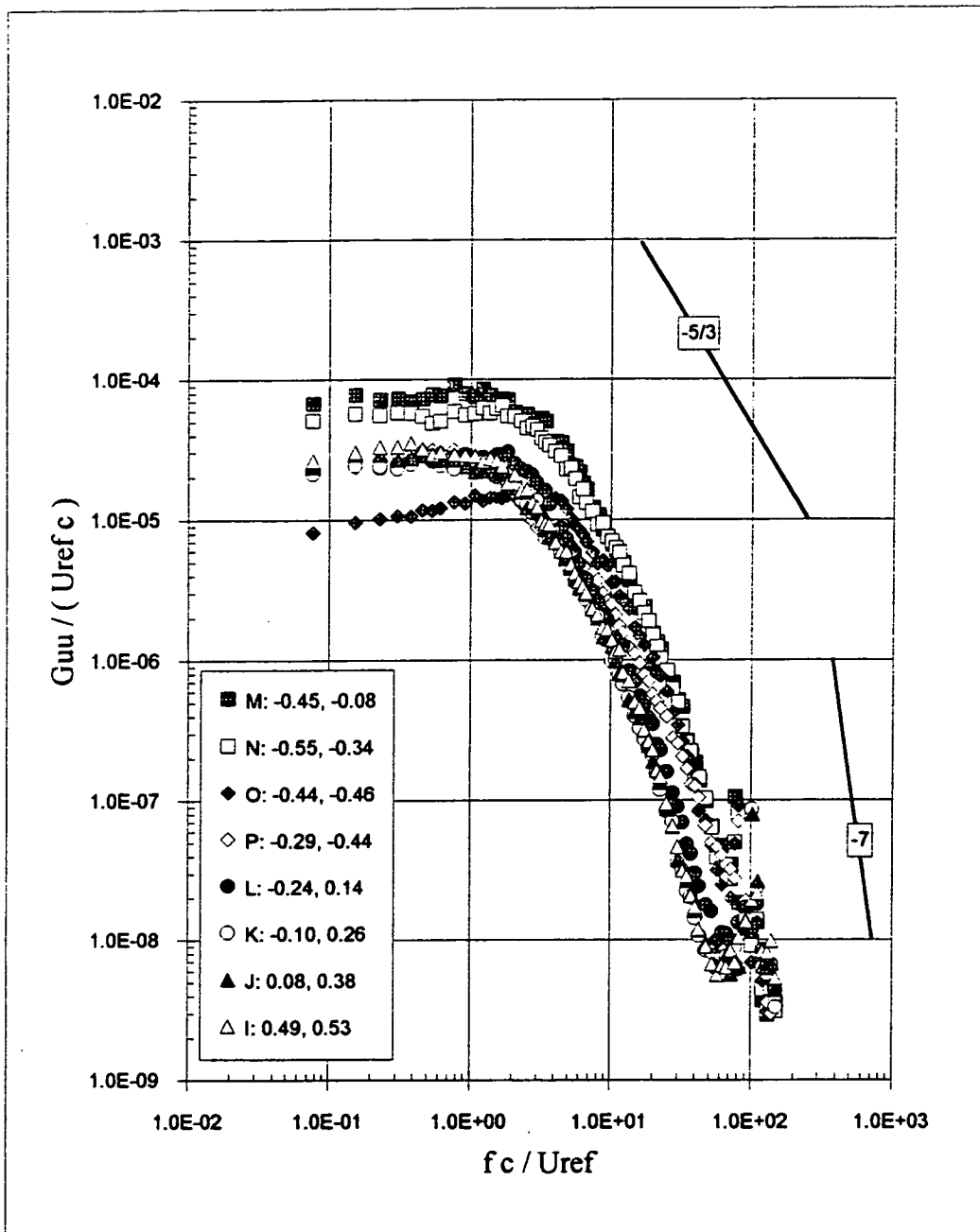
• Represents spectral measurement locations

Figure 3.87 Velocity autospectra,  $X/c=22.6$ ,  $\Delta/c = 0.0625$ . (a) Locations of spectral measurements relative to turbulence kinetic energy contours.



Numbers in legend represent the  $y/c$  and  $z/c$  locations respectively

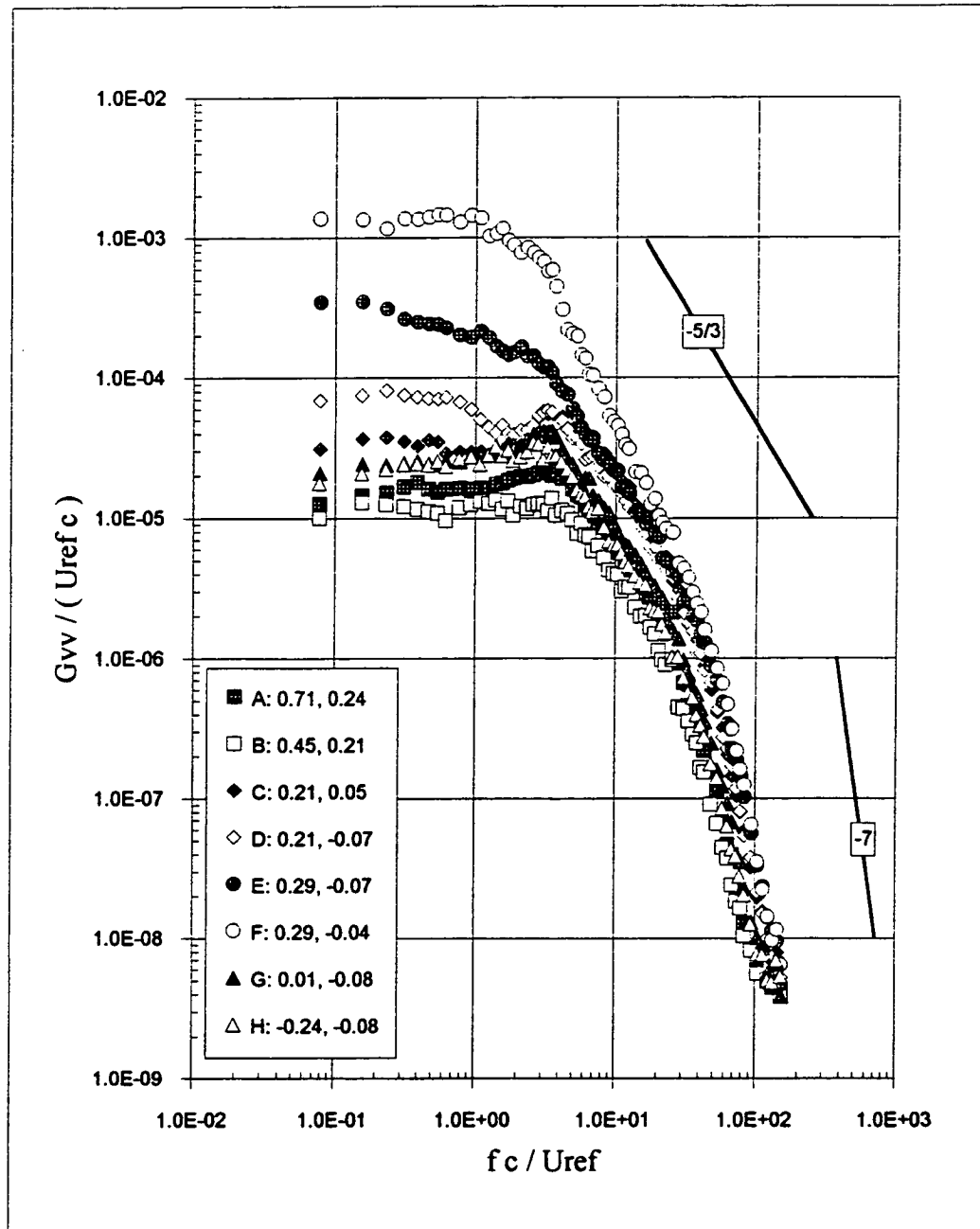
Figure 3.87 Velocity autospectra at  $X/c=22.6$ ,  $\Delta/c = 0.0625$ . (b)  $G_{uu}$



Numbers in legend represent the  $y / c$  and  $z / c$  locations respectively

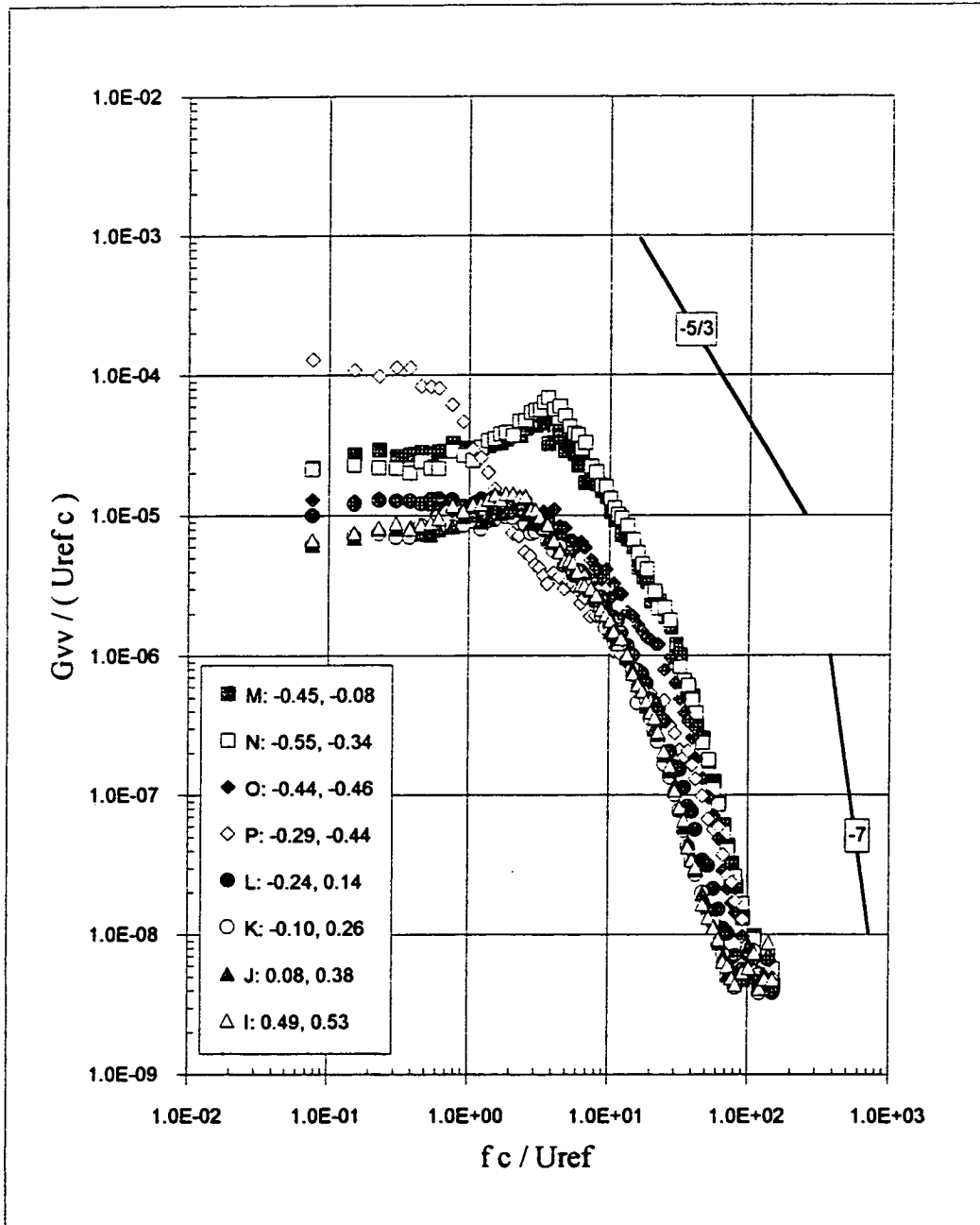
Figure 3.87 Velocity autospectra at  $X/c=22.6$ ,  $\Delta/c = 0.0625$ . (c)  $G_{uu}$  contd.





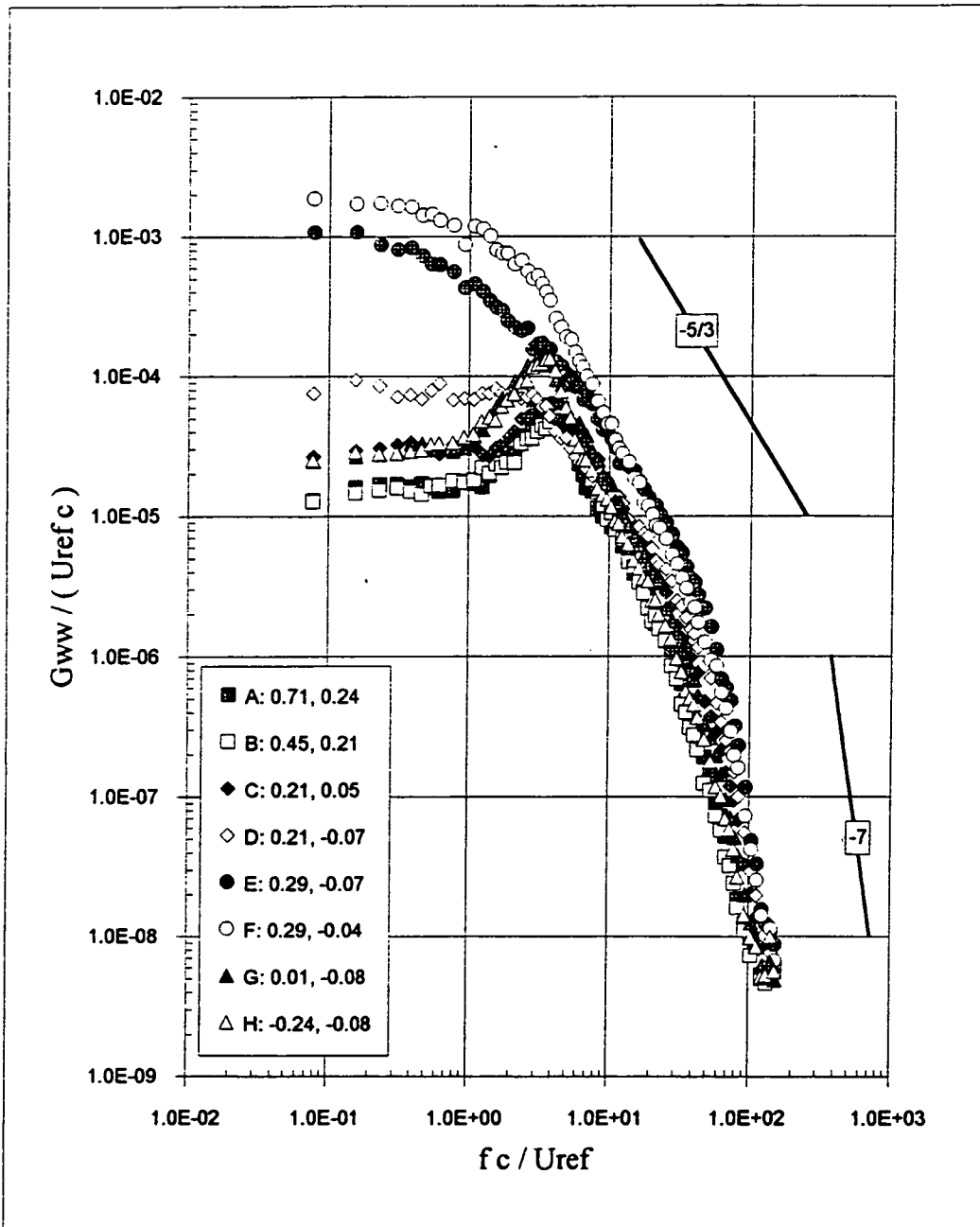
Numbers in legend represent the  $y / c$  and  $z / c$  locations respectively

Figure 3.87 Velocity autospectra at  $X/c=22.6$ ,  $\Delta/c = 0.0625$ . (d)  $G_w$



Numbers in legend represent the  $y/c$  and  $z/c$  locations respectively

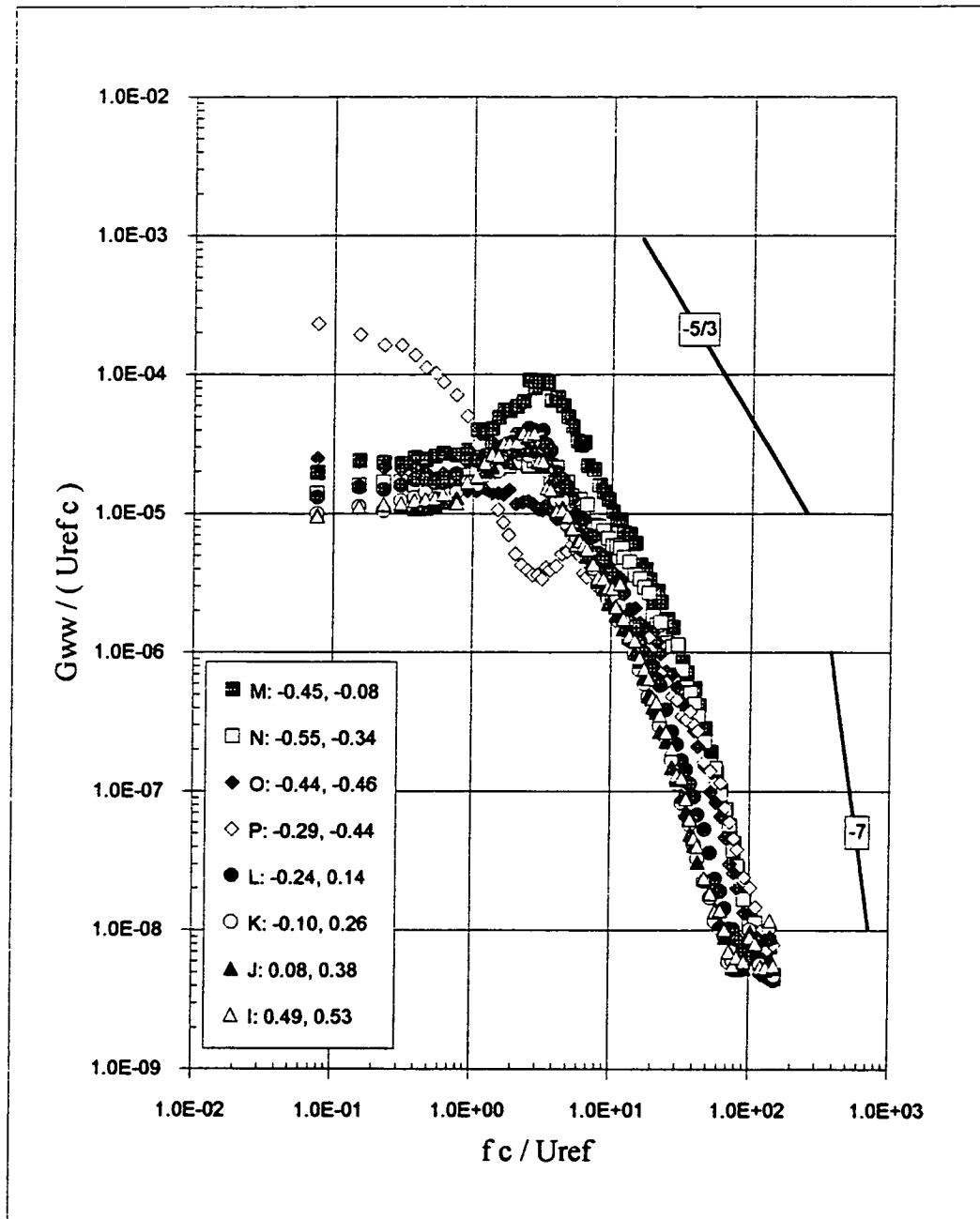
Figure 3.87 Velocity autospectra at  $X/c=22.6$ ,  $\Delta/c = 0.0625$ . (e)  $G_{vv}$  contd.



Numbers in legend represent the  $y/c$  and  $z/c$  locations respectively

Figure 3.87 Velocity autospectra at  $X/c=22.6$ ,  $\Delta/c = 0.0625$ . (f)  $G_{ww}$





Numbers in legend represent the  $y / c$  and  $z / c$  locations respectively

Figure 3.87 Velocity autospectra at  $X/c=22.6$ ,  $\Delta/c = 0.0625$ . (g)  $G_{ww}$  contd.

## 4. CONCLUSIONS

The flows produced by several different perpendicular blade vortex interactions have been studied in detail. Interactions were produced using two rectangular NACA0012 half wings separated by 14 chordlengths ( $c$ ) in the streamwise ( $X$ ) direction. The first wing, set at  $5^\circ$  angle of attack was used to generate the vortex. The second wing, also set at  $5^\circ$  was used as the interaction blade. Velocity measurements were made upstream and downstream of the blade for several different blade-vortex separations ( $\Delta$ ). All measurements were performed at a chord Reynolds number of 260,000. In all cases the vortex passed over the blade about  $0.85c$  from its tip the axis of the vortex being approximately normal to the blade span.

The measurements made upstream of the blade, at  $X/c=10$ , show the approach (primary) vortex to have a core  $0.076\%c$  in diameter containing 27% of the total circulation. Measured turbulence levels in the core are large, but this is mostly due to coherent wandering motions of the core which have an r.m.s. amplitude of about 7% of the core diameter. Judging from core velocity spectra, true turbulence levels in the core are very low, much lower than in the surrounding flow. These spectra show a large dissipation range of -7 slope extending to comparatively low frequencies and almost no inertial subrange, suggesting that the effective Reynolds number of core turbulence is low. The core is surrounded by the unrolled-up portion of the vortex generating wing, which forms a loose spiral. Moving along the wake toward the core, turbulence levels increase, reaching a maximum at the point where the wake begins to curve. Velocity spectra measured in this region appear similar to those of a two-dimensional wake. After the maximum turbulence levels fall, apparently because of a loss of energy at low frequencies. This may indicate that the formation and development of large scale structures is suppressed by the wake curvature and local straining of the flow field. Mean circulation and tangential velocity distributions outside the core are described well by Betz's theory.

The measurements made downstream of the blade, combined with information from prior flow visualization work give a detailed view of the effects of the blade vortex interaction. We regard the following observations derived from these results, as the most significant.

1. The nature of the blade vortex interaction depends upon the blade vortex separation ( $\Delta$ ). With the vortex passing on the pressure side of the blade ( $\Delta < 0$ ) it drifts inboard under the action of its image in the blade surface. The drift is outboard with the vortex passing on the suction side ( $\Delta > 0$ ). With the vortex impinging on the blade leading edge ( $\Delta = 0$ ) it appears to split into two filaments, each passing on the opposite side of the blade.

2. Regardless of  $\Delta$  the vortex becomes embedded in the blade wake downstream of the blade. Its interaction with the wake results in a region of turbulent flow of much greater cross-sectional area and intensity than that presented by the original vortex.

3. Perpendicular blade vortex interaction causes a loss in core circulation. This loss occurs because the vortex core entrains blade boundary layer and wake fluid containing negative streamwise vorticity. Both positive and negative streamwise vorticity are produced and shed by the blade because of the disturbance produced by the vortex on its spanwise lift distribution. The amount of the loss in core circulation appears approximately the same (40%) for a range of blade vortex separations (at least for  $\Delta/c = -0.125$ ,  $-0.0625c$  and  $0.0625$ ). It therefore seems likely that a simple model or correlation could predict this effect.

4. Perpendicular blade vortex interaction appears to alter the entire circulation distribution of the vortex outside its core as well. Comparisons with the same Betz's theory calculations described above showed very poor agreement downstream of the blade. Note, however, that some of this disagreement could have been due to inaccuracies in the methods used to determine the circulation distribution.

5. Perpendicular blade vortex interaction initiates a rapid growth of the vortex core. The point where the growth begins is a function of  $\Delta$ . For  $\Delta/c = -0.0625$  rapid growth in the core began between  $0.33c$  and  $7.6c$  downstream of the blade trailing edge, the core more than trebling in size by  $15c$  downstream. For  $\Delta/c = -0.125$ ,  $0.0625$  and  $0.125$  this growth began between  $7.6c$  and  $15c$  downstream. The rapid core growth is probably a consequence of the mixing of core and blade

wake fluid promoted by the turbulent structures of the wake. The delay in the onset of growth may simply reflect the distance take for the core and blade wake to meet and begin mixing.

6. Perpendicular BVI changes the spectral signature and turbulence structure of the core. Downstream of the blade true turbulence levels in the vortex core (judged from high-frequency velocity autospectra) were larger than in the surrounding wake flows, regardless of  $\Delta/c$  and distance downstream. In addition almost all velocity autospectra measured in the vortex core downstream of the blade displayed substantial inertial subranges, suggesting the effective Reynolds number of core turbulence was much higher than in the undisturbed vortex. In some cases, especially  $\Delta/c=-0.0625$  and 0 at  $X/c=30$  the core spectra had almost the same shape as those of the surrounding blade and vortex generator wakes.

7. In all cases perpendicular BVI was observed to accelerate the decay of the core axial velocity deficit.

8. Perpendicular blade vortex interaction has surprisingly little effect on the non-dimensional form of the core tangential and axial velocity profiles. This may indicate that turbulent vortex cores very rapidly achieve mean-velocity similarity - an fact that could be useful in the general modelling of these flows.

9. The properties of the blade wake near the vortex core are significantly altered by the blade vortex interaction. Firstly, the wake is significantly thicker outboard of the vortex core than inboard. Secondly, turbulence levels in the wake outboard of the core increase monotonically with  $\Delta$  over the measured range from  $\Delta/c=-0.125$  to 0.125. These effects are all due to the local influence of the vortex on flow over the blade. As already mentioned, streamwise vorticity is shed from the blade because of the disturbance of the vortex to its lift distribution. Specifically, the vortex increases the local angle of attack outboard of its core, and reduces it inboard. Thus the blade wake tends to be thicker outboard of the core. Finally, the rotational motion of the vortex lifts boundary layer fluid away from the blade surface. This, in combination with the local angle of attack changes, is responsible for the increase in outboard turbulence levels.



Perhaps the most important conclusion of this work is that, at least for the blade-vortex separations studied here, perpendicular blade vortex interaction substantially alters the flow structure in and around a trailing vortex. The nature of its interaction with all following blades is therefore likely to be altered. The effects of perpendicular blade vortex interaction are therefore likely to have a significant influence on helicopter noise.

The above conclusions do not address the effects of the blade tip vortex. The structure of the blade tip vortex appeared very similar to that of the primary vortex before it encountered the blade. Its principle effect downstream of the blade was to impose a secondary velocity field on the remainder of the flow, causing drift of the primary vortex core and distortion of the blade wake that would not have otherwise occurred. While these effects are themselves interesting they are not of great practical relevance, since the vast majority of perpendicular blade vortex interactions in helicopter rotors occur well inboard of the blade tip. In future work we recommend the use of a blade spanning the wind tunnel test section so that the effects of perpendicular blade vortex interaction can be studied in isolation. Such an investigation could examine with better accuracy and in more detail the functional form of the variation in vortex parameters with blade vortex separation, downstream distance, blade angle of attack and vortex strength. Empirical correlations of this type would be of great value in helicopter flow and acoustic noise computations.

## 5. REFERENCES

Antonia R A and Britz D, "Phase averaging in the turbulent far wake", *Experiments in Fluids*, vol. 7, pp 138-142, 1989.

Batchelor G K, "Axial flow in trailing line vortices", *Journal of Fluid Mechanics*, vol. 20, pp 645-658, 1964.

Bearman P W, 1971, "Corrections for the effect of ambient temperature drift on hot-wire measurements in incompressible flow", *DISA Information*, vol. 11, pp 25-30.

Brooks, T. F. and Martin, R. M., "Results of the 1986 NASA/FAA/DFVLR Main Rotor Test Entry in the German-Dutch Wind Tunnel (DNW)", NASA TM 100507, 1987.

Brooks T F, Marcolini M A and Pope D A, "Main Rotor Noise Study in the DNW", presented to the AMS Specialist Meeting on Aerodynamics and Aeroacoustics, Arlington, Texas, 1987.

Choi, K. and Simpson, R. L., "Some Mean-Velocity, Turbulence, and Unsteadiness Characteristics of the VPI&SU Stability Wind Tunnel", Report VPI-AOE-161, VPI&SU, Blacksburg, VA, 1987.

Devenport, W J, Glegg S A L and Sharma G, "Turbulence Measurements in Trailing Vortices for B.W.I. Noise Prediction", Report to NASA Langley under grant NAG-1-1119, June 1992.

Donaldson C duP and Bilanin A J, "Vortex wakes of conventional aircraft", AGARD AG-204.

Glegg S A L, "The prediction of blade-wake interaction noise based on a turbulent vortex model", AIAA 12th Aeroacoustics Conference, San Antonio, TX, April 10-12, 1989.

Ham N D, "Some conclusions from an investigation of blade vortex interaction", *Journal of the American Helicopter Society*, pp 26-31, October, 1975.

Jorgensen F E, " Directional sensitivity of wire and fiber film probes", *DISA Information*, No. 11, pp. 6-10, 1971.

Kalkhoran I M, Wilson D R and Seath D D, "Experimental Investigation of the Perpendicular Rotor Blade-Vortex Interaction at Transonic Speeds", *AIAA Journal*, vol. 30, No. 3, pp. 747-755, March 1992.

## Perpendicular BVI Part I

Mason W H and Marchman J F, "Farfield Structure of an Aircraft Trailing Vortex, Including Effects of Mass Injection", NASA contractor report C-62078, April 1972.

Moore D W and Saffman P G, "Axial flow in laminar trailing vortices", Proceedings of the Royal Society of London A, vol. 333, pp 491-508, 1973.

Müller R H G, "Special vortices at a helicopter rotor blade", Journal of the American Helicopter Society, October 1990, pp. 16-22.

Phillipe J J and Armand C, "ONERA Aerodynamic Research on Helicopters", Rotorcraft Design, AGARD CP-223, Jan. 1978.

Rife M C and Devenport W J, "Flow visualizations of perpendicular blade vortex interactions", Report VPI-AOE-197, AOE Dept., VPI&SU, 1993.

Reynolds G A, "Experiments on the stability of the Blasius boundary layer", MS thesis, VPI&SU, 1979.

Rossow V J, "Convective merging of vortex cores in lift-generated wakes", Journal of Aircraft, vol.14, pp 283-290, 1977

Seath D D and Wilson D R, "Vortex-Airfoil Interaction Tests", AIAA 24th Aerospace Sciences Meeting, AIAA Paper 86-0354, Reno, NV, Jan. 6-9, 1986.

Schlinker R H and Amiet R K, "Rotor-Vortex Interaction Noise", AIAA Eighth Aeroacoustics Conference, AIAA Paper 83-0720, Atlanta, GA, April 11-13, 1983.

Shabaka I M M A, Mehta R D and Bradshaw P, "Longitudinal Vortices Embedded in Turbulent Boundary Layers. Part 1. Single Vortex.", Journal of Fluid Mechanics, vol. 155, p. 37, 1985.

Wyganski I, Champagne F and Marasli B, "On Large scale structures in two-dimensional small-deficit turbulent wakes", Journal of Fluid Mechanics, vol. 168, pp 31-71, 1986.

Zsoldos J S and Devenport W J, "An Experimental Investigation of Interacting Wing-Tip Vortex Pairs", Report VPI-AOE-191, AOE Dept., VPI&SU, June 1992.

## APPENDIX. BETZ'S THEORY APPLIED TO AN ARBITRARY LIFT DISTRIBUTION

Consider a wing with a general circulation distribution

$$\Gamma = f\left(\frac{y}{s}\right) \quad (9)$$

Here  $y$  is spanwise distance measured from the root and  $s$  is the half span. Suppose the circulation shed by the wing rolls up into a single trailing vortex. Betz's theory implies that this vortex will have a variation of circulation with radius (see Donaldson and Bilanin (1975)) given by

$$\Gamma = f\left(\frac{y(r)}{s}\right) \quad (10)$$

where

$$r = \bar{y}(y) - y \quad (11)$$

and  $\bar{y}(y)$  is the centroid of the shed circulation distribution outboard of  $y$ . In general, therefore,

$$\frac{\bar{y}(y)}{s} = \frac{\int_{\eta}^1 \frac{d\Gamma}{d\eta} \eta \, d\eta}{\int_{\eta}^1 \frac{d\Gamma}{d\eta} \, d\eta} = -\frac{1}{\Gamma} \int_{\eta}^1 \frac{d\Gamma}{d\eta} \eta \, d\eta \quad (12)$$

where  $\eta = y/s$ . We may solve this integral by expressing the circulation distribution as a fourier sine series,

$$\Gamma = \sum_{n=1} A_n \sin n\phi \quad (13)$$

where  $\eta = -\cos(\phi)$  and the summation includes only odd terms (i.e. the circulation distribution is symmetrical about the root). This gives

$$\frac{d\Gamma}{d\eta} \eta \, d\eta = \frac{d\Gamma}{d\phi} \eta \, d\phi = -\sum_{n=1} A_n n \cos(n\phi) \cos\phi \, d\phi \quad (14)$$

and so



$$\int_{\eta}^1 \frac{d\Gamma}{d\eta} \eta \, d\eta = - \sum_{n=1} A_n n \int_{\phi}^{\pi} \cos(n\phi) \cos\phi \, d\phi \quad (15)$$

Using standard integrals the right hand side of this equation may be rewritten as

$$\sum_{n=3} A_n n \left( \frac{\sin(n-1)\phi}{2(n-1)} + \frac{\sin(n+1)\phi}{2(n+1)} \right) + A_1 \left( \frac{\phi}{2} - \frac{\pi}{2} + \frac{1}{4} \sin 2\phi \right) \quad (16)$$

We therefore have

$$\frac{\bar{y}(\phi)}{s} = \frac{\sum_{n=3} A_n n \left( \frac{\sin(n-1)\phi}{2(n-1)} + \frac{\sin(n+1)\phi}{2(n+1)} \right) + A_1 \left( \frac{\phi}{2} - \frac{\pi}{2} + \frac{1}{4} \sin 2\phi \right)}{- \sum_{n=1} A_n \sin n\phi} \quad (17)$$

This expression, along with equations 11 and 13 give, implicitly, the circulation distribution in the vortex. The coefficients  $A_n$  in the lift distribution may be calculated using, for example, lifting line theory.

## **PART II - NOISE PREDICTIONS**

## CONTENTS

1. INTRODUCTION	1-1
2. WAKE INTERACTIONS CAUSING BWI NOISE	2-1
3. THE NOISE PREDICTION METHOD	3-1
<b>3.1 The Acoustic Field</b>	3-1
<b>3.1 Modeling the Turbulence in the Vortex</b>	3-2
<b>3.3 Scaling the Turbulence Measurements</b>	3-4
<b>3.4 The Size of the Turbulent Region</b>	3-8
4. COMPARISON OF MEASUREMENTS WITH PREDICTIONS	4-1
5. REFERENCES	5-1

## PART II: NOISE PREDICTIONS

### 1. INTRODUCTION

Broadband noise from helicopter rotors is generated by the interaction of the blades with turbulent flow. At high frequencies the noise can be caused by the interaction of the blade boundary layers with the trailing edges of the blades, but this mechanism does not generate much power at the low or mid frequencies which have a major impact on the EPNL levels used for noise certification (Brooks et al (1987)). Mid frequency broadband noise was found by Brooks et al (1987) to be a strong function of the rotor tip path plane angle and this lead to the conclusion that noise was generated by the interaction of the blades with rotor wake turbulence. This was classified as Blade Wake Interaction (BWI) noise. Glegg(1991 ) showed how BWI noise could be correlated with the interaction of the blade tip vortices with the following blades and developed a noise prediction method based on a turbulent tip vortex model (Phillips and Graham(1983)). However measurements of the spectral characteristics of the turbulence in a tip vortex were not available in the literature and this lead to the study by Devenport and Glegg (1992) on the unsteady flow in a blade tip vortex, and its relevance to BWI noise. It was found that the largest velocity fluctuations in a tip vortex relative to the stationary frame were a consequence of the unsteady motion of the vortex core. Small lateral motions of the vortex can cause large *apparent* turbulent velocity fluctuations at a fixed point due to the large velocity gradients in the core. However these motions are not important for sound production when the vortex core is aligned parallel to the blade chord and normal to the blade span. This is the type of blade vortex interaction which causes BWI noise (Glegg(1991 )), and it was shown by Devenport and Glegg (1992) that core motion in this configuration was not an efficient mechanism for sound generation since it gives a source



which was of quadrupole order. This concurs with Howe(1990) who demonstrated that it is only the spanwise component of the vorticity that can radiate sound in a blade vortex interaction (this analysis is based on low frequency Greens functions and discards sources of quadrupole order).

Devenport and Glegg(1992) also showed that the turbulent flow in the wake of the blade evolved into a spiral region around the vortex, and the turbulence in this spiral was self similar. However there were some problems in modeling the extent of the turbulent flow for BWI noise prediction purposes, and in that study the turbulence was assumed to be confined to a small region of the wake close to the vortex. However noise predictions using this model were unsuccessful and it was concluded that some other mechanism such as vortex bursting was responsible for BWI noise. The study described in this report has considered the interaction of a tip vortex with a following blade and has given much better insight into the BWI noise mechanism. Firstly, flow visualizations have shown that vortex bursting only occurs when the vortex core is aligned very precisely with the downstream blade. Given the stochastic nature of the blade tip vortex paths close to a helicopter rotor, this precise alignment probably only occurs at discrete locations in the rotor disc plane, if at all. The noise generated by such an interaction would be intermittent or impulsive in nature and BWI noise does not have these characteristics. Secondly the interaction of the tip vortex from a blade with the wake of a downstream blade has been found to cause a region of turbulent flow which is significantly more dispersed than in the tightly wound spiral found in the isolated tip vortex. These observations have lead to the conclusion that it is the turbulence in the wakes of the blades which is the origin of the unsteady flow which causes BWI noise and this part of the report will describe how models of this wake turbulence can be used for noise prediction. First a discussion of the blade wake interactions which occur in different flight regimes will be given in section 2. Then in section 3 the noise prediction method and the scaling of the turbulence spectra will be described. Finally in section 4 the measurements described in part I of the report

will be used to predict measured levels of BWI noise (Brooks et al (1991 )) for 21 different flight regimes at two positions in the far field of the rotor.

## 2. WAKE INTERACTIONS CAUSING BWI NOISE

BWI noise has been shown experimentally to be caused by the interaction of helicopter rotor blades with turbulence generated by the blade wakes. The results presented in Part I of this report show that this can be separated into "wake turbulence" which is the blade boundary layer turbulence shed from the trailing edge of the blades and "vortex instabilities" which cause large velocity fluctuations at a fixed point due to unsteady motions of the vortex core. It is important to separate between these two mechanisms because in BWI vortex interactions, the vortex is aligned with the direction of blade motion and this causes a relatively weak noise generating mechanism. This argument suggests that it is the wake turbulence which is responsible for BWI noise. However the wakes shed from the trailing edge of the blades form a thin sheet which is both unstable and of limited extent in the axial direction. Calculations show that rotor blades interacting with this sheet only do so over a relatively small range of rotor tip path plane angles for a given advance ratio ( $-2.5^\circ < \alpha_{tpp} < 2.5^\circ$ ) whereas noise measurements show that BWI noise is significant over a much larger range of angles. In contrast the BWI noise prediction method developed by Glegg (1991) assumed that the turbulence responsible for BWI noise was associated with the trailing tip vortices. The model assumed a uniform distribution of turbulence over a circular region which was centered on the vortex core and scaled with the vortex core size. This gave reasonably good predictions of the measured noise levels, and especially for the dependence of the noise levels on tip path plane angle. However the measurements of Devenport & Glegg (1992) showed that this model was not a good description of the flow for an isolated trailing tip vortex. It was found that the vortex tended to wrap the wake turbulence into a spiral and reduce its intensity close to the vortex core, which is completely contrary to the model

used for the BVI noise predictions. The results presented in Part I of this report however give new insight into this phenomena, because they show that when a trailing tip vortex (the primary vortex) passes in the vicinity of a second blade a strong interaction takes place between the vortex and the wake turbulence of the second blade. The vortex acts as an attractor for the wake turbulence and distributes it over a region which surrounds the vortex core. The turbulent flow region therefore has strong similarities to the flow assumed in the original BVI noise predictions, providing that only interactions are included for which the vortices have passed close to a secondary blade.

In calculating the noise produced by a BVI type vortex interaction it is necessary to specify the unsteady flow velocity encountered by the blade. However it is also essential to distinguish between the unsteady flow associated with streamwise components of vorticity and those associated with spanwise components of vorticity, because the generated noise is only associated with the later. When a streamwise vortex interacts with the boundary layer on a downstream blade the resultant region of flow will include significant components of both unsteady streamwise vorticity (from the primary vortex) and spanwise vorticity (from the wake/boundary layer turbulence). Separating these two parts of the flow is not possible using existing technology but some fairly general conclusions can be drawn from the measurements which have been made. First we note that the streamwise vorticity is concentrated in a small region around the vortex core. In an isolated vortex ( before interaction with a secondary blade) the spectra of this type of velocity fluctuation has large low frequency components, and less energy than wake turbulence at high frequencies. As this vortex progresses more wake turbulence is wrapped around the core, but it is also laminarised and loses its high frequency content as it enters the core region. Spectra taken in the core of the vortex after an interaction with a secondary blade however show higher levels than the surrounding wake turbulence at high frequencies as well as the expected high levels at low frequencies. This suggests that the wake flow adds to and is uncorrelated with the streamwise vorticity, and



consequently can be treated as a separate component of the flow. Measurements of the wake turbulence in a isolated vortex have shown clearly that the wake flow maintains its self similar nature in spite of being stretched and wrapped around a developing vortex. The flow scales on the wake width which increases with the square root of the distance from the trailing edge where the wake was generated, and this rather than the stretching of the flow by the vortex appears to be the controlling feature. This leads us to suggest a flow model in which the turbulence in and around a trailing vortex which has passed close by a second blade has spanwise vorticity components which are solely determined by the wake turbulence of the secondary blade and scales with the distance from the second blade. The unsteady velocities associated with this spanwise vorticity have spectra which are self similar and can be modeled by the wake turbulence spectra found close to an isolated vortex. This model enables us to extract the component of the flow which is important for noise generation from the complex unsteady flow which has been measured.

We must also consider the size of the region in which this wake turbulence is significant. In the previous model (Glegg(1991 )) it was assumed that the region was circular and that the turbulence intensity decreased linearly from the center of the vortex to the outside edge of the vortex. The measurements however suggest a slightly more bell shaped distribution of turbulence intensity ( notwithstanding spurious peaks in the vortex core). This model will be discussed in more detail in section 3.

### 3. THE NOISE PREDICTION METHOD

#### 3.1 The Acoustic Field

The noise prediction method developed by Glegg (1991 ) assumes that BWI noise is produced by turbulence in the vicinity of trailing tip vortices interacting with the rotor blades. To evaluate the noise radiated to the acoustic far field it is first necessary to calculate the loci of the blade vortex interactions and their axial displacement from the rotor disk plane for a given flight condition<sup>1</sup> . These loci give lines on the rotor disk plane where noise is generated by blade turbulence interaction, and each of these lines are broken down into short linear segments of length  $\Delta\psi_A$  . To obtain the acoustic power spectrum in the far field of the rotor, the contribution of each linear segment is summed with a weighting which is proportional to the amount of time ( in observer co-ordinates) it takes for the blade to move across the segment (Glegg(1991)). The power spectrum, at the angular frequency  $\omega$ , of the acoustic pressure from each linear segment is calculated using

$$S_{pp}^L(z, \omega) = \left[ \frac{\omega \rho_o c z_3}{4\pi c_o r_o^2} \right]^2 \frac{2\pi^3 U b_c}{(1 - M_r)} |\chi_3|^2 \Psi_{33}(k_1, k_2) \quad (1)$$

where  $z=(z_1, z_2, z_3)$  defines the relative location of the blade to the observer,  $r_o=|z|$  is the distance between source and receiver,  $z_2$  is in the spanwise direction and  $z_3$  is the distance of the observer below the blade. In this equation  $c$  is the blade chord,  $\rho_o$  is the density of the fluid,  $U$  is the blade speed at the vortex interaction,  $M_r$  is the Mach number of the blade in the direction of the observer,  $c_o$  is the speed of sound and  $\chi_3$  is

---

<sup>1</sup> The vortex locations are calculated using a method developed by Egolf and Landgrebe(1983).

the blade response function for an upwash gust (Amiet (1975))<sup>1</sup>. The wavenumber spectrum of the upwash components is given by  $\Psi_{33}(k_1, k_2)$  where  $k_1 = -\omega(I-M_r)/U$  and  $k_2 = -\omega z_2/c_o r_o$ . All the parameters required to calculate the noise are defined by the rotor design apart from the wake width  $b_e$  and the wavenumber spectrum of the turbulence. In the following sections we will discuss how these parameters can be calculated from the measurements given in Part I of this report.

### 3.2 Modeling the Turbulence in the Vortex

As was discussed in section 2 we will assume that only vortices which have passed close to a downstream blade have sufficient turbulence associated with them to generate noise. Consequently the first time that a vortex interacts with a blade, its interaction is eliminated from the noise calculations. This is a relatively simple modification to the method outlined in section 3.1. The wavenumber spectrum of the turbulence however is more difficult to estimate.

In previous studies it has been assumed that the wavenumber spectrum of the turbulent flow can be modeled using the Von Karman interpolation formula. This gives for the wavenumber spectrum of upwash fluctuations

$$\Psi_{33}(k_1, k_2) = w^2 \frac{4}{9\pi k_e^2} \frac{(\hat{k}_1^2 + \hat{k}_2^2)}{(1 + \hat{k}_1^2 + \hat{k}_2^2)^{7/3}} \quad (2)$$

where

$$\hat{k}_i = \frac{k_i}{k_e} \quad \text{and} \quad k_e = \frac{3}{4L}$$

---

<sup>1</sup> Glegg (1991) included an unsteady thickness noise source in the BWI noise prediction scheme, but this has not been included here since it has a negligible effect on the predicted noise levels at the angles of interest.

and  $w$  is the rms turbulence velocity fluctuations and  $L$  is the integral lengthscale of the turbulence. For measurements of turbulence at a fixed point the spectral density (per Hz) for upwash fluctuations is given by this model as

$$G_{ww}(f) = w^2 \frac{2L}{3U_{ref}} \frac{(3 + 8\hat{k}_1^2)}{(1 + \hat{k}_1^2)^{11/6}} \quad (3)$$

where  $k_1 = 2\pi f / U_{ref}$  and  $U_{ref}$  is the mean flow velocity. The noise predictions require  $\Psi_{33}$  but it has only been possible to measure  $G_{ww}$ . To overcome this problem in the past, measurements of the spectrum at a point have been used to estimate the lengthscales and the turbulence intensity as a function of position in the flow, so that they may be used in formulae of the type given in equation (2) to obtain the wavenumber spectrum for noise calculations. However difficulties arise, as in this case, when the measured spectrum does not approximate to the Von Karman model given by equation (3). In these situations a relationship must be assumed between  $\Psi_{33}$  and  $G_{ww}$ , and it is customary to write this in the form

$$\Psi_{33}(k_1, 0) = \frac{1}{(2\pi)^2} G_{ww}(f) \mu(\hat{k}_1) U_{ref} \quad (4)$$

where  $\mu$  is the spanwise coherence lengthscale which, for the Von Karman interpolation formula, is given by

$$\mu = \frac{128\pi L}{27} \frac{\hat{k}_1^2}{(3 + 8\hat{k}_1^2)\sqrt{1 + \hat{k}_1^2}} \quad (5)$$

At high frequencies the coherence lengthscale  $\mu$  is given by  $2\pi U_{ref} / 9\omega$  which is independent of the integral lengthscale of the flow and is inversely proportional to the frequency. The maximum value of  $\mu$  is given by  $0.3\pi L$  and so this model specifies the coherence lengthscale as always being less than the integral lengthscale of the turbulence.



In the absence of two point measurements an estimate has to be used for the coherence lengthscale of the upwash velocity fluctuations and consequently we will assume that equation (5) may be used for this purpose. This is probably not a bad assumption since it gives a smooth interpolation between the largest lengthscale which we can expect  $\mu \approx L$  which occurs when  $\omega L / U_{ref} \approx 0.75$  and the coherence lengthscale at high frequencies which is independent of the turbulence scale.

### 3.3 Scaling the Turbulence Measurements

First we will consider the turbulent flow in an isolated vortex and show how the turbulence spectra evolve as the wake is wrapped around the vortex core. Figure 3.1 shows the turbulence intensity in the region around the vortex core at a location which is 10 chord lengths downstream from the leading edge of the primary blade. Four regions have been identified on this plot, a wake region which is that part of the flow dominated by the turbulent wake shed from the trailing edge of the blade, an outer spiral region where the wake is being wrapped around the vortex core, an inner spiral region which is close to the vortex core and the core region itself. The spectra of the upwash fluctuations in each region are plotted in figure 3.2. These show that the spectra in the wake region have a distinct peak which occurs at a non-dimensional frequency of  $fc / U_{ref} \approx 3.4$  and that the energy in that peak is significantly greater than in other parts of the flow with the exception of the core region which has large amounts of energy at very low frequencies. In the spiral regions the spectra show a steady reduction in energy as the core is approached especially in the frequency range around  $fc / U_{ref} \approx 10$ . The peak in the wake region spectra is very similar to the spectral peak in turbulent boundary layers in adverse pressure gradients (Bradshaw(1967)). This feature is attributed by Bradshaw to coherent

structures in the flow and may be indicative of spanwise vorticity. It is interesting to compare the upwash spectra in the wake region with the Von Karman interpolation formula given by equation 3. This comparison is shown in figure 3.3 using an integral lengthscale of  $L=0.2 L_o$  where  $L_o$  is the wake width at this location. This result shows (in contrast to earlier measurements Devenport & Glegg (1992)) that the Von Karman spectrum does not give a good fit to the measurements. The peak in the spectrum is not a feature of the Von Karman interpolation formula and the discrepancies at high frequencies are due to the effect of viscous dissipation (which is not been included in equation (3)). For BWI noise production the most important part of the spectrum is for non-dimensional frequencies which are close to the spectral peak and so it appears that the Von Karman formula is not a suitable model in this case, since any variation of the turbulence lengthscale will not give the measured spectral peak.

Next we consider the spectra in the wake after the primary vortex has passed a second blade. Figure 3.4 shows the distribution in turbulence intensity for a typical case where the vortex has passed a distance  $0.125c$  above the secondary blade located  $14c$  downstream of the primary blade. The measurement location is a further  $15c$  downstream of the secondary blade. The upwash spectra are again considered in four separate regions, a primary wake region (see figure 3.5) where the spectral shape is similar to the spectra in the wake region of the isolated vortex, a primary vortex core region where the low frequency vortex core motions are the dominant feature, a mixing region between the two vortices which has a dominant spectral peak similar to the wake region, and the secondary vortex core region with large low frequency motions. It was argued in the pervious section that BWI noise is primarily caused by the turbulent velocity fluctuations in the mixing region between the two vortices and that this would have the characteristics of the wake turbulence from the secondary blade and the results in figure 3.5 concur with this suggestion. To further test this hypothesis we will first scale the spectra in the wake

region of the isolated vortex into a self similar form and use these results to predict the spectra in different parts of the vortex after it has passed the second blade.

Wynanski et al (1986) have shown that the turbulence in the wakes of many different types of body can be scaled on the wake width  $L_o$  which can be defined in terms of the momentum thickness  $\Theta$  (see footnote<sup>1</sup>) of the wake as  $L_o = 0.32 \Theta \sqrt{(x/\Theta + 380)}$ . Consequently we can expect the spectra measured in the blade wakes to collapse when plotted as a function of  $fL_o/U_{ref}$ . Further equation (3) shows that the spectrum of the velocity fluctuations scales in magnitude as  $G_{ww}(f) \sim w^2 L/U_{ref}$  and Wynanski et al (1986) also show that the turbulence intensity scales as  $w/U_{ref} \sim \sqrt{(\Theta/x)}$ . For a given drag coefficient  $\Theta$  is proportional to the blade chord and, with  $L \sim L_o$ , the magnitude of the spectrum can be expected to scale as  $G_{ww}(f) \sim c L_o U_{ref}/x$ . Figure 3.6 shows the collapse of the  $G_{ww}(f)$  spectra from the wake region of the isolated vortex (figure 3.3) when they are normalized as  $G_{ww}(f)x/cL_oU_{ref}$  and plotted against  $fL_o/U_{ref}$ . A tenth order polynomial, least squares fit to these spectra has been obtained (and is also shown in figure 3.6) using the function

$$\frac{xG_{ww}(f)}{cL_oU_{ref}} = \exp\left(\sum_{n=0}^N c_n X^{N-n}\right) \quad X > 0.05 \quad (6)$$

where  $X = \ln(fL_o/U_{ref})$ ,  $N=10$  and the coefficients are given by

$$\begin{aligned} c_0 &= -4.094107911604283e-04 \\ c_1 &= -3.355736105268570e-03 \\ c_2 &= -9.101826421288446e-05 \\ c_3 &= 5.121995406807923e-02 \\ c_4 &= 4.419066392372003e-02 \\ c_5 &= -3.168685739499785e-01 \\ c_6 &= -2.193413116108480e-01 \\ c_7 &= 9.060883193917536e-01 \\ c_8 &= -2.801734323812800e-01 \\ c_9 &= -2.119234822914640e+00 \\ c_{10} &= -6.608767720927401e+00 \end{aligned}$$

---

<sup>1</sup> The momentum thickness is defined as  $\Theta = cC_D/2$  for these calculations which differs from the value assumed by Glegg (1991) which was based on an estimate of the boundary layer thickness.

To check the validity of this model the predicted spectrum has been compared with the measured spectrum at other locations. Figure 3.7 shows the fit to spectra measured at different locations after the vortex has passed by the second blade at a miss distance of  $0.125c$ . The flow is dominated by the wake from the second blade and so the  $x$  location has been taken relative to the trailing edge of the second blade. In general this scaling appears to give a good fit to the upwash spectrum in the wake region (see figure 3.4) but tends to underpredict the turbulence levels in the mixing region between the two vortices by as much as 10 dB. However the spectral shape is reasonably well modeled by the curve fit given in equation (7), and so this equation appears to be appropriate providing that a correction is applied to allow for the change in absolute level of the spectrum in different parts of the flow, and this will be discussed in more detail in the next section.

Finally in order to use equation (4) to obtain the wavenumber spectrum we need to estimate the integral lengthscale of the flow so that the coherence lengthscale can be obtained from equation (5). The peak in the measured spectrum occurs at  $fL_0/U_{ref} \sim 0.5$  which suggests that the coherent structure in the flow has a scale which is of order  $L \approx 2L_0$ . However as the wake is wrapped around the vortex core the turbulent eddies or coherent structures will be stretched and re-oriented relative to the spanwise direction. This will reduce the spanwise lengthscale. If we assume that the eddy stretching occurs at the same rate as the rate of flow development then we can expect the effective integral lengthscale to be reduced as  $1/\sqrt{x}$  while the wake scale increases as  $\sqrt{x}$ . These two effects will cancel and so the eddy lengthscale will be independent of the downstream location and can be estimated as twice the wake width at  $x=0$ . (This correction has a small effect on the final results but tends to improve the low frequency fit to the spectrum).



### 3.4 The Size of the Turbulent Region

To predict the radiated noise using equation (1) we also need to specify the spanwise extent of the turbulent region which is defined by the effective span  $b_e$ . This depends on the distribution of the mean square turbulence intensity over the region of the flow which interacts with the blade and is given by

$$b_e = \frac{1}{w_{\max}^2} \int w^2(z_2, z_3) dz_2 \quad (7)$$

In the previous study of BWI noise it was assumed that  $w$  was a maximum at the center of the vortex and decreased linearly to a zero value at the edge of the vortex core defined as  $a_0 = 0.15 \sqrt{xcC_L}$ . The measurements given in Part I of this report have shown that there is a significant variation in turbulence levels across the flow, as discussed in the previous section. Reviewing the turbulence measurements given in figure 3.41 of Part I suggests that it is more realistic to consider a distribution of turbulence which is of constant intensity in the vortex core region (providing that the peak associated with the core motions is disregarded) rather than the triangular shaped distribution which was assumed previously. The effect that these two alternatives have on the value of  $b_e$  are illustrated in figure 3.8 and can be compared with the measurements shown in figures 3.41 in Part I of this report. To estimate the size of the vortex the lift coefficient has been taken as the root circulation  $C_L = 0.5$  and the downstream location  $x$  as the distance from the primary blade. The measurements show that the turbulent region extends over a region of  $\sim 1.2 c$  in the spanwise direction and the model seems to estimate this quite well. The measurements also show that the levels on either side of the vortex core can differ by as much as a factor of two, but that they are constant in either region. Taking the

average between these two extremes would appear to be the best way to proceed in order to estimate the value of the effective span.

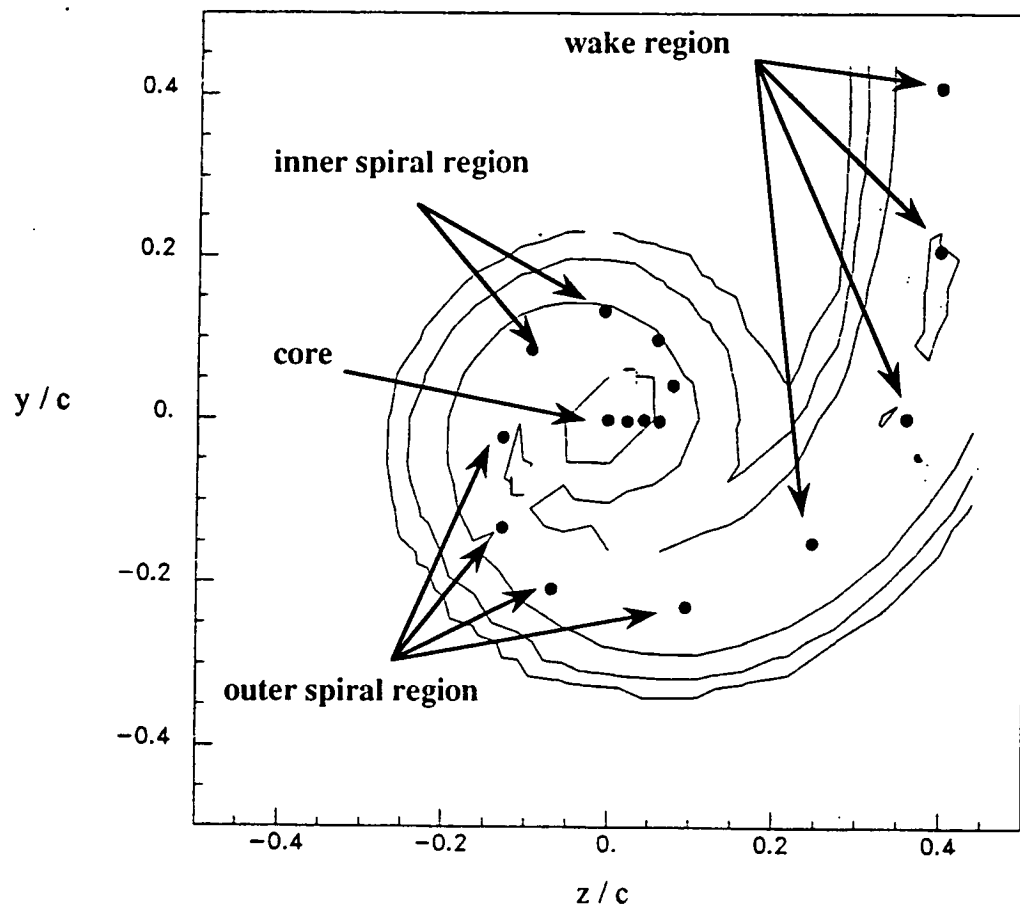
For a constant distribution of turbulence intensity we can define the effective span as

$$b_e = 2\sqrt{a_o^2 - z_3^2} \quad (8)$$

The linearly decaying model of the turbulence intensity considered by Glegg(1991) defines

$$b_e = 2a_o \left[ h^2 S + \frac{1}{3} S^3 - h^2 \ln \left( \frac{1+S}{|h|} \right) \right] \quad (9)$$

where  $h=z_3/a_o$  and  $S=\sqrt{1-h^2}$ . A comparison between these two different models is shown in figure 3.8(b) and we see that the major difference between them is maximum magnitude of  $b_e$  and the extent over which  $b_e$  remains significant.



• Represents spectral measurement locations

Figure 3.1 Contours of the mean square turbulence intensity in an isolated trailing tip vortex at a downstream location of  $x/c=10$ .

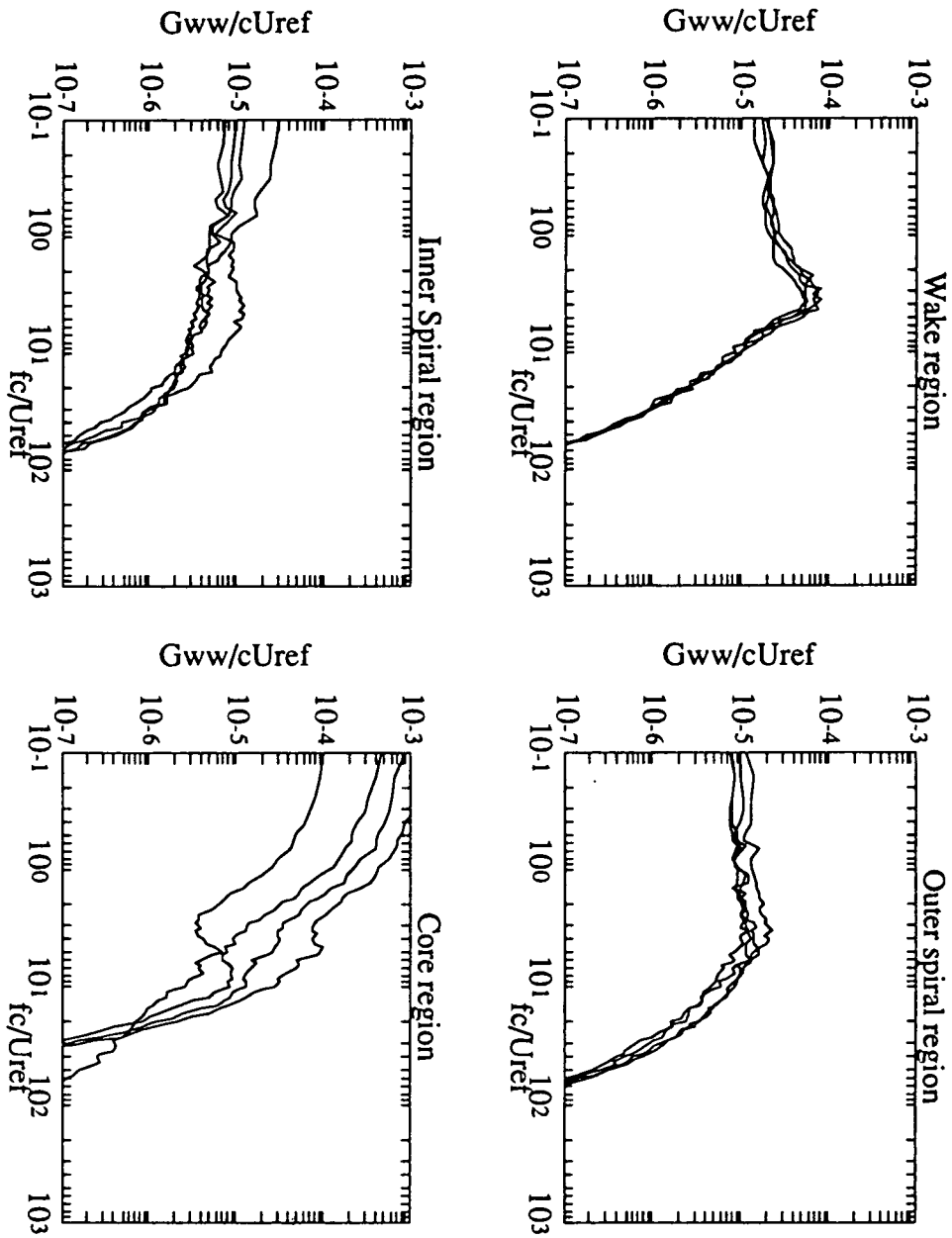


Figure 3.2: Spectra of Upwash Components in an Isolated Vortex  $x/c=10$



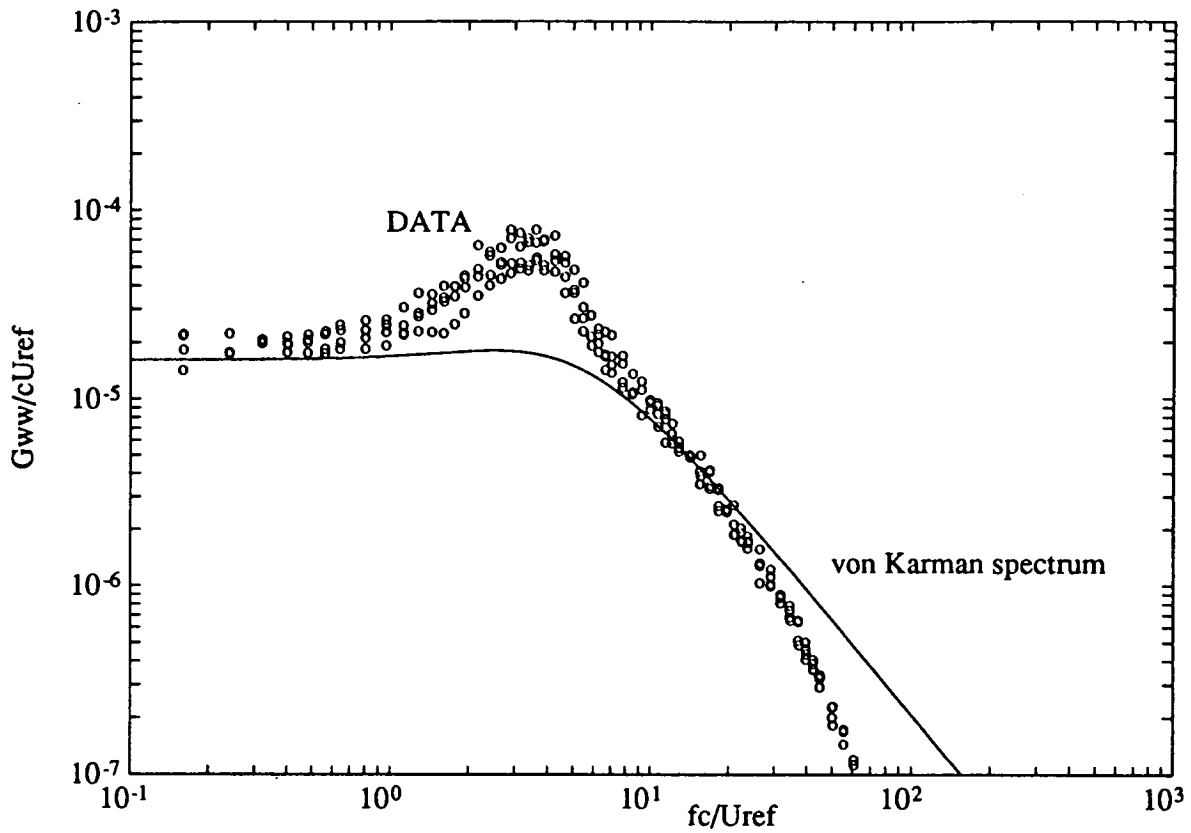


Figure 3.3: Spectra of Turbulence in Wake compared with Von Karman spectrum

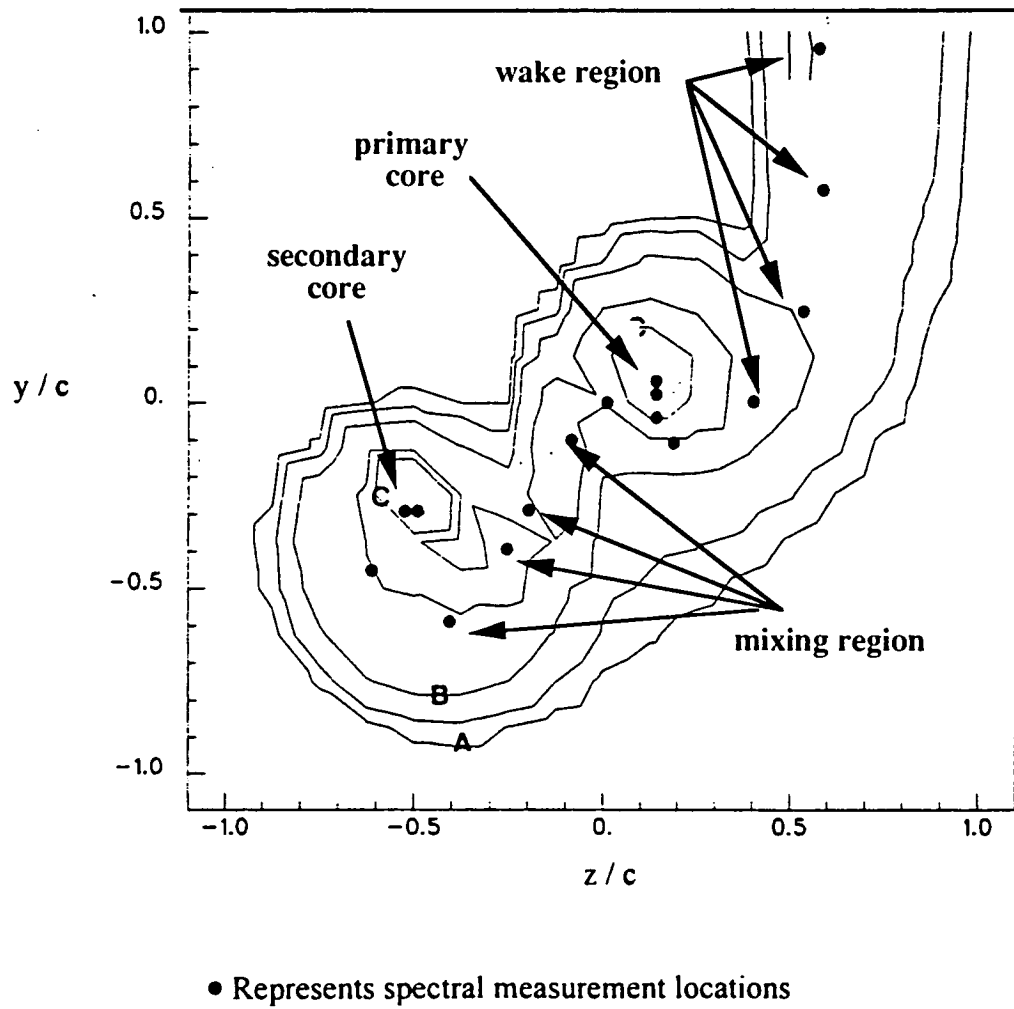


Figure 3.4 Contours of the mean square turbulence intensity in the wake region after the primary vortex has passed the second blade at  $x/c=30$

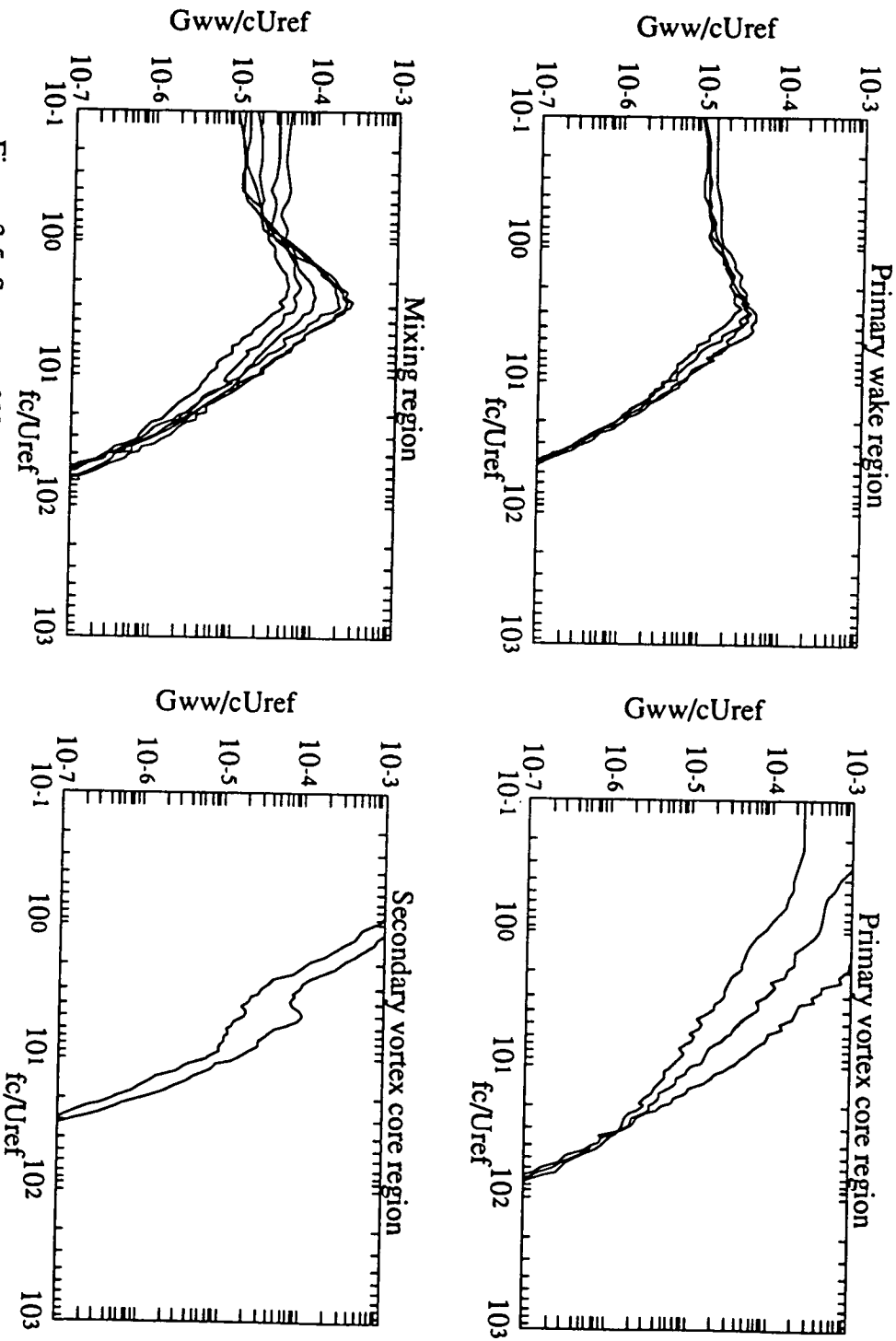


Figure 3.5: Spectra of Upwash Components in the Downstream Flow  $x/c=30$

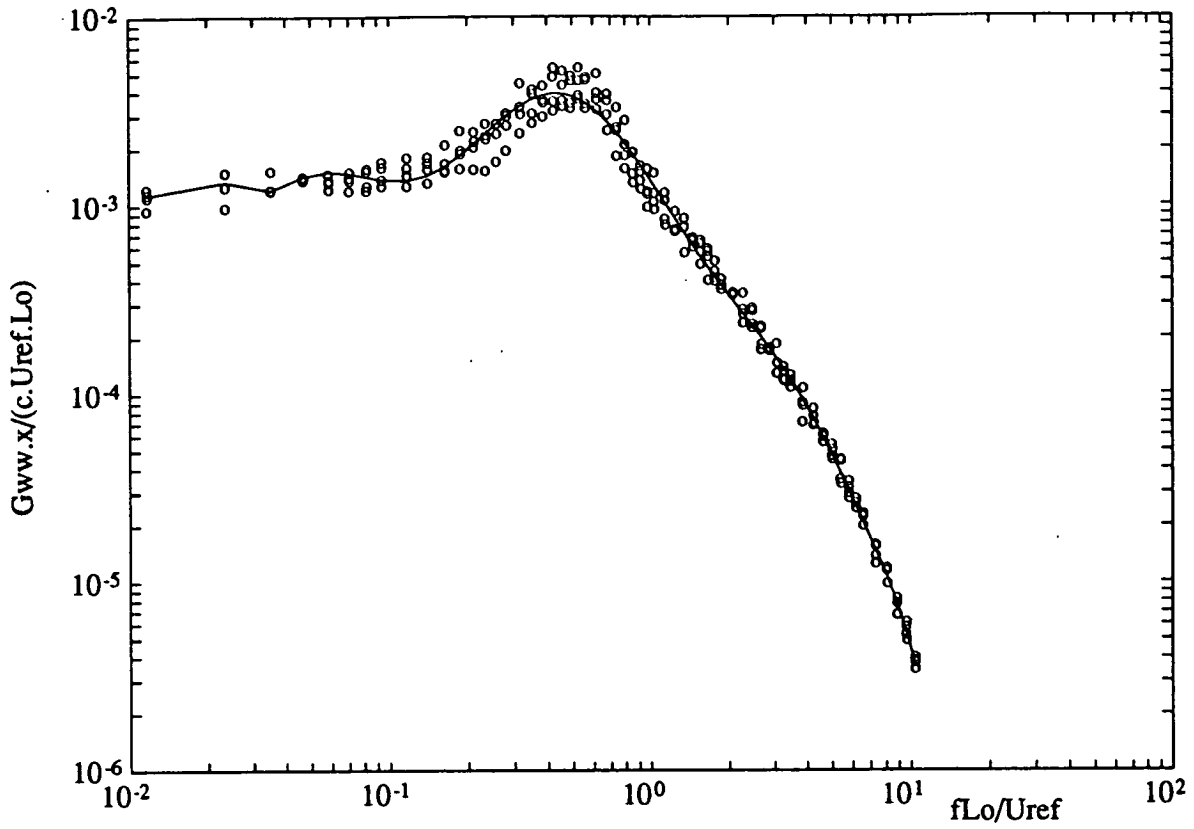


Figure 3.6: Wake region spectrum for an isolated vortex and least squares fit to the data



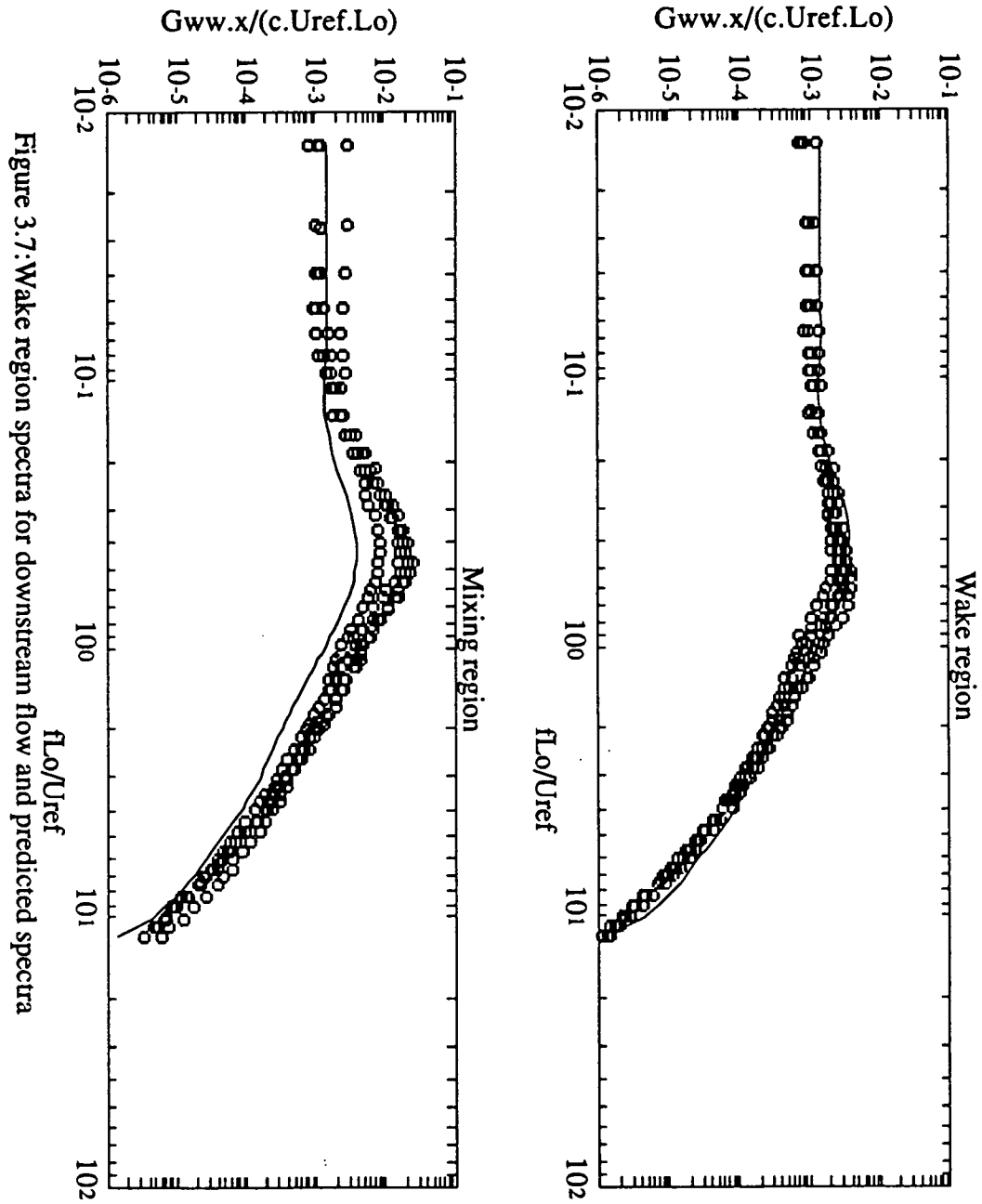
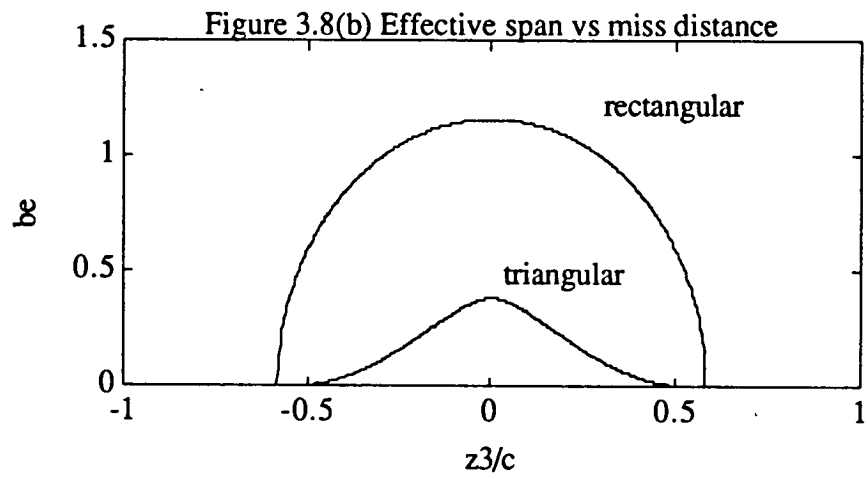
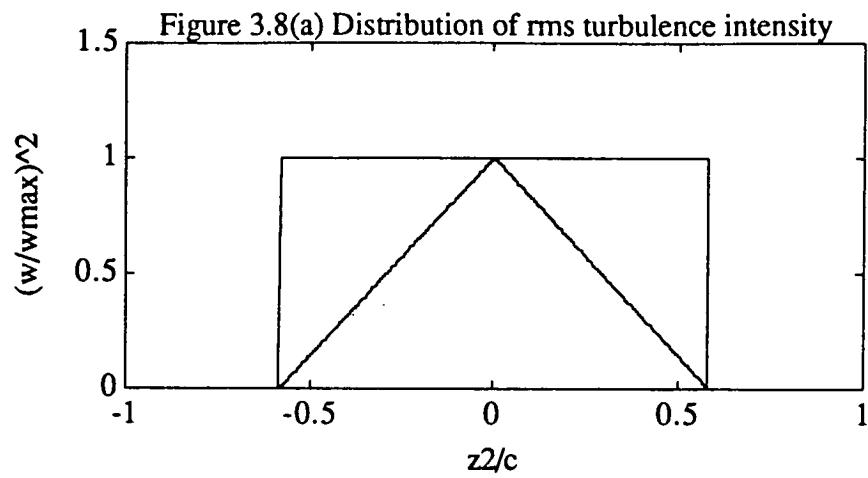


Figure 3.7: Wake region spectra for downstream flow and predicted spectra



#### 4. COMPARISON OF MEASUREMENTS WITH PREDICTIONS

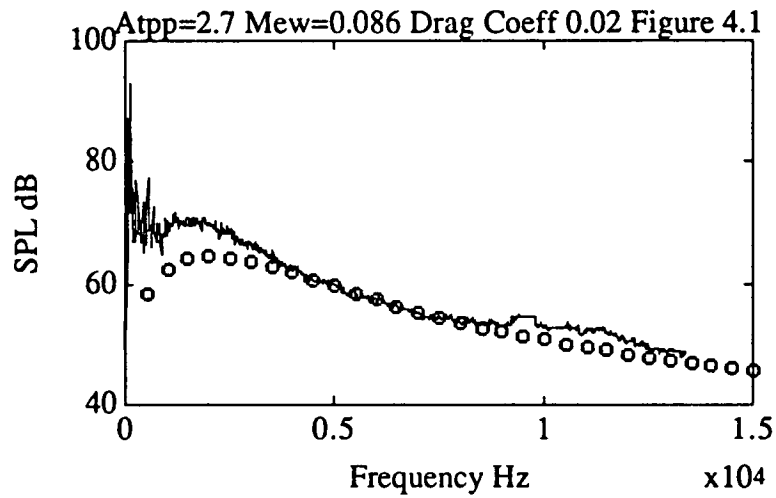
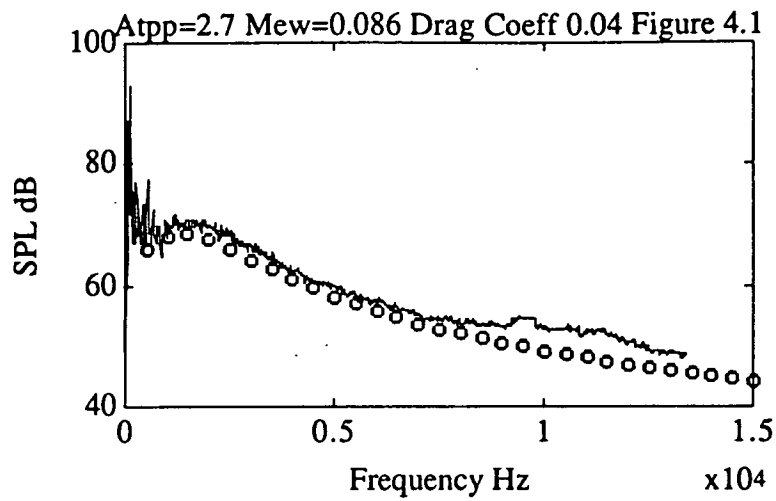
The noise prediction method described in the previous section has been compared with the data collected in the DNW anechoic wind by Brooks et al (1989). This data set comprises of 21 different flight conditions (including 3 different advance ratios and ~ 7-10 different tip path plane angles) and gives noise spectra at two different angles to the rotor axis in the acoustic far field. The predictions given are based on the theory described in the previous section using the blade design parameters as inputs (see Glegg (1991)). However the blade lift and drag coefficients are not known exactly and have to be estimated. The blade lift coefficient is required to estimate the vortex core size and in the previous study the lift coefficient was estimated from the rotor thrust coefficient as  $a_o = \beta R_t \sqrt{(\pi \psi_w C_T B)}$  where  $R_t$  is the rotor diameter,  $C_T$  is the thrust coefficient,  $\psi_w$  is the wake age, and  $B$  is the number of blades. The coefficient  $\beta$  is  $\sim O(1)$  and was evaluated to give the best fit to the noise measurements as  $\beta=0.8$  for the effective span given by equation (9). In this study the effective span is based on equation (8) and the data is matched better by using a value of  $\beta=0.5$ . The blade drag coefficient is required to determine the momentum thickness of the wake, but this is also not known, and may change with flight condition. To show the importance of this parameter predictions have been made using drag coefficients of  $C_d=0.04$  and  $C_d=0.02$  for a sample set of the data at three different advance ratios and two different tip path plane angles, as shown in figures 4.1 to 4.6. These results show three important features of the prediction method. At the lowest advance ratio a good fit to the data is obtained using a drag coefficient of 0.04, but at the higher advance ratio of 0.174 the spectral shape is predicted more accurately by using a smaller drag coefficient. This suggests that the drag coefficient a function of flight speed and is reduced as the advance ratio increases, as might be expected. At the highest advance ratio (figures 4.5 and 4.6) the scaling of the predicted spectrum with changes in tip path plane angle is not good and this is attributed to the

calculation of the vortex loci for this case, which has always been found to be inaccurate at high advance ratios.

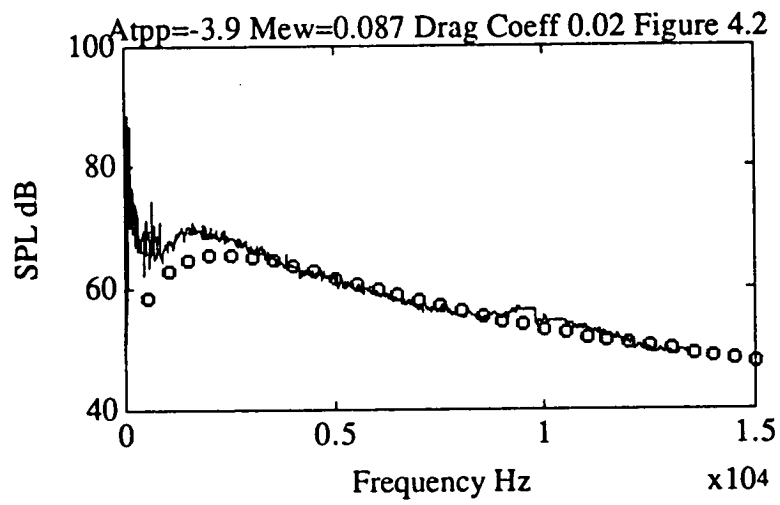
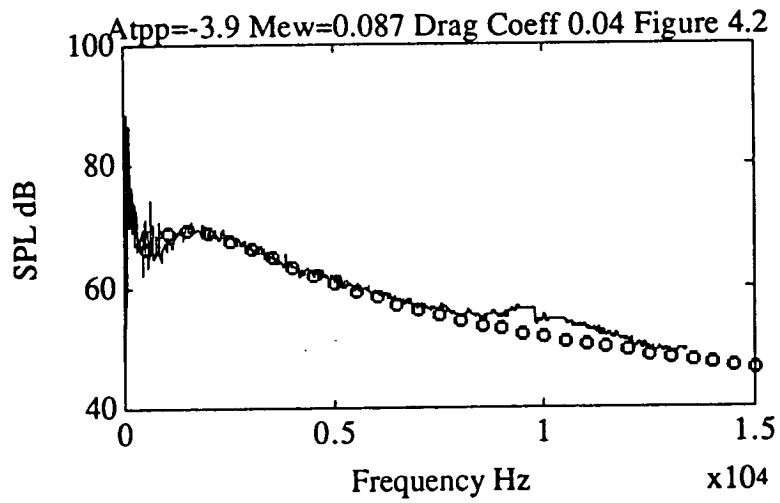
To give an overall view of the results a complete set of spectra and comparisons with the predictions are shown in figures 4.7-4.28 for two different microphone locations using a drag coefficient of  $0.04$ . (microphone 19 is at  $1.5^\circ$  and microphone 21 is at  $27.7^\circ$  to the rotor axis). In general the predictions shown here compare well with the data, and some marked improvements over the previous prediction method (Glegg(1991)) are apparent. In the previous study the spectral peak in the measurements at low frequencies (see for example figure 4.10 or figure 4.18) could not be identified in the predicted spectra which were based on the Von Karman interpolation formula. The new predictions given here clearly identify a spectral peak, which can be associated with a spectral peak in the turbulence spectrum (see figure 3.3). However as noted above, the best prediction of this peak at the advance ratio of  $0.174$  (see figures 4.18 and 4.4) is obtained with a smaller drag coefficient.

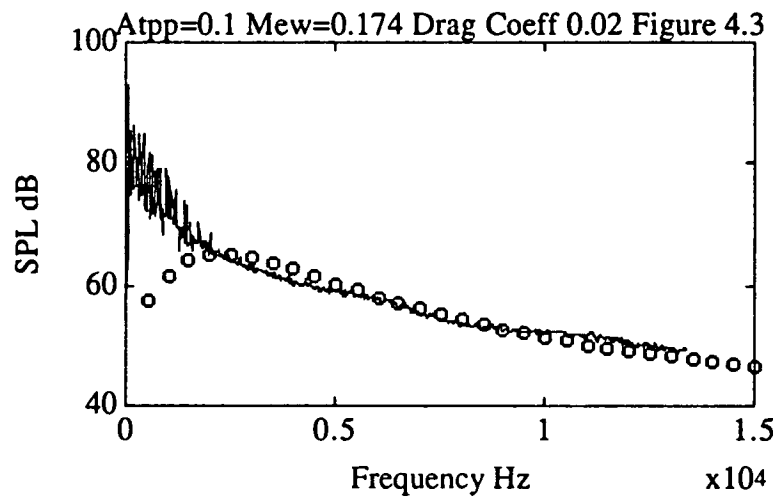
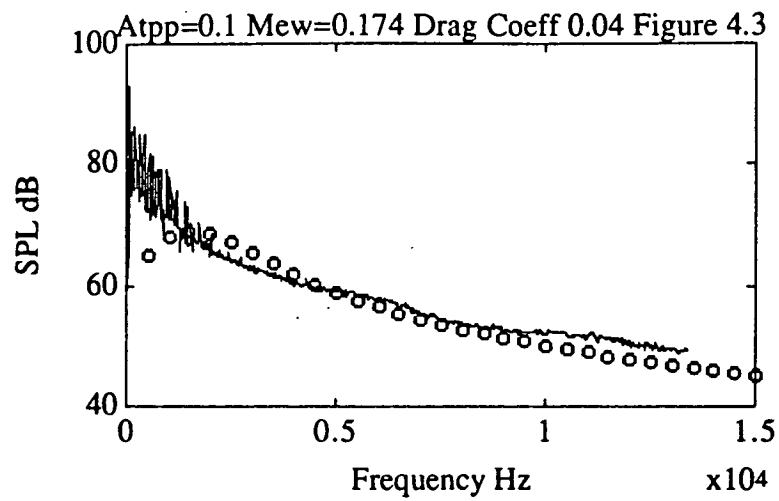
We conclude that by using the measured turbulence spectrum in the prediction method rather than assuming a spectrum given by the Karman interpolation formula, a significant improvement to the prediction method has been achieved. However the specification of the blade drag coefficient and the loci of the tip vortices as a function of the flight condition are important features of the prediction scheme and the method used here to obtain these appears, at present to be the limiting factor in improving the prediction of BVI noise. Further, but of less significance is the estimates which were made of the spanwise coherence lengthscale. The assumptions concerning this parameter affect the spectral shape and may warrant further investigation in the future.

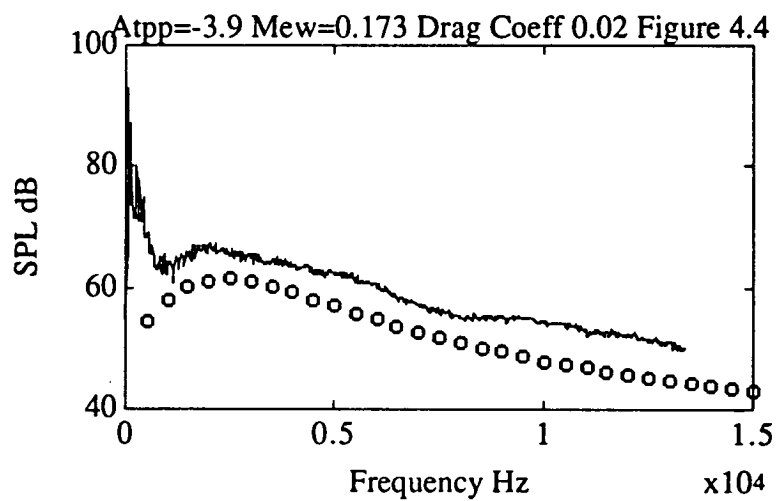
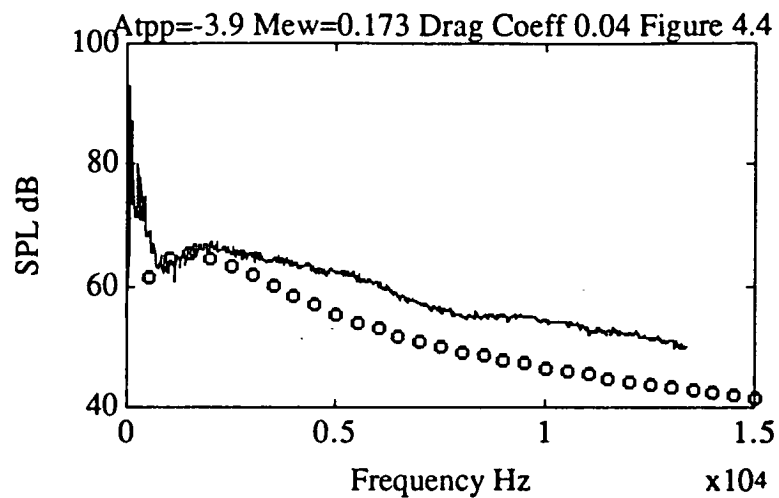




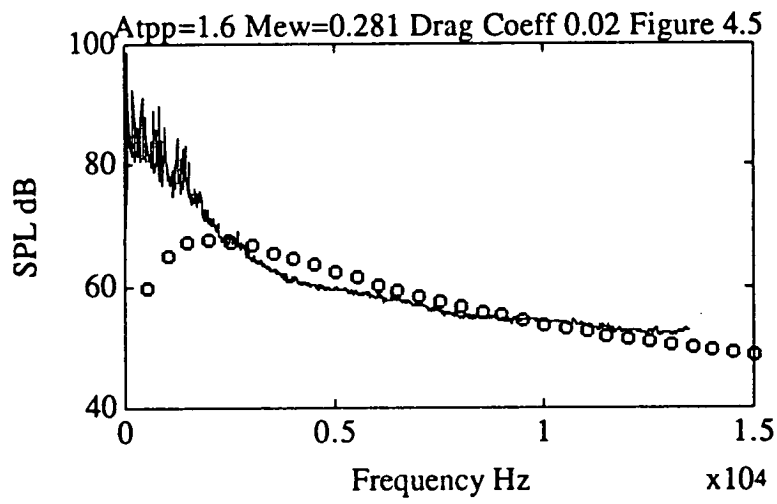
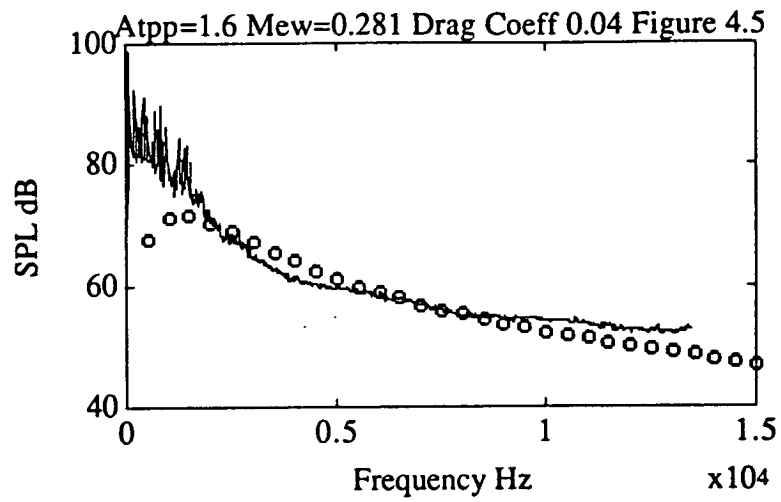
## Perpendicular BVI Part II

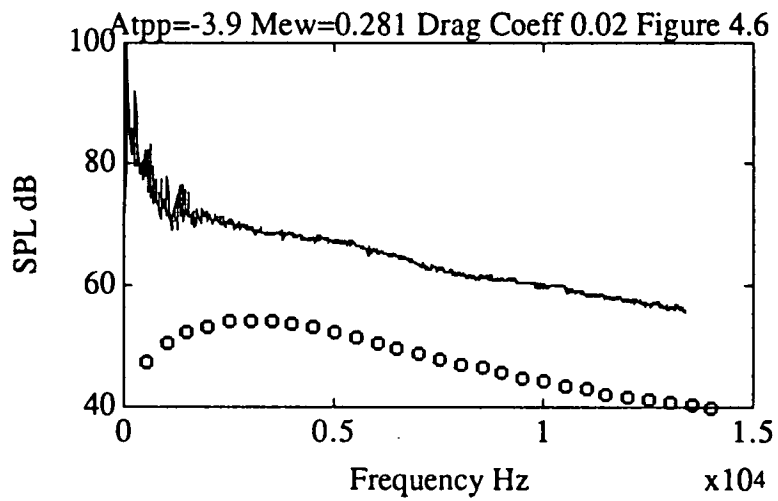
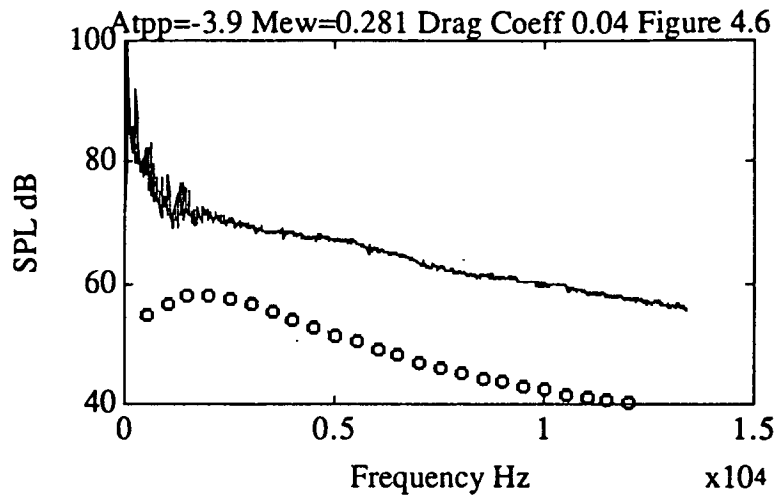


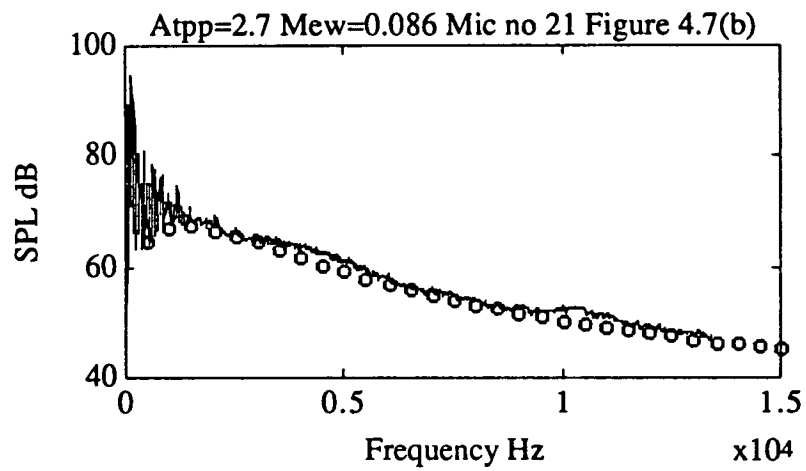
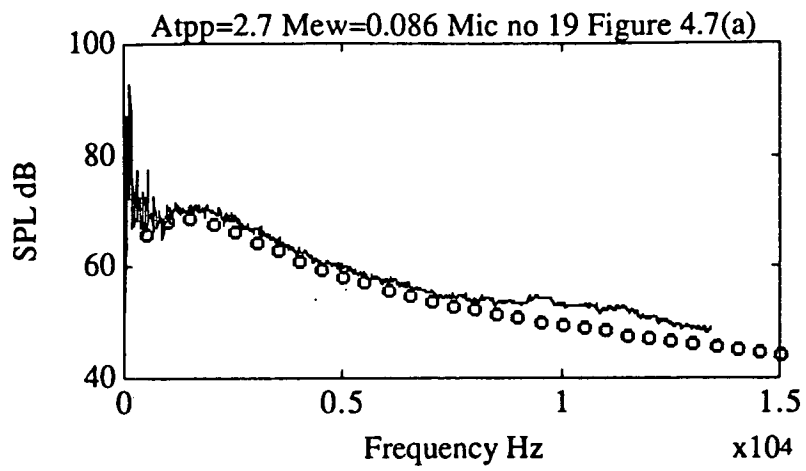


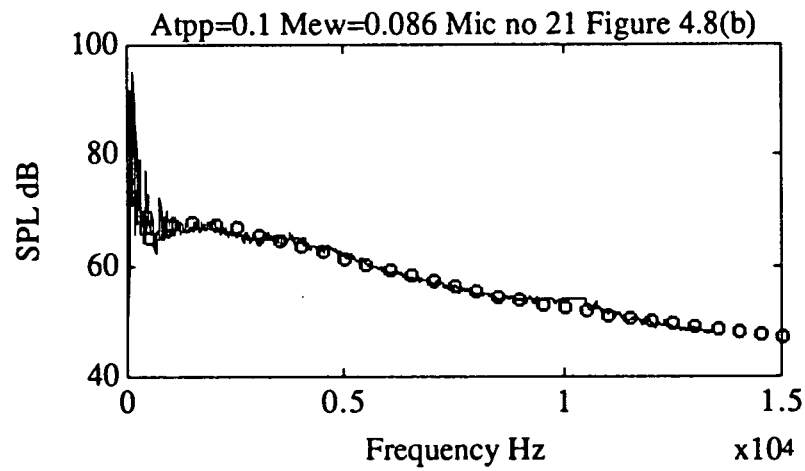
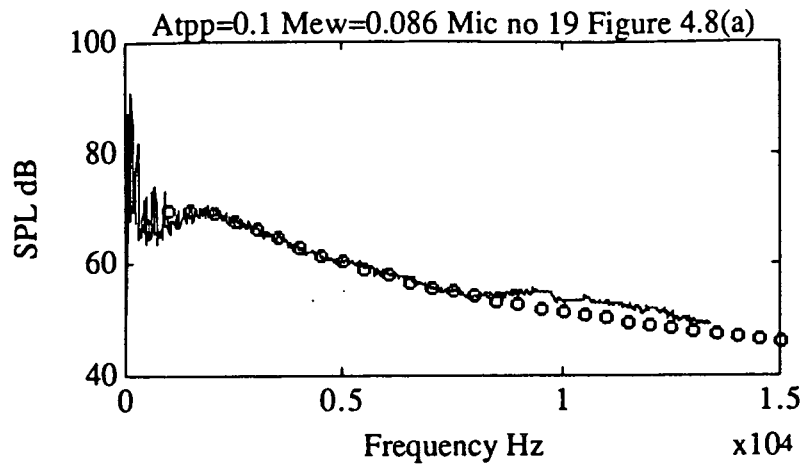




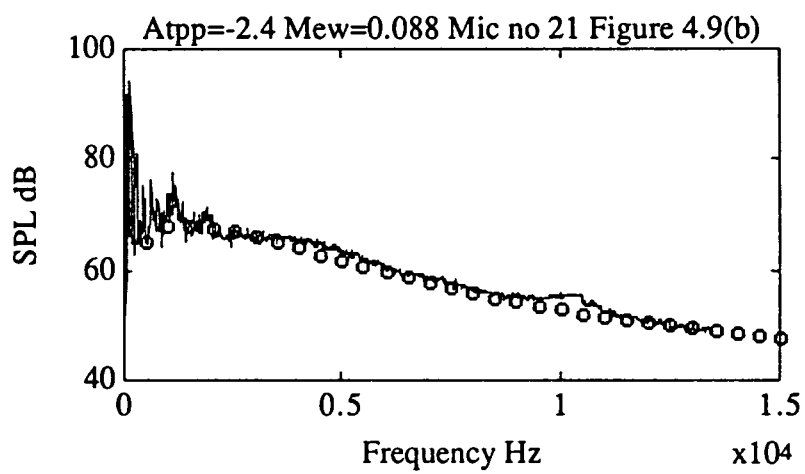
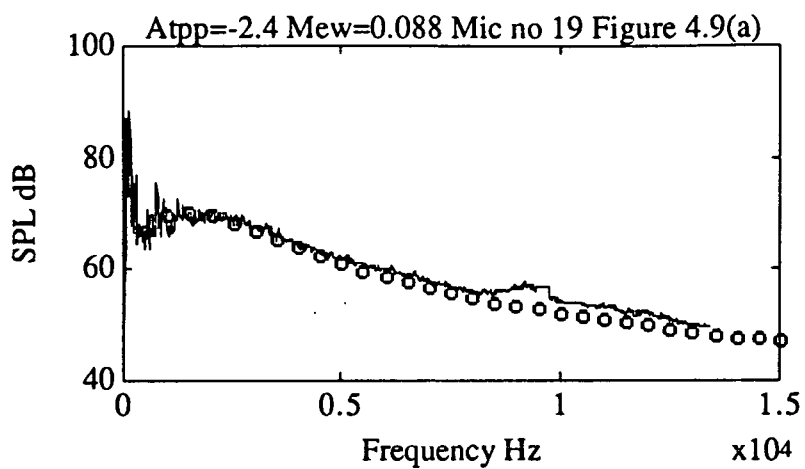


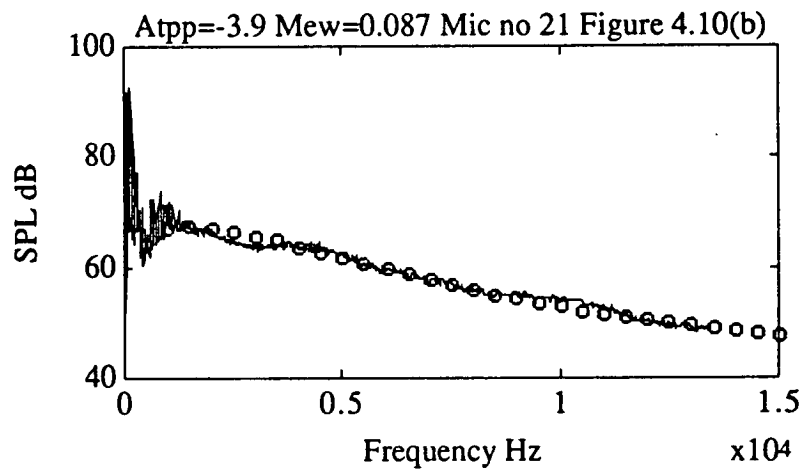
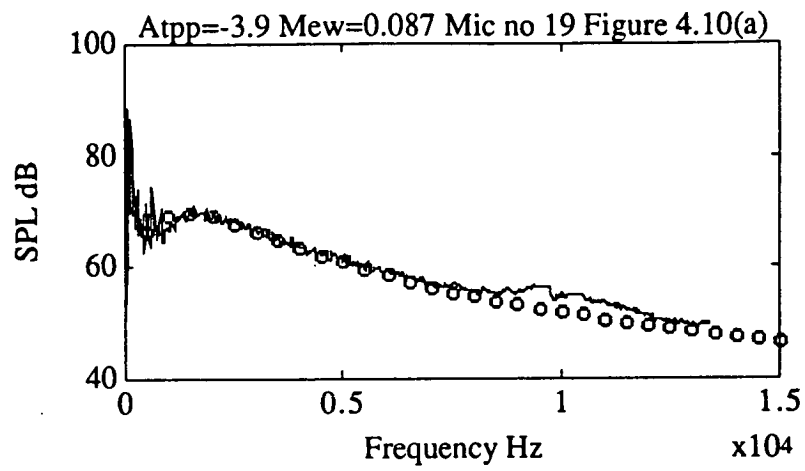


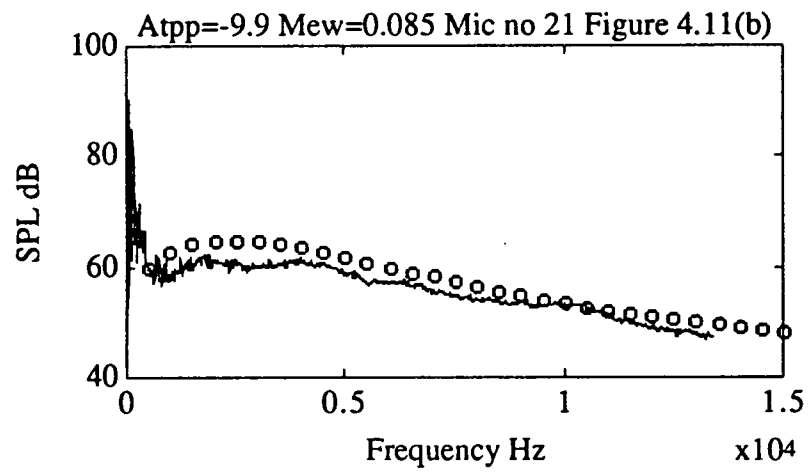
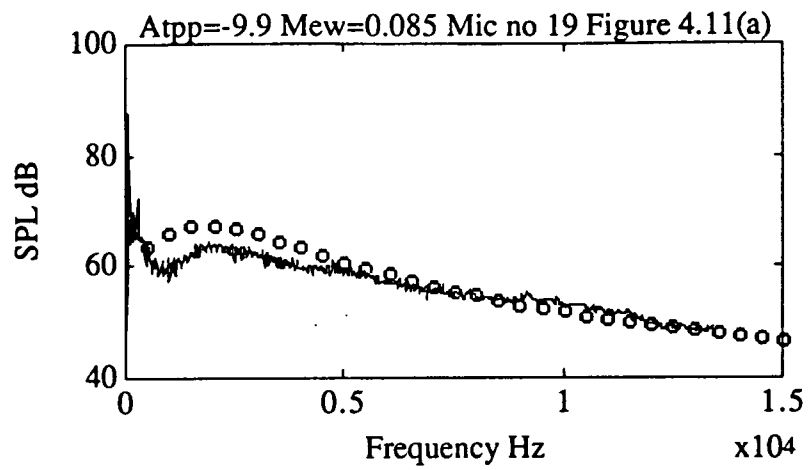


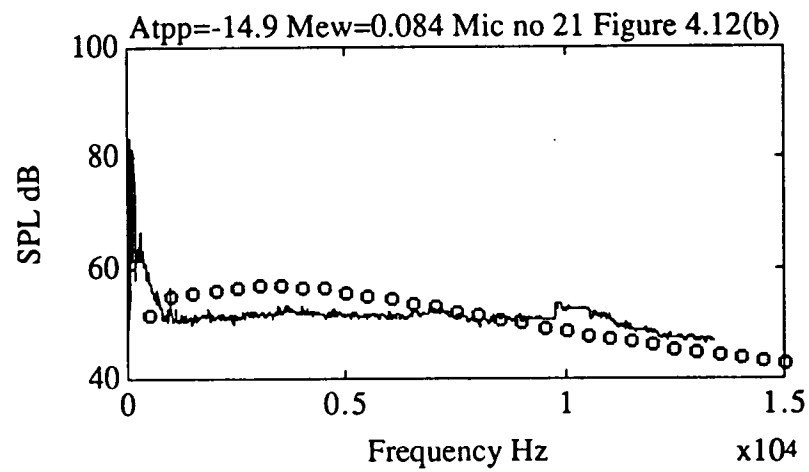
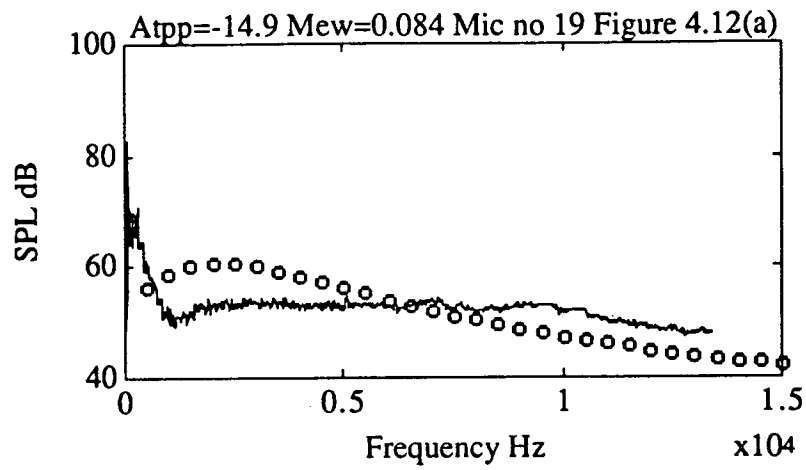




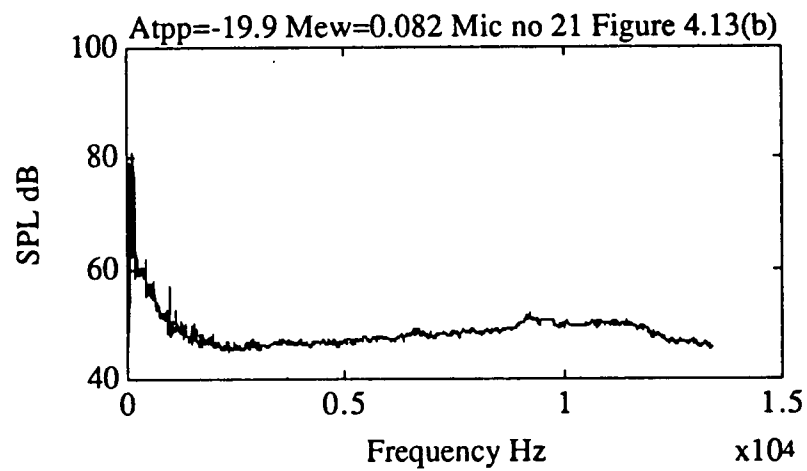
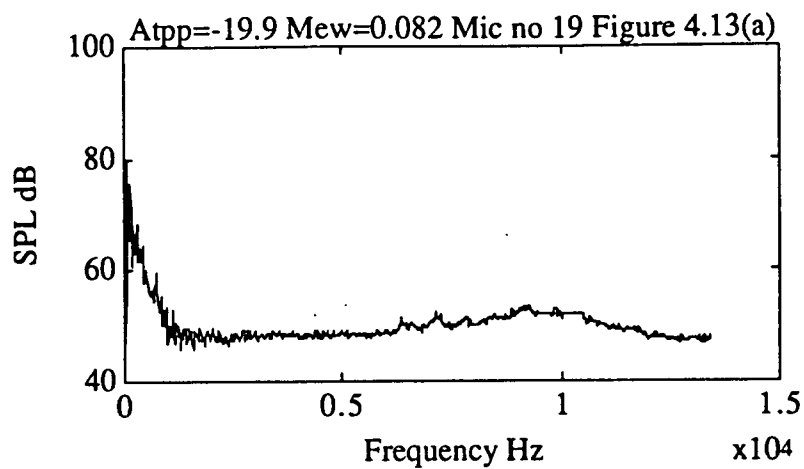


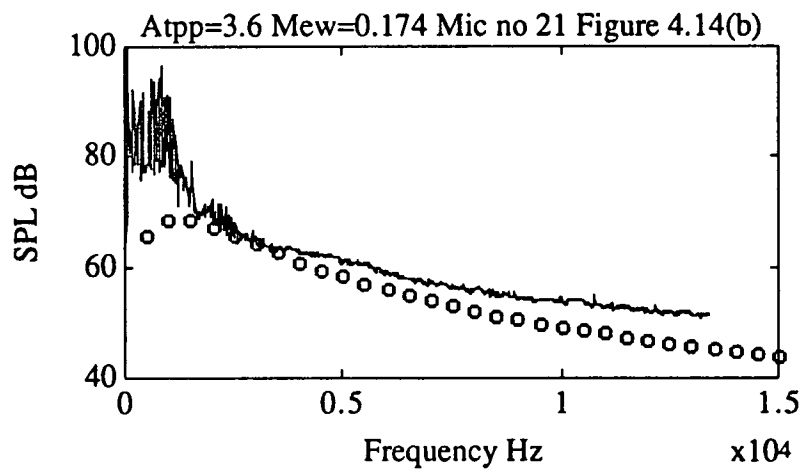
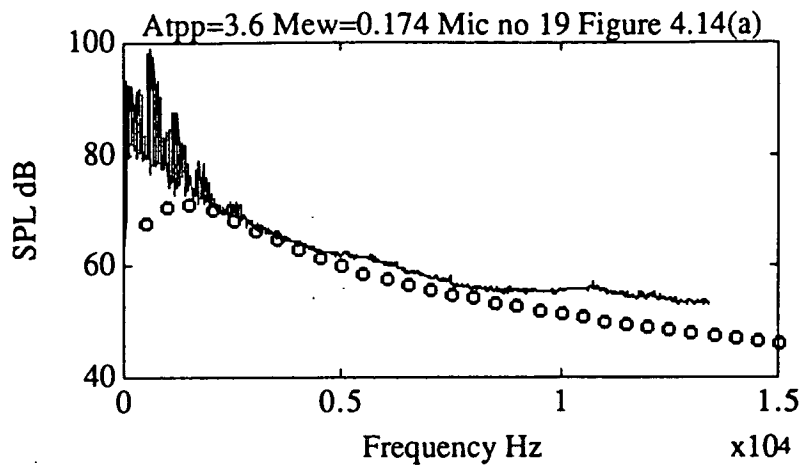


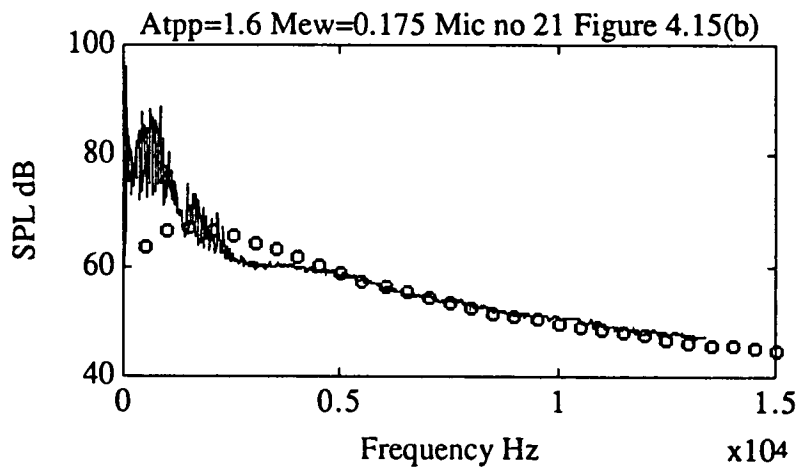
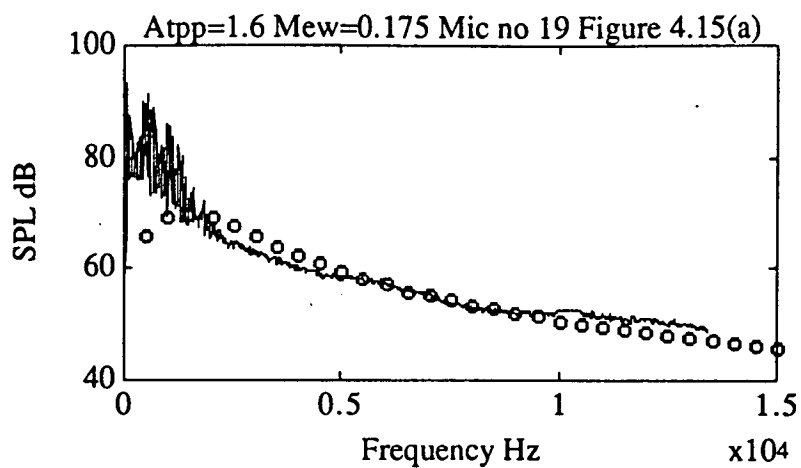


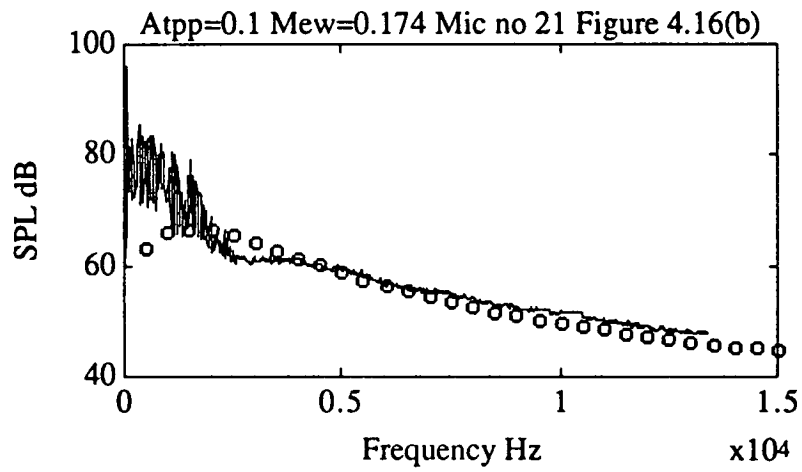
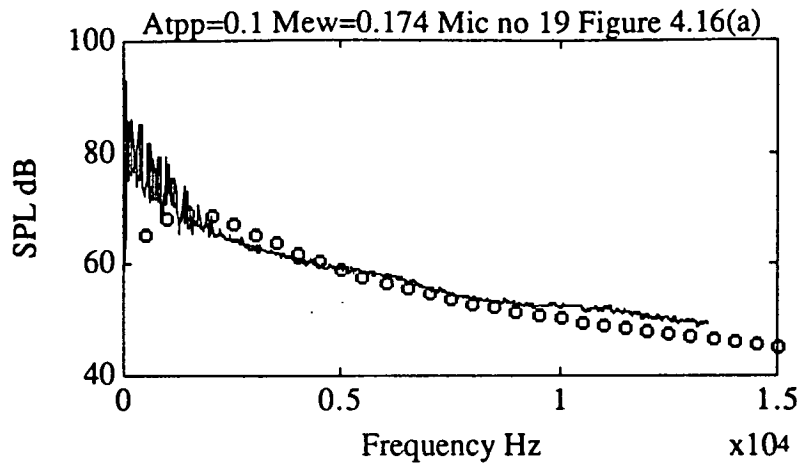




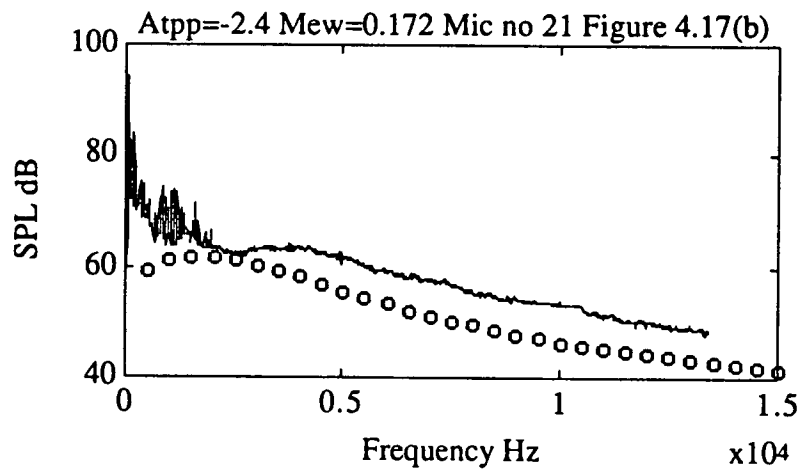
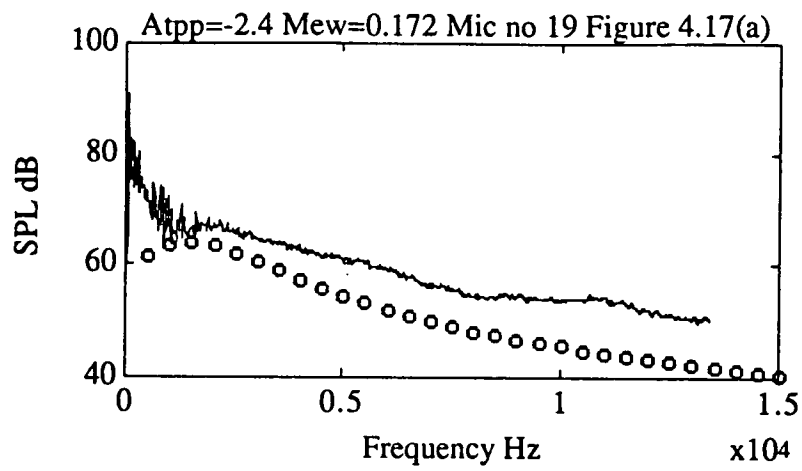


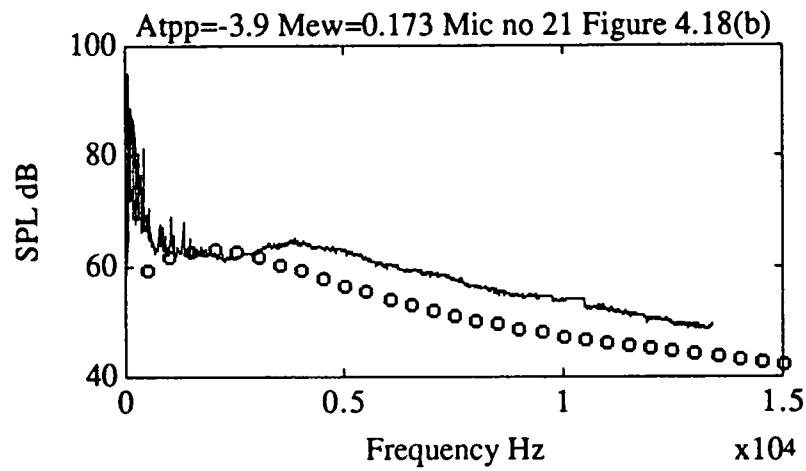
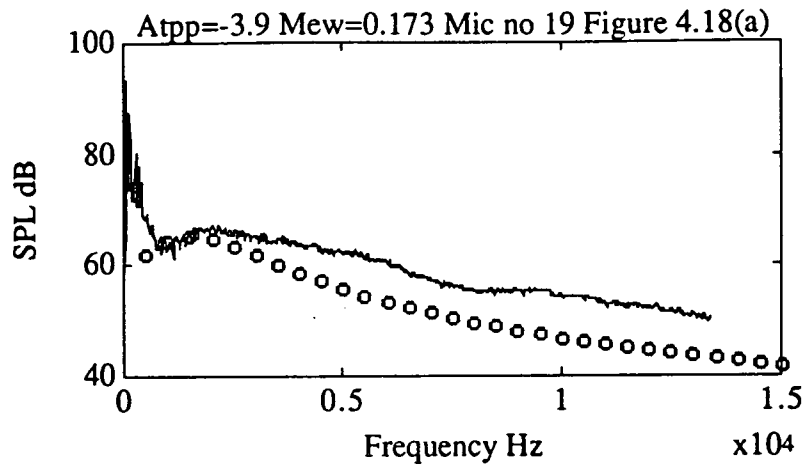


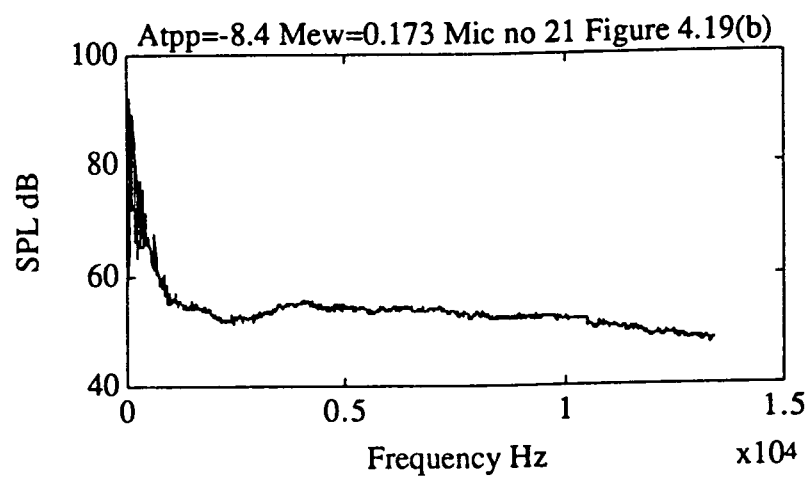
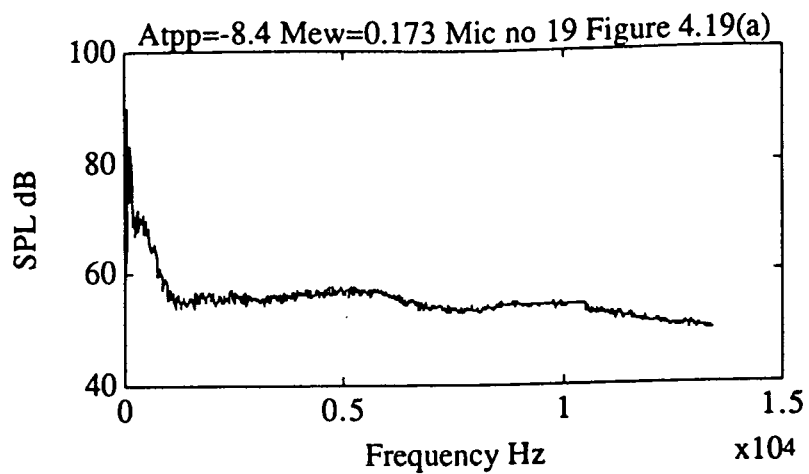


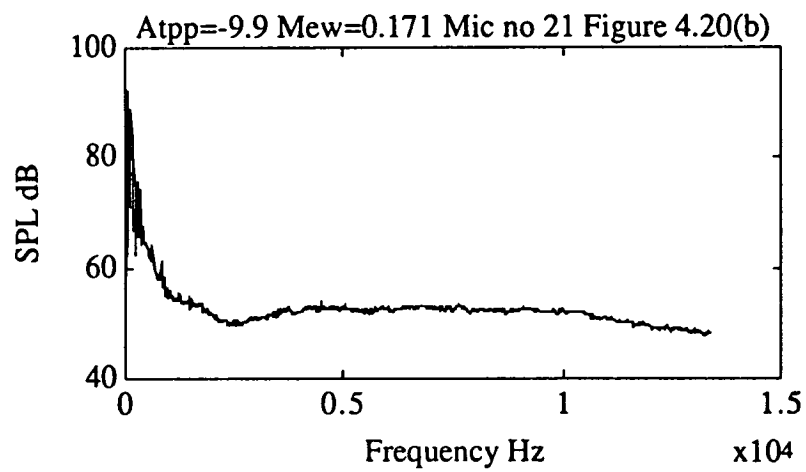
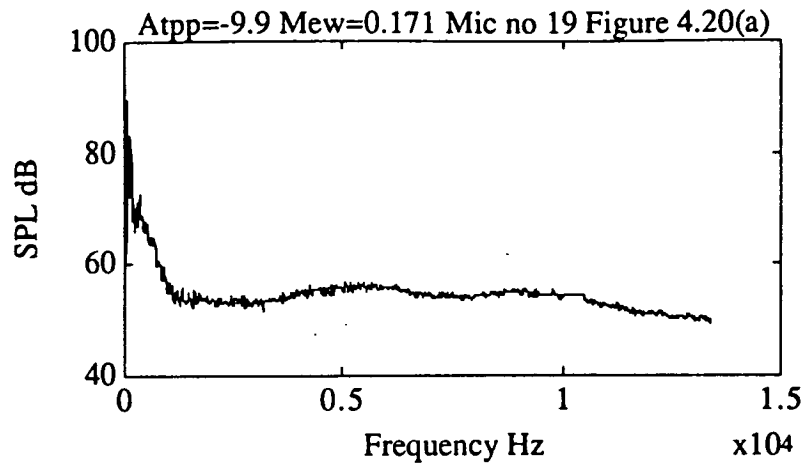




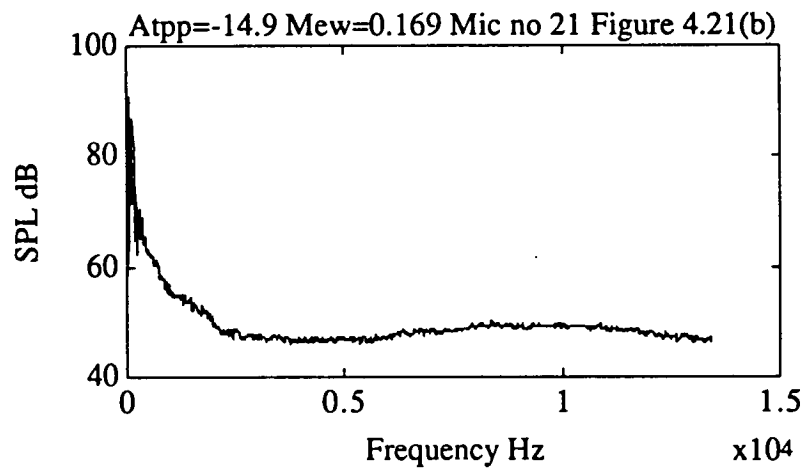
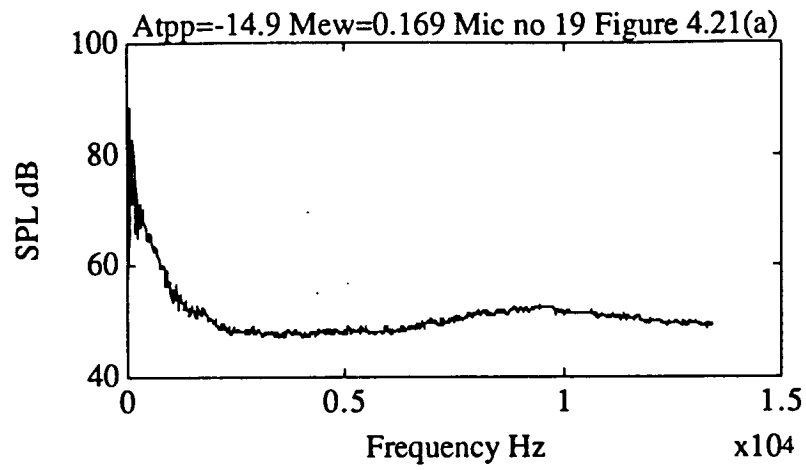


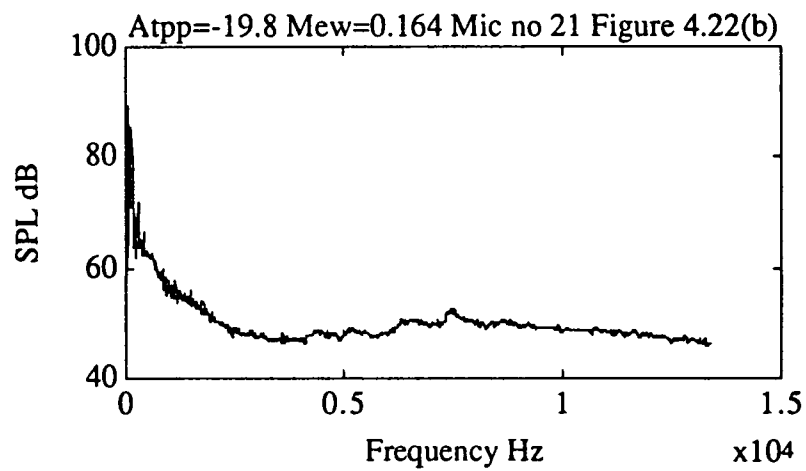
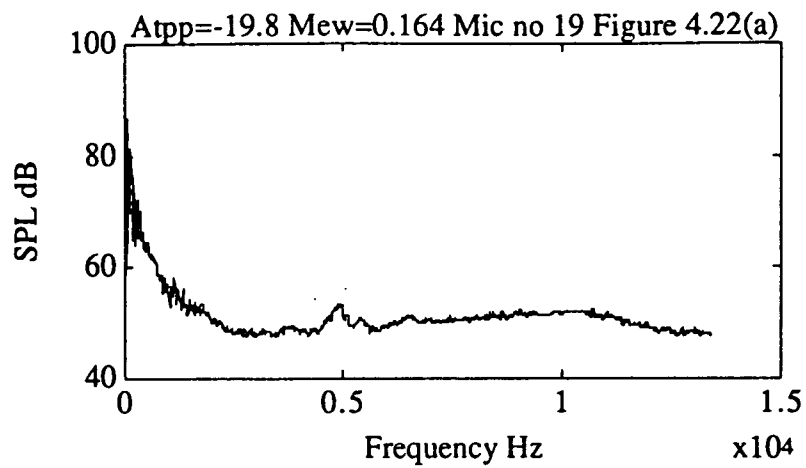


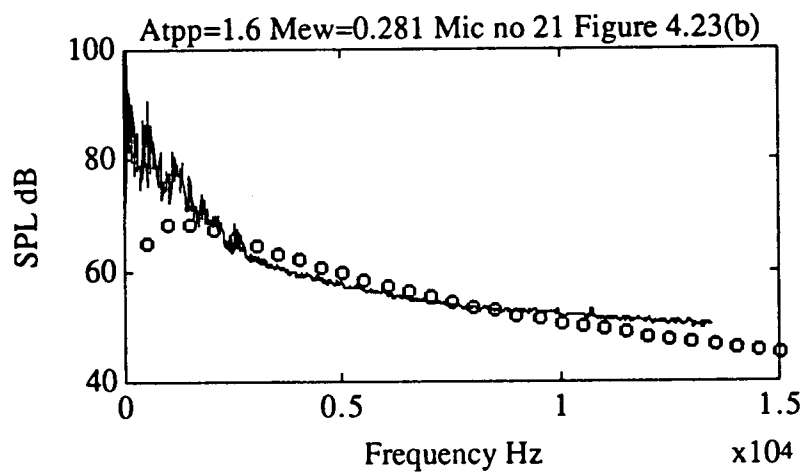
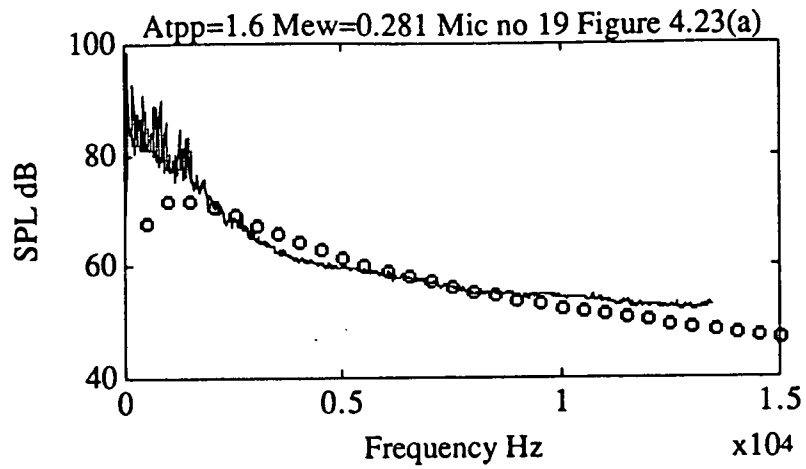


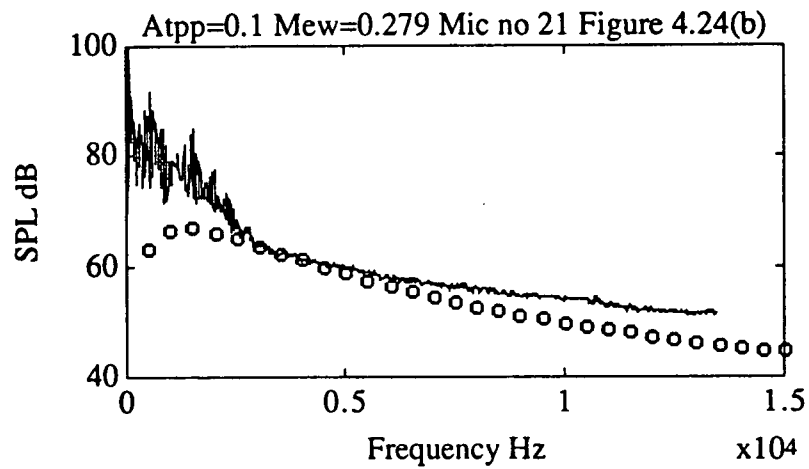
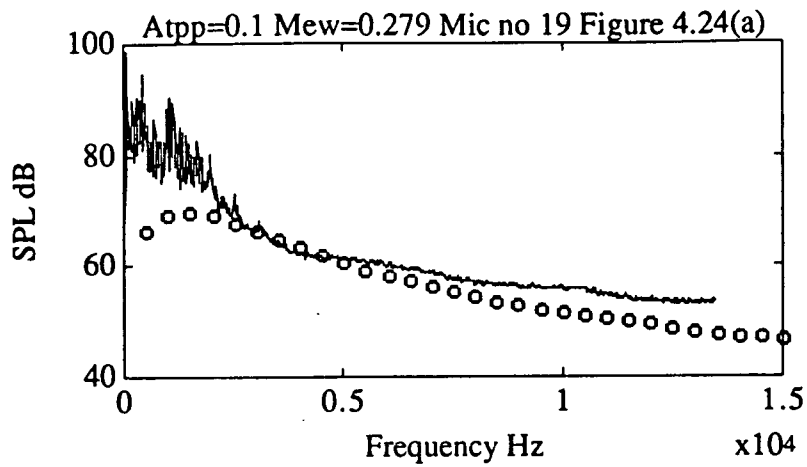




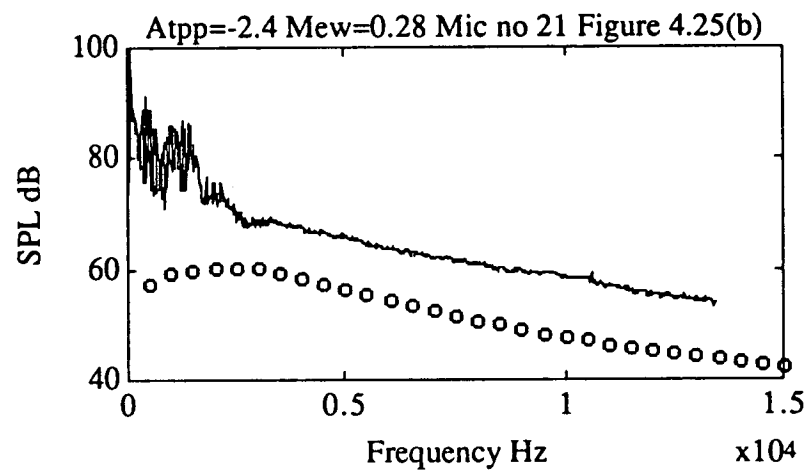
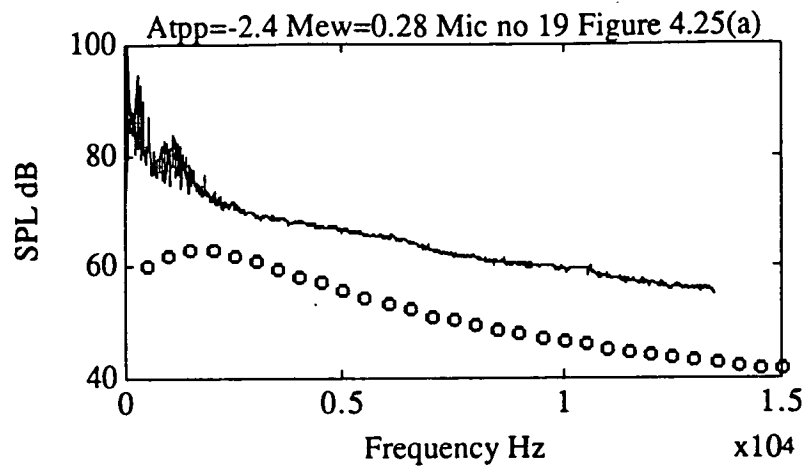


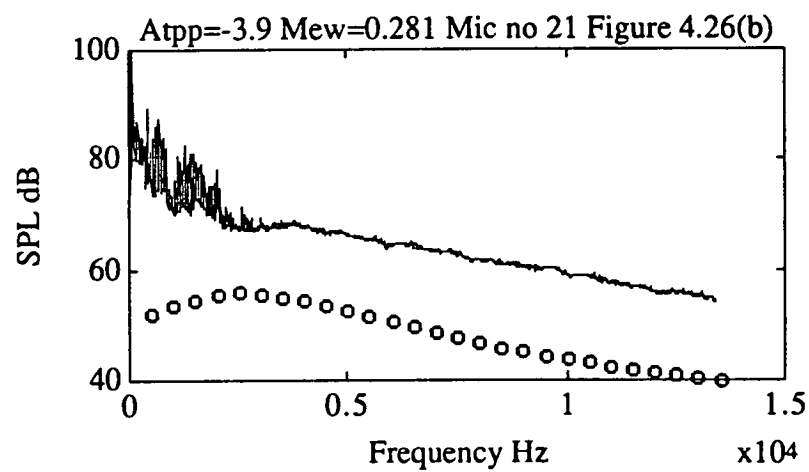
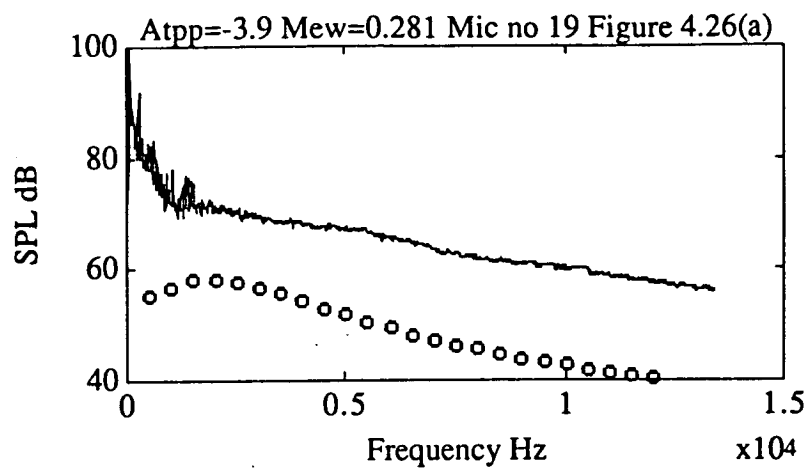


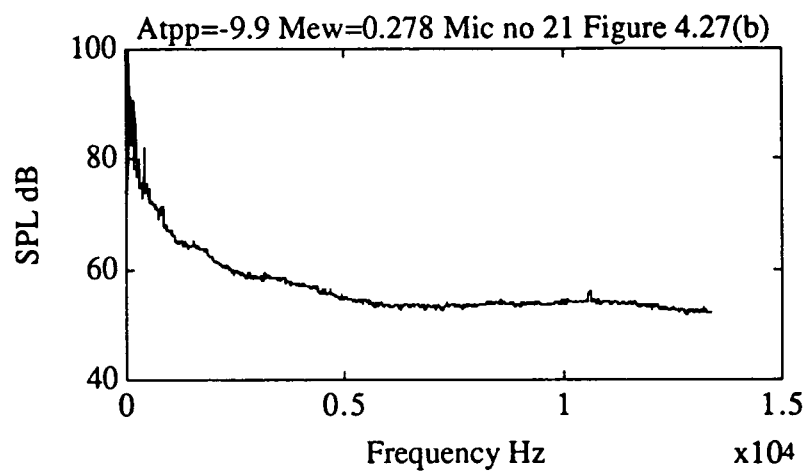
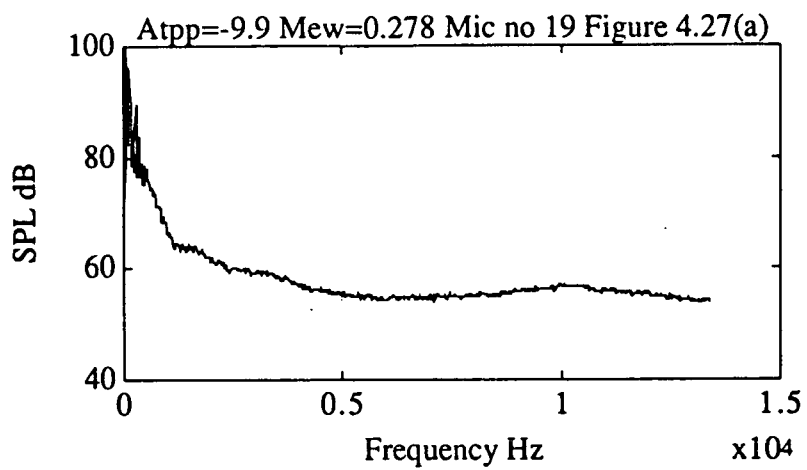












REFERENCES

- Amiet R., 1975, "Acoustic radiation from an airfoil in a turbulent stream", *Journal of Sound and Vibration*, Vol 41, pp 407-420
- Bradshaw P., 1967, "Inactive motion and pressure fluctuations in turbulent boundary layers", *J. Fluid Mechanics*, Vol 30, Pt 2, pp 241-258
- Brooks et al , T.F., Marcolini, M.A., and Pope D.S., 1987, "Main Rotor Broadband Noise Study in the DNW", Presented at the AHS Specialist meeting on Aerodynamics and Aeroacoustics, Arlington, Texas.
- Egolf T.A. and Landgrebe A.J. ,1983, "Helicopter Rotor Wake Geometry and its Influence in Forward Flight" NASA Contract Report 3726 and 3727
- Glegg S.A.L., 1991, "Prediction of blade-wake interaction noise based on a turbulent vortex model", *AIAA Jnl.* Vol 29(10), pp1545-1551.
- Howe M.S., 1988, "Contributions to the theory of sound production by vortex-airfoil interaction, with application to vortices with finite axial velocity deficit", *Proc. R. Soc. Lond.* A420, 157-182.
- Hinze J.O.,1975, "Turbulence", 2nd edition, McGraw Hill Inc., New York.
- Phillips W R C and Graham J A H, 1984, "Reynolds stress measurements in a turbulent trailing vortex", *Journal of Fluid Mechanics*, vol 147, p 353.
- Schlinker R.H. and Amiet R. K.,(1983), "Rotor-Vortex Interaction Noise", AIAA 83-0720, Presented at the 8th AIAA Aeroacoustics Conference, Atlanta, Georgia
- Wynnanski I., Champagne F.,and Marasli B., 1986, "On the large-scale structures in two-dimensional, small-deficit, turbulent wakes", *Journal of Fluid Mechanics* vol 168, pp31-71